TRAIN AERODYNAMICS

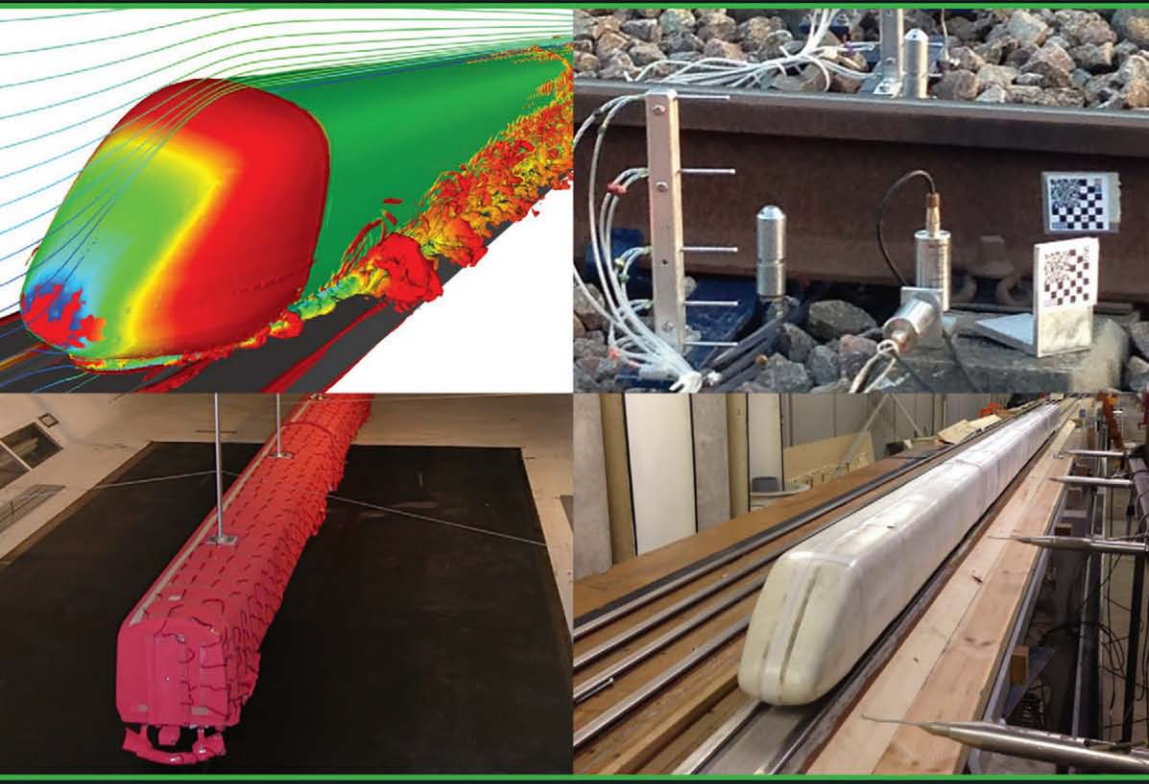

Fundamentals and Applications

Chris Baker | Terry Johnson
Dominic Flynn | Hassan Hemida | Andrew Quinn
David Soper and Mark Sterling

B H

TRAIN AERODYNAMICS

Fundamentals and Applications

CHRIS BAKER

TERRY JOHNSON

DOMINIC FLYNN

HASSAN HEMIDA

ANDREW QUINN

DAVID SOPER

MARK STERLING

Butterworth-Heinemann
An imprint of Elsevier

Butterworth-Heinemann is an imprint of Elsevier
The Boulevard, Langford Lane, Kidlington, Oxford OX5 1GB, United Kingdom
50 Hampshire Street, 5th Floor, Cambridge, MA 02139, United States

Notices
Knowledge and best practice in this field are constantly changing. As new research and experience broaden our understanding, changes in research methods, professional practices, or medical treatment may become necessary.

Practitioners and researchers must always rely on their own experience and knowledge in evaluating and using any information, methods, compounds, or experiments described herein. In using such information or methods they should be mindful of their own safety and the safety of others, including parties for whom they have a professional responsibility.

To the fullest extent of the law, neither the Publisher nor the authors, contributors, or editors, assume any liability for any injury and/or damage to persons or property as a matter of products liability, negligence or otherwise, or from any use or operation of any methods, products, instructions, or ideas contained in the material herein.

Library of Congress Cataloging-in-Publication Data
A catalog record for this book is available from the Library of Congress

British Library Cataloguing-in-Publication Data
A catalogue record for this book is available from the British Library

ISBN: 978-0-12-813310-1

Publisher: Matthew Deans
Acquisition Editor: Carrie Bolger
Editorial Project Manager: Carrie Bolger
Production Project Manager: Sruthi Satheesh
Cover Designer: Christian Bilbow

Typeset by TNQ Technologies

Preface

Textbooks on aerodynamics are usually concerned with the aerodynamic behaviour of streamlined bodies (e.g., aeroplanes and wings), operating well away from the ground in relatively low turbulence conditions. In such cases, the effects of turbulence are confined to thin regions, or boundary layers, next to the surface of the body. In all these respects, the subject of train aerodynamics is radically different. Even though parts of trains such as the nose may have been designed to be as streamlined as possible, trains are essentially nonstreamlined bluff bodies with large regions of separated flow around them. They operate close to the ground, and so aerodynamic interactions with the ground and with local topography are important. In this region, there are very high levels of ambient turbulence in natural wind conditions, which can have a considerable effect on the nature of the flow around the train. Furthermore, the boundary layers on trains, in which vehicle-induced turbulence is important, are by no means thin, and in places the thickness of such boundary layers can exceed the width of the train. Finally, whilst for aeroplanes, aerodynamic issues primarily affect the aeroplane itself, aerodynamic issues in train operation affect both the train itself and the surrounding environment and trackside infrastructure. Taken together, these effects make the study of the aerodynamics of trains extremely challenging.

In very broad terms, train aerodynamic effects increase in severity with the square of the speed of the train, and historically came to become of concern as the speed of passenger trains increased beyond around 100 km/h. In the first instance, attention was paid to reducing the aerodynamic drag of trains, both to reduce fuel consumption and to enable higher speeds to be achieved. A whole series of other issues rapidly emerged as train speeds of 200 km/h or more became common. The existence of severe pressure transients in tunnels causing considerable passenger discomfort was investigated in both Europe and Japan from the 1960s onwards. The stability of lightweight trains in high winds became an area of concern in the 1970s and has remained so to this day. Incidents involving pantograph dewirement in high winds also became increasingly common around that time. The effects of high wind velocities in train slipstreams on workers at the trackside, on passengers waiting on platforms and, most particularly, on pushchairs holding small children, caused largely by aerodynamically rough freight

trains, also raised concerns. As speeds increased still further to 300 km/h and beyond, not only did these issues became of increasing concern but also a further set became apparent: sonic booms from the exits of railway tunnels, failure of trackside structures such as noise barriers due to fatigue loading by train pressure transients and the lifting of large ballast particles beneath trains causing damage to both trains and track. Today, the range of aerodynamic issues that need to be taken into account in the design process for new trains and new routes is very extensive. Recent reviews of various aspects of train aerodynamics have been published by Schetz (2001), Ragunathan et al. (2002) and Baker (2010a, 2014a, 2014b).

This book will address these issues in a way that is intended to be accessible to a graduate engineer and, through the extensive references that are provided, will enable readers to access the source material and study these issues in greater depth. Before going any further, however, it is necessary to state the basic philosophy that underlies what follows. This is twofold. Firstly, the authors take the view that a proper understanding of the range of practical issues associated with train aerodynamics relies on an understanding of the fundamental nature of the flow field around trains, and secondly that, although physical model tests and computational flow calculations are undoubtedly useful and necessary, this understanding of the nature of the flow must primarily come from consideration of measurements of the highly unsteady and aerodynamically dirty flow around full-scale trains. In what follows, the nature of the flow around trains in various situations is thus discussed in detail before moving on to practical applications, and, wherever possible, experimental data obtained at full scale are given priority in this discussion.

Throughout this book, we will consider the flow around a number of different types of train. We will classify these as follows:

- High-speed passenger trains with maximum speeds between 250 and 350 km/h, and usually with streamlined noses. These trains usually operate as fixed formation multiple unit configurations, which sometimes run as double units with a discontinuity in the train geometry between them.
- Medium-speed passenger trains with maximum speeds of 175—250 km/h, consisting either of multiple units with a variety of different types of nose, with or without tilt, or formed from a locomotive and trailing carriages.
- Low-speed passenger trains, usually in multiple unit configuration, with maximum speeds of up to 175 km/h, usually with quite blunt noses.

- Freight trains, with maximum speeds around 120 km/h, usually formed of locomotives pulling a wide variety of different types of freight stock.

Other categorisations could have been used, based on aerodynamic properties, but the classification set out above has the virtue of simplicity. Generally, as train speeds increase, they become more streamlined, and generally longer (other than freight trains), and thus the classification does actually reflect aerodynamic behaviour to some degree.

This book itself is divided into two parts. Part 1 addresses a range of fundamental aspects (Chapters 1—6) and Part 2 (Chapters 7—13) considers a number of practical applications. The contents of the individual chapters are as follows:

Chapter 1. The historical context. This gives a brief historical context to the subject of train aerodynamics and how the field has developed over the last two centuries.

Chapter 2. Fluid mechanics concepts. This chapter sets out a number of fundamental fluid mechanics concepts that will be drawn on in the chapters that follow, at the level of graduate engineers with some fluid mechanics background.

Chapter 3. Testing techniques. This chapter provides introductions to full-scale testing and to physical model testing with wind tunnels and moving model rigs. Data processing is also discussed.

Chapter 4. Computational techniques. This chapter presents the basics of computational fluid dynamics as applied to train aerodynamics, and also to a range of optimisation techniques.

Chapter 5. The flow around trains in the open air. This chapter gives a description of the flow around trains in the open air with and without crosswind. The flow in different regions around the train is described in some detail, mainly drawing on a range of full-scale data.

Chapter 6. Trains in tunnels. This chapter discusses the special case of the flow around trains in tunnels, in particular considering the transient pressure waves created by the passing of trains through tunnels.

Chapter 7. Aerodynamic drag. This chapter describes methods for measuring and predicting train aerodynamic drag, presents a collation of drag data from a wide variety of trains and discusses methods of drag alleviation.

Chapter 8. Aerodynamic loads on trackside structures, passing trains and people. This chapter discusses both pressure loading and velocity (slipstream) loading caused by trains, presents methods for load measurement and prediction and considers how these loads can then be applied in the design and risk analysis process.

Chapter 9. Ballast movement beneath trains. This chapter considers the various mechanisms that cause ballast to move under trains, both aerodynamic and otherwise, and discusses the initiation of motion, ballast rolling and ballast flight. Applications to train authorisation and route risk analysis are also discussed.

Chapter 10. Aerodynamic effects on pantographs and overhead wire systems. This chapter describes the nature of the overhead line and pantograph system and considers methods for measuring and calculating the various aerodynamic loads within the system.

Chapter 11. Train overturning in high winds. This chapter describes the determination of the crosswind forces and moments on trains, the specification of the natural wind and calculation of the accident wind speed. The issues involved in train authorisation and route risk assessment are discussed, together with mitigation methods.

Chapter 12. Tunnel aerodynamic issues. This chapter considers a range of practical issues that arise when trains pass through tunnels — the effects of pressure waves on the ears, sonic booms at the outlet of long tunnels on high-speed lines, aerodynamic drag in tunnels, structural loading and specific problems associated with very long tunnels.

Chapter 13. Emerging issues. This chapter presents short introductions to a range of issues that may come to be of significant importance in the future.

References. A comprehensive reference list is provided. Most items have internet links that will take the reader to an electronic version of the item. However, the reader will require the appropriate permissions from the publishers to access the full copies of journal items in particular. In addition, for many items, the links are to the RSSB SPARK database and full access will require registration. Although the authors have tried to make the list as comprehensive as possible, it is inevitable that some potentially relevant papers have not been included, particularly where these are not easily accessed electronically.

Appendix 1. Train details for most of the different train types that are mentioned in the text, and in particular the nose shapes of those trains, using the categorisation described above.

Appendix 2. A collation of the very many journal and conference papers that present force and moment data for trains in crosswinds.

Two other points should be noted. Firstly, this book does not consider the application of aeroacoustics to train aerodynamics. This is a specialist subject in its own right with a large literature. This is well summarised

in Thompson (2008), to which interested readers are referred. Secondly, the material in this book inevitably, given the sphere of experience of the authors, has a British and European emphasis. Nonetheless, as the issues it addresses are common to all areas of the world, all that is included has a much wider geographical application.

Finally, it is necessary to give a note of explanation for non-British readers. In what follows, we will always refer to Great Britain or Britain, rather than the United Kingdom (UK). The full name for the UK is of course the United Kingdom of Great Britain and Northern Ireland. The railway administrations in Great Britain and in Northern Ireland are, however, quite distinct, and we will only be referring to the former in this book.

Acknowledgements

The first two authors have each been working in the field of train aerodynamics for over 40 years, whilst employed by a number of organisations. However, they both began their careers in the Aerodynamics Section of the British Rail Research Division in Derby, England. They would like to acknowledge the help and advice that they have received from colleagues in the Section over the years and in particular from Roger Gawthorpe and Clive Pope, the former being the head of the Section from 1970 to 1996, and under whose leadership much innovative and ground-breaking work was carried out. This book also draws on the results of a number of UK industry, Engineering and Physical Sciences Research Council and EU-funded research projects. The contributions to these investigations from a large number of research students and research fellows at the Universities of Nottingham and Birmingham and from colleagues from a number of other universities, railway administrations and railway companies in the United Kingdom and across Europe are gratefully acknowledged.

Notation

a	Parameter in Davis equation (N)
a_B	Ballast acceleration (m/s^2)
a_T	Train deceleration (m/s^2)
A	Reference area of train (m^2)
A_B	Ballast area (m^2)
A_{eq}	Equivalent leakage area (m^2)
A_{TU}	Tunnel area (m^2)
b	Parameter in Davis equation (Nsm^{-1})
b_1	Parameter in Davis equation (Nsm^{-1})
b_2	Parameter in Davis equation (Nsm^{-1})
B	Train cross-sectional area to tunnel cross-sectional blockage ratio
c	Parameter in Davis equation (Ns^{2}m^{-2})
c_a	Speed of sound in air (ms^{-1})
C_D	Drag coefficient
C_{DB}	Ballast drag coefficient
C_{DBO}	Drag coefficient of bogies
C_{DNT}	Drag coefficient of train nose and tail
C_{DW}	Contact wire drag coefficient
$C_D(\psi)$	Drag coefficient at yaw angle ψ
$C_{Df}(\psi)$	Drag coefficient increment at yaw angle ψ due to increased wheel/rail friction
$C_D(0)$	Drag coefficient at $\psi = 0$
C_f	Friction coefficient
C_{Fi}	Force coefficient in direction i
C_{LB}	Ballast lift force coefficient
C_{LW}	Overhead wire lift coefficient
C_{Mi}	Moment coefficient about axis i
C_{MxL}	Crosswind lee rail rolling moment coefficient
C_p	Pressure coefficient $\frac{p-p_r}{0.5\ \rho v^2}$
C_{p1}	Pressure coefficient on vertical surface
C_{p2}	Pressure coefficient on horizontal surface
C_S	Smagorinsky coefficient
C_{sp}	Specific heat at constant pressure (Jkg^{-1}K^{-1})
C_{sv}	Specific heat at constant volume (Jkg^{-1}K^{-1})
C_{ui}	Air velocity coefficient u_i/v
C_{uiB}	Ballast velocity coefficient u_{iB}/v
C_{uh}	Horizontal air velocity coefficient u_h/v
$C_{uh\ 95}$	95th percentile of horizontal gust velocity coefficient u_{h95}/v
C_{ux0}	Coefficient of velocity close to ballast bed u_{x0}/v
C_{ux2}	Square of air velocity coefficient $(u_x/v)^2$
C_μ	Constant in $k-\varepsilon$ model
d	Dispersion of extreme value distribution (m/s)
d_B	Ballast size (m)
d_W	Contact wire diameter (m)

E	Internal energy (J)
f_a	Admittance factor
f_c	Curvature factor
f_r	Track roughness factor
f_{s1}	Suspension factor − body roll
f_{s2}	Suspension factor − suspended mass movement
f_{s3}	Suspension factor − other effects
$F(\overline{u})$	Cumulative distribution function of mean speed
$F(\widehat{u})$	Cumulative distribution function of wind gust speed
F_{CWP}	Total contact force between a pantograph and the contact wire (N)
F_{HAB}	Horizontal aerodynamic force on ballast (N)
F_{HMB}	Horizontal mechanical force on ballast (N)
F_i	Crosswind aerodynamic force in direction i ($i = x,y,z$) (N)
F_R	Total train resistance (N)
F_{RC}	Train resistance due to track curvature (N)
F_{RG}	Train resistance due to gravity (N)
F_{VAB}	Vertical aerodynamic force on ballast (N)
F_{VMB}	Vertical mechanical force on ballast (N)
F_{VAWP}	Vertical aerodynamic force between pantograph and contact wire (N)
F_{VIWP}	Dynamic inertial force between pantograph and contact wire (N)
F_{VSWP}	Static vertical force between pantograph and contact wire (N)
F_W	Contact wire drag or lift force (N)
g	Acceleration due to gravity (m/s^2)
g_i	Body force per unit mass in Navier−Stokes equations (m/s^2)
G	Gust factor
$G(\overrightarrow{x}, r)$	Large eddy simulation filter function
h	Reference height (m)
h_{Fi}	Weighting function for crosswind force component $i(i = x,y,z)$
h_u	Under body gap height (m)
H	Boundary layer form parameter
H_{Fy}	Longitudinal point of action of side force
H_{Fz}	Longitudinal point of action of lift force (m)
i	Track gradient
I_i	ith component of turbulence intensity $\sigma_{ui} \Big/ \overline{u_x}$ ($i = x,y,z$)
I_R	Turbulence intensity relative to the train
k	Turbulent kinetic energy
k_i	Factor in resistance equations
k_{loss}	Pressure loss coefficient
k_{nose}	Coefficient showing the effect of the train nose
k_R	Factor on mass for rotating masses
k_{sim}	Factor used to correct Δp_{sim}
k_{s1}	Sand grain roughness of track (m)
k_{s2}	Sand grain roughness of train under body (m)
k_{VK}	Von Kármán constant
k_i	Factors used in drag coefficient equations in Chapter 7 ($k = 1$−7)
K	Constant in Eq. (2.13)
K_B	Bulk modulus of air (Pa)

K_1	Factor in Eq. (7.14)
K_2	Factor in Eq. (7.14)
K_{W1}	Factor in Eq. (7.8)
K_{W2}	Factor in Eq. (7.8)
l_i	Integral turbulence length scale (m)
l_K	Kolmogorov dissipation length scale (m)
l_{mix}	Mixing length (m)
l_S	Smagorinsky length scale
L	Train length (m)
L'	Adjusted train length (m)
L_c	Length of container (m)
L_g	Length of gaps between containers (m)
L_i	Length of intercar gap (m)
L_W	Overhead wire length (m)
L_{ui}	Integral length scale of velocity fluctuations ($i = x,y,z$) (m)
L'_{ux}	Integral length scale relative to train (m)
m	Mode of extreme value distribution (ms^{-1})
m_W	Mass per unit length of catenary wire (kgm^{-1})
M	Train mass (kg)
M_B	Ballast stone mass (kg)
M_i	Crosswind aerodynamic moments about axis i ($i = x,y,z$) (Nm)
M_p	Primary suspended mass (kg)
M_s	Secondary suspended mass (kg)
M_{xL}	Crosswind rolling moment about leeward rail (Nm)
Ma	Mach number
n	Frequency (Hz)
n_f	Reynolds number friction exponent
n_g	Characteristic gust frequency in Eq. (11.7) (Hz)
n_W	Natural frequency of catenary wire (Hz)
n_1	Crosswind force coefficient parameterisation constant
n_2	Crosswind force coefficient parameterisation constant
N_B	Number of bogies
N_P	Number of power cars
N_p	Number of pantographs
N_T	Number of trailing cars
P	Pressure (Pa)
p_{ext}	Train external pressure (Pa)
p_{int}	Train internal pressure (Pa)
p_{loss}	Stagnation pressure loss (Pa)
p_{max}	Maximum pressure (Pa)
p_{min}	Minimum pressure (Pa)
p_{MPW}	Peak value of the micropressure wave at a distance r_{MPW} from the tunnel portal (Pa)
p_o	Reference pressure outside tunnel portal (Pa)
p_r	Reference pressure (Pa)
p_1	Pressure on vertical structure (Pa)
p_2	Pressure on horizontal structure (Pa)

$\boldsymbol{P(\bar{u})}$	Extreme value probability of mean wind speed
$\boldsymbol{q}$	Centre of gravity height (m)
$\boldsymbol{Q}$	Heat transfer per unit length of tunnel ($Js^{-1}m^{-1}$)
$\boldsymbol{Q_{ij}}$	Residual stresses
$\boldsymbol{r}$	Radial coordinate (m)
$\boldsymbol{r_{MPW}}$	Distance between exit portal and point where micropressure wave is measured (m)
$\boldsymbol{r_{TR}}$	Track curve radius (m)
$\boldsymbol{R_g}$	Gas constant ($J\ mole^{-1}K^{-1}$)
$\boldsymbol{R_B}$	Ballast vertical reaction force (N)
$\boldsymbol{R_S}$	Velocity shear relative to the train
$\boldsymbol{R_T}$	Track radius of curvature (m)
$\boldsymbol{R_{TU}}$	Hydraulic radius of tunnel (m)
$\boldsymbol{R_{ui}(\tau)}$	Autocorrelation function of velocity component i
$\boldsymbol{R_{MxL}}$	Ratio of rolling moment coefficients at 90 and 30°yaw
$\boldsymbol{Re}$	Reynolds number
$\boldsymbol{Re_{li}}$	Reynolds number based on integral length scale
$\boldsymbol{s}$	Streamline coordinate
$\boldsymbol{S}$	Suspension coefficient
$\boldsymbol{Sc}$	Scruton number
$\boldsymbol{\overline{S_{ij}}}$	Mean strain rate tensor
$\boldsymbol{S_{Fi}(n)}$	Spectral density for force component i (N^2s) ($i = x,y,z$)
$\boldsymbol{S_{ui}(n)}$	Spectral density of air velocity in i direction (m^2s^{-1})
$\boldsymbol{S_V(n)}$	Spectral density for V (m^2s^{-1})
$\boldsymbol{S_m}$	Shields parameter for ballast roll
$\boldsymbol{S_x}$	Shields parameter for ballast slide
$\boldsymbol{S'_x}$	Shields parameter using friction velocity
$\boldsymbol{S_z}$	Shields parameter for ballast lift
$\boldsymbol{SS_E}$	Sum of the squared approximation errors (Eq. 4.25)
$\boldsymbol{SS_R}$	Sum of the squared approximation variation from mean (Eq. 4.27)
$\boldsymbol{SS_T}$	Sum of the squared true response variation from mean (Eq. 4.26)
$\boldsymbol{t}$	Time (s)
$\boldsymbol{Ta}$	Tachikawa number
$\boldsymbol{T_{abs}}$	Absolute temperature (K)
$\boldsymbol{T_{ui}}$	Integral timescale of velocity component I (s)
$\boldsymbol{T_W}$	Wire tension (N)
$\boldsymbol{u(x,t)}$	Wind velocity at point x and time t (ms^{-1})
$\boldsymbol{u(z,t)}$	Wind velocity at height z and time t (ms^{-1})
$\boldsymbol{u(h)}$	Wind velocity at height h above ground (ms^{-1})
$\boldsymbol{\widehat{u}}$	Wind gust velocity (ms^{-1})
$\boldsymbol{u_c}$	Characteristic wind speed (ms^{-1})
$\boldsymbol{u_i}$	ith component of air velocity ($i = x,y,z$) (ms^{-1})
$\boldsymbol{u_{iB}}$	ith component of ballast velocity ($i = x,y,z$) (ms^{-1})
$\boldsymbol{u_h}$	Horizontal component of velocity (ms^{-1})
$\boldsymbol{u_{h\ 95}}$	95% confidence limit of ensemble of one-second gust values of u_h (ms^{-1})
$\boldsymbol{u_{h\ average}}$	Average value of ensemble of one-second gust values of u_h (ms^{-1})
$\boldsymbol{u_{h\ gust}}$	One-second gust value of u_h (ms^{-1})
$\boldsymbol{u_{h\ sd}}$	Standard deviation of ensemble of one-second gust values of u_h (ms^{-1})

u_r	Velocity in radial direction (ms^{-1})
u_{x0}	Velocity close to ballast bed (ms^{-1})
u_{xr}	Representative air speed inside tunnel portal (ms^{-1})
$u_{x,\ z=\delta}$	Velocity at edge of boundary layer (ms^{-1})
u_θ	Velocity in angular direction (ms^{-1})
u_τ	Shear velocity $\sqrt{\tau_w/\rho}$ (ms^{-1})
u^+	u_x/u_τ
u_1	Lower velocity limit in cumulative probability distribution for human stability (ms^{-1})
u_2	Upper velocity limit in cumulative probability distribution for human stability (ms^{-1})
$\widehat{u}_{50}$	Once in 50-year gust speed (ms^{-1})
$u(\varepsilon)$	Wind speed at an incident angle ε to contact wire (ms^{-1})
$u(90)$	Wind speed at 90°to contact wire (ms^{-1})
v	Train speed (ms^{-1})
v_b	Balancing train speed (ms^{-1})
V	Wind velocity relative to train (ms^{-1})
$V(t)$	Wind velocity relative to train at time t (ms^{-1})
$V(x,t)$	Wind velocity relative to train at point x and time t (ms^{-1})
$V(h)$	Wind velocity relative to train at height h above ground (ms^{-1})
V_N	Velocity normal to train surface in panel method calculation (ms^{-1})
V_∞	Free stream velocity relative to train in panel method calculation (ms^{-1})
V_{FY}	Vertical point of action of side force (m)
w	Contact wire weight/unit length (kg/m)
x	Distance in train direction of travel, measured from train nose (m)
x_i	x coordinate of panel i
x_r	x coordinate of end of train
X_W	Longitudinal distance along contact wire span, measured from span centre (m)
X^2_{Fi}	Aerodynamic admittance for force component i
y	Lateral distance from the centre of the track (m)
y_i	y coordinate of panel i
y_p	Primary bump stop displacement distance (m)
y_s	Secondary bump stop displacement distance (m)
y_{TR}	Semitrack width (m)
Y	Lateral distance of vertical structure from the centre of the track (m)
Y_W	Maximum contact wire lateral displacement under wind loading (m)
z	Vertical distance from the top of the rail (m)
Z	Vertical distance of horizontal structure from the top of the rail (m)
Z_W	Vertical distance of contact wire from support points (m)
z_d	Velocity profile displacement height (m)
z_1	z at the bottom of train (m)
z_2	z at the top of train (m)
z_0	Surface roughness length (m)
z_{01}	Surface roughness of sleepers and ballast (m)
z_{02}	Surface roughness of train under body (m)
z^+	zu_τ/ν
α	Parameter in definition of characteristic velocity
α_0	Wheel unloading factor
β	Wind direction relative to track (degrees or radians)

β_i Angle of panel i to the flow direction (degrees or radians)
γ Ratio of specific heats
δ Boundary layer thickness (m)
δ_d Boundary layer displacement thickness (m)
δ_m Boundary layer momentum thickness (m)
Δ Size of computation cell
ΔC_p Peak-to-peak pressure coefficient
ΔC_{pB} Pressure coefficient across ballast particle
Δp Peak-to-peak pressure (Pa)
Δp_{95} 95% confidence limit of Δp (Pa)
$\Delta p_{average}$ Ensemble average of Δp (Pa)
Δp_{sd} Ensemble standard deviation of Δp (Pa)
Δp_{sim} Numerically simulated value of Δp (Pa)
Δp_{fr} Pressure change due to friction effects due to the entry of the main part of the train into the tunnel (Pa)
Δp_{HP} Pressure change in a tunnel due to the passing of a train nose (Pa)
Δp_N Pressure change due to the passing of the train nose, also initial pressure rise (Pa)
Δp_T Pressure change due to the entry of the train tail (Pa)
Δt Computational time step (s)
Δt_p Characteristic time interval for the initial pressure rise $= \frac{2k_{nose}R_{TU}}{v}$
Δx Distance between computational nodes (m)
ε Turbulence dissipation rate or overhead wire incident angle
ζ Train wetted perimeter (m)
η Wheel/rail friction coefficient
θ Angular coordinate
ϑ Parameter in Eqs. (3.5) and (3.6)
κ Weibull distribution shape factor
κ' Modified Weibull distribution shape factor
λ Weibull distribution scale factor (ms^{-1})
λ' Modified Weibull distribution scale factor (ms^{-1})
μ Dynamic viscosity of air ($kgm^{-1}s^{-1}$)
μ' Second viscosity of air ($kgm^{-1}s^{-1}$)
μ_B Ballast friction coefficient
μ_t Turbulent eddy dynamic viscosity ($kgm^{-1}s^{-1}$)
ν Kinematic viscosity of air (m^2s^{-1})
ν_t Turbulent eddy kinematic viscosity (m^2s^{-1})
ξ_W Mechanical damping ratio of catenary wire
π_1 Parameter in cumulative distribution function in Eq. (8.14)
π_2 Parameter in cumulative distribution function in Eq. (8.14)
ϱ Density of air (kgm^{-3})
ϱ_B Density of ballast (kgm^{-3})
ϱ_0 Reference density of air outside tunnel portal (kgm^{-3})
σ_{ui} Component of turbulence in direction i ($i = x,y,z$) (m/s)
τ Time (s)
τ_K Kolmogorov time scale (s)
τ_{dyn} Pressure tightness time (s)
τ_w Boundary shear stress (Pa)

$\boldsymbol{\phi}$	Velocity potential (s^{-1})
$\boldsymbol{\varphi}$	Stream function (s^{-1})
$\boldsymbol{\psi}$	Yaw angle (degrees or radians)
$\boldsymbol{\omega}$	Vorticity (s^{-1})
$\boldsymbol{\Omega_r}$	Accident risk cumulative density function in Eq. (8.9)
$\boldsymbol{\Omega_s}$	Pedestrian stability CDF in Eq. (8.12)
$\boldsymbol{\Omega}$	Solid angle associated with micropressure wave emission
$\boldsymbol{\Lambda}$	Source volume flow rate per unit length from point source
$\boldsymbol{\Lambda}'$	Source volume flow rate per unit length from panel
$\mathbb{e}$	Error in optimisation regression analysis
$\mathbb{k}_i$	Regression coefficients in optimisation regression analysis
$\mathbb{R}^2$	Coefficient of determination in optimisation regression analysis
$\mathbb{R}^2_{ad}$	Adjusted coefficient of determination in optimisation regression analysis
$\mathbb{x}_i$	Function variable in optimisation regression analysis
$\mathbb{y}_i$	Function variable in optimisation regression analysis
$\bar{}$	Time average, mean or filtered value
$'$	Fluctuating value
$''$	Subgrid component
$\hat{}$	Extreme or gust value
$\tilde{}$	Normalisation of velocities with characteristic wind speed
$\rightarrow$	Vector

PART 1

Fundamental aspects

CHAPTER 1

Historical context

1.1 Early developments up to 1930

From the early 19th century onwards, there was considerable interest in using air as a propulsion system for trains, and aerodynamics, viewed in this way, was seen as something to be exploited rather than as a cause of problems. This approach was perhaps typical of the entrepreneurial spirit of the age. As early as 1812, George Medhurst (Buchanan, 1992) made proposals for people and goods to be moved in capsules in sealed tubes, by a differential pressure between the ends of the capsule. The advantage of such a system was that the driving force could be applied by stationary, rather than moving, engines. Vallance in 1824, seems to have built a demonstrator system of something similar, with the annulus sealed by bearskin (Clayton, 1966), and this work resulted in the practical demonstration by Alfred Beach in New York in 1869 of his pneumatic railway as shown in Fig. 1.1 (Most, 2014).

However, the more 'successful' application of this principle was through what became known as the 'atmospheric railway' concept. Here, the train ran conventionally on track, but one or more of the vehicles was connected to a piston running in a pipe of diameter 30–60 cm that was laid between the tracks. This piston was driven by a pressure difference created by stationary engines. Obviously, the critical part of such a system was the sealing of the slot in the top of the tube through which the piston connector moved, and this proved to be the most difficult issue to overcome. A number of systems were built: one alongside the Kensington Canal in London in 1835 (Clayton, 1966); the West London Railway (d'A Samunda, 1841) from 1840 to 1842; the Dublin and Kingstown Railway from 1843 to 1853, which was reported to have achieved a speed of 65 mph with just one carriage connected to the piston (Mallet, 1844);

Train aerodynamics
ISBN 978-0-12-813310-1
https://doi.org/10.1016/B978-0-12-813310-1.00001-0

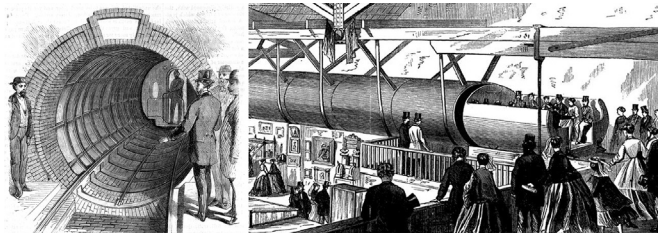

Figure 1.1 The Alfred Beach pneumatic railway.[1]

the London and Croydon Railway from 1846 to 1847 (Turner, 1977); the Paris to St Germain Railway from 1847 to 1860 (Clayton, 1966) — Fig. 1.2A — and, perhaps the most famously, Brunel's South Devon Railway from 1846 to 1848 (Buchanan, 1992) — Fig. 1.2B.

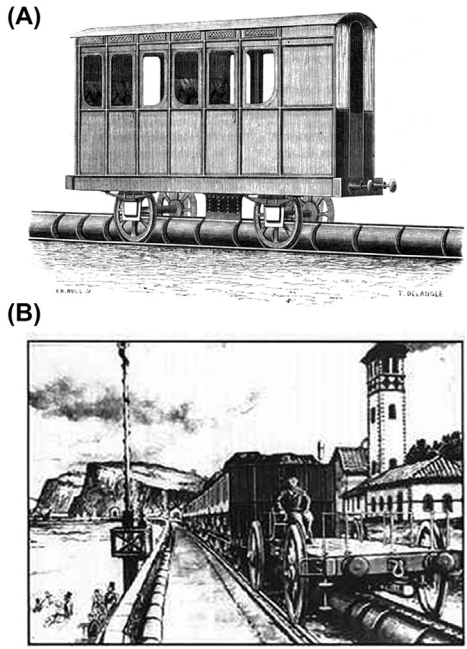

Figure 1.2 ***Atmospheric railways.*** (A) — Paris to St Germain Railway;[2] (B) — Brunel's South Devon Railway.[3]

[1] (Left) Public domain — https://commons.wikimedia.org/wiki/File:Beach_Pneumatic_Transit_01.jpg. (Right) — Public Domain.
[2] *A* - Public domain — https://en.wikipedia.org/wiki/Atmospheric_railway#/media/File:Wagon-directeur-chemin-atmospherique.jpg.
[3] *B* - Public domain.

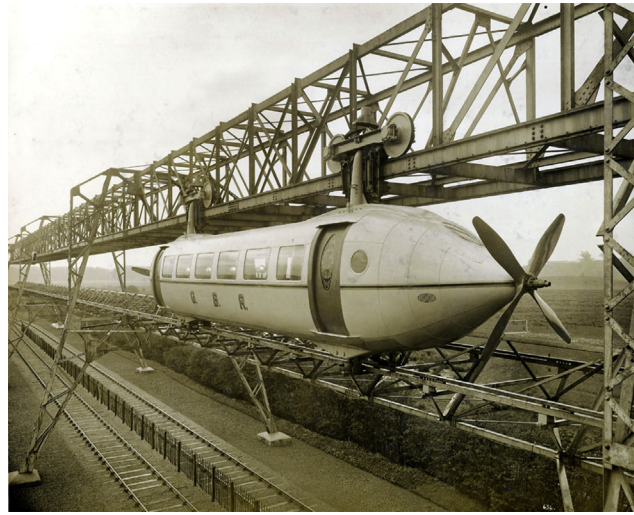

Figure 1.3 The Bennie railplane (Thwaite, 2005).

Although these met with some degree of success, for many of the schemes the unreliability of the seal led to their early abandonment, and even for others where this problem was solved, they ultimately proved uneconomic as steam engine power increased through the century. None of these systems seem to have survived after 1860. They do, however, have one modern successor at Porto Alegre airport in Brazil where the same principle is used today for a large airport people mover.

Another novel example of the merging of aeronautical and railway technology can be found in George Bennie's Railplane concept (Thwaite, 2005) shown in Fig. 1.3. This was effectively a monorail powered by an airscrew that was meant to run above railway tracks, allowing the latter to be used for slower moving vehicles. A 130 m demonstration track was built at Milngavie north of Glasgow and operated from 1930 for around 20 years. There were, however, major technical issues, and the project never attracted enough support for a commercial system to be built.

1.2 Train drag and streamlining – 1930 to 1960

Around the time of the development of the Bennie Railplane, the issues that are today of importance in the field of train aerodynamics were beginning to be considered, the first of these being that of the aerodynamic drag. In 1926, W. Davis derived the formula for train resistance that

eventually bore his name (Davis, 1926). This gives train resistance as a quadratic function of velocity, but was originally derived for quite a restricted set of conditions – freight cars and electric railcars for speeds of less than 40 mph. It has been modified and much used over the years since then, and the conventional explanation of its quadratic form is that the constant and linear velocity terms represent mechanical drag and the velocity-squared term represents aerodynamic effects.

In the 1930s, train speeds were approaching speeds of 100 mph (160 km/h) as locomotive power increased. This speed increase was driven partly through the need to increase passenger loads following the depression, partly as an expression of the modernist and technological cultural milieu and partly due to national pride and competitiveness in the countries involved. Engineers, therefore, began to consider seriously how the overall train resistance could be reduced. The obvious way in which this could begin to be achieved was through streamlining of the train, although of course this only affected the train nose, and as we shall see later, only addressed one component of train aerodynamic drag. Such streamlining was also very much consistent with the artistic attitudes of the age, and much appreciated by designers, stylists and poster artists. The first streamlined train appeared in Germany – the Schienenzeppelin, which ran between Berlin and Hamburg in 1931 (Fig. 1.4). It was first powered by an airscrew (and was thus a conventional vehicle equivalent of the Bennie Railplane), and in that form it reached a speed of 230 km/h. It was reengineered with a more conventional drive system and, in 1933, still achieved an impressive speed of 180 km/h. This led to the construction of a two-car, streamlined, diesel-electric vehicle known colloquially as the Flying Hamburger, which recorded an average speed of 124 km/h between Berlin and Hamburg in 1933 (Gottwaldt, 2006).

In the 1930s, in the United States, a fleet of lightweight, streamlined, diesel-powered locomotives were developed (the Zephyrs) that were able to attain high average speeds over long distances and top train speeds of around 180 km/h (Johnston et al., 2001). In Italy, a three-car electric FS Class ETR 200 achieved a speed of 201 km/h on the Rome–Naples route in 1937 (Cornolo, 1990). In Great Britain, the LNER Mallard, an A4 class locomotive (Fig. 1.5), was able to achieve a world record train speed for a steam locomotive of 203 km/h in 1938 (Hale, 2005).

Wind tunnel tests to measure train resistance seem to have been first carried out in the closing years of the 19th century (Goss, 1898), but it was not until the early 1930s that these became commonplace. A bibliography

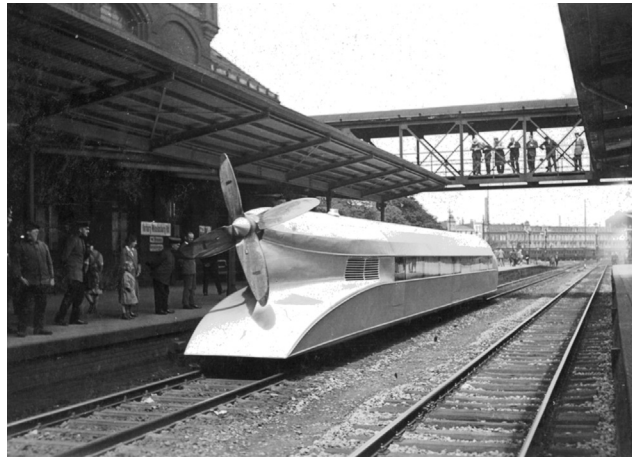

Figure 1.4 The Schienenzeppelin in its original form.[4]

Figure 1.5 Mallard locomotive at the National Railway Museum in York, Great Britain.[5]

listing these wind tunnel tests in France, Germany and the United States is provided in Peacock (1951). In Great Britain, wind tunnel tests to measure train resistance and smoke trajectories were carried out in a wind tunnel at the British National Physical Laboratory, for a range of LMS and LNER

[4] Can be used subject to conditions. https://creativecommons.org/licenses/by-sa/3.0/de/deed.en. Attribution-ShareAlike 3.0 Germany (CC BY-SA 3.0 DE).

[5] https://en.wikipedia.org/wiki/LNER_Class_A4_4468_Mallard#/media/File:Number_4468_Mallard_in_York.jpg. Creative Commons Attribution-Share Alike 3.0 Unported.

Figure 1.6 Wind tunnel tests on LNER steam locomotive at the National Physical Laboratory Great Britain, 1932.[6]

locomotives and coaches, including the A4 class (Johansen, 1936) — see Fig. 1.6. LMS Coronation class locomotives and coaches and short diesel multiple units were also investigated in a newly constructed wind tunnel in Derby (Peacock, 1951).

Around this time, studies were also carried out into the aerodynamic drag of trains in tunnels. Sutter (1930), for instance, describes full-scale tests in two Swiss tunnels to examine the increased aerodynamic drag of trains and, incidentally, made the first known attempt to calculate the unsteady flow in a tunnel (see Section 1.3.2).

As we move on into the post-war period, the need to reduce train resistance continued to be an issue, although the need for speed was less pressing in the light of the major reconstruction and restructuring that was underway throughout the industrialised world. However, when the Shinkansen series 0 trains began to be produced in Japan in 1964, it was clear that better estimates of resistance were needed. This led to the development of the coast down test technique, where speed was measured as a function of position as trains coasted from top speed down to rest (Ozawa, 1990). Ideally, many miles of straight level track are required for such tests, and suitable sites are not easily available. The data were then analysed to find

[6] Used with permission of IMechE Archive.

the deceleration and, thus, the resistance, and a quadratic curve fitted to the resistance/velocity data in accordance with the Davis approach, with the aerodynamic drag being determined from the velocity-squared term.

1.3 Emerging aerodynamic issues – 1960 to 1980

As the years passed, however, other aerodynamic issues came to prominence: pantograph aerodynamics; tunnel aerodynamics; pressure loads due to passing trains; the effects of train slipstreams and the effect of crosswinds on lightweight trains. We will consider these in turn below.

1.3.1 Pantograph aerodynamics

Pantographs can experience severe vertical aerodynamic forces (lift), either upwards or downwards, the former causing excessive wear on the overhead system and the latter leading to lack of contact. Thus, considerable effort was expended in designing pantographs to be aerodynamically neutral, through the addition of small wing sections on the frame (Garreau and Dupont, 1958). This was achieved by mounting and modifying full-scale pantographs on wind tunnel balances, in large aeronautical wind tunnels.

The other pantograph issue that emerged was the relative movement of overhead lines and pantograph in high crosswinds that was found to lead to dewirement, and in the worse cases, major damage to the overhead system as the wire became trapped beneath the pantograph. This led to studies of both wind-induced galloping oscillations of the overhead line (Gawthorpe, 1978b) and also of the displacement of the wire/pantograph system by turbulent crosswinds. To take account of the second effect, methods were developed in Great Britain to assess the exposure of sections of track and determine extreme wind loads on the wire. Where these were found to be excessive, extra pylons were inserted to reduce the overhead line span length and thus to restrict lateral movement. This resulted in a significant reduction in dewirement incidents (Gawthorpe, 1978b).

1.3.2 Tunnel aerodynamics

When trains pass through tunnels, a series of pressure waves are generated as the train nose and tail enter the tunnel – a positive increment of pressure for the former and a negative increment for the latter. These waves move along the tunnel at the speed of sound (i.e., much faster than the train) and are reflected at the end of the tunnel as pressure waves of the opposite sign.

This can result in very complex patterns of pressure variation along tunnels in even the simplest situations (Swarden and Wilson, 1969). The situation is further complicated when trains pass in double track tunnels. These pressure waves were found to cause much aural discomfort to some passengers, particularly as trains passed through narrow tunnels built in a previous era, at speeds for which they were simply not designed. In addition, it was found that the aerodynamic drag of trains in tunnels was significantly increased from the open-air value. This resulted in four areas of research.

The first of these was to develop methods for predicting the passage of pressure transients along tunnels. It was found that relatively simple gas dynamics calculation methods, based on the method of characteristics, could successfully be used for this, and a number of methods were derived in the 1960s and 1970s that form the basis of calculation methods that are still in use today (e.g., Fox and Vardy, 1973; Gawthorpe and Pope, 1976).

Secondly, in parallel with this, full-scale measurements began to be carried out to obtain field measurements of tunnel pressure transients to verify the models, and to give data for train entry pressure losses required by the models. These measurements required very considerable developments in instrumentation, and in the analysis of resultant data.

The third area of research was to investigate how people perceived pressure transients, through the use of volunteers in pressure chambers. This work led to the development of pressure transient limits that again formed the basis of limits that are still in force (Gawthorpe, 1978c). These took on several forms, but in general specified a maximum pressure rise that was allowed to occur over a suitable period (e.g., 3 kPa over 3 s). Rather stricter criteria were imposed where there was a possibility of regularly repeated changes in pressure, such as in long tunnels with airshafts or cross passages.

Finally, the issue of train drag in tunnels met with more attention. Here, it was found that, in long tunnels in particular, the effect of pressure transients on drag was small, and simple prediction methods could be used.

1.3.3 Pressure loads due to passing trains

Another problem that came to prominence in this period was the pressure load caused by a passing train on other trains, and on trackside structures. This seems to have been first investigated in a theoretical way by Tolmien (1927) using potential flow theory. Train pressure transients probably also

caused problems with broken windows as experienced in Le Havre in 1935. Experiments were first carried out to investigate the practical aspects of this phenomenon in Japan in 1962 (Hara and Okushi, 1962). It was found that as trains passed, there was firstly a positive pressure pulse, which was followed by a negative pulse. This problem saw the first tentative use of computational fluid dynamics (CFD) in the field of train aerodynamics in Britain, reported later in the history of BR Research written by Gilchrist (2006), with the application of inviscid panel methods to the calculation of flow around the nose of trains.

1.3.4 Effect of train slipstreams

The issue of the effect of train slipstreams also became important in the 1960s and 1970s, with instances of debris around the track being moved and causing damage (most notably to the windscreens of new cars being transported on trains) and also some near-accidents to passengers waiting on platforms. In both Great Britain and Germany, this occasioned various series of full-scale measurements to measure slipstream velocities (Gawthorpe, 1978a), which showed that there was a short acting gust near the nose of trains, related to the pressure pulse discussed above, and then a gradual build-up of the slipstream velocity along the train, within the boundary layer, reaching a peak in the near wake of the train. These measurements led to the initial development of criteria for the maximum allowable gusts experienced at the side of trains. However, at this stage, the nature of the flow within the slipstreams and wakes of the trains, and the need for many repeated measurements to obtain representative velocity values, was not fully appreciated.

1.3.5 Crosswind effects

In this period, the stability of lightweight trains in high crosswinds came to be of concern. There had been sporadic instances of trains being blown off tracks over the years, the most notable being at Leven Viaduct in Cumbria in Britain in 1903 (Railway Archive, 2018), and the Owencarrow Viaduct in Ireland in 1925 (Monreagh Heritage Centre, 2018), shown in Fig. 1.7. A range of other poorly reported events also occurred on narrow gauge railways in Japan and Switzerland.

Investigations were carried out to address this issue in Japan in the 1960s and early 1970s (Fukuchi, 1975), but it was with the advent of the lightweight, tilting high-speed Advanced Passenger Train, which was designed

Figure 1.7 Overturning accident on the Owencarrow Viaduct in 1925.[7]

to run on a very exposed line on the west of Great Britain, that this came to be a major concern by the mid-1970s. In addition, the move away from locomotive hauled trains to distributed traction has led to an increased vulnerability of leading vehicles even of conventional trains. This resulted in a number of tests to measure crosswind forces, such as that shown in Fig. 1.8, where the forces on a one-fifth scale model were measured on an open-air test track (Cooper, 1979), and to the first recorded use of moving model experiments for the measurement of crosswind forces (Baker, 1986).

1.4 High-speed train aerodynamics – 1980 to 2000

The period from 1980 to 2000 was mainly concerned with the development of high-speed trains with speeds up to 300 km/h, which resulted in an increasing number of aerodynamic issues becoming apparent. Coupled with this, a number of new tunnels were built that were significantly longer than most already in existence. This combination resulted in a further series of issues arising in the areas of tunnel aerodynamics, pressure loads due to passing trains and crosswind effects.

1.4.1 Tunnel aerodynamics

Firstly, there was a need for a fuller understanding of the air flow within tunnels, not only to specify the pressure transients more closely but also to

[7] With permission from Donegal County archives.

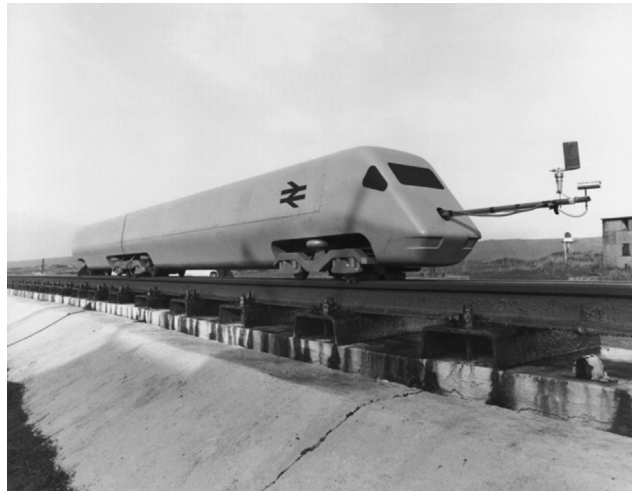

Figure 1.8 Crosswind force measurement on one-fifth scale Advanced Passenger Train model at the Pendine test track in South Wales.[8]

predict tunnel temperatures and to investigate emergency (fire) scenarios. This led to further developments in tunnel pressure transients and flow calculation methods to take account of complex geometries, and also to the undertaking of more full-scale tests to obtain data to calibrate these methods (Gawthorpe, 2000). It also resulted in the development, by British Rail Research, of a large moving model rig, in Derby in Great Britain, that was able to fire models along a long test track through model tunnels for more convenient measurements of pressure transients. The basic scaling parameter in this case is the Mach number, the ratio of train speed to the speed of sound, and thus the models need to be fired at full-scale train speeds to achieve the required similarity for simulating pressure waves in tunnels. Over the following years, this rig was used extensively to study a range of new tunnel developments across Europe. In Japan, two other issues arose. It was found that as Shinkansen speeds exceeded 300 km/h, loud sonic booms were heard at the exit of some of the tunnels on the line. Investigation showed that this was due to a significant steepening of the pressure waves caused by the train as they passed along long slab track tunnels, such that, although the majority of the energy was reflected at the end of the tunnel in the normal way, a significant proportion was transmitted to the

[8] Authors collection.

Figure 1.9 Tunnel entrance hood.[9]

environment as a 'micropressure wave' that had frequencies in the audible range. It was found that this effect could be alleviated by constructing a tapering entry hood at the *entrance* to the tunnel, that ensured the gradient of the initial pressure transient was reduced, and that even with steepening it would not achieve a critical value at the tunnel exit – see Fig. 1.9 (Yamamoto, 1965). This methodology has since been used, with variations, on a number of tunnels around the world.

In addition, in Japan, it was found that for some trains, there were large oscillations of the trailing coach as the train passed through tunnels. Later, unsteady flow CFD calculations (Diedrichs et al., 2007a) suggest that this was due to a complex instability of the flow between the train side and the tunnel wall that developed along the length of the train and was at its most severe around the end coach.

1.4.2 Pressure loads due to passing trains

As vehicle speeds increased, the effect of nose pressure pulses and their loading on passing trains and trackside structures became of more significance. ERRI (1994) reports full-scale experiments on measuring the pressure loading on noise barriers that were carried out to develop design rules for such structures. There was further development in CFD methodology in this area as well, as nose pressure pulses were within the

[9] Used with permission from RTRI, Japan.

capability of the calculation methods that were used at the time – see the reference list in Farhan (1991) for a collation of work in this area.

1.4.3 Crosswind effects

Finally, in this period, the crosswind issue gradually grew in importance, as train speeds increased, and the allowable risk of an accident was better defined. Codified methodologies for calculating risk were developed in Britain and Germany. In the latter, the concept of the characteristic wind curve was introduced – the relationship between the vehicle speed and a critical wind speed – and the determination of this curve now underlies many current methods for specifying risk relating to strong winds (Matschke and Schulte-Werning, 1997). CFD methods also began to be applied more regularly to the determination of aerodynamic force coefficients, although this proved, and was to continue to prove, to be a very challenging application of the methodology. One particularly interesting application of these techniques was to the case of the stability of the Channel Tunnel Shuttle vehicles, which carry trucks between England and France (Bradbury and Deaves, 1994). When empty in the ports of Folkestone and Calais, it was realised that these very light vehicles were at significant risk of blowing over at relatively low wind speeds and would need to be protected by wind fences. It was also found that the design of wind systems in that area were not the standard extratropical cyclones, but rather short duration, high-intensity thunderstorms.

1.5 Into the 21st century

Towards the end of the last century, the TRANSAERO project, a multipartner EU-sponsored project, was undertaken, lasting from 1995 to 1998 (Schulte-Werning, 2001). Work was concentrated in three areas: tunnel aerodynamics; loads due to passing trains and crosswind effects, which reflected the major issues that were of concern at that time. The TRANSAERO project itself was the precursor of a number of major international European collaborations from the early years of the 21st century – RAPIDE (RAPIDE, 2001), Aerodynamics in the Open Air (AOA) (Kaltenbach et al., 2008) and AeroTRAIN (Sima et al., 2011). The results from these projects have formed the basis of recent research and applications in train aerodynamics. The results from these projects will be used extensively in the following chapters.

CHAPTER 2

Fluid mechanics concepts

2.1 Outline

In this chapter, a number of basic fluid mechanics concepts will be set out that are of relevance to the subject of train aerodynamics. Only brief details are given, and readers who need to know more should consult standard texts on fluid mechanics – see for example Munson et al. (2013) and Davidson (2005). We begin with a discursive introduction to a number of concepts and then move on to give some analytical detail, in terms of the fundamental equations of fluid flow, which will be taken up in the following chapters. Finally, we describe, qualitatively and quantitatively, the nature of flow turbulence and the structure of the natural wind near the ground.

2.2 Dimensional analysis

In train aerodynamics, the primary physical parameters that are of interest are the flow velocities around trains, the aerodynamic pressure (force per unit area) on the surfaces of trains and railway infrastructure and the overall aerodynamic forces and moments on trains and railway infrastructure. The parameters are dependent on a wide range of train geometric and operational parameters and on the properties of the surrounding air. The conventional way of expressing these variables is based on a technique known as dimensional analysis. Very broadly, this technique allows the complexity of a relationship between a wide range of variables to be significantly reduced if these variables are expressed in a dimensionless form. For the parameters of most interest here, we will thus define the following dimensionless groups:

- The velocity coefficient $C_{ui} = \frac{u_i}{v}$, where u_i is the ith component of air velocity ($i = x$, y or z) and v is the train speed.
- The pressure coefficient $C_p = \frac{p - p_r}{0.5\rho v^2}$, where p is the surface pressure, p_r is a reference pressure (usually the pressure a long way from the train) and ρ is the density of air.

Train aerodynamics
ISBN 978-0-12-813310-1
https://doi.org/10.1016/B978-0-12-813310-1.00002-2

- The force and moment coefficients $C_{Fi} = \frac{F_i}{0.5\varrho v^2 A}$ and $C_{Mi} = \frac{M_i}{0.5\varrho v^2 Ah}$, where F_i and M_i are the ith component of the aerodynamic forces and moments, A is a reference area of the train and h is a reference height.

Dimensional analysis then allows us to say that these 'dependent' variables are functions of other 'independent' dimensionless variables — the dimensionless train and infrastructure geometries (expressed as, say, length over height ratios) and other dimensionless parameters representing the flow around the train. Of the latter, the two that will be seen to be of most importance to the study of train aerodynamics are the Reynolds number $\left(Re = \frac{\varrho v h}{\mu}\right)$ and the Mach number $\left(Ma = \frac{v}{c_a}\right)$, where μ is the dynamic viscosity and c_a is the speed of sound in air $\left(= \sqrt{\frac{K_B}{\varrho}}\right)$ and K_B is the bulk modulus of air. Physically, the Reynolds number is an indication of the ratio of inertial forces to frictional, viscous forces in the flow, and the Mach number is an indication of the effects of compressibility on the flow. In addition, for crosswind studies, the force and moment coefficients are strong functions of the yaw angle ψ, the wind direction relative to the vehicle direction of travel.

2.3 Frames of reference

In the study of aeronautics, it is usual to work in the frame of reference relative to the aircraft, and this frame of reference is often used in train aerodynamics. Thus, in this *train* frame of reference, a train moving at a speed v experiences a steady airflow of velocity v in the direction opposite to the train direction of travel, and the ground under the train is moving in that direction, also at a speed v. However, for train aerodynamics, it is sometimes more convenient to work in a frame of reference that is stationary relative to the ground, in other words that of a stationary observer, i.e., the *ground* frame of reference. In this case, the flow velocities produced by the train as it passes will increase from zero to some maximum values and then decrease again to zero, i.e., the flow is changing in time and is thus unsteady. In both frames of reference, we will adopt a coordinate system - x, y *and* z - where the origin of the system is at a point level with the top of the rails (TOR), midway between the tracks. x is measured from the train nose in the train frame of reference and is positive along the length of the train. In the ground frame of reference, x is the distance from the train nose to the observer and is positive when the train nose has passed the observer.

In both frames of reference, y is measured outwards from the centre of the track, and z is measured vertically from the TOR and is positive in an upward direction.

2.4 Forces and energy in fluids

As with any mechanical system, fluid flows follow the three basic conservation laws of mass (the continuity principle); momentum (Newton's second law) and energy (the first law of thermodynamics). In words, these can be expressed as follows:

Conservation of mass – the amount of fluid entering a region of space in unit time is equal to that leaving plus that stored within the region through density changes. For incompressible flows, the latter is of course zero.

Conservation of momentum can be expressed in one of two ways, either directly as the amount of fluid momentum leaving a region of space minus the amount entering in unit time being equal to the sum of the fluid forces on the boundaries of that space or indirectly as the mass of the fluid element multiplied by the total (i.e., spatial and temporal) acceleration being equal to the sum of the forces. There are three types of forces that act on the fluid – pressure forces which act perpendicular to the faces of the fluid element; friction forces which act parallel to the faces of the element and body forces such as gravity. The latter are usually small in low-speed atmospheric flows.

Conservation of energy – the energy leaving the region of space minus the energy entering the unit of space is equal to the heat transfer minus the work done by the fluid. The types of energy within the airflows we are considering here are kinetic energy, potential energy and thermal energy. The work done by the fluid is a function of the pressures at the faces of the fluid element, which do work on adjacent fluid elements.

The forces imposed on the surfaces over which the fluid passes, in our case trains and the local trackside infrastructure, are also of the two main types outlined above – pressure forces and friction forces. This distinction will be seen to be important in what follows. However, it is often difficult to distinguish between these two types of force in any one situation, and very often it is only possible to specify the overall forces and moments on structures caused by a combination of pressure and friction effects, usually specified by the force or moment coefficients in each of the three directions as defined above.

2.5 Free flows, boundary layers and turbulence

Any flow field can be divided into two regions — an external flow region away from any boundaries and a boundary layer region close to flow boundaries. In the former, friction forces are not significant, and changes in velocity are directly related to changes in pressure. In the latter, friction forces cause the velocity to fall to zero at the boundary, and there can thus be substantial velocity gradients (or shear) within the flow.

Within boundary layers, the flow can be of two types. At low values of the Reynolds number, the flow will be laminar and steady. However, as the Reynolds number increases, small instabilities in the laminar shear flow will grow and produce large-scale turbulence or unsteadiness, and the boundary layer will be composed of turbulent eddies over scales ranging from the thickness of the boundary layer to scales several orders of magnitude smaller than the boundary layer. For the study of train aerodynamics, the boundary layers that we are dealing with are almost always turbulent. The boundary layer over a train is of the order of 1—2 m in thickness at the end of a high-speed passenger train. There can, however, be occasions when carrying out experiments on small-scale physical or computational models for which the boundary layer will be laminar. In such an event, care needs to be taken, as this can result in flow patterns quite unlike those that would be observed at full-scale Reynolds number.

2.6 Bluff bodies, separation and wakes

Trains and most railway infrastructure can, in aerodynamic terms, be described as bluff bodies, as opposed to streamlined bodies such as aircraft. On both streamlined and nonstreamlined bodies, boundary layers will grow along the length of the body. Generally, at the downstream end of the former, the boundary layers on each side of the body will come together and create a wake that is characterised by a reduction in velocity from the free stream value, but where the flow is still in the original direction (Fig. 2.1). For bluff bodies, however, which are characterised by rapid changes in section, the flow within the boundary layer is often unable to remain attached to the surface of the body when the section changes and undergoes a process known as separation. This can result in large-scale wakes of the order of the body thickness, where the flow is in the opposite direction to the original flow. Such wakes can also be highly turbulent and unsteady, with large vortical flow structures. On occasion, these

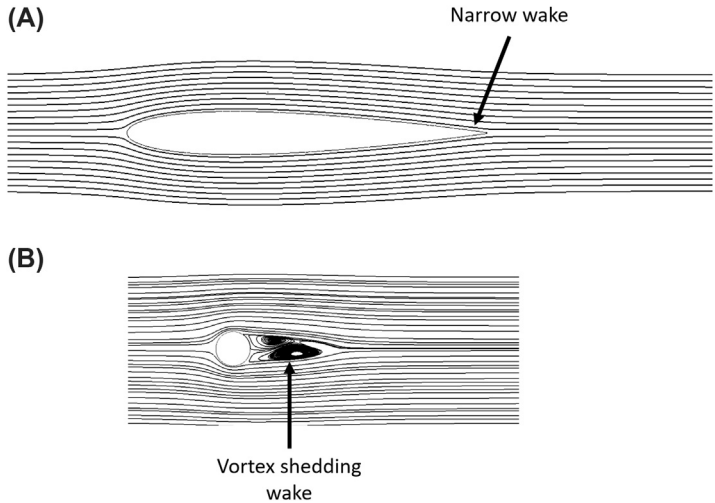

Figure 2.1 ***Streamlined and bluff body wakes.*** (A) – streamlined aerofoil; (B) – bluff cylinder.

structures can exhibit a well-defined periodicity (e.g., flow in the wake of a cylinder at low to medium Reynolds numbers), but for most of the applications that will concern us, the wake fluctuations will have a range of frequencies, with no dominant value.

2.7 Equations of motion

In this section and those that follow, we consider the equations of motion of fluid flow in a variety of forms that are relevant to later chapters. The main purpose is to show that the various analytical and numerical methods that will be presented in those chapters are all essentially derived from the same equation set, but with different assumptions and simplifications. From the start, however, we restrict our considerations to two dimensions (x and z) as the two-dimensional equation set is the most convenient for the basic understanding of the issues involved, which is the main concern of this discussion. For ease of understanding, we also present the equations of motion in Cartesian form rather than in the more concise vector/tensor form.

We begin with the two-dimensional, compressible, unsteady Navier–Stokes equations in the x-z plane. The continuity equation is written as

$$\frac{\partial \rho}{\partial t} + \frac{\partial (\rho u_x)}{\partial x} + \frac{\partial (\rho u_z)}{\partial z} = 0 \tag{2.1}$$

The x and z momentum equations are given by

$$\rho\left(\frac{\partial u_x}{\partial t}+u_x\frac{\partial u_x}{\partial x}+u_z\frac{\partial u_x}{\partial z}\right)=-\frac{\partial p}{\partial x}+\mu\left(\frac{\partial^2 u_x}{\partial x^2}+\frac{\partial^2 u_x}{\partial z^2}\right)+(\mu+\mu')\frac{\partial}{\partial x}\left(\frac{\partial u_x}{\partial x}+\frac{\partial u_z}{\partial z}\right)+\rho g_x \tag{2.2}$$

$$\rho\left(\frac{\partial u_z}{\partial t}+u_x\frac{\partial u_z}{\partial x}+u_z\frac{\partial u_z}{\partial z}\right)=-\frac{\partial p}{\partial z}+\mu\left(\frac{\partial^2 u_z}{\partial x^2}+\frac{\partial^2 u_z}{\partial z^2}\right)+(\mu+\mu')\frac{\partial}{\partial z}\left(\frac{\partial u_x}{\partial x}+\frac{\partial u_z}{\partial z}\right)+\rho g_z \tag{2.3}$$

In the momentum equations, the terms on the left-hand side describe the acceleration of the flow, and those on the right describe the pressure forces (first term), viscous forces (second and third terms) and body forces (final term). The second viscous term describes the effect of the bulk viscosity $(\mu+\mu')$ (due to compressibility of fluid elements), where μ' is known as the second viscosity. The second viscosity is not well specified but is often taken to be $\mu'=-\frac{2}{3}\mu$. For unsteady incompressible flow, where the variations in density can be neglected, the bulk viscosity terms also fall to zero through the use of the continuity equation, and we obtain

$$\frac{\partial u_x}{\partial x}+\frac{\partial u_z}{\partial z}=0 \tag{2.4}$$

$$\rho\left(\frac{\partial u_x}{\partial t}+u_x\frac{\partial u_x}{\partial x}+u_z\frac{\partial u_x}{\partial z}\right)=-\frac{\partial p}{\partial x}+\mu\left(\frac{\partial^2 u_x}{\partial x^2}+\frac{\partial^2 u_x}{\partial z^2}\right)+\rho g_x \tag{2.5}$$

$$\rho\left(\frac{\partial u_z}{\partial t}+u_x\frac{\partial u_z}{\partial x}+u_z\frac{\partial u_z}{\partial z}\right)=-\frac{\partial p}{\partial z}+\mu\left(\frac{\partial^2 u_z}{\partial x^2}+\frac{\partial^2 u_z}{\partial z^2}\right)+\rho g_z \tag{2.6}$$

The existence of turbulence within flow fields has been described above, and the question arises as to how this can be taken account of in the equations of motion. The method that is normally followed is to split the flow variables into mean and fluctuation components, the former denoted by an overbar $^-$ and the latter by $'$. The equations of motion are then time averaged. This process is called Reynolds Averaging and Navier-Stokes equations treated this way are abbreviated to RANS. Ignoring body

forces, this results in the following equation set for the steady, incompressible Navier–Stokes equations:

$$\frac{\partial \overline{u}_x}{\partial x} + \frac{\partial \overline{u}_z}{\partial z} = 0 \tag{2.7}$$

$$\rho\left(\overline{u_x}\frac{\partial \overline{u_x}}{\partial x} + \overline{u_z}\frac{\partial \overline{u_x}}{\partial z}\right) = -\frac{\partial \overline{p}}{\partial x} + \mu\left(\frac{\partial^2 \overline{u_x}}{\partial x^2} + \frac{\partial^2 \overline{u_x}}{\partial z^2}\right) - \rho\left(\frac{\partial \overline{u_{x'}^2}}{\partial x} + \frac{\partial \overline{u_{x'}u_{z'}}}{\partial z}\right) \tag{2.8}$$

$$\rho\left(\overline{u_x}\frac{\partial \overline{u_z}}{\partial x} + \overline{u_z}\frac{\partial \overline{u_z}}{\partial z}\right) = -\frac{\partial \overline{p}}{\partial z} + \mu\left(\frac{\partial^2 \overline{u_z}}{\partial x^2} + \frac{\partial^2 \overline{u_z}}{\partial z^2}\right) - \rho\left(\frac{\partial \overline{u_{z'}^2}}{\partial z} + \frac{\partial \overline{u_{x'}u_{z'}}}{\partial x}\right) \tag{2.9}$$

It can be seen that there are now additional terms in the momentum equations. These are known as the Reynolds stress terms, which are analogous to the viscous friction terms, representing the turbulent friction in the flow, caused by the mixing of turbulent eddies. In the two-dimensional case, here, there are four terms – in the fully three-dimensional case, there will be nine such terms, which make up what is often referred to as the Reynolds stress tensor. For most applications of computational fluid dynamic techniques (CFD) in train aerodynamics, the above equation set (but in its three-dimensional form) is the one that is most often used. The particular challenge is to determine adequately the terms in the Reynolds stress tensor. This will be taken up further in Chapter 4.

2.8 Steady boundary layer equations

Within boundary layers, the steady turbulent equations of motion take on rather simpler forms. Making the assumptions that $u_x \gg u_z$ and that gradients in the z direction are much greater than gradients in the x direction, i.e., the boundary layer is thin in comparison to its length, and looking at the magnitudes of the different terms, one obtains the equation set:

$$\frac{\partial \overline{u_x}}{\partial x} + \frac{\partial \overline{u_z}}{\partial z} = 0 \tag{2.10}$$

$$\rho\left(\overline{u_x}\frac{\partial\overline{u_x}}{\partial x}+\overline{u_z}\frac{\partial\overline{u_x}}{\partial z}\right)=-\frac{\partial\overline{p}}{\partial x}+\mu\left(\frac{\partial^2\overline{u_x}}{\partial z^2}\right)-\rho\frac{\partial\overline{u_{x'}u_{z'}}}{\partial z} \tag{2.11}$$

$$\frac{\partial\overline{p}}{\partial z}=0 \tag{2.12}$$

The last equation indicates that the pressure is constant across the boundary layer, taking the value at the edge of the boundary layer. Now similarity arguments applied to these equations lead to an explicit expression for the variation of $\overline{u_x}$ with height in the lower regions of the turbulent boundary layer

$$u^+=\frac{\overline{u_x}}{u_\tau}=\frac{1}{k_{VK}}ln(z^+)+K=\frac{1}{k_{VK}}ln\left(\frac{z}{z_0}\right) \tag{2.13}$$

where k_{VK} is the von Kármán constant (=0.41), $K=-\frac{1}{k_{VK}}ln\left(\frac{z_0u_\tau}{\nu}\right)$, $u^+=\frac{\overline{u_x}}{u_\tau}$, $z^+=\frac{zu_\tau}{\nu}$, ν is the kinematic viscosity ($=\mu/\rho$), z_0 is the surface roughness length and u_τ is the shear velocity defined by

$$u_\tau=\sqrt{\tau_w/\rho} \tag{2.14}$$

where τ_w is the boundary shear stress. $z=z_0$ at the point where the velocity falls to zero, a little way above the wall. This logarithmic expression holds in the lower regions of the boundary layer — see Fig. 2.2 — and above this the velocity tends to a constant value at the edge of the boundary layer where $z=\delta$, the boundary layer thickness δ. The latter is not well defined, and it

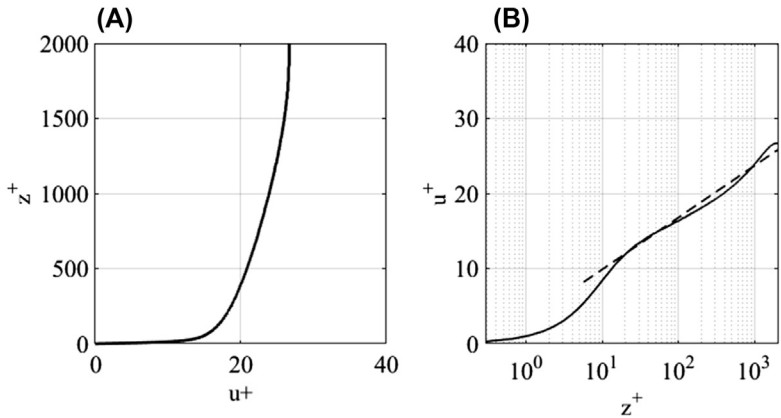

Figure 2.2 ***Boundary layer velocity profiles.*** (A) — plotted in conventional form; (B) — plotted in semi-logarithmic form showing logarithmic region as dotted line.

is usual to define two more precise integral boundary layer thicknesses – the displacement thickness δ^* and the momentum thickness θ given by:

$$\delta_d = \int_0^{\frac{z}{\delta}=1} \left(1 - \frac{u_x}{u_{x,z=\delta}}\right) d\left(\frac{z}{\delta}\right) \tag{2.15}$$

$$\delta_m = \int_0^{\frac{z}{\delta}=1} \left(\frac{u_x}{u_{x,z=\delta}}\right)\left(1 - \frac{u_x}{u_{x,z=\delta}}\right) d\left(\frac{z}{\delta}\right) \tag{2.16}$$

The ratio between δ_d and δ_m is the form parameter H. For equilibrium, zero-pressure gradient turbulent boundary layers, this has a value of around 1.4. Note that these two expressions are for a boundary layer growing on a stationary wall as the flow passes over it, in the train frame of reference in the terms of Section 2.3. For the ground frame of reference (measurements made with stationary instruments as a train passes by), the definition of δ_d needs to be modified somewhat to:

$$\delta_d = \int_0^{\frac{z}{\delta}=1} \left(\frac{u_x}{u_{x,z=\delta}}\right) d\left(\frac{z}{\delta}\right) \tag{2.17}$$

The definition of δ_m, however, remains the same.

2.9 Potential flow

The simplest way in which flow fields can be calculated is through the use of a potential flow analysis. This applies only for frictionless and what is termed irrotational flow. The latter implies that the vorticity, which describes the rotation of fluid elements, is zero. The basis of this method is the definition of two orthogonal functions – the stream function φ and the velocity potential ϕ. These are defined through the following equations:

$$u_x = \frac{\partial \phi}{\partial x} = \frac{\partial \varphi}{\partial z} \tag{2.18}$$

$$u_z = \frac{\partial \phi}{\partial z} = -\frac{\partial \varphi}{\partial x} \tag{2.19}$$

The stream function is constant along a streamline, whereas the velocity potential is constant normal to a streamline. Now the definition of vorticity (ω) for the two-dimensional case is

$$\omega = \frac{\partial u_x}{\partial z} - \frac{\partial u_z}{\partial x} \tag{2.20}$$

which goes to zero if the velocities are defined through the velocity potential as above, thus showing that such flows are irrotational. Furthermore, from the above equations and the continuity equation, we obtain:

$$\frac{\partial^2 \phi}{\partial x^2} + \frac{\partial^2 \phi}{\partial z^2} = \nabla^2 \phi = 0 \tag{2.21}$$

$$\frac{\partial^2 \varphi}{\partial x^2} + \frac{\partial^2 \varphi}{\partial z^2} = \nabla^2 \varphi = 0 \tag{2.22}$$

and thus both the potential and the stream function satisfy the Laplace equation. This formulation allows the use of the mathematical technique of conformal mapping for the prediction of flow fields and also the use of the straightforward numerical technique of panel methods for the calculation of more complex flows. These will be described further in Chapter 4, where computational methods based on the potential flow equations are set out, and in Chapter 8, where the flow around the nose of a train is considered. The important point to remember, however, is that such methods are only valid for frictionless, irrotational flows, where boundary layers and turbulence effects are not present and are essentially kinematic, only relying on the use of the continuity equation. To calculate the pressures in the flow and on any surfaces present, the zero vorticity condition is substituted in one of the momentum equations, which can then be straightforwardly integrated to give:

$$p + \frac{1}{2}\rho\left(u_x^2 + u_z^2\right) = \text{constant} \tag{2.23}$$

This is a simple statement of the steady flow energy equation known as the Bernoulli equation, and relates the local pressure to the local velocity.

2.10 Turbulent flows

The nature of turbulence has been briefly presented above. However, it will be seen in the following chapters that it is necessary to be able to describe turbulent characteristics in a quantitative fashion. Thus, in this section, some basic definitions will be set out that quantify both the magnitude and the spatial and temporal scales of turbulence.

The magnitude of the turbulence for velocity component u_i (where $i = x,\ y$ or z) is specified by the standard deviation of the fluctuating velocity σ_{ui}, but is more usually given by the turbulence intensity I_i, the ratio

of the standard deviation to the mean of the major velocity component, usually taken as that in the x direction.

$$I_i = \frac{\sigma_{ui}}{\overline{u_x}} \tag{2.24}$$

This definition applies to the train frame of reference. For the ground frame of reference it becomes:

$$I_i = \frac{\sigma_{ui}}{v - \overline{u_x}} \tag{2.25}$$

The size of the turbulent fluctuations can be specified in a number of ways. Firstly, the autocorrelation function of a velocity component u_i (where $i = x$, y or z) can be defined as:

$$R_{ui}(\tau) = \frac{\overline{\left(u_i(t) - \overline{u_i}\right)\left(u_i(t+\tau) - \overline{u_i}\right)}}{\overline{\sigma_i^2}} \tag{2.26}$$

This describes the correlation between the velocity at a time t and at a time $t + \tau$. The form of the autocorrelation is shown in Fig. 2.3A. As expected, the correlation drops off with time. A measure of the overall correlation is given by the correlation time and length scales, which are obtained from integrating the autocorrelation

$$T_{ui} = \int_0^\infty R_{ui}(\tau)d\tau \tag{2.27}$$

$$L_{ui} = \overline{u_i} T_{ui} \tag{2.28}$$

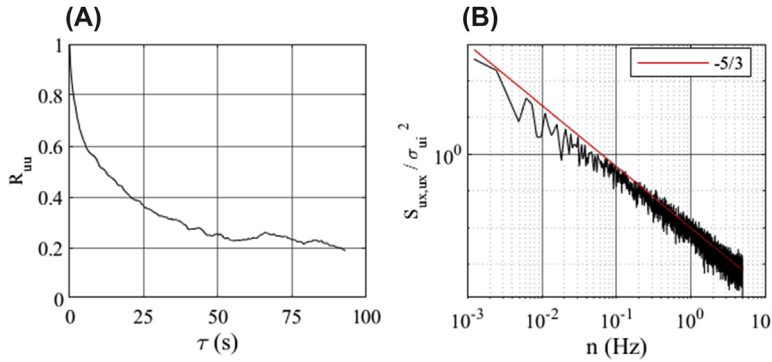

Figure 2.3 ***Autocorrelations and spectra.*** (A) — autocorrelations of wind velocity; (B) — power spectrum of wind velocity.

Clearly, these time and length scales can be defined for any velocity component, or indeed for any pair of velocity components. The ones most often used, however, are those associated with the main, streamwise component of flow. The frequency content within the fluctuating turbulent velocity can then be specified by the power spectrum, which is defined as the Fourier transform of the autocorrelation.

$$S_{ux} = \frac{1}{2\pi}\int_{-\infty}^{\infty}\left(u_i(t)-\overline{u_i}\right)\left(u_i(t+\tau)-\overline{u_i}\right)e^{-i2\pi n\tau}d\tau \qquad (2.29)$$

where n is the frequency. An important property of the power spectrum is that its integral over all frequencies is the variance σ_{ui}^2. Fig. 2.3B shows S_{ux}/σ_{ui}^2 plotted against n, as a log–log plot. At high frequencies, in what is known as the inertial subrange, $S_{ux} \propto (n)^{-5/3}$.

2.11 Atmospheric wind near the ground

Trains rarely run in still air, and some appreciation of the nature of the atmospheric wind is required in a number of areas of train aerodynamics, but particularly in terms of assessing the stability of trains in crosswinds. In this section, a number of basic concepts are set out that will be taken further in Chapter 11 in particular.

The first thing that must be appreciated is that the wind flow near the ground can be caused by a number of quite different meteorological phenomena. The most important storm types that result in high wind speeds near the ground are tropical and extratropical cyclones. Both of these cause high winds over periods of many hours and spatial distances of hundreds of kilometres, although the nature of their formation is completely different (Cook, 1985). These will be discussed first in what follows. In addition a range of small scale but high intensity storms can occur, and in particular thunderstorm downbursts and tornadoes. These will be briefly discussed in what follows.

With regard to the large-scale storm systems, perhaps the first thing to appreciate is that they contain energy over a wide variety of scales. This is illustrated in the well-known Van der Hoven spectrum (Fig. 2.4), which shows the energy content in extratropical cyclones over a very wide frequency range. It can be seen that there are two major peaks – one at a frequency of around 2×10^{-6} Hz, which represents the large-scale depressions passing over the site every few days (the macrometeorological winds), and one at 10^{-2} Hz which represents the mechanical turbulence

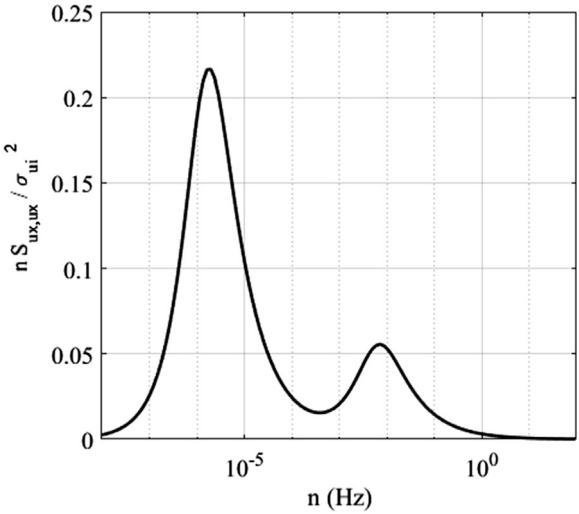

Figure 2.4 *Van der Hoven spectrum.*

within the boundary layer (the micrometeorological winds). Between them, there is the spectral gap, with little turbulence energy, at frequencies corresponding to around 1 hour, the existence of which implies that the macro- and micrometeorological winds can be treated separately. Similar conclusions can be drawn for the frequency content of tropical cyclones. This independence is extremely useful and allows separate consideration of hourly mean wind speeds (which specify the macrometeorological winds) from the shorter period gust speeds. Note that, the turbulence spectrum shown in Fig. 2.3 represents the high frequency end of the micrometeorological peak.

Consider first the hourly mean wind speeds. The cumulative probability distribution function $F(\overline{u}_x)$ that the hourly mean wind speeds will have velocity less than $\overline{u}_x$ (which is clearly important in any risk analysis that requires the identification of high wind conditions) is given by the Weibull distribution.

$$F(\overline{u}_x) = 1 - e^{-\left(\frac{\overline{u}_x}{\lambda}\right)^{\kappa}} \tag{2.30}$$

Here λ and κ are the Weibull scale and shape factor, respectively, whose values can be found from meteorological data. A typical distribution is shown for a 50-year time series of hourly mean values at Eskdalemuir in the north-west of England in Fig. 2.5.

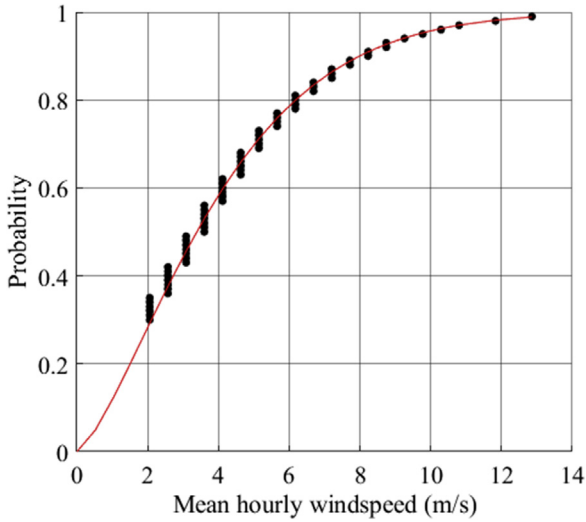

Figure 2.5 ***Weibull distribution for Eskdalemuir.*** $\kappa = 1.4$, $\lambda = 4.4$ m/s.

This expression is not fully adequate to describe the statistical nature of the macrometeorological wind speeds, and some way of describing the extreme values (the high velocity tail of the Weibull distributions) is also required. For this, we use an extreme value distribution and define the probability $P(\overline{u}_x)$ as the probability that the hourly mean wind speed will be exceeded at least once in a specified time period (usually 1 year). The most frequently used distribution is the Fisher–Tippett type 1 (or Gumbel) distribution.

$$P(\overline{u}_x) = 1 - e^{-e^{(\overline{u}_x - m)/d}} \tag{2.31}$$

where m is the mode of the distribution and d is the dispersion that can be obtained from an extreme value analysis of meteorological data. A methodology for fitting data to this curve is given in Cook (1985). A typical plot of the distribution, again for the Eskdalemuir time series, is shown in Fig. 2.6 in the conventional double exponential form. The mode for these data is around 16 m/s (the value of y at $x = 0$).

Now the train-operating environment is at the bottom of a very thick boundary layer – the atmospheric boundary layer, which is usually of the order of 1–2 km in depth. The hourly mean wind speeds will thus vary with height above the ground, surface roughness, topography, etc. Near the

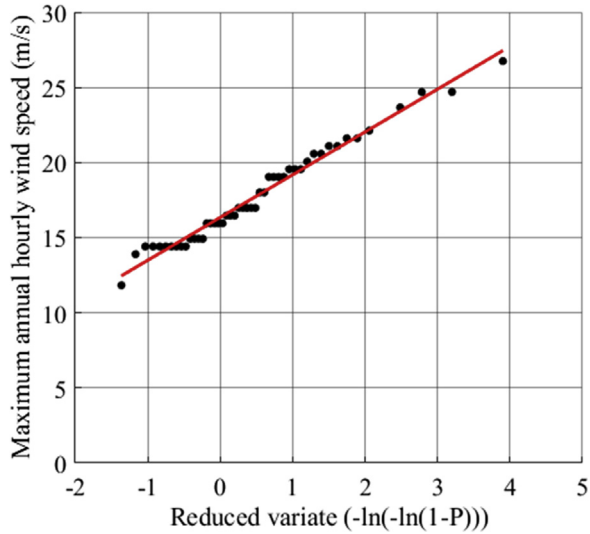

Figure 2.6 ***Gumbel distribution for Eskdalemuir.***

ground, in open country, the logarithmic law for boundary layers applies for the hourly mean wind speeds, i.e.,

$$\frac{\overline{u_x}}{u_\tau} = \frac{1}{k_{VK}} ln\left(\frac{z - z_d}{z_0}\right) \tag{2.32}$$

This is a slightly modified version of Eq. (2.13), to include the displacement height z_d, the height of the virtual ground plane. Typical curves are shown in Fig. 2.7A for a range of typical surface roughness values. Note that for low roughness, the velocity near the ground is faster than for high roughness. It should be noted that the terrain near railway tracks is rarely open and flat, and there are usually surrounding buildings and topographical features that have to be allowed for in determining the wind environment relative to any particular train.

Now consider the micrometeorological wind speeds, i.e., the turbulence gusts. In a neutral atmosphere (where thermal effects are not of significance), the streamwise, turbulence near the ground is given by

$$\sigma_{ux} = \frac{1}{k_{VK}} u_\tau \tag{2.33}$$

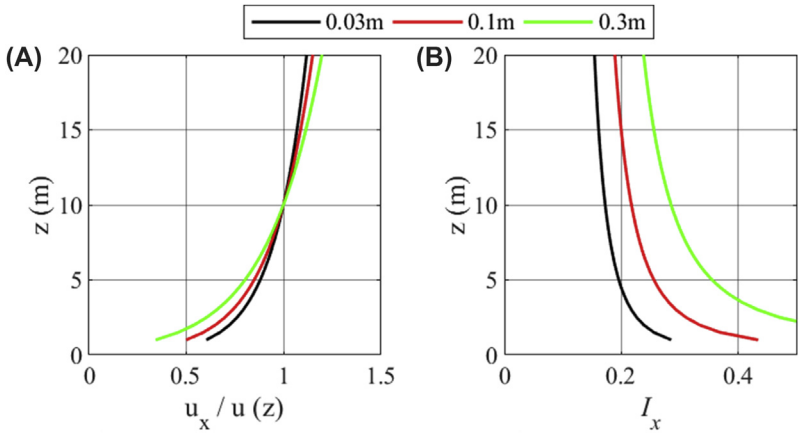

Figure 2.7 (A) Velocity profiles, (B) Turbulence intensity profiles.

Thus, the turbulence intensity that describes the magnitude of the short-term gusts is given by

$$I_x = \frac{\sigma_{ux}}{\overline{u_x}} = \frac{1}{ln\left(\frac{z - z_d}{z_0}\right)} \tag{2.34}$$

Typical values of I_x near the ground for rural and suburban terrains are shown in Fig. 2.7B. As expected, the values of turbulence intensity near the ground are higher for high roughness values than for low roughness values.

The scale of turbulence can be obtained from a consideration of the wind power spectrum. For near ground atmospheric flow, the von Kármán spectrum is a good approximation to the micrometeorological power spectrum of Fig. 2.3 (Fig. 2.8).

$$\frac{nS_{ux}}{\sigma_{ux}^2} = \frac{4\left(\frac{nL_{ux}}{\overline{u_x}}\right)}{\left(1 + 70.8\left(\frac{nL_{ux}}{\overline{u_x}}\right)^2\right)^{5/6}} \tag{2.35}$$

Here n is a frequency and L_{ux} is the streamwise turbulent length scale. The peak of the spectrum is at $\left(\frac{nL_{ux}}{\overline{u_x}}\right) = 0.146$ from which L_{ux} can be calculated. Typical values of L_{ux} near the ground are around 100–200 m.

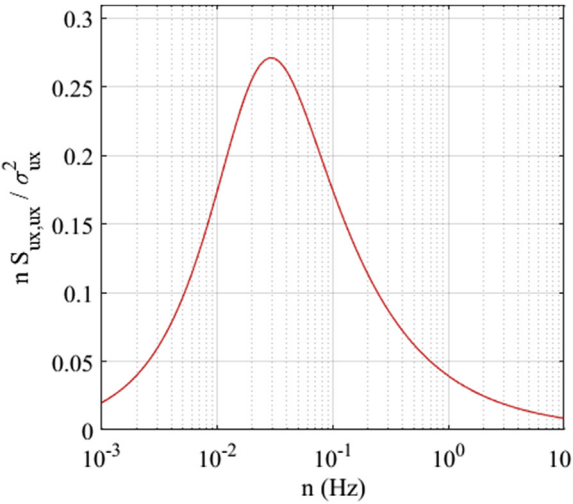

Figure 2.8 ***The von Kármán spectrum*** $\left(L_{ux} = 100\text{ m},\ \overline{u_x} = 20\text{ m/s}\right)$.

The lateral and vertical length scales L_{uy} and L_{uz} are much smaller — of the order of 10—20 m close to the ground.

In addition to the large-scale wind systems considered above, there are other shorter, but intense, meteorological events that can cause strong winds — in particular thunderstorms (downbursts) and tornadoes (Fujita, 1981). Often these are associated with convective conditions in the atmosphere. Thunderstorms, for example, can result in transient high velocity downbursts that impinge on the ground and then spread out in a radial direction. Complete thunderstorm events may only last a few minutes. Tornadoes by contrast are composed of a high intensity swirling flow with a central updraft. For both of these types of flow, research into their structure and the effect they have on buildings/vehicles, etc., is still in its infancy, and they will not be considered to any great extent in what follows, although in Chapter 11 some examples will be given for overturning incidents in which such wind systems were suspected of being of significance.

CHAPTER 3

Testing techniques

3.1 Full-scale testing

3.1.1 Instruments and data acquisition

Full-scale testing is, as one might expect, complex and difficult. The organisational aspects of such trials, in terms of train, track and human resource availability, are far from straightforward, and, as noted in Chapter 2, the aerodynamic environment near the ground is 'dirty', and the interpretation of results thus made is difficult. Nonetheless, full-scale measurements are real, with no modelling assumptions and, for all their difficulty, form a baseline against which the results of all other techniques can be judged.

The standard tools used for such measurements are two or three component sonic anemometers to measure wind and slipstream air speeds (Fig. 3.1A); static pressure probes and solid-state pressure transducers to measure pressure time histories (Fig. 3.1B) and, where required, accelerometers to measure aerodynamic forces and displacements (Fig. 3.1C).

The use of such instruments for specific measurements will be considered in the following chapters. Here, we will simply make some important, but general points.

- Care needs to be taken with positioning, calibration and accuracy. Positioning is usually measured in relation to the centre of the track for infrastructure measurements, and close liaison with the infrastructure owner will be required to gain the necessary permissions for the installation of the equipment. Obviously, the position of on-train instrumentation needs to be specified as tightly as possible, although there are often practical issues with the train construction that necessitate some compromise in instrument position.
- Most instrumentation comes with a factory calibration that can be expected to vary little over the lifetime of the equipment. Nonetheless, it is basic good practice to ensure that there is a regular calibration routine in place to check the factory calibrations.

Train aerodynamics
ISBN 978-0-12-813310-1
https://doi.org/10.1016/B978-0-12-813310-1.00003-4

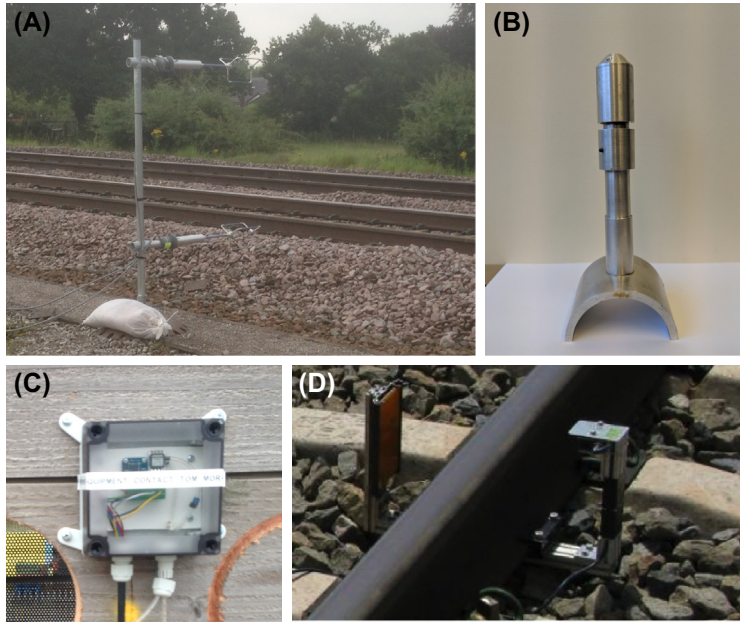

Figure 3.1 ***Full-scale measurement instrumentation.*** (A) Sonic anemometer at trackside, (B) pressure measuring probe, (C) pressure transducer and accelerometer mounted on wall at trackside and (C) light gates.

- Most instruments will have a specified uncertainty, often as a percentage of the maximum reading, and care needs to be taken to ensure that measurements are made in the instrument range where the uncertainty is small in comparison to the measured values.
- Care should be taken to set an appropriate sampling frequency. For trackside measurements, this should be as high as possible to obtain sufficient spatial resolution as trains pass and to capture the frequencies of interest in the measured data. For example, for trackside measurements, with a train moving at 80 m/s, a sampling rate of 100 samples/second results in a sample every 0.8 m along the train, which is rather coarse for some applications. If a sample is required every 0.25 m, then a sampling rate of 320 samples/second is needed; and if a yet tighter spatial resolution of 0.1 m is required, then a sampling rate of 800 samples/second is needed. Similar considerations are valid for on-train measurements.
- Measurements of meteorological conditions are often required, using standard meteorological instruments to measure reference environmental conditions. Such equipment should be positioned well away

from the train, but ideally the data should be collected in a way that can be synchronised with the more detailed trackside or on-train data.

- For trackside measurements, train position and velocity are normally required, usually using light gates mounted to the trackside that can identify the passing of the train (Fig. 3.1D). However, it has been found that measurements of the train head pressure pulse at a number of pressure tappings along the track can be used to measure the train speed, by measuring the time lag between the pressure maxima at individual probes (Quinn et al., 2010). Tube length for all probes needs to be the same to ensure that there are no issues with pressure signal lag and attenuation.

3.1.2 Data analysis

For trackside measurements, it is usually found that the results obtained are, for a given train type, variable between train passes for a number of reasons: slight changes in train geometry (this is particularly the case with freight trains where the consists can be very variable); changes in environmental conditions, such as crosswinds; and, perhaps most importantly, because each set of measurements is a realisation, from the point of view of a stationary observer, of a very unsteady turbulent flow field around the train. This has led to the concept of ensemble averaging of experimental results. The time histories of velocity or pressure for a large number of train passes are determined, and the measured parameters for each run are non-dimensionalised. The results for each of the runs are then averaged at discrete time/distance positions relative to the nose of the train (Baker et al., 2001). Typical results for such a process for slipstream velocities are shown in Fig. 3.2. These are from the measurements made on a 200m long S103 train for the recent AeroTRAIN experiments (Baker et al., 2014c). The individual runs and the ensemble average and standard deviations are shown, all normalized by train velocity. The run-by-run variation can be seen to be very significant indeed — but this is largely a function of the physics of the phenomenon rather than any experimental error. Note that, there are some flow regions where the uncertainty is very large in relation to the mean value, particularly in the region just behind the train, where the mean velocity also peaks. In general, it is found that around 20 runs are required to obtain stable averages for velocity fields, but only a small number (around three) to obtain stable averages for pressure transients.

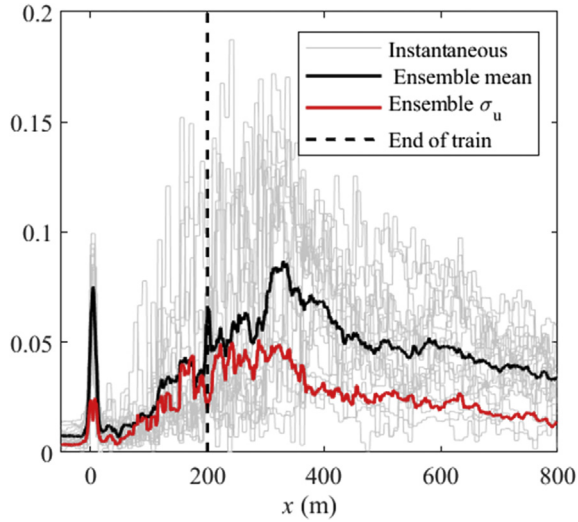

Figure 3.2 ***Ensemble average slipstream results for S103 (Velaro) using data from AeroTRAIN project.*** Measurements at height of 1.2 m above the rail, 3 m from the centre of the track.

3.2 Physical model testing

3.2.1 The purpose of physical models

In an ideal world, any detailed information regarding the flow field around trains and/or the corresponding wind-induced forces and moments would be ascertained from a series of full-scale experiments. However, as outlined in Section 3.1, full-scale experiments are not without their issues. They are relatively expensive, in terms of the time taken for the experiments themselves, as it may take a long time to ensure that the appropriate atmospheric conditions occur. This has a corresponding potential impact on the operation of existing rail networks. Thus, attention has frequently been turned to small-scale physical simulation, for example, wind tunnels. However, it is important to note that by their very nature, such simulations simplify the natural conditions and thus cannot hope to capture the true variability that is found in nature. They are only models of a complex process, which do not necessarily match reality. The common use of wind tunnels over the years has resulted in this warning being frequently neglected. Notwithstanding this fundamental drawback, significant progress has been made in train aerodynamics through the use of wind tunnels and the various other physical modelling techniques that will be considered in the following sections.

3.2.2 The effect of Reynolds number

It is possible, through the use of dimensional analysis, to demonstrate that the forces acting on train are a function of the Reynolds number (Section 2.2). The relatively small size of wind tunnels and the corresponding low speeds that are generated inevitably results in a mismatch between the Reynolds number at full scale ($\approx 10^6$–10^7) and that at model scale ($\approx 10^5$). This Reynolds number mismatch can particularly affect flow in separation regions. However, it is often assumed that bluff bodies such as trains are insensitive to Reynolds effects because the geometry of the train governs where flow separation tends to occur. Thus, as long as the Reynolds number is at least above $\sim 2 \times 10^5$, based on train height, for the results obtained in a model simulation, it is generally assumed that the results of wind tunnel tests can be applied to full scale. Caution is needed in this regard however. Hoxey et al. (1998) demonstrated that the surface pressure coefficients of a 1:100 model portal-framed structures compared with similar full-scale structure can vary significantly, i.e., up to 35% in the range of Reynolds number from 10^5 to 10^7. These large differences were observed to occur in regions of flow separation. Extending this work further, Lim et al. (2007) considered the surface pressure distributions of 1:25 and 1:75 cubes with those at full scale (i.e., Reynolds number varied in the range of 2×10^4–2×10^6). It was noted that in region of high flow separation, Reynolds number dependency was not significant in the mean parameters but could be observed in the higher-order statistics, i.e., the standard deviation of pressure coefficients. Similarly, Larose and D'Auteuil (2006, 2008) describe force measurements on rectangular prisms, which show Reynolds number effects up to values of 10^6. Work on model trains by Niu et al. (2016) also demonstrated some small Reynolds number dependency for force coefficients up to a value of 8×10^5. It was noted that this dependency also appeared to be a function of the yaw angle (the angle of the wind relative to the direction of travel of the train) which is perhaps not too surprising because the yaw angle governs the flow separation and thus the vehicle induced vorticity in the downstream flow. Thus, although for most purposes the conventional assumption that Reynolds number effects in physical models can be ignored if the model Reynolds number is greater than around 2×10^5 is probably adequate, the possibility that such effects might be present should be borne in mind.

3.2.3 Different types of simulation

There are two basic choices to be made in the specification of physical model tests. Namely,

- whether or not to attempt to model the relative motion between the ground and the train, either through the use of moving ground planes or by the use of moving models and
- whether to use a low turbulence, uniform onset flow or to simulate the atmospheric boundary layer.

Consider first the effect of the relative motion between the ground and the train. If a static model is used, the train will need to either be mounted on the wind tunnel floor on some simulation of railway track or, if a uniform onset flow is required, on a suitable ground board to minimize the size of the wind tunnel boundary layer ahead of the model. This will result in an underbody flow that is not at all representative of the real situation, because the flow in that region will be more like the flow in a pipe rather than the flow under a real train (see Chapter 5). For long stationary models with five to ten coaches, the boundary layer growth along the ground plane is considerable and at the rear of the train is very unrealistic. Nonetheless, such simulations are very straightforward and easy to set up (for example, Kwon et al., 2010). They are often used to investigate issues associated with train components away from the ground, where the correct simulation of underbody flow is not important, particularly for the leading car of the train. Such experiments are also used to measure crosswind forces, with the angle between the train model axis and the wind tunnel axis being taken as the yaw angle, the wind direction relative to the train. A comprehensive specification for setting up such tests is given in CEN (2018), and an example of such a test, albeit with a non-standard ground simulation, is shown in Fig. 3.3A.

As an alternative to fixed ground simulations, standard wind tunnels can be used with a moving belt (Kwon et al., 2001). The high length/height ratio of the train results in a number of issues, in particular the practicality of fitting a full model train (which is by definition long and thin) into a wind tunnel and of holding it in position a short distance above a moving ground plane. Such simulations can only properly be used for zero yaw angle conditions and are thus not suitable for crosswind measurements as the relative flow velocities between the wind and the ground will not be representative of the full-scale situation. In the past, the main use of such techniques has been for the measurement of train drag — Fig. 3.3B.

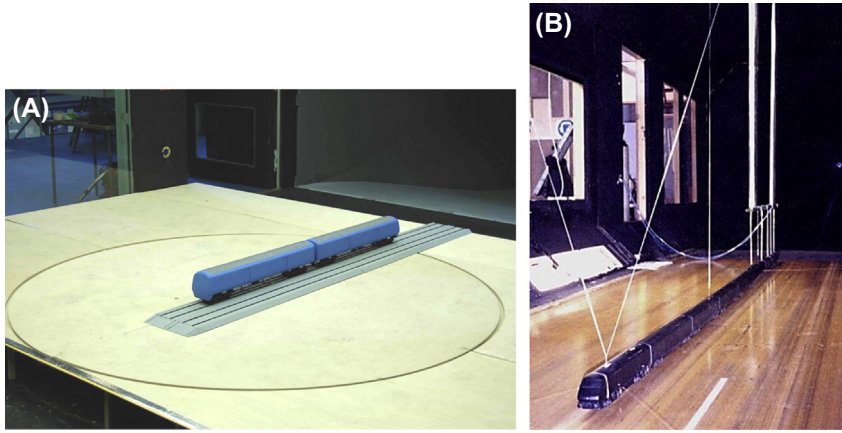

Figure 3.3 ***Stationary model wind tunnel tests with and without a moving ground.*** (A) — Class 321 force and moment measurement tests in BMT wind tunnel; (B) — moving ground aerodynamic drag on Class 43 HST in University of Southampton wind tunnel. *(A) © Copyright 2007 Rail Safety and Standards Board. Project No. 43762/00 Wind Loads on Trains, (9 July, 2007). Used with permission.*

More recently, moving model tests have been used, which more correctly model the train underbody flow, but at the expense of greatly increased experimental complexity. Further details of such experimental rigs are given in Section 3.2.5. These can be used to investigate a range of effects — pressure transients in tunnels, slipstream effects, transient loads on structures, etc., which will be considered in later chapters. Crosswind forces can also be measured through the generation of a flow across the track.

When the effects of crosswinds are being studied, consideration needs to be given as to whether the atmospheric boundary layer should be simulated. The nature of the flow near the ground has been discussed in Section 2.11, and expressions are given for the velocity profile, the turbulence intensity profile and the power spectrum. Fig. 3.4 shows a vector diagram of wind and train velocities.

The wind velocity relative to the train, $V(h)$, is given by

$$V(h)^2 = \left((u(h)cos(\beta) + v)^2 + (u(h)sin(\beta))^2\right) \tag{3.1}$$

where $u(h)$ is the mean velocity defined at some reference height h, often taken as 3 m, v is the train velocity and β is the wind direction. The angle of the wind relative to the train is given by the yaw angle ψ.

$$\tan\psi = \frac{u(h)\,\sin(\beta)}{u(h)\,cos(\beta) + v} \tag{3.2}$$

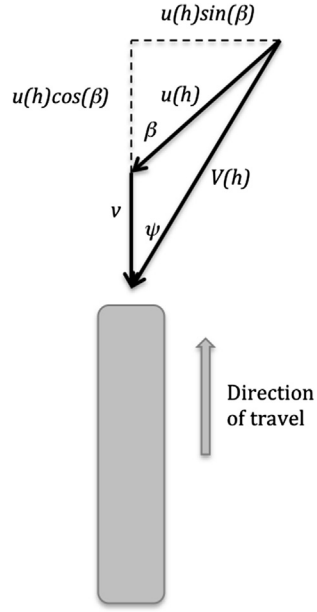

Figure 3.4 Wind vector diagram.

The shear can be characterised by the dimensionless shear relative to the train and is given by

$$R_S = (V(z_1) - V(z_2))/V(h) \tag{3.3}$$

where z_1 is the height of the top of the train (say 5 m), z_2 is the height of the bottom of the train (say 1 m) and h is a reference height. The turbulence intensity relative to the train is given by

$$I_R = I_u(h)u(h)/V(h) \tag{3.4}$$

Cooper (1984) derives the following formula for turbulence length scale relative to the train:

$$L'_{ux} = L_{ux}\left(\vartheta + \left(2\frac{L_{uy}}{L_{ux}}\right)^2(1-\vartheta)\right)^{0.5} \tag{3.5}$$

where

$$\vartheta = \left(\left(\frac{v}{V(h)}\right)\cos(\beta) + \left(\frac{u(h)}{V(h)}\right)\right)^2 \tag{3.6}$$

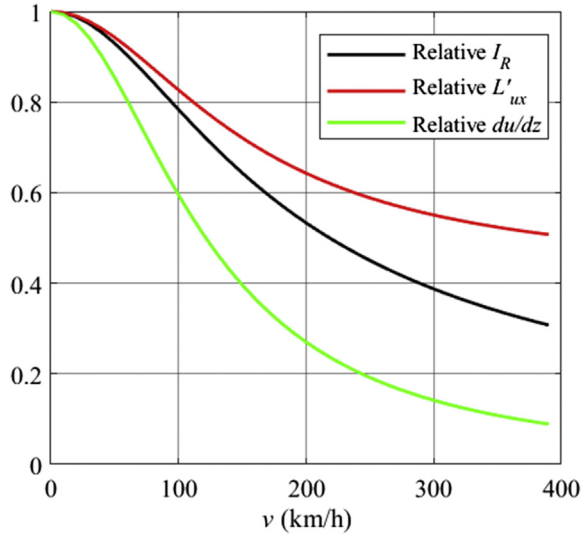

Figure 3.5 ***Atmospheric parameters relative to a moving train.***

Based on Eqs. (3.1)−(3.6), it is instructive to consider the wind as seen by the moving train. This is illustrated in Fig. 3.5 below, for a 30 m/s crosswind normal to the track ($\beta = 90°$). The shear, turbulence intensity and turbulence length scale are plotted against vehicle speed, each parameter normalised by the value at zero vehicle speed. It is clear that the shear, turbulence intensity and length scale as seen by the train all fall significantly as the vehicle speed increases. Using these results, it is possible to make a judgement as to whether or not the atmospheric boundary layer should be simulated in stationary model wind tunnel tests to measure crosswind forces. On the basis that if these ratios are high an atmospheric boundary layer simulation should be used, and if they are low a low turbulence simulation may be used instead, then it seems that for trains travelling at less than about 200 km/h atmospheric boundary layer simulations are most appropriate and for trains travelling above that value, low turbulence tests are sufficient. Of course, moving model tests with the correct atmospheric simulation is the most realistic case, if the most difficult to realise in practice.

3.2.4 Simulation of atmospheric boundary layers

As noted in the last section, to obtain realistic results in stationary wind tunnels for trains travelling at 200 km/h or less, the appropriate atmospheric

conditions need to be simulated. Thus, the approaching wind needs to have the appropriate flow profile – both in terms of mean quantities and turbulence statistics. To simulate this, a variety of passive or active mechanisms can be used. Typical passive mechanisms include the use of spires at the start of the wind tunnel section and roughness elements upstream of the model train. These devices essentially aim to create shear and vorticity within the flow, which lead to the development of suitable boundary layer velocity and turbulence intensity profiles with a suitably scaled turbulent length scale. Although guidance is available concerning the generation of appropriate profiles, the placement of the roughness elements and/or their size is likely to be a process of trial and improvement (ASCE, 2012). A typical setup is shown in Fig. 3.6.

Alternatively, active devices can be used. These are typically restricted to direct control of the fans and involve using a wind velocity time series obtained at full scale to drive the rotational speed of the fans (Sterling et al., 2003). This approach has the benefit of simulating the low frequency component of the wind and thus ensuring that power spectra generated in the wind tunnel and that obtained at full scale have the potential to match over a larger frequency range, thus increasing the likelihood simulating more realistic gusts.

Figure 3.6 ***Typical atmospheric boundary layer simulation.*** University of Birmingham wind tunnel showing multiple fans and floor roughness elements.

In reality, a combination of active and passive methods will result in the best approach, but given the usual physical confines of the wind tunnel, there will be a limit to vertical and lateral turbulence length scales and corresponding power spectral densities that can be simulated. Whatever method is used, the simulation of the correct level of turbulence is of paramount importance. More details of atmospheric boundary layer simulation in a railway context can be found in RSSB (2009).

3.2.5 Moving model experiments

In recent years, a number of moving model experiments have been developed where either the ground plane is moved relative to a stationary train or (more realistically) a model train is propelled at speed down a track. Baker (1986) and Howell (1986) led the field in such simulations with low vehicle speeds work to investigate crosswind forces. Research undertaken at the Politecnico di Milano (Bocciolone et al., 2008) led to the successful integration of a realistic atmospheric boundary layer simulation with a moving train. A ramp was used to accelerate a 1:20 scale model train to approximately 4 m/s, along a straight track, 4.5 m long (Fig. 3.7A).

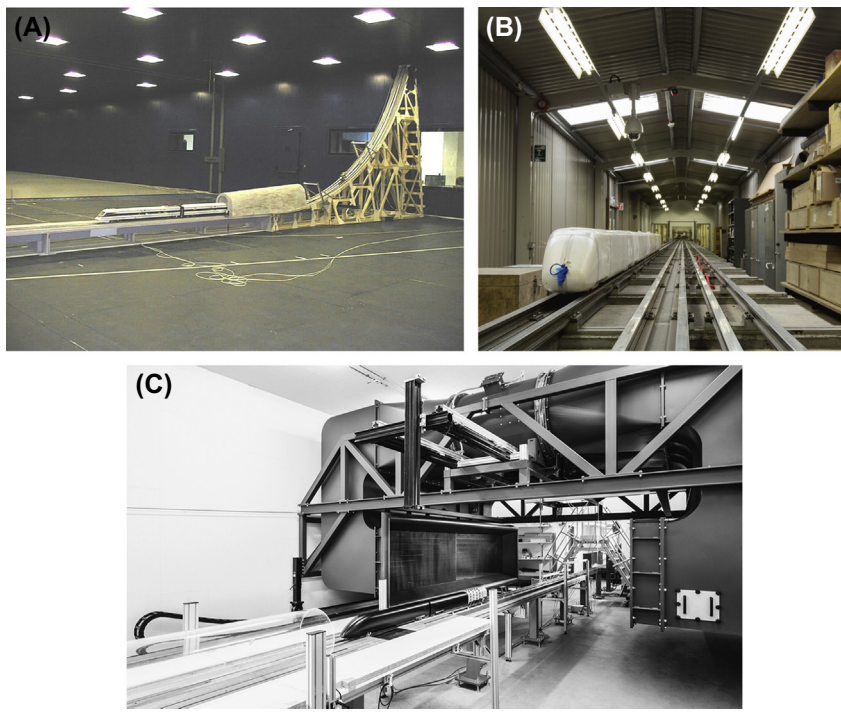

Figure 3.7 ***Moving model rigs.*** (A) — Politecnico di Milano, Italy (used with permission); (B) — University of Birmingham; (C) — DLR, Germany (used with permission).

Unfortunately, the limited speed resulted in a relatively low Reynolds number, and track-induced vibrations apparently resulted in mechanical noise with respect to the on-board force measuring system. A much larger scale system is the TRAIN (Transient Railway Aerodynamic Investigation) rig originally built by British Rail Research at the end of the 1980s — Fig. 3.7B. For a description of the rig, see Soper et al. (2014). The TRAIN rig consists of three parallel straight tracks of length 150m which are equipped with a mechanical propulsion system that can catapult 1:25 scale models at speeds of up to 75 ms^{-1}, i.e. Reynolds numbers of $\sim 5 \times 10^5$. The Mach numbers (the ratio of the vehicle speed to speed of sound) are thus representative of those at full scale, which is a requirement for the measurement of tunnel pressure transients. Similar rigs have been developed in China (Zhou et al., 2014; Yang et al., 2016) and Germany (Heine et al., 2013; Bell et al., 2015). The latter is shown in Fig. 3.7C. Rather different types of moving model tests are described in Doi et al. (2010) in Japan who developed a short, but very high speed (500 km/h) rig powered by compressed air; and Gil et al. (2010) who studied the flow around trains on a 4 m-diameter rotating rig.

3.2.6 Simulation of non-synoptic winds

The above discussion has been restricted to synoptic (boundary layer) winds, which can be regarded as stationary, i.e., the properties of the flow do not change over time at time scales that are of relevance to the flow around trains. This stationarity approximation does not hold for many short-term nonsynoptic events, e.g., thunderstorm downburst and tornadoes. Unlike boundary layer winds, there is at present no general consensus on the best way to simulate such events, although a number of downburst and tornado generators have been built — (Mishra et al., 2008; Refan and Hangen, 2018; Tang et al., 2018) — see Fig. 3.8 for examples from the University of Birmingham. Furthermore, the issue of scaling is an open question and one which (again at the time of writing) is subject to considerable debate with the academic community. It is thus hardly surprisingly that few attempts have been made to simulate trains is such environments (because the scaling associated with the train introduces yet another layer of complexity). However, there is growing awareness of the importance of nonsynoptic events and even videos on social media showing trains overturning as a result of tornadoes. Preliminary modelling work in this area has been reported by Suzuki et al. (2016a,b) and most recently by Bourriez et al. (2019), where pressures were measured on a 1/25th scale train moving through a tornado vortex generator.

Figure 3.8 ***Downburst and tornado generators.*** (A) — University of Birmingham downburst generator; (B) — University of Birmingham tornado vortex generator.

3.2.7 Instrumentation

Physical model tests are undertaken both to measure the nature of the flow around trains and also to measure the forces on the train itself, or the forces induced by the movement of the train on trackside infrastructure. Hence, the ability to be able to quantify both velocities and forces is of importance, and we will consider these in turn.

Velocity can be measured in a number of ways with differing levels of complexity. The simplest way is through the use of a pitot-static tube (also known as a Prandtl tube) which consists of two concentric tubes: the inner tube, open at the end, measures total pressure, whereas the outer tube, with holes around the circumference, measures static pressure. When connected to a suitable pressure transducer or manometer, the dynamic pressure and hence the velocity can be obtained from the difference between the total and the static pressure (Fig. 3.9A). Such devices have stood the test of time and are relatively insensitive to small changes in the direction of the approaching flow. However, they are unable to measure more than one component of velocity and are thus unable to determine the flow angle. A rake of these probes used to measure velocities beneath a train is shown in Fig. 3.9B.

To measure more than one component of velocity, recourse is often made to hot wire anemometers. Such devices have a series of thin wires, which are heated to a specific temperature and relate the rate at which the wires cool to the air velocity. The principles on which they are embodied are relatively straightforward, and a high degree of accuracy can

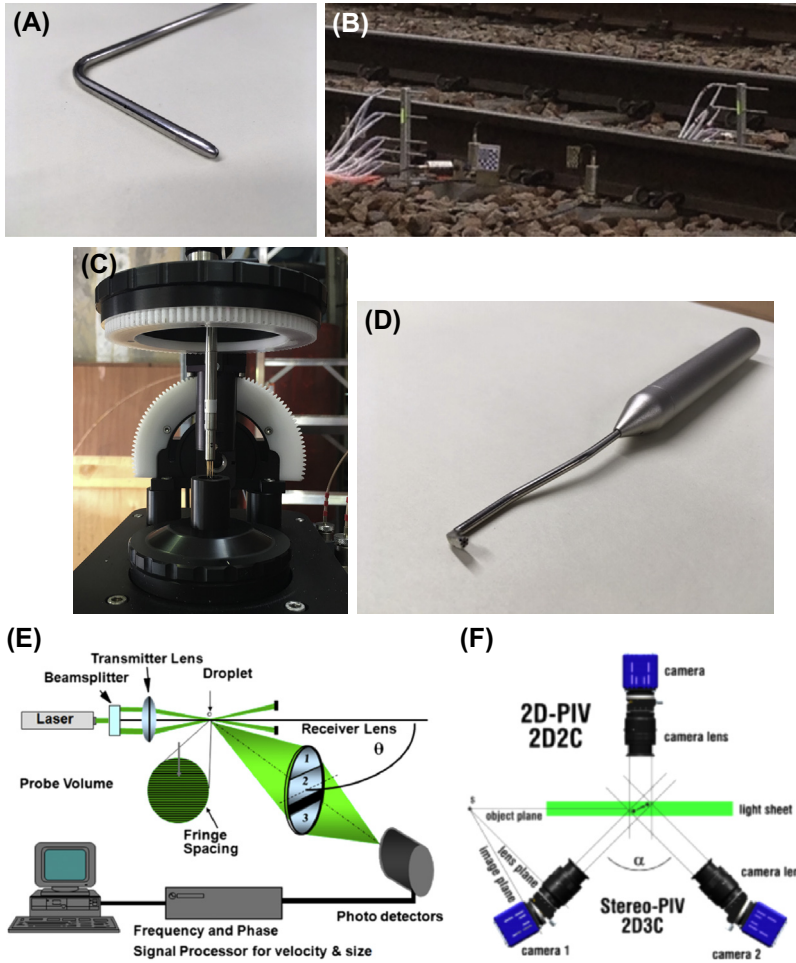

Figure 3.9 ***Velocity measurement probes.*** (A) pitot-static tube, (B) rake of pitot-static tubes at trackside, (C) hot wire anemometer in calibration rig, (D) multihole probe, (E) laser Doppler anemometer and (F) particle imaging velocimetry. *(E) and (F) used by permission of LaVision GmbH.*

be obtained (Fig. 3.9C). The use of probes with multiple wires at different angles to the flow allows two or three velocity components to be measured.

However, hot wire anemometers tend to be rather delicate and, as such, care needs to be undertaken when handling them. A more robust device which also enables more than one component of velocity to be obtained is a multihole probe (Fig. 3.9D) Such probes work on similar principles to

pitot-static tubes but have a number of holes (typically five, although there is at present no fixed standard) arranged at a variety of angle to the approaching flow and connected to a series of pressure transducers. By combining the results obtained from each hole, the three components of velocity can be determined. The number of holes and the angle at which they are placed with respect to the oncoming flow tends to govern their ability to measure the approaching flow, i.e., if the flow approaches from too large a flow angle (relative to the main axis of the probe), then a zero wind speed will be recorded. This flow angle limitation tends to be manufacturer specific. To circumvent the flow angle issue mentioned above, a variety of probes are available which are able to measure the flow from almost any direction (often referred to as 'omniprobes'). Such probes usually have a large number of holes, which are in turn connected to a series of pressure transducers.

Although hot wire anemometers and multihole tubes are small (typically, $\sim 1-5$ mm), they need to be directly inserted into the flow field into which they are measuring and as such have the potential to influence the flow. Laser Doppler anemometry (LDA) and particle image velocimetry (PIV) are two nonintrusive methods that enable the flow field to be measured. LDAs typically work by crossing two beams of lasers to create a measurement volume (Fig. 3.9E). Within this measurement volume, interference patterns (or fringes) are generated and as the flow, suitably seeded with very fine, ideally neutrally buoyant particles, crosses the fringes, light is reflected and causes a Doppler shift. The Doppler shift is proportional to the velocity of the seeded particles and thus enables the flow velocity to be obtained. The implicit assumption in this approach is that the seeded particles move at the same speed and in the same direction of the flow.

Similar to LDA, PIV is an optical measurement technique, which relies on the introduction of seeding particles. Unlike LDA, which makes measurements of the time history of the flow at a point, the PIV makes measurements of instantaneous spatial distributions of velocity (Fig. 3.9F). PIV in general involves tracking a number of seeded particles over a given period of time (a function of the frame rate of the optical instrument recording the motion, i.e., the camera) and establishing the distance travelled. From the frame rate and distance travelled, the velocity can be established using special analysis software. Typically, three or four cameras are required, particularly for flow areas of high vorticity, i.e., where the flow is expected to be highly three dimensional.

The overall forces and moments on the train are measured either by a force balance positioned directly below the train or by the measurement and subsequent integration of pressures acting on the train. In many respects, the term force balance is rather outdated and is a leftover from earlier days, where a series of balances and weights were used to measure the force on an object in the wind tunnel. However, these devices have come a long way from their early days and are now highly complex and capable of measuring, at high frequency, forces (and moments) in three mutually perpendicular directions (planes). Force balances are either internal (embedded within the model train) or external (outside the train and possibly outside the wind tunnel). The latter force balances typically interfere with the flow within the wind tunnel, although through careful design this effect can be minimised. However, in general, it is normally easier and quicker to change models using external balances. Modern force balances convert mechanical input (i.e., the forces/moments) into electrical signals, which are subsequently recorded. The conversion of the mechanical input into the electrical is undertaken by sensors, and it is usually a combination of the sensor coupled with the precision of manufacture that governs the choice of balance.

The alternative to directly measure the force is to measure the pressure acting on a train at a number of locations and then to assume that the pressure at a particular point is representative of the area around that point. Thus, by judicious placement of the pressure tappings (i.e., the points at which the pressure is measured), it is possible to gain an understanding of the force (or moment) acting over a number of small areas of the train, from which the overall forces (and moments) acting on the train can be determined. The position of pressure tappings requires careful consideration. For example, in areas which are expected to yield a large pressure gradient (e.g., in areas of flow separation), the spacing between the pressure tappings will need to be relatively small, otherwise the measure of pressure at that location may not be particularly representative of the pressure over a larger area, i.e., the estimate of the force acting on the area around the pressure may be over underestimated. As with most issues in physical modelling, the number of pressure tappings and their location depends on experience, but clearly it is better to use more tappings.

Measuring the pressure at a point is reasonably straightforward; however, there is, in general, one issue that needs consideration, and that is the response time of the pressure measurement system. The response time is simply the time taken for the pressure applied at a tapping to be registered

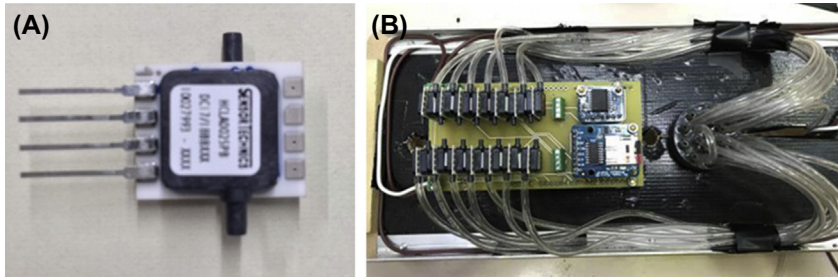

Figure 3.10 ***Pressure transducer system.*** (A) – single pressure transducer; (B) – pressure measurement system mounted within TRAIN rig model.

by the pressure measurement system. Thus, one should aim to place the pressure transducer as close as physically possible to the pressure tapping and, in doing so, minimise the length of tubing between the tapping and the transducer (Fig. 3.10).

Whether to use pressure tappings or a force balance to determine the overall loads acting on a train is very much down to the requirements. Pressure tappings provide a great deal of additional information about the pressure acting on the train and can identify critical/important areas. However, if one is only concerned about the global forces and moments, then there is merit in measuring these directly using a force balance because the pressure tapping approach introduces an additional layer of uncertainty. For a more in-depth discussion of instrumentation used in a wind tunnel, the reader is referred to Barlow et al. (1999).

CHAPTER 4

Computational techniques

4.1 Analytical and computational methods in train aerodynamics

In this chapter we consider a range of numerical techniques that are used in the study of train aerodynamics. In the main, these techniques are based on the Navier–Stokes equations, which can, in principle, be solved for any particular flow geometry. Eqs. 2.1–2.3 set out the two-dimensional unsteady form of these equations, and the incompressible form is presented in Eqs. 2.4–2.6. These equations are closed, i.e., if solved for given boundary and initial conditions, they lead to the pressure and velocity fields in both time and space. However, they are second-order nonlinear partial differential equations and it is only possible to solve these equations analytically for simple flow cases.

That point being made, there are some simple analytical techniques that are of use in the study of train aerodynamics. For example, boundary layer methods based on the boundary layer equations of Section 2.8 can be useful in understanding the flow along the sides and roofs of trains (Sterling et al., 2008) (see Chapter 5). A more complex, but still analytical, boundary layer solution for flow between two moving walls, a Couette flow, will be used in Chapter 9 to consider the underbody flow field and the movement of ballast (Garcia et al., 2011). Analytical potential flow methods (Section 2.9) have been used to predict the flow field around simple train nose shapes and the associated forces on trackside infrastructure, and these will be briefly discussed in Chapter 8 where loads on trackside structures are considered (Sanz-Andres et al., 2004a, 2004b; Barrero-Gil and Sanz-Andres, 2009). The main use of such analytical models is to identify the basic physics of the flow, to help develop a basic understanding of the issues involved and to act as a framework for the consideration of experimental results.

The simplest numerical solutions, for incompressible inviscid flows such as those around train noses, are also based on potential flow solutions to the

Train aerodynamics
ISBN 978-0-12-813310-1
https://doi.org/10.1016/B978-0-12-813310-1.00004-6

equations of motions, in particular, the range of techniques known as panel methods. These methods will be presented in Section 4.2.

The alternative, more complex, way of solving the equations of motion is to appropriately linearise them and then solve the resulting system of linear equations using high-performance computers. This approach has come to be known generically as computational fluid dynamics (CFD). To solve these equations numerically, the first step is to define the computational domain in which to solve for the velocity and pressure fields. The flow conditions at the boundaries of the domain are called the boundary conditions. The computational domain is then discretized into a finite number of computational cells and the solution is obtained for each cell. The linearised form of the governing equations requires that the size of the computational cell is very small, and the flow variables are effectively averaged in space over the computational cell.

There are two approaches for numerically solving the resulting governing equations. The first approach is to average these equations in time and then to solve the resulting equations (Eqs. 2.7–2.9) for each cell. This approach effectively damps out the turbulent fluctuations in time, and no turbulent scales are resolved. This approach is called Reynolds-averaged Navier–Stokes (RANS). By averaging over short time periods, this approach can be extended to capture large-scale unsteady flows using unsteady RANS (URANS). These methods, which are very widely used for all aspects of train aerodynamics, are discussed in Section 4.3.

The other approach is to solve the governing equations directly to resolve all the turbulent scales in the flow. This approach is called direct numerical simulation (DNS). As the spatial averaging associated with the computational grid in such methods means that only turbulent scales larger than the averaging space (or filter width) are resolved, for full DNS the computational cells have to very small, and the resources required for any practical calculations are prohibitively high. Thus the effect of the turbulent scales smaller than the filter width is usually modelled using simple turbulence models. This leads to one approach that solves the full unsteady equations of motion for large turbulence scales, but relies on modelling of the small turbulence scales (large eddy simulation – LES), and to a further approach that uses LES for most of the flow field and RANS-based methods for regions near flow boundaries (detached eddy simulation – DES). These methods are described in Section 4.4.

In Section 4.5, a very different numerical technique is then briefly considered, which solves the Boltzmann equation for interacting fluid

particles rather than the Navier–Stokes equations – the Lattice Boltzmann method (LBM), and in Section 4.6, a range of numerical optimization techniques that have become popular for design in recent years are set out. Finally it should be noted that the descriptions that follow will necessarily be brief and are aimed at applications in train aerodynamics. More detailed descriptions of a range of computational techniques in fluid mechanics can be found in standard texts such as Versteeg and Malalasekera (2007) and Wilcox (2002).

4.2 Panel methods

Around the noses of trains, the flow can be expected to be incompressible, inviscid and irrotational i.e., a potential flow (Section 2.9). For such flows, the velocity field can be expressed with only a scalar function (namely the velocity potential). In these flows, Laplace's equation (Eq. 2.21) can be solved numerically together with the boundary conditions to obtain the velocity potential. Once the velocity potential, ϕ, is obtained, the velocity components can be obtained using Eqs. 2.18 and 2.19. It is worth mentioning here that the Laplace's equation is the simplified form of the conservation of mass (continuity equation) for inviscid and irrotational flow. This means that for potential flow, the velocity field can be obtained using only the continuity equation without the need of the momentum equation. The simplified form of the momentum equation for potential flow (Eq. 2.23) is then used to calculate the pressure field once the velocity field is obtained. This simplicity resulted in potential flow methods being the first numerical methods to be used in train aerodynamics, particularly to investigate the flow around train noses (Khandhia et al., 1996; Berenger and Gregoire, 2001). However, the simplicity of such methods means that they are still useful in optimisation studies, where a large number of different geometries need to be considered, and for which the use of the other computational methods detailed in later sections would be prohibitively expensive.

Laplace's equation is a second-order linear partial differential equation whose solutions are called harmonic functions. The fact that the Laplace's equation is linear is particularly important as the sum of any particular solutions of the equation is also a solution. For example, if $\phi_1, \phi_2, \phi_3 \ldots \phi_n$ represent n separate solutions of Eq. 2.21, then the sum $\phi = \phi_1 + \phi_2 + \phi_3 + \ldots \phi_n$ is also a solution (see Fig. 4.1 for example). This makes it possible to superimpose a number of elementary flows, whose solutions

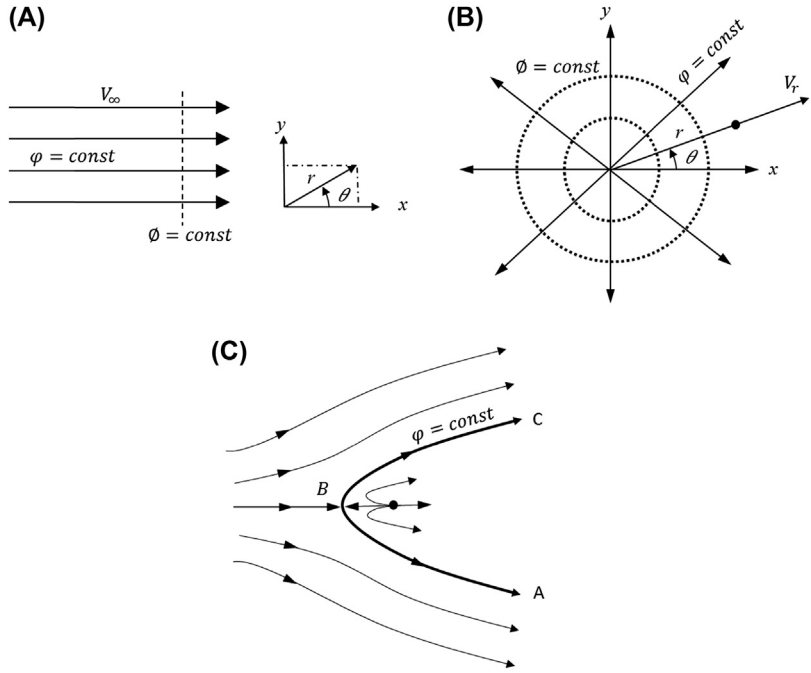

Figure 4.1 ***Superposition of elementary flow in potential flow.*** (A) Uniform flow; (B) line source, (C) addition of (A) and (B).

(velocity potential and stream function φ) are known, such that the resulting flow fields represent practical complicated problems—this is the idea behind the vortex panel method.

The velocity potential and stream function of the uniform flow in Fig. 4.1A can be represented in polar coordinate system as $\phi(r,\ \theta) = V_\infty r\cos\theta$ and $\varphi(r,\ \theta) = V_\infty r\sin\theta$. The velocity potential and stream function of the source flow in Fig. 4.1B in polar coordinate system can be expressed as $\phi(r,\theta) = \frac{\Lambda}{2\pi}\ln r$ and $\varphi(r,\theta) = \frac{\Lambda}{2\pi}\theta$, where Λ is the volume flow rate from the source per unit length. If the uniform flow and the source flow are combined, a potential flow pattern similar to the one in Fig. 4.1C is obtained. A streamline, ABC, is formed over which the flow cannot cross. A wall can be placed over this streamline and the flow will not be affected. The velocity potential and the stream function of the new flow are the sum of those from the uniform flow and the source flow, i.e., $\phi(r,\theta) = u_\infty r\cos\theta + \frac{\Lambda}{2\pi}\ln r$ and $\varphi(r,\theta) = u_\infty r\sin\theta + \frac{\Lambda}{2\pi}\theta$. These functions can then be used in Eqs. 2.18 and 2.19 to obtain u_r and u_θ.

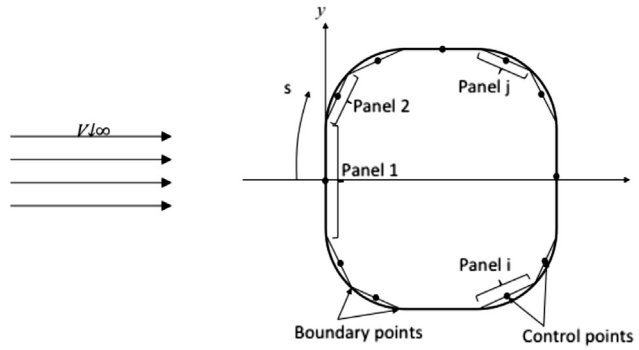

Figure 4.2 Panel methods.

It is, however, not always easy and straightforward to guess the combinations of elementary flows required to model complex flows. Instead the external structure of a complicated geometry, such as a train, is used to obtain the elementary flow around it by dividing the external structure into a number of panels, each panel representing a source sheet (consisting of an infinite number of line sources). Fig. 4.2 represents an example of a two-dimensional cross section of a train subjected to a uniform crosswind of velocity V_∞.

Denote $\Lambda' = \Lambda'(s)$ to be the source strength per unit length along s. The small portion of a panel of length ds has a volume flow rate equal to $\Lambda' ds$. It is assumed that the source strength Λ' per unit length is constant over a given panel, but it is allowed to vary from one panel to the next. The problem now is to find the known source strength Λ' for each panel that gives zero velocity in the normal direction of each panel. Using the superposition principle for the potential flow of number of sources from the panels and the uniform flow, it is straightforward to obtain the velocity potential at the control point of panel i due just to the other sources (i.e., ignoring the free stream crosswind) along the wall to be

$$\phi(x_i, y_i) = \sum_{j=1}^{n} \frac{\Lambda'_j}{2\pi} \int_j \ln r_{ij} ds_j \tag{4.1}$$

where j is the panel number and $r_{ij} = \sqrt{(x_i - x_j)^2 + (y_i - y_j)^2}$.

The velocity normal to the panel at panel i is the derivative of the velocity potential in the direction of the normal unit vector n. This gives

the normal velocity at the centre of panel i due to the sources at the other panel as

$$V_n = \frac{\Lambda_i'}{2} + \sum_{\substack{j=1 \\ j \neq i}}^{n} \frac{\Lambda_j'}{2\pi} \int_j \frac{\partial}{\partial n_j} (\ln r_{ij}) ds_j \tag{4.2}$$

The total normal velocity at panel i is the sum of the normal velocity due to the different sources at the different panels from j to n and the normal velocity due to the uniform free stream velocity. This normal velocity should be zero to satisfy the impermeability boundary condition at the wall of the train. This gives

$$\frac{\Lambda_i'}{2} + \sum_{\substack{j=1 \\ j \neq i}}^{n} \frac{\Lambda_j'}{2\pi} \int_j \frac{\partial}{\partial n_j} (\ln r_{ij}) ds_j + V_\infty \cos \beta_i = 0 \tag{4.3}$$

The angle β_i in Eq. (4.3) is the angle between the direction of the uniform flow and the unit normal direction at panel i.

Eq. (4.2) is one equation in n number of unknowns $\Lambda_1', \Lambda_2', \Lambda_3' \ldots, \Lambda_n'$. Similar equations can be obtained for each panel to create a system of linear equations that can be solved for the source strength at each panel. Once the source strengths are obtained, then the velocity potential and the velocity components can also be obtained. The smaller the panel length, the more accurate the solution will be. It is worth mentioning here that vortex sheets can be used instead of source sheets to account for the vorticity in the boundary layer of the train. If vortex sheets are used, then the method is called the vortex panel method. As this is a two-dimensional method, it can be used for calculating the flow on a train in a crosswind far from the nose (Chiu, 1991). If the nose of the train is to be included, or the wind is acting on the train with an angle other than 90 degrees, then more complex vortex panel methods can be used (Chiu, 1995).

4.3 Reynolds-averaged Navier–Stokes methods

4.3.1 Representation of turbulence

Turbulence is that chaotic state of motion characteristic of high Reynolds number flows. Resolving all the turbulent scales in space and time using DNS (see below) is feasible only for very fundamental and academic problems at very low Reynolds numbers. However, the flow around trains

is characterised by high Reynolds numbers, and resolving all turbulent scales is nearly impossible, even on present-day computers. It is worth mentioning that even if computers were able to solve a more complicated flow in an adequate time, there would still be a need to organise by averaging the huge amount of random data to understand the turbulent flow. It is easier to average the governing equations first and then to solve them afterwards. The time-averaged equations are called the RANS equations and are presented in Eqs. (2.7)−(2.9) for two-dimensional incompressible flow. RANS models are very widely used in train aerodynamics to study a range of problems, and these applications will be described in Chapters 7−12. It should be remembered, however, that these are, in general, steady flow methods, and thus where there is large-scale unsteadiness, this will not be captured by RANS calculations. In particular, in large-scale separated flows, the flow patterns will be time-average patterns, which will not fully represent the conditions found at full scale. Nonetheless, the relative simplicity of RANS models and the fact that they can be run on relatively small work stations make them a popular tool despite their acknowledged drawbacks.

From the point of view of the averaged motion at least, the problem with the nonlinearity of the instantaneous equations is that they introduce new unknowns, the Reynolds stresses, into the averaged equations. For three-dimensional flow, there are six individual stress components we must deal with; to be exact: $\overline{u'^2_x}$, $\overline{u'^2_y}$, $\overline{u'^2_z}$, $\overline{u'_x u'_y}$, $\overline{u'_x u'_z}$ and $\overline{u'_y u'_z}$. The absence of additional equations for these unknowns is often referred to as the turbulence closure problem and it is therefore necessary to model the Reynolds stress terms in some way. There exist mainly two different kinds of turbulence models for this purpose, turbulent viscosity models and Reynolds stress models, and we consider these in turn below (4.3.2 and 4.3.3), before moving on to look briefly at URANS models (4.3.4).

4.3.2 Turbulence viscosity models

The turbulent (or eddy) viscosity models act on the assumption that the Reynolds 'stresses' can be expressed in a similar way to the viscous stress term because they also resist the flow motion in some way − the Boussinesq eddy viscosity assumption. This assumption implies that the Reynolds stress tensor is proportional to the mean strain rate tensor. In tensor form, this leads to

$$-\rho\overline{u'_i u'_j} = \mu_t \overline{S_{ij}} - \frac{2}{3}\rho k \delta_{ij} \tag{4.4}$$

where δ_{ij} is the Kronecker delta, defined as

$$\delta_{ij} = \begin{cases} 1 & \text{if } i = j \\ 0 & \text{otherwise} \end{cases}, \tag{4.5}$$

k is the kinetic energy, expressed as

$$k = \frac{1}{2}\overline{u_i' u_i'}, \tag{4.6}$$

and $\overline{S_{ij}}$ is the mean strain rate defined by

$$\overline{S_{ij}} = \frac{1}{2}\left[\frac{\partial \overline{u_i}}{\partial x_j} + \frac{\partial \overline{u_j}}{\partial x_i}\right] \tag{4.7}$$

In Cartesian form, the term $-\rho\overline{u_x' u_y'}$ is represented as

$$-\rho\overline{u_x' u_y'} = \frac{1}{2}\mu_t\left(\frac{\partial \overline{u_x}}{\partial y} + \frac{\partial \overline{u_y}}{\partial x}\right) \tag{4.8}$$

The turbulent dynamic eddy viscosity, μ_t, in Eq. (4.8) has to be modelled. This term is not a property of the fluid, but a feature of the flow and it depends on position and time.

The simplest approach to specifying the turbulent viscosity is to use Prandtl's mixing length model. In this model, the effective viscosity μ_t is taken as being proportional to the square of a quantity having the dimensions of length, i.e., the so-called mixing length, l_{mix}, multiplied by the absolute value of the local velocity gradient $\nabla\overline{u}$. Thus

$$\mu_t = \rho\nu_t = \rho l_{mix}^2 |\nabla\overline{u}| \tag{4.9}$$

As Eq. (4.9) shows, the mixing length model does not need any extra transport equations to solve for the eddy viscosity and hence this model is called the zero-equation model. The main problem of this model is that there is no universal value for the mixing length and it is very difficult to decide the value for the different types of flows.

Other, more complex, models can be used where the turbulent viscosity is modelled by one or more equations. The most common of these is known as the $k - \varepsilon$ model, which is a two-equation model for the eddy viscosity μ_t. The turbulent viscosity is obtained by using the turbulent

kinetic energy k and the rate of dissipation ε. The turbulent kinetic energy is defined as

$$k = \frac{1}{2}\left(\overline{u'^2_x} + \overline{u'^2_y} + \overline{u'^2_z}\right) \tag{4.10}$$

These variables are determined from transport equations that have the same form for both k and ε and involve convection, diffusion, production and dissipation terms, which involve a number of empirically determined equations. The method effectively assumes that the flow is isotropic, i.e., the turbulence components do not vary with direction. Using dimensional analysis, the expression for the eddy viscosity can be found as follows:

$$\mu_t \propto k^a \varepsilon^b \tag{4.11}$$

Balancing the dimensions on both sides of Eq. (4.11) yields the following:

$$\mu_t = \rho C_\mu \frac{k^2}{\varepsilon} \tag{4.12}$$

where C_μ is the model constant, $C_\mu = 0.009$. The value of this constant has been arrived at by numerous iterations of data fitting for a wide range of turbulent flows.

In addition to the zero-equation model and the two-equation k-ε model, there is a large range of other turbulence models including one-equation models such as the Spalart–Allmaras (S-A) model (see Section 4.4.3 below) and two-equation models such as k-ω and Shear Stress Transport model (SST). Each of these models has advantages and disadvantages. Some of them will work very well to predict the mean flow in certain conditions but fail to predict the flow in another situation. At the present, there is no universal turbulence eddy viscosity model that can accurately predict the mean flow in all kind of engineering problems.

4.3.3 Reynolds stress models

Instead of modelling the turbulence viscosity, Reynolds stress models use the Reynolds stress transport equations to specify the Reynolds stress tensor in the Navier–Stokes equations. This accounts for the directional effects of the Reynolds stresses and the complex turbulent flow interactions.

As such, it is often claimed that Reynolds stress models offer significantly better accuracy than isotropic eddy viscosity–based turbulence models. Each of the six transport equations includes terms for transport of Reynolds stress by diffusion, turbulent pressure–strain interactions and rotations, together with production and dissipation terms. Most of these terms require modelling in some way, although these models are at a more detailed and more universal level than the modelling of eddy viscosity in the approaches outlined in the last section.

4.3.4 Unsteady Reynolds-averaged Navier–Stokes

In RANS modelling, the Navier–Stokes equations are time-averaged, and thus the time derivative disappears from the RANS equations. However, if the equations are averaged over a small time, then the time derivative remains in the equations and the variables in the equations represent the mean quantities during the small averaged time. This is called the URANS. The averaging process over the small averaging time produces Reynolds stresses similar to those in the RANS modelling, and the modelling of these stresses is done in the same way as those of the RANS models.

4.4 Direct numerical simulation

4.4.1 Cell size and time step limits

DNS involves the solution of the governing equations of the flow directly, without any assumptions or simplifications to obtain the exact instantaneous motions. In DNS, the number of equations is equal to the number of unknowns (i.e., four equations for four unknowns u_x, u_y, u_z and p). Now, it is a fact that the minimum turbulent eddy size that can be obtained from a numerical simulation is the size of the computational cell, Δ. Thus to resolve all the scales of the flow in DNS, the cell size should be of the order of magnitude of the smallest scale in the flow, which is given by the Kolmogorov dissipation scale l_K

$$l_K = l_i Re_{li}^{-\frac{3}{4}}, \tag{4.13}$$

where l_i is the integral length scale and Re_{li} is the Reynolds number based on this scale. Thus the number of cells needed for DNS increases with the Reynolds number. The time step, Δt, required by DNS also has to be very small to resolve the flow in time. There are two factors that control the choice of the time step. It should be smaller than the Kolmogorov time scale, τ_K, and to maintain numerical stability and accuracy, the time step

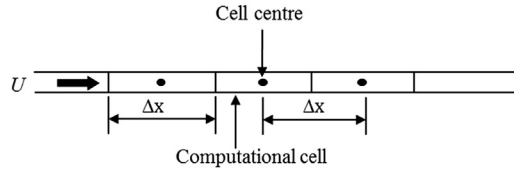

Figure 4.3 One-dimensional discretisation.

should also be small enough that the fluid particles do not move more than one grid spacing in each time step. For the one-dimensional flow shown in Fig. 4.3, this implies that

$$\frac{U\Delta t}{\Delta x} \leq 1 \tag{4.14}$$

where Δx is the spacing between nodes and U is the velocity.

The left hand side of Eq. (4.14) is called the Courant–Friedrichs–Lewy (CFL) number. To satisfy both limits, $\Delta t = min\left(\tau_K, \frac{\Delta x}{u}\right)$. For high Reynolds numbers, the flow is dominated by very fine structures associated with very small scales, and for any practical flow the total number of cells needed to resolve all the scales is very large, and hence the computational cost is also very high. This means that DNS is not feasible at the present time for solving high Reynolds number flow such as the flow around trains. There are, however, hybrid methods available that use DNS for the large-scale turbulence or for parts of the flow field, and some sort of turbulence modelling for small-scale turbulence and other parts of the flow, and these will be discussed in the following sections.

4.4.2 Large Eddy Simulation

LES decomposes the structures of the flow into large and small scales. The large motions of the flow are directly simulated, while the influence of the small scales on the large-scale motions is modelled. LES thus requires less computational effort than DNS, but more effort than RANS. The main advantage of LES over the computationally cheaper RANS approaches is the increased level of detail it can deliver. While RANS methods provide averaged results, LES is able to predict instantaneous flow characteristics and resolve turbulent flow structures. LES also offers significantly more accurate results than RANS for flows involving flow separation.

Now, Kolmogorov's assumptions about the energy cascade in turbulence flows from large-scale turbulence to small-scale turbulence imply that the small-scale structures behave in a universal way independent of the

boundary conditions used. The large flow structure, on the other hand, depends mainly on the boundary conditions and these depend on the problem under consideration. These attributes are the reason why it is useful to model only the small structures and simulate the big ones.

The first step in LES is to filter the equations. The actual velocity, $u(\overrightarrow{x}, t)$, is decomposed into a filtered part $\overline{u}(\overrightarrow{x}, t)$ and a subgrid component of velocity $u''(\overrightarrow{x}, t)$ as

$$u(\overrightarrow{x}, t) = \overline{u}(\overrightarrow{x}, t) + u''(\overrightarrow{x}, t) \tag{4.15}$$

The filtered velocity $\overline{u}(\overrightarrow{x}, t)$ is obtained by filtering the actual velocity as follows:

$$\overline{u}(\overrightarrow{x}, t) = \int G(\overrightarrow{x}, r)u(\overrightarrow{x} - r, t)dr \tag{4.16}$$

where the integration is over the entire flow domain, and $G(\overrightarrow{x}, r)$ is the filter function. The filtered velocity is not the same as the actual velocity field and the difference is the residual $u''(\overrightarrow{x}, t)$.

The equations for the large-scale eddies can be derived through filtering the Navier–Stokes equations. The filtered continuity and momentum equations for two-dimensional incompressible flows are

$$\frac{\partial \overline{u_x}}{\partial x} + \frac{\partial \overline{u_z}}{\partial z} = 0, \tag{4.17}$$

$$\rho\left(\overline{u_x}\frac{\partial \overline{u_x}}{\partial x} + \overline{u_z}\frac{\partial \overline{u_x}}{\partial z}\right) = -\frac{\partial \overline{p}}{\partial x} + \mu\left(\frac{\partial^2 \overline{u_x}}{\partial x^2} + \frac{\partial^2 \overline{u_x}}{\partial z^2}\right) - \rho\left(\frac{\partial Q_{xx}}{\partial x} + \frac{\partial Q_{xz}}{\partial z}\right) \tag{4.18}$$

$$\rho\left(\overline{u_x}\frac{\partial \overline{u_z}}{\partial x} + \overline{u_z}\frac{\partial \overline{u_z}}{\partial z}\right) = -\frac{\partial \overline{p}}{\partial z} + \mu\left(\frac{\partial^2 \overline{u_z}}{\partial x^2} + \frac{\partial^2 \overline{u_z}}{\partial z^2}\right) - \rho\left(\frac{\partial Q_{zx}}{\partial x} + \frac{\partial Q_{zz}}{\partial z}\right) \tag{4.19}$$

where Q_{xx}, Q_{xz}, Q_{zx} and Q_{xz} are the residual stresses.

The smallest eddies that can be resolved in any grid are of the size of the grid spacing. However, the flow includes smaller scales than the resolved ones. The residual stresses are a direct consequence of the filtering process and they compensate for the effect of the unresolved or subgrid-scale eddies on the resolved eddies.

The turbulence models for the residual stresses are analogous to the models used for the Reynolds stresses by RANS. It is known that small

scales tend to be more homogeneous and universal and less affected by the boundary conditions. Thus their models are simpler and require fewer adjustments when applied to different flows. The simplest formulation is the one-equation model proposed by Smagorinsky. It models the subgrid-scale Reynolds stress analogously to the way this is done in the eddy viscosity models. The anisotropic residual stress tensor, Q_{ij}, is related to the filtered rate of strain $\overline{S_{ij}}$ as $Q_{ij} = -\nu_t \overline{S_{ij}}$, where ν_t is the subgrid-scale eddy viscosity, which acts as an artificial viscosity and represents the eddy viscosity of the residual motion. It is modelled as the product of a length scale and velocity scale. According to Smagorinsky, this is modelled as

$$\nu_t = l_s^2 \sqrt{2\overline{S_{ij}}\ \overline{S_{ij}}}. \tag{4.20}$$

The length scale in Eq. (4.20) is modelled as $l_s = C_s \mathbf{\Delta}$, where C_s is the Smagorinsky coefficient and $\mathbf{\Delta}$ is the filter width.

The computational cost of LES is relatively low compared with that of DNS because all the turbulent scales are not resolved. In LES, the large eddies are solved directly and the influences of the small-scale eddies on the large-scale eddies are modelled. The size of the smallest scale eddy that can be resolved in LES is the size of the cell in the grid. Of course, the computational expense of LES is higher than that of RANS, but it is more accurate for flows in which large-scale unsteadiness is significant, such as the flow around trains. LES has been successfully applied for the flow around trains to obtain the train slipstream and aerodynamic forces (Hemida and Krajnović, 2008a, 2010; Krajnović, 2009b; Hemida and Baker, 2010; Flynn et al., 2014.

4.4.3 Detached Eddy Simulation

In the DES approach, URANS models are employed in the near-wall regions, while the filtered versions of the same models are used in the regions away from the wall, i.e., LES modelling. The LES region is normally associated with the core turbulent region where large turbulence scales play a dominant role. In this region, the DES method uses the LES subgrid models. In the near-wall region, the respective RANS models are used. One of the commonly used turbulent models with DES in the case of external flow is the one-equation S-A model. DES has been recently used intensively for train aerodynamics due to the fact that it is less computationally expensive than LES and provides much better time-averaged results than steady and URANS (Morden et al., 2015, Li et al., 2018a; Flynn et al., 2014).

4.5 Lattice Boltzmann method

LBM is a relatively new form of CFD that has come to be particularly popular in road vehicle aerodynamics in the last two decades. Rather than using the Navier–Stokes equations for a fluid continuum, LBM models the fluid as a large number of particles that are transported over a discrete lattice mesh, and collide with other particles, using the Boltzmann equation for the statistical behaviour of dynamic particle systems. This method can be shown to be equivalent to solutions of the Navier–Stokes equations for incompressible, low Mach number flows. It has effectively been used as a form of LES, with LBM being used to calculate the large-scale turbulence, and turbulence models of various types being used to calculate the small-scale turbulence. Its main advantage is its speed of calculation, as the model has been developed for massive parallel computation. The main disadvantage of this method is the fact that the mesh has to be uniform over the entire flow field and the mesh spacing in the three orthogonal directions needs to be similar. To date, the method has found little application to train aerodynamics, with the only works known to the authors being that of Wang et al. (2008), where it was used to calculate a range of flows around a short high speed train with and without crosswinds, and the work of Mohebbi and Rezvani (2018), where it is used to calculate the crosswind forces on trains behind windbreaks. The former used the method to calculate the large-scale turbulent flows and an embedded RANS model for small-scale flows and thus acted in some ways as the equivalent of LES. Neither paper gives details of the numerical methodology that was used. Notwithstanding this present lack of use, it is likely that this methodology will find more applications in train aerodynamics in the coming years.

4.6 Optimisation methods

4.6.1 Rationale

A train in motion experiences different kinds of aerodynamic forces and moments. It is known that the aerodynamics of train depend on its shape. For instance, as will be shown in Chapter 7, the total aerodynamic drag of a train is the sum on the aerodynamic drag contributions of the different parts of the train including drag from the nose, tail, bogies, intercarriage gaps, pantographs and the skin friction drag. To reduce the overall drag, the shape of these different parts needs to be modified.

The geometrical shape of trains is complex, and many variables can be optimised to enhance its aerodynamic design. Moreover, the flow around the trains is very complex, which makes it difficult to develop accurate and reliable design tools to predict an optimal shape. The design of the different variables has traditionally been based on simplified analytical methods and model tests. Optimisation has been handled in a trial-and-error design procedure that relies on the skills and experience of the aerodynamicist. Optimisation of the aerodynamic properties of trains is always a multi-objective (drag, lift, side force and aerodynamic moments) problem. Moreover, several aerodynamic objectives are known to be in conflict. For instance, reducing the drag of a train by changing its shape often produces high lift or high side forces. A resulting optimum shape should then compromise between these objective functions. There is thus a need for a more systematic approach, capable of identifying and comparing different trade-offs of multiobjective design.

4.6.2 Design approach

Without a clear strategy for a design method, the shape optimisation of one objective variable may require a large number of experiments (computational simulations or wind tunnel tests). This is not feasible and impractical in an engineering sense. Instead, an engineering approach should be used to limit the number of experiments and hence reduce design costs. For multi-objective optimisation, the first step is to define the objective functions (the desired variables or outputs that we need to reduce such as drag force, lift force, side force and rolling moment, for instance). Also, the design variables need to be defined before the optimisation process. If we take the train nose as an example, there is an infinite number of shape designs that can be thought of and this leads to infinite number of experiments required. The most common method to achieve this is to use a surrogate model to estimate responses of the experiments at small sequences of design points for the design variables. The design points chosen for the experiments are not selected randomly but follow a special strategy called design of experiments (DOE).

4.6.3 Design of experiments

The design of experiments (DOE) is a sequence of experiments (using CFD or wind tunnel testing) that will be performed for a number of chosen values of the design variables. There are several design strategies to pick the

design values. All of them start by determining the lower bound and upper bound of the design variables and then choose some points in between at which the experiments will be performed. The most common methods of generating these points are the cantered composite design (CCD) method and the optimal Latin hypercube sampling (opt.-LHS) method. In the CCD method, the design points are chosen at the lower and upper bonds and at the centre between them. This means that for two design variables, a minimum of nine design data points is needed. This method has been used by Hemida and Krajnović (2008c) for shape optimisation of a double-decker bus and Krajnović (2008) and Krajnović (2009a) for high-speed trains. The LHS design is constructed in such a way that each one of the design variables is divided into N equal levels and that there is only one point (or experiment) for each level. The final Latin hypercube design then has N design point. The opt.-LHS design augments the Latin hypercube design by requiring that the sample points be distributed as uniformly as possible throughout the design space in an optimum way (Viana et al., 2010). Fig. 4.4A shows a design space using the CCD method for two design variables $x1$ and $x2$, while Fig. 4.4B and C shows two possible design spaces for the same design variables using opt.-LHS and five design points. This method has been used for the shape optimisation of high-speed trains by Li et al. (2016), Yao et al. (2014) and Ming et al. (2016).

4.6.4 Surrogate model

Following the DOE, a relationship between the design space and the calculated/measured responses at the design points need to be constructed. This relationship is finally used for obtaining the optimal combination of design variables to fulfil the objectives. The response surface (RS) model is a

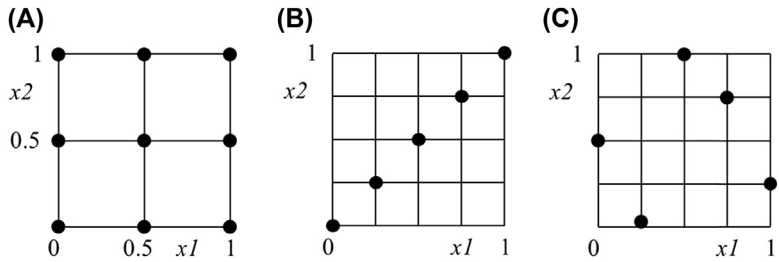

Figure 4.4 ***Design space for the two design variables*** **x1 *and*** **x2.** (A) Central composite design, (B) possible design for the Latin hypercube sampling (opt.-LHS), (C) another possible design for the opt.-LHS.

common method in surrogate model construction. This method is a statistical tool that is useful for modelling and analysis for situations in which the response of interest is a function of several input factors. The RS method has been widely used in practical engineering design optimisation problems, where the optimal searches are based on the RSs mimicking the physical processes or models. It is sometimes the only practical option for performing design optimisation, such as simulation based design optimisation, when simulations are usually computationally expensive. In conventional approaches, the RSs are built up using the group of sampling points based on the DOE scheme. The approximation of the true response in an RS can be represented by low-order polynomials that are normally quadratic. For RS, polynomials are advantageous in that their coefficients can be determined easily using the least square method and in that statistical evaluation can be made of them once their coefficients have been determined. For this reason, function approximations using the least square method are most often used with the RS methodology. For example, for the approximation $\widehat{\mathbb{Y}}$ of a variable $\mathbb{Y}$, which is a function of $\mathbb{X}$, one may write

$$\widehat{\mathbb{Y}} = \mathbb{k}_0 + \sum_{i-1}^{n} \mathbb{k}_i \mathbb{X}_i + \sum_{i-1}^{n} \mathbb{k}_{ii} \mathbb{X}_i^2 + \sum_{i-1}^{n} \mathbb{k}_{ij} \mathbb{X}_i \mathbb{X}_j \tag{4.21}$$

Representing the above with two variables $\mathbb{X}_1$ and $\mathbb{X}_2$ for simplicity gives

$$\widehat{\mathbb{Y}} = \mathbb{k}_0 + \mathbb{k}_1 \mathbb{X}_1 + \mathbb{k}_2 \mathbb{X}_2 + \mathbb{k}_{12} \mathbb{X}_1 \mathbb{X}_2 + \mathbb{k}_{11} \mathbb{X}_1^2 + \mathbb{k}_{22} \mathbb{X}_2^2 \tag{4.22}$$

Here, $\mathbb{k}_0$, $\mathbb{k}_1$, $\mathbb{k}_2$, $\mathbb{k}_{12}$, $\mathbb{k}_{11}$ and $\mathbb{k}_{22}$ are the model regression coefficients. The error between the approximation value $\widehat{\mathbb{Y}}$ and the actual value $\mathbb{Y}$ is $\mathbb{e}$. Assuming that the number of experiment points is n and the number of design variables is k, the linear regression model can be represented as

$$\widehat{\mathbb{Y}} = \mathbb{X}\mathbb{K} + \mathbb{e} \tag{4.23}$$

The regression coefficient $\mathbb{k}$ can be determined by minimising the sum of the square of the error $\mathbb{e}$. A good measure of the fit of the RS with the data is value of the coefficient of multiple determination, $\mathbb{R}^2$, which takes the form

$$\mathbb{R}^2 = \frac{SS_R}{SS_T} = 1 - \frac{SS_E}{SS_T} \tag{4.24}$$

Here, SS_E is the sum of the squared approximation errors at the n sampling points, SS_T is the true response's sum of squared variation from the mean $\widehat{\mathbb{Y}}$ and SS_R is the approximation's sum of squared variations from the mean, i.e.,

$$SS_E = \sum_{i-1}^{n} \left(\mathbb{Y}_i - \widehat{\mathbb{Y}}_i\right)^2, \tag{4.25}$$

$$SS_T = \sum_{i-1}^{n} \left(\mathbb{Y}_i - \overline{\mathbb{Y}_i}\right)^2, \text{ and} \tag{4.26}$$

$$SS_R = SS_T - SS_E = \sum_{i-1}^{n} \left(\widehat{\mathbb{Y}}_i - \overline{\mathbb{Y}_i}\right)^2. \tag{4.27}$$

In general, the coefficient of determination, $\mathbb{R}^2$, is used to decide whether a regression model is appropriate. The assessor $\mathbb{R}^2$ provides an exact match if it is 1.0, and if the residual increases, $\mathbb{R}^2$ decreases in the range from 1.0 to 0. As the number of variables increases, the residual increases so that the determination coefficient increases in value. For this reason, the coefficient of determination adjusted, $\mathbb{R}^2_{ad}$, is used to obtain a more precise regression model judgement. $\mathbb{R}^2_{ad}$ takes the form

$$\mathbb{R}^2_{ad} = 1 - \left(\frac{SS_E}{n-k}\right) \Big/ \left(\frac{SS_T}{n-1}\right) \tag{4.28}$$

where k is the number of design variables.

Although a higher value of $\mathbb{R}^2$ means a better fit, it is possible that the RS is not the correct representation of the actual data. One way to increase $\mathbb{R}^2$ is to increase the degree of the polynomial but it has other consequences. Increasing the degree of the polynomial by more than three results in a large amount of noise in the regression. The backward elimination procedure based on the t statistic is associated with the RS to discard terms and improve the prediction accuracy. The t statistic of the fitted coefficient is defined as its value divided by an estimate of the standard error of the coefficient. In the backward elimination, we begin with the full regression model obtained from the least square method. The t test is performed on all the regression coefficients to determine their influence on the model. A rule of thumb says that regressor terms with an absolute value of larger than 2.0 are significant at a 95% confidence interval. Thus the regressor

terms are removed from the model if the regressor's t is smaller than 2.0 and if R^2 increases after the regressor's removal. This method has been adapted by Hemida and Krajnović (2008c) and Krajonvić (2009). The method of Kriging explained in Li et al. (2016), Xu et al. (2017) and in Jakubek and Wagner (2016) is also used in shape optimisation for train aerodynamics.

4.6.5 Multi-objective optimisation

The constructed RSs are used an optimisation method to find the multi-objective optimum design. Optimisation methods are generally categorised into two groups: deterministic methods and stochastic ones. Deterministic methods are normally suitable for optimisation processes that only involve only one single peak in the optimisation space. However, if there are multiple peaks in the solution space, then the stochastic methods are more appropriate. In general, the objective functions of the train shape optimisation have plural peaks and thus stochastic methods are the suitable ones.

Among the stochastic approaches, there is an evolutionary algorithm that is widely used for obtaining the optimum shape of high-speed trains. At the beginning of the optimisation process using the evolutionary algorithm, an initial population of design candidates called individuals is randomly generated. Following this initial stage, a fitness function of each individual, which is related to the objective function, is evaluated. Another pair of individuals with higher fitness values is then selected to produce children for the next generation by exchanging and mutating their design parameters. The fitness functions of the new generation are then evaluated and the mating pairs are selected to reproduce the next generation again. As the evolutionary algorithm can sample as many solutions as the number of individuals during the alternation of generations, the Pareto optimal solutions can easily be obtained. The different steps involved in this method are explained in Suzuki and Nakade (2013) and in Deb and Datta (2010).

For shape optimisation of trains using the evolutionary multiobjective optimisation procedure, the so-called real-coded generic algorithm (NSGA-II) developed by Deb (2001) is normally used. The main aim of the algorithm is to find solutions such that there is no other solution for which at least one objective has better value while values of remaining objectives are the same or better.

CHAPTER 5

The flow around trains in the open air

5.1 Introduction

In general, when describing the flow around trains, we will utilise information from a range of full-scale experiments, rather than from model-scale experiments or computational fluid dynamics (CFD). It will be seen throughout this book that, although these modelling techniques are undoubtedly useful, they do not always fully represent what is in fact a very complex reality, and thus in describing the nature of the flow around trains, the use of full-scale data gives the most complete and realistic picture. Nonetheless, there will be points in the discussion that follows where information from physical model tests and CFD calculations will be used to illustrate flow phenomena, particular for those cases where full-scale observations are difficult to make. As a consequence of this use of full-scale data, primarily obtained from ground-based tests, the ground-based frame of reference will normally be used in what follows.

5.2 Trains on level ground in still air

5.2.1 Ensemble averaging and flow regions

The basic parameters that describe the flow field around a train are the velocity and pressure fields on and around the train — u_x, u_y, u_z and p, as defined in Section 2.2, all of which are functions of x, y and z. As is normally the case in aerodynamic studies, it is convenient to express these in a dimensionless form, and in what follows we will express the velocity and pressure fields in coefficient form as defined in Section 2.2, as $C_{ui} = u_i/v$ and $C_p = p/0.5\,\rho v^2$, where ρ is the density of air and v is the train velocity. We also define $C_{uh} = u_h/v$, where u_h is the overall horizontal velocity, the magnitude of the vector sum of u_x and u_y, as this is a parameter that is very often measured in trackside measurements.

Train aerodynamics
ISBN 978-0-12-813310-1
https://doi.org/10.1016/B978-0-12-813310-1.00005-8

Now, the flow around trains at full scale is inherently unsteady, and measurements of velocity and pressure at the trackside vary significantly from one train pass to another, and some sort of averaging procedure of velocity and pressure measurements is required to obtain a full appreciation of the underlying flow. Thus, in this section, we describe experimental data that have been obtained using the techniques of ensemble averaging, which has been outlined in Section 3.1.2. Typical velocity results have been shown in Fig. 3.2 for C_{uh} for the 200 m long Velaro S103 high-speed train obtained from the Aero-TRAIN experiments and show the significant run-to-run variability. Fig. 5.1 shows the ensemble average values of C_{uh} for the 364 m long ICE1 train, which, although classified as a high-speed train, has a less streamlined nose than the Velaro S103 of Fig. 3.2, with the velocities measured at a number of positions from the track centreline (RAPIDE, 2001, Sterling et al., 2008).

The data shown in Figs 3.2 and 5.1 suggest that a number of different flow regions can be identified around the train. Following and somewhat modifying, the definitions originally proposed in Baker et al. (2001), we define these regions as follows:

- The nose region, extending from upstream of the train to around 10 m behind the nose, where Figs 3.2 and 5.1 show that there are large velocity peaks.

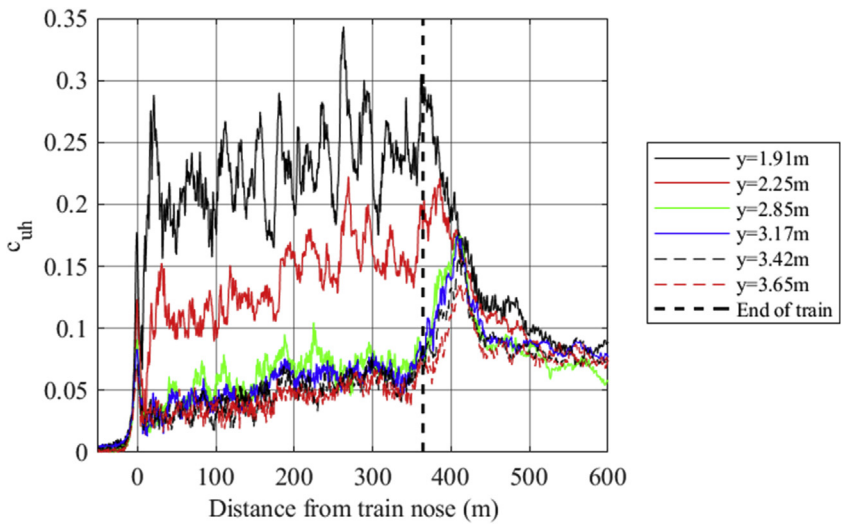

Figure 5.1 Normalised ensemble averaged horizontal velocities at different distances from the rack centreline for an ICE1 train. Measurements at a height of 0.5 m above the top of rail *(Data from RAPIDE project reported in Sterling et al. (2008) and RAPIDE et al. (2001).)*

- The boundary layer region of the train, extending from the end of the nose region to the end of the train (at $x = 200$ m for Fig. 3.2 and $x = 364$ m for Fig. 5.1). The figures show the gradual development of the flow in this region, with the measurements made furthest from the train having low velocities until the boundary layer grows sufficiently to envelope the measurement point. The boundary layer region will extend over the roof of the train. It is perhaps worth mentioning that the description of this region as being a boundary layer is potentially misleading in two ways. Firstly, boundary layers in aerodynamics are usually small in terms of the body scale, whereas for long trains, the thickness of the boundary layer is of the order of the train width towards the end of the train. Secondly, not only does friction on the train surface slow down the flow but also friction on the ground away from the train acts to slow the flow close to the ground. Thus, this region next to the train might be better thought to be a boundary region rather than a boundary layer.
- The near wake region extending around 100 m behind the train, where there can be large velocity peaks. It will be seen that, for some trains, coherent flow structures exist in this region, including longitudinal vortices.
- The far wake region, extending from the end of the near wake region, in which the velocities gradually decay to zero.

In addition, we can also define a further flow region for which data are not shown in Figs 3.2 and 5.1, but which will be seen to be of importance in later chapters.

- The underbody flow region, where the flow is dominated by highly sheared flow regions, where train and ground boundary layers meet. The flow in this region is determined both by the roughness of the train underbody and the roughness of the track bed.

5.2.2 Ensemble average velocities and pressures for different train types

Before we proceed with the discussion of different flow regions, it is convenient to set out here figures similar to Fig. 5.1 for a range of different train types, all of which are described in Appendix 1. Fig. 5.2A shows values of C_{uh} for a number of single unit high-speed trains — the S103 Velaro (the same data as Fig. 3.2); the S100 TGV, which is again a 200 m long train but with a more pointed streamlined nose; the S102 Talgo, again 200 m long, which has a beaklike nose and tail, all taken from the AeroTRAIN

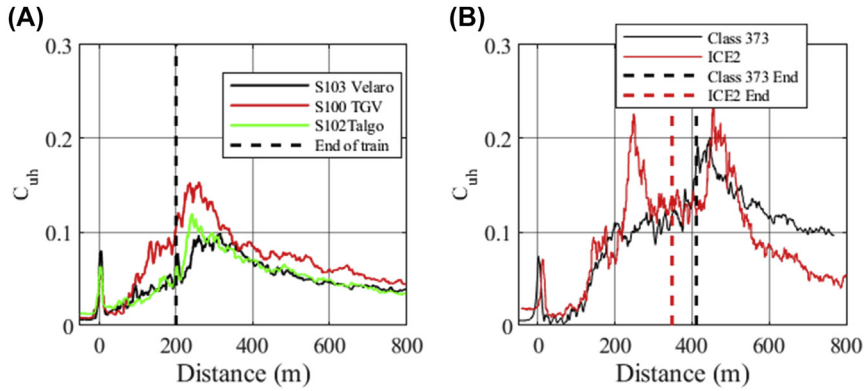

Figure 5.2 ***Slipstream measurements for high-speed passenger trains.*** (A) —single unit, (B) —double units. S100, S102, S103 and ICE2 data all from anemometers 0.2 m above the top of rail, 3 m from track centreline; Class 373 data were measured 0.2 m above the top of rail and 4 m from track centreline. *(Data from RAPIDE and AeroTRAIN projects reported in RAPIDE (2001), Sterling et al. (2008), Sima et al. (2011) and Baker et al. (2014c), with Class 373 data from Soper et al. (2017b).)*

experiments (Baker et al., 2014c). Fig. 5.2B shows similar measurements for two high-speed trains running as double units — the ICE2 (411 m long) (Baker et al., 2014c) and the Class 373 Eurostar (384 m long) (Soper et al., 2017b). Fig. 5.3A shows measurements for three medium-speed multiple unit trains — the Class 43 HST, with a length of 220 m and a sharp-edged

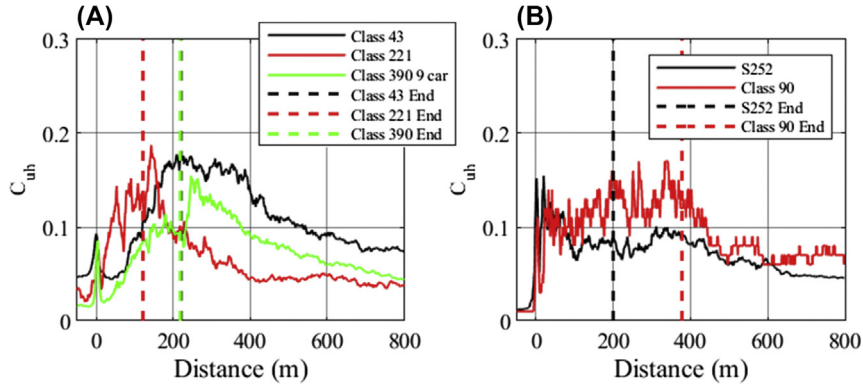

Figure 5.3 Slipstream measurement for medium-speed passenger trains. Class 43 measurements were made at 5.05 m from the centre of the track at 0.7 m above the top of the rail; Class 221 Voyager, Class 390 Pendolino, Class 90 and S252 measurements were made at 0.2 m above the top of rail and 3 m from the track centreline. *(Data from AeroTRAIN project reported in Sima et al. (2011) and Baker et al. (2014c), and Soper and Baker (2019).)*

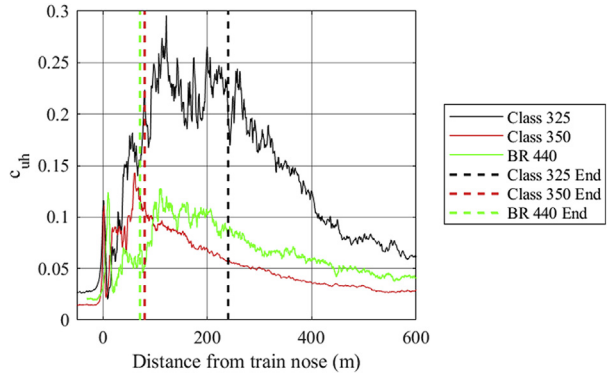

Figure 5.4 Slipstream measurements for low-speed multiple units All measurements were made at 0.2 m above the top of rail and 3.0 m from track centreline. *(Data from AeroTRAIN project reported in Sima et al. (2011), Baker et al. (2014c) and Soper and Baker (2019).)*

nose (unpublished data), a Class 221 Voyager train of length 121 m with a raked but somewhat blunt nose and a Class 390 Pendolino with a length of 218 m and a rounded, more streamlined nose (Soper and Baker, 2019). Fig. 5.3B shows measurements for the S252 locomotive plus trailing coaches (200 m long) (Baker et al., 2014c), and the Class 90 locomotive with sleeper carriages of length 378 m (Soper and Baker, 2019). Fig. 5.4 shows data for three multiple unit low-speed trains — the 71 m long BR440 (Baker et al., 2014c), the 240 m long Class 325 (a mail rather than a passenger train) and the 80 m long Class 350 (Soper and Baker, 2019). Fig. 5.5

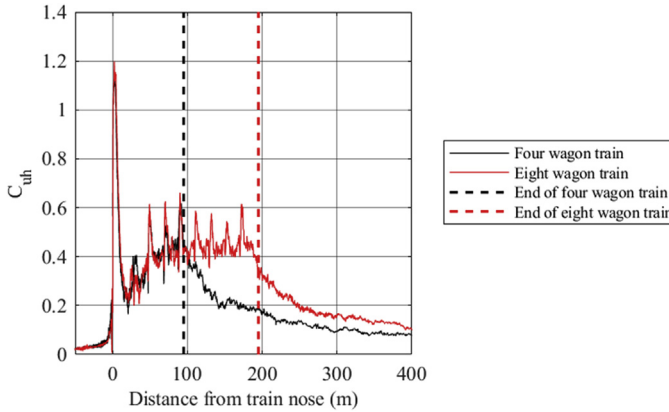

Figure 5.5 Slipstream measurements for two partially loaded container freight trains hauled by a Class 66 locomotive from Soper et al. (2014). Measurements were made 2.25 m above the top of rail and 1.75 m from track centreline. *(Copyright Elsevier.)*

shows moving model data for freight train measurements, for a Class 66 locomotive pulling two configurations of container train. Model-scale tests are used here, because of the large variation in freight train consists. The results are, however, consistent with the small amount of full-scale data that do exist for such trains (Sterling et al., 2008; Soper and Baker, 2019).

These trains reflect the broad range of train types, and although aspects of these figures will be considered in detail in what follows, it is worth making some general points at this stage. Firstly, it can be noted that the magnitudes of the ensembles for all passenger trains have a maximum of C_{uh} of between 0.1 and 0.2, i.e., 10%—20% of the train speed. The values for individual runs of course can be much higher. For the freight train results, the slipstream values are much higher at around 0.4. Secondly, although the single unit high-speed trains show a peak in C_{uh} in the wake of the train, the double unit high-speed trains also show a significant peak in C_{uh} at the junction of the two units. Thirdly, locomotive-hauled trains show a significant peak along the side of the train close to the front, presumably due to a discontinuity in cross-sectional area or profiles between the locomotive and the carriages.

The above discussion has been concerned with the velocity fields where the turbulent nature of the flow results in large velocity fluctuations between train passes. For train-induced pressures, however, the situation is rather different, and there is relatively little variation between train passes, and the pressure variations for all types of passenger train are similar in form. A typical plot is shown in Fig. 5.6 for a Class 43 HST (from unpublished

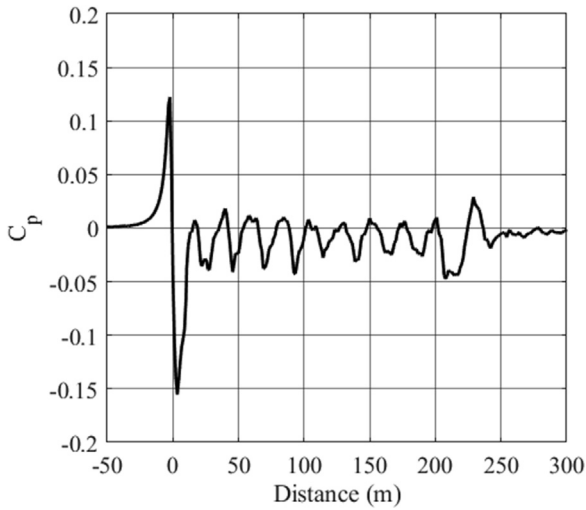

Figure 5.6 Pressure measurements for Class 43 HST passenger trains. Pressures were measured at 0.7 m above the top of the rail at 2 m from the track centreline.

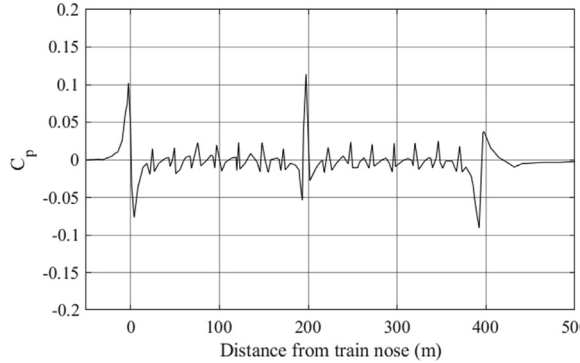

Figure 5.7 Pressure measurements for double unit passenger train. Measurements were made at 2.5 m from the track centreline and 1.5 m above the top of the rail. *(From AeroTRAIN data for Velaro S103 reported in Sima et al. (2011) and Grappein and Rueter (2015).)*

full-scale experiments). The results show a large positive/negative peak as the nose of the train passes, and smaller peaks can be seen along the train due to the passage of bogies and intercar gaps, with a small negative/positive at the train tail. As with the velocity plots, when trains travel in double units, then a peak in pressure can be observed at the junction between the two units — see Fig. 5.7 for the double unit S103 Velaro from the AeroTRAIN measurements (Grappein and Rueter, 2015). Fig. 5.8 shows similar results for the model-scale freight train experiments of Soper et al. (2014).

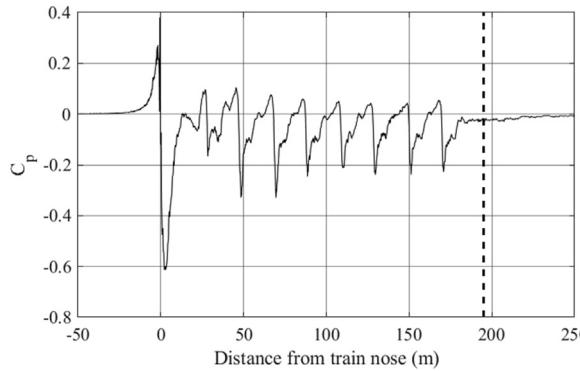

Figure 5.8 Pressure measurements for a freight train (Soper et al., 2014). Measurements were made at 2.25 m above the top of rail and 1.75 m from track centreline. Copyright Elsevier.

Very large nose peaks can be seen in this case due to the bluntness of the locomotives, and the passage of individual containers can also be detected. There is no noticeable tail peak in this case.

As noted above, in this chapter, we are following the approach of, in the main, using the results of full-scale experiments to describe the flow around trains. That is not to say that other techniques are not reliable under suitable circumstances. Physical modelling techniques with either moving models or moving grounds are useful for measuring slipstream behaviour, and a number of authors have used these techniques (see Soper et al., 2014; Xia et al., 2017a,b; Zhou et al., 2014). Jonson et al. (2012) report similar tests using a towing tank. The use of wind tunnel models with stationary ground is more problematic, but can nonetheless be used under certain circumstances where detailed flow measurements are required (Bell, 2015; Bell et al., 2014, 2015, 2016, 2017) or where the effect of the ground can be assumed to be small — for example, measurements of pressures on parts of the train well away from the ground plane. Relatively simple CFD techniques can be used to predict the pressure distribution around the noses of trains, and validation against full-scale data shows that these have a high degree of reliability if properly carried out (Grappein and Rueter, 2015). CFD predictions of slipstreams are more difficult and require resource-intensive unsteady methods to predict the turbulent boundary layer and wake flows (Flynn et al., 2014). Even here, care is needed with the interpretation, and if comparisons are to be made with full-scale experiments, then a large number of time histories of CFD velocities in the ground frame of reference need to be generated, and then ensemble averaged as at full scale (Flynn et al., 2016).

5.2.3 Nose region

The flow around the nose of many trains is largely inviscid with low turbulence, and the pressure and velocity variations are well defined. Typical pressure variations are shown in Fig. 5.9, above for the Class 43 HST (unpublished data) for a Class 66 locomotive pulling a train of partially loaded containers (Soper and Baker, 2019). In both cases, a positive peak is followed by a negative peak. Such results are typical of nearly all cases, although the magnitude of peak-to-peak pressure coefficient variation for different types of train can be substantial, as can be seen from the difference in magnitude of the two curves. The relative magnitudes of the positive and negative peaks are also rather different.

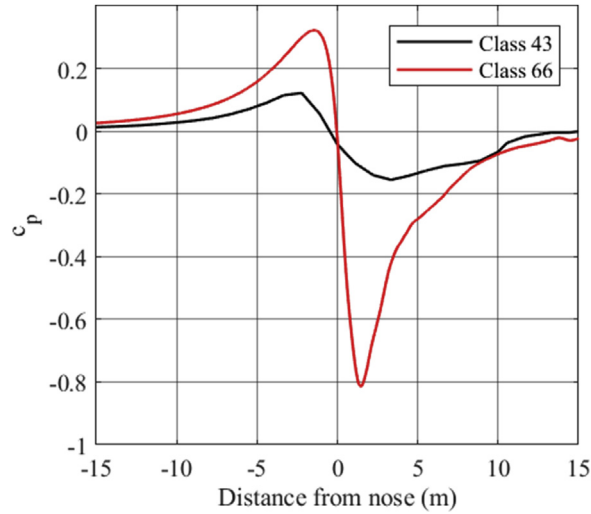

Figure 5.9 Typical nose pressure transients. Class 43 HST measurements were made at 0.7 m above the top of rail, 2 m from the track centreline; Class 66 measurements were made at 0.9 m above the top of rail and 3.0 m from the track centreline.

From the various full-scale data sets that are available, it is possible to determine the values of the peak-to-peak pressure coefficients around the train nose for a variety of different train types. This collation is shown in Table 5.1 below. Rather than present the data in the usual speed classification, it is presented here in order of peak-to-peak pressure coefficient. One should be circumspect in the interpretation of the data, as the measurement positions are not all the same, the train widths vary, and the sampling rates and filter characteristics of the data vary, but it is clear that, in general, the peak-to-peak pressure coefficients fall into three bands – 0.15 to 0.20 for streamlined nose shapes; 0.2 to 0.3 for intermediate nose shapes and 0.35 to 0.45 for blunt nose shapes.

Now, it is clear from Figs 5.2–5.5 that there are also large peaks in the horizontal velocity trace near the nose. However, this large peak is due to variations in the velocities in both the x and y directions. An example of this is shown in Fig. 5.10 for the Velaro S103 train (Baker et al., 2014c). The normalised x component of velocity C_{ux} follows the form of the pressure variation, with a positive and then a negative peak (i.e., reversed flow), but there is also a strong lateral velocity peak C_{uy} in the positive y direction, i.e., away from the train. If only the magnitude of the overall horizontal velocity is measured (C_{uh}), then this lateral velocity will dominate in the calculation.

Table 5.1 Nose peak-to-peak pressure coefficients.

	Streamlined						Intermediate			Blunt			
	S103 velaro	CRH2	Class 390	Class 221	S104	Emu V250	Class 325	Class 350	Class 43 HST	Class 90 loco	BR440	S252 loco	Class 66 loco
Data source	G&R 2015	G2018	S&B 2019	S&B 2019	G&R 2015	G&R 2015	S&B 2019	S&B 2019	U	S&B 2019	G&R 2015	G&R 2015	S&B 2019
Train speed (km/h)	300	350	201	201	300	250	144	144	200	120	160	200	120
Distance from track centreline (m)	2.5	3.15	3.0	3.0	2.5	2.5	3.0	3.0	2.0	3.0	2.5	2.5	3.0
Height above track (m)	1.5	1.4	1.4	1.4	1.5	1.5	1.4	1.4	0.7	1.4	1.5	1.5	1.4
Peak-to-peak pressure coefficient	0.146	0.17	0.170	0.170	0.171	0.196	0.240	0.240	0.277	0.36	0.394	0.395	0.43

Sources G&R 2015 – Grappein and Rueter, 2015; G2018 – Guo et al., 2018; S&B 2019 – Soper and Baker, 2019; U – unpublished data.

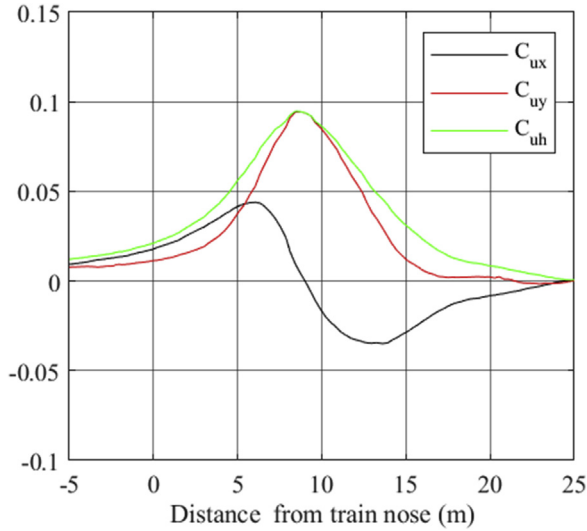

Figure 5.10 Velocities around train nose for S103 Velaro. Measurements were made at 0.2 m above the top of rail, 3 m from the track centreline. *(Data from AeroTRAIN project reported in Sima et al. (2011) and Baker et al. (2014c).)*

5.2.4 Boundary layer region on train side and roof

As might be expected, along the side and roof of trains, there is the development of a large-scale turbulent boundary layer. This boundary layer is, however, far from being two dimensional with a component of velocity up or down the train side, and divergence or convergence of velocity over the top of the train (Brockie and Baker, 1990). The development of the boundary layer can be clearly seen in Figs 5.1—5.5. The ICE1 results of Fig. 5.1 clearly show the development of the boundary layer along the side of the train, with the velocity remaining low for large distances from the train until the boundary layer grows out to that distance, and this gradual evolution of the boundary layer can be seen for the other high-speed trains in Fig. 5.2A. No significant effect of intercar gaps on the growth of the boundary layer can be observed. However, the double units of Fig. 5.2B show that this boundary layer evolution is severely disrupted by the gap between units. The medium-speed multiple unit passenger trains of Fig. 5.3A and the low-speed multiple units of Fig. 5.4 show the same gradual evolution of the boundary layer along the length of the train. The extent of the boundary layer growth on the very long Class 325 multiple unit is very obvious. The locomotive-hauled trains in Fig. 5.3B show a considerable difference, however, where it is clear that the flow separations

around the nose of the train and the disturbance caused by the discontinuity between locomotive and carriages result in a very rapid development of the shear layer along the side of the train. The freight train boundary layer in Fig. 5.5 is somewhat different, as it seems that the velocity develops very quickly after the train nose. It is difficult to generalise, however, for freight trains, because all consists will be different. For the pressure variations in the boundary layer region shown in Figs 5.6–5.8, the effect of intercar gaps and geometric discontinuities are more marked than in the velocity measurements, although this might well be a reflection of pressure variations caused by the passage of bogies.

The detailed measurements of Fig. 5.1 for the ICE1 also allow the boundary layer velocity profiles to be plotted, and typical results are shown in Fig. 5.11A. Perhaps, the most important point of note is the scale of the boundary layer – towards the rear of the train, the size of the layer is comparable with the width/height of the train itself with significant velocities at 3m from the track centre line. Fig. 5.11B shows boundary layer velocity profiles measured from the train side– for the ICE2 and the TGV using a laser anemometer (RAPIDE, 2001) and a Class 43 using a pitot tube rake (Brockie and Baker, 1990). These are also plotted in the ground frame of reference. The results of Fig. 5.11A and B can be seen to be broadly consistent with each other, with the side of the trains shown in Fig. 5.11B being around 1.5–1.7 m from the centre of the track. There does, however, seem to be a more rapid fall off in velocity at the midheight of the train than at the bogies, as would be expected.

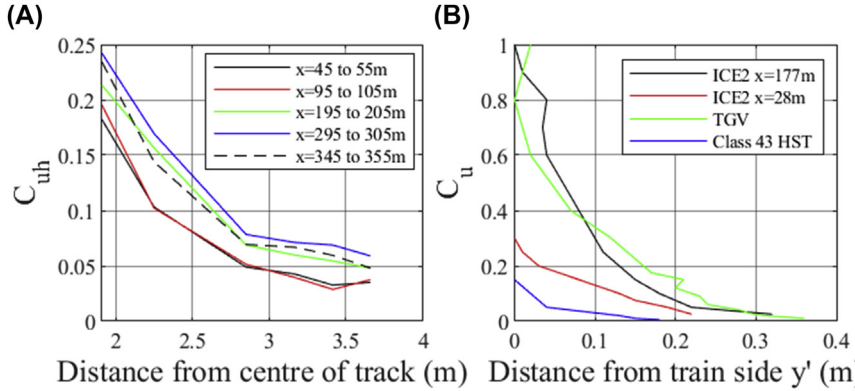

Figure 5.11 ***Boundary layer velocity profiles.*** (A) – ICE1 velocity profiles in ground frame of reference measured 0.5 m above the top of rail; (B) – ICE2, TGV and Class 43 measured from train at half body height, but plotted in ground frame of reference. *(Data from RAPIDE project reported in RAPIDE (2001) and Sterling et al. (2008), and from investigation of Brockie and Baker (1990).)*

Table 5.2 Skin friction coefficients.

Source	Train	C_f
RAPIDE (2001)	ICE2 $x = 177$ m	0.00197
RAPIDE (2001)	ICE2 $x = 28$ m	0.00297
RAPIDE (2001)	TGV	0.00208
Brockie and Baker (1990)	Class 43 HST	0.00109
Richards and Cooper (1977)	APT	0.0017 to 0.0024

From the measurements obtained on the train, the skin friction coefficient can be derived, by plotting the velocity profiles in the logarithmic law of the wall form (Eq. 2.13). The measured values are shown in Table 5.2, and it can be seen that the coefficient has values of between 0.001 and 0.003, although it should be noted that these values are quite sensitive to the curve fitting procedure used.

Fig. 5.12 shows plots of the displacement and momentum thicknesses and form parameter along the ICE1 (Sterling et al., 2008). These were

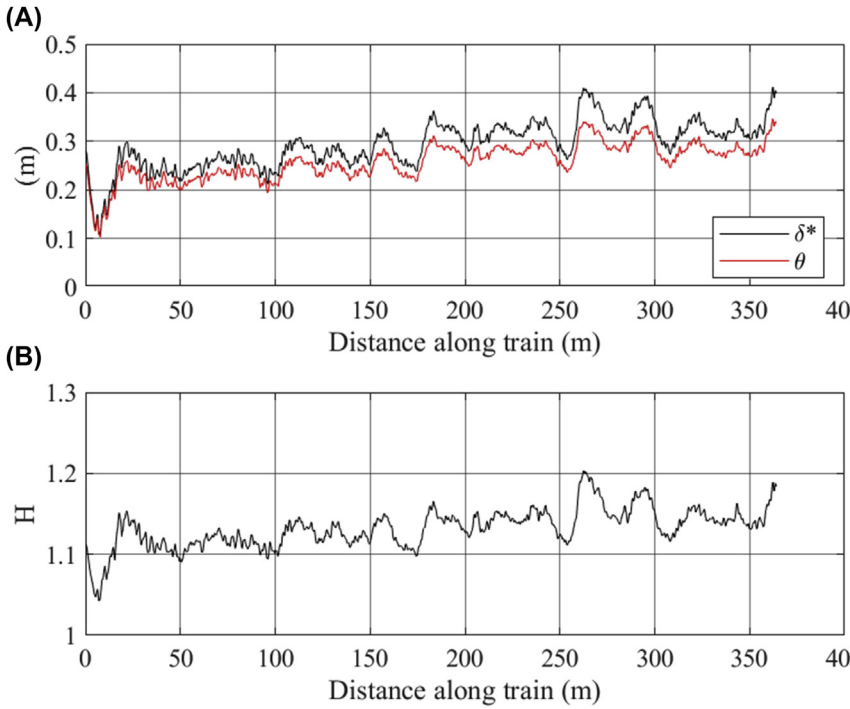

Figure 5.12 ***Boundary layer thicknesses and form parameter for ICE1.*** Measured 0.5 m above the top of rail; (A) — displacement and momentum thicknesses; (B) — form parameter. *(Data from RAPIDE project reported in RAPIDE (2001) and Sterling et al. (2008).)*

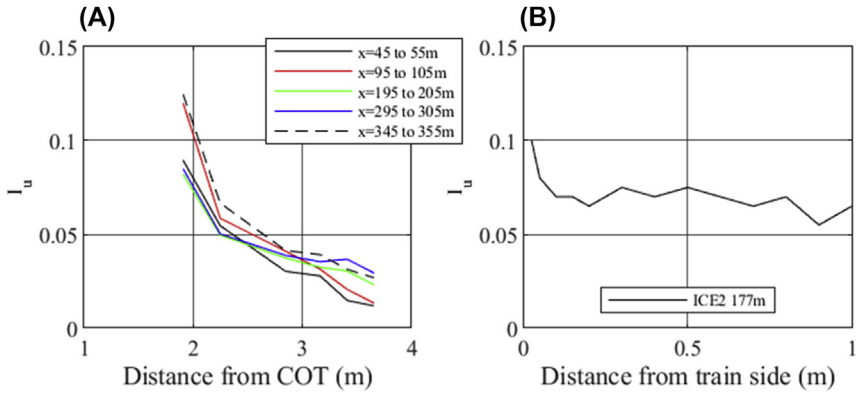

Figure 5.13 ***Turbulence intensity profiles in vehicle frame of reference.*** (A) – ground-based measurements for ICE1 (measured 0.5 m above the top of rail) (B) – train-based measurements for ICE2, but plotted in ground frame of reference. *(Data from RAPIDE project data reported in Sterling et al. (2008) and RAPIDE (2001).)*

calculated using the definitions appropriate to the ground frame of reference in Eqs (2.16) and (2.17). The displacement thickness has a value of 0.2 m very close to the nose of the train, suggesting a significant disturbance to the flow near the nose, then grows slowly along the train to a value of around 0.3 m. For normal equilibrium boundary layers, the actual thickness of the boundary layer is 8–10 times the displacement thickness. The form parameter (the ratio of the displacement thickness to the momentum thickness) has a value of 1.15 and is lower than for an equilibrium boundary layer and reflects the essential three dimensionality of the flow.

The turbulence intensity (in the ground frame of reference) is shown in Fig. 5.13 for both the results of Sterling et al. (2008) along the ICE1 (Fig. 5.13A), using ground-based measurements, and RAPIDE (2001) for the ICE2, using train-based measurements (Fig. 5.13B). These are broadly consistent with each other (with the edge of the train being about 1.75 m from the centre of the track) and show little variation along the train. Note, however, that these levels of turbulence intensity of around 0.05 to 0.1 as defined by equations 2.24 and 2.25 imply values of the standard deviations of the normalised ensembles of velocity in a ground-based frame of reference of the same order as the mean values of the ensemble, i.e., the velocities are very variable between train passes. The integral length scales of turbulence for these flows are of the order of 2.5 m. Thus, the coherence length of the turbulence eddies along the train is quite short. Note also that the turbulence intensities can be much higher than the values shown here

for rough trains — for freight trains, turbulence intensities in the vehicle frame of reference can be as high as 0.2 to 0.5.

The flow over the roof of a train is particularly important in the consideration of the aerodynamic importance of pantographs. In view of this, it is surprising that, very few detailed flow measurements have been made over the roof of trains. The only full-scale data set known to the authors was obtained from measurements to assess the safety of workers installing overhead equipment and was made at $z = 5.45$ m above the top of rail and at $y = 4.05$ m from the track centreline during passages of Class 43 HSTs, i.e., not over the roof of the train itself, but at the roof height and somewhat to the side (unpublished data). The results are shown in Fig. 5.14A, and they show some interesting points — in particular, a peak in the slipstream ensemble about 60 m along the length of the train, perhaps due to some major flow separation at the nose, and also very slow velocity decay in the wake. However, the tests were carried out in quite windy

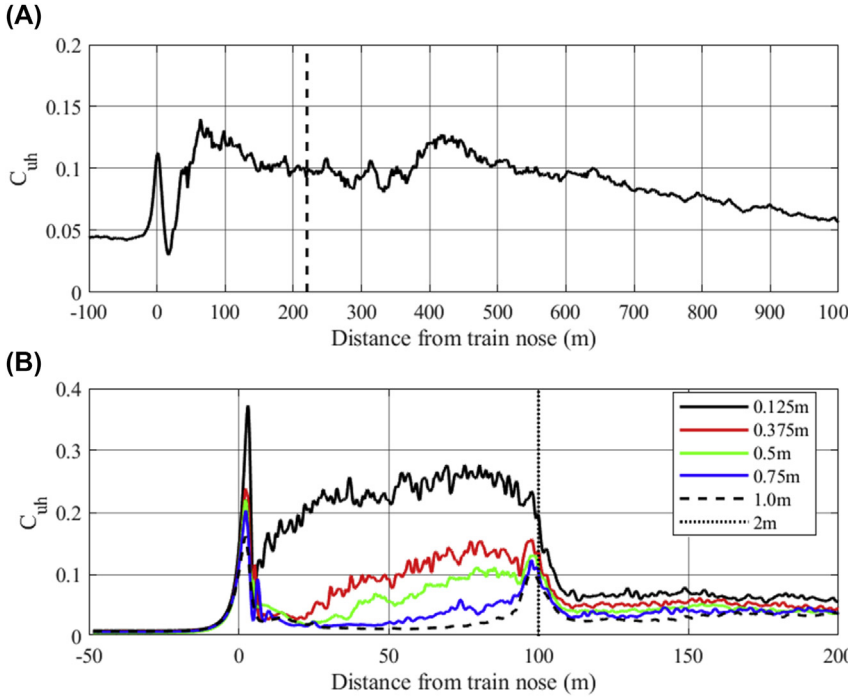

Figure 5.14 ***Roof boundary layer data.*** (A) — Class 43 HST results were made at $z = 5.45$ m and $y = 4$ m; (B) — ICE2 model-scale, Baker et al. (2001) measurements were made at $y = 0$ m, with the distances shown measured from above the top of the train — all distances are full-scale equivalents.

conditions as shown by the values of velocity before the train passes and cannot be considered to be wholly reliable.

For other roof data, we need to turn to the results of moving model tests. A short series of measurements were made on the University of Birmingham TRAIN Rig above a four-car ICE2 model in Baker et al. (2001), the results of which are shown in Fig. 5.14B. These show the expected boundary layer development along the train, reaching a full-scale equivalent thickness of over 1 m towards the end of the train, although the scale effects inherent in such measurements (and the lack of realistic roof roughness) makes these results difficult to interpret. The boundary layer development over the roof of the train clearly merits further investigation.

5.2.5 Near wake region

The near wake is the most complex of the flow areas around the train and can take on a variety of forms depending on the precise shape of the train. Typical pressure signatures for passenger trains can be seen in Figs 5.6 and 5.7 — these show the reverse of the nose situation with a negative peak followed by a positive peak. These are in general less severe than the nose peaks. For blunt-ended trains (as in Fig. 5.8), there seems to be little evidence of flow structure in this region, and large-scale separations occur (and one might argue that, for such trains, the near wake as a separate region does not exist, as there is a gradual falloff in velocity as in the far wake). However, for more streamlined trains, there is strong evidence from wind tunnel tests and CFD calculations of the existence of a pair of longitudinal trailing vortices behind the train. Fig. 5.15, taken from Bell et al., (2016), shows velocity and vorticity vectors in the wake of a two-car generic ICE3 train model mounted statically in a wind tunnel, and the inferred flow pattern. Fig. 5.16 shows visualisations from the calculations of Xia et al. (2017a), which show the difference between the trailing vortices for moving and stationary model cases for a model-scale CRH3 train. These differences can be seen to be substantial, but, nonetheless, the trailing vortex system can be seen in both cases. These can result in very high velocities in the train wake — see the wake peaks in Figs 5.2–5.5 — and thus low pressures.

There is also evidence that these vortices can be unsteady. In the full-scale data of Sterling et al. (2008), the individual runs of the ensemble only intermittently showed a wake peak or showed double or triple peaks. This led the authors to suggest that the technique of ensemble averaging might not be wholly suitable to analyse such structures. That being said the Strouhal numbers of the CFD simulation of Schulte-Werning et al. (2003)

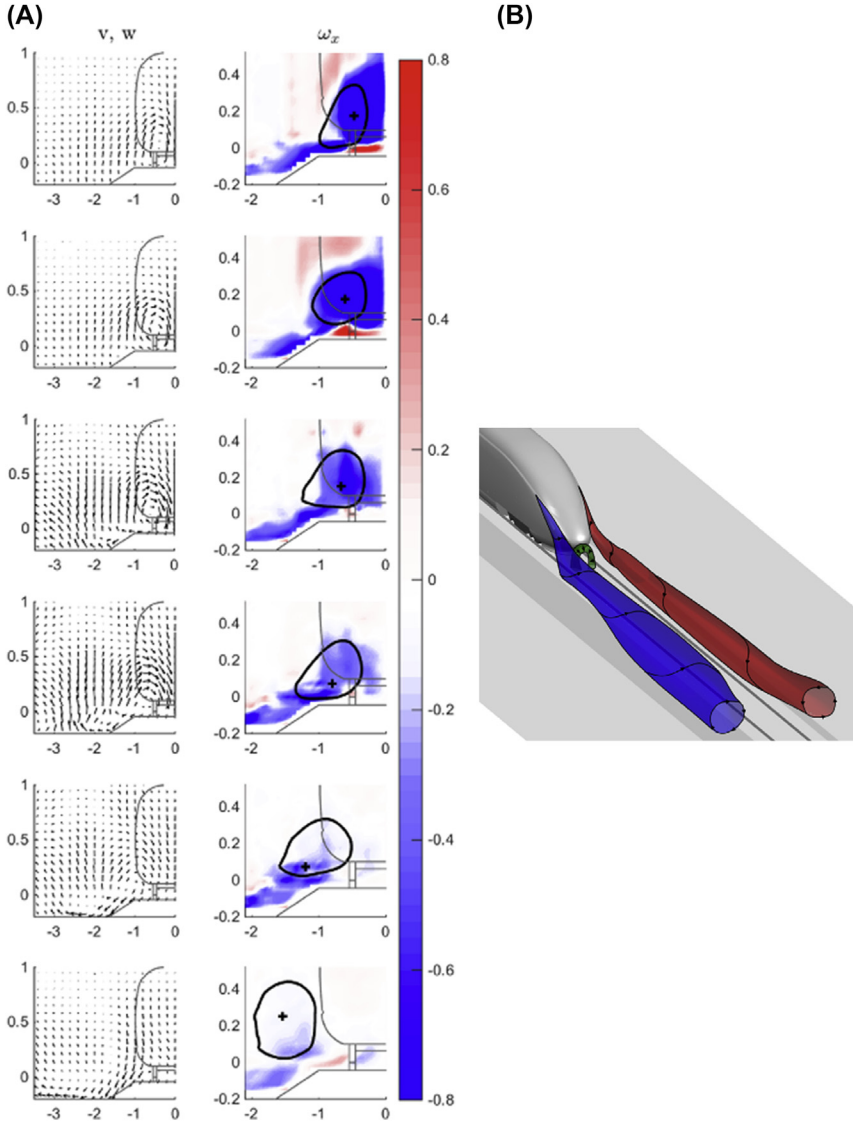

Figure 5.15 ***Longitudinal wake vortices from the wind tunnel results of Bell et al. (2016).*** (A) – velocity vectors and vorticity contours at 0.5, 1.0, 2.0, 5.0, 5.5 and 6.0 vehicle heights from the end of the train; (B) – shows the inferred vortex pattern. *(Copyright Elsevier.)*

and the full-scale experiments (Sterling et al., 2008), defined as oscillation frequency x body height/train velocity, were reasonably similar – 0.14 for the former and 0.11 for the latter. Muld et al. (2012, 2014) applied the powerful technique of modal decomposition to DES calculations around an

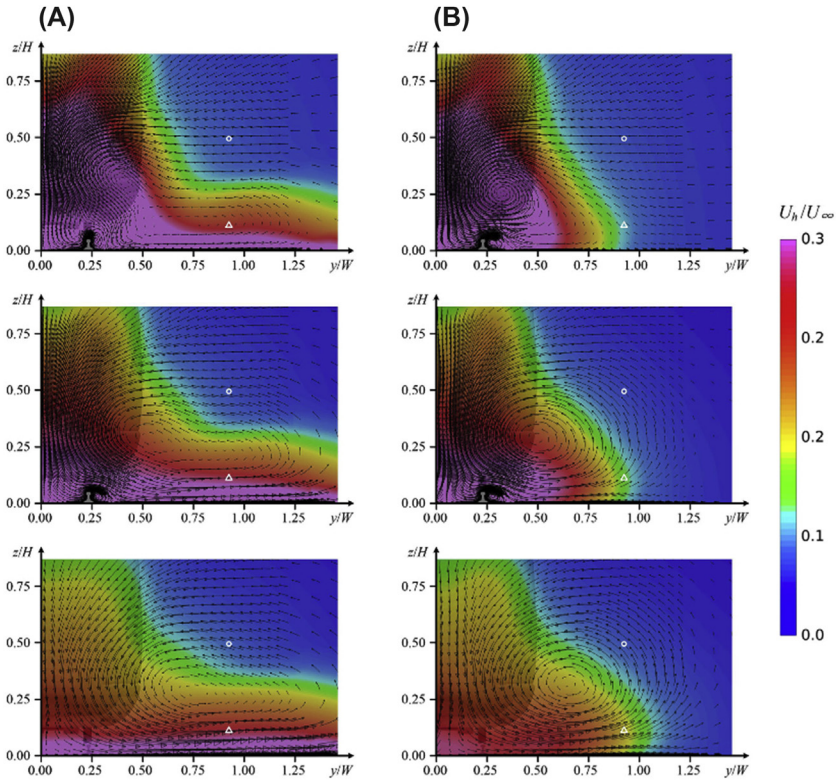

Figure 5.16 ***Longitudinal vortices in the near wake of a CRH3 train (Xia et al., 2017a).*** (A) – stationary ground; (B) – moving ground. *(Copyright Elsevier.)*

idealised high-speed train model (the Aerodynamic Train Model) to study these near wake oscillations. This technique can identify the spatial and temporal variability of coherent flow structures and has come to be widely used in a number of fluid mechanics studies in recent years. They identify two dominant modes – a vortex shedding mode at a Strouhal number of 0.085 and one related to the bending of the counter-rotating vortices. In Muld et al. (2014), they show that the frequencies and magnitudes of these modes are dependent on the boundary layer characteristics just ahead of the separation at the tail of the train, and thus on train length. The wind tunnel experiments of Bell et al. (2016) for the same train shape identified an interaction between the oscillations of the trailing vortex system and von Kármán-like oscillations from the side and top edges of the train, with a Strouhal number of 0.2. These oscillations have been visualised in the CFD

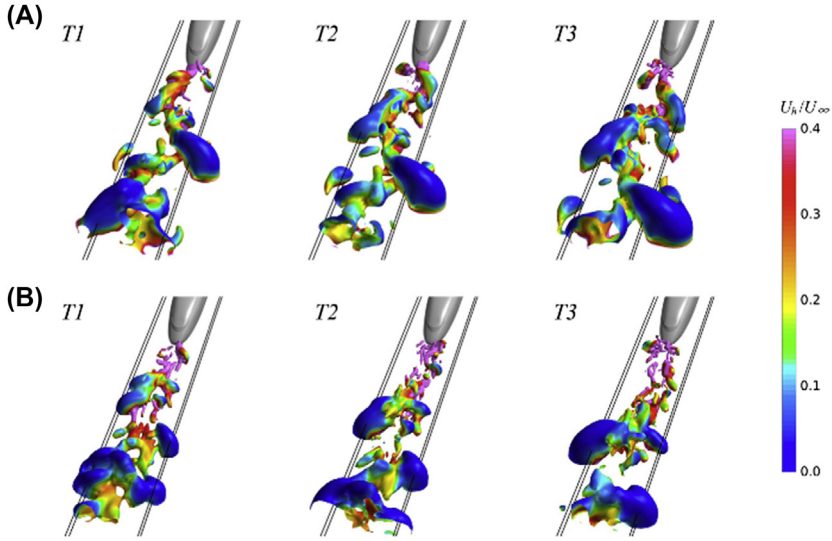

Figure 5.17 ***Wake vortex oscillations calculated by Xia et al. (2017a).*** (A) – stationary ground; (B) – moving ground). *(Copyright Elsevier.)*

calculations of Xia et al. (2017a) in Fig. 5.17, again for the stationary and moving ground cases. Similar oscillations have been observed in the CFD DES calculations of Huang et al. (2016) for the Chinese CRH2 train. Clearly, the flow pattern in the near wake is complex and probably quite train and model geometry specific.

5.2.6 Far wake region

In the far wake behind trains, there is little pressure variation and a gradual reduction in the flow velocities – see Figs 5.2–5.5 for example. Baker (2001) applied the rather complex formulation of Eskridge and Hunt (1979) for the wake of road vehicles to describe this variation, and it was found that a number of curve fit parameters were required that varied for the wakes of different vehicles. In Baker et al. (2014c), a much simpler empirical power law form was fitted to train wake data, with the velocity being taken to be proportional to $(x - x_t)^n$, where x_t is the position of the tail of the train. For a wide range of trains, the exponent n was found to be close to 0.5. This is illustrated in Fig. 5.18 for some of the velocity ensembles of Figs 5.2–5.5. The same exponent seems to be appropriate for both streamlined high-speed trains and blunt-ended medium-speed passenger trains.

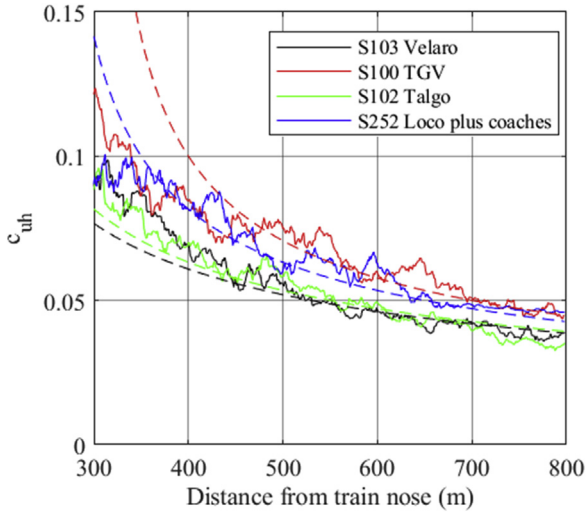

Figure 5.18 Wake decay using data from AeroTRAIN project and reported in Sima et al. (2001) and Baker et al. (2014c). The lines show fits with an exponent of −0.5.

5.2.7 Underbody region

A number of authors have made measurements of velocities and pressures beneath trains in recent years, mainly in investigations of the ballast flight problem (see Chapter 9). Typical pressure and velocity measurements, for the Eurostar Class 373 train (which is essentially a TGV), are shown in Figs 5.19 and 5.20 for the train running over a ballasted track (Quinn et al., 2010; Soper et al., 2017b). This is an 18-coach train, 384m in length, which is effectively two identical units with articulated coaches with a non-articulated connection at the centre of the train. Again, these are shown in the form of ensemble averages, which masks rather large unsteadiness, particularly in the velocity measurements. The nose pressure peak is very obvious, but the nose suction peak is somewhat obscured by high levels of unsteadiness beneath the train. The velocity rises to a constant level within the first car along the train and remains constant till half way along the train where there is a rapid increase due to the nonarticulated bogie mentioned above. It then remains constant to the end of the train. The pressure trace clearly shows the positions of the bogies, with small peaks and troughs at each bogie position. The tail trough and peak is obvious. The magnitudes of both pressures and velocities are much higher than at the side of the train (Figs 5.2 and 5.6).

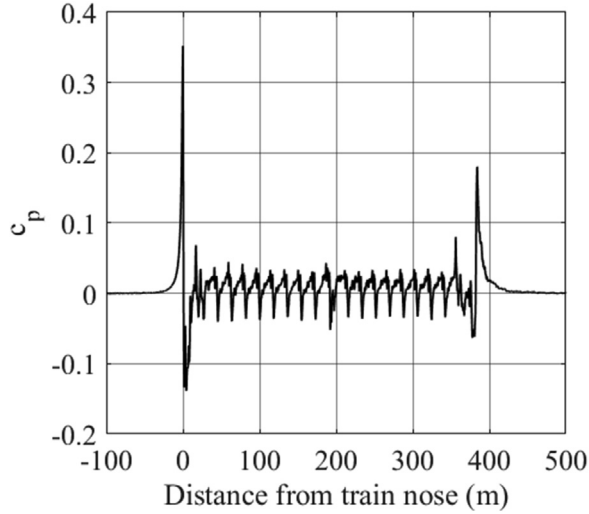

Figure 5.19 Pressures on ground plane beneath the Class 373 Eurostar from Soper et al. (2017b). Measurements made at $y = 0.16$ m. *(© Elsevier, Soper et al., 2017b.)*

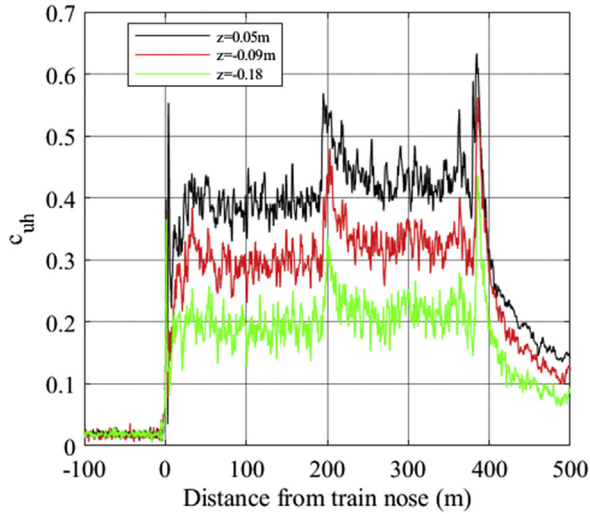

Figure 5.20 ***Ensemble average velocities beneath the Class 373 Eurostar data from Soper et al. (2017b).*** Measurements made at $y = 0$ m. *(© Elsevier, Soper et al., 2017b.)*

Fig. 5.21A and B shows the velocity profiles and the turbulence intensity beneath the train (Soper et al., 2017b). These are plotted in a frame of reference relative to the stationary ground. These profiles extend vertically about half the height of the underbody gap. The boundary layers

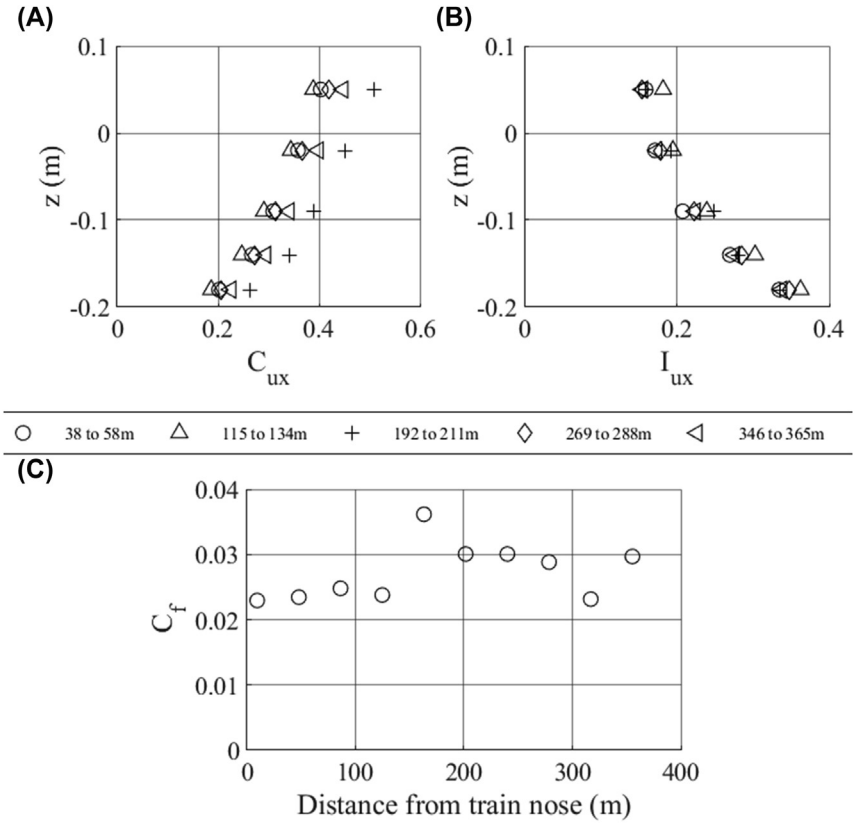

Figure 5.21 ***Underbody boundary layer parameters for Class 373 Eurostar data from Soper et al. (2017b).*** (A) – velocity profiles; (B) – turbulence intensity profiles; (C) – friction coefficient. *(Copyright Elsevier.)*

quickly attain a level of equilibrium and show only minor changes along the train, and the turbulence intensity profiles are also relatively constant. The bed friction coefficient can be calculated from fitting a logarithmic curve to the velocity profiles to find the friction velocity u_τ and then using $C_f = \tau/0.5\rho v^2 = 2(u_\tau/v)^2$. The values thus obtained are shown in Fig. 5.21C. The friction coefficient can be seen to be roughly constant at around 0.03.

Other authors have measured velocity and pressure variations across the complete underbody gap – see Fig. 5.22 for example (Ido et al., 2008), where moving ground wind tunnel results for a three-car Shinkansen train, and full-scale results obtained beneath a 16-vehicle train have been replotted in a frame of reference relative to the ground. These results show

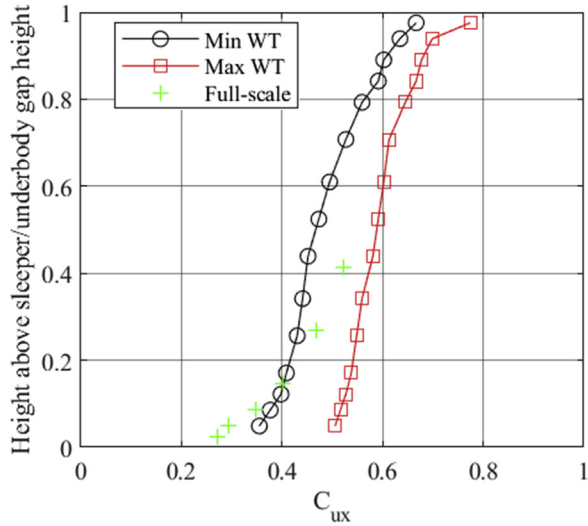

Figure 5.22 Velocity profile across complete underbody gap for Shinkansen train. *Square symbols* show maximum wind tunnel values; *circles* show minimum wind tunnel values; and crosses show full-scale measurements. *(Adapted using data from Ido et al. (2008).)*

a characteristic 'S' shape, with a point of inflection at about half height. Essentially, the flow beneath the train consists of two merging boundary layers — one on the under surface of the train and one on the track i.e., a sort of classic Couette flow.

Such velocity profile measurements enable the skin friction coefficient at the ground to be determined, and the results are shown in Table 5.3 below for a number of investigations. Fitting a log law to the data is not straightforward, particularly in terms of determining the virtual origin, so the values given should only be regarded as approximate. Nonetheless, they do suggest that for ballasted track, the skin friction coefficient is of the order of 0.02—0.06 and is somewhat lower for slab track. These values are an order of magnitude higher than the skin friction coefficient on the side of vehicles (see Table 5.2 above).

5.2.8 Pressures on trains

Up to this point, we have been concerned with the velocity and pressure fields around trains. However, pressure fields also develop on the trains themselves and, thus, result in aerodynamic forces on trains. For the case of trains in the open air on level ground in still air conditions, the pressure variations on the train surface are usually quite small, with the exception of

Table 5.3 Skin friction coefficients in the underbody gap.

Tests	Track	Train	u_v/v	C_f
Ido et al. (2008)	Ballast	Shinkansen – equipment faired	0.129	0.0334
Ido et al. (2008)	Ballast	Shinkansen – side skirts	0.043	0.0036
Kwon and Park (2006)	Ballast	KTX	0.113	0.0247
Deeg et al. (2008)	Ballast	ETR500	0.141	0.0398
Lazaro et al. (2011)	Ballast	S103 Velaro	0.172	0.0590
Premoli et al. (2015)	Ballast	Unidentified train 13 car	0.136	0.0367
Premoli et al. (2015)	Ballast	Unidentified train 13 car	0.125	0.0310
Premoli et al. (2015)	Ballast	Unidentified train 11 car	0.107	0.0229
Soper et al. (2017b)	Ballast	Class 373 Eurostar	0.120	0.0289
Deeg et al. (2008)	Slab	ETR500	0.070	0.0098

the regions around the train nose and tail. Fig. 5.23 shows the pressure around the nose of three trains measured in wind tunnel tests; the medium-speed Class 43 HST passenger train with a raked but sharp-edged nose shape Morden et al. (2015); the high-speed CRH3, with a convex curved streamlined nose shape (Xia et al., 2017a) and the high-speed CRH380A,

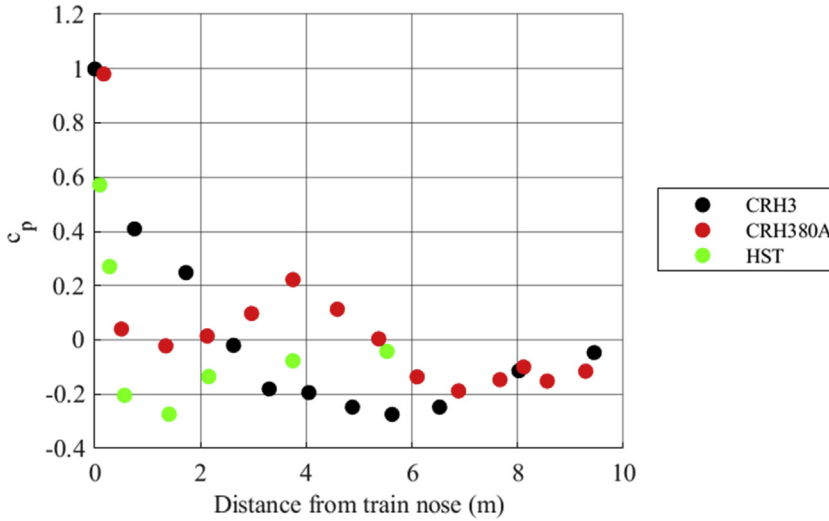

Figure 5.23 Nose pressures for high-speed and medium-speed trains. *(Data from Morden et al. (2015), Xia et al. (2017a), Guo et al. (2016).)*

with an elongated slightly concave nose shape (Guo et al., 2016). Details of all the trains are shown in Appendix 1. In addition, Zhang et al. (2018) also provide pressure data for the CRH380 at a range of yaw angles. The HST results show a positive pressure coefficient at the nose itself ($x = 0$ m), with a negative pressure peak at around $x = 1.5$ m, and the pressure then approaches zero at $x = 5$ m. The CRH3 pressure again has a positive pressure peak at $x = 0$ m with a negative pressure coefficient peak at $x = 5.5$ m and approaches zero at $x = 10$ m. The CRH380A shows rather different behaviour, with a positive pressure coefficient at the nose, but with a region of positive pressure coefficient around the concave dip in the elongated nose at $x = 4$ m and a negative peak at $x = 7$ m.

5.3 Trains on level ground in windy conditions

5.3.1 Flow around trains in crosswinds

Perhaps the most important parameter that needs to be specified when considering trains in crosswinds is the yaw angle ψ, the angle between the wind velocity vector relative to the train and the vehicle direction of travel. This is defined in terms of wind speed, wind direction and vehicle speed in Eq. (3.2). For small yaw angles of the order of 0−5 degrees, i.e., low crosswinds, the flow field around a train can be modified in small but potentially significant ways. For example, the boundary layer development along the train can be skewed, with a thicker lee side boundary layer and a thinner windward side boundary layer. The near wake seems to be particularly sensitive to small crosswinds. The AeroTRAIN project slipstream measurements (Baker et al., 2014c,d) show that the ensemble averages of velocities can be significantly changed by even low crosswinds − see Fig. 5.24A, for example. This is presumably because the longitudinal trailing vortices in the wake are moved laterally (towards or away from the measuring instruments) in crosswind conditions. The same effect can be seen in the one second gust measurements from individual train passes shown in Fig. 5.24B. These show the maximum measured gust in each train pass, and it can be seen that, in a statistical sense at least, these values are quite sensitive to small changes in yaw angle. The use of one second gusts in characterising the slipstreams will be further discussed in Chapter 8. Now as for most of the time trains will not experience still air conditions, but will be operating in a flow at a small yaw angle, these results suggest that the still air case discussed at length above is to some degree only an abstraction or an average of measurements that fluctuate about a zero yaw angle.

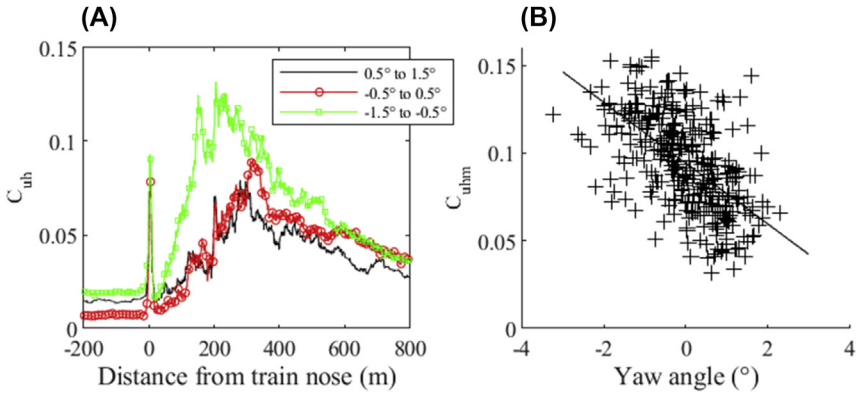

Figure 5.24 ***Effect of crosswinds on slipstream behaviour for S103 Velaro train.*** (A) – ensemble average velocities; (B) – one second maximum gust velocities; slipstream velocities measured at 1.2 m above the top of the rail and 3 m from the track centreline. *(Data from AeroTRAIN project reported in Sima et al. (2011) and Baker et al. (2014d).)*

At larger yaw angles, from 5 to 40 degrees, it is generally accepted that longitudinal trailing vortices form on the leeward side of streamlined trains. Early wind tunnel work at Cambridge (Mair and Stewart, 1985; Copley, 1987) studied this vortex pattern in detail around an idealised train shape above a ground board and revealed a complex vortex structure along the train (Fig. 5.25). Similar flow patterns have been revealed in more recent CFD calculations (Fig. 5.26) (Gallagher et al., 2018).

It might be expected that such longitudinal vortices in the wake will have a significant effect on slipstream velocities. Indeed, the collation of gust results for a wide variety of trains given in Baker et al. (2007) suggests

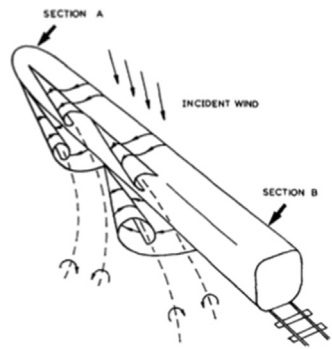

Figure 5.25 Inclined vortices in the wake of an idealised train from Mair and Stewart (1985), Copley (1987). *(Copyright Elsevier.)*

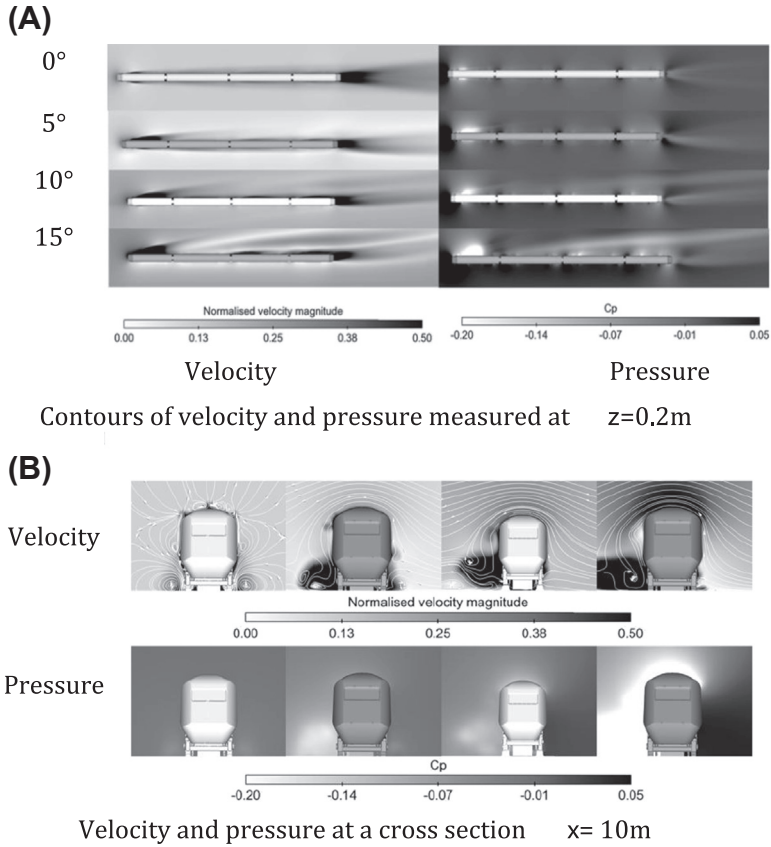

Figure 5.26 ***Inclined vortices in the wake of a Class 43 HST in crosswinds from Gallagher et al. (2018).*** (A) Contours of velocity and pressure measured at $z = 0.2$ m, (B) velocity and pressure at a cross section $x = 10$ m. *(Copyright Elsevier.)*

an increase in slipstream velocities with yaw angle, although the data are very scattered. Similarly, the moving model measurements of freight train slipstreams of Soper et al. (2014) and the related CFD calculations of Flynn et al. (2014) suggest a magnification of peak slipstream velocities as the yaw angle increases.

The extent to which such complex structures exist in highly turbulent natural conditions, with turbulent winds and complex train geometries, is debatable. This is illustrated by the results given in Fig. 5.27 (Gallagher et al., 2018), which shows the variation in yaw angle and side force coefficient per unit length on a loop on the power car of a Class 43 HST in operational conditions (effectively describing the difference in the pressures

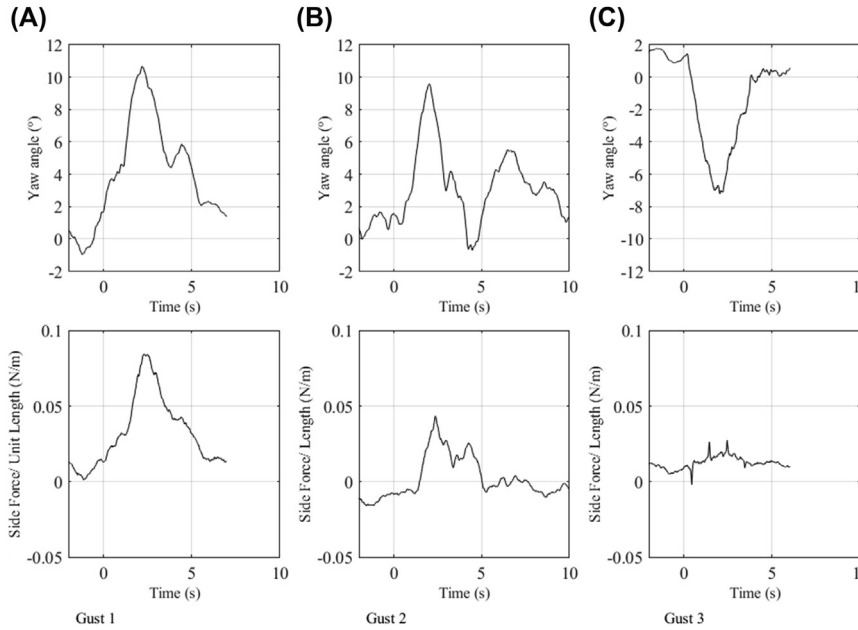

Figure 5.27 ***Crosswind pressure development on a Class 43 HST for discrete gusts from Gallagher et al. (2018).*** (A) Gust 1; (B) Gust 2 and (C) Gust 3. *(Copyright Elsevier.)*

on the leeward and windward sides of the train) for a small number of discrete wind gusts. Although the correlation between yaw angle and force coefficient can be seen to be respectable for gust 1, it is poor for gust 2 and nonexistent for gust 3. This reflects the variability of the wind conditions, the time taken for the flow around the train to develop and the nature of topography over which the train travels. These results serve as a warning that the much more stable and deterministic results of physical model tests and CFD are only a realisation of a much more complex reality.

At the higher yaw angles (above 60 degrees), which are only relevant for slow or stationary trains, such evidence as exists suggests that the flow field around trains more closely resembles that around a prism normal to the flow, with large-scale separation and some degree of vortex shedding, although the latter is inhibited by the effect of the ground. Fig. 5.28 shows a useful diagram from the work of Chiu and Squire (1992), which gives an indication of how the flow patterns develop along the length of the train as yaw angle changes. It can be seen that, in the intermediate yaw angle range, someway away from the nose, there is a region in which the flow switches intermittently between the low and high yaw angle regimes.

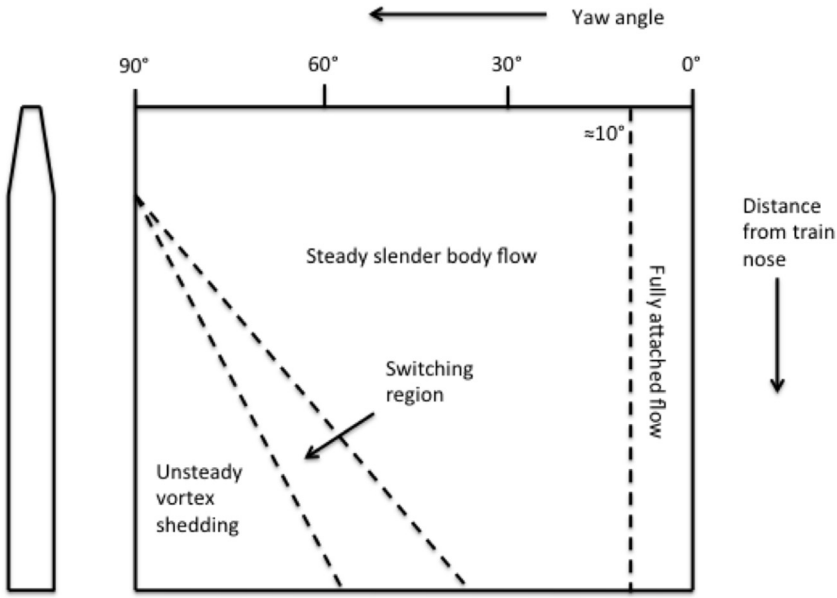

Figure 5.28 Development of wake for different yaw angles from Chui and Squire (1992). *(Copyright Elsevier.)*

5.3.2 Pressures and forces on trains in crosswinds

These major changes in flow field of necessity have a significant effect on the pressure field around trains. To illustrate this, we use the full-scale, physical modelling and CFD data described in Gallager et al. (2018) for the Class 43 HST, a medium-speed passenger train with sharp edges around the nose. Fig. 5.29 shows contour plots of the pressure on the leading vehicle as the yaw angle increases, obtained from low turbulence wind tunnel results with a stationary ground simulation. It can be seen that, as the yaw angle increases, the pressure increases on the windward side of the vehicle and decreases on the leeward side, and a suction develops over the leading edge of the roof, near the nose at lower yaw angles, but progressively extending all down the vehicle. This results in overall side and lift forces on the vehicle, which have obvious implications for crosswind stability (Chapter 11).

More detailed plots of the pressure around a loop close to the downstream end of the leading car are shown in Fig. 5.30 from stationary wind tunnel tests, moving model tests and DES CFD calculations. In general, the agreement between the techniques can be seen to be very good, with the

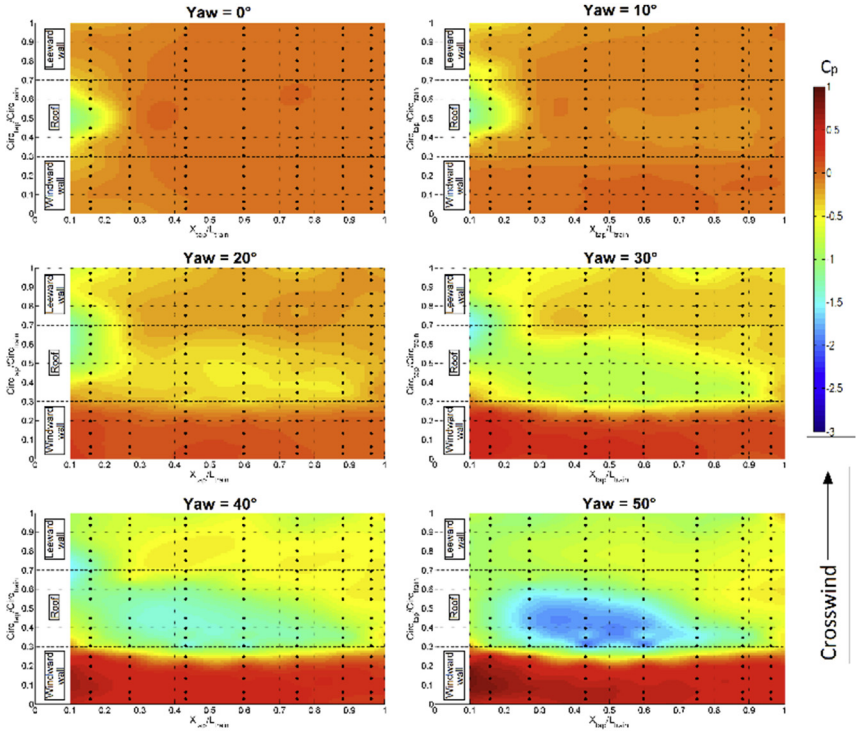

Figure 5.29 Contour plots of pressure coefficient from wind tunnel tests around the leading car of a Class 43 HST from Gallagher et al. (2018). *(Copyright Elsevier.)*

developing suction over the windward edge of the roof being very apparent.

Fig. 5.31 shows a comparison between the wind tunnel pressure coefficient data at low yaw angles and measurements made at full scale. Although the overall comparison is quite good, the large uncertainty bands that give the standard deviations of the full-scale measurements are worthy of note. Again, the physical model and CFD techniques give something of a false impression as to the steadiness and repeatability of the overall flow.

The form of the results in Figs 5.30–5.32 is quite typical for passenger trains. The major variability between trains is in the development of the large suction peak around the front of the roof of the vehicle. For freight trains, because of the large variations in train consist, generalisations are difficult to make. However, for the specific case of a container train, Soper (2014) and Soper et al. (2015) report moving model rig measurements of container pressures in crosswinds, and Flynn (2015) and Flynn et al. (2016)

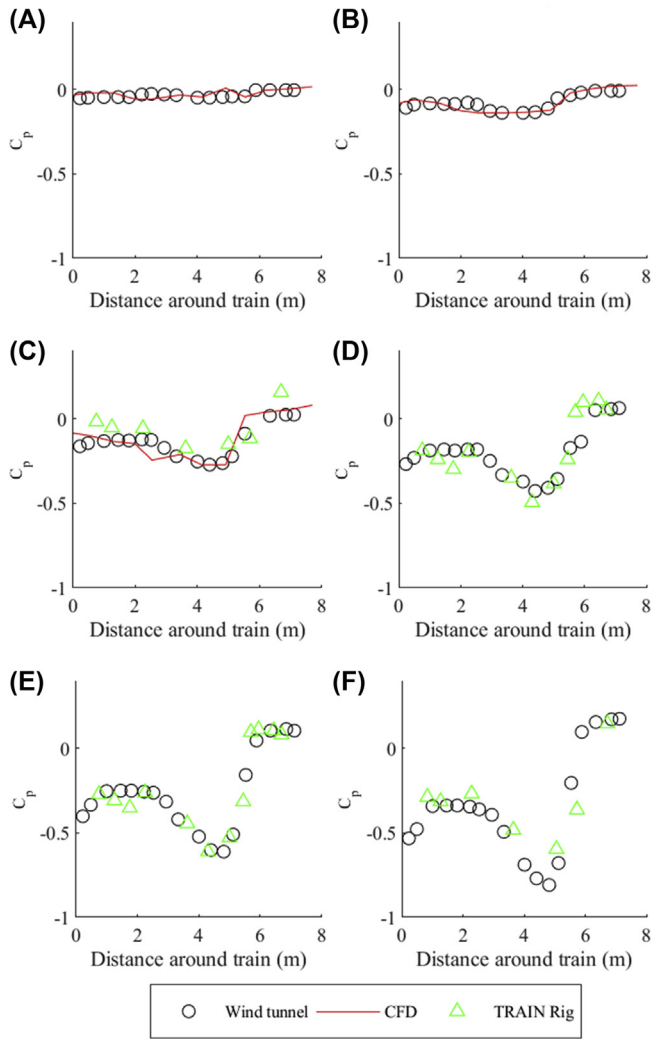

Figure 5.30 ***Pressure development around the Class 43 HST as the yaw angle increases data from Gallagher (2018).*** Distances below 2.5 m are on the leeward wall; from 2.5 to 5.5 m on the roof and above 5.5 m on the windward wall; (A) − 5 degrees yaw; (B) − 10 degrees yaw; (C) − 15 degrees yaw; (D) − 20 degrees yaw; (E) − 25 degrees yaw; (F) −30 degrees yaw. *(Copyright Elsevier.)*

report associated DDES CFD calculations. The configuration studied was a Class 66 freight locomotive followed by four fully laden container wagons. The pressure distributions for the container on the third wagon at a yaw angle of 30 degrees are shown in Fig. 5.32. As with the Class 43 data above,

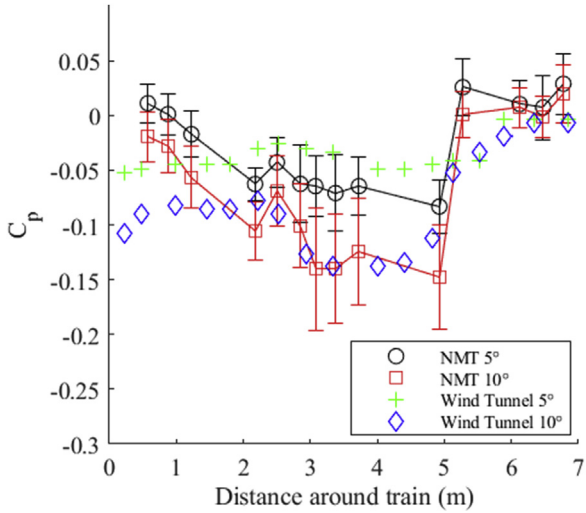

Figure 5.31 Comparison of wind tunnel pressures and full-scale measurements for Class 43 HST. *(Copyright Elsevier.)*

there is a low-pressure region over the top of the container but of a significant greater extent, presumably due to a large-scale separation over the container itself.

5.4 Trains travelling through different railway environments

Railways of course travel through a range of environments, both natural and man-made, that one might expect to have an effect on the air flow around the train, and these effects will be considered briefly in this section. Specifically, we will consider the effects of route topography — ballast platforms, embankments and viaducts — and then move on to consider the effects of railway infrastructure — platforms and flow confinements such as overbridges and stations.

The ballast platforms that support many lines can be of very variable height — from close to zero above the surrounding ground level to 1.5 or even 2 m above ground level. The effect of variable ballast platform height has been investigated by Soper et al. (2017a) and Bell et al. (2014). The former describes moving model rig tests with a range of ballast shoulder heights and three different types of train — a high-speed train, a medium-speed passenger train and a freight train. In general, very little effect of

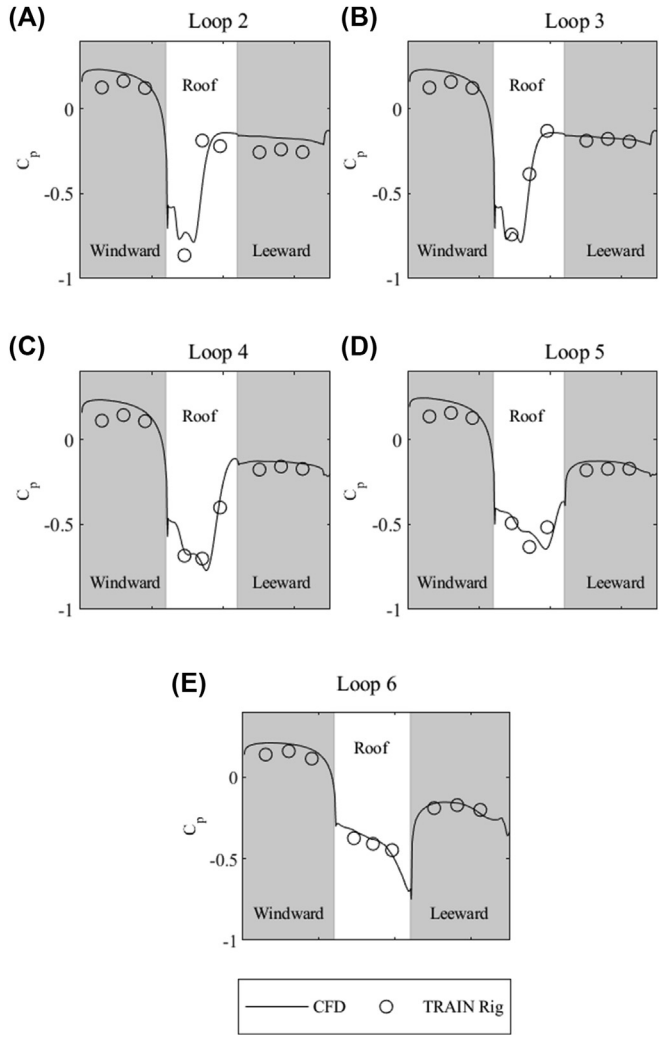

Figure 5.32 Pressure distributions around freight container in a crosswind from Flynn et al. (2016). *(Copyright Elsevier.)*

ballast platform height on the train slipstream velocities and pressure transients could be detected, except for very small ballast platforms. In such cases, there was a marked shift in the ensemble average slipstream velocities from the values for higher ballast platforms, particularly in the near wake of the vehicle. Bell et al. (2014) carried out stationary model wind tunnel tests with a flat ground simulation and a ballast platform simulation, and thus

there are issues concerning the adequacy of the simulation. Nonetheless, they did show that the platform simulation allowed the wake trailing vortices to diffuse rather more before coming into contact with the ground and moving away from the track than was the case for the flat ground, where the trailing vortices moved rapidly away from the track behind the train. The results of the two investigations are broadly consistent in showing the importance of simulating a ballast platform, but the height of that platform does not seem to be too important.

Two of the major items of railway infrastructure are embankments and viaducts, and the effect of increased wind speeds over such structures is important in the assessment of train crosswind stability. Attention has been in the main directed to measuring the forces on trains on embankments and bridges (see, for example, Cheli et al., 2010a), and there does not seem to have been a great deal of work on understanding how the flow around trains changes in such situations. The wind speed up over embankments has been investigated widely by the wind engineering community and is now included in most loading codes of practice (CEN, 2010). Very broadly, for winds normal to the embankment, the wind near the ground speeds up, and at the top of the embankment the velocity profile is flatter (i.e., change less with height) than at ground level. The turbulence level stays the same, and thus the turbulence intensity at the top of the embankment is less than that at an equivalent height at ground level. For nonnormal winds, the assumption often made in the calculation of vehicle overturning risk is that the normal component of flow is speeded up, whereas the component of flow parallel to the embankment remains constant. This has been named the 'Baker Hypothesis' by some in the industry on the basis of a paper from the 1980s (Baker, 1984). However, it is worth remembering that reliability of this hypothesis should not be assumed as, at best, this suggestion was tentative and based on a very small number of full-scale experimental data points.

Similarly, one can expect that the wind will speed up over viaduct structures, due to the increased local blockage of the flow, although the amount of speed up will depend on the precise geometry of the structure, in particular the under- and along-track structure, such as arches and parapets as they affect underbody blockage and offer shielding, respectively.

The effect of station platforms on the development of train slipstreams is of importance in determining the safety of waiting passengers. This effect was studied in the AeroTRAIN project (Baker et al., 2014d), where it was found that, within the limits of experimental uncertainty, the effect of low

platforms (less than 0.4 m in height) on gust values at any particular height above the track was minimal. However, a rather fuller analysis of the ensemble averages does reveal an effect of platforms as can be seen in Fig. 5.33. Fig. 5.33A and B show measurements at the trackside and above platforms of heights 0.18 and 0.38 m for the ICE-T train, at heights of $z =$ 1.2 m and 1.38 m above the track and a height corresponding to 1.2 m above the platform ($z = 1.38$ m and $z = 1.58$ m). This difference, however, lay within the uncertainty bounds of the gust measurements of Baker et al. (2014d). Fig. 5.33C shows measurements for a Class 91 locomotive and trailing coaches at trackside at $z = 0.7$ m and above a higher 0.9 m platform at $z = 1.6$ m (i.e., 0.7 m above the platform). Here, the effect is obvious, with lower platform speeds than at the equivalent trackside height. Thus, it can be conjectured that low platforms may amplify the slipstream velocities, perhaps by forcing the low level flow over the platform, whereas higher platforms may give a sheltering effect.

Finally, there is a class of vehicle environments that is intermediate between the open-air case and the tunnel case that will be considered in Chapter 6. These may be called semi-confined flows, where the flow around the vehicle is constrained to the side of the track and above the track — for example, deep vertical sided cuttings, long overbridges, etc. One would expect the flow around trains in such environments to show characteristics that are somewhere between those of trains in the open air and those in tunnels. Such cases have not been considered to any great extent in the past, the exception being the work of Gilbert (2013) and Gilbert et al. (2013a,b), who looked at the flows with varying levels of idealised confinements, and the tests carried out on enclosed station environments by Takei et al. (2008) and Zhou et al. (2014). Gilbert et al. found that the pressure transients for low levels of confinement are very similar to those outlined in Section 5.2.3 with nose and tail peaks. As the degree of confinement increases to 100%, both the nose and tail peaks increase in magnitude and spread out spatially, and the nose peak takes on the form for tunnels that will be discussed below. However, when there is some degree of connection into the confined area, no pressure waves can be observed. When the confinement is complete however, then the oscillations caused by pressure waves are very apparent. For the situation considered, the 'tunnel' was very short and thus the waves pass up and down the tunnel very rapidly, showing pressure peaks that are very close together. Thus, there can be seen to be a gradual change from the open-air case to the fully enclosed tunnel case. The nature of this variation can be expected to be very dependent on the precise confinement geometry.

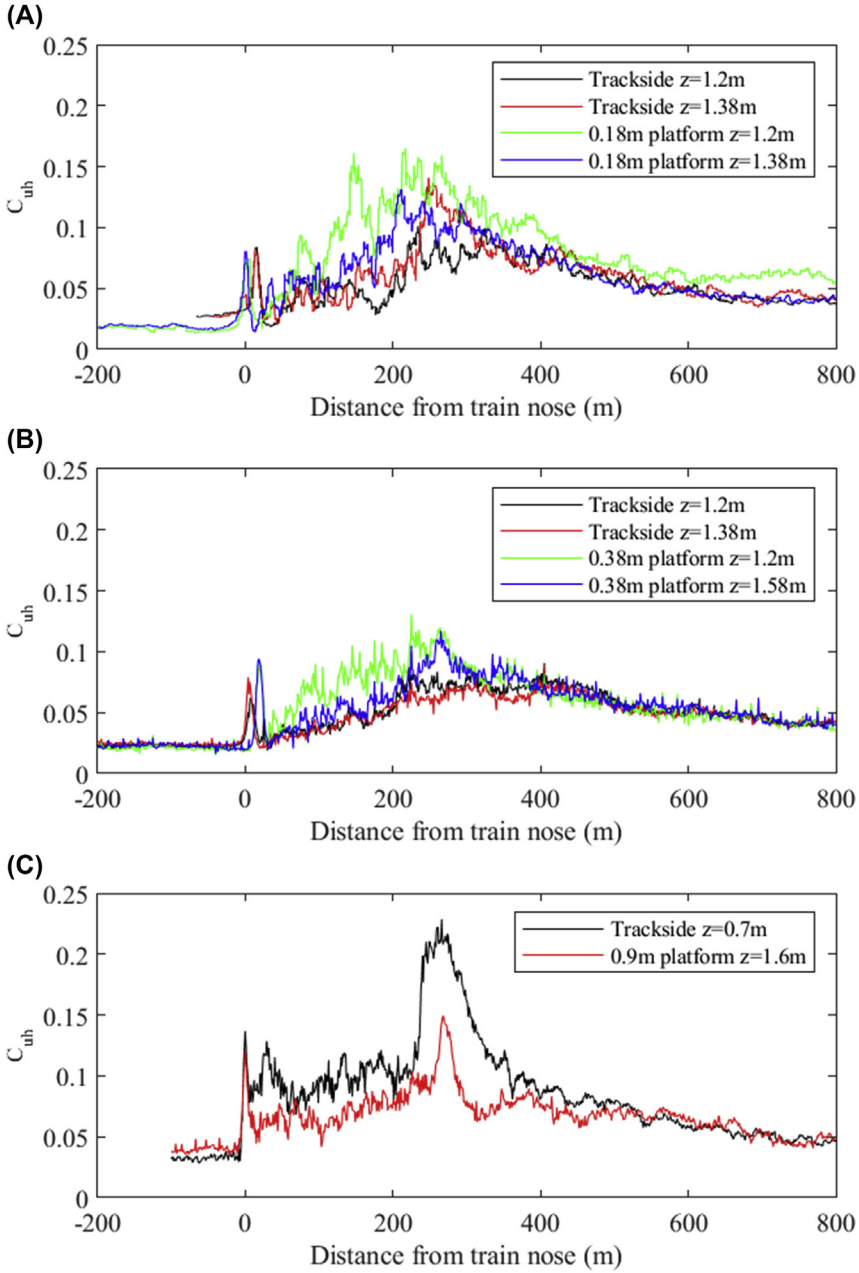

Figure 5.33 ***Effect of platforms on slipstream velocities.*** (A) — ICE-T 0.18 m platform; (B) — ICE-T 0.38 m platform; (C) — Class 91 (IC225) locomotive plus coaches, 0.9 m platform. *(Data from AeroTRAIN project reported in Sima et al. (2011) and Baker et al. (2014c).)*

Similar transition forms of pressure transient were measured by Takei et al. (2008) for an enclosed station environment, but the relatively unenclosed geometry of the station simulated in the moving model tests of Zhou et al. (2014) were much more similar to the unconfined flow case. These investigations will be considered further when the loads on trackside structures are considered in Chapter 8.

CHAPTER 6

Trains in tunnels

6.1 Introduction

When trains enter and travel through tunnels, a number of aerodynamic effects occur. These include

- pressure changes that may cause aural discomfort to people on the train and load the train structure and equipment and fitments in the tunnel,
- air movements displaced by and around the train that increase the aerodynamic drag of the train and exert loads on equipment located in the tunnel or personnel working therein, and
- pressure emissions into the ambient surroundings of the portals.

The basic mechanisms by which these phenomena are generated will be described in the following sections. The practical aspects, including methods of calculation and the issues that arise from these phenomena, are discussed in Chapter 12, together with methods of alleviation.

6.2 Pressure changes

When a train enters and leaves a tunnel, it generates pressure changes, also called pressure waves, a few percent above or below ambient atmospheric pressure. These pressure waves move along the tunnel at the speed of sound, reflecting at any interface with the open air, such as at the portals or at the top of any airshafts that are present. Closed surfaces, such as a blocked shaft, will also reflect pressure waves. When reflected at these open-air interfaces, the pressure waves are modified such that waves above ambient pressure return into the tunnel as waves below ambient pressure and vice versa. This means that a train moves through a complex superposition of pressure changes as it travels through the tunnel. These waves can combine to give relatively large positive or negative pressure transients over short periods of the order of a few seconds.

In the first instance, it is convenient to consider the pressure waves as step changes. As a train enters the tunnel through the entrance portal,

Train aerodynamics
ISBN 978-0-12-813310-1
https://doi.org/10.1016/B978-0-12-813310-1.00006-X

it behaves like a leaky piston and it instantaneously increases the pressure in the tunnel at the nose of the train. As a result, a step change of pressure above ambient pressure propagates along the tunnel at the speed of sound towards the opposite tunnel portal. This step change is called the initial compression wave or nose entry wave. It progresses to the exit portal, where it is reflected back towards the train entrance portal as a second pressure step change, called a rarefaction or expansion wave, at a few percent below ambient pressure. Not all the energy is contained in the reflected wave, however, and some energy is emitted into the region outside the portal. This process continues as the pressure wave proceeds up and down the tunnel, reflecting and changing sense at each portal. Under this reflection process with energy losses at each portal, and due to the friction of the tunnel walls and ballast bed, the magnitude of the pressure wave gradually reduces and the wave dies away.

The reflection of pressure waves differs at open boundaries, such as portals, and at closed boundaries, such as capped airshafts or cross-passages with doors. Fig. 6.1 shows a finite width compression wave approaching an open and a closed boundary from a tunnel tube. In Fig. 6.1A and D, the wave is moving to the right at the speed of sound. In Fig. 6.1B, the wave meets the open boundary and is reflected back into the tunnel tube as a rarefaction wave. In Fig. 6.1E, the wave encounters a closed boundary and is reflected back into the tunnel as a compression wave. In Fig. 6.1C and F, the different reflected waves return into the tunnel tube.

As the train continues to enter the tunnel after nose entry, the pressure rises due to frictional effects between the tunnel and the train. When the train tail enters the tunnel, a rarefaction wave is generated which

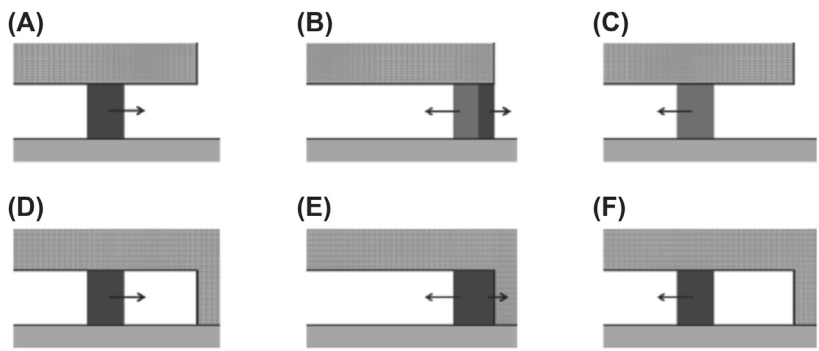

Figure 6.1 ***Reflection of a finite width compression wave.*** (A–C) At an open boundary; (D–F) at a closed boundary –*dark grey* = compression, *light grey* = rarefaction.

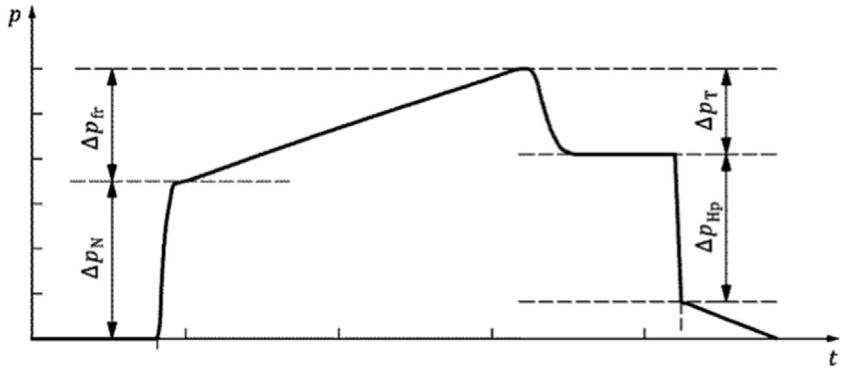

Figure 6.2 Idealised 'pressure signature' measured at a location in a tunnel due to the entrance of a train. *(From CEN (2010b) - used with permission.)*

propagates forward, again at sonic speed, first alongside the train and then into the tunnel.

Fig. 6.2 shows the idealised pressure change time history caused by a train at particular location in a tunnel. Δp_N is the pressure rise due to the train nose entry compression wave, Δp_{fr} is the pressure rise due to frictional effects as the train body enters the tunnel, Δp_T is the pressure drop due to the train tail rarefaction wave and Δp_{HP} is the pressure drop caused by the train nose passing the measurement point.

The standard way to represent pressure waves generated by trains travelling through tunnels is by using a wave diagram. Fig. 6.3 shows a wave diagram for a 400 m long train travelling through a tunnel 2000 m long. The train nose enters at time zero, and it leaves the tunnel at 36 s. The train tail enters at 7.2 s and leaves at 46.2 s. It can be seen that the train nose and tail also generate pressure waves when they exit the tunnel and waves remain in the tunnel after train exit. The wave diagram can be used to determine where combinations of waves can result in large pressure changes, e.g., at a location 800 m from the entry portal and at about 22 s, two rarefaction waves coincide with the passing of the train tail.

Although the wave diagram is useful in determining the sequence of compression and rarefaction waves occurring at fixed points in the tunnel or alongside the train, it does not tell us anything about the combined magnitudes of these waves. Computational methods are generally required to determine the amplitudes of the pressure waves, and these will be discussed in Chapter 12. One such method has been used to predict the pressure changes at the tunnel midpoint for the tunnel and train shown in Fig. 6.3.

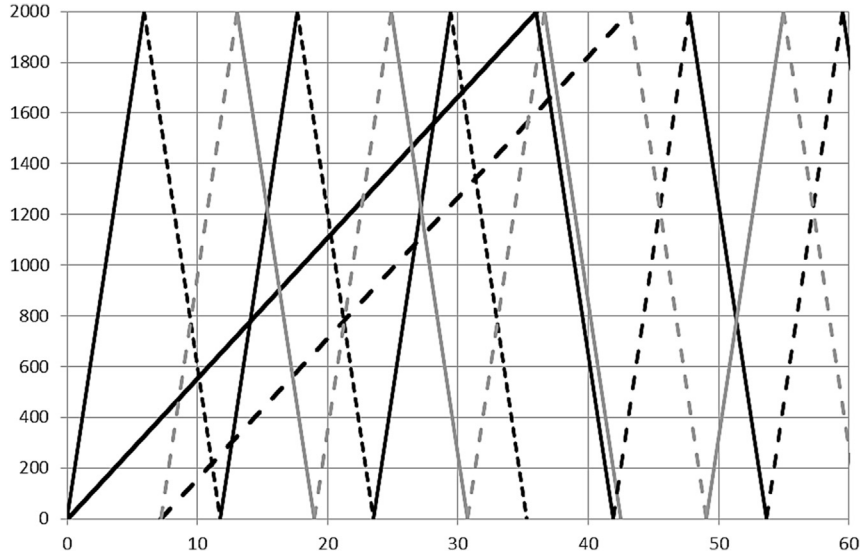

Figure 6.3 Wave diagram for a train travelling through a 2000 m long tunnel. $v = 200$ km/h, $L = 400$ m, *solid black* = nose waves, *solid grey* = tail waves, *thick black solid* = nose path, *thick black chained* = tail path, *solid line* = compression, *dashed line* = rarefaction.

The relationship between the wave diagram and the pressure variations is shown in Fig. 6.4. It shows how the passing of different pressure waves, indicated by the vertical chained lines, generates the pressures at particular locations in the tunnel.

The pressure waves shown in Fig. 6.4 will also cause pressure changes along the train. For an unsealed train, these pressure variations are propagated directly into the vehicles of the train, whereas for partially sealed or sealed trains the pressure changes are attenuated by the sealing, leading to slower, modified pressure variations inside the train. Rapid or large pressure changes may cause aural discomfort for people travelling in the train, and in rare cases could pose a medical aural health problem.

It is also instructive to see an instantaneous distribution of pressures in a tunnel once a train has fully entered; an example is shown schematically in Fig. 6.5. The arrow on the nose entry wave indicates the direction of propagation of the pressure waves at this instant; the train has entered from the left.

The factors that influence the magnitude of the generated pressure waves in a tunnel due to a single train are many and are summarised in Table 6.1, and some are briefly discussed below.

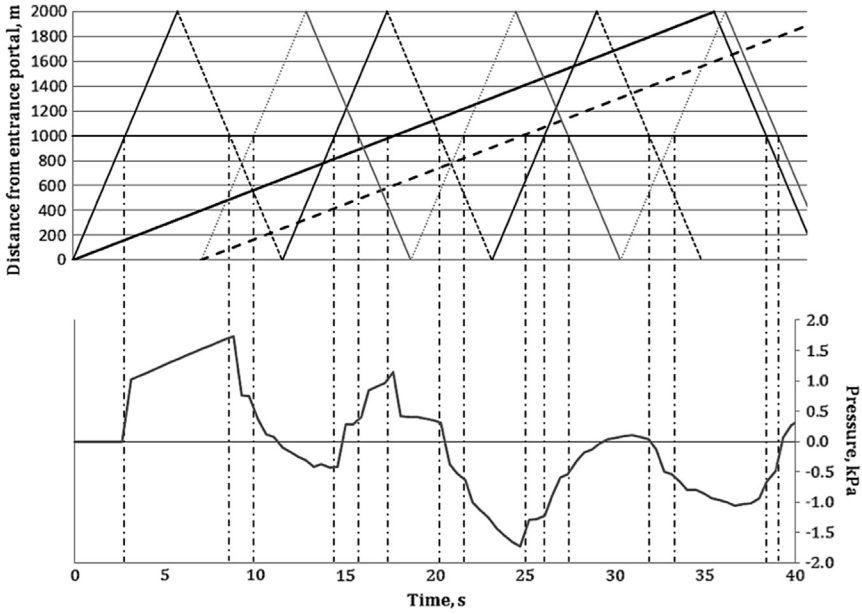

Figure 6.4 Relationship between the wave diagram (top) and pressure predictions (bottom) at the tunnel midpoint; pressures are in kPa. Tunnel length = 2000 m, v = 200 km/h, L = 400 m; pressure calculation undertaken using ThermoTun Online.

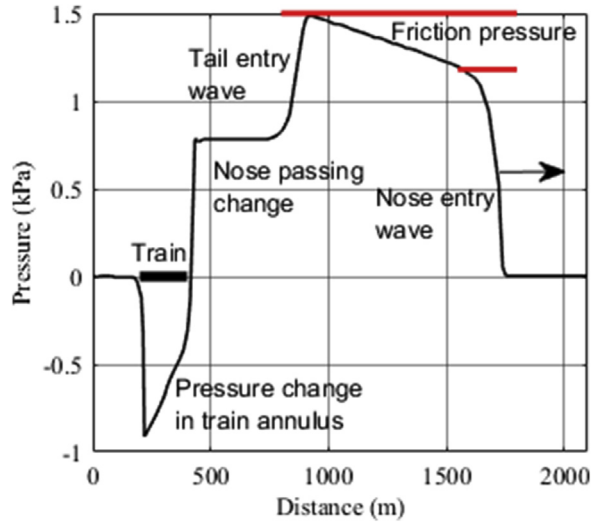

Figure 6.5 Pressure distribution along a tunnel after a train has fully entered. Tunnel length = 6500 m, v = 270 km/h and L = 200 m.

Table 6.1 Relevant factors affecting the magnitude of train pressure changes.

Pressure change	Relevant factors
Nose entry	Train to tunnel area ratio, train speed, ambient airflow speed in the tunnel before train entry, train nose aerodynamic design, local speed of sound and air density.
Frictional rise	As for the nose entry *plus* train area and perimeter, tunnel area and perimeter, train length, train friction factor, tunnel friction factor.
Tail entry	As for the frictional rise *plus* train tail aerodynamic design, pressure loss coefficient of the portal.
Nose passing	As for the frictional rise *plus* train tail aerodynamic design.

The speed of the train during entry is a key parameter, and the amplitude of the pressure changes depends approximately on the square of the speed. Ambient airflows in the tunnel before train entry effectively add to or subtract from the train speed and affect all of the pressure changes. Airflows opposing the train direction of travel increase the amplitude of the train nose and tail entry waves, whereas the amplitudes of these waves reduce when air flows in the same direction as the train.

The train to tunnel area ratio, usually called the blockage ratio, is a fundamental parameter and for relatively small changes of blockage ratio, the pressure changes are proportional to it.

The aerodynamic design of the train, particularly the design of the nose and tail and the friction factor (i.e., roughness due to the surface finish, the effects of window recesses, intercar gap design), also affects the magnitudes of the pressure changes. The nose and tail aerodynamic designs result in local pressure losses, with larger losses occurring from bluff noses and lower losses resulting from streamlined noses.

The pressure superpositions acting in a tunnel more generally also depend on the tunnel length as this affects the timing of waves and their reflections. In addition, the effect of tunnel friction becomes more significant as tunnel length increases, thereby reducing wave magnitudes.

The entry of a second train into a tunnel following the entry of an initial train will increase the number of waves and their reflections, making the wave combinations more complex at points in the tunnel or on the outside of the trains travelling through the tunnel (as may be envisaged by considering Fig. 6.3). It is clear that pressure time histories will also change

along the length of the trains themselves. In addition, the relative difference in entry times of the two trains will also affect how the train waves superimpose, and therefore their amplitudes.

If tunnels have airshafts, they will usually offer relief of pressures in the running tunnel by providing alternative paths to the external ambient air, although the number of pressure waves in the tunnel will increase.

To a lesser degree, the design of the tunnel portals can also affect pressure waves in tunnels. The use of perforated entrances or trumpet-shaped portals can affect the rate at which entry pressure waves are formed and may thus alter the amplitude of wave combinations.

The pressures alongside trains will propagate into the interior of trains and will affect the aural comfort of passengers or staff on the trains. The degree to which the external pressures propagate into the interior of vehicles depends on the degree of pressure sealing of those vehicles. In many older passenger coaches, the degree of sealing was more or less non-existent, due to the design of the intercar gaps, interior doors and the use of drop-light windows at the vestibule ends or openable hopper windows located in the coach windows. In this type of coach design, passengers and staff on the trains were exposed to the unattenuated pressure changes alongside the exterior of the train. More modern railway coaching stock has varying degrees of sealing, due in part to changes in window and vestibule design and also due to the drive for greater pressure comfort levels required by the train operators. This issue will be returned to when the issue of aural pressure comfort is dealt with in greater detail in Chapter 12.

6.3 Tunnel air velocities

The movement of pressure waves in tunnels sets up pressure differences in the tunnel which then lead to movement of air along the tunnels. The greatest generator of air movements is the moving train itself, which acts like a leaky piston in a cylinder, with air being displaced ahead of, around and behind it.

Fig. 6.6 shows the predicted airflows and the transient pressures at 500 m from the train entry portal of a 2000 m long tunnel, generated by a train travelling at 200 km/h.

Initially, up to about $t = 1.4$ s, there is no air movement, but once the nose entry pressure wave arrives, the air starts to move in the direction of train movement. It can be seen that there is some correlation between the

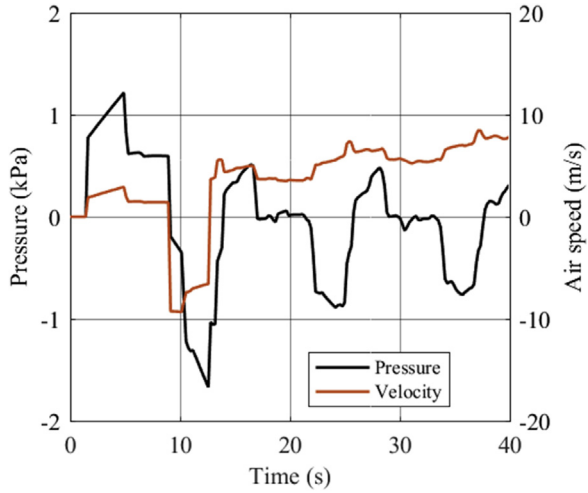

Figure 6.6 Air speeds at 500 m into a tunnel compared with transient pressures. $L = 2000$ m, $A = 8$ m^2, $A_{TU} = 50$ m^2, $v = 200$ km/h; calculations undertaken using ThermoTun Online.

air speeds and the pressure changes. At around 9 s, the train nose passes the location and the air reverses back towards the entry portal. Just after 10 s, the reflection of the nose entry wave passes and the air speed slows towards the entry portal. As the train continues to enter, the air speed in the gap between the tunnel and the train reduces due to friction. Once the train tail passes, the air changes direction again and starts to flow in the train direction. Thereafter, the air continues flowing in this direction, gradually increasing in speed, but with small variations due to the pressure waves passing the point.

It can be seen that air speeds reach a maximum of about 9.8 m/s in the direction of the train entry portal. Air speeds can exceed these levels in tunnels with smaller cross-sectional areas or for trains with less aerodynamic nose designs or travelling at faster speeds and need to be considered if workers have to be in the tunnels when trains are operating. If this is the case, safety niches (a volume cut out of the sidewall of a tunnel, sufficient to hold two or three people and/or equipment out of the main airflows in the tunnel) or handles have to be provided to provide protection for workers when trains pass.

In general, the pressures and airflows in tunnels can be considered as constant across tunnel cross sections except within about 50 m of the

portals, around the bases of airshafts and in the region around the train itself. There have been very few full-scale measurements of the airflows around trains, but Pope and Richards (1984) describe some interesting tests to measure the slipstream and wake flows generated by a train in the 1218 m long Stanton Tunnel in Nottinghamshire. A 200 m long test train, consisting of a Class 47 locomotive hauling nine Mark 1 coaches, was used. Comprehensive air speed measurements were undertaken at 412 m from the tunnel entrance at eight positions spanning the tunnel at two levels, 1.5 and 6.0 m, above the tunnel floor using eight ERA gust anemometers. Tests at each height were undertaken on separate days. Three of the measurement positions at each of the two heights were in the path of the test train, so the anemometers at these locations were mounted on a moveable gate. This was held open as the gate was approached and passed by the train and then closed once the train had passed to enable full measurements of the wake across the tunnel cross section. Based on their analysis of the measurements, Pope and Richards (1984) proposed a model of the annular gap flow between the sides of the train and the tunnel and in the train wake, shown in Fig. 6.7.

Sakuma et al. (2010) also report measurements of airflows in a 3 km long, double-track tunnel and relative to the side of a Shinkansen train travelling through it, at speeds of 250 km/h and above. They present some

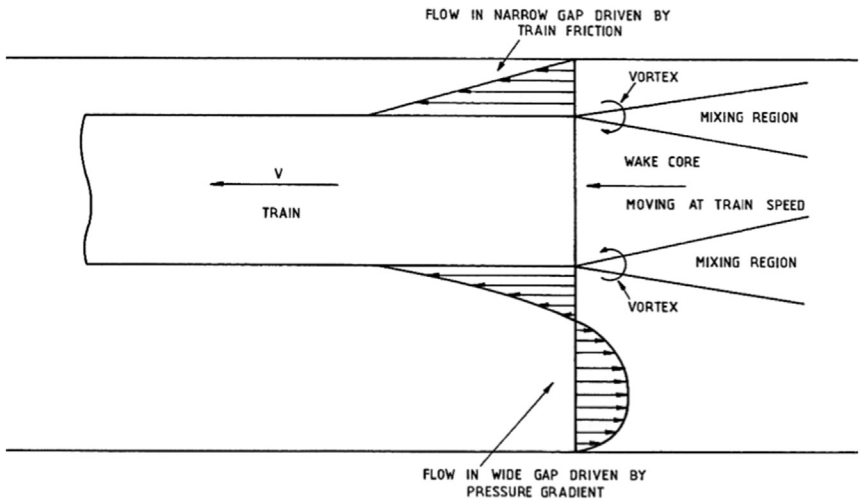

Figure 6.7 Model of the airflow behaviour in the train annulus and wake. *(Adapted from Pope and Richards (1984).)*

velocity profiles at two locations along the train and on the near-wall side and the near-tunnel-centre-side of the train. The streamwise velocity profiles followed the classic 1/nth power law turbulent boundary layer profiles well, with n being in the range of 8−10. Different boundary layer thickening behaviour was observed on either side of the train, in keeping with the Pope and Richards (1984) model.

The presence of an airshaft will have an influence on both the pressures and the airflows in a tunnel. An airshaft, with an area of 5 m^2, was introduced at the midpoint of the 2000 m tunnel considered in Fig. 6.6. The effect of the airshaft on the pressures and air speeds at 500 m from the train entry portal were predicted and are shown in Fig. 6.8, together with the air speeds in the airshaft. The main effects on the pressures are the wave reflections from the bottom of the shaft, seen, for example, between 6.9 and 9.3 s. The airflows in the tunnel are slightly reduced. What is notable are the high air speeds in the airshaft, which varies between 25.5 m/s up the shaft (positive values) and 26.8 m/s down the shaft (negative values). Air speeds of these magnitudes may lead to other issues. These are explored in Chapter 12.

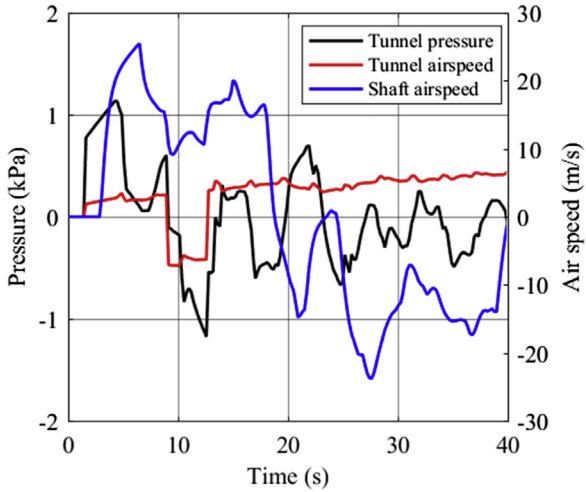

Figure 6.8 Air speeds at 500 m into a tunnel and in a shaft compared with transient pressures. $L = 2000$ m, $v = 200$ km/h; calculations undertaken using ThermoTun Online.

6.4 External pressure emissions and sonic booms

It was stated in Section 6.2 that when a pressure wave meets a boundary with the external atmosphere, such as at the portals, some energy from the wave is lost into the external environment. Under certain circumstances, which will be described later, this energy will be emitted in the audible spectrum and can make a sound described as varying between a gunshot and a booming noise.

It was also stated in Section 6.2 that it is convenient to consider pressure waves as step changes; however, in reality this is not the case. The evolution of the full train cross section during train entry can be considered as a series of infinitely thin slices in the longitudinal direction, each of which generates its own forward-running pressure wave, and in this way the full nose entry pressure wave, for example, is developed as function of time. This is illustrated in Fig. 6.9 based on Woods and Pope (1976) and shows the nose entry pressure wave at 100 m from the train entry portal caused by the entry of a Class 47 locomotive. Note that the pressure wave starts to develop before the leading wheelset enters; this is due to the equivalent of a ship's

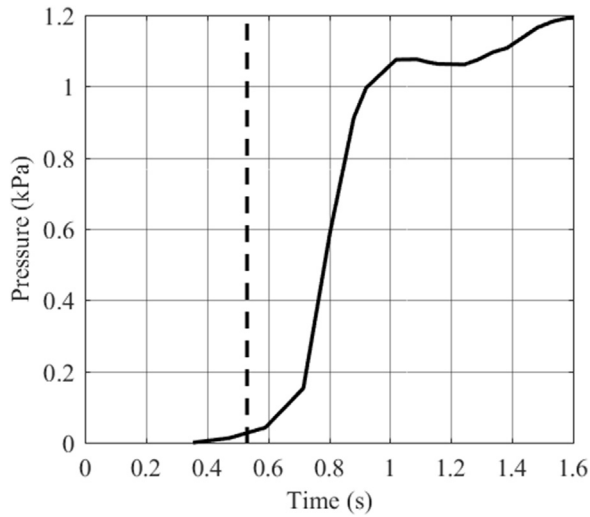

Figure 6.9 Development of the nose total pressure generated by a Class 47 locomotive, $v = 105$ km/h, and measured 100 m from the train entry portal, with the derived equivalent blockage ratio from Woods and Pope (1976). *Dotted line* indicates where leading wheelset enters tunnel portal.

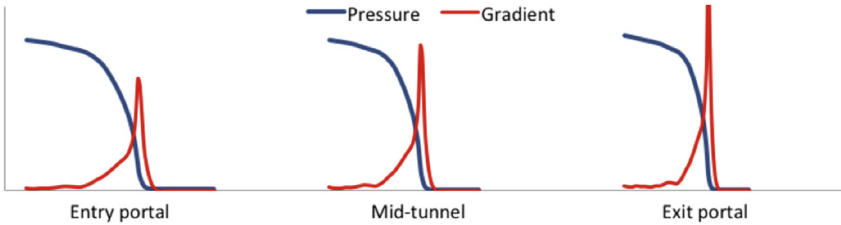

Figure 6.10 Steepening of the nose entry wave along a tunnel from left to right, showing the increase in pressure gradient.

bow wave travelling ahead of the physical front of the locomotive. The increase of the pressure wave follows the development of the full body cross-sectional area of the vehicle as it enters the tunnel and is thus related to the geometric blockage (train: tunnel). Flow separations due to sharp edges on the front of the locomotive lead to an overshoot of the pressure rise; this may be thought of as due to a virtual increase in the train cross section due to the separated flow region.

As this pressure wave progresses along the tunnel, the gradient of the rise between about 0.7 and 0.9 s usually decreases due to frictional effects at the tunnel walls and particularly over the ballast bed. However, under certain conditions, the gradient increases and the wave steepens as it progresses along the tunnel, as illustrated in Fig. 6.10 (which shows part of the nose pressure rise shown to the right of Fig. 6.5 from 1500 m onwards).

There are several processes affecting the pressure gradient as it progresses from inception along the tunnel. The first is steepening of the wave due to inertia. The front of the wave is propagating through stationary air, but the back of the wave moves through air that has already begun to move in the direction the wave is propagating and so travels more quickly than the front.

On the other hand, friction in the tunnel, due to surface roughness, installed tunnel equipment or other general discontinuities (such as cross-passages, niches or airshafts), dampens air movements and reduces the wave gradient. In addition, ballast in the track form appears to permit air from the pressure wave to move into gaps between the ballast stone, which spreads the pressure wave over a longer distance. Wave interaction effects from open cross-passages, deep niches and airshafts can also reduce wave steepening.

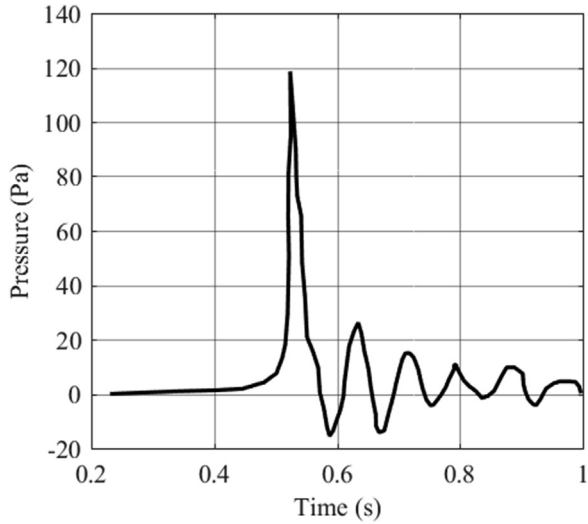

Figure 6.11 Typical micropressure time history outside the train exit portal of a tunnel.

These processes vary in magnitude depending on the tunnel construction and the track form type. In slab track tunnels, inertial steepening of the pressure wave dominates frictional and ballast effects, and smooth tunnel walls and long tunnels further increase the pressure wave gradient at the tunnel exit, where critical micropressure waves can be emitted.

Micropressure waves are pulses of pressure emitted from a tunnel whenever any pressure wave is reflected at a portal (tunnel portal or airshaft portal). Thus, they occur in every tunnel; only when they occur at audible frequencies with sufficient amplitude are they problematical. In this case loud, booming noises can be heard and windows, doors and shutters will rattle in buildings near to the portal. This was the problem experienced during test runs on the Sanyo Shinkansen line in 1974, leading to a number of complaints from nearby residents, Maeda et al. (2000). Fig. 6.11 shows an example of the micropressure wave variation with time at approximately 20 m outside a tunnel.

Conversely, on ballasted track, the ballast effect is dominant, and in long tunnels the wave pressure gradient reduces significantly, reducing the micropressure wave frequencies and amplitudes.

It should be noted that critical micropressure waves can be caused by any pressure wave having a sufficiently steep gradient at an entry or exit portal,

but the most important and the most studied are those caused by train nose entries into tunnels.

For wave steepening to occur, a tunnel has to be long, train speed has to be high enough and the tunnel track construction and track form conducive to reducing tunnel friction. Maeda et al. (2000) give the following expression for the maximum pressure gradient of the initial pressure rise, based on the expression for the pressure rise derived by Hara (1961):

$$\left(\frac{\Delta p_N}{\Delta t}\right)_{\max} = \frac{\rho v^3\left[1-(1-B)^2\right]}{4k_{nose}R_{TU}\left[(1-Ma)\left(Ma+(1-B)^2\right)\right]} \tag{6.1}$$

This can be seen to depend on the cube of train speed, the train Mach number Ma, the train to tunnel area blockage ratio B, the hydraulic radius of the tunnel R_{TU} and the train nose loss coefficient k_{nose}. In a short tunnel, the change of the initial wave from the entrance portal to the exit portal is small and frictional effects have little effect, so the pressure gradient is still closely proportional to the cube of the train speed.

Due to the complexity of the propagation of the nose entry pressure wave along the tunnel, there are no simple formulae describing the process. However, Japanese researchers developed an approximate relationship based on acoustic theory between the compression wave arriving at the tunnel exit portal and the amplitude of the emitted micropressure wave (Maeda et al., 2000), as a function of the distance between the portal and measurement point, r_{MPW}, as shown in Eq. (6.2):

$$p_{MPW}(r_{MPW}) = \frac{2A_{TU}}{\Omega r_{MPW} c_a} \cdot \left(\frac{dp}{dt}\right)_{exit} \tag{6.2}$$

The solid angle, Ω, can be thought of as an empirical factor describing the local topography outside the tunnel and takes theoretical values of between π and 2π, but typically taking a value between three and four. The relationship shows that the peak value of the micropressure wave is inversely proportional to the distance on the measurement point from the exit portal, but proportional to the gradient of the compression wave arriving at the portal.

The variation of the peak value of the emitted micropressure waves from four tunnels for a range of different train speeds is shown in Fig. 6.12. Two of the tunnels have ballasted track and the other two have slab track.

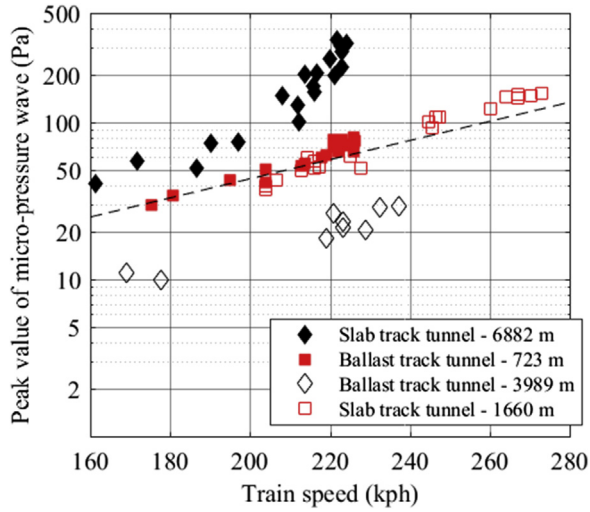

Figure 6.12 Variation of micropressure wave peak values with train speed and track form in different tunnels. *(Adapted from Maeda et al. (2000).)*

In the shorter tunnels, the peak values vary approximately with the cube of train speed, irrespective of the track form. The peak values for the longer tunnel with ballasted track lie below those of the shorter tunnels at each train speed, but seem to follow approximately the same trend with train speed variations. However, the longer tunnel with slab track shows the peak values increase at a rate greater than train speed cubed.

PART 2

Applications

CHAPTER 7

Aerodynamic drag

7.1 The specification of aerodynamic drag – the overall context

We begin our consideration of aerodynamic drag by thinking about the context in which drag information is used, which is primarily to give information concerning the overall resistance of trains. In the past, such information has been required by train designers to be able to specify the necessary power of the traction system and, for electric trains, the power that is required from the electricity supply system. While such calculations are still required, in recent years the focus has changed somewhat, and there is an increasing use of train resistance equations in train simulators to attempt to minimise energy consumption through optimising speed profiles and similarly for timetable optimisation. Whatever the requirement, there is a need to be able to specify the overall train resistance. Conventionally this has been given by the Davis equation (Davis, 1926; Rochard and Schmid, 2000).

$$F_R = a + b_1 v + b_2 V + cV^2 \tag{7.1}$$

Here v is the train speed relative to the ground, V is the train speed relative to the air and a, b_1, b_2 and c are train-specific constants. The first two terms are taken to be mechanical resistance terms, the third term is the air momentum drag due to the ingestion of air for cooling and air conditioning purposes and the fourth term is taken to be the aerodynamic component – i.e., the aerodynamic drag increases with the square of wind speed relative to the train. Note that V is a function of wind speed and wind direction. The constant c in the Davis equation can be related to the aerodynamic drag coefficient $C_D(\psi)$ as follows.

$$c = 0.5\rho A C_D(\psi) \tag{7.2}$$

where the drag coefficient is a function of yaw angle ψ (defined in Eq. 3.2). A is a reference area usually taken as 10 m^2. The Davis equation implies that

Train aerodynamics
ISBN 978-0-12-813310-1
https://doi.org/10.1016/B978-0-12-813310-1.00007-1

aerodynamic effects will become of increasing importance as vehicle speed increases, and indeed the aerodynamic resistance of trains dominates over mechanical resistance for medium-speed passenger trains at vehicle speeds greater than around 200 km/h, and at 250 km/h aerodynamic drag is around 75%–80% of the total resistance (Gawthorpe, 1978a).

In train performance calculations, the resistance formula is only one aspect of a wider set of issues. Consideration also needs to be given to the routes over which the train will run, the train speed profiles, the number of services and so on. In other words, a duty cycle for a particular train needs to be defined. Trains of course run across their full speed range and only achieve the speeds at which the aerodynamic component of resistance is dominant for part of their journey. As a rule of thumb, the ratio of the percentage energy saved to the percentage reduction in aerodynamic drag coefficient is of the order of 0.3 for low-speed trains and 0.5 for high-speed trains (Baker, 2014b; Orellano and Sperling, 2009). However, this is a very approximate figure and is very sensitive to the nature of the service that is operated and the timetable. To give some further context, Baker (2014b) showed that on a three-mile section of reduced speed running at 50 km/h on a section of track in England between Birmingham and London where the line speed was 200 km/h, resulted in a 4% increase in overall energy usage for the journey, due to the energy consumed in accelerating and decelerating. This was the equivalent of around a 7%–8% increase in aerodynamic drag coefficient. Thus any reduction in drag coefficient can easily be nullified in terms of energy usage if there are operational difficulties.

Now, let us consider the nature of the drag coefficient itself in a little more detail. We consider, first, the case of no crosswind, i.e., $V = v$. The drag coefficient can, in principle, be divided into a number of components. The first is a pressure drag caused by the pressure differences on the nose and tail of the train and which can be expected to be a function of nose and tail shape – the length/height ratio, degree of streamlining, etc. The second component is caused by the pressure difference across the bogies and under floor equipment and is, to a first approximation, a function of train length (L) because the drag losses are repeated along the length of the train. The third component is a friction drag caused by the friction on the train side, roof and underbody. Again, one might expect that this component would broadly scale on the length of the train. However, flat plate boundary layer theory suggests that this component would also vary with a Reynolds number based on train length and with the overall 'roughness' of the

train – some sort of integral measure of the irregularities along the length of the train. One would expect this variation to be proportional to $(vL/\nu)^{-n_f}$, where n_f is of the order of 0.1–0.2 for a smooth train and close to zero for a rough train. It is this friction term that makes physical or CFD modelling at reduced scale problematic, particularly for smooth trains where the friction component will be considerable and can thus be expected to vary significantly between model scale and full scale.

Approximate breakdowns of the drag components for high-speed and regional trains have been presented by Nolte and Wurtenburger (2003), Orellano and Sperling (2009) and Orellano and Kirchhof (2011) and are shown in Fig. 7.1. Whilst the details are somewhat different, the overall message is the same – that the drag arises because of a number of different physical causes, with skin friction playing a major role. The higher contribution of the nose for (usually blunt ended) regional trains than for the later high-speed data is also obvious.

At this point, the essential arbitrariness of the basic assumption of the Davis equation is becoming clear. It assumes that all the aerodynamic effects are included within the (velocity)^2 terms. Whilst this is probably a good

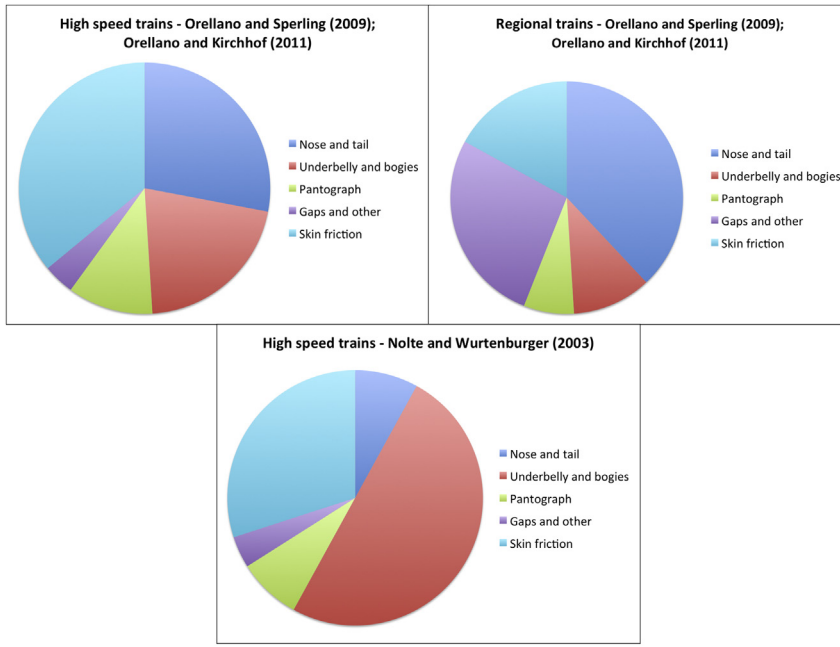

Figure 7.1 Drag breakdown. *(From Orellano and Sperling (2009), Orellano and Kirchoff (2011) and Nolte and Wurtenburger (2003).)*

engineering approximation to reality, the Reynolds number effects on friction drag make this formulation somewhat problematic overall.

In addition to this arbitrariness of definition, the determination of drag coefficient as so defined is subject to considerable uncertainties. In Section 7.2, we will describe the different techniques that can be used to determine $C_D(\psi)$ — full-scale tests, physical model tests and CFD calculations. Lukaszewicz (2007), following a thorough investigation of errors and biases, suggests that, even for well-performed full-scale coasting tests, the uncertainty in values of drag coefficient is of the order of ±8%. It is difficult to be precise about the absolute error associated with physical model tests because such a determination would require tests being repeated in different wind tunnels using different ground simulations. However, experience within the automotive industry suggests that an uncertainty in drag coefficient of ±5% is probably appropriate. CFD results rarely come with any indication of uncertainty, but these calculations are subject to a range of choices in terms of grid, turbulence model, boundary conditions, etc., and an uncertainty estimate of ±5% again seems appropriate.

In addition to these experimental uncertainties, we also have environmental uncertainties, in particular the effects of winds. The average wind speed at 3 m above ground in Britain is of the order of 3 to 4 m/s. Assuming this blows at 90 degrees to the track, this gives a yaw angle of around 4 degrees for a train travelling at 50 m/s (180 km/h). For higher wind speeds, this yaw angle experienced by the train can frequently be of the order of 5 to 10 degrees. It will be seen in Section 7.3 that the drag coefficient increases with yaw, even over this low yaw angle range, and, if not allowed for in energy consumption calculations, can result in further uncertainties in the results.

Thus in conclusion these considerations lead to some cautionary points that need to be borne in mind in what follows.

- Values of drag coefficient come with considerable uncertainties, and this must be appreciated in interpreting the results of energy consumption calculations.
- Experimenters and modellers need to be explicit about the uncertainties of the results that they produce and avoid implicitly giving an impression of much greater certainty than is actually possible.
- Where possible, crosswind effects need to be considered in duty cycle analysis.
- When attempts are made to optimise train shape to reduce nose drag (Section 7.6), consideration needs to be given to optimisation at small yaw angles and also, ideally, for rapidly changing yaw angles.

In Section 7.2, we will briefly consider the different methods that can be used to obtain train aerodynamic drag coefficients. Section 7.3 then considers the effects of crosswind on train drag. In Section 7.4 we consider a number of different methodologies for specifying the overall resistance, as used in different countries around the world. Section 7.5 then attempts a compilation of drag coefficients for a wide range of trains from different sources, and Section 7.6 looks at methods of drag reduction and optimisation.

7.2 Determination of train drag

7.2.1 Full-scale coasting tests

The basic technique for full-scale measurement of train resistance is the coasting test, in which trains are allowed to coast to a rest without power from their top speed, and some or all of the acceleration, velocity, time and distance travelled measured. The former can be measured with accelerometers of different types and the other parameters either using direct methods (using for example Doppler radar units) or tachometry methods (based on the measurement of wheel rotation). Care needs to be taken with the latter as wheel slip can cause inaccuracies. The standard procedure in Europe for such tests is outlined in CEN (2013). The formulation that is used does not include the b_2 term and assumes there is no crosswind so that the Davis equation becomes

$$F_R = a + bv + cv^2 \tag{7.3}$$

where the constant b_1 has been replaced by b. Newton's law for a coasting train is given by

$$Mk_R a_T = F_R + F_{RG} + F_{RC} \tag{7.4}$$

where M is the train mass, k_R is a factor that allows for the inertia of rotating masses (wheels in particular), a_T is the train deceleration, F_{RG} is the resistance force due to track gradient and $F_{RC}$is the resistance force due to curves. In an ideal situation, these tests would be carried out on straight, level track ($F_{RG} = F_{RC} = 0$), although usually there will be some slope on the track that has to be allowed for. For nonlevel curved track, F_{RG} and F_{RC} are given by

$$F_{RG} = Mgi,\ F_{RC} = \frac{0.8Mg}{r_{TR}} \tag{7.5}$$

where i is the track gradient (in the form of vertical increment in track height/horizontal distance — effectively in radians) and r_{TR} is the curve radius. Note that the constant 0.8 in Eq. (7.5) is dimensional and has units of m. From Eqs. (7.3)—(7.5), we thus obtain

$$Mk_R a_T - Mgi - \frac{0.8Mg}{r_{TR}} = (a + bv + cv^2) \tag{7.6}$$

The basic approach is then to obtain values of a, b and c by a curve fit to the experimental data using one of the two methods. CEN (2013) specifies that for both methods, the a term should be found through a low-speed hauling test and that coasting tests should be carried out to obtain b and c over as great a speed range as possible. In the first method (the regression method), the sum of the terms on the left hand side of Eq. (7.6) is calculated as a function of v with the acceleration term being determined from the experimental results and thus b and c determined directly by a regression analysis. A typical deceleration velocity plot is shown in Fig. 7.2. For the second method (the speed history identification method), Eq. (7.6) is written as

$$\frac{dv}{dt} = \left((a + bv + cv^2) - Mgi - \frac{0.8Mg}{r_{TR}} \right) \Big/ Mk_R \tag{7.7}$$

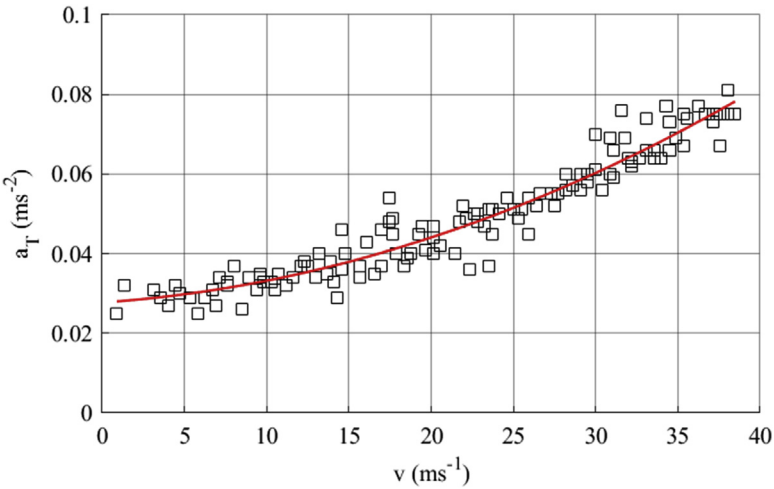

Figure 7.2 Deceleration/velocity curve from tests of Baker et al. (1982) for Class 45 locomotive and six-passenger coaches.

Values of b and c are assumed and Eq. (7.7) is integrated numerically to give a velocity/time curve which is then compared with that obtained from the experimental data. b and c are then altered iteratively until good agreement is found. Experience with such methodologies suggests that the fitting of a quadratic velocity curve is far from straightforward, with the values of the constants being sensitive to the precise methodology that has been used.

Somaschini et al. (2018) also describe a third method to obtain the coefficients b and c. They suggest carrying out tests on the same short section of track at two different speeds. Thus two different expressions can be obtained from Eq. (7.6) and by subtraction the gradient and curving terms can be eliminated to give an expression between the differential acceleration between the two runs and the differential velocity between the runs. A plot of these expressions across all speed ranges thus enables the coefficients b and c to be determined.

It is worth noting at this point that other methods other than coasting tests have been used in the past to obtain full-scale drag coefficient data. These include measuring the force in a link between the train and a towing vehicle (which of course will result in inaccuracies as the nose aerodynamic drag will be affected) or through the measurement of traction power at different speeds, either from engine performance or through the measurement of voltage and current inputs from the overhead. Neither method is in regular use at present.

Finally, a word of warning on the practical use of the Davis equation is appropriate. The constants in the equation have been expressed in many units in previous work, depending on the way in which the velocity is expressed. The simplest way is to consistently use SI units so that the units of c, for example, are $Nm^{-2}s^2$. However, many authors express speed in km/h or mph and resistance in kN, and the value of the constants in the Davis equation will change accordingly. The most complex formulation for c seen by the authors in the preparation of the data collation in Section 7.5 is $dN/(mph)^2$. SI units are definitely to be preferred.

7.2.2 Physical model scale measurements

There are a number of different model scale drag determination techniques, each with their own advantages and disadvantages. At the simplest level, there is the 'image' technique, in which a model is mounted above an upside down (image) model to represent the effect of the ground. Although this was in vogue in the automotive industry in the mid- to late 20th

century, it has been little used in railway research. See Brockie and Baker (1990) for details of such experiments on a small-scale Class 43 HST model.

A more conventional modelling technique is to mount a stationary model on a ground plane in a wind tunnel, with or without some mechanism for removing or minimising the ground boundary layer upwind of the train. For trains, the primary difficulty is the increase in the train/ground boundary layer along the length of the train, which will not be simulated accurately because there is no relative movement between train and ground. As such, this type of test is best restricted to short trains (two or three coaches) or for the investigation of the drag of train components such as pantographs, where the movement of the ground will be unimportant, or to investigate relative drag between different configurations, rather than absolute drag values. They are also useful for looking at the effects of crosswind, as stationary trains can easily be yawed in the wind tunnel. Tests of this type have been described by Mancini et al. (2001) for a 1:7.5 scale ETR500 to investigate the effect of bogie fairings; Golovanevskiy et al. (2012) to investigate the drag of individual 1/40th scale railcars with and without crosswind effects and Kwon and Oh (2013) for a 1/20th four-carriage HEMU-430X to investigate the effect of different train components.

To more accurately model the train/ground interaction, a moving ground plane can be used. The issue here is simply the practicality of suitably mounting a long train shape above a moving floor. Also, long moving floors are required, which are not routinely available. Nonetheless, these tests can be used to measure long train models with three or more carriages (see Fig. 3.3). Tests of this type have been reported by Guiheu (1981) for 1:20 scale five- and three-vehicle TGVs; Brockie and Baker (1990) for a Class 43 HST; Paradot et al. (1999) for a 1/15th scale TGV-R with five vehicles and Ido (2003) for a three-car Shinkansen looking specifically at the drag of underfloor components. The latter two experiments were carried out with only part of the floor beneath the trains in motion due to lack of a suitable length of moving ground.

More recently work has been reported using moving models by Li et al. (2017, 2018d) for a 1:16.8 scale three-car high-speed multiple unit. These are effectively coasting tests, with the deceleration of the train being measured by onboard and trackside sensors to detect the passage of the train.

The work of Tschepe et al. (2016a,b) also needs to be mentioned. These investigators have developed a methodology that uses a water towing tank for measuring train drag, with the model being moved over the floor of the

tank at speeds of up to 5 m/s. The use of water in this way enables a high Reynolds number to be achieved at fairly low speeds where flow visualisation and measurement is possible. They identified a maximum speed limit of about 8 m/s to avoid the issue of cavitation or air bubbles coming out of solution in regions of low pressure.

Finally, it is worth once again raising the issue of Reynolds number dependence that was touched on earlier. The early work of Baker and Brockie (1991) for 1/76th and 1/40th scale Class 43 HSTs (with a maximum Reynolds number of around 0.3×10^6), and comparison with full-scale values, suggests steady, if small, decrease of drag coefficient throughout the entire Reynolds number range (based on train height) of up to 10^7. That work shows that the measured friction coefficients at 1/40th scale are between 0.0033 and 0.0037, whilst those at full scale are between 0.0012 and 0.0014, a substantial decrease. Baker and Brockie (1991) also report on the work of Guiheu (1981), which shows that 1/20th scale TGV model tests indicates that the drag results are still falling at their maximum wind tunnel Reynolds number of around 0.8×10^6, although the equivalent full-scale values (measured from coasting tests with all the inherent uncertainties) are similar to the maximum wind tunnel values. By contrast, the work of Willemson (1997) for a range of different passenger train shapes shows a fall in drag coefficient for low Reynolds numbers but suggests there are no further variations with Reynolds number above 0.5×10^6. Similarly the towing tank tests of Tschepe et al. (2016b) show no drag coefficient variations above Reynolds numbers of 0.3×10^6. The wind tunnel and CFD work of Xia et al. (2017a) suggest variations in drag coefficients with Reynolds number up to values of 1.8×10^6. Finally, the work of Li et al. (2018) mentioned above suggest that a Reynolds number of around 0.8×10^6 gives good comparison between model-scale and full-scale results for smooth passenger trains. Thus, one may conclude, somewhat tentatively, that although there might be small changes in drag coefficient with Reynolds number throughout the Reynolds number range (and indeed one would expect this because of the skin friction component) this is probably not discernible in the experimental uncertainty for Reynolds numbers above 0.5 to 1.0×10^6.

7.2.3 CFD calculations

In considering the application of CFD to train aerodynamics, we restrict our attention to investigations from 2008 onwards, as the field is changing rapidly

with new computational methodologies being developed. CFD techniques have mostly been used in the past to investigate the drag of individual train components, such as nose drag and pantograph drag. In general, RANS methodology has been used extensively over that period – see for example Paul et al. (2009) for studies in the reduction of freight train drag; Golovanevskiy et al. (2012) for calculations of the drag of individual freight vehicles within a longer train; Pereira and Andre (2016) for drag calculations for a short concept train and Zhang et al. (2016) for pantograph and train nose calculations. There has been a more recent emphasis on more complex unsteady methods such as Unsteady RANS (URANS), Lattice Bolzmann (LB), detached eddy simulation of different types (DES) and large eddy simulation (LES) – see for example Wang et al. (2008) for LB calculations for three-coach multiple unit; Maleki et al. (2017) for URANS and LES calculations for a double-stack freight wagon and Li et al. (2017) for DES calculations for a three-car HEMU. Most work has been carried out to investigate the drag of individual vehicles or train components, but a small number of investigators have also looked at complete, albeit short, trains – Kwon and Oh (2013) for a four-car HEMU-430X with and without a moving ground simulation and Li et al. (2017, 2018d) for a three-car CRH2.

Normal practise would be to use between 10 and 100 million grid points with a moving boundary beneath the trains, constant velocity boundaries at the inlet and outlet of the domains and constant pressure boundaries at the side of the domains. Mesh sensitivity tests and convergence tests need to be carried out to give confidence in the results that are obtained.

The work of Maleki et al. (2017) is worthy of further comment. They carried out a comparative study using embedded large eddy simulation (ELES), SAS (a hybrid LES/RANS method), URANS and various RANS turbulence models for their double-stack freight wagon and the results were compared with the results of physical model tests. Interestingly, they found that although the ELES and SAS produced the best agreement with the model tests and URANS and RANS did not predict the flow in the separated areas well, this came at the cost of very high CPU usage – 66 times that used by RANS for the ELES and 33 times for SAS. The authors of the paper argue that this implies that RANS will continue to be a viable option for calculations into the future, particularly where large-scale computer resources are not available, although its inaccuracy needs to be appreciated.

7.3 Train drag and crosswinds

In reality, trains do not often run in the still air conditions assumed above, and one might expect the drag coefficient to be affected by crosswinds. Indeed, Beagles and Fletcher (2013) suggest that for a freight train in a 4 m/s wind, the drag may be up to 2.5 times higher than in still air conditions. A typical variation of drag coefficient with yaw angle is shown in Fig. 7.3 for a container train with a variety of different loading configurations from Beagles and Fletcher (2013) who used data from Vollmer (1989) and for a freight train with wagons from Golovenevskiy et al. (2012). To a first approximation, for small yaw angles, one may write

$$C_D(\psi) = C_D\,(0)(1 + K_{W1}\psi^{K_{W2}}) \tag{7.8}$$

where ψ is the yaw angle (in radians), $C_D(0)$ is the drag coefficient at zero yaw and K_{w1} is of the order of 2−5. The exponent K_{W2} is somewhere between 1.0 and 2.0. Over the yaw angle range of practical importance (<10 degrees), a value of 1.0 is probably adequate.

7.4 Predictive formulae

In the early stages of train design, there is a requirement for information on train resistance that can be used to specify power trains, electricity supply

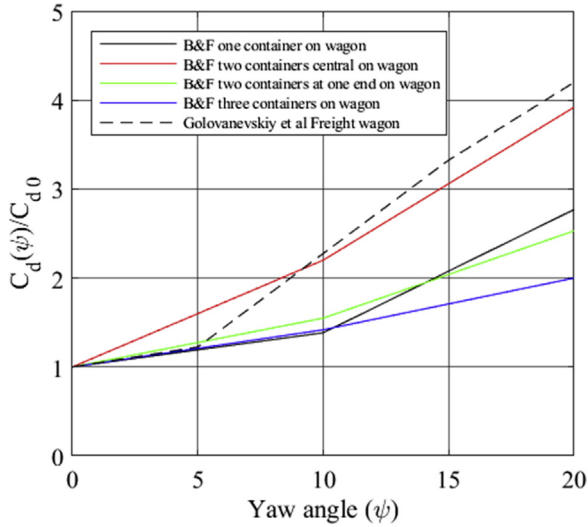

Figure 7.3 Effect of crosswinds. *(Data from Beagles and Fletcher (2013) and Golovenevskiy et al. (2012).)*

systems and operational characteristics, and a number of these have been developed over the years in different countries. These are usually in forms that are consistent with the Davis equation, i.e., a quadratic formulation with velocity. In this section, we present the forms that are used for the aerodynamic term in the Davis equation – readers are directed to the specific references given below for information on the other terms.

The British method of Armstrong and Swift (1990) gives the following expression for c in the Davies equation.

$$\begin{aligned} c = &[0.6125AC_{DNT} + 0.2566N_p] + [0.00197\ (\zeta L)] \\ &+ [0.0021(\zeta L_i)(N_T + N_P - 1) + 0.2061C_{DBO}N_B] \end{aligned} \tag{7.9}$$

Here C_{DNT} is the drag coefficient of the nose and tail, C_{DBO} is the bogie drag coefficient, ζ is the train wetted perimeter, L is the train length. L_i is the intercar gap length, N_T is the number of trailer cars, N_P is the number of power cars, N_p is the number of pantographs and N_B is the number of bogies. The first term represents the nose/tail/pantograph drag, the second is the skin friction drag and the third term gives the repeating drag along the train, coming from features such as intercar gaps and bogies.

Profillidis (1995) and Michalek (2018) give the following form used in France.

$$c = k_1 A + k_2 \zeta L \tag{7.10}$$

where the constants k_1 and k_2 vary for different train types. The first term represents nose and tail drag, and the second term represents repeating roughness along the train and skin friction.

From Germany we have the Strahl and Sauthof formulae (from Sachs, 1973; Michalek, 2018; Rochard and Schmid, 2000). The former is given by

$$c = k_3 M(0.007 + k_4) \tag{7.11}$$

and the latter by

$$c = k_5(2.7 + N_T)A \tag{7.12}$$

where k_3, k_4 and k_5 are again train-specific constants and M is the train mass. The use of mass in the Strahl equation is physically unreasonable, as the aerodynamic forces cannot be affected by mass. Neither does it reflect the breakdown of drag between its components outlined above. The Sauthof formula is used with the velocity v adjusted to allow for a 4.2 m/s (15 km/h) headwind, i.e., instead of cv^2 in the Davis equation, $c(v + 4.2)^2$ is used. Again the first term will represent nose and tail drag, and the second

the repeating drag along the train. In Korea, Kim et al. (2006) present the following equation for the Korean KTX high-speed train.

$$c = k_6 + k_7 N_T \tag{7.13}$$

which again contains a nose/tail term and a term dependent on train length.

So it can be seen that most of the predictive formulae that are used can be reduced to a generalised form that consists of a constant term that represents the nose and tail drag and a term that is linear in an adjusted train length L' – the length of the train without the nose and tail components. In dimensionless terms, this can be expressed as

$$C_D = K_1 + K_2 \frac{L'\zeta}{A} = \frac{2c}{\rho A} \tag{7.14}$$

This expression, although perhaps lacking in sophistication, will be used in the collation of train drag data in Section 7.5. Note that the parameter K_2 is effectively an overall friction factor for the train, which takes into account the drag caused by friction, bogies, and all other repeating effects.

At this point, however, it is worth mentioning the work of Beagles and Fletcher (2013). They identified another drag term due to crosswinds, caused by the increased rail friction due to the lateral wind force on the train and a consequently increased lateral wind force on the track. For the freight containers they studied, this extra increment to drag coefficient was given by $C_{Df}(\psi)$

$$C_{Df}(\psi) = 0.23\eta L_c \psi^2 \tag{7.15}$$

where L_c is the container length and η is the lateral wheel/rail friction coefficient.

7.5 Collation of whole train drag coefficient values

A collation of the drag coefficient data for a wide range of trains is given in Table 7.1A–E for high-speed passenger trains, medium-speed passenger trains as multiple units, medium-speed locomotive hauled passenger train, low-speed passenger trains and freight trains, respectively. The drag coefficients in the table are plotted against the parameter $\frac{L'\zeta}{A}$ in Fig. 7.4 for the full-scale coasting tests only. All drag coefficients have been normalised with an area of 10 m^2. The length L' is given by the train length minus 10 m (the length of the nose and tail region being assumed to be 5 m each) for all trains. The total perimeter ζ is taken as twice the sum of the train

Table 7.1 Collation of drag coefficient for whole train formations.

A – High-speed passenger trains					
Author	**Country**	**Train**	**Test type**	***L (m)***	C_D
Peters (1990)	Germany	ICE 1 (2 + 1)	Coasting	64	0.59
		ICE 1 (2 + 2)	Coasting	90	0.72
		ICE 1 (2 + 3)	Coasting	115	0.75
Bernard (1995)	France	TGV (2 + 0)	Coasting	37	0.31
		TGV (2 + 2)	Coasting	75	0.41
		TGV (2 + 3)	Coasting	94	0.54
		TGV (2 + 5)	Coasting	133	0.65
		TGV (2 + 8)	Coasting	190	0.90
SYSTRA (2011)	France	TGV-R (2 + 8)	Coasting	200	1.10
Rochard and Schmid (2000)	Japan	Shinkansen series 0	Coasting	400	2.52
		Shinkansen series 100	Coasting	400	2.51
		Shinkansen series 200	Coasting	300	1.87
	Great Britain	Class 373 eurostar 18 car	Coasting	384	2.37
Mancini et al. (2001)	Italy	ETR500 (2 + 3)	Coasting	250	1.55
		ETR500 (2 + 8)	Coasting	119	0.95
Kim et al. (2006)	South Korea	KTX (2 + 5)	Coasting	145	0.73
Kwon and Oh (2013)	South Korea	HEMU-430x (2 + 2)	Wind tunnel stationary ground	100	0.36
		HEMU-430x (2 + 2)	CFD stationary ground	100	0.37
		HEMU-430x (2 + 2)	CFD moving ground	100	0.38
Hillmansen (2014)	France	AGV (2 + 9)	Coasting	200	1.08
SYSTRA (2011)	France	AGV (2 + 9)	Coasting	200	0.97
Li et al. (2017)	China	CRH2 (2 + 8)	Coasting	201	1.10
		CRH2 (2 + 1)	Moving model	73	0.44
		CRH2 (2 + 1)	Wind tunnel stationary ground	73	0.39
		CRH2 (2 + 1)	CFD stationary ground	73	0.40
		CRH2 (2 + 1)	CFD moving ground	73	0.43

Table 7.1 Collation of drag coefficient for whole train formations.—cont'd

B – Medium-speed passenger trains – multiple units					
Author	**Country**	**Train**	**Test type**	***L (m)***	***C_D***
Gawthorpe (1978a)	Great Britain	Class 43 HST (2 + 8)	Coasting	300	1.92
Baker and Brockie (1991)	Great Britain	IC225 (2 + 8)	Wind tunnel moving ground	197	1.85
Lukaszewicz (2001, 2006, 2007)	Sweden	X2-7 (2 + 5)	Coasting	159	1.29
		X2000 (2 + 4)	Coasting	139	1.15
		X2-5 (2 + 3)	Coasting	109	1.04
Hillmansen (2014)	Great Britain	Class 390 pendolino	Coasting	218	1.69

C – Medium-speed passenger trains – locomotives and coaches					
Author	**Country**	**Train**	**Test type**	***L (m)***	***C_D***
Baker et al. (1982)	Great Britain	Class 47 locomotive + 5 mark 1 coaches	Coasting	137	1.64
ERRI (1993) (from Lukaszewicz, 2006)	International collaboration	Loco + 10 eurofirma	Coasting	245	2.12
		Loco + 6 eurofirma	Coasting	155	1.68
		Loco +10 SJB7	Coasting	245	2.48
		Loco + 6 SJB7	Coasting	155	1.86
Lukaszewicz (2001, 2006, 2007)	Sweden	Loco + 18, coaches	Coasting	356	3.10
		Loco + 9 coaches	Coasting	251	2.45
		Loco + 5 coaches	Coasting	145	1.80
		Loco + 1 coach	Coasting	40	1.15

D – Low-speed passenger trains					
Author	**Country**	**Train**	**Test type**	***L (m)***	***C_D***
BRB (1986)	Great Britain	Class 150 dmu 3 car	Coasting	60	0.75
BRB (1994)	Great Britain	Class 165 dmu 2 car	Coasting	46	0.48
BRB (1991)	Great Britain	Class 319 emu 4 car	Coasting	79	1.03
BRB (1991)	Great Britain	Class 319 emu 8 car	Coasting	158	1.84
Pritchard and Preston (2018)	Great Britain	Class 357 emu 4 car	Unknown	82	0.90

Continued

Table 7.1 Collation of drag coefficient for whole train formations.—cont'd

E – Freight trains					
Author	**Country**	**Train**	**Test type**	***L (m)***	***C_D***
Baker et al. (1982)	Great Britain	Class 47, coach, 5 partially loaded container flats	Coasting	137	3.1
		Class 47, coach, 11 coal wagons	Coasting	100	2.7
Lukaszewicz (2001, 2006, 2007)	Sweden	Partially loaded container	Coasting	514	8.2
		Partially loaded container	Coasting	355	6.2
		Partially loaded container	Coasting	195	3.6
		Fully loaded container	Coasting	294	3.5
		Fully loaded trucks	Coasting	294	3.7
		Fully loaded hoppers	Coasting	294	3.5
		Empty container flats	Coasting	256	5.0
Michalek et al. (2018)	Czech Republic	Locomotive plus loaded container flats	Coasting	598	6.1

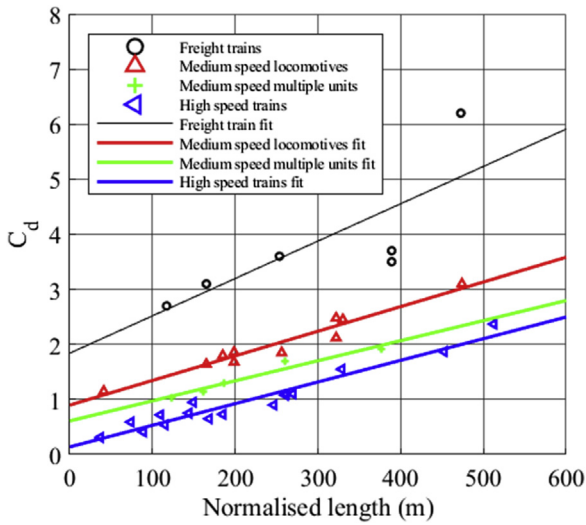

Figure 7.4 Drag collation for whole trains (coasting tests).

height and train width for each train. For each category of train, the experimental results and a best fit line are shown. The form of the graph is insensitive to the precise assumptions for L' and ζ. Note that the small number of low-speed train results have not been included on the figure because of the difficulty of drawing reliable trend line through a small number of points and also because the nose correction just described becomes problematic for short train lengths. The magnitudes of the low-speed data are, however, generally consistent with the other data presented.

When considering the results shown in Fig. 7.4, it needs to be noted that the precise values of the slope and intercept of the best fit lines are somewhat dependent on the data that are included in each train category. For example, all the Shinkansen train data are included in the high-speed train data set, even though some of the earlier series do not fit the precise definition used here in terms of speed, and could be included in the medium-speed multiple unit category, which would affect the slope and intercept of the best fit line for both categories. Nonetheless, very broadly, the drag coefficients increase linearly with effective train length as would be expected, with high-speed trains having the lowest values and freight trains the highest (although of course there is considerable scatter in the latter due to highly variable consists). Plots such as these enable a rough estimate of drag coefficient to be obtained for the design of new trains and also act as a benchmark against which the aerodynamic performance of new trains can be judged.

Table 7.2 shows the calculated values of intercept K_1 and slope K_2 (Eq. 7.14). The values of K_1, the drag coefficient for $L' = 0$, show the expected variation with the values for high-speed trains being the lowest and for freight trains the highest, with the medium-speed trains in between, reflecting the nose shape of the trains. The value of the slope K_2, which reflects the friction drag, is similar for the three passenger train categories, at around 0.004, and somewhat higher for the freight train category. Whilst this similarity in slope must be to a degree coincidental and is certainly a

Table 7.2 Intercept and slope of drag coefficient/length graphs.

	Intercept K_1	Slope K_2
High-speed passenger trains	0.14	0.0039
Medium-speed multiple units	0.61	0.0036
Medium-speed locomotive and coaches	0.90	0.0045
Freight trains	1.84	0.0067

function of the limited data that are available, it is at first sight surprising, as one would expect this parameter also to increase in the same way as the intercept. Now, as noted above, the slope K_2 is an effective friction factor around the train. This can be expected to be some sort of weighted average of the friction factors on the train sides, roof and underbody. The data in Chapter 5 for high-speed trains suggest that the train side and roof values are of the order of 0.002 (Table 5.2) and can be expected to act on (say) 80%–90% of the train surface, whilst the underbody value is of the order of 0.03 (Table 5.3) and acts on the remaining 10%–20%. A simple calculation shows that, for high-speed trains, the overall magnitudes of the friction drag on the side/roof and the underbody are very similar. This suggests that the parameter K_2 will be to a significant extent determined by the value of the underbody friction coefficient, which will be similar for all trains as it is determined both by train underbody roughness and by ballast roughness. This is a very crude argument of course, but it does have an interesting implication in that it suggests that train resistance and energy consumption could be significantly improved by making the track smoother particularly when it is noted (Table 5.3) that the underbody friction factor for slab track falls to 0.01 (Deeg et al., 2008). An indication of this is given in the Shinkansen data described in Rochard and Schmidt (2000), where the overall resistance for slab track is 7% less than for ballasted track, although this is attributed to the linear velocity term in the Davis equation in the correlation that is given there.

Finally, note that the wind tunnel, moving model rig and CFD data for short high-speed passenger trains from Li et al. (2017), which are not shown on the graph, are between 80% and 90% of the value that can be obtained from the average values using Eq. (7.14) and the values of K_1 and K_2 in Table 7.2. The wind tunnel and CFD results of Kwon and Oh (2013) are only around 60% of the calculated value. These reduced values may reflect the fact that experimental and computational values of the drag coefficient do not include the aerodynamic drag due to rough track.

7.6 Drag reduction methods

Methods for reducing drag, and thus energy consumption, can be divided into three (overlapping) categories – overall train design, optimisation of train components and modification of train operation. These will be considered in turn below.

The methods through which train drag can be reduced by overall train design are in a sense obvious and have been known for many years (Gawthorpe, 1978a). These include the following:

- The streamlining of the nose and tail. However, note that for long trains, this component of drag is relatively small and the law of diminishing returns applies as the degree of streamlining is increased. The purpose of the extreme streamlining seen on some modern trains is actually to reduce pressure transients in the open air and in tunnels. Nonetheless, Tian (2009) proposes that the length of streamlined noses should be around 4 m at speeds of 200 km/h rising to 9 m at 350 km/h.
- Ensuring the surface of the train is as uniform and free from protuberances as possible. This involves detailed design of door handles and pantograph mountings, for example, and perhaps most importantly, the faring of intercar gaps, where small-scale flow separations can result in significant energy losses. For freight trains, this would involve ensuring that, as far as is practically possible, the wagons are as smooth as possible, without discontinuities. This may involve fairings between containers, covers on open wagons, etc., and, where possible, avoiding gaps in loading (see below). As an example, Paul et al. (2009) give results indicating that around 20% drag reduction of freight trains is possible simply by ensuring that there are few protruding external ribs on hopper and gondola cars. Similar magnitudes of drag reductions for freight trains using end fairings and load covers are reported in Watkins et al. (1992). Giappino et al. (2018) show, unsurprisingly, that the optimum drag coefficient values for containers are obtained when the gaps between containers are minimised.
- The fairing, as far as practicality allows, of the underbody and the bogies, so that the roughness is reduced and flow separation around the bogies reduced as far as is possible. The CFD analysis of Zhang et al. (2018a) also shows that the actual shape of the bogie cavity has a small but noticeable affect on the overall train drag.

Orellano and Sperling (2009) suggest that there is a greater potential for drag reduction of regional trains than high-speed trains (essentially because the issue of the blunt nose shape can still be addressed). Their calculations suggest that drag reductions of 20%–25% are possible, which when used to assess typical energy usage on typical routes translates into 6%–8% energy savings. For high-speed trains, they argue that the potential for drag reduction is significantly less at around 14%, giving similar energy reductions of between 6% and 8% on typical routes.

In recent years, there has been a move to optimise aspects of train design to achieve certain design requirements – and in particular the train nose and tail to achieve minimum drag, lift and side forces. The methodology for this is in concept quite simple but in practise quite complex. It begins by deciding on 'objective functions' – the desirable outcomes to be achieved. Then a range of CFD tests are carried out (usually by RANS methods where many variations can be investigated rapidly) for a range of parameters across the design space (for example, train nose length, curvature, etc.) to establish a data set of drag, lift values, etc., for a range of design parameters. A range of optimisation techniques (such as those outlined in Section 4.6) can then be used to choose parameters such that the objective functions are minimised. Such methods are described in Monneyer et al. (2006) for optimising nose drag coefficient; Krajnovic (2008, 2009a) for optimising nose shape for maximum crosswind stability and optimising vortex generators for maximum drag reduction; Suzuki et al. (2013) to optimise nose shape for drag, the nose pressure pulse and the rolling moment; Yao et al. (2014) for tail lift and nose volume; Ming et al. (2016) for nose shape; Jakubec et al. (2016) for drag and head pressure pulse; Li et al. (2016) to optimise the total drag and lift coefficient of the nose and tail of the CRH2 and Zhang et al. (2018b) for nose drag, side and lift forces.

It is appropriate at this point to make some cautionary remarks concerning such optimisation. Firstly, nose and tail drag, whilst significant, is not the largest contributor to overall drag, and optimisation focused on these areas may produce only a small effect overall – which indeed may be well within the order of uncertainty in full-scale and physical model tests. For example, the results of Zhang et al. (2018b) for train nose optimisation result in drag coefficient reductions of only 2.4% for the nose and thus a much smaller value for the overall train, which are insignificant in practical terms. Secondly, optimisation should consider crosswind effects. The most common operating condition for trains is at a few degrees of yaw and thus optimisation should take place around this condition. Also, the yaw angle can change rapidly between positive and negative in a few seconds (Gallagher et al., 2018) and ideally optimisation should take such rapid fluctuations into account. Finally, optimisation should not neglect the wider picture of flow around trains, and, coming back to the case of nose and tail optimisation, care should be taken to ensure that the optimised designs do not result in adverse effects to the development of the boundary layer and wake. In short, optimisation for drag reduction is a powerful technique, but the overall context needs to be remembered and care taken that the

optimisation is about appropriate environmental conditions and does not adversely affect the wider flow field.

Finally, we consider the possibility of using changes in train operation to reduce aerodynamic drag. The importance of train operation has already been noted in Section 7.1, where it was shown that for a typical, conventional main line journey, the effect of a small disruption resulting in reduced speeds for a short distance can cause a rise in energy consumption that is equivalent to a change of 8% in aerodynamic drag. This point perhaps needs to be more widely appreciated — ensuring smooth operation of train services is more important and in the long term more significant than detailed train design to reduce, say, the drag of the nose of the train or raising the maximum train speed.

However, there are specific instances where simple changes to train operation can have major effects. Lai and Barkan (2005), Lai et al. (2007), Lai et al. (2008) and Kumar et al. (2011) developed algorithms to help intermodal freight yard operators to load containers onto trains in the most efficient manner to reduce overall drag and fuel consumption. They coupled these algorithms with machine vision technology so that the aerodynamic efficiency and fuel usage of individual trains could be identified on leaving the yard. Such techniques offer a powerful method for training yard operators to minimise drag and energy consumption during the loading of trains.

CHAPTER 8

Aerodynamic loads on trackside structures, passing trains and people

8.1 Pressure loads and slipstream loads

In the operation of freight and passenger trains, the velocity and pressure fields around the train interact with adjacent infrastructure, other trains, moveable objects such as pushchairs and people on platforms and at the trackside. The loadings imposed by the passage of trains take two forms — pressure loading and loading due to the high air speeds in the train slipstream. The effect of such loads is strongly dependent on the nature of the infrastructure, object or person, distance from train, train type and train speed. In this chapter, we will first consider pressure loads (Sections 8.2—8.5) and then move on to slipstream loads (Sections 8.6—8.9), considering in both cases the nature of these loads, the various methods for measuring and quantifying them, a collation of the most important available data and how these loads can be applied to calculate specific 'load effects'.

8.2 The nature of pressure loads

It has been shown in Chapter 5 that when a train travels through the air, the flow stagnates on the front of the train causing a positive pressure region to develop. As the train passes, this positive pressure gives way to a region of negative pressure caused by acceleration around the edges of the front vehicle — see Figs. 5.6—5.10 for example. Along the train there are also pressure variations of lower magnitude, which occur because of the intercarriage gaps and bogies and their cavities. Around the tail of passenger and high-speed trains, a negative to positive pressure transient exists, but this is usually smaller than the nose transient. In the frame of reference of the train (Chapter 2), these pressure transients are relatively steady.

Train aerodynamics
ISBN 978-0-12-813310-1
https://doi.org/10.1016/B978-0-12-813310-1.00008-3

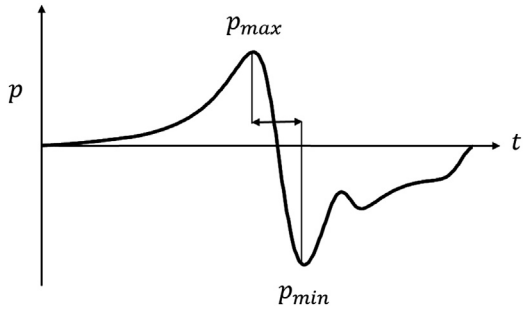

Figure 8.1 Schematic of nose pressure pulse.

However, to a stationary observer at trackside, the local pressure fields around the train appear as transient pulses. In what follows we will define these pressure transients by a pressure coefficient based on the peak-to-peak value of the nose transient (Fig. 8.1):

$$\Delta C_p = \frac{p_{max} - p_{min}}{0.5\rho v^2} = \frac{\Delta p}{0.5\rho v^2} \tag{8.1}$$

Clearly these pressure transients will create a transient pressure field on any infrastructure close to the track, and integration of that pressure field over the surface will give the overall pressure loading on that structure. This transient loading can either cause direct static or dynamic failure or can result in a fatigue failure when repeated over many thousands of train passings. When these pressure transients impact on other trains, they can result in considerable, and very sudden, train lateral displacements, with consequences both for structural loading and passenger comfort.

8.3 Methods for measuring and quantifying pressure loads

8.3.1 Full-scale measurements

There are two basic methodologies for the measurement of pressure transients at full scale. Pressures can either be measured in the open air with no structure present or they can be measured on the structure of concern. A methodology for both is given in detail in CEN (2013). The former method, although not of relevance to any practical situation, is relatively easy to achieve and is used as a method of train authorisation and acceptance and is required because of the split between rolling stock and infrastructure issues in the Technical Standards for Interoperability (TSIs)

(EU, 2007, 2008, 2011a,b, 2014a,b). We will return to this issue a number of times in this and later chapters. For this method, measurements are required 2.5 m from the track centre line at heights of 1.5, 1.8, 2.1, 2.4, 2.7 and 3.0 m above the top of rail using static pressure probes connected to a reference pressure source. Acceptable track dimensions are specified — essentially the height of the top of the rail should not be more than 1 m above the surrounding ground level. Details of sampling rate, uncertainties and various data corrections for nonstandard test conditions are given. At least 10 runs need to be carried out at the reference train speed (which is usually the maximum speed) and the mean and standard deviation of the peak-to-peak pressure ensemble determined, Δp and $\sigma_{\Delta p}$. The 95% confidence level is then found from

$$\Delta p_{95} = \Delta p_{average} + 2\Delta p_{sd} \tag{8.2}$$

The standard gives a maximum allowable value of Δp_{95} of 800 Pa for train speeds of 160 km/h or greater. Typical measurements of this kind were carried out as part of the AeroTRAIN project and the results are described in Grappein and Rueter (2015).

For the measurement of pressure forces on trackside structures, a similar methodology is proposed, but with pressures measured on the surface of the structures themselves. Details of suitable pressure measurement systems are given. Examples of this type of measurement can be found in Yang et al. (2015) for overbridges; Tokunaga et al. (2016) and Lachanger et al. (2016) for noise barriers and Takei et al. (2008) for enclosed stations.

8.3.2 Physical model experiments

CEN (2013) specifies a methodology for moving model tests very similar to that of full-scale tests, outlining the measurement and data acquisition requirements at some length, for both freestream pressures and pressures on structures. Once again, at least 10 runs are required, and Δp_{95} is to be calculated as in Section 8.3.1. A minimum Reynolds number based on train height of 2.5×10^5 is specified. Experiments of this type are described in Jang et al. (2008) for acoustic barriers; Takei et al. (2008) for enclosed stations and Zhou et al. (2014) for platform screens. Baker et al. (2014a,b) describe a very extensive series of measurements using different train types (ranging from streamlined to bluff noses) and different infrastructure types (vertical hoardings, overbridges, canopies, platforms, etc.). The models used in these tests are illustrated in Fig. 8.2.

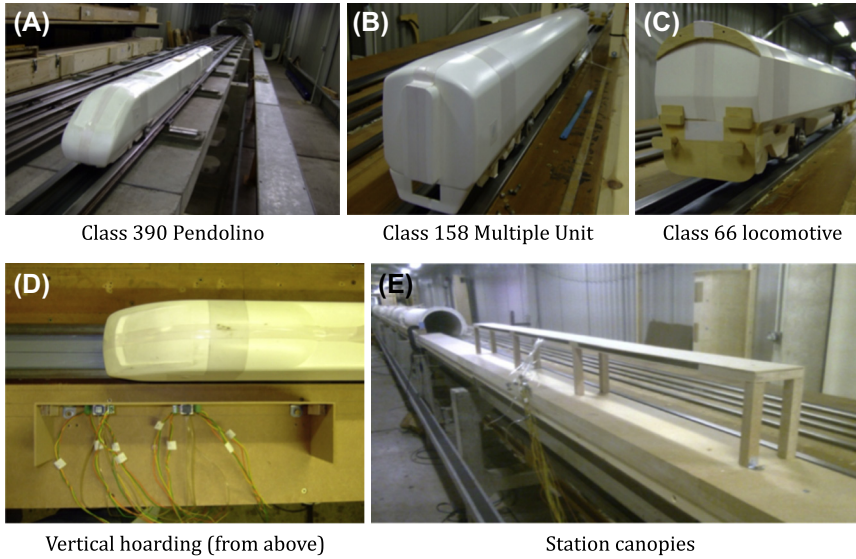

Figure 8.2 ***Models used in the investigation reported in Baker et al. (2014a,b).*** (A) Class 390 Pendolino, (B) Class 158 multiple unit, (C) Class 66 locomotive, (D) Vertical hoarding (from above) and (E) station canopies.

CEN (2013) also allows for static model tests to measure pressure around the train nose, with the measured pressures (in the train frame of reference) transformed into pressure transients in a ground frame of reference. This methodology is useful for examining the influence of a range of different nose shapes and investigating pressure variations over a range of distances from the train. An example of such measurements is given in Belloli et al. (2009).

8.3.3 CFD calculations

CFD techniques can be reliably used for the measurement of free air pressures around trains and also, to a certain extent, to determine pressure transient forces on structures. Indeed, the study of nose pressure transients was one of the first to be tackled by computational methods, in the form of panel methods (Khandia et al., 1996; Berenger and Gregoire, 2001). This capability is recognised in CEN (2013) where a suitable methodology is outlined, which gives details of simulation requirements. RANS and lattice Bolzmann methodologies are allowed. Clearly steady RANS methods will

not give the run-to-run variation found at full scale and the 95% peak-to-peak pressure is alternatively specified as

$$\Delta p_{95} = k_{sim} \ \Delta p_{sim} \tag{8.3}$$

where Δp_{sim} is the measured peak-to-peak pressure in the simulation and k_{sim} is a constant with a value of either 1.03 or 1.05 depending on the nature of the simulation and the shape of the vehicle. The standard also set out procedures for the use of unsteady CFD methods, equivalent to those for full-scale or moving model tests. For examples of such CFD calculations, see Belloli et al. (2009) for loads on acoustic barriers and Yang et al. (2015) for pressure loads on overbridges.

8.3.4 Analytical models

Finally, it is worth making brief mention of some analytical methods that have been used to study nose pressure transients and in particular the use of potential flow theory (Chapter 2), for example, the work of Sanz-Andres et al. (2004a,b), Barrero-Gil and Sanz-Andres (2009) and Rutschmann et al. (2013). Relatively simple analysis can be used to provide a framework for the consideration of experimental and computational results — see for example Baker (2014a), where the method of Sanz Andres et al. (2004a) is used to help explain variations in the form of the nose pressure and velocity transients. More complex methods (in the form of the panel methods) have been shown to compare well with standard CFD methodology. Simple potential flow methods can also be used in conjunction with other methods for complex situations — for example, Takei et al. (2008) used a potential flow method to predict nose pressures couple with a one-dimensional pressure transient calculation to look at the pressure distributions within confined station geometries.

8.4 Collation of pressure load data

8.4.1 The CEN standard and UIC guidance

The CEN (2013) methodology assumes an idealised 'rectangular' pressure transient distribution of the form shown in Fig. 8.3 and gives peak-to-peak correlations for a variety of different train and infrastructure geometries. The latter include vertical structures next to the track (hoardings, platform screens); horizontal surfaces above the track (over bridges); horizontal surfaces next to the track (canopies); mixed horizontal and vertical surfaces

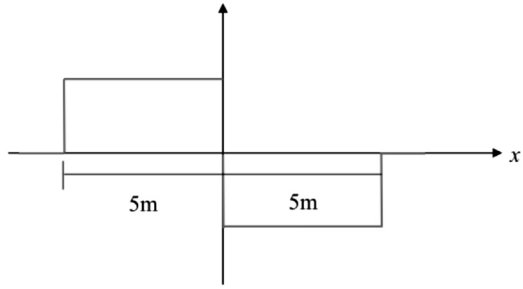

Figure 8.3 Rectangular pressure transient used in CEN (2013). *(Used with permission.)*

(noise barriers) and short enclosed sections up to 20 m long. The information in this standard is also contained in a UIC Guidance document (UIC, 2013). The information in these documents applies to standard European track spacings and train gauge widths. The experiments of Baker et al. (2014a,b) described above report on a series of moving model tests to obtain equivalent data for GB railways. Experiments were carried out with a variety of train types (Class 390 Pendolino, Class 158 multiple unit and Class 66 freight locomotive) for various types of infrastructure (vertical hoardings, overbridges, station canopies and platforms) — see Fig. 8.2. These data have also been incorporated into a guidance note — RSSB (2014a).

In the sections that follow (Section 8.4.2 and 8.4.3), we consider only the information given in these documents for vertical and horizontal surfaces. The interested reader is referred to the documents themselves for the more complex geometries. We then move on to consider two other situations not covered in CEN (2013), UIC (2013) or RSSB (2014a) — forces on structures in enclosed station environments and forces on passing trains.

8.4.2 Vertical structures at the trackside

Based on full-scale experiments carried out in the early 1990s in Europe (ERRI, 1994), CEN (2013) and UIC (2013) give the following expressions for the pressure coefficient C_{p1} and pressure p_1 for the loading on a vertical wall next to the track:

$$p_1 = \rho \frac{v^2}{2} k_1 C_{p1} \tag{8.4}$$

$$C_{p1} = \frac{2.5}{(Y + 0.25)^2} + 0.02 \tag{8.5}$$

Y is the distance of the structure from the centre of the track. k_1 is a constant with values of 1.00 for freight trains, 0.85 for conventional passenger trains and 0.6 for streamlined passenger trains. Although it is not made explicit in CEN (2013) and UIC (2015), the values of C_{p1} are based on experimental values averaged over a 2.5 m distance in the x direction and on moment-averaged values in the z direction.

For the more constrained GB loading gauge, the moving model experiments of Baker (2014a,b) resulted in the following expression for C_{p1}:

$$C_{p1} = \frac{6}{(Y + 1.75)^2} \tag{8.6}$$

This correlation was formed by averaging pressures over a 5 m length in the x directions (which is more consistent with its application in the code — see Fig. 8.3 above) and on moment-averaged values in the z direction. For trackside structures, k_1 has values of 1.0 for bluff trains, 0.53 for blunt-ended multiple units and 0.43 for more streamlined trains.

These data were further used in RSSB (2014a), but this time averaged over a 2.5 m length in the x direction to be consistent with CEN (2013), and resulted in the following correlation.

$$C_{p1} = \frac{8}{(Y + 2.10)^2} \tag{8.7}$$

The values of k_1 were 1.0 for bluff trains, 0.613 for blunt-ended multiple units and 0.43 for more streamlined trains.

These correlations are plotted together in Fig. 8.4, for the streamlined train case together with some unpublished experimental results for maximum wall pressure coefficients from Great Britain, Japan (Tokunga et al., 2016), South Korea (Jang et al., 2008) and China (Xiong et al., 2018) for high-speed trains. It can be seen that the CEN correlation for European-sized trains (2.9—3.0 m in width) lies above that from RSSB for the smaller British trains (2.6—2.7 m in width), which in turn lies just above the correlation of Baker et al. (2014a,b) due to the longer averaging length of the latter. The results of Soper and Baker (2019), for European-sized trains, agree well with the CEN correlation as would be expected — but remember that these are maximum rather than length-averaged values. The Chinese, Korean and Japanese data (for trains with widths of 3.2—3.4 m) lie above the CEN correlation, again as would be expected.

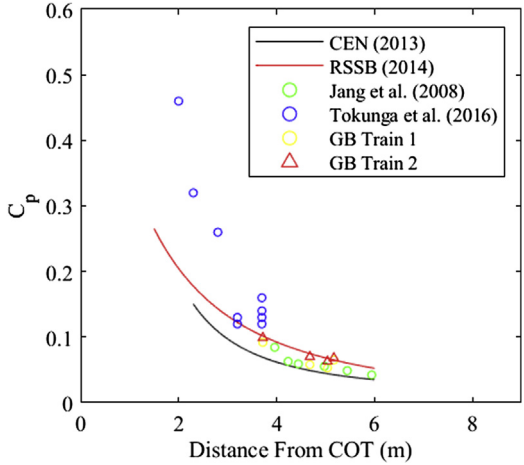

Figure 8.4 Correlations for peak-to-peak pressures on vertical trackside structures with the experimental results. *(Data from Tokunga et al. (2016), Jang et al. (2008) and Soper and Baker (2019).)*

Taken together, these correlations and experimental data suggest that care should be taken in design to use data or correlations obtained under conditions relevant to the local railway infrastructure and train sizes under consideration.

8.4.3 Horizontal structures over the track

In a similar way to vertical structures, correlations have been produced for the pressure transient peak-to-peak values for horizontal structures. CEN (2013) and UIC (2013) again use information provided in ERRI (1994), but there was only very limited experimental data (for a TGV passing beneath one bridge) that were supplemented by the (early) use of panel method calculations for a wider range of trains. This time the correlation was based on maximum pressures in the x direction, rather than length-averaged pressures

$$p_2 = \rho \frac{v^2}{2} k_2 C_{p2} \tag{8.8}$$

$$C_{p2} = \frac{2}{(Z-3.1)^2} + 0.015. \tag{8.9}$$

where Z is the height of the structure above the top of the rail. k_2 takes the same values as the CEN (2013) k_1 values above. Baker et al. (2014a,b) again present experimental results for this case for GB railways, but these were

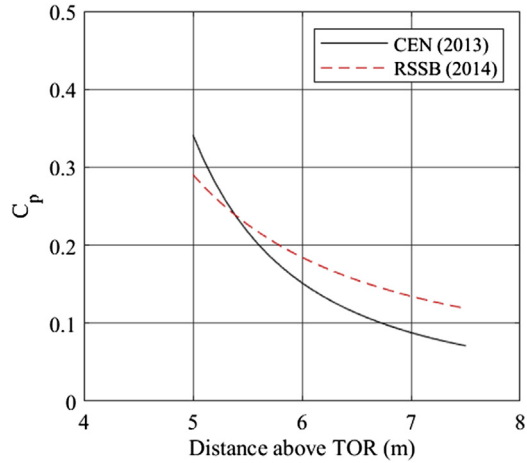

Figure 8.5 Surface pressures on horizontal structures from CEN (2013) and RSSB (2014) correlations.

analysed in the same way as for the vertical wall pressures above and are thus not consistent with the CEN (2013) approach in this case and, for the sake of clarity, are not included here. The data were used in RSSB (2014a) and, for a 10-m wide structure, (along the track) give the following equivalent formula, again based on maximum rather than averaged pressures:

$$C_{p2z10} = \frac{8.5}{(Z - 1.9)^2} + 0.1 \tag{8.10}$$

with $k_2 = 1$ for bluff trains and 0.432 for intermediate and streamlined trains. RSSB (2014a) also gives expressions for the variation of design pressure coefficient for different widths and lengths of overbridges.

These correlations of Eqs. (8.9) and (8.10) are plotted together in Fig. 8.5 for a 10 m wide bridge for high-speed trains. This time there is significant variability between the curves, which reflects a very conservative approach in forming the correlation in RSSB (2014a,b). Also the nature of the calculations leading to the CEN (2013) correlation (from early and uncheckable panel methods) must cast doubt on the reliability of this curve.

8.4.4 Station environments

Most station environments are quite open and the pressure transients caused by passing trains are similar to those described above and the correlations of the last section can be used to give values for the design of (say) platform screens. However, some stations are very enclosed and, in

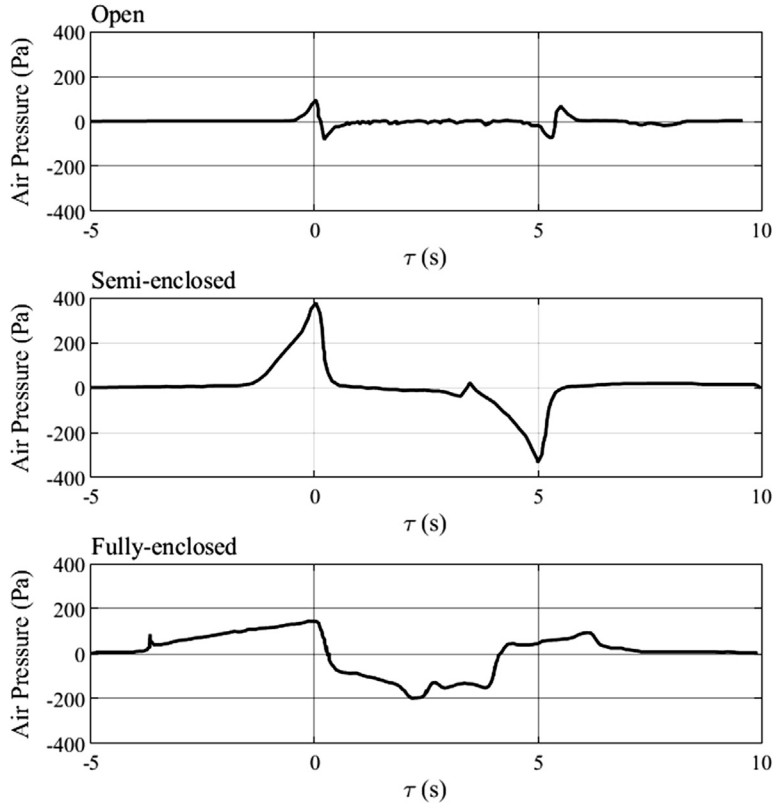

Figure 8.6 Pressure transients in enclosed stations. *(Data from Takei et al. (2008).)*

aerodynamic terms, come close to becoming tunnels. This confined flow situation has been discussed in Section 5.4, and the pressure transients that may occur in such a situation are well illustrated in Fig. 8.6, adapted from the work of Takei et al. (2008), which shows the pressure coefficient variation with time as a train passes through a station for different degrees of confinement. Three situations are shown — an open station, where the nose and tail pressure transients are clear; a semi-enclosed station, where the pressure time history begins to resemble that seen in a tunnel; and a fully enclosed station, where the pressure transients have wholly tunnel characteristics. The intermediate form has particularly high pressures.

8.4.5 Passing trains

Knowledge of the pressure transient on passing trains is of importance for the determination of train load assessment and displacements. Indeed, until recently, in GB measurements of transient pressures were specified to be

measured on the surface of a stationary train as the assessed train passed, rather than in free air as in CEN (2013), which may well be argued to be the more rational approach. It may be expected that the pressure transient magnitudes will be similar in form to those on a vertical wall next to the trackside and thus scale on the speed of the passing train, although the peak-to-peak times will be lower than the stationary case because of the relative motion of the trains. Such transients were measured by Komatsu et al. (1999) for a Shinkansen series 300 train being passed by a variety of other Shinkansen trains. Within experimental uncertainty, the pressure coefficients formed with the velocity of the passing train were constant with speed for any one passing train type, suggesting that the assumption above is correct. In the TRANSAERO project (Johnson and Dalley, 2001), full-scale measurements were made of the pressure transients on a static ETR500 as it was passed by another ETR500, and these experiments were duplicated in moving model tests. Agreement between the two sets of measurement was found to be excellent.

Both Komatsu et al. (1999) and Johnson and Dalley (2001) investigated the effect of nose length on the pressure transients, and the results are plotted in Fig. 8.7 for the peak-to-peak pressure variation with nose length. The three sets of results shown are for different track spacings, so they cannot be directly compared, but the sharp fall as nose length increases is clear.

Liu et al. (2014) describe a comprehensive series of large eddy simulation (LES) calculations of the pressure on the side of a stationary freight

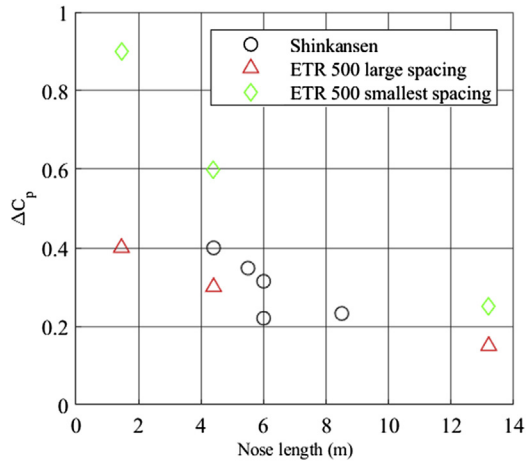

Figure 8.7 Effect of nose length on nose pressure transients with data from Komatsu et al. (1999) and Johnson and Dalley (2001).

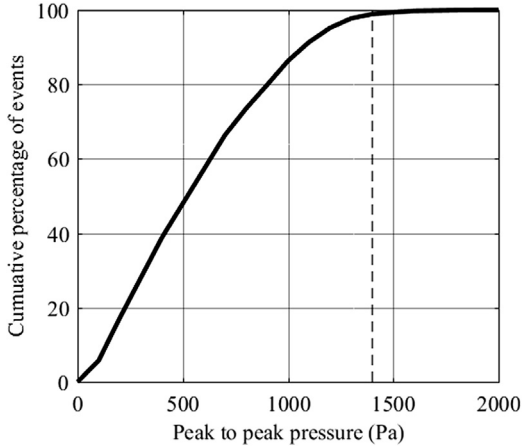

Figure 8.8 ***Train passing pressure histogram from investigation described in Gallagher et al. (2018).*** *Dotted line* shows the GB limit value.

wagon with double-stack containers, as it is passed by an ICE2. They present data for pressure and force transients, which, not surprisingly, show that the magnitudes of the peaks of pressure and force increase with decreasing train separation. Interestingly, there are significant drag and lift force coefficient transients due to pressure variations over the roof and ends of the wagon, as well as the expected side force coefficient transients.

The full-scale experimental campaign reported in Gallagher et al. (2018) obtained a large amount of data from the GB New Measurement Train as it travelled around the country, including the pressure transients due to a variety of passing trains. These results have not, at the time of writing, been published, but the pressure transients were of the expected form, although there was significant variability as measurements were made for a wide variety of passing trains, track spacings and weather conditions. Fig. 8.8 shows a histogram of peak-to-peak pressure values that were measured. Whilst most train passings resulted in quite low peak-to-peak values, around 1% of the train passing pressures exceeded 1.4 kPa — the British Rail limit value.

8.5 Application of pressure loads to structural loading

The knowledge of the pressure transients caused by passing trains is not of course an end in itself, but rather provides data for loading calculations. There are four types of calculations that can be carried out.

- Quasi-static loading calculations in which measured or codified pressures are applied to a structure to calculate the transient stresses and forces within structural members assuming no dynamic response. An ultimate limit state design can then be carried out to ensure that the failure stresses within structural members are not exceeded. This is effectively the methodology outlined in CEN (2013) and only applies to static structures. It can be nonconservative for structures that exhibit dynamic behaviour.
- For structures that exhibit some kind of dynamic behaviour, such as noise barriers, the dynamic stresses and forces can be calculated using a dynamic amplification factor approach, where a dynamic factor is applied to the quasi-static forces in the ultimate limit state design. Such methods are set out in UIC (2013) and CEN (2016b). The dynamic amplification factor can be calculated by a variety of methods, but usually just focuses on the dynamic behaviour of the primary oscillation mode. Lachinger et al. (2016) compared these methods to the results of a large data set of full-scale data for noise barrier stresses, strains and displacements measured in Austria and showed that they were both mildly conservative in marked contrast to the quasi-steady method which was very non-conservative.
- Where greater accuracy is required than can be provided by the dynamic amplification factor approach, a full structural dynamics calculation is required that takes into account all the dynamic properties of the structure, and usually requires a finite element structural calculation. Carassale and Brunenghi (2013) carried out such an analysis of the behaviour of noise barriers. They found that obtaining adequate experimental data to test any such methods is difficult, as very often there will be a need to separate ground-borne vibrations from the train passing from aerodynamic effects, which is far from straightforward. Tokunaga et al. (2016) also carried out a full dynamic analysis of noise barriers, but this time for low-speed, high-speed and very high-speed trains. They found that for low train speeds (130 km/h), the ground-borne vibrations dominate and produce strains and displacements in the barrier that reflect the passing of wheels and bogies. At normal high-speed train speeds (340 km/h), the pressure transients can excite the fundamental mode of oscillation of the barrier if the natural frequency is low enough, resulting in damped strain and displacement oscillations that persist well beyond the passage of the nose and tail peaks. Similar oscillations can also be seen in the data of Lu et al. (2018). At very high speeds (up

to 500 km/h), a complex phenomenon occurs with interactions between the vibrations caused by the nose transient and those caused by the tail transient, which can significantly amplify the latter. As train speeds increase in the future, this effect may well prove to be of some importance.

- Static and dynamic loading calculations of the above type will give forces that correspond with the ultimate design case. These are rarely exceeded in practise, and more often than not the critical loading case is that of fatigue loading. Failure by fatigue loading can occur after a load much lower than the ultimate design load has been applied a large number of times. Again there are varying levels in design for fatigue loading. At the simplest level, the peak-to-peak stresses calculated in quasi-static or dynamic loading analyses can be regarded as the design stress range for fatigue loading, and an analysis of structural properties carried out to ensure that this stress does not exceed the failure stress corresponding to a fixed number of occurrences. UIC (2013) specifies this number of occurrences as 5×10^6, but this can be varied depending on the operational characteristics of the line. Calculations of this sort are given in Takei et al. (2008). More complex methods, such as the 'rainflow' method — see for example Downing and Socie (1982) — can use full-scale test data to give a histogram of the magnitudes of stress cycles from the passage of a large number of trains, which can then be used as input to a more complex fatigue design methodology.

8.6 The nature of slipstream loads

The nature of the flow in train slipstreams has been presented in Chapter 5. Essentially for single multiple unit passenger trains, there is a slow buildup in wind speed along the side of the train (the boundary layer), but the major peaks in speed are to be found in the trailing vortex wake and can occur 100 m or so behind the tail of the train (see Figs. 5.1 to 5.4). These peaks last for only a short time — for 1 s at the most. For double-unit trains or locomotive-hauled passenger trains, high slipstream velocities can occur along the side of the train in the boundary layer region because of discontinuities in the train profile. For freight trains, the situation is different, with a much thicker boundary layer and high wind speeds along the side of the train for a sustained period of many seconds. Whilst the air speeds in slipstreams can reach levels where passengers and trackside workers could become unstable, the effect of train slipstreams on pushchairs and

wheelchairs is of particular concern. Between 1973 and April 2005, there were 30 slipstream-induced incidents on the GB rail network (Figura-Hardy, 2008). The incidents in question were mostly correlated with the passage freight trains of containers with large spacings or with car carrying trains. The most recent incident occurred at Twyford railway station in April 2016 (RAIB, 2017) where a braked wheelchair carrying a disabled teenage girl was pulled into the side of a freight train passing through the station at 45 mph, with the girl fortunately sustaining only minor injuries. RSSB (2017) shows a graphic video of an empty pushchair being moved by a freight train passing through a station.

To assess the safety of passengers and trackside workers, and the stability of items such as pushchairs and wheelchairs, the ideal procedure would have two parts. Firstly, measurement would be made of slipstream velocities for the train and site under consideration and the equivalent forces calculated. Alternatively, the forces caused by the slipstreams could be measured directly on human dummies or pushchairs. Secondly, the stability or otherwise of humans and objects would be assessed through a suitable mechanical model. However, much of this ideal procedure has proved problematic, in particular the direct measurement of forces and the assessment of stability, and current methods essentially specify limit slipstream velocities as the criteria for train authorisation purposes. This is again a logical consequence of the split between infrastructure and rolling stock TSIs mentioned above, with the limit slipstream velocities effectively acting as surrogate indicators of safety. Thus, in Sections 8.7 and 8.8, we will discuss the methods available for measuring slipstream velocities and present a collation of experimental results for a variety of trains in terms of the limit velocities. In Section 8.9, we will return to the fuller assessment outlined above and discuss ways in which the risk of human and object instability can be calculated.

8.7 Methods for measuring and quantifying slipstream loads

8.7.1 Full-scale measurements

A procedure for quantifying the strength of gusts in slipstreams is set out in CEN (2013). The procedure requires measurements from at least 20 train passes at trackside and gives details of site location, probe positions and data sampling rates. For trackside measurements, the velocities must be sampled at 3 m from COT (Centre of Track) and 0.2 and 1.4 m above

TOR (Top of Rail). These positions are intended to be representative of the chest height/centre of mass of the majority of the adult population. Ambient wind conditions also need to be measured and only data for runs with ambient wind speeds less than 2 m/s are used. It is possible to reduce the number of train passes required by positioning multiple probes along the track at the same lateral and vertical positions. However, to ensure that the obtained results are independent, the anemometers must be spaced by at least 20 m. The measured air speeds need to be adjusted to allow for the different train speeds in each run, usually to the standard operating speed of the train.

The air speed time history from each train passage is then filtered with a 1-second moving average filter. The fundamental assumption here is that the 1-second gust duration is appropriate in considerations of human stability. A typical spread of 1-s gust values and the position relative to the train where they occur is given in the histograms of Fig. 8.9 for the S103 Velaro. The level of variability can be seen to be significant as one might expect, with most of the peaks occurring in the 200 m after the train has passed. In the same way as for the pressure measurements described in Section 8.3.1, the maximum allowable horizontal air speed, u_{h95}, is calculated from

$$u_{h95} = u_{haverage} + 2u_{hsd} \tag{8.11}$$

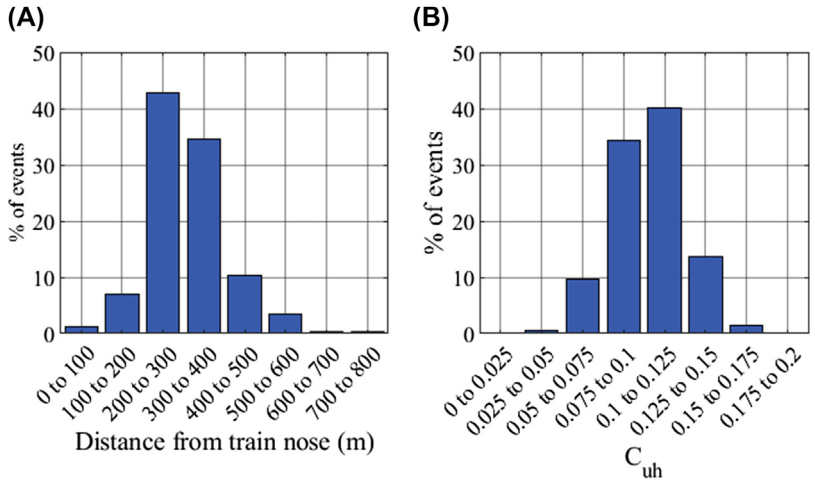

Figure 8.9 ***Gust values for S103 Velaro.*** Nose of train at 0 m. Tail of train is at 200 m. *(Data from AeroTRAIN project.)*

where $u_{haverage}$ is the mean of the peak velocities from each train passage after the 1-s moving average procedure and u_{hsd} is the standard deviation of these peak velocities. The values of u_{h95} are then compared with the values set by CEN (2013), which will be discussed in Section 8.9. Tests to measure slipstream velocities are reported in Baker et al. (2014c,d) for the Aero-TRAIN project and Soper and Baker (2019) for a variety of trains on GB lines. The results of these will be considered further below.

8.7.2 Physical model measurements

With regard to model-scale measurements, there are two possibilities – using standard wind tunnels with stationary models or using moving model rigs. Tests of the first type are reported, for example, in Bell et al. (2017) and of the second in Soper et al. (2014, 2017a). The former require measurements to be made at a range of points along and behind the train and are unrealistic in that the correct relative vehicle to ground motion is not simulated. This deficiency is corrected for in moving model tests. Both types of test are unrealistic in that it is difficult at model scale to simulate a full-length train (because of geometrical constraints of experimental facilities) and thus the boundary layer along the train will not be fully developed. Attempts have been made to artificially thicken the boundary layer on the train, but such techniques are still in development (Berenger et al., 1997; Sima et al., 2016; Bell et al., 2017). Also of course the Reynolds number will be much lower than at full scale for both types of test.

These issues mean that at present scaled model tests are not included in CEN (2013) as a means of certification for train slipstream loads, but they are allowed as a means of assessment of the air flow around a particular design during the concept phase of development. A detailed procedure is given, which in essence mirrors the procedure for full-scale experiments.

Despite the fact that physical model tests cannot be used in Europe for train authorisation purposes, nonetheless, they have proved useful both in understanding the flow field around trains of different types and in obtaining approximate values of the limit speed. Baker et al. (2013) provides a comparison between the results of moving model tests and full-scale data for the ICE2 train. The agreement was found to be good and within the margins of uncertainty. Soper et al. (2014) provide data for the development of the flow field around container freight trains with different loading arrangements. The slipstream velocities were found to be very high in this case and are sustained along the length of the train. Bell et al. (2017) compared moving-model, wind tunnel and full-scale data to determine a

method of slipstream analysis for train prototype design. Instantaneous and gust velocities were compared with reasonable accuracy.

8.7.3 Computational fluid dynamics

Similarly to moving-model tests, CFD is not yet considered sufficient to be used as a certification method for train slipstream analysis, regardless of train speed. There are currently no agreed methods in which train certification could be performed using CFD. However, like model-scale testing, its use as a means of prototyping has been documented in CEN (2013). Basically resource-intensive unsteady flow methods (DDES, LES) are required to adequately model the large-scale turbulence found in slipstreams – see for example the work of Hemida et al. (2012) and Wang et al. (2017). Whilst such calculations can, quite straightforwardly, give mean and standard deviations of velocity at a point relative to a train, they do not in the first instance give information on the gust velocities as defined in CEN (2013). To achieve this, time histories relative to a stationary observer have to be derived – effectively by moving an observer at the train speed at a section alongside the train for at least 20 separate occasions. These time histories can then be analysed in the same way as full-scale and model-scale time histories to give u_{h95}. However, the need to continue the calculation for enough time to provide sufficient data for obtaining 20 separate time histories is another constraint on resources (see Flynn et al., 2014).

8.8 Collation of slipstream load data

The AeroTRAIN project carried out slipstream velocity measurements on a wide range of trains and has produced a database of measured TSI velocities (Baker et al., 2014c,d). In addition, a number of other full-scale tests have been reported in the literature, and some moving model rig information is available for a small number of trains. Some of the AeroTRAIN measurements were made at a range of heights, and the variation of u_{h95} with height above track is shown in Fig. 8.10A for high-speed trains and in Fig. 8.10B for low-speed trains. There is perhaps an indication in these figures of a slight fall off in u_{h95} with height, but the uncertainties are large (of the order of ± 0.03). In what follows we present data mainly from the TSI measurement position at 0.2 m above the top of the rail, although some data are from a somewhat greater measurement height. It can be expected that these data will be representative of the slipstream velocities up to about 1.5 m above TOR.

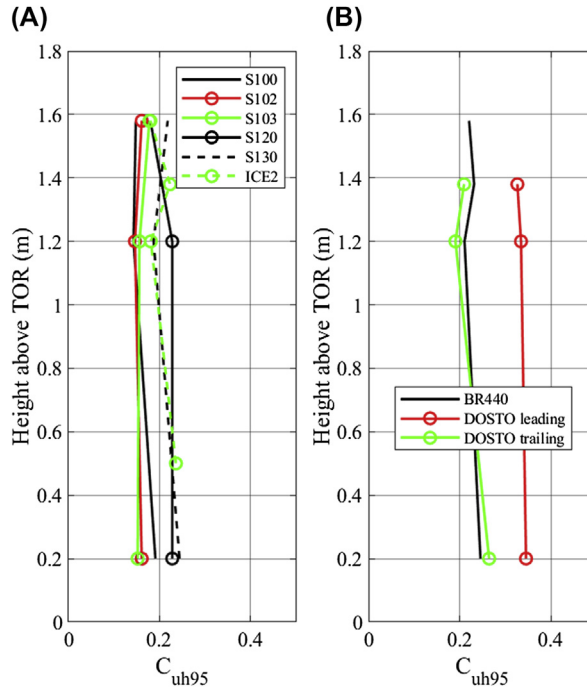

Figure 8.10 ***Variation of C_{uh95} with height above top of rail.*** (A) High-speed trains, (B) low-speed trains. *(Data from AeroTRAIN project.)*

These data are collated in Table 8.1, which shows u_{h95} values, normalised with train speed v (C_{uh95}) for trackside tests only. Note that some of the values were obtained from small ensembles (less than 10 train passes) and uncertainties can be large (up to ± 0.05). A number of points arise from the collation.

- For high-speed trains, the C_{uh95} values range from 0.15 to 0.28, with the more streamlined trains (such as the S103 Velaro) showing the lower values and the trains with more sharp-edged noses (such as ICE-2) showing the larger values.
- For double-unit trains, the C_{uh95} values are in general noticeably higher than for single-unit trains, as the overall C_{uh95} value is heavily influenced by large gusts in the interunit gap region.
- Medium- and low-speed trains have (with one exception) a wide range of C_{uh95} values from 0.18 to 0.35 with the higher values being associated with the more blunt-ended vehicles. For locomotive-hauled trains, large gusts can occur around the front part of the train at the junction

Table 8.1 Collation of C_{uh95} values.

A High-speed trains

	Baker et al. (2014d)	Baker et al. (2014d)	Baker et al. (2014d)	Baker et al. (2014d)	Baker et al. (2014d)	Baker et al. (2014d)	Baker et al. (2014d)	Gilbert (2013)	Gilbert (2013)	Soper et al. (2017a)	Baker et al. (2014d)	Baker et al. (2014d)	Baker et al. (2014d)
Train	S100	S102	S103	S120	S130	ICE-1	ICE-2	ICE-2	ICE-2	ICE-2	S102 (double)	S103 (double)	ICE-2 (double)
Technique	FS	FS	FS	FS	FS	FS	FS	MM	MM	MM	FS	FS	FS
Distance from track centreline (m)	3.0	3.0	3.0	3.0	3.0	2.5	2.5	2.5	3.0	3.0	3.0	3.0	3.0
Height above TOR (m)	0.2	0.2	0.3	0.2	0.2	0.5	0.5	0.5	0.2	0.2	0.2	0.2	0.2
C_{uh95}	0.191	0.161	0.152	0.228	0.244	0.221	0.251	0.278	0.276	0.277	0.226	0.17	0.275

B Medium-speed trains

	Soper and Baker (2019)	Unpublished (network rail)	Soper et al. (2017a)	Soper and Baker (2019)	Soper and Baker (2019)	Baker et al. (2014d)	Baker et al. (2014d)	Baker et al. (2014d)
Train	Class 390 Pendolino	Class 43 HST	Class 43 HST	Class 221 Voyager	Class 90 locomotive and sleeper coaches	S252	ICE-T	Class 91 (IC225)
Technique	FS	FS	MM	FS	FS	FS	FS	FS
Distance from track centreline (m)	3.0	3.05	3.0	3.0	3.0	3.0	3.0	2.5
Height above TOR (m)	0.2	0.7	0.2	0.2	0.2	0.2	0.5	0.7
C_{uh95}	0.24	0.215	0.329	0.24	0.18	0.215	0.236	0.305

C Low-speed trains					
	Baker et al. (2014d)	**Baker et al. (2014d)**	**Baker et al. (2014d)**	**Soper and Baker (2019)**	**Soper and Baker (2019)**
Train	BR440	DOSTO loco leading	DOSTO loco trailing	Class 325 mail multiple unit	Class 350
Technique	FS	FS	FS	FS	FS
Distance from track centreline (m)	3.0	3.0	3.0	3.0	3.0
Height above TOR (m)	0.2	0.2	0.2	0.2	0.2
C_{uh95}	0.245	0.345	0.264	0.38	0.22

D Freight trains			
	Unpublished (network rail)	**Soper et al. (2017a)**	**Soper and Baker (2019)**
Train	Misc. Freight	Container train	Class 66 locomotive and containers
Technique	FS	MM	FS
Distance from track centreline (m)	3.05	3.0	3.0
Height above TOR (m)	0.7	0.2	0.2
C_{uh95}	0.50	0.549	0.47

between the locomotive and the carriages. The exception is the Class 325 mail multiple unit, which is 240 m long, and the value of 0.38 probably reflects the growth of the boundary layer along the side of the train.

- The values for freight trains are highly variable and reflect both the variability of train consist from run to run and the variability in the flow field. However, the very high values of C_{ul95} are clear (around 0.5). Note that as freight train speeds are quite low (around 100 km/h), these dimensionless values do not necessarily result in very high absolute values.

8.9 Application of slipstream loads

8.9.1 The assessment of the effects of slipstreams

The diagram of Fig. 8.11 illustrates the range of methods for assessing the effects of slipstreams on people and objects. It essentially shows four pathways leading to the following four outcomes.

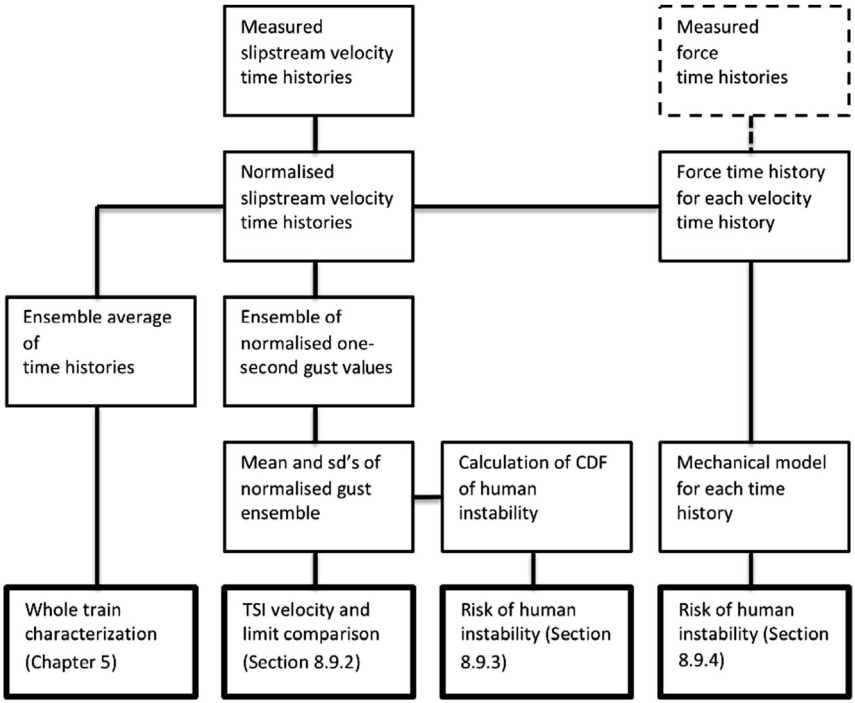

Figure 8.11 ***Train slipstream assessment methodologies.*** *CDF*, cumulative density function; *TSI*, Technical Standard for Interoperability.

- The calculation of ensemble averages of slipstreams, such as those used to illustrate the nature of the flow around trains in Chapter 5.
- The calculation of values of C_{uh95} that can be compared with limit values for train authorisation.
- The calculation of the risk of object and human stability based on stability measurements conducted in idealised conditions.
- The calculation of the risk of object and human stability based on the calculation of aerodynamic forces and the use of mechanical models.

The utility of the first of these is in providing a description and understanding of the flow and a characterisation of the whole flow field around a train. The results of this method have been fully discussed in Chapter 5 and will not be discussed further here. The second method is that set out in CEN (2013) and represents current practise and will be discussed in Section 8.9.2. The third and fourth methods address the wider issues of risk of accidents and will be discussed in Sections 8.9.3 and 8.9.4.

8.9.2 Comparison with limit values

If a person becomes unstable because of a train slipstream while standing on a station platform, there is potential for them to fall causing injury. Research into human stability is yet to reach a consensus about what wind speed or gust can unsteady a person. The reason for this is the wide range of contributing factors involved, such as gust duration, the person's age, weight, height, response time, dress and physical fitness to name a few. Further factors include whether the person is walking or standing and what their orientation is to the wind. The level of disagreement of what constitutes an unsteadying wind speed is highlighted by the range of critical wind speeds in the literature where mean values of between 10 and 20 m/s and gust values of between 15 and 30 m/s have been suggested by a range of authors - see Jordan et al. (2008) for a collation of these data. In the light of the above, the limits given in CEN (2013), that are based on a benchmarking principle, can thus only be regarded as approximate surrogates for safe wind gust speeds. These values are shown in Table 8.2 below.

In view of the lack of sensitivity of u_{h95} to height, the value at 1.4 m above TOR is likely to be the critical one. The values for C_{uh95} for $u_{h95} = 15.5$ m/s are thus shown in Table 8.3 for a range of vehicle speeds. It can be seen that at the higher speeds the values of C_{uh95} approach the measured values for a range of high-speed trains with speeds of around 300 km/h (Table 8.1).

Table 8.2 Limit values from CEN (2013).

Train maximum speed (km/h)	Height above top of rail (m)	u_{h95} m/s
<160	–	No assessment required
160–250	0.2	20
	1.4	15.5
>250	0.2	22
	1.4	15.5

Table 8.3 Limit values of C_{uh95} for $u_{h95\%} = 15.5$ m/s.

Train speed (km/h)	C_{uh95} for $u_{h95\%} = 18.5$ m/s
200	0.279
250	0.223
300	0.186
350	0.159

8.9.3 Risk of instability through the use of experimental stability data

As in almost every other context, human behaviour when exposed to train slipstream velocities is very variable and can only really be considered in statistical terms. In an attempt to understand this variability, Jordan et al. (2009) reported tests carried out to measure human response in a large wind tunnel, where test subjects were subjected to sudden gusts following the removal of a windshield as shown in Fig. 8.12B. Data have been obtained from these tests to derive cumulative density functions (CDFs) for the probability of incipient instability as a function of gust speeds (Fig. 8.12B). These data can be used in the following way (Baker, 2015).

- Determine from experiments the mean and standard deviations of the 1-second gust values from full-scale or model-scale measurements, $u_{haverage}$ and $u_{hsd,}$ and assume these values are normally distributed – see Baker et al. (2014d) for justification for this.
- Determine the cumulative distribution function for the stability of different categories of people – passengers, trackside workers, etc. The data of Fig. 8.12B suggest this might be of the following form.

$$\begin{aligned} \Omega_s &= 0 && \text{for} && u_{hgust} < u_1 \\ \Omega_s &= (u_{hgust} - u_1)/u_2 && \text{for} && u_1 < u_{hgust} < u_1 + u_2 \\ \Omega_s &= 1 && \text{for} && u_1 + u_2 < u_{hgust} \end{aligned} \tag{8.12}$$

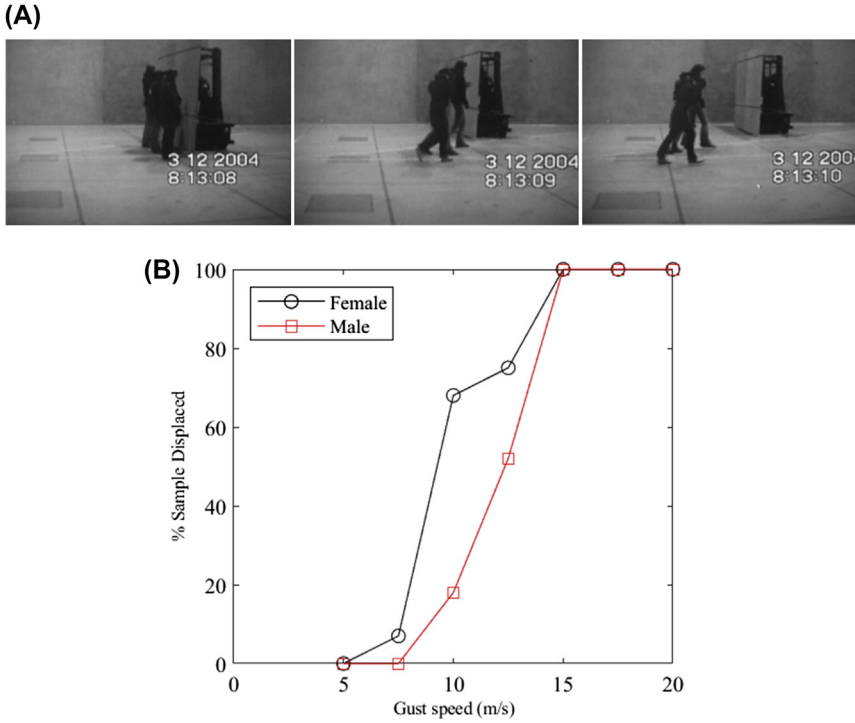

Figure 8.12 ***The experiments of Jordan (2008).*** (A) The wind tunnel experiments; (B) cumulative density functions of human stability for subjects facing the flow.

$u_1$and u_2 can be expected to be functions of the assumed gender breakdown of the exposed population (gender here being a broad surrogate for passenger size and weight). Ω_s is the cumulative probability that u_{hgust} will not be exceeded.

- Through a convolution of train gust speed probability distributions and the cumulative probability distribution of human stability, calculate the risk of an accident (i.e., a person becoming unstable) for one train passing a particular location. After some manipulation, this can be shown to be given by

$$\Omega = 0.5(1 - \mathrm{erf}(\pi_2)) + \frac{1}{(\pi_2 - \pi_1)}\left(\frac{1}{\sqrt{\pi}}\left(e^{-\pi_1{}^2} - e^{-\pi_2{}^2}\right) + \frac{\pi_1}{2}(\mathrm{erf}(\pi_1) - \mathrm{erf}(\pi_2))\right) \tag{8.13}$$

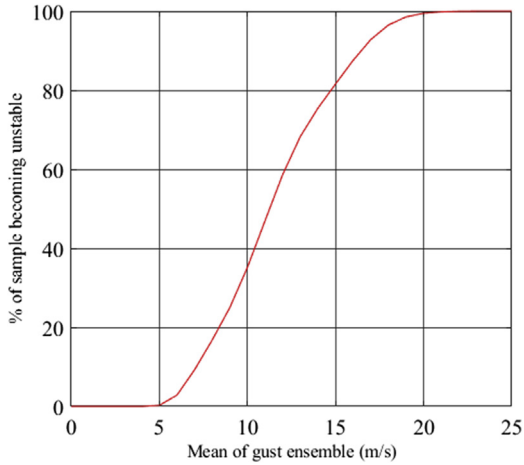

Figure 8.13 Cumulative density functions of human stability.

where

$$\pi_1 = \frac{u_1 - u_{haverage}}{u_{hsd}\sqrt{2}} \quad \pi_2 = \frac{u_1 + u_2 - u_{haverage}}{u_{hsd}\sqrt{2}} \tag{8.14}$$

Fig. 8.13 shows a typical CDF for a range of values of $u_{haverage}$ with a fixed ratio of $u_{hsd}/u_{haverage} = 0.2$ and values of $u_1 = u_2 = 7.5$ m/s, which Fig. 8.12 suggests is broadly representative of the general population. This CDF gives the risk of human instability for one train passage at a particular site and can be combined with operational information on the number of train passes and the likelihood of people being present to obtain an overall risk of an accident.

8.9.4 Risk of instability from mechanical models

In the past test techniques with dummies and vertical cylinders have been used in some countries to measure forces of relevance due to train slipstreams (see RAPIDE, 2001; Tsai et al., 2003; Li et al., 2009). There are significant difficulties with such tests. However, both practical in that resonance at the natural frequency can contaminate the results and make analysis difficult and also conceptual – it appears that cylinders only react to pressure transients (such as those around the nose and tail of the train) and dummies only to velocity transients (RAPIDE, 2001). In neither case was there a good correlation between slipstream velocity time histories and force time histories as one might expect. These issues have led to the

general abandonment of this type of methodology, and it is thus represented in the chart of Table 8.1 as a dotted box.

Where forces are used in the assessment of the safety or otherwise of train slipstreams, they are generally obtained from the slipstream speed time histories using a drag coefficient approach, i.e.,

$$F = 0.5\ C_{Fx} A \rho u_h^2 \tag{8.15}$$

where A is the frontal area of the object exposed to the flow and u_h is the instantaneous horizontal slipstream speed. For pushchairs, a drag coefficient value of 1.4 is appropriate (Jordan, 2008). The value of u_h for instability of rigid trackside objects or object on platforms can then be calculated using this equation and a simple static model of the forces on the object or subject that includes appropriate allowance for weight, friction, etc. An assessment can then be made of the risk of instability for a particular train at a particular site.

To calculate the appropriate values for human instability is, however, not so straightforward, because of the inherent variability found within the population as mentioned above. The method adopted in Jordan et al. (2008, 2009) was to use the experimental data for drag coefficient to calibrate a spring mass damper mathematical model to replicate human response to a wind gust. A schematic of the model is shown in Fig. 8.14 where the head, torso and legs each accounts for a portion of the total body mass. Furthermore, the connectivity between the components was modelled as springs and dampers to represent the influence of the muscles and joints. Typical values of drag area (drag coefficient × area) for humans are given in Jordan et al. (2008). For men at a wind speed of 15 m/s, the average value is 0.59 m^2 when facing the flow and 0.34 m^2 when sideways on, and the equivalent figures for women are 0.46 and 0.30 m^2. All values

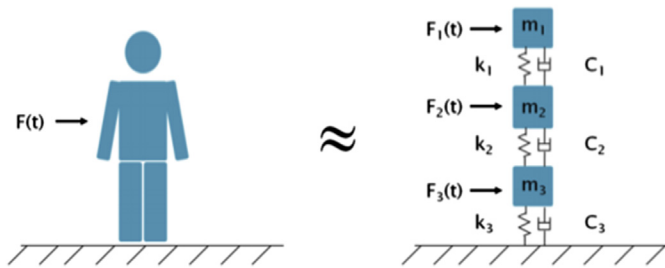

Figure 8.14 Schematic of spring mass damper model of person stability subjected to wind gust from Flynn et al. (2016). *(Copyright Elsevier.)*

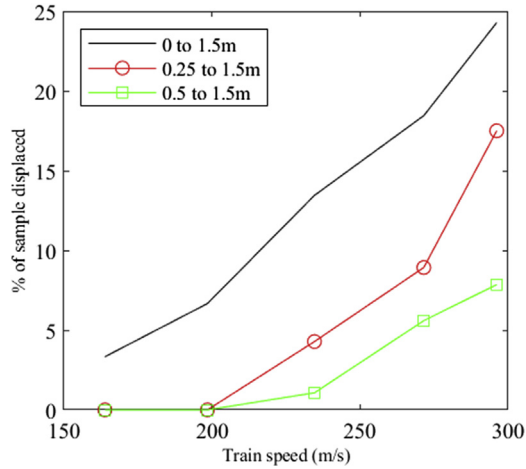

Figure 8.15 Stability of passengers on platforms passed by passenger trains in different distance bands from the platform edge. *(From Jordan (2008).)*

decrease as wind speed increases, presumably because of the 'streamlining' of clothing. Forces were applied to each component of the model using these drag coefficients distributed across the different components of the model body. The person model was then subjected to experimentally measured or analytically generated slipstream wind speeds and used to find the probability of an accident occurring at different positions from the edge of the platform (Fig. 8.15).

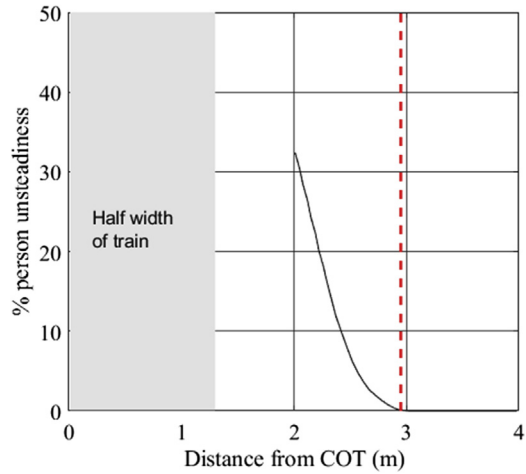

Figure 8.16 Percentage of population becoming unstable as a freight train passes against distance from train side for no cross wind. *(Copyright Elsevier.)*

The spring mass damper model has also been used with CFD-generated velocities (Flynn et al., 2016). Fig. 8.16 shows the percentage of a randomly selected population who became unstable at different distances from the train side. The position of the safety line on many station platforms at 3 m from the centre of the track can be seen to be somewhat vindicated by these results.

CHAPTER 9

Ballast flight beneath trains

9.1 The issues

The problem of ballast flight beneath trains is one that has made itself felt very forcibly over recent years, with a variety of (usually unpublicised and unpublished) events occurring on high-speed lines, where ballast has been lifted from the track, seemingly by aerodynamic effects, and caused considerable damage to train underbody equipment and tracks. The phenomenon seems to manifest itself in different ways in different countries. In parts of Europe, incidents have occurred in normal weather conditions, where large quantities of quite large ballast have become airborne and caused extensive pitting of train under bodies. In particular, this occurred during ICE3 tests in French and Belgium lines in 2003 and 2004, where major damage was caused to the trains, but other incidents have been reported in Italy and Spain (Kaltenbach et al., 2008). In other parts of the world, the problem seems to be due to ice particles falling from trains, which then displaces ballast and causes train and track damage (Kawashima et al., 2003). In Great Britain, the problem appears to be due to smaller ballast particles being lifted onto the track, where they are crushed by either the train that caused the ballast to lift or a following train, leading to pitting of the wheel and rail as shown in Fig. 9.1, and the need for more regular maintenance. Indeed, discussion with operators in Great Britain suggests that the flight of ballast has been a problem for many years on medium-speed trains, with long-term requirements for extra wheel maintenance (through grinding) for the front and rear wheel sets and regular observations of ballast high up in the underfloor equipment during maintenance periods. Without a doubt, the most severe issues occur on ballasted high-speed lines when operating around and above 300 km/h. This phenomenon has initiated a significant amount of research work around the world, particularly within Europe, through the Aerodynamics in the Open Air (AOA) (Kaltenbach et al., 2008) and AeroTRAIN (Sima et al., 2011) projects. As a part of these projects, measurements have been made of the train

Train aerodynamics
ISBN 978-0-12-813310-1
https://doi.org/10.1016/B978-0-12-813310-1.00009-5

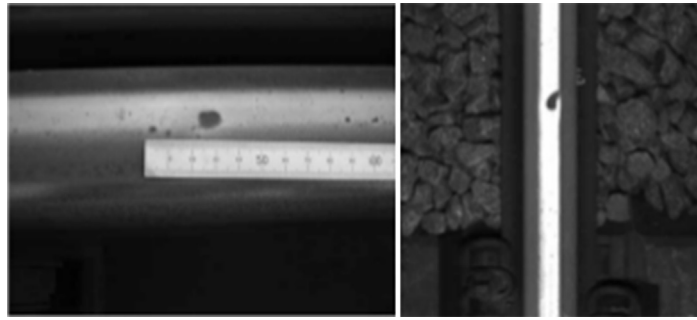

Figure 9.1 Pitting of rails due to ballast crushing.

underbody flow field at full scale and in a variety of facilities at model scale, and equivalent CFD calculations have also been made. Some of these have already been reported in Chapter 5 where the underbody flow field was discussed.

The problem of ballast flight can of course be alleviated by measures that require no knowledge of the aerodynamic issues, such as protecting the track using 'ballast bags' or ballast shields, or by ballast gluing – see RSSB (2016a). The disadvantage of such methods is the initial cost and that track maintenance becomes much more difficult and costly. Another way of alleviating the problem is to develop an understanding of when the initiation of ballast flight occurs, in terms of train aerodynamic behaviour and ballast and track properties, and to ensure that the conditions for ballast flight are avoided by careful design and operation. A further approach might be to allow ballast flight to take place but ensure that ballast stones do not impact on the train. It is with these last two concepts that this chapter is chiefly concerned.

In what follows we firstly recap on the nature of the flow field beneath trains in Section 9.2. We then move on to consider in Section 9.3 the aerodynamic and mechanical forces that act on stationary ballast stones and consider the conditions necessary for ballast movement to be initiated. In Section 9.4 we review what is currently known of the movement and flight of ballast after movement has been initiated, and in particular the issue of whether or not ballast stones will impact on the underside of trains or fall onto the tracks. Section 9.5 considers the ejection of ballast from the bed, either by the impact from other ballast or by ice or similar particles falling from moving trains. Section 9.6 then discusses the possible way forward for train authorisation and route risk analysis.

9.2 The flow field beneath trains

The flow field beneath trains has already been described in Section 5.2.7, and here we recap on the main points of what was said there and also add some detail of relevance to the ballast flight issue. Fig. 5.20 shows that the air flow velocities beneath a train can have high values (i.e., a significant proportion of the train speed) quite close to the bed. The velocity field is highly unsteady, and a mean value can only be obtained by forming an ensemble average of measurements from several train passages. The ensemble standard deviations are large and of the same order of size as the ensemble means. This unsteadiness needs to be borne in mind in what follows. Significant pressure transients can also be observed, particularly around the train nose and tail, which can also be best discerned from ensemble averages of measurements from a number of train passages (Fig. 5.19). A number of investigators (Kwon and Park, 2006; Ido et al., 2008, 2013; Deeg et al., 2008; Quinn et al., 2010; Lazaro et al., 2011; Premoli et al., 2015; Soper et al., 2017b) have measured the velocity profile beneath trains close to the bed and have thus been able to obtain indirect measurements of bed roughness and shear velocity through the fitting of logarithmic profiles to the measured velocity values. In particular, friction coefficients of around 0.02–0.03 have been determined for ballasted track and values of around 0.01 for slab track. In both the pressure and velocity time histories, the presence of the bogies is clearly discernible, with peaks and troughs in pressures and velocities occurring as bogies pass over the measurement point. A number of authors have commented that the effect of bogies in producing velocity peaks may result in conditions more favourable to ballast movement. Detailed investigations have been carried out using large-scale physical models (Jönnson et al., 2012) and high-resolution CFD techniques (Zhu and Hu, 2017; Paz et al., 2017) to measure the variations of the flow field around particular bogie configurations.

Of particular interest and utility is the analysis that has been carried out by Garcia et al. (2011). Through a simple analysis of the flow field beneath the train, they arrived at the following expression for the velocity profile:

$$\frac{u_x}{u_\tau} = 2.5\left(\ln\left(\frac{\sin\left(\frac{\pi z}{2h_u}\right)}{\frac{\pi z_{01}}{2h_u}}\right) - \ln\left(\cos\left(\frac{\pi z}{2h_u}\right)\right)\right) \tag{9.1}$$

where

$$u_\tau = \frac{v}{2.5\left(\ln\left(\frac{2h_u}{\pi z_{01}}\right) + \ln\left(\frac{2h_u}{\pi z_{02}}\right)\right)} \tag{9.2}$$

Here u_x is the velocity at a height z above the bed, u_τ is the friction velocity, h_u is the underbody gap, v is the train speed and z_{01} and z_{02} are the surface roughness lengths at the ballast bed and at the train surface, respectively. The surface roughness lengths are related to the corresponding equivalent sand grain roughnesses by the expressions

$$z_{01} = k_{s1}/30 \quad z_{02} = k_{s2}/30 \tag{9.3}$$

The form of this solution is shown in Fig. 9.2. It can be seen to have the characteristic 'S' shape of the mean velocity profile beneath trains and

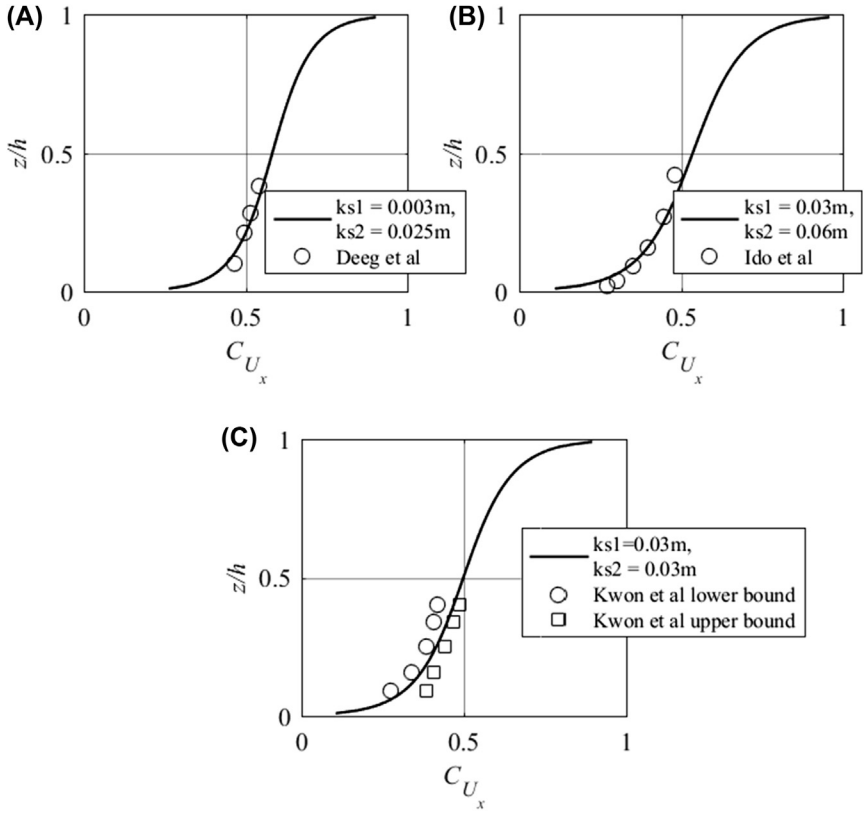

Figure 9.2 ***The analytical formulation of Eq. (9.1).*** A - Experiments of Deeg et al. (2008), B - Experiments of Ido et al. (2008), C - Experiments of Kwon et al. (2006).

represents a type of Couette flow. Garcia et al. (2011) used this formulation to determine the equivalent sand grain roughnesses for a variety of train and track configurations. Curve fits to the data of Deeg et al. (2008) for slab track and Ido et al. (2008) and Kwon and Park (2006) for ballasted track are shown in Fig. 9.2, together with the required values of k_{s1} and k_{s2}. Whilst the agreement is good, it should be noted that the definition of what constitutes the underbody height is far from clear and that the methodology produces values of the ratio u_τ/v that are significantly below the values obtained from the log law plots of the same data in Section 3.2.7. Nonetheless, it will be seen below that the formulation of Garcia et al. (2011) offers a potential methodology of use in train authorisation and route risk assessment.

9.3 Forces on stationary ballast and initiation of motion

9.3.1 Forces on ballast

In this section, we will consider the forces acting on ballast stones, both mechanical and aerodynamic, and then move on in the next section to consider the initiation of motion of ballast caused by these forces. The analysis is very simple and is not intended to provide precise criteria for incipient motion of ballast, but rather to identify the main parameters involved and their relationship to each other. Note that the analysis that follows has many points in common with those of Sanz-Andres and Navarro-Medina (2010), Jing et al. (2012), Navarro-Medina et al. (2015) and Paz et al. (2017). We begin our discussion by setting out the forces that act on ballast stones beneath trains and attempt to give rough orders of magnitude for these. We consider the situation shown in Fig. 9.3 of a ballast stone on top of others exposed to the flow. For the sake of simplicity and clarity, we consider the ballast stone to be defined by just one length scale d_B, although this is of course a major assumption.

The aerodynamic forces that act in the vertical direction, F_{VAB}, are as follows:

$$F_{VAB} = -0.5\rho A_B \Delta C_{pB} v^2 + 0.5\rho A_B C_{LB} u_{x0}^2 \tag{9.4}$$

A_B is the ballast horizontal area which will be taken as d_B^2, v is the train speed and ΔC_{pB} is the difference in pressure coefficient beneath the top and bottom of the ballast stone, which can be taken from curves such as Fig. 5.19 (Soper et al., 2017b). C_{LB} is a ballast lift force coefficient and u_{x0} is a flow velocity close to the bed. The first term on the right hand

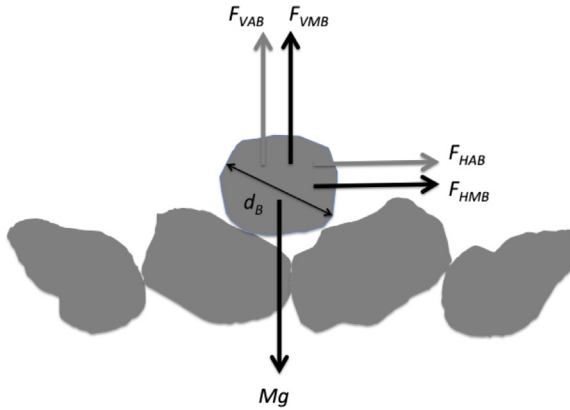

Figure 9.3 Aerodynamic and mechanical forces on a ballast stone.

side is due to the pressure transients underneath the train, assuming that the pressure beneath the stone does not vary with time. Note the negative sign, as a negative pressure will cause a positive force on the stone. The second term is due to a vertical component of the force caused by the changes in velocity around the train (the lift). Using the velocity and pressure coefficient data for one train pass of the Class 373 Eurostar at $z = -0.18$ m from the top of the rail (i.e., just above the ballast surface), travelling at 84 m/s and assuming the ballast has a length scale of 0.03 m with a density of 2650 kg/m^3 and a lift coefficient of 0.5, the overall vertical aerodynamic force on the ballast can be calculated and is shown in Fig. 9.4. The effects of the nose and tail pressure transients are clear, with very unsteady fluctuating forces between them.

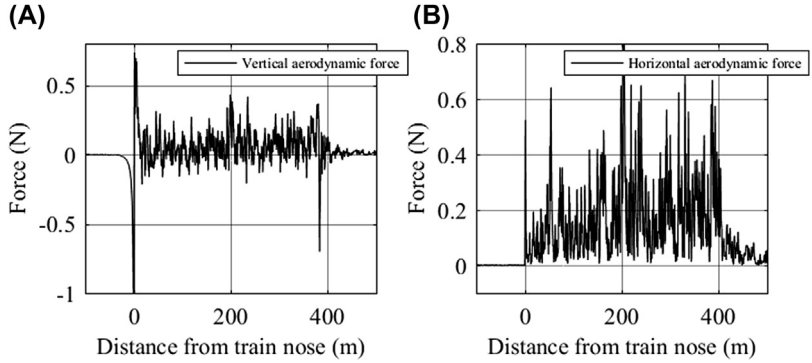

Figure 9.4 ***Aerodynamic forces on 3 cm ballast stone beneath the Class 373 Eurostar travelling at 84 m/s.*** (A) Vertical aerodynamic force; (B) horizontal aerodynamic force.

The horizontal aerodynamic force, F_{HAB}, can be expressed using the normal drag coefficient formulation

$$F_{HAB} = 0.5\rho A_B C_{DB} u_{x0}^2 \tag{9.5}$$

where C_{DB} is a ballast drag coefficient, which one would expect to have values of around 1.0. A time history of the horizontal forces thus calculated for a 3 cm cubic stone is also shown in Fig. 9.4B. For the conditions chosen, these can be seen to be somewhat larger than the vertical forces in magnitude. Overall the aerodynamic forces fluctuate between ±0.5 N.

The vertical mechanical force is an inertial force caused by track acceleration. If the acceleration is measured in a positive vertical direction, the inertial force will have a negative sign. This is given by

$$F_{VMB} = -M_B a_B \tag{9.6}$$

where a_B is the ballast acceleration and M_B is the ballast mass. The measurements of ballast accelerations described in Soper et al. (2017b) enable time histories of this force to be determined for a 3 cm ballast stone. Typical results are shown in Fig. 9.5A for the same conditions as in Fig. 9.4. It can be seen that these forces oscillate as the train passes, with discrete oscillations as wheels and bogies pass, with peak magnitudes of around ±0.5 N. Note, however, that track accelerations and thus the mechanical forces can vary very significantly with levels of track quality. The results shown in Fig. 9.5A are for well-maintained track with vertical displacements of the track itself of the order of 0.3 mm as the train passes over. For poorly maintained track or for track where there are poor underlying ground conditions, these displacements, and thus accelerations and forces, can increase by an order of magnitude.

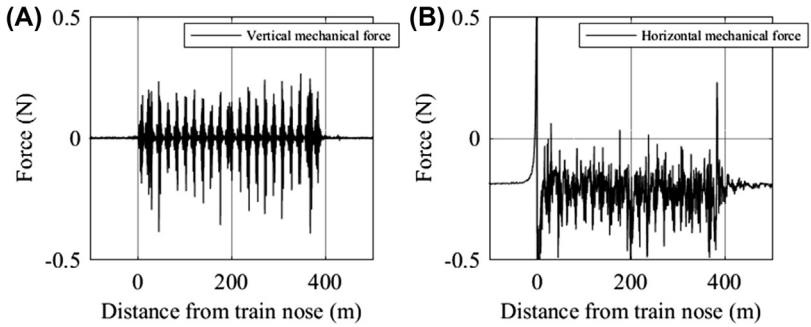

Figure 9.5 ***Mechanical forces on 3 cm ballast stone beneath the Class 373 Eurostar travelling at 84 m/s.*** (A) Vertical mechanical force; (B) horizontal mechanical force.

The horizontal mechanical force F_{HMB} is simply a friction force that is the overall vertical reaction force R_B multiplied by a friction coefficient μ_B. The overall vertical reaction force is given by

$$\begin{aligned} R_B &= -F_{VAB} - F_{VMB} + M_B g \\ &= 0.5\rho A_B \Delta C_{pB} v^2 - 0.5\rho A_B C_{LB} u_{x0}^2 + M_B a_B + M_B g \end{aligned} \tag{9.7}$$

and thus

$$F_{HMB} = -\mu_B\left(0.5\rho A_B \Delta C_{pB} v^2 - 0.5\rho A_B C_{LB} u_{x0}^2 + M_B a_B + M_B g\right) \tag{9.8}$$

Again, a typical horizontal time series is shown in Fig. 9.5B assuming friction coefficient of 0.6. Of course this force cannot in reality take positive values, as it is essentially a friction force that opposes motion.

9.3.2 Initiation of ballast movement

Ballast movement can occur due to three mechanisms.

- Overall vertical force $> M_B g$
- Overall horizontal force > 0
- Rolling moment about leeward edge $> M_B g d_B/2$

We assume horizontal and vertical areas of d_B^2 and a moment arm of $d_B/2$. The first of the above conditions gives

$$F_{VAB} + F_{VMB} = -0.5\rho d_B^2 \Delta C_{pB} v^2 + 0.5\rho d_B^2 C_{LB} u_{x0}^2 - M_B a_B > M_B g \tag{9.9}$$

The second gives

$$\begin{aligned} F_{HAB} + F_{HMB} = 0.5\rho d_B^2 C_{DB} u_{x0}^2 - \mu_B\big(&0.5\rho d_B^2 \Delta C_{pB} v^2 \\ &- 0.5\rho d_B^2 C_{LB} u_{x0}^2 + M_B a_B + M_B g\big) > 0 \end{aligned} \tag{9.10}$$

The third condition gives

$$\begin{aligned} (F_{VAB} + F_{VMB})\left(\frac{d_B}{2}\right) + (F_{HAB})\left(\frac{d_B}{2}\right) = \big(&-0.5\rho d d_B^2 \Delta C_{pB} v^2 \\ &+ 0.5\rho d d_B^2 C_{LB} u_{x0}^2 - M_B a_B\big)\left(\frac{d_B}{2}\right) \\ &+ \left(0.5\rho d_B^2 C_{DB} u_{x0}^2\right)\left(\frac{d_B}{2}\right) \\ &> M_B g\left(\frac{d_B}{2}\right) \end{aligned} \tag{9.11}$$

After some manipulation these three criteria give

$$\text{For lifting} \quad S_z = \frac{0.5\rho v^2\left(C_{LB}C_{uxo}^2 - \Delta C_{PB}\right)}{\rho_B d_B(a_B + g)} > 1 \tag{9.12}$$

$$\text{For sliding} \quad S_x = \frac{0.5\rho v^2\left(\mu_B\left(C_{LB}C_{uxo}^2 - \Delta C_{PB}\right)\right) + C_{DB}C_{uxo}^2\right)}{\mu_B\rho_B d_B(a_B + g)} > 1 \tag{9.13}$$

$$\text{For rolling} \quad S_m = \frac{0.5\rho v^2\left(\left(C_{LB}C_{uxo}^2 - \Delta C_{PB}\right)\right) + C_{DB}C_{uxo}^2\right)}{\rho_B d_B(a_B + g)} > 1 \tag{9.14}$$

These three ratios S_z, S_x and S_m are effectively Shields parameters. This parameter has long been recognised as of importance for the movement of sediment (Bagnold, 1941). C_{uxo} is given by u_{x0}/v. The instantaneous values of these three criteria are shown in Fig. 9.6A–C for the conditions

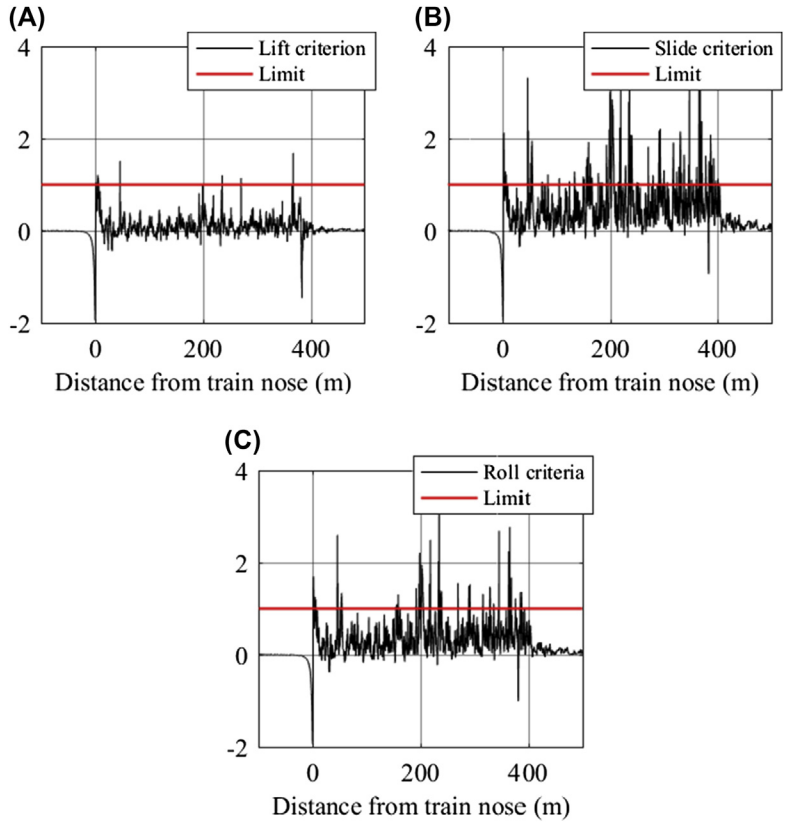

Figure 9.6 ***The three Shields number criteria for ballast movement initiation.*** (A) Lift criterion; (B) slide criterion; (C) roll criterion.

of Figs. 9.4 and 9.5. It can be seen that the limit of unity is exceeded at times for each of the three criteria. It needs to be remembered of course that these calculations are for just one train pass and one assumed set of conditions, and the results can be expected to vary significantly between train passes, for different stone sizes and different train speeds, etc. In this case, the horizontal sliding mode is the most common, with the limit of unity exceeded 13.7% of the time, followed by the rolling limit for 5.6% of the time and the lift limit for 3.6% of the time. It is of interest to see that most of the exceedances of the criteria occur around the central bogie (180–220 m), where there is an increase in underbody velocity, and in the second half of the train where the velocity is generally higher than in the first half (see Fig. 3.20).

Kaltenbach et al. (2008) use the classic definition of the Shields parameter to analyse experimental data from wind tunnel tests that measured the horizontal movement of ballast stones, with no vertical acceleration and ignoring vertical aerodynamic forces. This parameter is given by

$$S'_x = \frac{\rho u_\tau^2}{\rho_B d_B g} \tag{9.15}$$

In effect, the horizontal aerodynamic forces are specified by a shear force rather than a direct drag force. S'_x can of course be directly related to S_x as defined above. Kaltenbach found ballast flight initiation occurred at S'_x values of around 0.02–0.03, rather higher than the classical value of 0.01 given in Kinds (1975). A sample of these results is shown in Fig. 9.7, where the number of ballast stones moved in a fixed period is plotted against S'_x. Kaltenbach et al. (2008) emphasise that these results cannot be taken as representative of the full-scale situation because of the idealised nature of the experiments, but they are interesting in that they show the marked effect of the nature of the sleeper on the initiation of ballast flight. Unsurprisingly, the more exposed the ballast is to the flow (as with biblock sleepers), the greater the likelihood of movement occurring.

9.3.3 Implications of the incipient motion analysis

The analysis set out above must be regarded as very idealised and simplified. Nonetheless, it does give an indication about the nature of ballast flight, which is essentially a complex multivariate problem, and suggests possible methods for reducing ballast flight initiation. This is of practical importance,

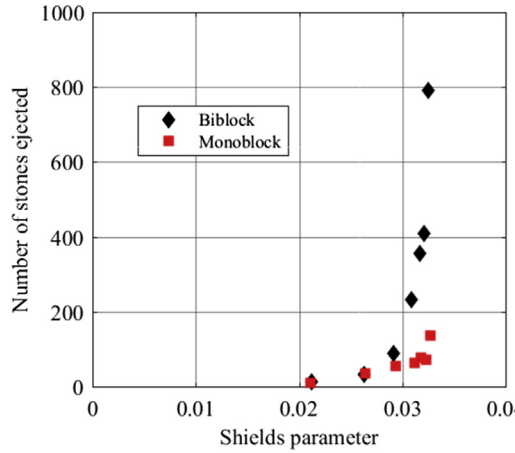

Figure 9.7 Number of ballast stones moved plotted against the classical Shields parameter S'_x. *(Data from AOA project reported in Kaltenbach et al. (2008).)*

as the most obvious method for reducing the impact of ballast flight is to stop ballast flying in the first place. Specifically the following points arise from the analysis above.

- If one piece of ballast is sheltered by other pieces, one would expect the horizontal aerodynamic forces to be significantly reduced. As the horizontal sliding motion seems to be the most likely to occur, then the initiation of ballast movement becomes much less likely. This is hardly a surprise but does indicate the desirability of avoiding an uneven ballast bed with exposed stones. Indeed, the basic precaution taken against ballast flight is to lower the ballast bed as far as possible and to ensure that no isolated ballast is left on top of the sleepers.
- Eqs. (9.12)–(9.14) indicate that for identical flow fields beneath the train (C_{uxo} and ΔC_{PB} constant), constant ballast force coefficients (C_{LB} and C_{DB}) and constant track accelerations, the boundary between ballast flight and no ballast flight is defined by an expression $d \propto v^2$, i.e., the larger the train velocity, the larger the size of ballast stone that will move. The fact that the square of the velocity is important indicates the sensitivity of ballast movement to velocity changes, which will be of most importance where relatively small increases in train maximum velocities are made.
- The analysis also suggests that tamping and stone-blowing practises that result in the creation of small ballast particles, particularly on the ballast surface, should be avoided.

- The importance of track vibration in initiating ballast movement is clear, with negative accelerations effectively reducing the damping effects of gravity (in the denominators of Eqs. 9.12–9.14). The results shown here are for well-maintained track where vibration would be expected to be low. For poorly maintained track, the accelerations may be up to an order of magnitude higher. Thus ballast flight issues can be reduced through a proper track inspection and maintenance regime.
- The most important variables that can be related to the train are the train speed v and the ratio of the near ballast velocity to the train speed, C_{uxo}, which is effectively a measure of the shear stress at the bed (and can indeed be directly related to the bed friction coefficient). Thus in terms of train authorisation and certification, the parameter would seem to be the one to concentrate on – as indeed is the case in much current practise. This will be considered further below.

9.4 Ballast in motion

As noted in Section 9.1, other possibilities for specifying a safe behavioural boundary for ballast flight might be the conditions either when ballast can land on the rail and be crushed or when ballast flies high enough to hit the underbody of the train. In this section, we will thus consider the movement and flight of ballast in a little more detail, although it must be stressed at the outset that all that follows is provisional with many assumptions. It is intended again to only serve as an indication of what parameters are of importance rather than giving absolute indications of ballast velocities, trajectories, etc.

After ballast movement has been initiated, if the flow conditions are suitable, the ballast will continue to either move along the ballast bed by either rolling or sliding – see Sanz-Andres and Navarro-Medina (2010) and Navarro-Medina et al. (2015) for a discussion of this – or will perhaps lift and begin to fly through the underbody flow field. Rolling or sliding is of less practical importance because ballast moving near the bed will not cause damage, and it is the flight of ballast that is of most interest and will be considered here. That being said, vigorous along bed movement may result in collisions that then result in ballast stones moving upwards and beginning to fly.

For flying ballast, the forces acting on the stone take on different forms to those set out in Section 9.2. The pressure forces will cease to be of relevance, as the pressure changes due to train pressure transients will

equalise around the stone. Similarly the mechanical forces will cease to be of importance, as the ballast is no longer in contact with the bed. The force coefficients can be expected to change as a ballast changes its orientation to the flow — and will continue to do so. The situation thus becomes simpler on one hand and more complex on the other. To analyse the flight of ballast in a relatively simple way, we thus assume that as the ballast flies through the air the only forces that act on it are an aerodynamic drag force in the direction of the instantaneous flow and the weight acting downwards. The drag coefficient is taken to be constant. Thus applying the compact debris equations outlined in Baker (2007) to the situation, we obtain

$$\frac{dC_{uxB}}{d\left(\frac{tg}{v}\right)} = Ta\left(\left(C_{ux} - C_{uxB}\right)^2 + \left(C_{uz} - C_{uzB}\right)^2\right)^{0.5}\left(C_{ux} - C_{uxB}\right) \tag{9.16}$$

$$\frac{dC_{uzB}}{d\left(\frac{tg}{v}\right)} = Ta\left(\left(C_{ux} - C_{uxB}\right)^2 + \left(C_{uz} - C_{uzB}\right)^2\right)^{0.5}\left(C_{uz} - C_{uzB}\right) - 1 \tag{9.17}$$

Here C_{uxB} and C_{uzB} are the dimensionless ballast velocities in the horizontal (x) and vertical (z) directions, (u_{xB}/v and u_{zB}/v), respectively; C_{ux} and C_{uz} are the dimensionless air velocity in the horizontal and vertical directions (u_x/v and u_z/v) and Ta is the Tachikawa number given by

$$Ta = \frac{C_{DB}\rho A_B v^2}{2M_B g} \tag{9.18}$$

For ballast stones of length scale d_B, this becomes

$$Ta = \frac{C_{DB}\rho v^2}{2\rho_B d_B g} \tag{9.19}$$

We assume boundary conditions at $t = 0$ of $u_{xB} = 0$ and u_{zB} is input as a variable in the calculations. We take the horizontal velocity in the underbody gap to be given by the form developed by Garcia et al. (2011) — Eq. (9.1). This is a useful approximation, but cannot be wholly adequate, particularly in the vicinity of bogies. For the initial calculations below, we assume there is no vertical component of velocity beneath the train.

These equations can be solved relatively straightforwardly, although a numerical solution is required. Typical results of the ballast flight calculations are shown in Fig. 9.8A for a small ballast stone with length scale 0.02 m.

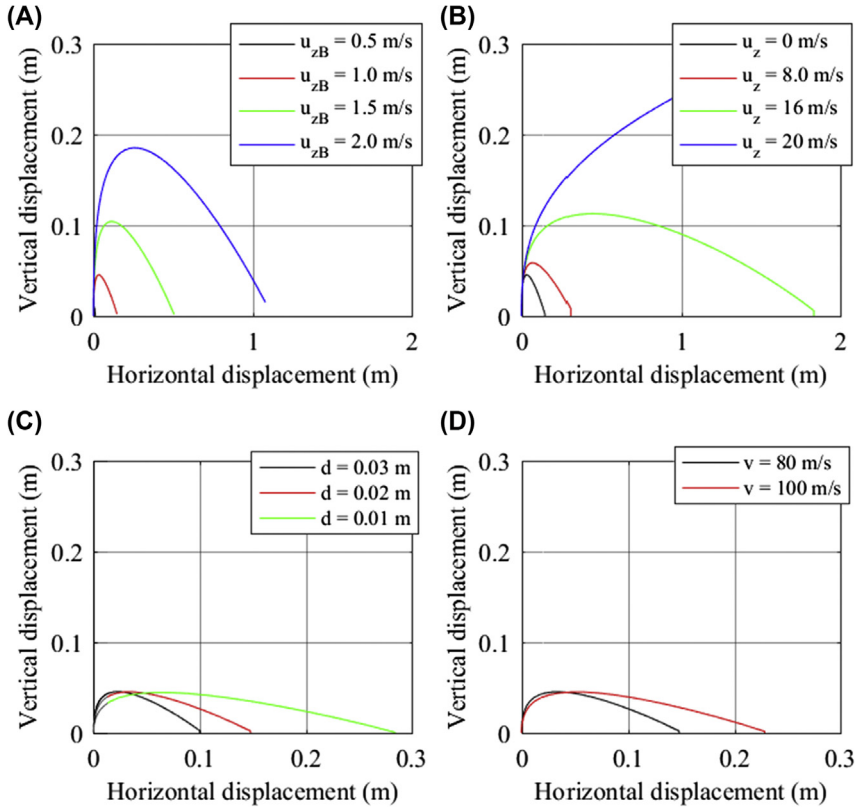

Figure 9.8 ***Ballast flight.*** Base case is vehicle speed of 80 m/s, ballast diameter of 0.02 m, initial vertical velocity of 1 m/s and zero vertical flow velocity component. (A) Variation in initial vertical velocity, (B) Variation in underbody vertical component of wind speed, (C) Variation in ballast size, (D) Variation in train speed.

It was found that a non-zero initial vertical velocity was required to initiate ballast flight, and the results in Fig. 9.8A are for a range of initial vertical velocities between 0.5 and 2 m/s. One would expect these initial velocities to be generated partly by the vibration of the track and partly from the vertical aerodynamic forces at the condition of incipient motion. It can be expected that the ballast will continue to move upwards as the ballast bed passes its maximum vertical displacement and starts to fall. The track displacement data given in Soper et al. (2017b) indicate track velocities of only around 0.02 m/s — not enough for ballast stones to fly to any significant extent. However, the same paper gives track velocities of over 0.5 m/s for track with voided sleepers. This implies that ballast is most likely to fly significantly where there is poor quality track.

There are other possibilities, however, that might result in a greater upward ballast velocity. Firstly, the flow beneath the train may exhibit 'bursts' and 'sweeps' in the same way that flat plate boundary layers do. Bursts are large-scale coherent turbulence structures that eject significant momentum away from the bed, and sweeps are the reverse, bringing significant momentum down to the bed. Bursts can thus have a significant upward vertical component. Secondly, it may be that in the vicinity of bogies there may be considerable upward flows. Indeed, these can be inferred from the detailed computational work of Zhu and Hu (2017). To investigate the effect of such velocity components, trajectories were calculated for a constant vertical velocity component of between 0 and 20 m/s throughout the ballast flight, with an initial vertical velocity of 1 m/s. It can be seen from Fig. 9.8B that the height and length of the ballast trajectory increase significantly with increasing upward velocity. Further work is required to analyse full-scale and experimental data to confirm that such upward flows do in fact exist. Fig. 9.8C and D shows further ballast flight trajectories for different train speeds and different ballast sizes for an initial vertical velocity of 1 m/s. Unsurprisingly, the ballast trajectories are longer for higher train speeds and smaller ballast stone sizes. In physical terms, the ballast is extracting energy from the flow beneath the train.

This analysis also allows one to calculate the energy in the stones at the end of the trajectory and the angle of impact. For the cases shown in Fig. 9.8, the ballast stone kinetic energy at impact is of the order of 10 J, with impact angles of between 20 and 40 degrees. These values will be used in considering the ballast impact issue in the next section.

From the above consideration of ballast flight, perhaps the most important point to emerge from the analysis is that a vertical flow in the underbody gap is required to lift the ballast particles into the high-velocity areas near the train and to impart significant kinetic energy. This suggests that care should be taken to ensure that such regions of flow are minimised, particularly concentrating on the bogie cavity region where the work of Zhu and Hu (2017) show large vertical velocities.

9.5 Ballast stone impact and ejection

As noted in Section 6.1, some ballast flight incidents appear to be initiated by pieces of ice becoming detached from trains, hitting the ballast at speed

and ejecting a large number of ballast stones with considerable momentum (a ballast avalanche). These ballast stones themselves can impact either the train or the track and can cause further ballast movement, resulting in the worst case in a ballast avalanche. RTRI (2001) reports model results to measure ballast ejection and showed that lumps of ice of 2 kg in weight could cause ballast to be ejected to the height of the train underbody at collision speeds above 20 m/s, corresponding to impact kinetic energies of 400 J. The number of ejections that reached the underbody height naturally increased with the weight of the ice block and the speed of impact. Impact speeds between 20 and 50 m/s can be expected to be typical for ice falling from rapidly moving trains. Experiments and calculations carried out as part of the AOA project and reported in Kaltenbach et al. (2008) have indicated that flying ballast impact kinetic energies of the order of 10 J can cause other ballast stones to become dislodged after an impact. For higher impact energies of the order of 100–200 J, the experiments and calculations suggested that significant numbers of ballast stones could be dislodged and ejected from the bed. Such impact energies can be reached by ballast stones that are lifted high in the underbody gap. Thus 'ballast avalanches' might be caused by either (or both) ice falling from trains or by high-energy ballast particles themselves. Clearly the most fundamental way to avoid the issue of ice falling from trains is careful design to ensure that there are no suitable surfaces on which large quantities of ice can form. Some guidance on the nature of icing in bogie cavities is given in the extensive CFD investigation of Wang et al. (2018). If it is known that ice accretion is likely to occur on a specific train in certain conditions, then the appropriate way of ensuring that a ballast avalanche is not initiated when ice falls is to reduce the speed of the train in such conditions. This is in fact the method used in Switzerland, Germany and France (RSSB, 2016a).

9.6 Train authorisation and infrastructure operation

The aim of much of the work described in this chapter has been to develop methods that will allow for the development of a methodology for the authorisation of new trains and give information to infrastructure operators on the likelihood of ballast flight incidents. The split of the TSIs between rolling stock and infrastructure responsibilities is a particular issue for the study of ballast flight, which of course depends on both train and track characteristics. There would appear to be two different methodologies that are being considered.

- The measurement of velocities beneath the train over a section of track where a smooth sheet had been laid for around 100 m (to eliminate the localised effect of the ballast roughness itself, as proposed in the AeroTRAIN project (Sima et al., 2011). This methodology implicitly gives a measure of shear above the ballast bed.
- The use of a standard physical element on the track over which pressures are measured as the train passes over. Sanz-Andres and Navarro-Medina (2010) and Navarro-Medina et al. (2015) propose the use of a hemispherical cylinder for such purposes. The technique involves the identification of pressure 'impulses' and integrates in some way the effects of both horizontal and vertical aerodynamic forces.

The first of these methodologies more readily relates to the analysis of previous sections, as values of C_{uxo} are directly measured. Current discussions are focused on how best to use these data – either through the use of the ensemble-averaged value of the square of the normalised velocity $C_{ux2} = (u_x/v)^2$ (either the average value or some sort of peak value) or though the use of a temporally and spatially integrated version of this parameter, somewhat misleadingly referred to as the 'power' of the flow (Saussine et al., 2015). In effect, both are surrogates of the shear stress at the bed, which is more difficult to measure, as either an analysis of the fluctuating components of velocity to obtain the Reynolds stresses or the measurement of a velocity profiles would be required.

A limit value for the parameter C_{ux2}, in whatever form is chosen, which is suitable for train authorisation purposes, is yet to be derived. Also, how this parameter can be used to take account of different track formations is still under discussion. Saussine et al. (2015) propose a methodology where the probability distribution of the 'power' under a particular train can be derived, which is then convoluted with the probability distribution of the strength of the track, with a correlation between 'power' and the number of grain movements. Another possible way to address this issue would be to fit experimental velocity data to the formulation of Garcia et al. (2011) outlined in Section 9.1 to determine the roughnesses of both the experimental track surface and the train and then using this formulation to predict the near track velocities for other track configurations. More work is required in this area.

Full-scale tests of the type required by the proposed methodologies are expensive and time-consuming and are affected by uncontrollable environmental conditions. It would be convenient if such tests could be carried out at model scale or using computational methods. Ido et al. (2008, 2013) describe a methodology that involves propelling a 1/8th-scale model train

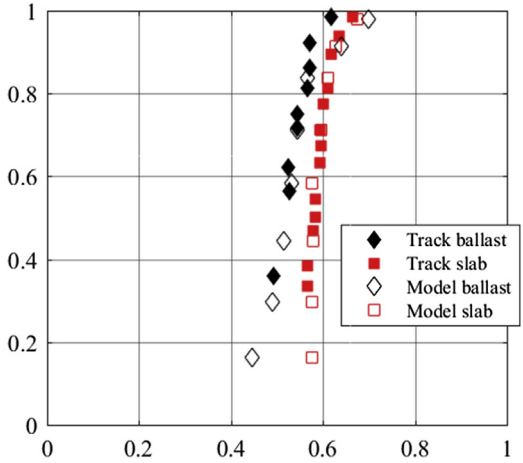

Figure 9.9 Velocity measurements for full-scale track tests and towing wind tunnel tests for ballast and slab track. *(Data from investigation of Ido et al. (2013).)*

over a ground plane using a car behind a train with various track simulations through what they describe as a towing wind tunnel facility. Clearly this replicates the full-scale situation and the velocity measurements made using probes mounted on the vehicle are similar in form and magnitude to those measured in the same way in the full-scale situation – see Fig. 9.9. Soper et al. (2018) measured the flow beneath a 1/25th-scale model of the Class 373 Eurostar train on a moving model rig. To enable this to be done, the model had to be mounted upside down on the rig and fired beneath a simulated ground plane (Fig. 9.10). Measurements were made of the velocity

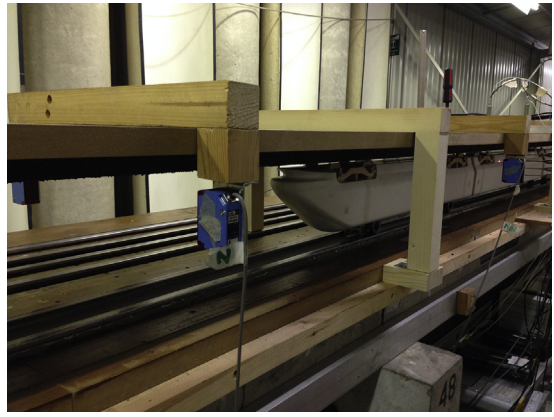

Figure 9.10 Underbody flow measurements on Class 373 Eurostar on a moving model.

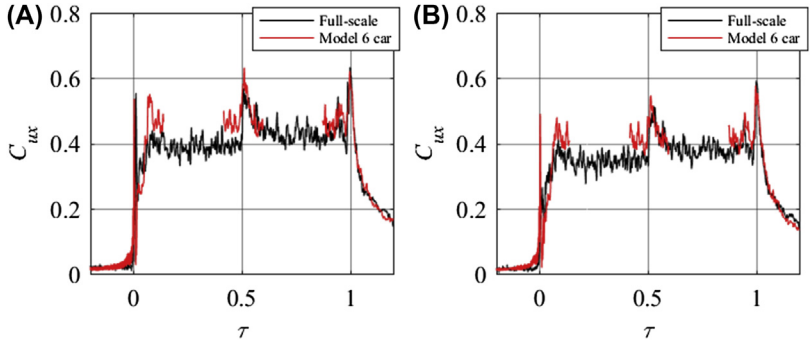

Figure 9.11 ***Results of underbody flow measurements on Class 373 Eurostar on a moving model.*** (A) 0.05 m above TOR, 0 m from COT, (B) −0.02 m above TOR, 1.085 m from COT. *(Data from investigation of Soper et al. (2018).)*

using Cobra probes, and a 20 run ensemble of the data was constructed and compared with equivalent full-scale measurements. The results are shown in Fig. 9.11. It can be seen that the level of agreement between the two sets of data is very encouraging and suggests that this methodology might be useful in determining the parameter C_{uxo}. More work is needed, however, to look at the turbulent properties of the flow in such situations.

In principle, CFD calculations also look to be a useful methodology for calculating the underbody flow field, thus arriving at a value of the parameter C_{uxo}. Such calculations can also give details of the flow that it is difficult to measure at full scale or on physical models — such as the flow around bogies where experimental data suggest that there may be an increase in velocities. However, there are significant difficulties in specifying the extent of the mesh — should flows around all the train be calculated, with significant resource costs, or just flows underneath the train, and if the latter, what boundary conditions should be applied. Also, the specification of the ground is not straightforward — should individual sleepers be modelled or a more generalised roughness (Paz et al., 2017). Difficulties such as these have meant that CFD calculations of the underbody flow field are not as far advanced as might be expected — for example, the CFD calculations presented in Soper et al. (2018) do not match the full-scale data and the physical model tests.

CHAPTER 10

Aerodynamic effects on pantographs and overhead wire systems

10.1 Background

Electrically powered trains collect current for traction and ancillary services either, from a third rail using a collector shoe mounted on the bogie or from an overhead wire. The former method presents no significant aerodynamic problem and will not be considered further. In the second method, the current from an overhead wire is picked up using a pantograph, an electrical contact mechanism supported above the train. The pantograph was invented in the late 19th century and replaced the simpler trolley pole for the transfer of current from the overhead wire to the train, as it permits higher vehicle speeds. Such overhead line equipment (OLE) systems can either provide DC power (with a range of different voltages) or AC power (with a range of different voltages and frequencies). Clearly such systems are susceptible to a range of different aerodynamic effects. The overhead wire itself is subject to the effects of the natural wind and also potentially to a range of aerodynamic instabilities. Pantographs are exposed to the general flow over the roof of the train and experience drag forces, which add to the overall train drag; side forces, which can cause lateral displacements; and lift forces, which can either increase or decrease the contact force between the pantograph and the overhead wire. In extreme cases, the differential displacements between the overhead wire due to crosswind effects, and the pantograph due to train and pantograph displacement, can result in the phenomenon known as dewirement, where the overhead wire can get trapped beneath the pantograph resulting in major damage to the OLE system.

Section 10.2 gives a general description of the overhead current collection system. The aerodynamic issues associated with overhead line

Train aerodynamics
ISBN 978-0-12-813310-1
https://doi.org/10.1016/B978-0-12-813310-1.00010-1

systems are then described in Section 10.3, and the issues with the pantograph are set out in Section 10.4. Section 10.5 describes methods for optimising the aerodynamic forces that act on pantographs to ensure good current collection. Finally, in Section 10.6, pantograph dewirement issues are discussed.

10.2 Description of the overhead current collection system

Before looking at the aerodynamic aspects of the overhead wire and the pantograph, we provide here a brief description to explain the terminology and functions of some components of the OLE. This specifically describes the usage in Great Britain but has a fairly general validity (Network Rail, 2015). Fig. 10.1 shows a typical system. This consists primarily of the contact wire, which carries the current that is supplied to the train by direct contact with the pantograph; the catenary wire, which supports the contact wire; and masts alongside the tracks or frames across the tracks that support the wires and OLE components. The contact wire is a copper extrusion which has grooves formed into the sides of the wire for clips.

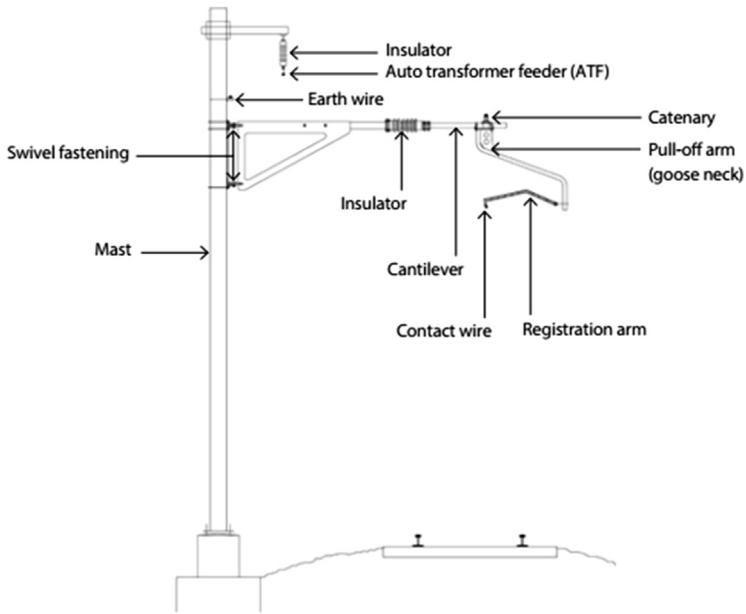

Figure 10.1 Example overhead line equipment mast, cantilever and associate components. *(Used with Permission of Network Rail.)*

These fit into dropper wires that hang from the catenary wire and support the contact wire. Both the catenary and contact wires are tensioned between supporting structures to ensure that the movements due to crosswinds or temperature variations of the contact wire are minimised. On high-speed routes, autotensioning equipment is used to apply loads of typically between 9 and 20 kN (8.9 and 13.2 kN in GB) along the wires over lengths of up to 1500 m. Support structures are normally spaced about 50 m apart, but the spacing can typically vary to give span lengths between 10 and 75 m.

At the top of the pantograph, there are usually two graphite strips (the 'carbons'), which provide the contact surfaces with the contact wire. The carbons provide good electrical conduct and conductivity, as well as lubricating the contact wire interface. However, a carbon is brittle and can become chipped and will wear down during operation. To ensure even wear of the pantograph carbons, the contact wire is designed to take a zigzag path along the centreline of the track. Registration arms and pull-off arms set the horizontal position of the contact wire to achieve the correct lateral deviation or stagger. The mean contact wire height varies between about 5.0 and 5.75 m (4.2—5.94 m in GB), but it varies with line speed and vehicle gauge and at tunnels, bridges and level crossings, where safe electrical clearance to passing road vehicles is needed.

The pantograph is mounted on the top of a train vehicle and thus moves with the dynamic lateral motion of the train caused by the movement of the train on the rails, track roughness and irregularities, train speed, cant deficiency and the corresponding response of the upper body train mass on the secondary suspension. A further influence is that of unsteady crosswinds introducing additional dynamic movements of the vehicle. The lateral movement of the pantograph head is further increased when the contact wire is at higher heights. An additional, but secondary, effect on the movement of the pantograph head is caused by the lateral flexibility of the pantograph itself. Collectively, these movements of the pantograph are referred to as pantograph sway.

The OLE fixed infrastructure itself is vulnerable to pantograph sway, as it forms an interface with the train pantograph. Pantograph sway affects two aspects at the interface:

- Intentional contact — the contact wire needs to remain in contact with the pantograph to supply traction current. If the contact wire deviates too far laterally from the pantograph centre, the vertical contact force may displace the contact wire further, allowing the pantograph to rise without restraint causing major damage to the train or the OLE.

- Essential clearance – mechanical clearance must be retained between the swaying pantograph and parts of the OLE fixed infrastructure at a common electrical potential; electrical clearance must be retained between the swayed pantograph and parts of the OLE-fixed infrastructure, or adjacent civil infrastructure, at earthed potential or isolated.

To demonstrate both interface aspects are achieved, dewirement risk and gauge clearances have to be considered.

10.3 Aerodynamic issues of the overhead wire

10.3.1 Self-induced forces and displacements

The contact wire is a cable hanging under its own weight, albeit with support from the catenary and droppers, and therefore hangs in a classic catenary shape. The shape of the unsupported catenary is given by the following equation

$$Z_W = \frac{T_W}{w}\left[\cosh\left(\frac{wX_W}{T_W}\right) - \cosh\left(-\frac{wL_W}{2T_W}\right)\right] \tag{10.1}$$

where Z_W is the height relative to the span end points, X_W is the longitudinal distance into the span, T_W is the wire tension, w is the contact wire weight per unit length and L_W is the span wire length. Fig. 10.2 shows a typical catenary shape. The height difference between the ends and the centre is known as the sag of the wire.

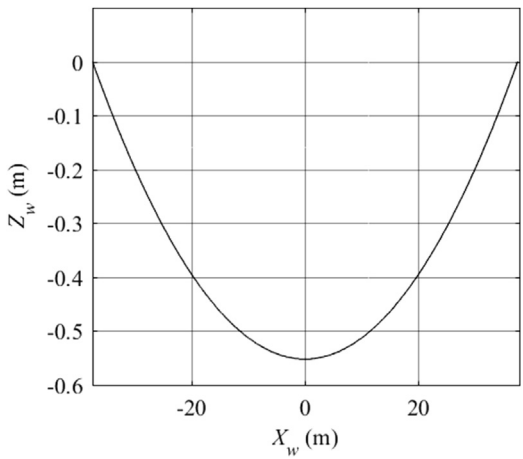

Figure 10.2 Typical catenary shape of the contact wire. ($T_W = 11.9$ kN, $w = 9.34$ N/m, $L_W = 75$ m).

10.3.2 Wind effects

As the wire hangs in a catenary shape, lateral loads generated by the wind will displace the wire laterally, reducing the sag, and will change the relative position of the wire and the pantograph. Traditionally, the OLE design has accounted for the effect of wind displacement and maximum stagger with tolerance/allowance budgets. Those for GB railways are shown in Fig. 10.3, where two positions are considered; midspan and at the fixed support points, e.g., at the registration arm. In Fig. 10.3, the worst case at midspan is considered when the vehicle sways into the wind away from the contact wire displaced in the direction of the wind. At support and registration points, the worst case is considered as when the vehicle sways with the wind away from these points. The aim of the budget is to ensure that the contact wire does not move further from the pantograph centreline

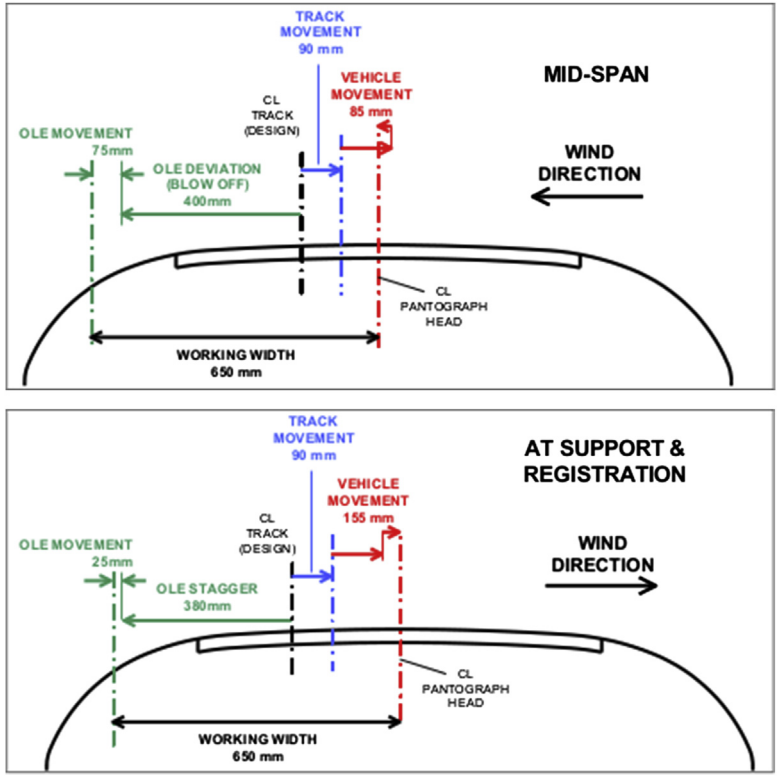

Figure 10.3 Current GB overhead line equipment (OLE) buildup of maximum deviation and maximum stagger.

than the working width of the pantograph (650 mm). Various tolerances also considered are as follows:

- Movement of the centreline of the track from its nominal value due to track shifting within maintenance tolerances;
- Dynamic movements of the vehicle including wind loading;
- Movement of the wires due to wind loading on masts;
- Design contact wire stagger and midspan offsets.

Consideration of these movements at midspan shows the maximum allowable deviation due to wind, termed blow off, to be 400 mm. (Note that any designed stagger effect or midspan offsets will reduce this value.) At the fixed points, the value of maximum stagger is calculated to be 380 mm.

Now, standard thin wire theory gives the maximum lateral displacement of the contact wire, Y_W, under wind loading as

$$Y_W = \frac{\left(\frac{1}{2}\varrho d_W u(90)^2 C_{DW}\right) L_W{}^2}{8T_W} \tag{10.2}$$

where ϱ is the air density, d_W is the contact wire diameter, C_{DW} is the contact wire aerodynamic drag coefficient and $u(90)$ is the wind speed at right angles to the wire. The bracketed term represents the along-wind aerodynamic drag force acting on the contact wire. A more complex formula can be derived (e.g., Cooper, 1975), which takes into consideration the interaction with the droppers and the catenary wire. However, it has been found that the additional effect of including the interaction does not generate enough of a difference to be included, when considered against the uncertainty in estimating a suitable local wind speed to use. Note that this formula does not give an averaging time for this wind speed, but it must represent a gust that lasts long enough for the deflection to fully establish itself. Neither does this take into account the lack of lateral correlation of the wind along the span. More recently, Song et al. (2018) use a nonlinear finite element model of the catenary wire, the contact wire and droppers to calculate the galloping responses of the overhead system to a stochastic wind for different wire tensions (Section 10.3.3).

If the stagger effect and midspan offset are known for a given span, then the blow off due to wind, Y_W, can be calculated as outlined above. Rearranging Eq. (10.2) then allows the span length, L_W, to be calculated. This is the process used to design OLE span lengths, when the base wind speed is chosen to be an extreme wind speed (for example, the once in

50 years return period of a gust with a suitable averaging time), modified by allowing for local wind factors to allow for different upstream roughnesses or topography.

10.3.3 Galloping instabilities

Cables in crosswinds are known to suffer from a range of instabilities, the most important of which is known as galloping. When a cable moves in the wind, its motion is damped by both mechanical damping due to its supports, self-weight and cable tension and aerodynamic damping due to the motion-induced aerodynamic velocities and forces. Galloping occurs when the displacement of a cable by wind forces leads to a change in shape or orientation and a change in aerodynamic forces, which results in a negative aerodynamic damping of a sufficient magnitude that the overall damping is reduced to zero. Very large amplitude oscillations can result. This particularly affects those cables which are asymmetric about one or more axes and is commonly observed on power transmission lines, bridge cables, etc. Indeed, the change of shape of cables caused by rivulets of rainwater and by ice accretion has been known to initiate major galloping episodes (Demartino and Ricciardelli, 2015). Typical contact wire cross sections for overhead wires are shown in Fig. 10.4, and they can be seen to be asymmetric about the horizontal axis. Furthermore, the shape of the contact wire is known to change due to wear to the bottom of the wire caused by the passage of pantographs and also during winter conditions by ice accretion, which can (temporarily) significantly change the cross-sectional shape. Thus, it can reasonably be concluded that overhead wires might, under certain circumstances, undergo galloping oscillations.

For galloping to occur, it can be shown that (Stickland and Scanlon, 2001; Song et al., 2018)

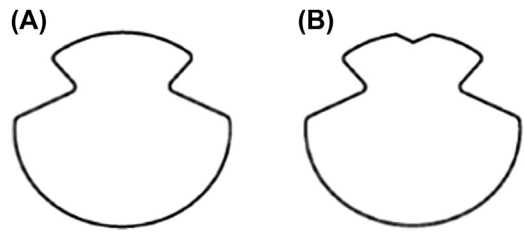

Figure 10.4 ***Typical cross sections of contact wires.*** (A) Standard with side grooves; (B) standard with top and side grooves.

$$\frac{dC_{LW}}{d\varepsilon} + C_{DW} < 0 \tag{10.3}$$

and u_G, the critical galloping velocity, is given by

$$\frac{u_G}{2\pi n_n d_W} > -\frac{2Sc}{\frac{dC_{LW}}{d\varepsilon} + C_{DW}} \tag{10.4}$$

In these equations, n_W is the natural frequency of the cable; d_W is the cable diameter; Sc is the Scruton number given by $2\xi_W m_W / \rho d_W^2$; ξ_W is the mechanical damping ratio and m_W is the cable mass per unit length. C_{DW} is the wire aerodynamic drag coefficient; C_{LW} is the wire aerodynamic lift coefficient and ε is the incident wind angle on the cable. The force coefficients are defined as

$$C_{DW} = \frac{F_D}{\left(\frac{1}{2}\varrho L_W d_W u^2(\varepsilon)\right)} \quad C_{LW} = \frac{F_L}{\left(\frac{1}{2}\varrho L_W d_W u^2(\varepsilon)\right)} \tag{10.5}$$

where F_D is the drag and F_L is the lift force; L_W is the wire length and $u(\varepsilon)$ is the wind speed at an incident angle of ε (Fig. 10.5).

Thus, if $\frac{dC_{LW}}{d\varepsilon} + C_{DW} < 0$, the cable will be stable below a critical velocity that is dependent on the mechanical properties of the cable and galloping will occur above that velocity. If this parameter is greater than zero, the cable will always be stable. This implies that there needs to be a negative slope for the C_{LW} versus ε curve for galloping to occur, as C_{DW} will always be positive. (It should be noted that the incident wind angle on the contact wire will be generated by the upward and downward movements of the wire, as well as rotation of the wire due to the restraints of the droppers and catenary, even if the natural wind is perfectly parallel to the ground).

The drag and lift coefficients required for an assessment of galloping are generally determined in wind tunnel tests, although Song et al. (2018) used

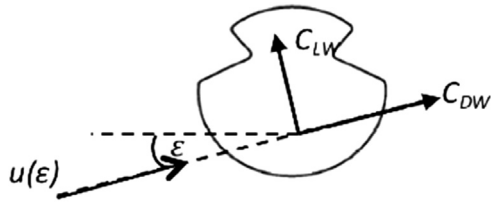

Figure 10.5 Definition sketch for the force coefficients on a contact wire.

Large Eddy Simulation CFD calculations to determine the aerodynamic coefficients of a contact wire with varying degrees of wear. An early series of such wind tunnel tests was carried out following an incident of major overhead oscillations on the West Coast Main Line in the north of England in the early 1970s (Gilchrist et al., 1974) to measure lift and drag forces on sections of contact wire and the catenary. These are reported in Cooper (1975). Measurements were made with varying wind tunnel speed (hence varying Reynolds number) and varying the turbulence level between 1% and 10%. Fig. 10.6 shows typical results of the measured drag and lift coefficients. The variation with incident angle is shown for a fixed wind speed and a turbulence level of 1%. There was little variation with Reynolds number or with turbulence intensity up to a value of 10% (Gawthorpe, 1978a). It can be seen that there is a negative slope to the lift coefficient term for incident wind angles between −5 and +10 degrees. However, the calculated values of $\frac{dC_{LW}}{d\varepsilon} + C_{DW}$ are generally slightly positive and thus galloping would not be expected to occur.

Stickland and Scanlon (2001) describe a further wind tunnel test to measure aerodynamic characteristics of catenary wires. A 1:10 scale model of a section of contact wire was mounted between two end plates, which minimised end effects, in a low-turbulence wind tunnel and an underfloor balance was used to measure lift and drag forces and the pitching moment. The maximum wind speed could be set to about 50 m/s and turbulence levels were typically 1%. Variation of the wind angle of incidence was

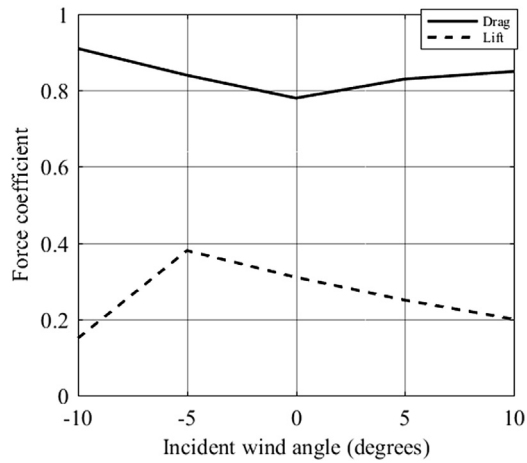

Figure 10.6 Variation of contact wire drag and lift coefficients from Cooper (1975). $V_w = 36.6$ m/s, $I = 1\%$.

accomplished by rotating the contact wire model. They undertook an experimental analysis of the aerodynamic characteristics of a range of contact wires having cross sections representing normal and worn conditions, as well as modified cross sections to investigate galloping. They found that large negative values of $\frac{dC_{LW}}{d\varepsilon} + C_{DW}$ only occurred over a narrow range of incident angles in some cases, but this range increased somewhat with contact wear. The galloping velocities that they calculated depended on the cable mechanical properties that they assumed. They noted that increasing wire tension was the most effective way of increasing mechanical damping and thus increasing the critical galloping wind velocity. This was also the conclusion of the work of Song et al. (2018). In a further paper, Liu et al. (2012) reviewed the effects of icing of railway contact wires in China. In particular, the work only looked at galloping caused by ice accretion on the contact wire, but the authors commented that 'galloping of the overhead contact wire caused by icing is rare'.

In view of the, albeit limited, evidence presented above, it seems that there is only a narrow set of favourable circumstances in which wire instability occurs and that wire galloping may not occur under most realistic railway scenarios, particularly on high-speed lines where catenary wire tensions are high. Other factors, such as of loss sag, may be the cause of large wire amplitudes.

10.4 Aerodynamic issues and testing of pantographs

10.4.1 Types of pantograph

There are a range of different designs of railway pantographs, but they broadly fall into two main types: single arm or multiple arms. Fig. 10.7 shows these generic types. Most pantographs are more usually of the single-arm type and this design will be considered herein. Fig. 10.8 shows the components of a typical pantograph — the Brecknell-Willis high-speed (single-arm) pantograph. The stowed position of the pantograph is shown in dotted outline in the side elevation.

10.4.2 Pantograph forces

As previously stated, the purpose of the pantograph is to transmit electrical energy from the contact wire to the train. To ensure good electrical contact with the contact wire, a constant static upward force is required. However, the total upward force has to be limited during running to ensure that the

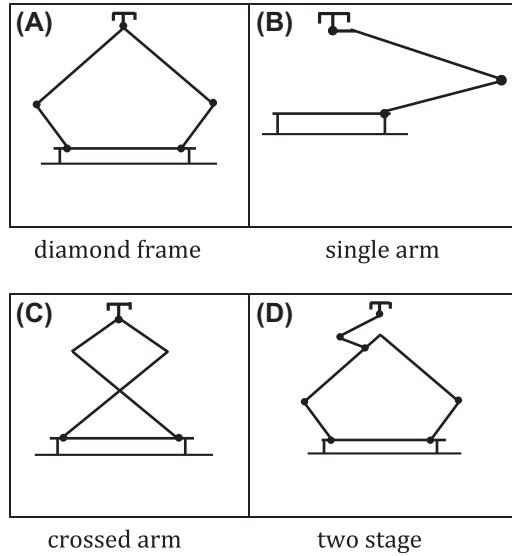

Figure 10.7 ***Generic types of pantographs.*** (A) Diamond frame; (B) single arm; (C) crossed arm and (D) two stage.

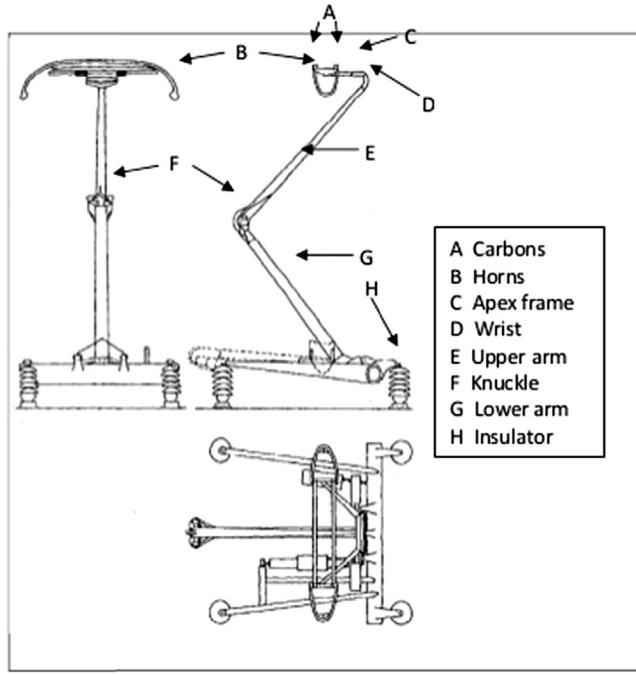

Figure 10.8 Components of the Brecknell-Willis high-speed pantograph. *(Harrison, D., 1998.)*

carbons and wires do not undergo excessive wear or that the upward force exceeds OLE design limits. On the other hand, it should not be reduced such that there is loss of contact with the wire leading to electrical arcing, which can cause damage to the carbons. Measuring the additional forces due to aerodynamic effects under different relative wind conditions is thus essential to ensure that the total force exerted on the contact wire remains within design limits. CEN (2012) gives limits for the maximum and minimum mean contact forces permissible in different European countries. For Great Britain, the range is 0−120 N, although British Rail used to apply the range 80−120 N for running in still air conditions (Harrison and Rigby, 1990).

The total force between the contact wire and the pantograph when running can be expressed as

$$F_{CWP} = F_{VSWP} + F_{VIWP} + F_{VAWP} \tag{10.6}$$

where F_{CWP} is the total contact force, F_{VSWP} is the static vertical force, F_{VIWP} is the dynamic inertial force due to pantograph vertical oscillations and F_{VAWP} is the aerodynamic force due to the relative wind acting on the pantograph. In common with other aerodynamic forces, F_{VAWP} varies with wind speed acting on it, in this case the relative wind speed created by the vector addition of the forward speed of the train and the crosswind speed.

Consideration of Fig. 10.8 shows that pantographs are aerodynamically complex mechanisms, having a complicated head, consisting of the apex frame, on which is mounted the carbon strips, and tubular, rectangular or elliptic sectioned upper and lower arms meeting at the knuckle. These are mounted on the roof frame and electrically insulated from the rest of the train. Further complications arise as the pantograph extends and retracts, changing height as it follows the contact wire height variations. In addition, it is expected to perform satisfactorily for both directions of travel of the vehicle on which it is mounted. These are referred to as the knuckle leading or knuckle trailing directions when related to the pantograph.

In addition to the factors mentioned above, the aerodynamic characteristics of pantographs are also affected by the train roof geometry, in particular the layout of the pantograph cutout region of the train roof, the position of the pantograph vehicle in the train and the speed and direction of the relative wind speed acting on them. Fig. 10.9 shows how the pantograph location, pantograph cutout length and roof equipment vary for

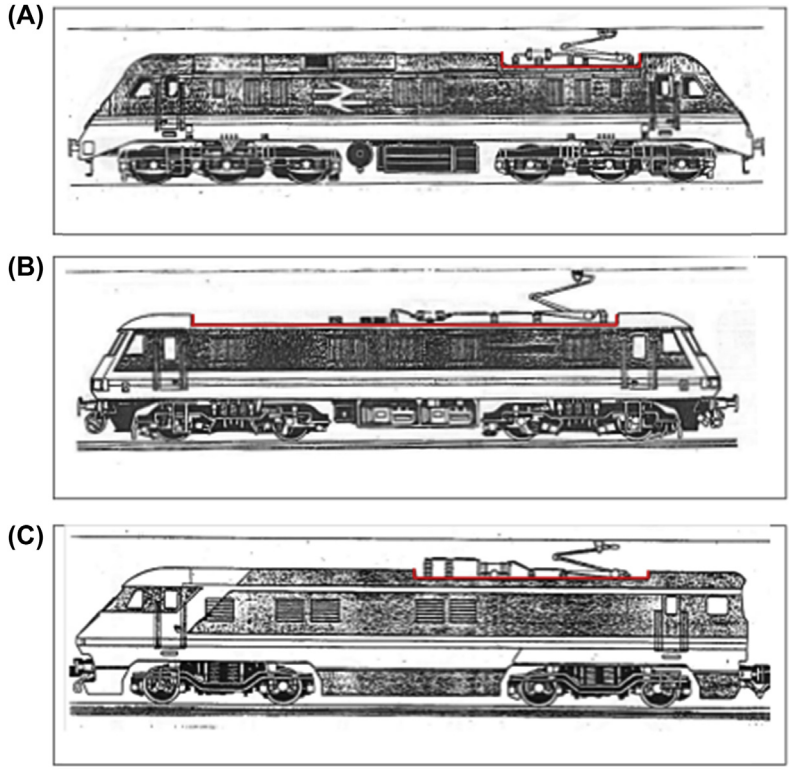

Figure 10.9 ***Roof cutouts on locomotives.*** (A) Class 89; (B) Class 90; (C) Class 91.

the British Class 89, Class 90 and Class 91 locomotives. (Note that the Class 91 operates in both directions and, in one, has the pantograph just behind a bluff-fronted locomotive nose). It is clear that such variations could have an effect on the longitudinal wind speeds along the locomotive roofs affecting different parts of the pantograph, when considering both the flow off the roof and into the cutout, as well as the boundary layer growth along the roof. Such effects will reduce when there is a crosswind, but other issues such as flow angularity will then play a part.

Due to this complexity of pantograph design, it is difficult to specify their aerodynamic characteristics *a priori*, and some sort of testing methodology is required to determine the aerodynamic characteristics of pantographs, most important of which are the aerodynamic lift and drag. The next three sections describe the use of wind tunnel testing, full-scale testing and CFD to obtain these parameters.

10.4.3 Wind tunnel tests on pantographs

In wind tunnel tests to investigate pantograph behaviour, it is usual for a full-scale pantograph, mounted on dummy insulators, to be used, which obviates potential problems with Reynolds number scaling of the smaller components of the pantograph and includes realistic bearing friction forces in the pantograph. However, there has been some pantograph testing using scaled models; for instance, Takaishi and Ikeda (2012) used a 1:3.15 scale model pantograph and Lee et al. (2015) used quarter-scale models. It is common practice to mount the assembly directly onto a rotatable turntable, set either into the wind tunnel floor or just above it to remove any boundary layer growth. However, it is also usual to mount the pantograph onto a deck, to at least partially model the local vehicle roof profile and the pantograph cutout region (see Fig. 10.10 for example). All sharp edges are faired to ensure a smooth and parallel flow over the pantograph. The length of the deck is limited by the requirements to ensure minimisation of downstream end effects and to permit rotation within the wind tunnel. The deck is also pivoted on its centreline to allow the pantograph to roll to simulate the effect of canted track or onset wind angle such as might be encountered on an embankment.

Pantograph uplift forces are measured using two strain-gauged load cells mounted on a supporting beam, which is in turn attached to the lower frame of the pantograph. These are connected via fixed-length retractable cords to each of the two carbon strip carriers on the pantograph head. This setup measures the total uplift forces on the pantograph due to the static uplift, applied throughout testing to raise the pantograph, and any aerodynamic uplift forces generated during testing.

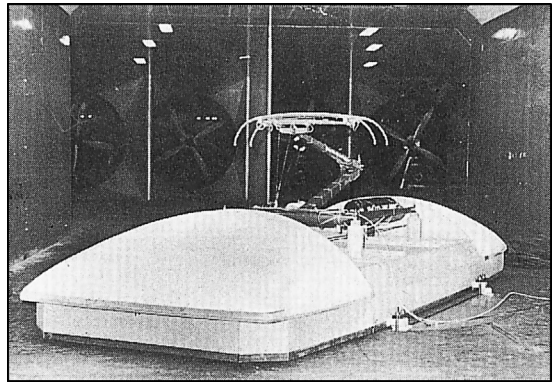

Figure 10.10 The Brecknell-Willis high-speed pantograph in a full-scale wind tunnel.

A drawback of wind tunnel testing is that the real train roof and pantograph cutout is not accurately modelled because of the space limitations in most wind tunnels. Additionally, atmospheric turbulence is not usually included in such testing and so real-life atmospheric turbulence is not simulated (although the turbulence intensity 'seen' by high-speed train pantographs will be much lower than in natural wind, due to the dominant effect of the forward movement of the train – see Section 3.2.3). Takaishi and Ikeda (2012) recognised this deficiency and proposed a method of simulating the boundary layer on the roof of a Shinkansen train, upstream of their model pantograph. They used triangular spires of two different sizes and an L-shaped angle to modify the boundary layer in a small-scale low-noise wind tunnel in tests to measure the noise generated by the pantograph. The wind tunnel profiles at the pantograph were compared with full-scale measurements. The L-shaped angle produced wind profiles closest to those measured at full scale. Although Reynolds number trends for the lift coefficient followed those observed at full scale (measured using the tethered head technique), the lift coefficients measured in the wind tunnel were generally lower than the full-scale values.

Strictly, with regard to the issue above, testing of pantographs in low-turbulence wind tunnels will only represent situations where the train is running in still air or in relatively small crosswinds. When considering high-speed trains, most wind tunnels will not be able to generate airflows of sufficient speed to simulate the relative wind speed past the pantograph, so there is the likelihood of Reynolds number effects affecting the results. On the other hand, such tests are useful, and sufficiently reliable, to investigate the trends of behaviour of uplift with yaw and wind angles, as well as for investigating the relative effect of pantograph component designs. It is generally held to be best practice when investigating pantograph aerodynamics to use both wind tunnel testing and full-scale tests to confirm results, with fine-tuning when necessary.

10.4.4 Full-scale testing of pantographs

Testing of a pantograph's aerodynamic characteristics in situ on a train appears, at first, to be a more realistic alternative to wind tunnel testing. This is because the pantograph will operate in the correct position on the train, thus ensuring a realistic onset airflow as conditioned by the upstream vehicles and pantograph cutout, and any crosswinds will contain the appropriate turbulence. However, there are significant drawbacks as the boundary conditions cannot be controlled, e.g., crosswinds will usually be

present (especially when unwanted!) and will vary due to the gusty nature of the wind and localised sheltering or embankments, and the pantograph height will vary with variations in the height of the contact wire, etc. In addition, there are inertial contributions to the uplift due to vehicle motions. However, these will be the conditions under which the pantograph will ultimately have to perform.

There are two methods of track testing: tethered head running or using an instrumented head. In the tethered head method, the pantograph is restrained by retractable cords, attached at the base to load cells, as in the wind tunnel test method above, and the total uplift can be determined by adding the load cell forces. The augmentation to aerodynamic uplift is derived by subtracting the static uplift from the measured (total) uplift. In this form of testing, the pantograph is restrained to run below the contact wire and so does not draw current.

Instrumented head tests are specified for the dynamic measurement of the total contact force exerted on the contact wire by the pantographs in CEN (2016a). They may also be used to determine the aerodynamic uplift. Put simply, optical load cells (to obviate problems with electromagnetic interference) are placed underneath the carbons (or under the complete collector strips) and measure the forces exerted between the carbons and the carbon carriers. Accelerometers, mounted near to the load cells, permit the determination of inertia forces on the mass of components between the load cells and the contact wire. This is required because the load cells do not measure the total contact force on the wire because of their location. Furthermore, any aerodynamic uplift caused by the components above the load cells will also not be measured. To accommodate the later, the method in CEN (2012) requires an aerodynamic correction to account for the deficiency. This can be determined by applying known uplifts to the pantograph in a bench test and correlating these to the outputs of the instrumented head. There is a danger that admittance effects may be missed if this determination is undertaken in a quasi-static way. Finally, the effect of the instrumentation itself will probably affect the aerodynamic characteristics of the pantograph and this too needs determination; CEN (2012) suggests using a tethered head test for this purpose and measuring uplifts with and without the instrumentation fitted.

Nevertheless, the use of such an instrumented head means that with a certain amount of work, the aerodynamic uplift can be determined, again by subtracting the static uplift from the total derived contact force. However, the tethered head method is more straightforward if all pantograph working heights can be catered for.

10.4.5 CFD modelling of pantographs

The use of CFD for the prediction of pantograph aerodynamic force has not, until recently, been a practical tool for the rail industry to use. As has been noted in previous sections, the different shapes of the pantograph components, some bluff and some streamlined, and the orientations of these present a significant challenge for CFD methods. When considered in the context of the whole train, or part train if the pantograph on a leading vehicle is considered, there are significant meshing issues to resolve to ensure the appropriate resolution of the mesh in regions where strong flow gradients are expected. These aspects imply computational domains requiring very many cells. A further aspect is the adequacy of single-turbulence models to accurately replicate the differing flow regimes that occur. However, CFD is increasingly used for general train aerodynamics predictions in the rail industry, particularly by train manufacturers, as the power and costs of computers have fallen and the use of parallelisation in solving has increased. Thus, in the last few years, a number of studies have been published of the aerodynamics of whole pantographs. Carnevale et al. (2017) provide a good review of the use of CFD for this purpose. Li et al. (2018b) used the delayed detached eddy simulation approach to simulate the unsteady aerodynamic performance of a high-speed train pantograph in crosswinds at yaw angles of 0−30 degrees to determine how yaw angle influences the aerodynamic forces and the wake behind the pantograph. Once validated against full-scale measurements, CFD offers a much more granular way to analyse the aerodynamic forces on pantographs with, in particular, the ability to determine how different components contribute to the lift or drag force budgets, an ability that the measurement methods cannot generally deliver. This ability of CFD is potentially very helpful to manufacturers designing new pantographs or refining existing designs.

As noted above when testing pantographs in wind tunnels, the pantograph is a mechanism such that the total uplift exerted on the contact wire is the result of the aerodynamic uplift and any bearing friction forces present. It is therefore possible that aerodynamic uplift predicted by CFD will be greater than that actually generated by a particular pantograph.

10.5 Pantograph aerodynamic force optimisation

10.5.1 Lift force

In common with many other aerodynamic phenomena, pantograph aerodynamic forces vary with the square of the relative wind speed acting

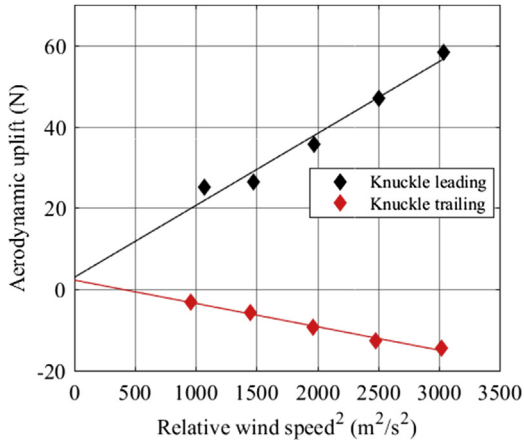

Figure 10.11 The variation of a single-arm Schunk pantograph aerodynamic uplift with relative wind speed. *(Data from Carnevale et al. (2017). Copyright Elsevier.)*

on the pantograph, as is shown for the aerodynamic lift force in Fig. 10.11. It has long been known that, for most pantograph designs, the majority of the lift is generated by the pantograph head (Peacock, 1967). Pimputkar (1971) suggests, based on previous research from France, Russia and Britain, that 80% of the aerodynamic lift force is generated by the head with only 20% coming from the frame.

The ideal pantograph would have aerodynamic lift that is neutral with increasing train speed and also in each direction of running if the pantograph is asymmetric, as is the single-arm pantograph. Historically, there have been a large number of studies and measurements of aerodynamic lift and the effect of different pantograph component design on lift. One of the complicating factors is that apparently small design changes can cause significant effects on lift. For instance, Fig. 10.12 shows work undertaken in France in the 1950s and reported in Pimputkar (1971) on the impact of design variations to the carbon strip holders (shown in cross section on the right) on pantograph lift force.

Other aspects that are of concern when considering pantograph lift are the effects of varying yaw angle, as obviously the natural wind can act at any angle to the direction of track, and also the roll angle of wind acting on pantographs, which can occur as a result of train pantograph vehicles running on canted track and flow angularity due to steep, high embankments. A final issue that affects lift is the height of the pantograph (as the constituent parts of the pantograph will be at different angles to the

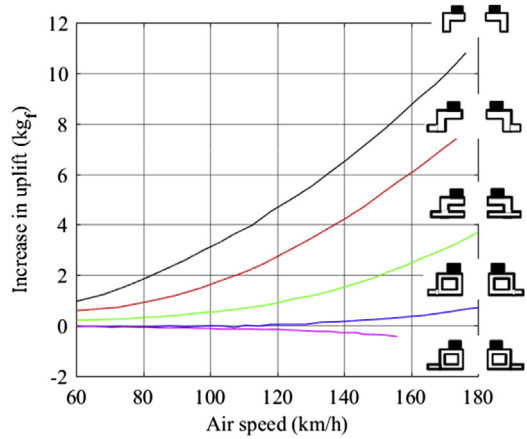

Figure 10.12 Relative increase in pantograph uplift for different carbon holder designs. *(Data from Pimputkar (1971).)*

onset relative wind), but this has not been widely studied in any detail. However, see Coxon (1981) for details of some full-scale tests and Harrison (1988) for descriptions of wind tunnel tests investigating this aspect.

Fig. 10.13 shows wind tunnel measurements of the variation of aerodynamic lift coefficient (based on an area of 10 m^2) for a resultant air speed of 30 m/s for the Faiveley single-arm AMBR pantograph as reported by Rigby and Gawthorpe (1979). Measurements were made for the full range

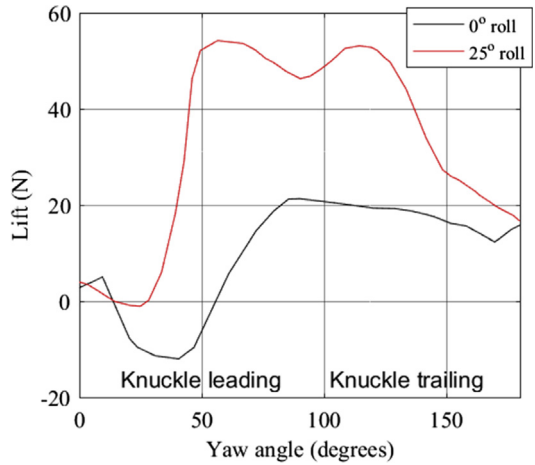

Figure 10.13 Lift coefficient variations for the AMBR one pantograph at 0 and 25 degrees roll angles. *(Data from Rigby and Gawthorpe (1979).)*

of yaw angles, with the angle 0 degree representing the flow along the train longitudinal axis with the pantograph knuckle leading and 180 degrees representing the flow along the train longitudinal axis with the pantograph knuckle trailing. Two roll angles were also tested: 0 degree representing a horizontal resultant onset wind acting on the pantograph and 25 degrees representing an extreme combination of canted track and a steep embankment. It can be noted that the lift behaviour is quite different in the knuckle leading and knuckle trailing directions of operation and that roll angle has a strong effect, increasing the lift values.

Fig. 10.14 shows the variation of the aerodynamic lift for the AMBR pantograph in both the knuckle leading and trailing directions as a function of train speed with no crosswind. Although the uplifts are relatively small, there is still a difference in lift depending on the pantograph direction and it can be seen that the behaviour is quite different from that of the Schunk pantograph shown in Fig. 10.11.

These asymmetries in the behaviour of aerodynamic lift, depending on pantograph travelling direction and increasing with train and crosswind speeds, have driven the search to determine which components of pantographs affect the lift and how, as exemplified in Fig. 10.12, in particular the search to correct for the directional lift asymmetry.

During the development of the British Rail/Brecknell-Willis high-speed pantograph in the 1970s and 1980s, a great deal of work was undertaken to overcome the asymmetrical aerodynamic lift behaviour. Coxon (1981) describes the chronology of the development of this pantograph and the tests undertaken. Of particular interest was the use of aerofoils fixed to the apex

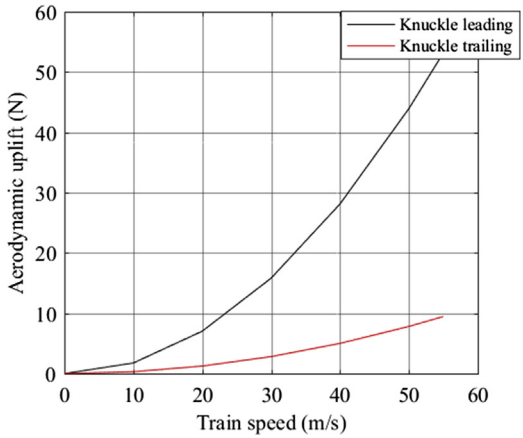

Figure 10.14 Variation of the aerodynamic lift force for the AMBR pantograph.

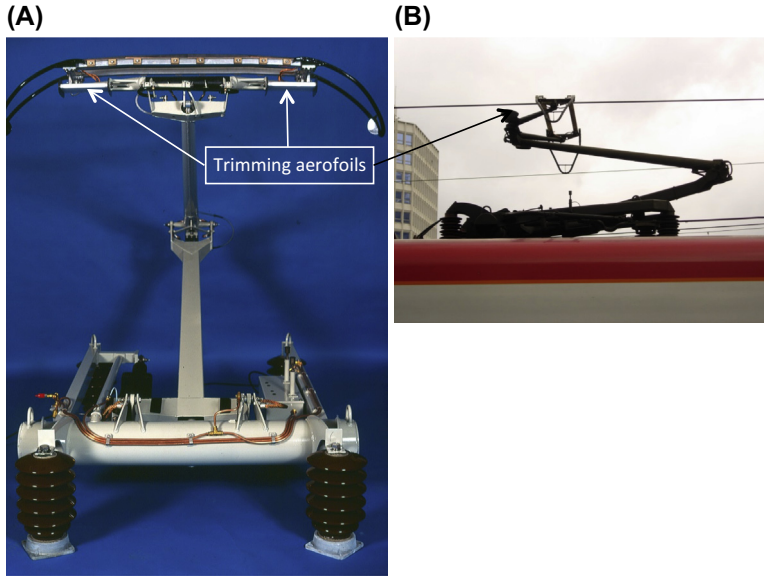

Figure 10.15 ***Views of the Class 390 pantograph fitted with apex frame aerofoils.*** (A) Front view; (B) mounted on class 390. *(Used with permission from Brecknell-Willis.)*

frame to try to balance the values of aerodynamic lift in each direction of travel. These aerofoils are still used on Brecknell-Willis pantographs, as can be seen in Fig. 10.15, which shows the pantograph fitted to the Class 390. To improve their efficiency, they are fitted with end plates, which can be observed in Fig. 10.15A.

Other approaches used to improve the uplift performance of the British Rail/Brecknell-Willis pantograph using wind tunnel testing are described in Harrison (1988). Geometric changes included fairing various parts of the pantograph frame, altering the pantograph head by changing the carbon strip spacing, changing the number of fitted carbon strips and filling in the space between the strips. These variations were expected to change the aerodynamic characteristic of the pantograph, although it was realised that some of them would not be practical to apply to a service pantograph. Indeed, some of the changes made uplift performance worse, but nevertheless indicated important trends. An attempt was also made to improve performance for the pantograph operating at maximum wire height by fitting an auxiliary aerofoil fixed to the pantograph upper arm. In general, no single modification produced large improvements in lift performance over the full range of possible operating conditions, although the use of fairings and the auxiliary aerofoil showed some promise. Fig. 10.16 shows

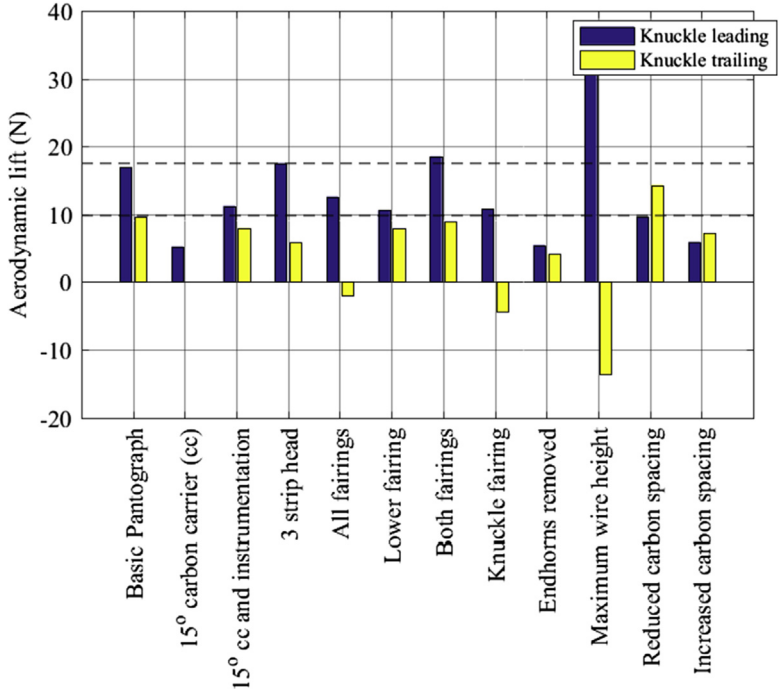

Figure 10.16 Effect of pantograph component modifications on aerodynamic lift. *(Data from Harrison (1988).)*

an example of the impact of the component modifications on the aerodynamic uplift. (The horizontal lines show the uplift in the knuckle leading and trailing positions for the unmodified pantograph.)

The use of aerofoils to adjust the asymmetric lift performance of a pantograph does, however, lead to a difficulty ensuring that the aerofoil angle is chosen optimally. Harrison and Rigby (1990) describe full-scale tests undertaken on the Classes 89, 90 and 91 locomotives (see Fig. 10.9), using the tethered head method for measurement of aerodynamic lift. All the locomotives could provide propulsion to trains with the pantograph knuckle leading or trailing. The Class 89 only operated in hauling mode, whilst the other two locomotives operated in hauling and propelling modes. Furthermore, the Class 91 has a streamlined and a bluff end. This made for a complex series of tests involving setting the aerofoils at 5, 10 and 15 degrees and testing under all possible operating modes. It can be seen that the airflow approaching the pantographs in all the different modes can be modified by the length of train and pantograph cutout upstream. The results showed that the compromise optimum aerofoil angles were about 10, 8 and

10 degrees for the Class 89, 90 and 91 locomotives, respectively. Under certain combinations of operating conditions, uplift limits could be exceeded for these choices, and no lift characteristic was neutral with train.

A different approach to correct for lift asymmetry of single-arm pantographs was taken by the Central Japan Railway Company when developing the Series N700 Shinkansen train, see Nakamura et al. (2011). A major concern for high-speed Japanese trains is aeroacoustic noise, one significant source of which had been found to be the pantographs. The proposed noise-reducing design of the N700 pantograph, which was based on Series 700 pantograph, included a fairing over the lower arm of the pantograph. The separate contributions of the pantograph head and the lower and upper pantograph arms were determined by wind tunnel testing for the original Series 700 pantograph and the N700 pantograph. This showed that the lift forces on the arms of Series 700 pantograph broadly cancelled each other, leaving just the lift on the head. (The lift forces in the knuckle leading and trailing cases were neither negligible nor equal, but were presumably within acceptable limits.) However, the lower arm fairing on the N700 pantograph led to a significant increase in lift asymmetry in the two running directions. The use of an aerofoil on the head was ruled out as this would have increased the pantograph aeroacoustic noise. The solution proposed was to increase the tilt angle of the head, which introduced a drag force on the head with an additional component of lift.

In general, these studies of lift force have been undertaken in wind tunnels or full-scale tests, but more recently CFD studies have increasingly been used. Carnevale et al. (2016) and Carnevale et al. (2017) used CFD to investigate the total pantograph uplift and contributions to uplift of different pantograph components. Using wind tunnel measurements of uplift from a full-scale single-arm Schunk pantograph, the same pantograph with an upstream wind shield and the pantograph with an instrumented head, they validated their CFD model in the knuckle leading and knuckle trailing directions. The method used was RANS simulation with the k-ω SST model for turbulence, and the domain was divided into 20 million cells. The agreement between the wind tunnel measurements and the CFD predictions was generally excellent. A full train CFD model, using 40 million cells, was used to compare with full-scale track measurements of the uplift of the instrumented head pantograph. Comparing the uplift measurements and predictions showed that the CFD performed well. Some notable differences were observed between the wind tunnel results and the track tests in the uplift behaviour in the knuckle leading direction, which was ascribed to the

development of the train boundary layer and effects of upstream roof recesses.

Zhang et al. (2017) also used CFD to simulate uplift on the CX-PG pantographs of an eight-car train model of 200 m length at full scale. The domain comprised 33 million cells and they also used a RANS simulation with the k-ω SST turbulence model. Simulations were made for the knuckle leading and trailing directions with the pantograph at the front and rear of the second and seventh train vehicles. Not surprisingly, the pantograph uplift is significantly higher when the pantograph is nearest the front of the train.

When specifying the required uplift performance of pantographs, it might seem appropriate to consider using the maximum train speed in conjunction with some allowance for a particular headwind speed. However, when trains enter tunnels, there can be a significant reversed airflow back from the tunnel towards the entry portal because of the air being displaced by the train. In this way, train entry into a tunnel having a high blockage ratio may be the most appropriate scenario for defining the maximum relative air speed along the train. Although high uplifts can be generated by crosswinds, they are generally not considered in pantograph specifications. Such scenarios should, in future, be considered within a risk assessment framework to ensure that high uplifts do not occur with unacceptable probabilities.

10.5.2 Drag force

The greatest research focus has been on the aerodynamic uplift of pantographs and much less on the aerodynamic drag. Nevertheless, some studies have been undertaken using wind tunnel tests and CFD.

Fig. 10.17 shows wind tunnel measurements of the aerodynamic drag coefficient variation for a resultant air speed of 30 m/s for the Faiveley single-arm AMBR pantograph as reported by Rigby and Gawthorpe (1979). The drag coefficient, based on a reference area of 10 m^2, in the knuckle leading direction (0 degree) is quite similar to that in the knuckle trailing direction (180 degrees). The value of approximately 0.033 is broadly consistent with that reported by Carnevale et al. (2017) of 0.045 from wind tunnel tests.

Allain et al. (2016) used CFD to investigate the aerodynamic behaviour of pantographs and the contribution of pantograph components to lift and drag. A five-car TGV train was modelled, consisting of a power car fitted with a pantograph, two trailer cars and a trailing power car.

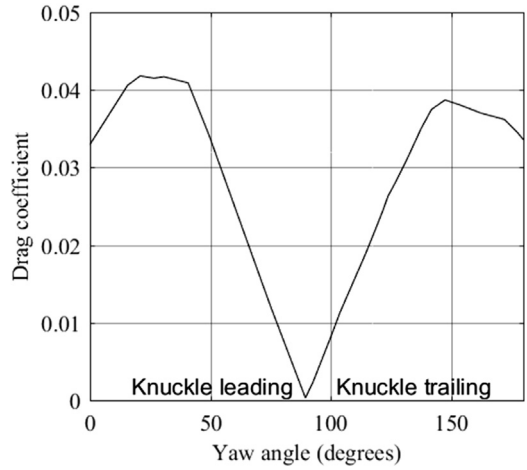

Figure 10.17 Variation of the aerodynamic drag coefficient for an AMBR pantograph. *(From Rigby and Gawthorpe (1979).)*

A steady-state RANS approach using the realisable K-ε turbulence model was used. The computational domain consisted of between 10 million and 15 million cells. The train was simulated running at 320 km/h, accelerating from stationary to constant speed and travelling in the open air before entering a tunnel. Fig. 10.18 shows the calculated pantograph uplift and aerodynamic drag. Of note is the increase in both forces as the train enters the tunnel.

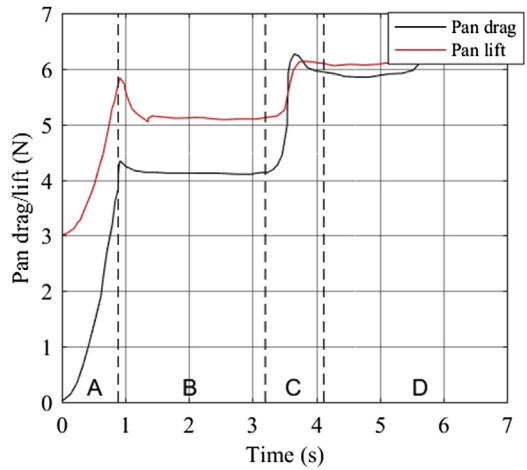

Figure 10.18 Variation of pantograph lift and in the open air and in a tunnel (not to same scale) using data from Allain et al. (2016). *A*, acceleration phase; *B*, running in open air at constant speed; *C*, tunnel entry phase; *D*, running in tunnel at constant speed.

10.6 Dewirement analysis

Dewirement is the movement of the contact wire laterally beyond the ends of the rail vehicle pantograph, leading to loss of electrical contact and damage to the OLE and pantograph. There are many causes of dewirement, including vandalism and wind-blown objects on the overhead equipment, but some incidents are thought to be caused by the wind blowing the contact wire laterally.

Modern OLE design addresses the dewirement due to wind. This is accomplished by assessing a local wind speed, called the 'OLE Design Wind Speed', based on site-specific factors, and limiting the span length to ensure the maximum lateral deflection of the contact wire from track centre is controlled using Eq. (10.2).

The maximum lateral deviation of the contact wire relative to track centre is caused by the combination of the following:

- Contact wire stagger.
- Midspan offset and blow off due to wind.
- Track and OLE tolerances.
- Support structure deflection.

Span lengths at a given site with a specified OLE Design Wind Speed are limited by maximum deviation rules, whereby the maximum wire lateral deviation is limited to 400 mm for a pantograph height of 4.7 m; the maximum deviation reducing by 40 mm/m of pantograph rise above 4.7 m.

Deviation of the contact wire relative to a pantograph centre is caused by sway of the vehicle to the left or right and the lateral component of the pantograph uplift force on the wire. Previous design assessment of OLE deviation limits considered a series addition of parameter values as show in Fig. 10.3.

These hard and fast tolerances do not occur with uniform probabilities in practice; they have statistical distributions that need to be considered in a deeper analysis of dewirement risk. Such a probabilistic approach was taken in a research project to investigate the dynamic and wind-induced sway of railway vehicles, RSSB (2011), which also considered the risk of dewirement. The latter took the same general approach as the overturning risk assessment given in Section 11.9.

The cause of dewirements, which certainly do occasionally occur causing thousands of pounds worth of damage to the OLE and causing train delays and disruption, was long an issue of contention in British Railways.

As more information was gathered following incident investigations, it became evident that a large number were caused by equipment being out of specification. Both OLE and pantographs were found to be severally at fault. The need to set different aerofoil angles on the Brecknell-Willis pantographs on individual trains, for instance, led to some incidents before procedures were put in place at depots to obviate the problem.

The risk of dewirement was usually reduced either by supertensioning the overhead wires at incident sites or introducing additional support structures, thereby reducing span length. Some novel approaches were also considered. For instance, the use of midspan offsets in the direction of the predominant south westerly winds in Britain. This was first suggested by Cooper (1975) and developed in Bellfield (1983) and Johnson (1985). A probabilistic approach was used to determine the amount of midspan offsets. Although Johnson (1985) found that offsetting by about 100 mm could be more advantageous than supertensioning, the use of offsetting was never implemented. This could prove to be a viable technique for future installations, however, where wind conditions are well documented.

On balance, it would seem that dewirements are low-risk events, except in exceptional wind conditions, provided that train equipment and OLE infrastructure are operating within their allowed tolerances.

CHAPTER 11

Train overturning in high winds

11.1 The issues

There are a variety of different issues relating to the effects of crosswind on trains. The first, which has received by far the most attention and will be the one discussed at length in this chapter, is the overturning of trains in crosswinds. Such incidents are not as unusual as might first appear and can be traced back to the blowing over of trains on the approach to the Leven Viaduct in Cumbria in Britain in 1903 and the Owencarrow Viaduct in Ireland in 1925 — see Fig. 1.7 (Railway Archive, 2018; Gawthorpe, 1994). More recent events have taken place in Japan (Fujii et al., 1999; Imai et al., 2002; Tamura, 2009), China (CNN, 2007) and Switzerland (Euronews, 2018), where passenger trains have been blown off the track, and in Great Britain (RAIB, 2009, 2015) and Canada (Global News, 2017) where freight containers have been blown off flat cars, or complete freight wagons have been blown over.

There are a number of other wind-related issues that affect trains and railway infrastructure. Strong crosswinds on vehicles can also result in excessive lateral force on the tracks, leading to possible track deflections and wheel climbing, and also result in gauge infringement, i.e., the vehicle being moved laterally so that it exceeds its maximum allowable displacement. Issues also occur in lower wind speed conditions. As has been shown in Chapters 7, 8 and 10, there are significant crosswind effects on train drag, train slipstream behaviour and the displacement of the train pantograph with respect to the overhead wire. Also the problem of trees and other debris falling or blowing onto railway track is an ever-present problem for many railway administrations and can result in severe disruption (Johnson, 1996). That being said, this chapter will concentrate on the overturning of trains in high winds.

The first serious study of this issue seems to have been in connection with the development of the Advanced Passenger Train in Great Britain in the late 1970s (Cooper, 1979). However, the advent of high-speed trains in many parts of the world means that this is an issue that has received

Train aerodynamics
ISBN 978-0-12-813310-1
https://doi.org/10.1016/B978-0-12-813310-1.00011-3

considerable attention across Europe and elsewhere in the last 20 years. A review of much of this work is given in Baker et al. (2009). The current situation in Europe is that railway interoperability legislation EU (2014a) requires an assessment to be made of train stability in high winds for all new trains that will travel faster than 140 km/h (although all rail vehicles irrespective of speed have to be assessed in Great Britain). Various methodologies for addressing the issues involved are given in the associated CEN standard (CEN, 2018), although at the time of writing this is in the process of revision.

Finally, it should be noted that in this chapter we mainly consider the effects of large-scale cyclonic or extra cyclonic storms. Strong wind conditions that can be dangerous to trains may also occur in smaller storms such as thunderstorm downbursts or tornadoes, but work in this area is in its infancy and the effects of such storms will only be considered briefly in what follows.

11.2 Outline of methodology for assessing crosswind stability of trains

An outline of the generic methodology used in the European train authorisation and route risk assessment processes is given in Fig. 11.1. It begins with knowledge of the vehicle design, its geometry characteristics and the vehicle aerodynamic characteristics. The first two usually come from other parts of the design process, whereas the last needs to be obtained in some way — usually either from wind tunnel tests or from CFD calculations (where these are permitted). These are considered in Section 11.3. The wind conditions are then simulated in some way (Section 11.4) and then used in the calculation of aerodynamic forces and moments on the train (Section 11.5). This information is then applied to some sort of vehicle system model (Section 11.6) to determine what has come to be known as the characteristic wind curves (CWCs) (Section 11.7). A CWC is nominally a plot of the wind gust speed at which a specific level of wheel unloading will occur against vehicle speed and wind direction. In vehicle authorisation, the CWCs thus derived are compared with standard reference values for a class of train (Section 11.8). In the assessment of route risk, the wind speeds given by the CWCs are used in conjunction with meteorological information of wind conditions along the route to determine the risk of an overturning accident occurring (Section 11.9). Finally, a brief description of mitigation methods is given in Section 11.10. Note that this outline methodology is similar in many aspects to the SNCF methodology developed for the TGV

Figure 11.1 Generic assessment methodology.

Mediterranean line, outlined in Cleon and Jourdain (2001), although the objective of that method was to identify appropriate wind protection and wind warning systems.

11.3 Specification of aerodynamic characteristics

11.3.1 Definitions

When trains are subject to a crosswind, they experience three aerodynamic forces (drag force F_x, side force F_y and lift force F_z along the x, y and z axes, respectively) and three aerodynamic moments (rolling moment M_x about the x axis, pitching moment M_y about the y axis and yawing moment M_z about the z axis). The origin for the coordinate system is usually taken to be

at the centre of the track at rail level, below the geometric longitudinal centre of the vehicle being considered. These coefficients are defined as

$$C_{Fx} = \frac{F_x}{0.5\rho A V^2} \quad C_{Fy} = \frac{F_y}{0.5\rho A V^2} \quad C_{Fz} = \frac{z}{0.5\rho A V^2}$$
$$C_{Mx} = \frac{x}{0.5\rho A h V^2} \quad C_{My} = \frac{y}{0.5\rho A h V^2} \quad C_{Mz} = \frac{M_z}{0.5\rho A h V^2} \qquad (11.1)$$

where ρ is the density of air, A is a reference area (conventionally taken as 10 m^2 although the side area is also used in some cases), h is the reference height (usually taken as 3 m) and V is the air velocity relative to the train (i.e., the vector sum of the wind and vehicle velocities – Eq. 3.1). In addition, we define a rolling moment coefficient about the leeward rail (which is the most relevant parameter to the overturning issue) as

$$C_{MxL} = \frac{M_{xL}}{0.5\rho A h V^2} \qquad (11.2)$$

The points of action of the aerodynamic forces are also of interest. Making the assumptions that the drag force acts along the body axis at the same vertical position as the side force and that the lift force acts through the centre of the track, then the longitudinal points of action for side and lift force relative to the centre of the train (H_{Fy}/h) and (H_{Fz}/h) and vertical point of action for side force relative to the ground (V_{Fy}/h) are given by

$$\frac{H_{Fy}}{h} = \frac{C_{Mz}}{C_{Fy}} \quad \frac{H_{Fz}}{h} = \frac{C_{My}}{C_{Fz}} \quad \frac{V_{Fy}}{h} = \frac{C_{Mx}}{C_{Fy}} \qquad (11.3)$$

Note that all the coefficients above can either be defined in terms of mean values of the forces and moments and mean values of the resultant velocity V or in terms of maximum values of the forces and moments and the maximum values of V obtained from the gust wind speed. The latter formulation is of relevance when the forces and moments are obtained from wind tunnel tests with an atmospheric boundary layer – see below. In what follows, the assumption will be that mean forces, moments and velocities are used, unless otherwise stated, and that the coefficients will be denoted as above. If there is a specific need to distinguish between the 'mean' coefficients and the maximum 'gust' coefficients, they will be denoted by $\overline{C}_{Fi}$, $\overline{C}_{Mi}$ and $\widehat{C}_{Fi}$, $\widehat{C}_{Mi}$, respectively.

In what follows, we consider firstly how these force and moment coefficients may be obtained – from full-scale experiments (Section 11.3.2),

from physical model tests (Section 11.3.3) or from CFD calculations (Section 11.3.4). In Section 11.3.5 we then consider the form of the variation of these coefficients with yaw angle using experimental data for high-speed trains presented in CEN (2018), and in Section 11.3.6 we propose a parameterisation of these coefficients that will be of use in subsequent sections.

11.3.2 Full-scale measurements

The determination of aerodynamic force and moment coefficients from full-scale experiments is extremely difficult, largely because strong wind conditions are required in which to obtain these data, and thus experimental periods can be protracted and can consume significant operational resources. They are, however, useful in that they provide base data against which physical modelling and computational techniques can be checked and also provide an appreciation of the nature of the flow around trains in complex and unsteady wind environments. There are two basic types of such experiments.

- Experiments with stationary trains, usually in an exposed location with forces being measured for a range of wind directions. Such tests are reported in Baker et al. (2004) for the Class 390 Pendolino and a Mark 3 coach on reasonable-level topography (a beach) and in Kikuchi and Suzuki (2015) and Suzuki and Hibino (2016) for 1:1 commuter coach models on a mock viaduct.
- Experiments with moving trains, either on an experimental track or in normal operation. Tests of this type are reported in Matschke and Heine (2002), Cheli et al. (2016), Gallagher (2016) and Gallagher et al. (2018).

These experiments show the very high level of unsteadiness in full-scale data, and many data samples are required to enable robust averages to be obtained. For moving vehicle experiments, the determination of wind velocity and direction at any point is far from straightforward and requires onboard measurements that need to be calibrated in some way. That being said, datasets have been produced that allow some limited comparisons to be made with physical model measurements and CFD calculations. Perhaps the major point to arise from these experiments is that they reveal the unsteady and transient nature of the flow fields around trains. As an example of this, Fig. 11.2 shows a plot of one-second gust values of side force coefficient per unit length for a Class 43 HST train (Gallagher et al., 2018) against yaw angle, for train speeds greater than 20 m/s and wind speeds greater than 4 m/s. The scatter can be seen to be very significant and

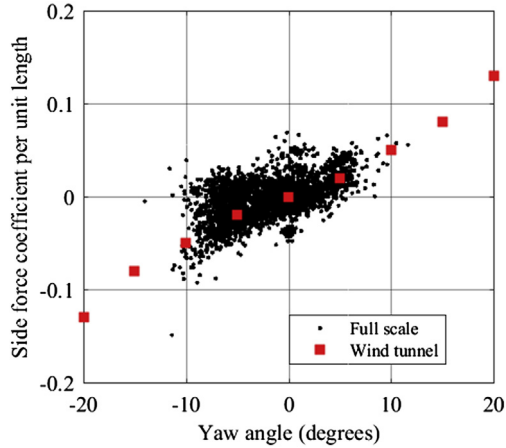

Figure 11.2 One-second side force coefficient values versus yaw angle for a Class 43 High Speed Train. *(From Gallagher et al. (2018). Copyright Elsevier.)*

reflects the fact that aerodynamic forces take time to develop, are highly transitory and are significantly affected by local topographic effects. Fig. 5.2 (also from Gallagher et al., 2018) shows the development of side force coefficient during three individual gust events lasting several seconds. It can be seen that only in one of these events does the coefficient time history closely follow the velocity time history. Such results should be borne in mind in what follows — physical model tests and CFD calculations can only be regarded as poor approximations of a very complex and transient reality.

11.3.3 Physical model tests

Detailed data for forces and moment coefficients can be obtained from physical model tests that require a number of modelling choices to be made including the following.

- The model scale and air velocity that should be used.
- Whether or not to simulate atmospheric turbulence.
- Whether or not to simulate vehicle motion.
- The nature of the ground simulation.

We will consider these in turn. In terms of model scale, the basic concept is to make the Reynolds number (Section 2.2) as high as possible because the Reynolds number controls the nature of the flow around the train, which implies making the scale and velocity as high as possible. CEN (2018) indicates that a Reynolds number above 2.5×10^5 should be achieved. This figure is partly confirmed by the results of Cheli et al. (2013)

for a two-car multiple unit, which shows no change in the side force coefficients for Reynolds numbers greater than 2.8×10^5, although lift force coefficients continue to vary with Reynolds number up to values of 7.0×10^5. The model scale is usually limited by the size of the facility available – an area blockage of around 5% at the maximum yaw angle studied is the maximum that is usually desirable. Similarly, the velocity is usually limited by the capabilities of the tunnel. Wind tunnels with maximum speeds of up to 40 m/s are typical of those used.

In terms of the simulation of turbulence, there are basically two possibilities – working in a low turbulence flow, with a uniform flow profile (as in aircraft testing), or simulating the atmospheric boundary layer. For high-speed trains, a low-turbulence flow is most realistic, for reasons explained in Section 3.2.3. For low-speed or stationary vehicles, however, it is necessary to model the atmospheric turbulence and shear. Again, this is an approximation that, whilst absolutely valid for stationary vehicles, becomes less so as the vehicle speed increases. Section 3.2.3 shows that this is a better approximation to the actual wind conditions seen by the train than the low-turbulence tests for speeds of up to around 200 km/h. The modelling of atmospheric turbulence in wind tunnels is well established (see Cook, 1985), although there remain difficulties in generating turbulence length scales that are consistent with physical model train scales – the former can most easily be achieved at scales of 1/100 or less, whereas model scales are usually of the order of 1/25 or greater. Higher effective length scales can be achieved by partial spectral simulation of the wind (i.e., matching the small-scale turbulence between full-scale and model rather than the integral length scale), but this is not an approach that has often been taken in train aerodynamics in the past. To obtain statistically rigorous maximum values of forces, moments and velocities, an extreme value analysis of some sort needs to be carried out as is often done in the study of wind loads on buildings (see Cook, 1985). Experimental comparison between low turbulence and atmospheric boundary layer measurements are given in Baker (1991a,b) and Cheli et al. (2013), both for two-car multiple units. The results are complex but very broadly seem to show a significant variations in side and lift force coefficients in the high yaw angle range with both turbulence and length scales. It is also worth noting that the full-scale and model scale atmospheric boundary layer results of both Baker et al. (2004) and Kikuchi and Suzuki (2015) are in very good agreement.

Now consider the simulation of train/ground relative motion. Measurement of train forces and moments using static models is relatively

straightforward, and measurements are usually made with either standard force balances or by the use of an array of surface pressure measurements (Section 3.2.7). The use of moving models for the measurement of cross-wind forces is much more complex and has not often been attempted. In physical model terms, some sort of firing mechanism is required, and the forces and moments on the vehicle need to be measured using an internal balance or a large number of pressure tappings, with the data acquisition system and reference pressure reservoir mounted within the model. Details of experiments of this type are given in Humphreys (1995) for container trains, Yongle et al. (2012) for trains passing behind bridge towers, Sakuma and Hibino (2013) for a generic vehicle shape, Dorigati (2013) and Dorigati et al. (2015) for the Class 390 Pendolino and Gallagher (2016) and Gallagher et al. (2018) for the Class 43 HST. For the Class 390 Pendolino, there is good agreement between moving model and stationary model tests with the same atmospheric boundary layer simulation. For the Class 43 HST, reasonable agreement was found between static model wind tunnel and moving model rig results and, for lower yaw angles, with CFD DES results, Fig. 11.3, and also with full-scale results (Fig. 11.2).

Finally, let us consider the nature of the ground simulation. In the past, a number of standard simulations have been used — plain flat ground with no rails, single- and double-ballasted track and rail representations, etc. The standard simulation that has been adopted by CEN (2018) is the 'single-track ballast and rail' or STBR, which is shown in Fig. 11.4.

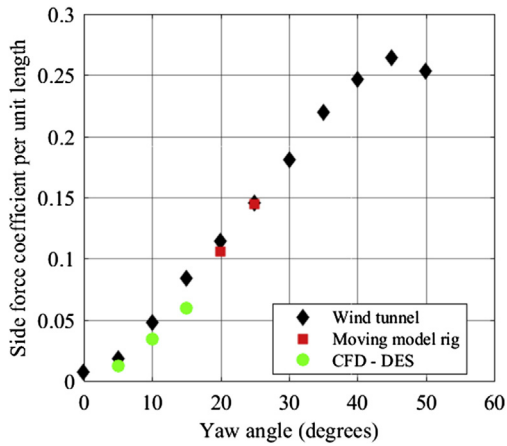

Figure 11.3 Comparison between different modelling techniques for the Class 43 HST. *(From Gallagher et al. (2018). Copyright Elsevier.)*

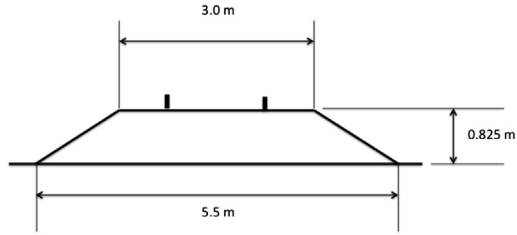

Figure 11.4 Single-track ballasted rail ground simulation as required by CEN (2018). Full-scale dimensions.

CEN (2018) contains a comparison of the various methods, which shows that the force coefficients can vary by 10%–20% depending on which simulation is used. Thus force coefficients comparisons between different trains are only really meaningful when a common ground simulation is used. Whatever simulation is used for low-turbulence tests, care must be taken to ensure that the wind tunnel floor boundary layer is kept as thin as possible, either through the use of boundary layer suction or by the use of a ground plane mounted above the floor of the wind tunnel.

There can thus be seen to be potentially a wide variety of methods that can be used to obtain aerodynamic force coefficients, and this is reflected in the literature, where wind tunnel tests with stationary ground and moving model tests with and without atmospheric boundary layer simulations are reported, both for the level ground case and for other ground simulations. Experiments have also been carried out for vehicles on different infrastructure scenarios such as embankments, viaducts, etc. Details of these experiments and calculations are tabulated in Appendix 2, which allows the interested reader to follow-up specific types of investigations as required.

The simplest wind tunnel test, and the most often used, is thus to use a stationary model mounted on some sort of representation of the track, with the effect of different wind directions modelled by turning the model at different angles to the oncoming flow. Simulations of this type usually ignore both the effects of atmospheric turbulence and shear and the effects of vehicle movement relative to the ground. Nonetheless, simulations of this type are in common use and, as noted above, are quite valid for high-speed trains.

11.3.4 CFD calculations

In carrying out CFD simulations to obtain the crosswind force and moment characteristics, similar choices need to be made to those for physical model

tests in terms of scale and Reynolds number, vehicle/ground motion, turbulence simulation and track simulation. CFD calculations are not of course, in principle, restricted by scale, and RANS calculations in particular can be carried out at 1:1 scale. The more complex unsteady methods usually require smaller scales. However, because of resource limitations, CEN (2018) recommends the same lower Reynolds number as for physical model experiments. The simulation of natural wind conditions in CFD calculations is possible, but requires care in the input specification to ensure that the correct turbulence, shear and length scales are used at the inlet (Garcia et al., 2015, 2017). It is somewhat easier to achieve a moving vehicle simulation in CFD calculations than in model tests by moving the floor of the computational domain, but the specification of the crosswind inlet conditions on two sides of the computational domain is then complex (Flynn et al., 2016). In an extensive series of calculations made for the AeroTRAIN project, Sima et al. (2015) and Eichinger et al. (2015) show that well-performed RANS CFD calculations are quite capable of replicating experimental results for train aerodynamic coefficients.

CFD calculations using a range of RANS, URANS, DES and large eddy simulation methods have also been made by a number of authors in recent years, and these are included in the table of Appendix 2 for reference purposes.

11.3.5 Force and moment characteristics

In the first instance, we will consider the side and lift force coefficients only. Figure 11.5 shows the variation of these coefficients with yaw angle for the leading vehicles of the high-speed ETR500, TGV Duplex and the ICE3 trains from the data given in CEN (2018). For static experiments or calculations, the yaw angle is simply the angle of the vehicle axis to the flow direction. These coefficients were obtained from low-turbulence wind tunnel tests with the standard STBR ground configuration and are thus formed with the mean values of the forces, moments and wind tunnel velocity. It can be seen that at low yaw angles, coefficients increase with yaw angle (up to around 40 degrees), before levelling off for yaw angles between about 40 and 70 degrees, and then decreasing at higher yaw angles. The upper and lower yaw angle ranges reflect the flows described in Section 5.3.1, i.e., an inclined vortex wake at low yaw angles and a fluctuating vortex shedding wake at high yaw angles. The intermediate yaw angle range is often very unsteady, with the flow switching between the low and high yaw angle states. In recent decades, measurements have been

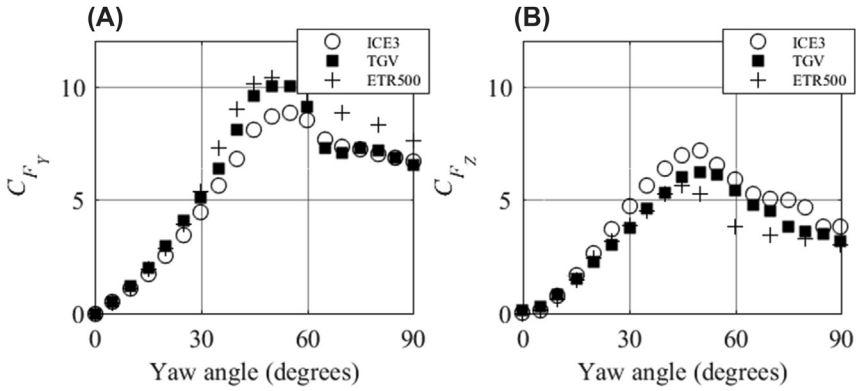

Figure 11.5 ***Variation of side and lift force coefficients with yaw angle for leading ICE3, TGV and ETR500 vehicles.*** (A) Side force coefficient, (B) Lift Force coefficient. *(Data from CEN (2018).)*

made for a wide variety of different train types, and this behaviour seems quite general, although the fall off at high yaw angles is not always apparent. Also the high yaw angle values are very sensitive to small changes in wind tunnel geometry. The latter point is particularly true of tests that have been carried out with a turbulence simulation (Baker et al., 2004). Similar results have been found in tests for trailing vehicles.

Fig. 11.6 shows the points of action of side and lift forces obtained from the three moment coefficients and the three force coefficients for the leading vehicles of the same three trains. These are expressed in a dimensionless form, normalised by the reference height of 3 m. The longitudinal position variation of the side force, which is measured relative to the centre of the vehicle, is consistent for all trains — moving steadily from close to the train nose at low yaw (where there is a high suction peak around the train nose) to the train centre at high yaw, with a levelling off in the midyaw angle range. The longitudinal position of the lift force, again measured relative to the centre of the vehicle, moves from in front of the train centre at low yaw to be behind the train centre for most yaw angles, before coming close to the train centre at the highest angles. The vertical point of action of side force, measured from above the track bed, is consistent and constant for the three trains at a little over half the reference height. The behaviour of points of action of side and lift forces for trailing vehicles follows similar trends, although the variation of the side force point of action is much less marked as there is no open front end.

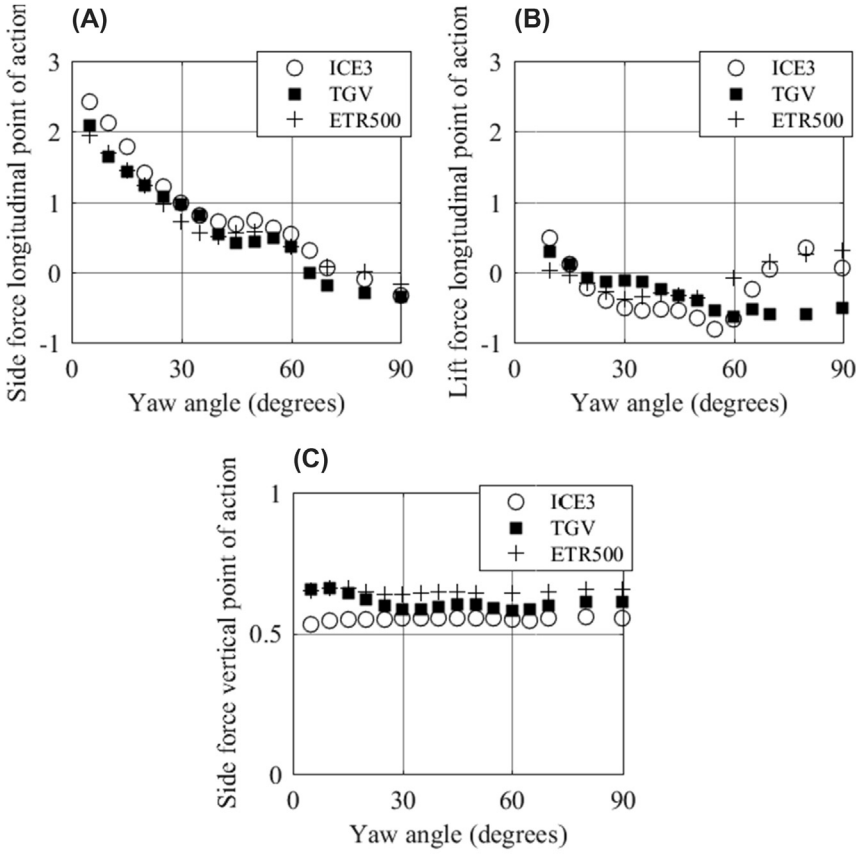

Figure 11.6 ***Variation of the normalised side and lift force points of action with yaw angle for the leading ICE3, TGV and ETR500 vehicles.*** (A) Side force longitudinal point of action, (B) Lift force longitudinal point of action, (C) Side force vertical point of action. *(Data from CEN (2018).)*

11.3.6 Parameterisation of force and moment coefficients

Recent work has suggested that it is possible to develop a generalised form for side force, lift force and rolling moment. In Baker (2013), a large dataset of side force, lift force and lee rail rolling moment coefficients was considered and the author showed that if the data were normalised by the value at 40 degrees then, at least in the low yaw angle range (which is actually the range of practical importance for high-speed trains), the data collapse onto a single curve for different categories of train, which is easily parameterised. However, the data used in that paper were of variable

quality and the precise nature of the parameterisation could only be regarded as provisional. Since that paper was written, however, the extensive dataset from the AeroTRAIN project (Paradot et al., 2015) has become available, where crosswind force and moment coefficients were measured on a wide variety of trains in one wind tunnel with a single ground simulation. This offers the opportunity for a more thorough test of the earlier parameterisation. In what follows, we thus apply the following forms to the side and lift force coefficients measured in the AeroTRAIN project. At low yaw angles, we assume

$$\frac{C_{Fi}(\psi)}{C_{Fi}(30)} = \left(\frac{\sin(\psi)}{\sin(30)}\right)^{n_1} \tag{11.4}$$

and at high yaw angles

$$\frac{C_{Fi}(\psi)}{C_{Fi}(90)} = \left(\frac{\sin(\psi)}{\sin(90)}\right)^{n_2} \tag{11.5}$$

These forms modify and extend the earlier parameterisation introduced in Baker (2013) in two ways. Firstly, the low yaw angle normalisation uses the force coefficients at 30 degrees rather than 40 degrees – the AeroTRAIN data suggest that this results in a somewhat better fit. The two forms are, of course, directly equivalent and related to one another. Secondly, the earlier high yaw angle parameterisation assumed constant force coefficients – effectively $n_2 = 0$, in the absence of coherent data. Again, the AeroTRAIN data allow a rather more sophisticated form to be used. This dataset is fully described in Paradot et al. (2015). Essentially ten train models were tested in the CSTB wind tunnel in Nantes using a low-turbulence simulation with the standard STBR simulation. Three force and three moment coefficients were measured for a yaw angle range from −45 to +90 degrees. The details of the trains that were modelled are given in Appendix 1. These trains can all be classified as medium- or low-speed passenger trains with top speeds of between 160 and 200 km/h. Here we also consider the three high-speed reference trains in the CEN standard for which the data were obtained in a similar way to the AeroTRAIN data – the ICE3, TGV and ETR500 (CEN, 2018). All but one of the leading vehicles that were tested have streamlined nose shapes, whatever their top speed, the exception being the blunt-ended Silberling train. Fig. 11.7 shows the data for side force coefficient for the leading vehicles. On each figure, curves representing the parameterisation of Eqs. (11.4) and (11.5) are shown.

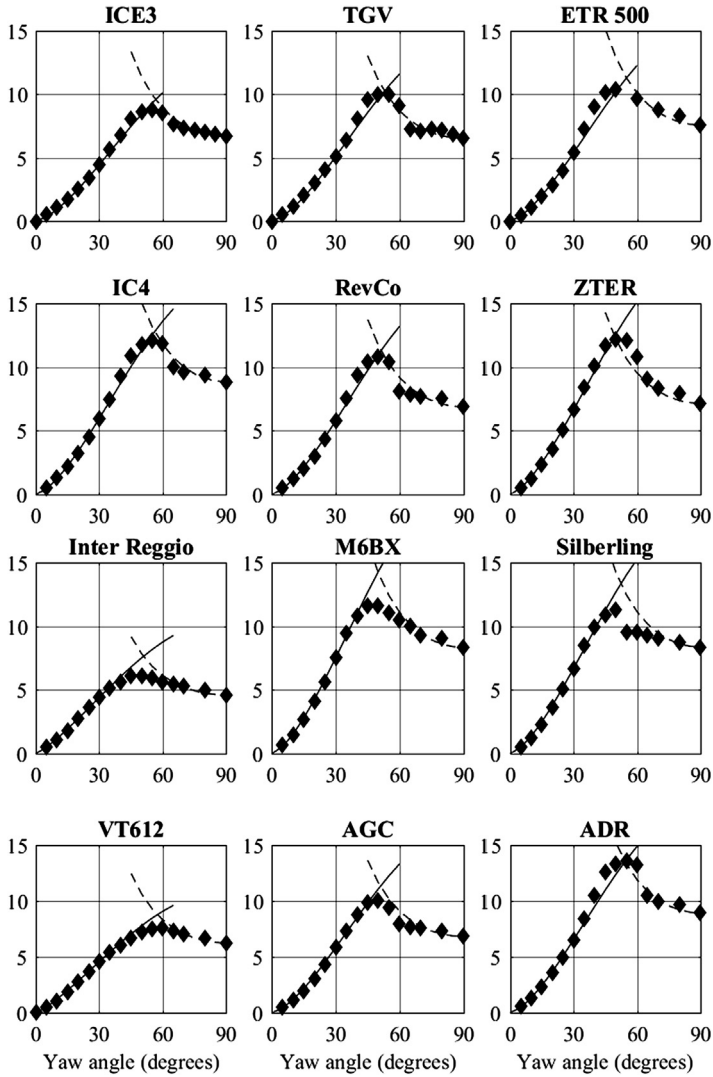

Figure 11.7 Side force coefficients for CEN and AeroTRAIN leading vehicle data on the single-track ballast and rail configuration. (*x* axis gives yaw angle in degrees; *y* axis gives coefficient value. *Black diamonds* are experimental data; *solid line* is the low yaw angle correlation with $n_1 = 1.5$ or 1.25 (for the Inter-Reggio and Silbering only); *dotted line* is the high yaw angle configuration with $n_2 = -2.0$.)

For most of the cases $n_1 = 1.5$ and $n_2 = -2$, whilst for the Silberling and Inter-Reggio $n_1 = 1.25$ and $n_2 = -2$. It is of course perfectly possible to find best-fit values of n_1 and n_2 for each train, but using the same values in general for each vehicle allows a comparison to be made for the

different train geometries. It can be seen that the expected three regions of yaw angle can be seen – an increase in coefficient at low yaw angles up to 40 degrees, a decrease at high yaw angles above 60 degrees and a transition region between 40 and 60 degrees. These data are very consistent and for most trains the above parameterisation works well with $n_1 = 1.5$ and $n_2 = -2.0$. The value of n_1 is consistent with the work of Baker (2013) for a wide variety of 'historic' data. There are two trains for which this does not apply – the Inter-Reggio and the Silberling, where a curve fit of $n_1 = 1.25$ is better at low yaw angles, and the distinction between the transition and high yaw angle regions is not so clear. The data for the latter is consistent with the work of Baker (2013) where a lower value of n_1 was found to be appropriate for blunt nosed trains such as the Silberling. It is not clear, however, why the Inter-Reggio, which is from appearances a relatively streamlined train, should have these values. From this figure, it can be seen that all trains follow the same pattern: the differences arising from the relative extent of the low and high yaw angle regions and the nature of the transition between them.

The lift force coefficients are shown in Fig. 11.8. Again, the data are in general a good fit with the parameterisation $n_1 = 1.5$ and $n_2 = -2.0$. There is, however, a deviation at the higher yaw angles for ICE3 and TGV, and for the Inter-Reggio the high yaw angle region is of very limited extent. Fig. 11.9 shows the side force coefficients for trailing vehicles. Baker (2013) suggested that values of $n_1 = 1.7$ and $n_2 = 0$ were appropriate in this case, and these values seem to adequately represent the AeroTRAIN data. For the trailing vehicle lift coefficients, Fig. 11.10, there is however a poor fit to the parameterisation, and these data seem to have a somewhat different form from the trailing vehicles considered in Baker (2013). This is particularly true for the AGC.

Thus it can be seen from the above discussion that the parameterisation of Eqs. (11.3) and (11.4) provides an excellent way of describing the measured data using effectively four parameters for each force coefficient – the values of n_1 and n_2, and the values of the coefficients at 30 and 90 degrees. However, the curve fitting approach is essentially empirical and observational and does not of itself explain the form of the fitted functions. The 'sine' form has perhaps some justification. A linear sine term implies that the force coefficients are proportional to the area of the train projected normal to the flow, and a sine squared form would indicate that the force coefficients are proportional to the wind speed normal to the axis.

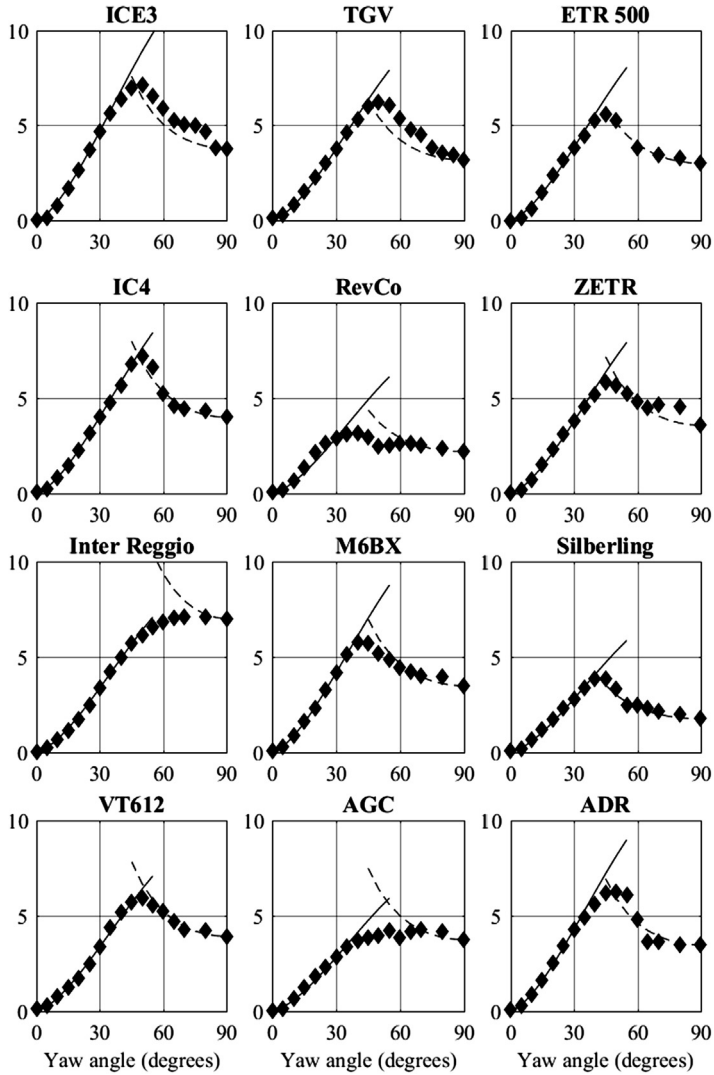

Figure 11.8 Lift force coefficients for CEN and AeroTRAIN leading vehicle data on the single-track ballast and rail configuration. (*x* axis gives yaw angle in degrees; *y* axis gives coefficient value. *Black diamonds* are experimental data; *solid line* is the low yaw angle correlation with $n_1 = 1.5$; *dotted line* is the high yaw angle configuration with $n_2 = -2.0$.)

However, for leading vehicles, the form of the coefficients is significantly affected by the low-pressure peak around the train nose, which seems to exist throughout the yaw angle range. The form of the parameterisation is thus best regarded as a convenient and plausible fit to experimental data.

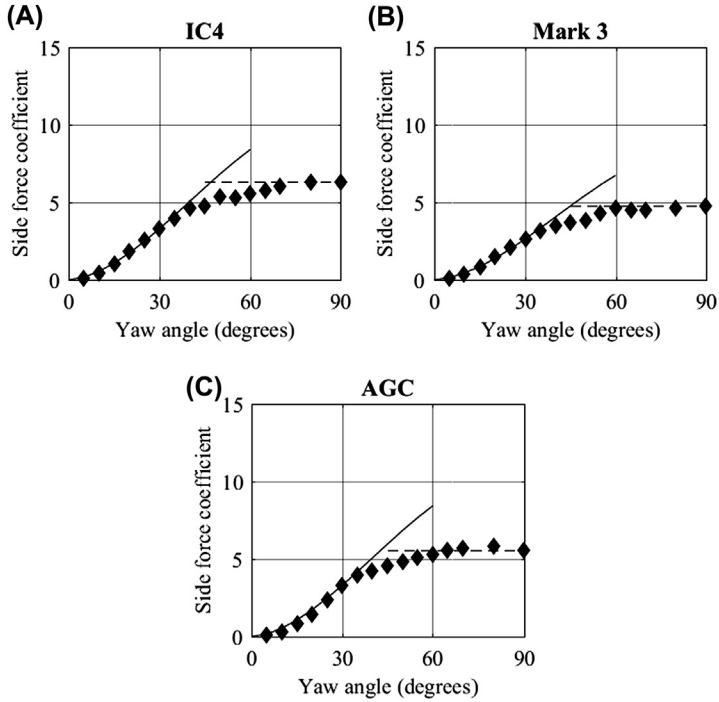

Figure 11.9 Side force coefficients for AeroTRAIN trailing vehicle data. (*x* axis gives yaw angle in degrees; *y* axis gives coefficient value. *Black diamonds* are experimental data; *solid line* is the low yaw angle correlation with $n_1 = 1.7$; *dotted line* is the high yaw angle configuration with $n_2 = 0$.).

11.4 Wind simulations

11.4.1 Specification of wind speeds

The natural wind impinging on the train can be specified with varying degrees of complexity as follows.

- The specification of the maximum gust speed that the train will experience, $\widehat{u}$.
- The specification of a typical extreme gust, which will vary both in space and time, $\widehat{u}(x, t)$.
- The simulation of a spatially varying stochastic wind time history, $u(x, t)$.

In each case, the wind relative to the train has to be calculated from the vector equation 3.1, which involves the train speed, wind speed and wind direction. In the first case this results in a maximum gust speed relative to the train $\widehat{V}$, whilst in the second two cases this results in a time history of wind speed relative to the train $V(x, t)$. These three different types of wind specification are considered in turn below.

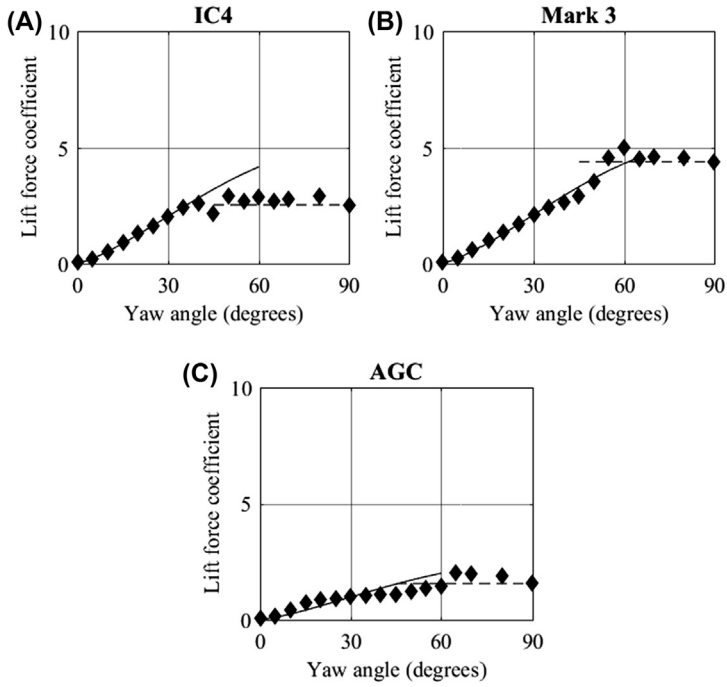

Figure 11.10 Lift force coefficients for AeroTRAIN trailing vehicle data. (*x* axis gives yaw angle in degrees; *y* axis gives coefficient value. *Black diamonds* are experimental data; *solid line* is the low yaw angle correlation with $n_1 = 1.3$; *dotted line* is the high yaw angle configuration with $n_2 = 0$.)

11.4.2 Gust wind speed specification

The gust speed of most relevance to the issue of train overturning will have a period of between 1 and 3 s, this being the time it will take for any train to rotate sufficiently to overturn. The gust wind speed $\widehat{u}$ is related to the mean wind speed $\overline{u}$ through an equation of the form:

$$\frac{\widehat{u}}{\overline{u}} = 1 + GI_x \tag{11.6}$$

where I_x is the turbulence intensity and G is a gust factor that will have a value of around 3.5, depending on the precise averaging time used.

11.4.3 Typical extreme gust – the Chinese hat method

The method in CEN (2018) is to use a typical extreme gust that has come to be known as the Chinese hat gust (Fig. 11.11). This was developed in wind loading studies for wind turbines as a time-dependent gust to be

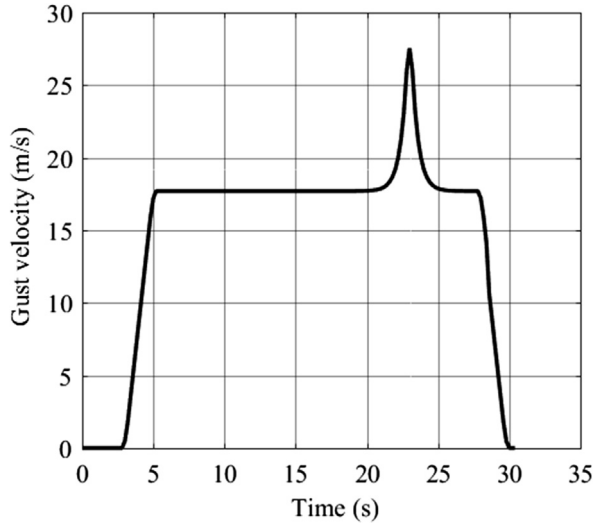

Figure 11.11 Chinese hat profile superimposed on a mean wind speed profile as specified in CEN (2018).

applied to calculate wind turbine loading at one fixed location (Bierbooms and Cheng, 2002). As such, it is perfectly adequate and a good representation of an average extreme gust in high wind conditions. In the methodology of CEN (2018), however, it is reinterpreted as a stationary spatially varying gust and, for a wind normal to the track, is given by

$$\frac{u}{\overline{u}} = 1 + 0.694e^{-16\left|\frac{n_g x}{\overline{u}}\right|} \tag{11.7}$$

where n_g is the 'characteristic frequency' of the gust calculated from standard wind engineering methods for temporally, rather than spatially, varying gusts, and x is the distance along the track. Note that this gust profile is for a fixed probability of a gust of the specified amplitude, for a value of surface roughness length of 0.07 m and for a fixed value of turbulence intensity (i.e. one topography upwind of the line). The time dependence is recovered through the passage of the train passing through this gust at a speed v to give

$$\frac{u}{\overline{u}} = 1 + 0.694e^{-16\left|\frac{n_g vt}{\overline{u}}\right|} \tag{11.8}$$

The gust thus has a maximum value when $t = 0$. The velocity relative to the train is then found by the vector addition of this gust velocity with the vehicle velocity to give a time varying value $V(t)$. CEN (2018) requires

that the resulting gust profile then be averaged over the length of the vehicle under consideration. The methodology thus does not fully describe a typical gust as seen by a moving train, which would vary both spatially and temporally, and can at best be regarded as an approximation. Ideally, if such an approach is to be used, a gust that varies both in space and time to give a value $V(x,t)$ is really required. Such a gust was used in the SNCF route assessment method of Cleon and Jourdain (2001), where the shape of the gust is appropriately described as a rugby ball. Nonetheless, the use of the Chinese Hat gust method gives a simple gust shape that can be used to benchmark the performance of different trains.

An alternative, stochastic, gust model is presented in Wetzel and Proppe (2007) and Proppe and Wetzel (2010) that produces an extreme gust embedded in a stochastic unsteady wind field.

11.4.4 Stochastic simulation of wind time series

CEN (2018) also contains, as an informative annex, a methodology that derives a full stochastic simulation of the spatially and temporally varying wind field based on the work of Cheli et al. (2012). The analysis is complex but rigorous, involving the calculation of wind characteristics that are consistent with the wind power spectrum throughout the frequency range and that also display the correct spatial correlation. In Cheli et al. (2012), a spatially (x) and temporally (t) varying wind field is calculated and the wind speed experienced by a train is calculated by following the $x = vt$ line in this plane. Ding et al. (2008) follow a similar procedure, but add the local wind simulation to the simulation of the temporal and spatially varying mean velocities in large-scale storms, so as to simulate the wind conditions over the complete route a train might take. Baker (2010b), Yu et al. (2013, 2015, 2016) and CEN (2018) use a rather simpler method to generate local wind conditions, in which the spectrum of wind relative to a moving vehicle is used as the target spectrum for wind simulations (after Cooper, 1984). The wind speed and direction relative to the train can then be found from the vector addition of wind speed and vehicle speed. Such a method results in a theoretically sound representation of $V(x, t)$ with the correct statistical properties (turbulence intensity, length scales, etc.).

11.4.5 Small-scale storms

Implicit in the above discussion is the assumption that the wind conditions being simulated are due to large-scale storms — tropical or extratropical cyclones. These are of course not the only storm type that can cause

dangerous wind conditions. Bradbury and Deaves (1994) describe the effect of thunderstorm downbursts on large freight vehicles in Great Britain, and Tamura (2009) describes the effect of tornadoes on train operation in Japan. Model descriptions of such wind conditions are in the process of development – see Holmes and Oliver (2000) for downburst models and Baker and Sterling (2018) for tornado models – and whilst capturing some of the features of these storms, they are not wholly realistic. The latter paper actually applies the wind model to the stability of trains passing through tornadoes, but the work is at an early stage and verification of the loading model is still required.

11.5 Aerodynamic forces and moments

In general, the aerodynamic forces imposed on the vehicle are taken directly from the definitions of the force coefficients and the wind speed relative to the train – either as a gust or as a time series. For example, the side force is given by

$$\widehat{F}_y = \left(0.5\rho A \widehat{V}^2\right) C_{Fy} \tag{11.9}$$

if wind gust values are used or

$$F_y(t) = \left(0.5\rho A V(t)^2\right) C_{Fy} \tag{11.10}$$

if wind time series are used. This is effectively a quasi-steady approach, which assumes that forces and moments are directly related to the wind speed relative to the train. However, the reality is rather more complex and for a time varying wind field, the time varying force is more properly split into mean and fluctuating components and is given by

$$F_y = \overline{F}_y + F'_y = \left(0.5\rho A \overline{V}^2\right) \overline{C}_{Fy} + \left(\rho A \overline{V}\right) \overline{C}_{Fy} \int_0^\infty h_{Fy}(\tau) V'(t-\tau) d\tau \tag{11.11}$$

where $h_{Fy}(\tau)$ is the aerodynamic weighting function (Baker, 2010b; Yu et al., 2015, 2016). This implies that as the train passes through a time varying wind field, the forces and moments lag behind the wind field to some extent. The weighting function is given by the Fourier Transform of the aerodynamic admittance, which is given by

$$X^2_{Fy} = \frac{1}{\left(\rho A \overline{V} C_{Fy}\right)^2} \frac{S_{Fy}(n)}{S_V(n)} \tag{11.12}$$

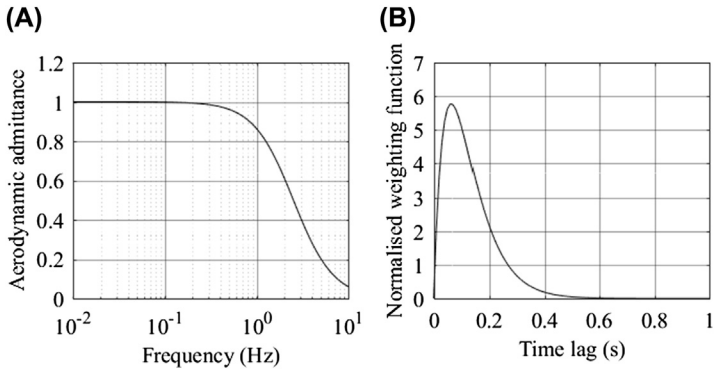

Figure 11.12 ***Typical side force admittance and weighting functions for a 20 m long vehicle, with a mean wind speed of 20 m/s and a vehicle speed of 50 m/s.*** (A) Aerodynamic admittance, (B) Normalised weighting function.

where X^2_{Fy} is the side force aerodynamic admittance, which relates the spectra of the wind speed relative to the train, $S_V(n)$, to the side force spectra on the train, $S_{Fy}(n)$. Typical curves of admittance and weighting functions are given in Fig. 11.12 using the methodology of Baker (2010b). It seems that the magnitude of the admittance is close to 1.0 at low frequencies (and thus force and moments follow the lower frequency fluctuations in wind speed with no lag or attenuation) but falls off at high frequencies, and thus high-frequency force fluctuations are both lagged and attenuated in comparison to those obtained from the quasi-steady assumption. The weighting function shows non-zero values for lag times less than 0.4s, showing the forces react to flow changes in the previous 0.4s. Experimental and computational results for aerodynamic admittances for a number of train types can be found in Baker (1991b), Baker et al. (2004), Baker and Sterling (2009), Tomasini and Cheli (2013), Garcia et al. (2015, 2017), Duan et al. (2016) and Yan et al. (2018).

An alternative, but completely equivalent, approach is to use the admittance function and the wind spectrum to calculate a force spectrum and then to find a fluctuating force time history from an inverse Fourier Transform of the force spectrum (Cheli et al., 2012; Yu et al., 2013).

Fig. 11.13A shows the side force on a train calculated using this methodology. The quasi-steady side force, calculated from a simulated wind time history and Eq. (11.10), is shown, together with the side force calculated by Eq. (11.11) allowing for weighting function/aerodynamic admittance effects. It can be seen that the latter filters out the high-frequency fluctuations of the former, together with introducing a lag of around 0.2 s.

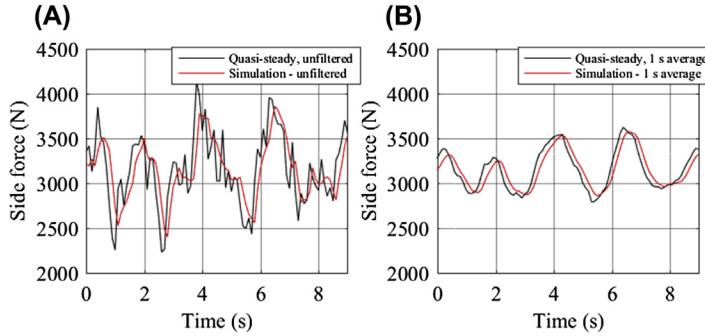

Figure 11.13 ***Simulated and quasi-steady side force time histories for a generic train shape.*** (A) Unfiltered values, (B) one second average values.

Fig. 11.13B shows the one-second averages of both curves, and it can be seen that they are very similar, suggesting that the complication of using aerodynamic admittance functions is not necessary if values of forces averaged over 1 s or more are required, as will generally be the case when train overturning is considered.

11.6 Vehicle system models

The next stage in the process of calculating the risk of overturning is to use a model of the vehicle dynamic system, suitably loaded by the aerodynamic forces and moments described in the last section, to determine the loads on the leeward wheels. These models, often termed multibody system (MBS) models, can have varying degrees of complexity. Three types of vehicle model are set out in CEN (2018).

- The simplest is a three-mass model (consisting of an unsprung mass, a primary suspended mass and a secondary suspended mass), which allows for some representation of the sprung and unsprung masses and makes some simple allowance for suspension effects by requiring the calculation be carried out with the sprung masses at their maximum lateral displacement (RSSB, 2014b). This is essentially a two-dimensional method and ignores the yawing and pitching moments that differentially affect the loads on the front and back bogies. The simplicity of such a model is attractive, and it will be seen below that it can be used to aid understanding of the interaction between wind and dynamic effects.
- A five-mass method (consisting of an unsprung mass for each bogie, primary suspended masses for each bogie and a secondary suspended

mass for the car body, with suitable spring/damper connections) gives a fuller representation of the vehicle dynamic system and allows the variation of the wheel unloading between the front and back bogies (Diedrichs, 2006; Diedrichs et al., 2004).

- The most complex is the multidegrees of freedom simulation (with many elements and their connections modelled), which fully specifies the vehicle dynamic system (Carrarini, 2008; Thomas et al., 2015; You et al., 2017, Yu et al., 2013, 2015, 2016). Such models are developed routinely for modern trains for assessing dynamic behaviour and are only validated for this purpose, not for overturning calculations, which increases the uncertainty using MBS for this purpose. They have also been used to study the effects on wheel unloading of crosswinds alone (with the wind forces and moments usually applied at the vehicle centre) and also the combination of crosswinds with other effects. Baker et al. (2010) and Rathakrishnan et al. (2013) studied the contribution of track roughness to wheel unloading, and Thomas et al. (2015) studied the particular effects of travelling around curves. Li et al. (2011) and Cui et al. (2014) investigated the interaction between train movement and the flow around trains, using integrated MBS and CFD techniques, and found relatively small, but noticeable, effects on the predicted forces and moments. There have been a number of investigations of the effects of crosswind on trains on flexible bridges with significant absolute track movement (see Guo et al., 2007; Li et al., 2005; Li et al., 2015; Xia et al., 2000; Xia et al., 2001; Xu et al., 2003; Xu et al., 2004; Xu and Ding, 2006). For these more complex methods, care needs to be taken such that the uncertainties are balanced across the overall calculation process shown in Fig. 11.1 — for example, although the dynamic calculations may be very accurate, the specification of wind conditions and train forces andmoments have very considerable uncertainties attached to them, and highly accurate MBS simulations may not always be justified.

The methodology in CEN (2018) directs that calculations should be carried out for different degrees of unbalanced lateral accelerations — effectively simulating the passage of trains around curves with either cant deficiency or cant excess, (i.e., where the centrifugal forces are not balanced by the train weight component because of the cant, or camber, of the track and where there is thus a lateral force on the track). This is mirrored to some extent by RSSB (2018), which considers tilting trains running at enhanced permissible speed (i.e., at cant deficiency around curves).

The generally accepted criterion for the precursor to the occurrence of an incident is for 90% unloading of the windward wheels of the vehicle. This value is also in some sense a safety factor that allows for uncertainties in the estimation of CWCs.

Finally, it is worth considering the work of Sesma et al. (2012) who carried out a detailed comparison between a simple three-mass model and a full MBS model. They showed that if yaw and pitching moments were not included in the MBS calculation (as is often the case as these are difficult to measure and specify), the CWCs obtained from the two types of models are very similar. This suggests that the simple two-dimensional three-body model might have a wider range of applicability and utility than has been appreciated in the past.

11.7 Characteristic wind curves

11.7.1 Outline

The next step in the process is to calculate the CWCs. In general, the simpler the mode that is used, the more straightforward is the analysis — for example, Giappino et al. (2016) use the three-mass method to compare the CWCs of different vehicles, and Baker (2013) uses the gust wind model and the three-mass vehicle model to present a straightforward analytical procedure for the calculation of overturning wind speeds for any vehicle speed. The next section discusses this approach in rather more detail, as it yields some important physical insights.

The methodology in CEN (2018) is, however, to use the Chinese hat gust with a full MBS vehicle model, which can only be solved numerically, and needs to be repeated a number of times in a search procedure for each train speed and wind direction to find the critical wind speed. CWCs calculated using this methodology for the vehicle given in CEN (2018) with a top speed of 200 km/h are shown in Fig. 11.14 — the variation of overturning wind speed with wind angle for a given train velocity or the variation with vehicle speed for a given wind direction (usually a wind direction of 90 degrees, normal to the track). The form shown in this figure is typical. The variation with wind direction typically shows a minimum for a wind direction of around 70–80 degrees to the direction of travel. The variation with vehicle speed, as would be expected, shows a fall off in the wind speed required for an accident to occur as the vehicle speed increases.

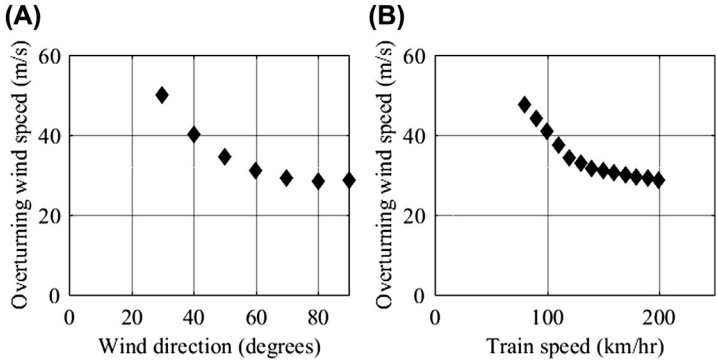

Figure 11.14 ***Characteristic wind curves for CEN (2018) vehicle 2.*** (A) Variation with wind direction at 200 km/h and (B) variation with train speed at wind direction $\beta = 90$ degrees.

The most complex methodology is to use the full stochastic wind field with a full dynamic model. This approach to calculating CWCs was taken by Cheli et al. (2008, 2010b, 2012) and the CWCs were calculated over a large number of realisations of the stochastic wind field, using simulated wind time series. This leads to a distribution of vehicle overturning wind speeds at each vehicle speed, and thus the CWCs become essentially statistical, rather than deterministic as in CEN (2018).

11.7.2 Simplified model

Baker (2013) sets out a relatively simple method for calculating the CWCs, which aims to provide a simple, yet potentially useful, method that can be easily applied. This method effectively assumes a three-mass quasi-static model. Using the expressions for the overall velocity and yaw angle given in Eqs. (3.1) and (3.2), and the coefficient formulation outlined in Section 11.3.6, for the lee rail rolling moment (Eqs. 11.4 and 11.5), one can obtain the following equations for the CWCs in the low and high yaw angle ranges, respectively:

$$\widetilde{u}^2 + \widetilde{v}^2 + 2\widetilde{u}\widetilde{v}\cos(\beta) = (\widetilde{u}\sin(\beta))^{\frac{2n_1}{n_1-2}} \tag{11.13}$$

$$\widetilde{u}^2 + \widetilde{v}^2 + 2\widetilde{u}\widetilde{v}\cos(\beta) = (2^{n_1}/R_{MxL})^{\frac{2}{n_2-2}}(\widetilde{u}\sin(\beta))^{\frac{2n_2}{n_2-2}} \tag{11.14}$$

Here R_{MxL} is the ratio of the lee rail rolling moment coefficients at 90 and 30 degrees. $\widetilde{u}$ and $\widetilde{v}$ are normalised values of the overturning wind

speed and vehicle speed. β is the wind direction relative to the track. The normalisation velocity is a characteristic wind speed u_c given by

$$u_c^2 = \frac{\alpha M g \gamma_{TR} (\sin(30))^{n_1}}{0.5 \rho C_{MxL}(30) A h} \tag{11.15}$$

where M is the train mass, γ_{TR} is the track semi-width, ρ is the density of air, A is a reference area and h is a reference height. α is given by

$$\alpha = f_{s1}(\alpha_0 - f_{s2} - f_{s3} - f_a - f_r - f_c); \tag{11.16}$$

where

- $\alpha_0 = 0.9$ (the assumed wheel unloading).
- f_{s1} is a factor that allows for train body roll, given explicitly by $(1 + S)/(1 + 2S)$ where S is the suspension coefficient, details of which are given in CEN (2016c). f_{s1} is of the order of 0.8–0.9 for different trains.
- f_{s2} is a factor that allows for suspended mass movement to the bump stops and is given explicitly by $\left(\frac{M_p \gamma_p}{M \gamma_T}\right) + \left(\frac{M_s \gamma_s}{M \gamma_T}\right)$ where M_p and M_s are the primary and secondary suspended masses and γ_p and γ_s are the primary and secondary bump stop displacements. f_{s2} is approximately 0.05–0.1 for different trains.
- f_{s3} is a factor that allows for other (dynamic) suspension effects, which has been calibrated against a simple suspension model and is approximately ± 0.02.
- f_a is a factor that allows for aerodynamic admittance effects and is approximately -0.02.
- f_r is a factor that allows for track roughness effects, which has been calibrated through a simple suspension model with variable track roughness and is approximately 0.03.
- f_c is a factor that allows for curvature and cant, given explicitly by $\left(\left(\frac{v_b}{v}\right)^2 - 1\right)\frac{qv^2}{\gamma_{TR} g R_T}$ where v_b is the balancing vehicle speed, q is the overall centre of gravity height and R_T is the radius of curvature of the track. In the terms of CEN (2018), this is given by $\frac{q a_u}{\gamma_{TR} g}$ where a_u is the unbalanced lateral acceleration.

Note the relationships in Eqs. (11.13) and (11.14) are slightly different from those in Baker (2013) because of the revised formulation of Eqs. (11.4) and (11.5). These equations have to be solved iteratively, but this is quite straightforward.

Now the results of the recent AeroTRAIN project presented in Paradot et al. (2015) allow this methodology to be validated through the following process.

- Determine n_1, n_2 and R_{XML} for the lee rail rolling moment coefficients for each train type (here restricted to leading vehicles) and thus determine the normalised CWCs from the above equations.
- Using the CWCs calculated from a full dynamic analysis presented in Paradot et al. (2015), determine the value of u_c that allows the best fit between the calculated CWCs and the CWCs determined from the current method.

The results of this process are shown in Fig. 11.15 for trains on straight track with no unbalanced acceleration. It can be seen the two sets of data agree well – and certainly the form of Eqs. (11.13) and (11.14) fit the calculated CWC data very well. Note that the discontinuity in the curves is at the yaw angle where the high and low yaw angle formulations cross. The best-fit values of u_c are given in Table 11.1 together with those from a similar analysis for an unbalanced acceleration of 1 m/s^2. The table also shows, for trains where the data is available, the values of u_c calculated from Eq. (11.15) and Eq. (11.16), assuming $f_{s3} = f_a = f_r = 0$. Consider first the values for straight track, Very broadly, high-speed trains have values of u_c of around 38–40 m/s, whilst the values for lower speed trains are generally around 30–34 m/s. There are two exceptions to this – the 200 km/h Inter-Reggio and the 160 km/h ADR; both have values of 38.5 m/s. The CEN CWC for high speed trains (not shown here) has a value of u_c of 38 m/s which is consistent with the values for the ICE3 and the TGV. The effects of track curvature can be seen to reduce all the CWCs by about 5 m/s, showing the destabilising nature of unbalanced lateral acceleration. The calculated values of the characteristic velocity were obtained with $f_a = f_r = 0$, thus replicating the CEN (2018) calculation method, and also assuming that dynamic suspension effects were not significant ($f_{s3} = 0$). These values of u_c for straight track can be seen to be close to the best fit values, with an average variation of 2%. Assuming values of f_{s3}, the factor that allows for dynamic suspension effects, of between 0.01 and 0.02 for the different cases makes the characteristic velocities agree closely. This strongly suggests that the effect of train suspension on train overturning is very largely quasi-static and dynamic effects are small. The calculated and best fit values of the characteristic velocity for the unbalanced acceleration case

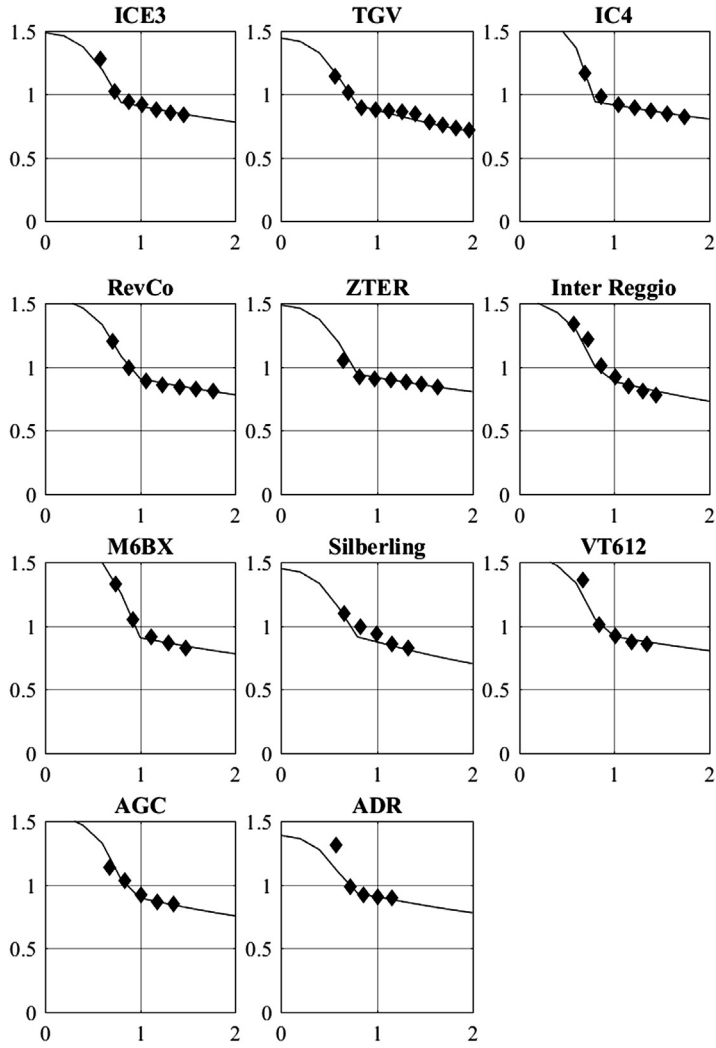

Figure 11.15 Characteristic wind curves for AeroTRAIN data. (*x* axis shows $\widetilde{v}$ and *y* axis shows $\widetilde{u}$. *Solid line* is calculated from Eqs. (11.13) and (11.14) for $\beta = 90$ degrees. *Symbols* are from AeroTRAIN analysis, normalised with the best-fit value of u_c).

have an average difference of 7%, suggesting some effect of the suspension on the curving behaviour of the train. Here again, assuming values of f_{s3} of 0.02−0.03 makes the calculated and best fit values of the characteristic velocities agree closely.

Table 11.1 Train parameters and calculated values.

Train	Max speed km/h	N_1	n_2	$C_{MxL}(30)$	R_{MxL}	u_c from curve fit (m/s)		u_c from calculation m/s)	
						Straight track	Curvature	Straight track	Curvature
ICE3	330	1.5	−1.9	3.63	1.28	38.0	33.0		
TGV	320	1.35	−1.9	3.91	1.22	39.5	33.0		
IC4	200	1.55	−2.5	4.84	1.06	32.0	25.0		
M6BX	160	1.5	−1.7	5.92	0.96	30.0	24.5		
RevCo	200	1.5	−1.3	4.75	1.18	31.5	26.0	32.0	27.8
ZTER	200	1.55	−1.9	4.83	1.32	33.7	28.5	34.1	30.0
Inter-Reggio	200	1.4	−1.4	3.29	1.14	38.5	30.5	40.0	34.7
Silberling	200	1.35	−1.9	3.53	1.21	33.5	29	33.3	29.0
VT612	160	1.55	−1.5	4.07	1.19	33.0	28.0	34.1	30.0
AGC	160	1.45	−1.5	4.15	1.12	33.0	27.5		
ADR	160	1.5	−1.6	4.35	1.47	38.5	33		

Before closing, one further issue is worth raising. If we consider the low yaw angle solution of Eq. (11.13) for high values of train speed and $\beta = 90$ degrees (i.e., a pure crosswind), one obtains the following simple solution for the CWC

$$\widetilde{u} = \widetilde{v}^{\frac{n_1-2}{n_1}} \tag{11.17}$$

For $n_1 = 1.5$, which is a good fit to the aerodynamic data for high-speed trains, this reduces further to

$$\widetilde{u} = \widetilde{v}^{-1/3} \tag{11.18}$$

which is extraordinarily simple, considering the overall complexity of the problem. Eqs. (11.17) and (11.18) can be regarded as high train speed asymptotes of the CWC.

11.8 Train authorisation

EU (2014a) states that for all new trains with design speeds between 140 km/h and 250 km/h, the CWCs must be evaluated using the methods of CEN (2018) and suitably recorded in the vehicle reference file. For high-speed trains travelling at speeds greater than 250 km/h, there are two possible approaches – one that mirrors that for lower speeds and simply requires a calculation and recording of the CWCs and the other that requires the methodology of EU (2008) to be followed – essentially wind tunnel tests on a completely flat ground and on an embankment scenario and comparison with specified reference CWCs. A further set of reference CWCs for high-speed trains on a single-track ballasted rail simulation is given in CEN (2018). This situation came about because the relevant standard, CEN (2018), has no reference CWCs for trains with these speeds, which will have to be remedied in a future revision by adding CWC curves for all speed classes of vehicle. These will have to be developed in a future research project.

The simple analysis presented in the last section suggests an alternative method based on the normalisation velocity u_c. The parameter effectively defines the CWCs and gives a straightforward way of comparing different train types, perhaps offering a simple limit value. The results given in Table 11.1 suggest values of, say, 38 m/s for high-speed trains and 30 m/s for conventional trains. Clearly more calibration work is required here to ensure that any values chosen are consistent with current practice, but it does offer a reasonably straightforward way of specifying the stability of new vehicles.

11.9 Calculation of route overturning risk

11.9.1 Wind probability distributions

However the crosswind characteristics are derived, they can then be used, together with meteorological data, to find the probability that, at a particular section of track, the wind speed will exceed the precursor or accident wind speed and that the wheel unloading limit will be exceeded or an overturning incident will occur. A number of such methods (those used in Germany, France, Italy and Great Britain) were considered during the Aerodynamics in Open Air project (Masson and Hoefener, 2008), during which a comparative exercise was carried out. At the core of each of these methods is some sort of probability distribution that relates the wind conditions at the site to the overturning wind speeds as defined by the CWCs to give a probability that those wind speeds are exceeded at the site. It is normal practice to carry out such a calculation for 6–12 directional sectors around the site in question and then to sum the probabilities from each wind direction to obtain the overall probability.

The earliest calculation of this type is reported in Cooper (1979). He used a Gumbel extreme value distribution to give the probability $P(\widehat{u})$ that the overturning wind gust speed $\widehat{u}$ will be exceeded at least once a year on average at a particular site for a particular wind direction:

$$P(\widehat{u}) = 1 - \exp\left(- \exp\left(- \frac{\left(\frac{\widehat{u}}{\widehat{u}_{50}} - 0.712 \right)}{0.074} \right) \right) \tag{11.19}$$

where $\widehat{u}_{50}$ is the once in 50 year return period gust speed at the site under consideration, which is expected to occur once on average in any 50-year period. This is obtained from building design codes, which will be discussed further in the next section. This allows the possibility of further exceedances of the overturning wind speed in that year. Bradbury et al. (2003) developed a formula that moves away from predicting the probability of one extreme gust in a given period to a more general methodology for predicting the overall gust probability by asymptotically matching the extreme value distribution with the Weibull distribution to give the following cumulative probability distribution that the overturning wind speed will be exceeded:

$$F(\widehat{u}) = e^{-20.1\left(\frac{\widehat{u}}{\widehat{u}_{50}}\right)} \tag{11.20}$$

The German method outlined in Herb et al. (2007) also uses the extreme value distribution and the Weibull distribution and arrives at the equivalent expression for the cumulative probability that the overturning gust wind speed will be exceeded:

$$F(\widehat{u}) = e^{-\left(\frac{\widehat{u}}{\lambda'}\right)^{\kappa'}} \tag{11.21}$$

where λ' and κ' are modified Weibull parameters that are obtained from meteorological measurements and are given as functions of $\widehat{u}_{50}$. A similar procedure was adopted by Araki et al. (2013) based on analyses of 10 min meteorological datasets.

In Baker (2013) it is proposed that a modified Weibull distribution could be used:

$$F(\widehat{u}) = e^{-\left(\frac{\widehat{u}}{\lambda}\right)^{\kappa'}} \tag{11.22}$$

where λ is the Weibull parameter appropriate to mean wind speeds and κ' is a modified value of the Weibull parameter κ, which is a function of turbulence intensity I_{ux} and given by

$$\kappa' = \left(1 + 0.5088I_x - 1.0747I_x^2\right)\kappa - \left(0.3404I_x + 0.1395I_x^2\right)\kappa^2 \tag{11.23}$$

This allows wind gust probabilities to be determined rather than the mean hourly wind probabilities usually associated with the Weibull distribution.

It can be seen that all these probability distributions are similar in form, although the probabilities that result can be very different.

11.9.2 Risk calculation

With the probability of the local wind speed exceeding the accident wind speed at a particular site having been obtained, the overall route risk can be obtained by summing the probabilities over all route sections. This implies that the meteorological parameters (either $\widehat{u}_{50}$ or the Weibull parameters λ and κ) need to be established at each site, through the complete wind direction range for the overall probabilities to be calculated. For a long route, this can be a considerable task. These data can either be obtained from meteorological stations, with suitable transfer functions to relate these measurements to the trackside sites (Gautier et al., 2001; Freda and Solari, 2010; Burlando et al., 2010; Misu and Hishiara, 2018), or from the wind

maps in building design codes (Cooper, 1979; Herb et al., 2007). The transfer functions can be derived from comparing trackside measurements with the measurements at meteorological stations or from numerical calculations of the wind flow over the local terrain. However they are obtained, these data then have to be corrected for surface roughness, height, topography and gust effects, usually through a series of discrete factors that are set out in design codes. In the railway situation, it is important that the speed-up over embankments and viaducts is taken into account (Baker, 1984; Herb et al., 2007). In calculating the route probability, train operations must also be taken into account – how often and for how long trains will be in a particular section of route – see Cooper (1979) for example.

The resulting risks are then considered either by comparing the risk with the risk of an accident on existing reference operations (train plus route) that are perceived to be safe or by calculating an absolute risk level and can be used to inform the construction of wind protection along the track or the development of traffic restriction strategies during strong winds.

Other issues can also be taken into account. RSSB (2018) allows for the probability of the train exceeding the speed limit at a particular site (an issue particularly for tilting trains where there is large cant deficiency) due to driver error. Andersson et al. (2004) use a risk matrix approach to assess the consequences of an accident, with the potential number of fatalities, etc. The German methodology outlined in Tielkes et al. (2008) also explicitly includes the consideration of consequences of an accident (i.e., number of fatalities) in the calculation of risk and its acceptability.

Whatever the precise methodology that is used, it is found that the final risk value is firstly very sensitive to small changes in the input parameters and can only really be specified to the nearest order of magnitude, and secondly, a very large proportion for the risk comes from just a few exposed sites on any particular route.

11.10 Mitigation methods

If the calculated risks are such that mitigation methods are required, then two basic methodologies are available – wind warning systems that allow operational measures, such as reducing train speed or stopping operations, to be implemented, or the protection of exposed section of the track by wind fences.

Wind warning systems can either be based on data from established meteorological stations or from trackside instrumentation. These can either

offer short-term predictions of high wind conditions of the order of a few minutes or long-term predictions over the next few hours. The use of the former is reported in Gautier et al. (2001) and Sourget et al. (2004) for France, Hoppman et al. (2002) for Germany and Liu et al. (2015) for China. In Great Britain, where the rail system is characterised by high-density traffic at near-capacity conditions and where real-time changes to operation are not usually possible, operational requirements require warnings several hours before the high winds are predicted, and thus information from meteorological stations is usually used. Indeed, in Britain the major risk to trains in windy periods seems to be due to wind-blown debris on the track or from tree fall onto the track or overhead (which may provide mitigation of a sort from overturning). In Japan, a tornado wind warning system has been developed based on ground-based measurements and also on radar and Lidar measurements of wind speeds, which is able to track the formation and path of tornadoes as they approach specific railway routes (Fujiwara and Suzuki, 2013).

With both short- and long-term warnings, when high wind conditions are forecast, then either train can be slowed down or operations can be halted. The GB guidelines for such traffic restrictions are given in the Route Weather Resilience Plans that are given in Network Rail (2018) and are based solely on wind velocity magnitudes. Imai et al. (2002) describe a rather more refined method that can be used on specific well-defined routes that bases warnings on both wind velocity magnitude and direction.

If normal operation needs to be maintained even in very high winds, then the use of wind fences can be considered. These can reduce the aerodynamic forces and moments on trains very significantly, see Fig. 11.16 below from Imai et al. (2002), and can be installed at the most exposed sites, resulting in a significant reduction in overall accident risk. CFD calculations of the effect of wind fences in a range of situations are given in Niu et al. (2018), He et al. (2018) and Mohebbi and Rezvani (2018).

Finally, two novel developments are worthy of mention. Alfi et al. (2011) describe a conceptual methodology for using active vehicle suspension to decrease overturning risk by changing suspension characteristics when high winds are detected. Secondly, Fu and Easton (2018) investigated the geographical spread of wind-related delays in the East Anglian region in Great Britain by integrating a range of spatial and temporal datasets for train delay, climate, vegetation and geographical databases (Fig. 11.17). Through a sophisticated regression analysis, they were able to identify those geographical areas particularly prone to wind-related delays and the wind

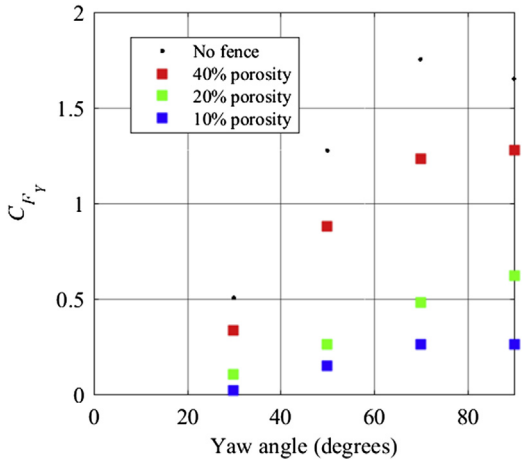

Figure 11.16 Effect of wind fences from Imai et al. (2002). *(Copyright Elsevier Imai et al. (2002).)*

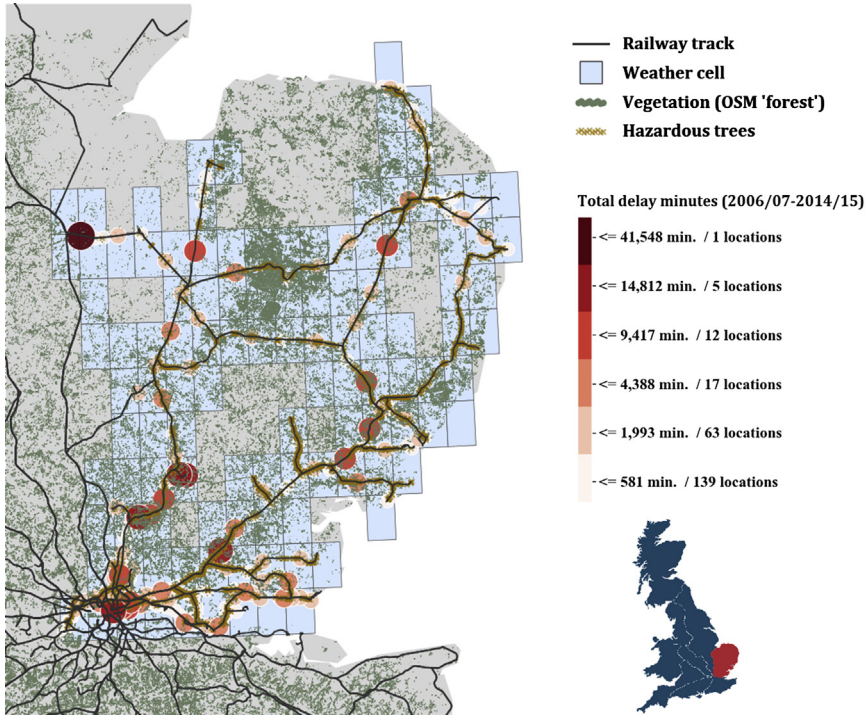

Figure 11.17 Wind-related delays and geographical databases. *(Adapted from Fu and Easton, 2018.)*

gust speeds and directions that caused these delays. Having established the regression model from a particular set of weather events, they also attempted, somewhat inconclusively, to develop their analysis for use as a predictive tool for other events. This is clearly a work in progress, but it is an illustration how the manipulation of large geographical and climate datasets may contribute to the field in the future in helping to develop wind warning systems.

CHAPTER 12

Tunnel aerodynamics issues

12.1 Introduction

In this chapter we return to the subject of aerodynamic effects in tunnels, which was described in Chapter 6, and focus on a number of practical issues. However, before considering these in detail, in Section 12.2, we will describe how tunnel aerodynamic pressures and airflows are calculated. Many aspects of the aerodynamics of trains in tunnels rely on prediction methods, rather than more complex analytic approaches or full- or model scale measurements, because of the many factors that influence the effects. This is particularly important for new tunnel constructions, where aerodynamic effects may lead to tunnel cross-sectional area increases or configuration changes and there is a potential for increased civil engineering costs. Sections 12.3 and 12.4, which comprise the major part of this chapter, then consider pressure transients effects on passenger aural safety and comfort and Section 12.5 then addresses the issue of micro-pressure wave emissions. In Sections 12.6–12.8 we then briefly consider the aerodynamic drag of trains in tunnels, structural loading on trains and infrastructure items in tunnels and the special problems of very long tunnels.

12.2 Calculation of pressure transients

12.2.1 Modelling basics

Flows and pressures in railway tunnels behave as unsteady pipe flows and can, in most circumstances, be treated satisfactorily using a one-dimensional basis. This means that flow properties are functions of distance, e.g., from a portal, and air velocities and pressures can be considered as constant (in an averaged value sense) across cross sections. There are regions where this assumption does not hold such as at portals and around the nose and tail of a train, and here special modelling is required to account for three-dimensional effects.

Over the years, a large number of one-dimensional prediction methods have been devised for calculating the unsteady aerodynamics of trains in tunnels.

Train aerodynamics
ISBN 978-0-12-813310-1
https://doi.org/10.1016/B978-0-12-813310-1.00012-5

The drive to develop such methods came from a number of sources, in particular the development of the Shinkansen high-speed lines in Japan; an early scheme for a tunnel between Britain and France in the late 1960s; early design studies for the Gotthard Base Tunnel and the development of European high-speed lines.

The one-dimensional unsteady, compressible continuity and momentum equations can be derived from Eqs. (2.1) and (2.2) as

$$\frac{\partial \rho}{\partial t} + \frac{\partial (\rho u_x)}{\partial x} = 0 \tag{12.1}$$

and

$$\frac{\partial p}{\partial x} + \rho \left(\frac{\partial u_x}{\partial t} + u_x \frac{\partial u_x}{\partial x} \right) = -\frac{\tau_w \zeta}{A_{TU}} \tag{12.2}$$

where u_x is the longitudinal velocity, P is pressure, t is time, ρ is density, A_{TU} is the tunnel area, τ_w is the shear stress acting on the tunnel wall and ζ is the tunnel wetted perimeter. The body force and viscous terms in Eq. (2.2) have been replaced by the wall shear stress term. In addition, for the flow in tunnels, the energy conservation equation (the first law of thermodynamics) is often used and can be written as

$$-\frac{\partial p}{\partial t} + \rho C_{sp} \left(\frac{\partial T_{abs}}{\partial t} + u_x \frac{\partial T_{abs}}{\partial x} \right) + \rho \left(u_x \frac{\partial u_x}{\partial t} + u_x^2 \frac{\partial u_x}{\partial x} \right) = \frac{Q}{A_{TU}} \tag{12.3}$$

Here T_{abs} is the absolute temperature, C_{sp} is the specific heat at constant pressure and q is the heat transfer through the tunnel wall. The equation set is completed by the general gas equation:

$$p = \rho R_g T_{abs}, \tag{12.4}$$

where $R_g = C_{sp} - C_{sv}$, where C_{sv} is the specific heat at constant volume and where the speed of sound satisfies

$$c_a^2 = \gamma R_g T_{abs} \tag{12.5}$$

and γ is the ratio of specific heats.

12.2.2 Compressible flow models

Pope (1980) lists five types of flow model that can used to solve the set of Eqs. (12.1)–(12.3):

1. The variable entropy (non-homentropic) model;
2. The constant entropy (homentropic) with friction model;

3. The constant density, finite speed-of-sound model;
4. The constant entropy (isentropic) without friction model;
5. The incompressible (constant density, infinite speed-of-sound) flow model.

In the variable entropy model (1), wave propagation and thermal effects are modelled strictly in accordance with the above equations, together with a definition of entropy from the second law of thermodynamics. Usually there are three dependent variables: the velocity, the speed of sound (rather than pressure) and the entropy. However, this model is overly complicated, uses a relatively large amount of computing time and is difficult to extend to predict the flows in generalised train-tunnel complexes Its' use therefore tends to be limited to modelling single trains in a plain tunnel.

The other models represent the flow behaviour but make certain simplifications. In model (2), the entropy is assumed constant (implying an inferred heat transfer across the tunnel walls), but the effect of friction is included. This makes the energy equation redundant. The boundary conditions for the nose and tail of a train are derived from the local continuity equation and an extended form of the compressible Bernoulli equation with terms included describing the pressure losses across the boundaries. This type of model has been used by a number of workers, in particular Henson and Fox (1974) and Fox and Vardy (1973), whose methods have resulted in very comprehensive commercial software able to model multitunnel complexes with airshafts, adits and many trains (see for example ThermoTun Online, 2018).

In model (3), the constant density, finite speed-of-sound model, density changes are ignored and the speed of sound is assumed constant. This method was used by Yamamoto (1965) for predictions of a single train in a plain tunnel. Using a finite speed of sound means that, although density changes are ignored, pressure waves can still propagate. The boundary conditions use continuity and the extended incompressible Bernoulli equations over the train ends.

The isentropic flow model (4) is similar to model (2) but friction is not included. It requires the isentropic relationship instead of the energy equation:

$$\frac{p}{p_0} = \left(\frac{\rho}{\rho_0}\right)^{\gamma} \tag{12.6}$$

where the subscript 0 refers to some reference condition, e.g., conditions just outside a tunnel portal.

Model (5) is the classical unsteady, incompressible flow method, and as the speed of sound is infinite, pressure waves cannot propagate. This method has been used by several workers, Sutter (1930), Gaillard (1973) and Green (1978) among others, but is only useful for indicating trends of behaviour.

Overall, models (1), (2) and (3) have been shown to represent the flows realistically, whilst the others (4) and (5) have limitations that restrict their effectiveness. In addition, models (2) and (3) are particularly economical in computing time and lend themselves to generalisation.

12.2.3 Methods of solution

The one-dimensional Eqs. (12.1)–(12.3) are usually solved using the method of characteristics, which may give rise to some of the complexities of application noted above. This method is explained in more detail in Shapiro (1977). Other methods have been applied; for example, Howe (1998) developed analytical solutions based on an acoustical analogy for the compression wave generated by a train entering a tunnel; Proverbio (2009) used the discontinuous Galerkin method and Tabarra and Sturt (2010) used finite difference methods. Three-dimensional RANS CFD or other complex approaches are also starting to be used, but these methods require moving meshes and more computational resources (e.g., Forassi, 2016; Chen et al., 2017). Currently there do not seem to be any significant alternatives to the use of the method of characteristics with an appropriate entropy model, which can offer both the speed and ability to model complex tunnel systems.

12.2.4 Empirical inputs

As stated above, some of the above models require the input of certain terms to account for local pressure losses. These are necessarily based on empirical measurements, either at full scale or at model scale. Vardy (1996a) discusses these terms in some detail, as well as the train and tunnel geometrical parameters, in the context of train aerodynamic drag in tunnels. He states that the most important for use in one-dimensional calculations are skin friction coefficients, stagnation pressure loss coefficients and drag coefficients. These describe different aspects of identical physical phenomena and can be connected theoretically. The friction and pressure coefficients are of most use for analysis and the drag coefficients for the practical assessment of train drag.

Local stagnation pressure losses occur at portals, tunnel junctions with other tunnels, airshafts or cross adits and where tunnel areas change. These losses take the form:

$$p_{loss} = k_{loss} \times \frac{1}{2}\rho {u_{xr}}^2 \tag{12.7}$$

where p_{loss} is the stagnation pressure loss, k_{loss} is the loss coefficient and u_{xr} is a representative air speed just inside the portal or other tunnel features.

The pressure losses at the train nose and tail take the same form as Eq. (12.7), but the reference air speeds are then the relative air speed just ahead of the nose and the relative air speed in the annulus just upstream of the tail, respectively.

The local shear stresses on the tunnel and on the train are defined by

$$\tau_w = C_f \times \frac{1}{2}\rho {u_{xr}}^2 \tag{12.8}$$

Here, C_f is the appropriate skin friction coefficient, and the representative air speed is either the air speed in the annulus relative to the tunnel or relative to the train for the tunnel and train, respectively.

Vardy (1996a) has developed relationships between the nose drag coefficient, the tail drag coefficient and skin friction drag and the stagnation pressure losses and train skin friction coefficient.

Whilst the pressure losses and shear stresses can be determined using Eqs. (12.7) and (12.8), knowledge of the different coefficients is required for their evaluation. As stated in Section 4.7, various workers such as Hara (1961), Peacock (1971), Gawthorpe et al. (1979a,b), Pope et al. (1982), Gregoire et al. (1997) and Sockel (2003) have produced equations for the prediction of loss coefficients and friction factors. These are based on full-scale or moving model scale measurements of pressure variations for trains in tunnels.

An equation for the nose loss and pressure loss coefficient is given in Gawthorpe et al. (1979a) and is shown in Eq. (12.9) as an example. Referring to Fig. 6.2 for the train 'pressure signature' on tunnel entry for the definition of Δp_n, the nose loss coefficient is

$$k_{nose} = (1 - B^2)\left(1 + \frac{2\Delta p_N}{\rho\left(\frac{\Delta p_N}{\rho c_a} - v\right)^2}\right) - 1 \tag{12.9}$$

Similar, sometimes more complex, equations are given in all the previously mentioned references for the various losses and friction coefficients.

To give the pressure loss coefficients and skin friction coefficients generality, it is necessary to be able to transform the values determined in the full- or model scale reference scenario to other tunnels and trains. Vardy (1996b) gives ways to do this. Very often the tunnel friction factor is estimated from a generalised description of its surface finish, but Pope (1981) describes an interesting way to determine this from the decay of the air speed in the tunnel after a train has exited using just a single air speed measurement and an assumption about the velocity profile in the tunnel.

12.3 Aural pressure comfort and health limits

12.3.1 Physiological effects

In Section 6.2, the way in which pressure changes are generated by trains entering and leaving tunnels was described, together with how pressures are then propagated in tunnels ahead of the trains and reflected at portals, creating a complex series of pressure variations through which the train passes, see Fig. 6.4. For unsealed trains, the pressure variations in the tunnels are propagated directly into the vehicles of the trains, whereas for partially sealed or sealed trains, the pressure changes are attenuated by the sealing, leading to slower, modified pressure variations inside the train.

Some people can be quite sensitive to these pressure changes as they affect their ears, particularly when they are suffering with head colds or ear infections, whilst others may be completely unaware of the effects. The cause of the sensitivity is related to their ability to tolerate and to relieve the induced pressure changes across their eardrums. The problem is therefore subjective and response can be further affected by any distracting activities being undertaken at the time and also the state of health of the particular individual. The prescription of aural pressure limits is solely a comfort issue and therefore is not generally an issue for safety standards; it is rather an issue for the service provider or entities procuring trains.

A very small percentage of the travelling public with existing aural health issues could suffer permanent hearing damage if pressure changes exceed certain levels. For this reason, the Locomotive and Passenger TSI, EU (2014a), has requirements limiting the pressure changes generated by TSI compliant trains travelling in tunnels, and requirements are placed on Infrastructure Managers in the Infrastructure TSI, EU (2014b), to ensure

that pressure changes do not exceed limit values in tunnels when compliant trains travel on their infrastructure.

Thus, to ensure aural medical health and pressure comfort for train travellers, some limits have to be applied to the generated pressures changes. In the tunnel design process, the tunnel area has to be large enough, or other alleviation methods applied, for the intended speed of operation to satisfy both the intended passenger aural comfort criteria and the medical health criterion.

12.3.2 Subjective pressure tests

British Rail Research undertook a range of subjective tests (Myring, 1973, Fletcher, 1974 and Gawthorpe et al., 1984) mainly in the 1970s and 1980s using a pressure chamber, see Fig. 12.1. This had a diaphragm in its ceiling, which could be adjusted in real time to produce variations in the internal pressure by varying the chamber's air volume. Pressures corresponding either to simple pressure time histories, such as ramps, sinusoidal variations or to realistic train pressures measured on trains in tunnels or predicted from

Figure 12.1 The British Rail Research pressure chamber.

theoretical models could be simulated. Volunteers sat in the chamber as the pressures were varied and were then asked to score individual pressure events for aural comfort on a ranking sheet.

The results showed that the subjects varied greatly in their responses to the same pressure changes, that responses are partly physiological and partly psychological and, critically, that the change of pressure, both in terms of range and the time over which it occurs, is most important.

The same pressure chamber was also used by DB to undertake subjective tests, in connection with the introduction of sealed ICE trains on the Neubaustrecke in Germany, Gawthorpe et al. (1984, 1988), Glöckle (1991). Due to the difference in the way pressures change within sealed trains (i.e., slower changes, generally reduced amplitudes compared with the pressures outside the train), DB pressure comfort limits derived from the tests focused much more on rates of change of pressures than did British Rail's limits.

More recently, Schwanitz et al. (2013b) have demonstrated a good agreement between comfort rating scores obtained in a pressure chamber and those obtained during a real train journey.

12.3.3 Pressure comfort limits

Interest in determining pressure comfort limits for passengers travelling on trains in tunnels originated in Japan (Myring, 1971). The issue was taken up in Great Britain during studies for the Advanced Passenger Train. It is clear from Myring (1971) that the intention was for the APT to be pressure-sealed to limit internal pressure changes.

Gawthorpe (1970) made a preliminary proposal for comfort limits for British unsealed train operations, based on discussions with medical consultants, but commented that more research work would be necessary before firm limits could be determined. These initial approaches led to the development of the British Rail Research pressure chamber and the subsequent pressure comfort assessment tests described in Section 12.3.2.

Since then, aural pressure comfort limits have been developed and formalised in Great Britain for unsealed trains, and various European railway organisations also developed comfort limits for sealed train operations. Table 12.1 gives the aural pressure comfort limits in place for sealed and unsealed trains used in a number of different countries from UIC (2005). The limits for trains in Great Britain generally take the form of a maximum pressure change for unsealed trains over a period of 3 or 4 s, with no expressed limit to the rate of change of pressures. This form of limit was

Table 12.1 Aural pressure comfort criteria in different countries, UIC (2005).

Country	Comfort criterion	Operating conditions
Japan	Maximum change of pressure = 1000 Pa Maximum rate of pressure change = 200 Pa/s	Sealed rolling stock High-speed trains 210–270 km/h Tight bore, double-track tunnels
Great Britain, mainline railway tunnels	Pre-1986: Maximum change of pressure = 3000 Pa within a period of 3 s Post-1986: Maximum change of pressure = 4000 Pa within a period of 4 s	Unsealed rolling stock Moderate-speed trains 160–200 km/h Tight bore, double-track tunnels
Great Britain, Channel Tunnel Rail Link	Maximum change of pressure = 2000 Pa within a period of 4 s for single-track tunnels Maximum rate of pressure change = 3500 Pa within a period of 4 s for double-track tunnels	Unsealed rolling stock High-speed trains 225–300 km/h Large bore, single- and double-track tunnels
Great Britain/ France: Channel Tunnel	Maximum change of pressure = 3000 Pa within a period of 3 s Maximum change of pressure = 450 Pa for frequently repeated pressure pulses caused by passing pressure relief ducts	Twin-bore tunnels with connecting pressure relief ducts Moderate-speed trains, 160 km/h Moderately sized bore single-track tunnels
Germany	Maximum change of pressure = 500 Pa in 1 s and 800 Pa in 3 s and 1000 Pa in 10 s	Single train only (i.e., not crossing a second train in the tunnel) Sealed rolling stock High-speed trains 240–800 km/h Large bore tunnels
Italy	Maximum change of pressure = 1500 Pa Maximum rate of pressure change = 500 Pa/s	Sealed rolling stock High-speed trains Moderately sized bore tunnels
United States of America, UMTA	Maximum change of pressure = 700 Pa within a period of 1.7 s Maximum rate of pressure change = 410 Pa/s (as an average over periods greater than 1.7 s)	Underground rapid transit systems Unsealed rolling stock Low-speed trains 80–100 km/h Small bore tunnels

Pressure comfort limits and maximum train speeds may have been changed since publication in some European countries.

based on the findings from the British Rail Research pressure comfort tests. In contrast, pressure comfort limits for sealed trains usually include a limit on the rate of pressure change as well, which reflects a sensitivity of passenger response to the rate of pressure change in such trains.

Although these pressure comfort limits were based on pressure comfort ratings, the link to them was not highlighted, so it is not clear if a common standard of passenger pressure rating has been used. Furthermore, the limits for trains passing in tunnels do not take into consideration other relevant factors such as the type of service, the density of tunnels on the route and the rarity of the maximum pressure change occurring.

Gawthorpe (1991), also summarised in UIC (2005), recognised this omission when proposing revised pressure comfort criteria for unsealed trains based on expert judgement. Four operational scenarios were postulated and three parameters taken into consideration: the type of service (intercity or short distance commuter), the number of pressure changes on the journey and the different comfort standards applied (i.e., sealed or unsealed trains) — see Table 12.2. Gawthorpe recognised that aural pressure comfort depends on the whole journey experience, not just single tunnels in isolation, and that both the pressure changes experienced every time a single train passes through a tunnel (the normal case), and the likelihood of worst case passing pressures when trains pass in tunnels (the extreme case) need consideration.

Table 12.2 Aural pressure comfort criteria proposed for unsealed trains, Gawthorpe (1991).

Operational scenario	Extreme case (two trains passing in tunnel)	Normal case (single train, occurs each time in tunnel)
Conventional intercity and regional services, unsealed trains, up to 4 tunnels per hour, less than 10% of route length is tunnels	4.0 kPa in any 4 s period (comfort rating = 4.5)	2.5 kPa in any 4 s period (comfort rating = 4.5)
Intercity unsealed train services with about 30% of route length in tunnels	3.0 kPa in any 4 s period (comfort rating = 3.5)	2.0 kPa in any 4 s period (comfort rating = 3.5)
Sealed train operations	Not considered	Not considered
Rapid transit, metro or urban underground unsealed train services, with large number of stations with connecting tunnel sections	1.0 kPa in any 4 s period	0.7 kPa in any 4 s period

Since these limits were proposed, other analytic approaches trying to address this complexity have been reported in the literature. Before looking at these approaches in more detail, it is useful to further understand the reasons for the complexities.

Pressure chamber tests of subjective responses to pressure changes on simulated train journeys through several tunnels on a route led Gawthorpe et al. (1994) to confirm the possibility of basing pressure comfort limits based on operational scenarios, as proposed in Table 12.2. This is because a passenger's aural comfort assessment of a complete journey depends not only on the worst pressure change in one tunnel but also on the cumulative impression of all the tunnel pressure changes experienced, see Schwanitz et al. (2013b).

Maximum pressure transients generated by a single train in a tunnel will occur every time the train passes through it at the same speed, so it is logical that pressure comfort limits will be lower than for two trains crossing in the same tunnel. However, maximum pressure changes for two trains passing depend on a number of parameters, including the relative entry times of the two trains. Such entry time will occur because of normal perturbations in the nominal train timetable. Fig. 12.2 gives an example of the variations of the maximum pressure changes in periods of 4 s for two trains passing in a tunnel of length 2500 m with a cross-sectional area of 90 m^2. The trains are 400 m long and travel at 270 km/h, and the down train enters at 0 s whilst the time at which the up train enters is delayed between 0 and 38.5 s.

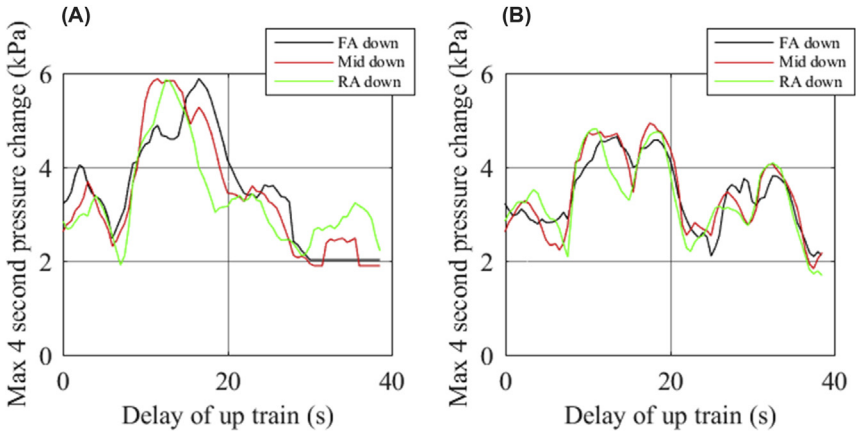

Figure 12.2 ***Maximum pressure changes as a function of train entry delay time.*** (A) Maximum pressure changes on down train; (B) maximum pressure changes on up train; *FA*, front of train annulus; *Mid*, centre of train; *RA*, rear of train annulus.

Predictions have been made of the pressures at the front, in the middle and at the rear of the trains. These pressures were then analysed to determine the maximum change within any period of 4 s.

It can be seen that the maximum pressure changes vary with the relative entry time, the position on the train and which train is considered. The maximum pressure changes on the down train at the different locations are very similar, but occur for different relative delay times of between 10 and 20 s. This also means that a passenger's exposure to worst pressure changes during the event of a train passing in a tunnel depends on which train they are travelling and whereabouts in the train they are sitting.

Johnson et al. (2000) sought to bring these factors into a novel decision tool for train operators to use to set comfort levels for a particular journey involving passing through tunnels. The tool combines the factors of train speed, tunnel area, the probability of particular pressure changes occurring and the level of comfort desired. A prerequisite of the tool is to have a relationship between pressure changes in 4 s (in this case) and the number of people who would rate them at a particular comfort level. To achieve this, the pressure histories of a journey along the Italian high-speed Direttissima route were simulated in a pressure chamber. The simulated route had 23 tunnels of various lengths along it and the maximum 4-s pressure changes varied between 0.74 and 2.8 kPa. Thirty volunteers, broadly representatives of the British travelling public, were exposed to the simulation and asked to rate each part of the journey in a tunnel on a seven-point rating scale. This scale was uncommented except at the extreme ends, with one being at the end marked 'Not at all unpleasant' and seven being at the end marked 'Extremely unpleasant'. The results were extended to include higher maximum pressure changes to cover the worst predicted cases from other studies and the lower percentile values.

Analysis of the data allowed rating curves to be generated as functions of percentile values and maximum pressure changes in 4 s, see Fig. 12.3. From this, the likely passenger response to a given pressure change could be estimated.

The following steps were taken to determine the likelihood of different numbers of passengers finding pressure changes unpleasant at a rating level chosen by the train operator.

- Determine the probabilities of a train crossing another train in the tunnel or passing through with no crossing; the train travelling on the up or down lines; passengers being in the front, middle or rear third of the train.

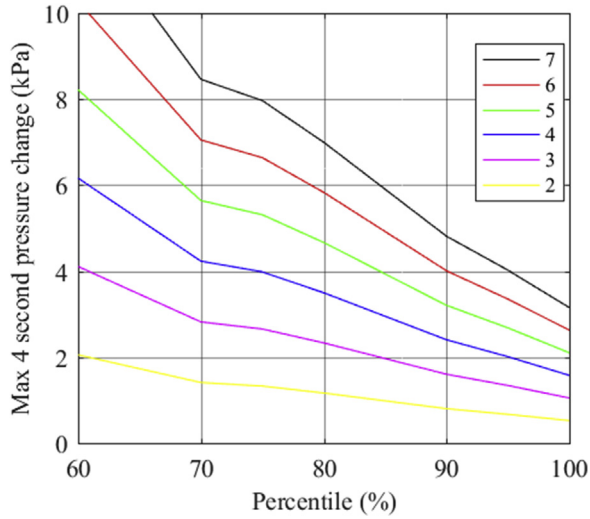

Figure 12.3 Population percentile values rating maximum pressure changes at or below specific rating levels. *(From Johnson et al. (2000).)*

- For a single (non-crossing) train, allocate to the predicted maximum pressures at the three prediction locations, a percentile value at the appropriate rating level. This percentile estimates the proportion of people in the relevant part of the train who might score the matching maximum pressure change at a rating higher than the rating level.
- For trains that pass, determine the probability of a certain delay time occurring and for each train allocate to the predicted maximum pressures at the three prediction locations a percentile value (e.g., using Figs. 12.2 and 12.3).
- For both single and crossing trains, sum the probabilities for each percentile value to obtain a probability distribution describing the rating scores through the tunnel.

  This process is summarised simply in Fig. 12.4.

Fig. 12.5 shows an example of the comfort rating probability distributions determined by the method for a tunnel with varying cross-sectional area.

One way in which an absolute pressure comfort level can be met is by increasing the tunnel area, with the consequent increase in construction costs. An advantage of the method of Johnson et al. (2000) is that increasing tunnel areas to meet a pressure comfort criterion can be assessed on a probabilistic basis.

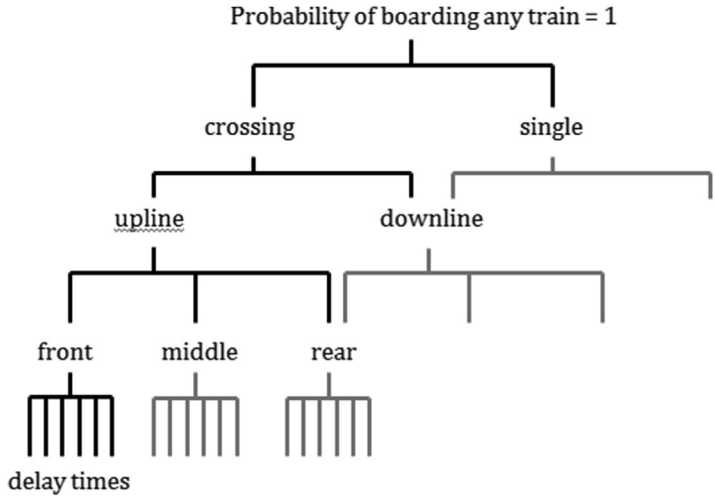

Figure 12.4 Schematic of probability process for aural pressure comfort assessment. *(From Johnson et al. (2000).)*

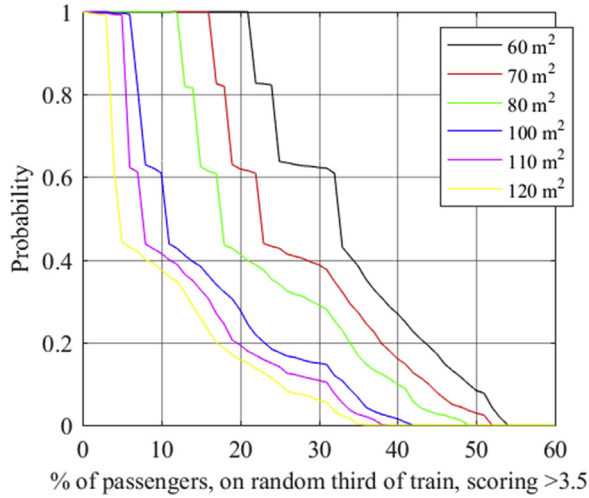

Figure 12.5 Example of comfort rating probability distribution for different tunnel areas. *(From Johnson et al. (2000).)*

Schwanitz et al. (2013a) have also made a systematic analysis of pressure changes and the perception of discomfort felt by passengers in the context of other influencing factors affecting passengers on train journeys. The pressure chamber at the German Aerospace Centre (DLR) was used to

determine subjective responses to a range of pressure changes. The pressures considered are more applicable to German sealed train operations, see Table 12.1.

12.3.4 Medical safety limit for pressure

A potentially more serious outcome of tunnel pressure changes is the possibility of damage to the ears. Work was undertaken by the European Railway Research Institute (ERRI) on behalf of UIC to determine an allowable pressure change limit from a medical health point of view. Five doctors having particular knowledge of ear function and pathology, comprised the technical experts in the working group. They concluded, on the basis of experience and judgement, that the maximum peak-to-peak pressure change to which train passengers and crew are subjected, must not exceed 10 kPa within any part of the time taken for a train to pass through a tunnel, ERRI (1998). A proviso was added which stated that the small minority of passengers with certain ear conditions should follow medical advice before using high-speed trains, much in the same way as they should when travelling by air (see also UIC, 2005). People with these ear conditions form a very small proportion of the total population and, hence, of the train-travelling population.

For unsealed trains, the criterion makes sense given the limit value is accepted, but for sealed trains, where internal pressure changes are significantly attenuated by the sealing, it does pose a problem. For passengers to be exposed to such a large pressure change in short or moderately long tunnels, there would have to be a catastrophic failure of the pressure sealing locally along the train for the external pressures to be able to influence the internal coach volume. Therefore, for sealed trains, the probability of sealing failure needs to be considered. It is, however, possible for pressures to drop to 10 kPa or more alongside a train if the tunnel is sufficiently long, and on train exit this pressure will return to ambient over a relatively short period depending on the degree of sealing of the train.

Nevertheless, the medical health criterion is used (successfully) to be able to characterise high-speed trains and to ensure the cross-sectional size of the tunnel is sufficient or the train speed is appropriate in tunnels. EU (2014a) references CEN (2010b), which provides the limiting values of the components of the train pressure signature, (see Fig. 6.2), necessary to ensure that the medical health criterion is never exceeded at the train speed of operation. The scenario considered is the entry of two trains of the same type with a specific relative entry time and then passing in a reference

Table 12.3 Maximum tunnel characteristic pressure changes, CEN (2010b).

Maximum design speed	Reference case		Criteria for the reference case		
Km/h	Reference train speed, km/h	A_{tu} m^2	Δp_N Pa	$\Delta p_N + \Delta p_{fr}$ Pa	$\Delta p_N + \Delta p_{fr} + \Delta p_T$ Pa
$v < 200$	No requirement	No requirement	No requirement	No requirement	No requirement
$200 \leq v < 250$	200	53.6	$\leq$1750	$\leq$3000	$\leq$3700
$250 \leq v$	250	63.0	$\leq$1600	$\leq$3000	$\leq$4100

tunnel of a length such that the full pressure signatures of both trains, perhaps after reflection at portals, superimpose in such a way, with the additional pressure change due to the train nose passing, so as to generate the most adverse peak-to-peak pressure change alongside one of the trains. The limit values are shown in Table 12.3.

The train designer can meet these pressure change limits by designing an aerodynamic nose and tail for the train and ensuring the train body and underbody is smooth to reduce the skin friction and pressure drag.

EU (2014b) requires infrastructure managers to design tunnels such that any train satisfying the pressure requirements of Table 12.3 (called a reference train) running through their tunnels do not generate a maximum pressure change exceeding the medical health limit. This can be achieved, for instance, by modifying the tunnel areas or by adjusting the operational speeds of trains using the tunnels (see the next section).

UIC (2005) provides minimum cross-sectional areas for plain railway tunnels (i.e., without airshafts or junctions, etc.) for unsealed standard or high-speed passenger train operations, considering just train aerodynamics. The areas have been determined using tunnel pressure calculations made using the AEROTUN/4 one-dimensional characteristics program, an earlier version of THERMOTUN (ThermoTun Online, 2018). Tunnel areas are provided for a range of tunnel and train parameters for single- and double-bore tunnels. Three different time periods for the maximum pressure change are presented: 1, 4 and 10 s. In addition, minimum areas are also presented for tunnels to just meet the medical health criterion. These results are best used to understand trends of behaviour and approximate tunnel areas for general design purposes, and specific calculations should be undertaken for particular tunnel design and train operations.

12.4 Alleviation of tunnel pressures

12.4.1 Methods of alleviation

There are a number of ways to address tunnel pressures as they affect the aural comfort of passengers, besides using a probabilistic analysis, such as that proposed in Section 12.3.3. These include the following:

- choosing the tunnel area to ensure pressure comfort limits are satisfied for the design speed of the tunnel;
- choosing the design speed of the tunnel;
- constructing airshafts along the length of the tunnel;
- constructing cross-passages to link separate twin-bore tunnels;
- pressure sealing the trains;
- modifying the tunnel portal designs.

These methods will be briefly considered in the following sections.

12.4.2 Modification of tunnel area

Choosing the optimum cross-sectional area of a tunnel for new tunnels on a route is one of the main ways to alleviate pressure wave effects. There is a trend for railways to use certain fixed cross-sectional areas depending on whether tunnels are single- or double track and according to train operating speed ranges. This appears to be related to the size of tunnel boring machine sizes and the target pressure comfort to be achieved. Existing tunnels have a range of cross-sectional areas, as they were often constructed by hand excavation with the use of explosives, and tunnel pressures were not considered.

Increasing tunnel areas to mitigate tunnel pressures has the significant disadvantage in increased boring costs and may have the further disadvantage of requiring more powerful fans for normal ventilation, if required, or for emergency ventilation during fires. Therefore, during new tunnel construction, the choice of tunnel area will be considered in the wider context of desired train operations and ventilation, with construction costs being a key parameter. Other means of reducing pressure changes, such as those outlined in what follows in tunnels, are often considered in conjunction with choosing tunnel areas, depending on relative costs.

12.4.3 Adjustment of train speed

Pressure changes caused by trains travelling in tunnels reduce as train speeds are reduced. This is an effective method as the pressures increase is in proportion to the square of train speed but may conflict with the target line

speeds for the complete route. Speed reductions need to be only applied as trains enter or leave tunnels, which is generally where the major pressure changes are generated. However, applying such speed reductions is not particularly practical and, in addition, may be contrary to the desired operations through the tunnel. The choice of tunnel design train speed should be considered as part of the wider design and operations of tunnels on a route.

12.4.4 Airshafts

The use of airshafts in 19th century railway tunnels in Great Britain came about for two reasons: to ease and speed up construction and also to permit smoke from steam locomotives to escape from the tunnel and reassure passengers they would not be asphyxiated by smoke. This aspect of airshafts, i.e., the connection to the open air, is also beneficial in relieving pressure transients in tunnels by releasing some pressurised air from the tunnel to atmosphere.

Fig. 12.6 shows the effect of an airshaft on the pressure changes at the rear of a 200 m long train travelling at 200 km/h through a 2000 m long tunnel. In the plain tunnel, the worst pressure change within 4 s (ending at 17.3 s) is 1.59 kPa alongside the rear of the train. When the airshaft is included, the maximum pressure change in 4 s is reduced to 1.38 kPa and occurs within the 4 s ending at 26 s.

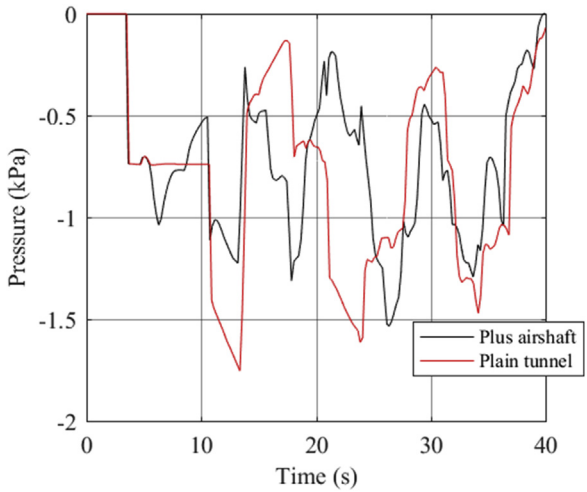

Figure 12.6 Pressure changes to the rear of a train in a 2000 m tunnel, with and without an airshaft at the midpoint. Calculations undertaken using ThermoTun Online.

The ability of airshafts to relieve tunnel pressure transients has been recognised since the 1970s, e.g., Vardy (1976). Systematic studies have been undertaken by Henson and Pope (1997) and Figura-Hardy (2000). The former investigated the reduction of the maximum pressure change in 4 s in an 1140 m long tunnel using small diameter airshafts. A one-dimensional unsteady compressible flow model using the characteristics method was used for the pressure predictions. Shaft spacings and diameters were varied and it was found that small bore airshafts are an effective and low-cost method to reduce tunnel pressure transients; about 50 one metre diameter shafts provided an almost 60% reduction of the most severe pressure change and would be reasonably cost-effective in relatively soft rock. They found that the use of 20 airshafts of appropriate area gave a greater reduction in maximum pressure change in 4 s than doubling the tunnel area.

Figura-Hardy (2000) investigated the general trends and benefits of using airshafts to reduce pressure transients in tunnel using one-dimensional unsteady compressible flow method. Prior to the study, a literature study was undertaken by ERRI on behalf of the UIC (UIC, 2005). The reported efficacy of a range of tunnel pressure alleviation devices was assessed, and it was concluded that the use of airshafts was the most cost-beneficial. The work reported by Figura-Hardy (2000) was the follow-up to the literature study and consisted of some 132,000 pressure simulation runs. Two train lengths and two different aerodynamic characteristics were considered. Train speeds were varied between 175 and 350 km/h. Tunnel lengths were varied between 500 and 5000 m, with five blockage ratios modelled. Up to seven airshafts were located in each tunnel subject to a minimum shaft separation of 250 m; these were of 6 m^2 in cross-sectional area, which had been found separately to be near optimal for pressure alleviation. Single-train tunnel transits, as well as crossing scenarios between trains of both aerodynamic types, and unsealed and sealed trains were modelled. Fig. 12.7 gives some sample results from the paper.

To illustrate the use of airshafts in complex engineering projects, let us consider the upgrade of the West Coast Main Line in Britain in the early 2000s. Calculations of transient pressures in several tunnels were undertaken prior to the introduction of the new high-speed, pressure-sealed tilting Class 390 Pendolino (Temple, 2006). A very important aspect of this study was that although the Class 390 trains were pressure-sealed, and therefore meeting comfort limits was easy for passengers on these trains even for the higher speeds proposed, existing trains using the tunnels were not. Thus, the burden of increased tunnel pressures arising from the Class 390

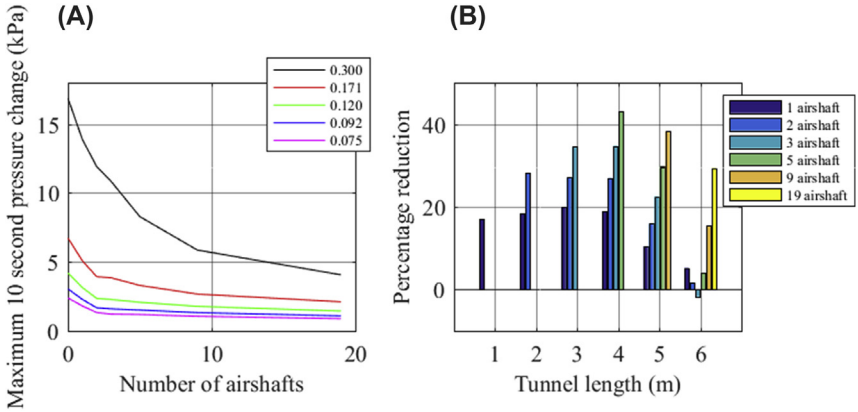

Figure 12.7 ***Examples of the results of the pressure reductions achieved by the introduction of airshafts from Figura-Hardy (2000).*** (A) Variation of maximum pressure changes in 10 s: two passing streamlined trains with moderate sealing at 250 km/h, $L_{tu} = 5000$ m; (B) average percentage reduction in maximum pressure change in 4 s: two unsealed trains passing (over all blockage ratios, train speeds and train lengths.

travelling at faster speeds, and meeting pressure comfort limits for passengers, fell on these trains. Only by choosing the operational speeds of the Class 390 appropriately, or introducing pressure transient alleviation methods into the affected tunnels, could an equitable situation be achieved. In all, fifteen, 19th century tunnels were investigated, six of which already had airshafts. It was found that pressure mitigation measures would be required in two tunnels on the route to ensure that the aural comfort of passengers on unsealed vehicles passing the new trains would not be compromised. In Stowe Hill Tunnel, which runs below open countryside, four airshafts were eventually constructed to meet increased train speeds in the tunnel and meet the desired pressure comfort criterion. The other tunnel, Northchurch, runs below a housing estate, which limited the number of airshafts that could be constructed to just one. Due to the emergence of the top of the airshaft into the housing estate, it was necessary to give considerable attention to the design and appearance of the shaft head structure to make it visually acceptable, secure and safe and that any modifications did not impair the efficacy of the pressure relief of the airshaft. The proposal for the airshaft construction also had to pass the hurdle of a public inquiry. Although the tunnel was lined with an acoustic lining, there were complaints about the levels of noise emanating from the shaft once it was constructed and Class 390 operations had commenced because of the high air speeds generated in it by passing trains.

Generally, the use of airshafts can be a relatively inexpensive option allowing smaller tunnel cross-sectional areas while still meeting pressure limits and will also reduce the aerodynamic drag of trains using the tunnels. They may also assist with ventilation and temperature control as well as assist with smoke removal in the case of tunnel fires. Alternatively, airshafts may not be an option when the tunnels are very deep or in adverse rock formation or urban areas, and they may give rise to the generation of noise caused by the air flows induced in them by train movements.

12.4.5 Cross-passages

Cross-passages are usually installed between twin-bore tunnels for safety reasons but they may in some cases reduce pressure transients. They were considered as an option for pressure relief purposes as part of the studies for Northchurch Tunnel described above. Northchurch Tunnel consists of two single tunnels containing the slow lines and a double-track tunnel for the fast lines. The proposal was to link the double-track tunnel with adits to one of the single-track tunnels. However, it was found that this option increased worst case pressure transients in both connected tunnels when train operations in all the tunnels were considered (Temple, 2006).

The use of cross-passages for pressure relief has a number of drawbacks as operations in the two connected bores have to be considered, because the cross-passages allow pressures to be transmitted from one tunnel into the other. This cross-connection may also cause problems for smoke control if there is a fire in the tunnel. There may also be issues with strong induced air flows in the cross-passages, as exemplified by the Channel Tunnel (Section 12.8).

12.4.6 Train pressure sealing

Pressure sealing trains is a very effective way of reducing transient pressures affecting onboard passengers and staff (although it is of no benefit for meeting the medical health criterion). Pressure fluctuations outside a sealed train coach can change the pressures inside the coach via two main mechanisms:

- The coach becomes deformed by the external pressure with a consequent change of volume. It has been estimated that the internal pressure may vary by up to 10% of the external pressure change via this mechanism.
- The pressure difference between the interior and exterior of the coach forces air through any leakage paths so that the internal pressure follows the external pressure changes with a time delay.

As a result of these two mechanisms, some means is needed to describe how the internal pressure responds to the external pressure changes. This is most commonly achieved by defining the air-tightness of a train coach in terms of either a pressure tightness time, τ_{dyn}, or an equivalent leakage area, A_{eq}. It is also a common assumption that the coach volume is considered as constant, despite it being dynamically deformable, so that the effects due to coach deformation can be ignored.

The air-tightness of a coach differs when it is static compared with when it is moving. In the latter case, small movements of the components of the structure of the coach relative to each other may alter the leakage paths or, perhaps, leakage paths may open up under movement of the coach, which are relatively sealed when it is static. This leads then to the concept of dynamic and static values of air-tightness. This becomes more complicated as some leakage paths may open when there is an external underpressure and close when there is a relative overpressure, or vice versa.

The air-tightness of a railway coach subject to a dynamically varying external pressure, τ_{dyn}, is defined as

$$\frac{dp_{int}}{dt} = -\frac{1}{\tau_{dyn}}\left(p_{ext} - p_{int}\right) \tag{12.10}$$

in which $p_{ext}(t)$ is the pressure external to the train and $p_{int}(t)$ is the train internal pressure. τ_{dyn} is always positive and varies from 0 to infinity such that, for a completely unsealed train, $\tau_{dyn} = 0$, and for an ideal train which is perfectly sealed, $\tau_{dyn} = \infty$. It should be noted that these extreme values due to complete openness or complete tightness are difficult to achieve. Furthermore, as noted previously, τ_{dyn} may have two values: $\tau_{dyn}(p_{ext} > p_{int})$ and $\tau_{dyn}(p_{ext} < p_{int})$.

Because of its ease of measurement, static values of air-tightness are often used to approximate the dynamic air-tightness of a coach even though the latter may be several times larger than the former. More information about train pressure sealing can be found in Johnson (1999), CEN (2010b) and Sima (2003). Fig. 12.8 shows the effect of pressure sealing at the front and back of a train travelling in a 2000 m long tunnel with a central airshaft. Pressures outside and inside the train are shown for comparison. Liu et al. (2017) describe full-scale tests on a CRH2A train operating on the Hefei–Wuhan rail line in China, running through twelve tunnels with lengths between 72 and 10,766 m. Pressure measurements were made outside and inside the train to investigate how variations of exterior pressures affected the train interior pressures. Significant differences in the variation of internal pressures were observed between short and long tunnels.

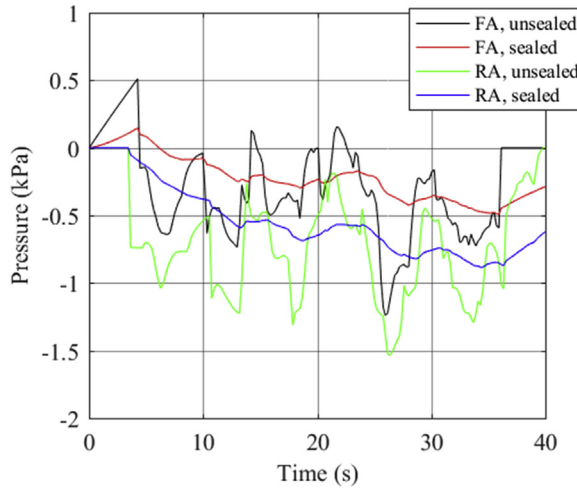

Figure 12.8 ***Example of pressure sealing on train pressures.*** $\tau_{dyn} = 10$ s; *FA*, front of train; *RA*, rear of train. Calculations undertaken using ThermoTun Online.

12.4.7 Portal design

One other way in which pressure changes in tunnels can be altered favourably for pressure comfort is by using modification of the design of the entry portals of tunnels. The two main methods that have been proposed is the use of flared or porous entrances. The way in which these methods work is by slowing the buildup of the initial pressure rise as a train enters a tunnel. This is illustrated in Fig. 12.9, which shows the external pressures at the rear of a train running in a 2000 m long tunnel. The effect of adding a 200 m long flared entrance section, with cross-sectional area varying from 80 m^2 at its entrance to the tunnel area of 50 m^2, is shown. The pressure plots show the pressures with a time base beginning when the train enters the main tunnel in each case. The steep pressure drop when the tail of the train enters plain the tunnel at about 3.5 s is modified by the flare to a more rounded variation, and the worst pressure change in 4 s ending at about 18.5 s is reduced by the flare from 1.6 to 1.2 kPa.

Henson and Pope (1997) also investigated numerically the effect of flares on a double-tracked 1140 m long tunnel. Each flare was 380 m long and had cross-sectional areas varying linearly from 205 m^2 to the tunnel area 82 m^2. The peak pressure transient was reduced by 60% from the plain tunnel. These sized flares theoretically produce the best benefit but are generally not cost-effective to construct, unless there is a significant trade-off compared to reducing the main tunnel cross-sectional area.

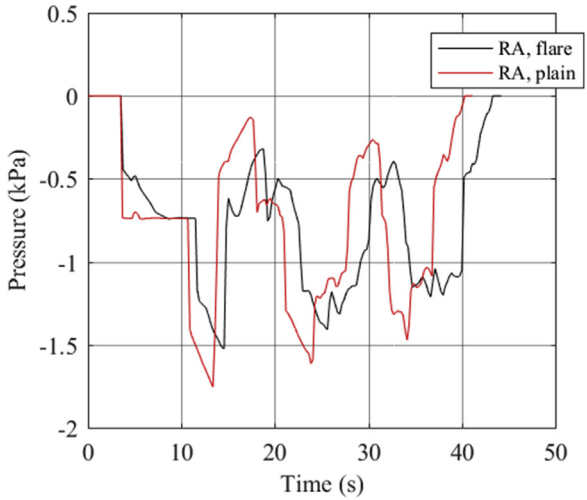

Figure 12.9 Effect of a flared entrance on pressure alongside a train. *RA*, rear of train. Calculations undertaken using ThermoTun Online.

Perforated entrances to tunnels were investigated numerically by Vardy (1975) and experimentally and numerically by Dayman et al. (1979) and found to produce beneficial results in reducing pressure transients.

During aerodynamic design studies using numerical methods for the Channel Tunnel Rail Link in 1997 by AEA Technology, a porous tunnel entrance was proposed for the twin-bore single-track London Two tunnel as a means of meeting the tunnel aural pressure comfort criterion. In the tunnel as designed, the train entry pressure changes were predicted to violate the comfort criterion for single-track tunnels (Table 12.1). Johnson and Dalley (2000) undertook an experimental study using moving model tests to verify the effect of porous entrances on pressure changes in the tunnel (and hence alongside a train travelling through the tunnel). Model trains at a scale of 1/25 were fired through a 45 m long tunnel, the first 2 m of which was drilled with 576 six mm sharp-edged holes. Filling or leaving open the holes allowed the entrance section porosity to be varied. Four pressure tappings along the tunnel allowed the pressures generated in the tunnel by the train to be measured; the second was at 3.75 m from the train entry portal.

Fig. 12.10 shows the effect of a porous entrance on the measured pressure changes caused by a train entering the tunnel and passing the second pressure tapping position. X is the point in the wave evolution where the train's full cross section has entered the tunnel; Y is the point

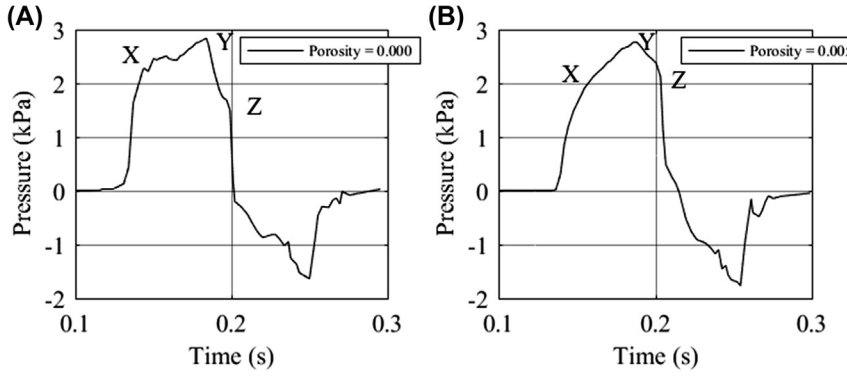

Figure 12.10 ***Effect of a porous entrance on the train pressure signature in a tunnel from Johnson and Dalley (2000b).*** (A) Nonporous tunnel entrance; (B) porous tunnel entrance, porosity = 0.005 m^2/m.

after the frictional pressure rise when the tail entry wave reaches the second tapping; Z marks the start of the train nose passing the second tapping position. The porous entrance has a significant effect on the evolution of the pressure, but not the amplitude, up to point Y. In the case of the London Two tunnel, this modification was sufficient to allow the aural pressure comfort criterion to be met on the train, and the experiment demonstrated that the prediction method could be relied on.

12.5 Assessment and alleviation of sonic booms

12.5.1 Methods for assessing micro-pressure wave generation

In Section 6.4, we saw that the generation of micro-pressure waves, which might result in sonic booms at the train exit portal of a tunnel, comprises four different phases. These are pressure wave generation as a train enters the tunnel; wave transmission at sonic speed along the tunnel ahead of the train; emission of the micro-pressure wave from the exit portal and then transmission of the micro-pressure wave outwards from the exit portal into the surroundings.

Different methodologies are capable of predicting the four phases above and to predict the whole process, but methods have to be combined with outputs from one method forming the inputs to another method.

Full-scale tests are of course possible for existing tunnels and trains. Pressures may be measured about 100 m inside the tunnel to evaluate the

pressure wave generation and the gradient of this wave front. The wave transmission and wave steepening can be determined by further pressure measurements along the tunnel. Finally, the micro-pressure wave emission and transmission is measured outside the tunnel using pressure transducers and low-frequency microphones. However, such measurements will not prevent problems arising in other tunnels and so prediction methods are essential for tunnel design.

For all phases, three possible methods may be used – simple formulae, three-dimensional CFD and scale model testing, although the latter may be limited by space for suitably long tunnel models and the exterior environment which may influence micro-pressure wave transmission.

For pressure wave generation alone, several methods are suitable: simple formulae, such as given in Eq. 6.1 developed by Hara (1961), three-dimensional solutions, e.g., Howe (1999), Howe et al. (2000, 2006), Iida and Howe (2007) and three-dimensional CFD and scale model testing, e.g., Gregoire et al. (1997). For pressure wave transmission, one-dimensional methods, described in Section 12.2, are also suitable.

Hieke et al. (2009, 2011) describe a chain of calculations for the assessment of micropressure waves using unsteady three-dimensional CFD to predict wave generation by a train entering a tunnel. At the tunnel cross section where the pressure wave front became essentially one-dimensional, an unsteady one-dimensional Euler equation method was then applied to predict the wave transmission along the tunnel, using the results from the CFD as inputs. A formula similar to Eq. (6.2) was then used to predict the emission of the micropressure wave outside the train exit portal. The various calculations were verified against full-scale measurements made in the German Euerwang Tunnel and showed good agreement. In the second paper, there is a discussion of the noise generated by the micropressure wave emission in the context of German and European noise legislation.

Vardy (2008) presents simplified ways of estimating the generation, transmission and emission of micropressure waves for tunnel designers to be able to determine whether further more detailed studies are required. Some empirical inputs are required for the theoretically derived equations used.

12.5.2 Methods for micro-pressure wave alleviation

From the above description and Eq. (6.2), the gradient of the pressure front arriving at the exit portal generated by the train entering the tunnel determines whether there will be a noise problem associated with the micropressure wave outside the tunnel. Therefore, reduction of this gradient

is the aim of micropressure wave alleviation. This can be addressed when the entry pressure wave is generated, as the wave travels along the tunnel or at the exit portal itself. Vardy (2008) provides a good engineering discussion of methods that can be applied.

The aim of modifying the entry pressure wave is to reduce the initial gradient of the wave sufficiently that, despite any subsequent wave steepening that may occur during transmission, the gradient of the exit portal pressure wave is not great enough to result in a noise problem outside the tunnel. There are two ways of accomplishing this at the entry portal: one by reducing the wave front amplitude or the second by increasing the time over which it reaches its maximum amplitude.

Ozawa (1984), Ozawa and Maeda (1988) and Ozawa et al. (1991) describe the approach used in Japan to address the problem using tunnel extensions ('hoods') located at the entry portal of between 18 and 70 m in length, dependent on train speed, see examples in Fig. 12.11A. These typically have cross-sectional areas 1.3—1.5 times the tunnel cross-sectional

Figure 12.11 ***Example of tunnel entrance portal hoods.*** (A) Japanese hoods; (B) German hoods. *(A) Used with permission from Tokuzo Miyachi of JRRI, (B) Photographs by Michael Hieke, DB, used with permission.)*

area and have a number of window-like apertures in their sides, which allow air and pressures to escape through them as the trains enter. The size and distribution of these apertures was originally determined via trial-and-error testing using moving model rigs (Maeda et al., 2000). The hoods reduce both the amplitude and the maximum gradient of the train entry pressure wave.

These devices have proved very effective in reducing micro-pressure wave noise problems for Shinkansen tunnels for train speeds up to 250 km/h. The use of tunnel hoods has been widely taken up and studied in other countries since then, e.g., Liu et al. (2010), Hieke et al. (2011), Rety and Gregoire (2002). A typical German examples are given in Fig. 12.11B.

Johnson (2001) presents pressure results described in Johnson and Dalley (2000) obtained from moving model tests of a tunnel with a 50 m entrance section having a range of porosities, see Fig. 12.12A. It was shown that when the porosity is 0.25 m^2/m, the initial pressure gradient is reduced by almost 70% compared with the zero porosity entrance section. This suggests that the use of porous entrances is a viable way of addressing the problem. Fig. 12.12B shows more recent modelling work on a rectangular hood of varying area and porosity, used to help develop tunnel hood designs for the HS2 project in Great Britain (HS2, 2014; Sturt et al., 2015).

Even the shape of the tunnel portal can have a beneficial effect on reducing the initial pressure wave gradient. Réty and Gregoire (2002), for example, found that a scarfed portal, i.e., one having a sloped entrance, reduced the pressure wave gradient by 17% compared with a portal with a vertical plane face. Other investigations of the impact of tunnel portal design include Zhang et al. (2018c), who describe work including CFD and

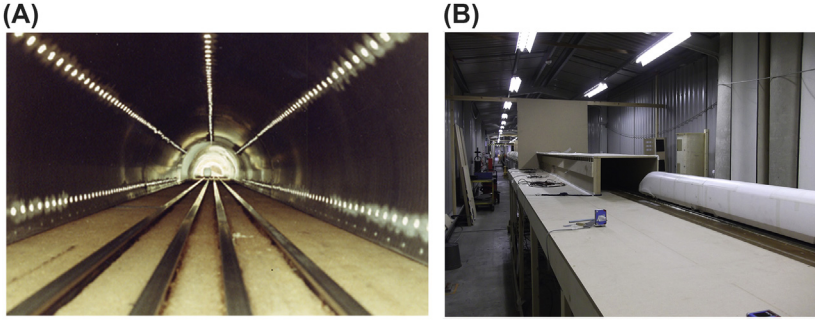

Figure 12.12 ***Physical model testing of tunnel hoods.*** (A) View inside the model porous tunnel section; (B) rectangular porous hood model for HS2. *(B) Used by permission of HS2.)*

moving model tests. Miyachi et al. (2016) describe full-scale tests of the effect of two tunnel hood designs on the generation of the initial compression wave generated by the entrance of the train.

However, where space is limited at tunnel entrances or as further speed increases have been planned, these hoods cannot deliver sufficient alleviation and attention has shifted in Japan to the design of the leading vehicle of trains. Kikuchi et al. (2011) and Muñoz-Paniagua et al. (2014), among others, have numerically investigated the optimum variation of the cross-sectional area of a train nose to reduce the maximum pressure gradient of the initial pressure wave for tunnels with and without entrance hoods. Such studies have led to the development of long, rather exotic looking train nose shapes on Japanese high-speed trains, e.g. see Fig. 12.13.

Another potential way that train operations can influence the initial pressure wave gradient is suggested by Vardy (2008). He notes that the pressure gradient can be significantly reduced by slowing down train speeds on entry to tunnels, due to an approximate dependence on the cube of train speed, and that this speed reduction needs only to be applied as the train enters the tunnel. For example, a train speed reduction on tunnel entry from 300 to 250 km/h is calculated to reduce the pressure gradient by 40% at the cost of less than 5 s in journey time.

A way in which pressure wave gradients can be limited during pressure wave transmission along tunnels is by installing shafts or side-branches to them. These fragment wave fronts due to the wave action in them, reducing the amplitude of the transmitted wave. As complexity in wave patterns increases with the introduction of these devices, there is the possibility that pressure wave gradients may not necessarily decrease at the tunnel exit portal, and so specific studies are advisable to ensure the benefit is actually derived.

Figure 12.13 JR East E5. *(Attribution-ShareAlike 3.0 Unported (CC BY-SA 3.0).)*

A second way that pressure wave gradients can be reduced during wave transmission is by using ballast. There seems to be no evidence of micro-pressure wave problems in tunnels with ballasted track, so introducing ballast into slab track tunnel will reduce the tendency for problems to occur. There is no clear understanding of how ballast influences the transmission of pressure waves. Vardy (2008) suggests that wave fronts moving along tunnels with ballasted track reach an equilibrium situation in which the tendency for the wave to steepen is balanced by the effect of the ballast spreading out the pressure wave. This means it is difficult to determine the optimal degree of ballasting to minimise micro-pressure wave problems in otherwise slab-tracked tunnels. However, there is practical evidence that mixing track types up in this way can be used to alleviate the problem, Mancini and Violi (1999).

In December 2005, test runs were being undertaken on a high-speed line in Germany, linking Nuremberg and Ingolstadt, when loud sonic booms occurred at the portals of the Euerwang and the Irlahüll tunnels. These were, respectively, 7700 and 7260 m long. Both were originally planned to be fitted with ballasted track but were changed to be slab track without any changes to the design to avoid micro-pressure wave issues. To reduce micro-pressure wave emissions, it was decided to equip the two tunnels with acoustic track absorbers, between and either side of the rails. These absorbers are designed not only to counteract railway noise but also to affect the pressure wave steepening process by dispersion and friction. So the use of such acoustic material is another way to prevent wave steepening during transmission of pressure waves along tunnels.

Other devices have been proposed to prevent pressure wave steepening at tunnel exit portals by introducing additional local wave interactions. Ehrendorfer and Sockel (1997) undertook model scale experimental and numerical studies of chamber structures at the exit portal to investigate their impact on emitted micropressure wave amplitudes outside a tunnel. Some of the structures considered are shown in Fig. 12.14. The types that were horizontally split were found to be effective as long as the dimensions of the chamber and the upstream pressure wave are of the same order.

Pesava and Sockel (2000) undertook a combined model scale experimental and numerical study of baffle plates introduced into a tunnel to determine effect on propagated pressure gradient. Different tunnel blockages and baffle separations considered. Baffle plates with 15% reduction of tunnel cross-sectional area and close spacing led to suppression of wave steepening.

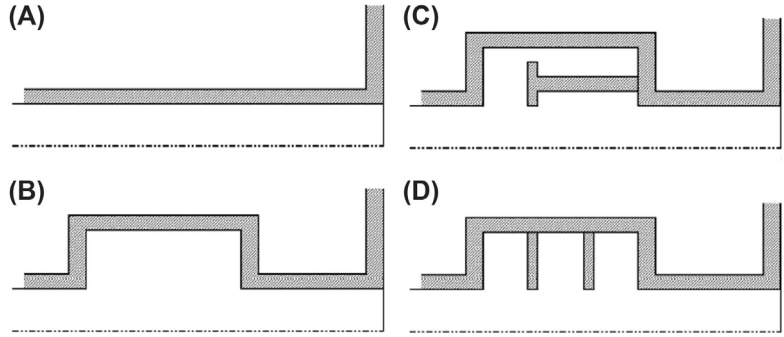

Figure 12.14 ***Exit portal chambers considered by Ehrendhorfer and Sockel (1997).*** (A) Plain tunnel, (B) plain chamber, (C) horizontally split chamber, (D) vertically split chamber.

Another way that is being studied to reduce micro-pressure wave emissions by modifying the incident wave front at the exit portal is by the use of active pressure control. Matsubayashi et al. (2004) describe experiments in which servo-actuators and air tanks were installed in a side-branch at the end of a model tunnel. When an entry pressure wave is detected passing an upstream monitoring point, air is released from the high-pressure air tanks ahead of the advancing wave. The effect of this is to reduce the overall pressure gradient of the combination pressure wave as it reaches the exit portal. Other active pressure control methods have been proposed which act in a similar way to noise cancelling devices and aim to generate pressure changes equal to and opposite from the transmitted pressure wave. Drawbacks of all such devices in practice are that they are mechanical and subject to failure and also require regular maintenance.

12.6 Aerodynamic drag in tunnels

The subject of aerodynamic drag for trains in open air is addressed in detail in Chapter 7. It was pointed out there that drag or resistance is the force on a train resisting its forward motion and arises from mechanical and aerodynamic processes. The mechanical resistance is unaffected by travelling in a tunnel, but the aerodynamic drag increases. The latter is proportional to the square of train speed and consists of the following:

- pressure drag, caused mainly by the pressure difference between the nose of the train, where pressure is high, and behind the tail of the train where the pressure is low. Pressure drag will increase if the nose and tail

of the train are unstreamlined. Components of the train, such as pantographs, intercar gaps and bogie design, will also add to the pressure drag.
- Skin friction drag, which arises from shear forces acting on the train surface. The train surface finish, intercar gap and bogies all contribute to skin friction drag.

In tunnels, these constituents of aerodynamic drag increase because of the constraints of the tunnel walls on the airflows around the trains. In particular, the boundary layer thickness is forced to be constant along the train, except near the train nose and thus the pressure varies along the length of the train. This increases the pressure differences between the front and rear of the train increasing pressure drag. The presence of the tunnel wall, where the air speed must be zero, changes the gradient of the velocity at the train surface and thus the shear force acting on the train surface. Additionally, air speeds around and over the train surface are increased in a tunnel; both effects increase skin friction drag.

The aerodynamic drag of a train in a tunnel is not constant but varies during the transit through the tunnel. Fig. 12.15 shows an example of the variation of the aerodynamic drag coefficient (defined as in Section 2.2 for a train travelling at constant speed). The drag coefficient rises at first from its initial value until 4 s, when the train tail enters the tunnel. Variations of the drag coefficient occur thereafter as pressure waves move up and down the tunnel and the local air speed around the train varies. The balance between pressure drag and skin friction drag thus varies along the tunnel.

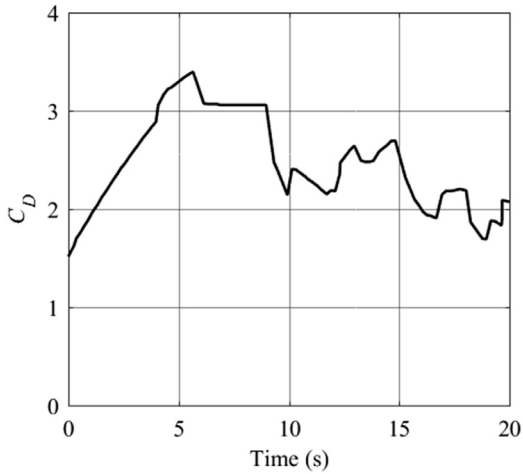

Figure 12.15 Example variation of aerodynamic drag coefficient for a train in a tunnel. *(From Sockel (2003) with a Mach number of 0.3 and a blockage ratio of 0.18.)*

Whilst train aerodynamic drag in tunnels can be many times that of trains in the open air, with the subsequent increase in traction energy being required, it is generally only considered if there are long tunnels on a particular route.

12.7 Structural loading in tunnels and on trains

In the previous sections of this chapter, we have seen that trains travelling singly or crossing in tunnels generate aerodynamic pressures and airflows in the tunnels. In addition, trains also generate static pressure pulses, primarily associated with the nose and tail passing. These effects will generate loads on trackside objects in a tunnel as the train passes or on the train itself and have to be considered in the design of tunnel equipment and the train structure.

When considering aerodynamic exceptional and fatigue loads, all load sources need to be considered for the lifetime of the train for some notional operation, and determining a representative set of open air and tunnel scenarios to consider poses a significant problem. An attempt to address this is given in CEN (2010b).

For the train structure, the pressure loads caused by pressure waves are most important and will act positively and negatively on the train surfaces. The pressures inside the train will vary with the external pressure distribution, but with some delay depending on the degree of pressure sealing of each vehicle. The net load on the structure will then be the difference between the internal and external pressures at any given time.

The aerodynamic pressures may not produce the most significant exceptional load case for the train structure as a whole but should be considered for train components such as doors, windows, gangways, etc. For fatigue load calculations, both tunnel pressure transients and open-air train passing loads have to be considered (Section 8.5). The relevant load effects on the body structure have to be appropriately combined using e.g. a rainflow analysis of the relevant pressure curves (see for instance Downing and Socie, 1982).

For equipment and infrastructure installed in tunnels, both pressure and airflow effects may be relevant for the design. Any closed structures that have sealed enclosed volumes should consider pressure loads generated by the pressure waves in their design. Structures, such as signals or gantries, have to withstand the train-induced air speeds and require the determination of a suitable drag coefficient to combine with the square of the air speed and the structure area to evaluate the induced wind load.

12.8 Special problems with long tunnels

Long tunnels pose problems additional to those of normal length tunnels. These will be illustrated by reference to two specific long tunnels: the Channel Tunnel between England and France, and the Lötschberg Tunnel in Switzerland.

The Channel Tunnel is a twin-bore tunnel, 50.45 km in length in which trains travel at a maximum speed of 160 km/h (Kirkland, 2002; Wikipedia, 2018a). The running tunnels are 7.6 m in diameter and are 30 m apart. Between the running tunnels is a 4.8 m diameter service tunnel. This tunnel is linked to the running tunnels at 375 m intervals by cross-passages, which are closed during normal operations. In addition, 2 m diameter piston relief ducts link the two running tunnels every 250 m (see Fig. 12.16).

Several problems had to be addressed during the design of the Channel Tunnel. The first was to reduce the aerodynamic drag of trains travelling through the Tunnel. If trains had to travel through a single-bore tunnel from England to France, significant energy would be required to overcome the drag; air would, however, be induced to run through the tunnel and provide some ventilation. The solution was to introduce the piston relief ducts, which allowed air to flow into the second running tunnel ahead of the train in one running tunnel and back from the second tunnel into the first behind the train. In the first instance, this design led to unacceptably high air speeds in the ducts with high loads imposed on the trains, until flow restrictors were installed where the ducts joined the running tunnels and train speeds were reduced. The ducts led to the second problem, which was for adequate ventilation of the tunnel, as air heated by the traction equipment and drag would not be forced through the tunnel by the piston effect of the trains.

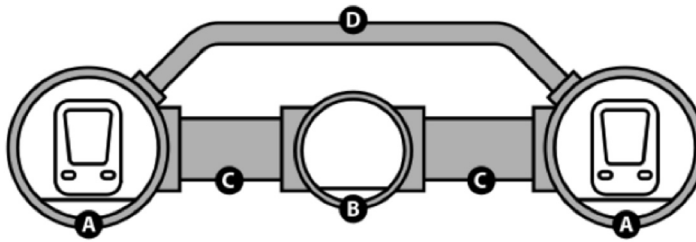

Figure 12.16 ***Typical Channel Tunnel cross section.*** (A) Running tunnel, (B) service tunnel, (C) cross-passage, (D) piston relief duct. *(Public domain https://commons.wikimedia.org/w/index.php?curid=3581241.)*

Two factors had to be considered in the design of the ventilation system. One was the ventilation requirement in normal operations and the second was for emergency conditions such as a fire in one of the running tunnels. During normal operations, the air pressure is maintained at a higher value in the service tunnel than in the running tunnels to preclude smoke entering the service tunnel if there is a fire. The service tunnel would be used as a safe space for the emergency evacuation of detrained passengers during a fire. The ventilation system is required to maintain safety and comfort and is supplied by shafts from each end of the Tunnel at Shakespeare Cliff and Sangatte. If there is a fire in the tunnel, the ventilation system keeps smoke from the service tunnel and drives air in one direction in the tunnel bore containing the fire, permitting clean air for passengers escaping from the train.

A second aspect of tunnel cooling was the use of water pipes in each running tunnel, through which chilled water from refrigeration plants at each end of the tunnel is pumped to help limit Tunnel temperatures to 30°C.

Finally, three pumping stations have been installed to remove rainwater and water infiltrating from the undersea rock strata out of the tunnel.

Despite these problems being related to ventilation, cooling and safety management, they had to be considered and refined with the tunnel aerodynamics issues as the latter have direct influences on the problems.

The second long tunnel we will consider is the Lötschberg Tunnel, which is half-finished because of financing problems, but nevertheless opened for traffic in 2007. It currently consists of a single-track bore for about 20 km, which then becomes two single-track bores for about 14 km, and has a total length of 34.6 km. The single-bore section will be converted to twin bore in the future. Traffic travels in the tunnel at up to 250 km/h (Wikipedia, 2018b; BLS Ltd, 2018).

Along the tunnel the altitude varies between 654 and 828 m and the line gradient varies between 3 and 13%. The major issue was that the tunnel runs through geothermal rock, and a peak rock temperature of about 40°C was expected before construction. Naturally occurring water in the rock strata was estimated to have temperatures of between 19 and 22°C. It is Swiss practise to make use of this geothermal heat by extracting it from infiltrating water, Wilhelm and Rybach (2003).

The Lötschberg Tunnel shares many of the design issues seen in the Channel Tunnel. The tunnel is equipped with three ventilation control centres: two air supply centres and one air extraction centre. In addition, there are eight jet ventilators at each of the tunnel entrances. The different ventilation options permit a range of ventilating modes to meet

various operating scenarios. The air supply centres supply fresh air, which is particularly important during maintenance of the tunnel. However, air extraction is only used to remove polluted air through a ventilation shaft, such as smoke, during emergencies.

As may be imagined, the climatic conditions in the base tunnel are hot and very humid. 44 refrigeration units and 396 air circulation cooling units ensure a stable climatic environment for personnel and electronic equipment. Maximum temperatures in the tunnel are limits by the cooling units to a maximum of 31°C.

Water, including infiltrating heated mountain water, in the tunnel is managed in an environmentally friendly way and is separately treated depending whether is clean or polluted. The actual temperature of the clean mountain water is about 18°C, and it is collected in the tunnel and is used for cooling. Polluted tunnel waste water is channelled into containment tanks for checking for contaminants.

The important lesson for long tunnels is that whilst aerodynamics issues are still important, there may be other aspects which have to be considered, and a system approach to the design has to be taken.

CHAPTER 13

Emerging issues

13.1 Future context

In this chapter, we will look forward to the aerodynamic issues that might be expected to emerge in the railway of the future. This is a process fraught with difficulty, and perhaps the only thing that can be said with any certainty is that future predictions of this sort will never be wholly correct. Whilst other chapters in this book will, it is hoped, retain their relevance for some years, this chapter is likely to go out of date very quickly.

That being said, the following fairly general comments that can be made concerning the future context for rail travel over the next few decades.

- There will be increasing pressure for a reduction in carbon-based transport energy consumption, both because of supply issues and because of the need to minimise carbon production to mitigate against climate change effects. This will lead to the need to maximise the capacity of non−carbon based transport modes.
- The effects of climate change will become increasingly significant for transport networks, particularly in terms of an increased frequency of extreme weather events.
- There will be an increasing pressure to improve air quality, particularly in urban areas where poor air quality is a cause of large numbers of early deaths.
- The development of new materials will result in lighter vehicles.
- New conventional speed forms of rail-based transport are likely to be developed, particularly arising from current research on autonomous vehicles.
- New very high-speed modes of transport will be developed, partly in response to some of the above issues and partly because technological advances make them possible.

In the sections that follow, we consider what might be the aerodynamic issues that will need to be addressed in the light of these developments. We will consider, firstly, in Section 13.2, how the tools and techniques that are

Train aerodynamics
ISBN 978-0-12-813310-1
https://doi.org/10.1016/B978-0-12-813310-1.00013-7

used to address aerodynamic issues might change. These developments will all be underpinned by developments in digital technology, both in terms of processing power and in terms of full-scale data acquisition systems. We then move on to consider specific issues outlined above – reducing energy consumption and maximising capacity (Section 13.3); the development of resilient rail networks (Section 13.4); air quality issues (Section 13.5); the use of new materials (Section 13.6), new conventional speed transport systems (Section 13.7) and very high-speed transport (Section 13.8).

13.2 Tools and techniques

Since the early days of the development of CFD, there has been an ongoing expectation that such techniques will replace physical model testing within the next decade, but the 'decade' has expanded somewhat, and with the present state of development of CFD, the study of train aerodynamics still requires the use of wind tunnel and other physical modelling techniques, particularly where unsteady turbulent flows need to be studied. Thus, whilst CFD techniques can now routinely be used for predicting trackside pressures and loading on simple trackside structures (Yang et al., 2015), for the prediction of train drag (Maleki et al., 2017), for optimising nose shapes (Krajnović, 2009a,b), the flow around trains in tunnels (Forasassi, 2016) and to some extent for predicting crosswind force and moment coefficients (Eichinger et al., 2015), they are as yet unable to deal with unsteady crosswind loading on trains; the prediction of unsteady slipstream effects; complex and unsteady train underbody flow and so on. In particular, the modelling of atmospheric turbulence and shear and the interaction of such flows with trains are very challenging because of the large range of turbulent scales of importance. Even where CFD methods can be used, they are resource intensive, and care is required to ensure that the modelling is carried out robustly. However, developments in unsteady CFD methodologies are progressing very rapidly, and unsteady large eddy simulation and detached eddy simulation methodologies are more and more able to be used at higher and more realistic Reynolds number. It can be expected that the next decade will really be the time when the capabilities of CFD will reach a level sufficient of reliability to replace the necessity for physical model tests in many areas, although those areas where consideration of highly complex and unsteady turbulence flows are of importance will probably still require physical modelling.

That being said, CFD calculations are as much a model of reality as are physical model tests and still need calibrating against some sort of

fundamental truth. So whilst we may well see a movement away from physical model testing to CFD analysis, there will be a continuing need for full-scale experimentation to provide the necessary calibration data. The need for this is made graphically clear by the full-scale measurements of crosswind effects by Gallagher et al. (2018) described in Chapter 11, where both physical model tests and CFD simulations were at best shown to give only a reasonable representation of the highly complex and transient flow around trains. Such full-scale tests are expensive and complex — and will almost certainly require high levels of national and international, academic and industry co-operation. However, there have been significant developments in instrumentation technology and analysis methodologies for such complex experiments, and it is likely that it will become easier to instrument service trains and obtain large amounts of aerodynamic data remotely via wireless links. Real-time monitoring of aerodynamic and other effects will also lead to significant improvements to inspection and maintenance regimes for both rolling stock and infrastructure.

Over recent years, results from CFD, physical model testing and full-scale testing have been used to develop robust codes of practise and this work will continue. In Europe, this will involve the further development of the CEN aerodynamic standards, and in particular the inclusion of CFD-based methods in areas where they are currently not included. Note that the use of these standards is not confined to Europe, but they are also used in an increasing number of other countries around the world.

13.3 Reducing energy consumption and maximising capacity

The need to reduce transport carbon-based energy consumption can be expected to lead to a modal shift from road to rail, the latter, in principle at any rate, being the more energy efficient mode and for which a range of non—carbon based power systems are available. This will lead to continued pressure to reduce the aerodynamic resistance of trains to enhance this efficiency, which will require more detailed aerodynamic design of even low-speed conventional trains. Orellano and Sperling (2009) suggest there is significant scope for drag reduction for such trains, with resultant lower energy consumption. Novel drag reduction methods might also become of use, such as the plasma actuator methods described by Park et al. (2013), but there are significant practical and operational obstacles to the deployment of such methods.

Any modal shift to rail will of course result in capacity issues and thus the need to use the existing network more efficiently. In terms of future aerodynamic issues, at a mundane level it can be expected that there will be more emphasis on understanding the aerodynamic behaviour of conventional passenger and freight train designs, which are likely to be required to run at higher speeds, with larger vehicles, on networks that were not designed for such sizes and speeds. Work will also be required to investigate the pressure and slipstream loads on trackside structures caused, at least in the short term, by complex and aerodynamically rough freight trains running at enhanced speeds (see Soper et al., 2014 for example) and to investigate the behaviour of such freight trains in relatively high blockage tunnels, in terms of pressure wave generation and drag. Similarly more attention needs to be paid to aerodynamic loading in terms of the maintenance and the design of trackside structures, which can have nominal design lives of decades, during which train types, speeds and the nature of the network operation can change significantly.

13.4 Resilient rail networks

To maximise the capacity of the existing network, work will also be required to improve the resilience of the system to environmental shocks. In aerodynamic terms, this mainly implies increasing system resilience to wind effects, through better understanding of pantograph dewirement (Section 10.6), tree fall on the railway (Johnson, 1996), tree and vegetation management and remote monitoring of tree fall and debris movement onto tracks (RSSB, 2018). In terms of nonconventional vehicles, Britcher et al. (2012) show that urban maglev vehicles, if they run on elevated tracks, may suffer significantly from crosswind effects, which could cause substantial redistribution of the levitation forces. Further refinement to wind warning systems will be also be required so that short-term real-time warnings can be incorporated into traffic operations, even on high capacity and heavily congested networks – see Section 11.10.

As railways develop around the world, there are more and more developments in areas where wind-blown sand in extreme weather conditions is an actual or potential problem (Bruno et al., 2018). The problems on the Qinghai–Tibet railway, where train windows have been broken by sand and stone particles picked up in high winds, show this problem at its most extreme (Xiong et al., 2011; Cheng and Xue (2014); Xie et al., 2017).

However, there are other, less-dramatic issues, with sand being blown onto tracks, sand ingested into engines, etc., all of which pose significant aerodynamic challenges that will need to be addressed (Paz et al., 2015).

13.5 Air quality

It is likely that there will be an increased pressure to minimise the negative effects of trains on air quality. There are increasing problems in major cities, and emissions from transport have recently become a major issue in many parts of the world, with the recognition that such emissions cause significant health hazards and excess deaths in many countries (DEFRA, 2017). Air quality research in the railway environment is at an early stage, but there are indications of very high levels of the oxides of nitrogen and particulate matter, mainly from diesel trains, in main line railway stations (Hickman et al., 2018) and subway stations and tunnels (Aarnio et al., 2005; Cha et al., 2016; Kam et al, 2011; Onat et al, 2014; Querol et al., 2012). The particulate matter from rail, brake and pantograph wear (and thus trains of all types) is of concern in some places because of its carcinogenic effects (Abbassi et al., 2011; Bukoweicki et al., 2007). The airflow around and under trains is one of the major factors in the dispersion of such pollutants, but its role is little understood. Work is required on how relatively slow-moving trains disperse pollutants within station environments and how trains of all types and speeds disperse pollutants both in tunnels and on the open track — see Gerhard and Kruger (1998) for some early work on this aspect. In parallel to this, further developments of station air conditioning systems are required to take more account of the removal of pollutants, as well as the provision of clean air, and to lower the high temperatures that occur during summer on some underground railway networks. This is of particular importance for underground railways of course (Lin et al., 2008). Also, the importance of providing clean air to passenger and driver compartments of trains is becoming clearer, with some recent measurements on a commuter train in Great Britain showing high levels of cabin pollutant, even on electric trains (BBC, 2016; Fridell et al., 2010). BBC (2019) in the United Kingdom, Fridell et al. (2010) in Sweden and Cheng et al. (2012) in Taiwan also report enhanced particulate and carbon dioxide levels inside commuter trains and highlight the need to control the resuspension of particulate matter by trains.

13.6 New materials

Very significant advances have been made in the field of materials science in the last few decades, and a range of lightweight, strong and environmentally sustainable materials have been developed and are likely to find a use in the railway environment (Arup, 2014). In aerodynamic terms, lighter trains will have lower rolling resistance, and thus aerodynamic drag will become of greater overall significance. Also, lightweight trains will be more susceptible to wind-induced accidents.

13.7 New conventional speed forms of transport

The digital revolution is likely to have a major effect on rail operations over the coming decades. One of the major developments is likely to be in the field of autonomous transport technology, facilitated by rapid, high broadband digital technology. Such technology may well lead to a blurring of the lines between public and private transport and between road and track based transport, with small personal or public rapid transit vehicles running at a range of speeds on roads or tracks, often in platoon formation, bringing all the aerodynamic issues that are involved in the running of vehicles in close proximity (see ULTRA (2018) for details of the Heathrow Airport system and Daimler (2018) for the Mercedes-Benz FutureBus for example). Such systems may well replace less highly used rail systems and in some ways can naturally be considered as a new generation of train-like vehicles. Work is also underway in Great Britain to look at high-speed coupling and uncoupling of high-speed rail vehicles using modern wireless communications, and Le et al. (2015) report on a study of 'virtual coupling' with vehicles running close together in close wireless communication. The concept of lorry platoons has also reached the stage where on-road tests are possible (TRL, 2018) and here again we see an example of road vehicles becoming conceptually very close to rail vehicles, with a lorry platoon looking very similar to a freight train. There is thus the need to understand the aerodynamic issues associated with high-speed road and rail vehicles moving in close proximity. These issues include the effect of impinging wake flows on trailing vehicle stability (Tsuei and Savos, 2001), the growth of slipstreams, the nature of the pressure loading on trackside structures as platoons pass, pollutant dispersion, aerodynamic noise, etc. Also, there are suggestions that, to reduce urban congestion, such vehicles could run in platoon formation in high blockage tunnels (Guardian, 2016), which again would result in a range of aerodynamic issues that would need to be considered. Similar schemes for urban rail freight tunnels are being

advanced by a number of organisations (Arup, 2014), and even though these might be relatively low speed, the confined nature of the flow may well lead to significantly increased aerodynamic drag.

13.8 Very high-speed transport

The need for reduced journey times to facilitate modal shift, particularly from air for medium-haul international journeys, is often put forward as an incentive for the development of very high-speed vehicles with speeds of above 400 km/h. Maglev trains, for example, have undergone significant development over recent decades and high-speed services are now operational in China and Japan (Railway Technology, 2018a, b), and speeds of above 600 km/h have been recorded. Maglev developments in Europe, however, have come to a halt following the 2006 accident in Germany (Guardian, 2006). Tielkes (2006) points out that the aerodynamic issues are similar to those of current high-speed vehicles, although much more severe, particularly with regard to tunnel aerodynamics as blockage ratios for recently designed systems tend to be higher than for conventional trains. The high speeds of such vehicles also have the potential to cause structural deformations to trackside infrastructure or to vehicles passing in the opposite direction (Monaco and Dignath, 2008). There are also potential issues of vibration, particularly when cornering in a crosswind, which have been addressed in a preliminary fashion by Han and Kim (2017).

Finally, there is the possibility that evacuated tube transport might become viable for very long distance, very high-speed transport — see for example Kim et al. (2011). The most high-profile example of such systems is the Elon Musk Hyperloop scheme described in Spacex (2018). In this system, it is proposed that 2.2 m diameter capsules, 10—15 m in length, will run in tubes with pressures of around 1 mbar at speeds of over 700 km/h, supported on an air cushion and propelled by linear induction motors. The major issues here are at a system level — constructing the infrastructure, maintaining the vacuum, safety issues, etc (Guardian, 2017). Also, the capacity of such systems is relatively small — one Hyperloop tube has roughly 10% of the capacity of a high-speed rail line. The aerodynamic problems of such schemes are formidable, with complex transonic flows predicted around the proposed vehicles, the potential for flow instabilities, the transmission of pressure waves in the near vacuum, and these will require detailed aerodynamic design to ensure acceptable performance in terms of drag and ride quality (Braun et al., 2017).

But such considerations bring us back almost to where we began. The use of low-pressure tubes has a long history, and some of the early developments outlined in Chapter 1, in particular George Medhurst's evacuated tube railway scheme of 1812 and Alfred Beach's Pneumatic Pneumatic Railway in New York in 1869 are eerily similar to what is being currently proposed. Whether schemes such as Hyperloop represent progress or regress is left for the reader to decide.

APPENDIX 1

Train information

This Appendix presents some basic information concerning most of the trains that appear in the text, arranged in the four categories used throughout the book: high-speed passenger trains, medium-speed passenger trains, low-speed passenger trains and freight locomotives. Within each category, the trains are arranged by order of the country where they operate. There is one exception to this categorisation — all Shinkansen trains have been placed in the high-speed category, even though some of the earlier series fit into the medium-speed category.

HIGH-SPEED PASSENGER TRAINS

Train		Normal maximum service speed (km/h)	Service dates	Configuration	Manufacturer	Country of operation
CRH2		380	2007–Present	8 or 16 passenger cars	Kawasaki/ CRRC	China
CRH3 velaro		380	2007–Present	8 or 16 passenger cars	Siemens/ Tangshan	China
CRH380A		350	2010–Present	8 or 16 passenger cars	CRRC	China
ICE1		280	1990–Present	2 power cars + 12 passenger cars	Siemens	Germany
ICE2		280	1995–Present	2 power cars + 7 passenger cars	Adtranz/ Siemens	Germany

Train		Normal maximum service speed (km/h)	Service dates	Configuration	Manufacturer	Country of operation
ICE3 velaro		330	2000–Present	2 power/passenger cars + 6 passenger cars	Siemens	Germany
Class 373 TGV		280	1994–Present	2 power cars + 16 passenger cars	GEC Alstom	Great Britain/France
Class 374 velaro		320	2015–Present	2 power cars + 14 passenger cars	Siemens	Great Britain/France
V250		250	2012–2013	8 passenger cars	AnsaldoBreda	Holland
ETR 480 pendolino		250	1997–Present	9 passenger cars	Fiat ferroviaria/Alstom	Italy
ETR 500		360	2000–Present	11 cars	Trevi	Italy
ETR 1000-v300 zefiro		400	2015–Present	2 power cars + 8 passenger cars	AnsaldoBreda/Bombardier	Italy
AGV		360	2012–Present	7 passenger cars	Alstom	Italy
Shinkansen series 0		220	1964–2008	4, 6, 8, 12 or 16 passenger cars	Hitachi + others	Japan

Train		Normal maximum service speed (km/h)	Service dates	Configuration	Manufacturer	Country of operation
Shinkansen series 100		220	1985–2012	4, 6, 12 or 16 passenger cars	Hitachi + others	Japan
Shinkansen series 200		240	1982–2013	8, 10, 12, 13 or 16 passenger cars	Hitachi + others	Japan
Shinkansen series 300		270	1992–2012	16 passenger cars	Hitachi + others	Japan
Shinkansen E5 series		320	2009–Present	2 end cars and 8 intermediate cars	Hitachi + others	Japan
KTX TGV		305	2004–Present	20 passenger cars	Alstom/ Rotem	South Korea
HEMU-430x		370	2012–2015	8 passenger cars	Hyundai Rotem	South Korea
S100 TGV		300	1992–Present	2 power + 8 passenger cars	Alstom/ CAF	Spain
S102 talgo		330	2005–Present	2 power + 12 passenger cars	Talgo/ Bombardier	Spain
S103 velaro		350	2007–Present	2 power/ passenger + 6 passenger cars	Siemens	Spain

Train		Normal maximum service speed (km/h)	Service dates	Configuration	Manufacturer	Country of operation
S104		250	2005–Present	2 power/passenger + 2 passenger cars	Alstom/CAF	Spain
S120		250	2006–Present	4 passenger cars	CAF/Alstom	Spain
S130 talgo		250	2010–Present	2 power + 9 passenger cars	Talgo/Bombardier	Spain

MEDIUM-SPEED PASSENGER TRAINS

Train		Normal maximum service speed (km/h)	Service dates	Configuration	Manufacturer	Country of operation
IC4		200	2007–Present	4 cars	AnsaldoBreda	Denmark
RevCo driving trailer		200	1975–Present	Passenger cars with locomotive and driving trailer	Societe franco-Belge/Alstom	France
ZTER		200	2003–Present	3 passenger cars	Alstom/Bombardier	France
ICE-T pendolino		230	1999–Present	7 or 5 passenger cars Tilting	Siemens	Germany

Train		Normal maximum service speed (km/h)	Service dates	Configuration	Manufacturer	Country of operation
InterRegio - Bimdzf269 driving trailer		200	1995–Present	Operates with locomotive and carriages		Germany
APT		200	1980–1986	14 passenger cars Tilting	BREL	Great Britain
Class 43 HST		200	1975–Present	2 power cars + 4–9 passenger cars	BREL	Great Britain
Class 221 voyager		200	2001–Present	4 or 5 passenger cars. Titling	Bombardier	Great Britain
Class 390 pendolino		200	2002–Present	9 or 11 passenger cars Tilting	Alstom	Great Britain
Class 89 locomotive		201	1987–2002	Locomotive plus coaches	BREL	Great Britain
Class 90 locomotive		180	1987–Present	Locomotive plus coaches	BREL	Great Britain
Class 91 locomotive plus coaches (IC225)	 	225	1989–Present	Class 91 locomotive, 9 mark 4 coaches and driving trailer Top figure shows locomotive, bottom figure shows driving trailer	Brel/GEC-Alstom/ Metro-cammell	Great Britain

Train		Normal maximum service speed (km/h)	Service dates	Configuration	Manufacturer	Country of operation
Mark 3 coach		200	1975–Present	Coach	BREL	Great Britain
S252 locomotive		200	1991	Locomotive	CAF/ Siemens	Spain
X2/X2000		200	1990	Locomotive plus variable number of carriages Tilting	Asea Brown Boveri/ Adtranz	Sweden

LOW-SPEED PASSENGER TRAINS

Train		Normal maximum service speed (km/h)	Service dates	Configuration	Manufacturer	Country of operation
M6BX		160	2007–Present	Locomotive, driving trailer and double deck coaches	Bombardier	Belgium
AGC		160	2004–Present	3 or 4 cars	Bombardier	France
BR440		160	2008–Present	3 passenger cars	Alstom	Germany
DOSTO BR111	 	160	2005–Present	Loco, double deck coaches and driving trailer Top figure shows locomotive, bottom figure shows driving trailer	Bombardier	Germany

Train		Normal maximum service speed (km/h)	Service dates	Configuration	Manufacturer	Country of operation
Silberling BDnrzf 740 driving trailer		160	1971–1977	Operates with locomotive and carriages		Germany
VT612		160	1998–Present	2 passenger cars Tilting	Adtranz/ Bombardier	Germany
Derby lightweight dmu		100	1954–1969	2 or 4 passenger cars	British Rail	Great Britain
Class 141 dmu pacer		120	1984–1997	2 passenger cars	British Leyland	Great Britain
Class 158 dmu		140	1990–Present	2 or 3 passenger cars	BREL	Great Britain
Class 165 dmu		145	1990–Present	2 or 3 passenger cars	BREL	Great Britain
Class 319 emu		160	1987–Present	4 passenger cars	BREL	Great Britain
Class 325 emu		160	1995–Present	4 passenger or parcel cars – can run as two or three coupled units	ABB Derby	Great Britain
Class 350 emu desiro		160	2005–Present	4 passenger cars	Siemens	Great Britain

Train		Normal maximum service speed (km/h)	Service dates	Configuration	Manufacturer	Country of operation
Class 357 emu		160	1999–Present	4 passenger cars	Adtranz/ Bombardier	Great Britain
AREX 1000 (incheon airport express)		110	2006–Present	6 passenger cars	Hyundai Rotem	South Korea

FREIGHT LOCOMOTIVES

Train		Normal maximum service speed (km/h)	Service dates	Configuration	Manufacturer	Country of operation
Class 47 locomotive		120	1962–Present	Locomotive	Brush	Great Britain
Class 50 locomotive		160	1967–1994	Locomotive	English Electric	Great Britain
Class 66 locomotive		120	1998–Present	Locomotive	EMD	Great Britain

The license details for the above pictures can be found at the following links.

S100 TGV - https://commons.wikimedia.org/wiki/File:Renfe_AVE_S-100_Sevilla_Santa_Justa.JPG

S102 Talgo - https://commons.wikimedia.org/wiki/File:AVE_Tarragona-Madrid.jpg

S103 Velaro - https://commons.wikimedia.org/wiki/File:RENFE_Class_103_Vinaixa.jpg

S104 - https://commons.wikimedia.org/wiki/File:Renfe_avant.jpg
https://commons.wikimedia.org/wiki/File:Zaragoza_-_Delicias_7_-_Avant.JPG
S120 - https://commons.wikimedia.org/wiki/File:Alvia_120-861_Madrid-Hendaya.jpg
S130 Talgo - https://es.wikipedia.org/wiki/Archivo:S130_Torredembarra_(5183918409).jpg
https://commons.wikimedia.org/wiki/File:130-07_en_el_Cambiador_de_Valdestillas.jpg
ICE 1 - https://commons.wikimedia.org/wiki/File:ICE_1_Hannover-Berlin_Gardelegen.jpg
ICE 2 - https://commons.wikimedia.org/wiki/File:ICE2_Hilpodrom.jpg
ICE3 - https://commons.wikimedia.org/wiki/File:ICE_3_Oberhaider-Wald-Tunnel.jpg
Class 373 - https://commons.wikimedia.org/wiki/File:3015_at_Calais_Frethun.jpg
Class 374 - https://commons.wikimedia.org/wiki/File:Eurostar_Class_374_on_HS1.jpg
ETR480 - https://commons.wikimedia.org/wiki/File:ETR_480_Alta_Velocit.JPEG
ETR500 - https://commons.wikimedia.org/wiki/File:Naples,_Central_station,_gorgeous_long-distance_train.jpg
https://commons.wikimedia.org/wiki/File:ETR500mono-23B.jpg
ETR1000-V300 - https://commons.wikimedia.org/wiki/File:Mockup_of_Frecciarossa_1000_on_InnoTrans_2012.jpg
AGV - https://commons.wikimedia.org/wiki/File:Italo_NTV_Class_ETR_575_No_575-154.jpg
V250 - https://commons.wikimedia.org/wiki/File:Fyra_V250_4806.jpg
Shinkansen Series 0 - https://commons.wikimedia.org/wiki/File:Shinkansen_Series0_R67_JNRcolor.jpg
Shinkansen Series 100 - https://commons.wikimedia.org/wiki/File:100_V9_Grand_Hikari_Tokyo_199701.jpg
Shinkansen Series 200 - https://commons.wikimedia.org/wiki/File:200_H6_Yamabiko_43_Tokyo_20020601.jpg
Shinkansen Series 300 - https://de.wikipedia.org/wiki/Datei:Shinkansen_Series_300_at_Okayama.JPG

Shinkansen E5 - https://commons.wikimedia.org/wiki/File:E5_S11_Sendai_20090725.JPG
KTX TGV - https://commons.wikimedia.org/wiki/File:KTX-Sancheon.jpg
HEMU-430X - https://en.wikipedia.org/wiki/HEMU-430X#/media/File:HEMU-430X_Test_run.jpg
CRH2 - https://commons.wikimedia.org/wiki/File:China_railways_CRH2_unit_001.jpg
CRH3 Velaro - https://commons.wikimedia.org/wiki/File:CRH3.JPG
CRH380A - https://commons.wikimedia.org/wiki/File:CRH380A-2820@BCR_(20151204164747).jpg
S252 locomotive - https://commons.wikimedia.org/wiki/File:Bf_Sevilla_S.J._252_003.jpg
S252 X2/X2000 - https://commons.wikimedia.org/wiki/File:SJ_X2_in_snow_Jonsered_2007-01.jpg
APT - https://commons.wikimedia.org/wiki/File:Carlisle_InterCity_APT.jpg
Class 43 HST - https://commons.wikimedia.org/wiki/File:Taunton_-_Abellio_ScotRail_43149.JPG
Class 221 Voyager - https://commons.wikimedia.org/wiki/File:221129_Durham.JPG
Class 390 Pendolino - https://commons.wikimedia.org/wiki/File:Alstom_Pendolino_departing_Stoke.jpg
Class 89 locomotive - https://commons.wikimedia.org/wiki/File:89001_at_Doncaster_Works.JPG
Class 90 locomotive plus sleeper - https://commons.wikimedia.org/wiki/File:90012_and_train_London_Liverpool_Street.jpg
Class 91 locomotive - https://commons.wikimedia.org/wiki/File:91116_at_Kings_Cross.jpg
Class 91 driving trailer - https://commons.wikimedia.org/wiki/File:NXEC_Mk4_Driving_Van_Trailer.jpg
Mark 3 coach - https://commons.wikimedia.org/wiki/File:IC125@40_-_TF_41146_at_Cardiff_Central.JPG
ICE-T Pendolino - https://commons.wikimedia.org/wiki/File:ÖBB4011_Schneewalchen.jpg
Inter Regio Bimdzf269 Driving trailer - https://de.wikipedia.org/wiki/Datei:DBAG_Bimdzf269.2_MuenchenHbf.jpg

IC4 - https://commons.wikimedia.org/wiki/File:Hugh_llewelyn_5615_(5707052179).jpg
RevCo driving trailer - https://commons.wikimedia.org/wiki/File:B5uxh_à_Montbéliard_(25).jpg
ZTER - https://fr.wikipedia.org/wiki/Fichier:Z21796_à_Angers_par_Cramos.JPG
BR440 - https://de.wikipedia.org/wiki/Datei:Bahnhof_Mering_BR_440.JPG
DOSTO BR111 - https://de.wikipedia.org/wiki/Datei:BR_111_147_IMGP7151.jpg
DOSTO Driving Trailer - https://commons.wikimedia.org/wiki/File:DBpbzf_763.5_Remagen.jpg
Silberling BDnrzf740 Driving Trailer - https://commons.wikimedia.org/wiki/File:Bn-Wendezug.jpg
https://de.wikipedia.org/wiki/N-Wagen#/media/File:BA_KK,_BDnf_1998-05-01_16-40_Rennsteig_RB_14741_Erfurt_-_Themar.jpg
VT612 - https://commons.wikimedia.org/wiki/File:612_078_Möhren.jpg
Derby lightweight dmu - https://commons.wikimedia.org/wiki/File:Derby_Lightweight_79018_at_Bewdley.JPG
Class 141 dmu Pacer - https://commons.wikimedia.org/wiki/File:141108_at_Colne_Valley_Railway.jpg
Class 158 dmu - https://commons.wikimedia.org/wiki/File:Arriva_Trains_Wales_Class_158,_158818,_Ruabon_railway_station_(geograph_4024571).jpg
Class 165 - https://commons.wikimedia.org/wiki/File:Reading_-_GWR_165102_Basingstoke_service.JPG
Class 319 emu - https://commons.wikimedia.org/wiki/File:319373_and_319_number_438_to_Sevenoaks_2E45_by_Train_Photos.jpg
Class 325 emu - https://commons.wikimedia.org/wiki/File:Hugh_llewelyn_325_002_(6520031505).jpg
Class 350 emu Desiro - https://commons.wikimedia.org/wiki/File:Hugh_llewelyn_350_101_(6314709436).jpg
Class 357 emu - https://commons.wikimedia.org/wiki/File:357206_Upminster.jpg
M6BX - https://fr.wikipedia.org/wiki/Fichier:M6Bx_65046_-_Bruxelles-Midi_-_IC1938_-_10-08-18.jpg

AGC - https://fr.wikipedia.org/wiki/Autorail_grande_capacité#/media/File:AGC_Z_27500.jpg
AREX 1000 (Incheon Airport Express) - https://commons.wikimedia.org/wiki/File:Q707519_Yongyu_station_A01.jpg
Class 47 - https://commons.wikimedia.org/wiki/File:47424_47607_Bangor1987.jpg
Class 50 - https://commons.wikimedia.org/wiki/File:50050_Fearless_at_Hardingham.jpg
Class 66 - https://commons.wikimedia.org/wiki/File:EWS_unit_66138.JPG

APPENDIX 2

Data for aerodynamic crosswind force coefficients

The tables that follow list the available data for crosswind force coefficients for the four categories of train used throughout the book – high-speed passenger, medium-speed passenger, low-speed passenger and freight. They are presented initially by the nature of the track geometry – flat ground (FG) with or without a track simulation first (Single Track Ballasted Rail (STBR) or Double Track Ballasted Rail (DTBR)) and other ground simulations next, such as viaducts or bridges. They are then categorised as being either low-turbulence simulations (LT) or atmospheric boundary layer simulations (ABL). The individual results are then tabulated by reference and date (Tables A2.1–A2.4). Full scale tests are indicated by FS, wind tunnel tests by WT, moving model tests by MM and CFD tests by CFD followed by the type of CFD simulation as described in Chapter 4.

Table A2.1 High-speed passenger trains.

(A) Flat ground

Geometry	Turbulence	References	Vehicle	Type	Scale
Flat ground with track	ABL	Bocciolone et al. (2008)	ETR 500 leading	WT	1:20
Flat ground with track	LT	Bocciolone et al. (2008)	ETR 500 leading	WT	1:20
Flat ground with STBR	LT	CEN (2018)	ICE3 leading	WT	Not given
Flat ground	LT	CEN (2018)	ICE3 leading	WT	1:7
Flat ground with DTBR	LT	CEN (2018)	ICE3 leading	WT	1:15
Flat ground with STBR	LT	CEN (2018)	TGV leading	WT	Not given
Flat ground	LT	CEN (2018)	TGV leading	WT	1:7
Flat ground with DTBR	LT	CEN (2018)	TGV leading	WT	1:15

Continued

Table A2.1 High-speed passenger trains.—cont'd

(A) Flat ground

Geometry	Turbulence	References	Vehicle	Type	Scale
Flat ground with STBR	LT	CEN (2018)	ETR 500 leading	WT	Not given
Flat ground	LT	CEN (2018)	ETR 500 leading	WT	1:10
Flat ground with track	LT	Cheli et al. (2010c)	EMUV250 leading	WT	1:10
Flat ground with track	LT	Cheli et al. (2010c)	EMUV250 leading	CFD/ RANS	1:7
Flat ground	LT	Cheli et al. (2010a)	ETR 500 leading	WT	1:10
Flat ground	LT	Cheli et al. (2010a)	ETR 500 trailing	WT	1:10
Flat ground	LT	Diedrichs (2003)	ICE2 leading	CFD/ RANS	1:1
Flat ground	LT	Diedrichs (2003)	ICE2 trailing	CFD/ RANS	1:1
Flat ground	LT	Hemida and Krajnović (2008a)	ICE2 leading	CFD/ LES	1:10
Flat ground	LT	Munoz-Paniagua et al. (2017)	ICE2 leading	CFD/ various	1:10
Flat ground	LT	Kwon et al. (2010)	KTX leading	WT	1:20
Flat ground	LT	Kwon et al. (2010)	KTX trailing	WT	1:20
Flat ground with STBR	LT	Niu et al. (2017)	CRH2C leading	CFD/ DDES	1:8
Flat ground with STBR	LT	Niu et al. (2017)	CRH2C leading	WT	1:8
Flat ground with STBR	LT	Premoli et al. (2016)	ETR 500 leading	CFD/ RANS	1:15
Flat ground with STBR	LT	Premoli et al. (2016)	ETR 500 leading	WT	1:15
Flat ground with track	LT	Sanquer et al. (2004)	TGV leading	WT	1:15
Flat ground with track	LT	Sanquer et al. (2004)	TGV trailing	WT	1:15

Table A2.1 High-speed passenger trains.—cont'd

(A) Flat ground

Geometry	Turbulence	References	Vehicle	Type	Scale
Flat ground	LT	Schober et al. (2010)	ICE3 leading	WT	1:15
Flat ground with STBR	LT	Sima et al. (2015)	ICE3 leading	CFD/ RANS/ URANS/ DDES/ DES	1:15
Flat ground	ABL	Giappino et al. (2016)	ETR 500	WT	1:10

(B) Embankments/bridges/viaducts

Geometry	Turbulence	References	Vehicle	Type	Scale
Viaduct	LT	Bocciolone et al. (2008)	ETR 480 leading	WT	1:20
Viaduct	LT	Bocciolone et al. (2008)	ETR 480 trailing	WT	1:20
Viaduct with fences	LT	Bocciolone et al. (2008)	ETR 480 leading	WT	1:20
Embankment	LT	Bocciolone et al. (2008)	ETR 480 leading	WT	1:20
Viaduct	LT	Bocciolone et al. (2008)	ETR 480 leading	MM	1:20
Viaduct	LT	Bocciolone et al. (2008)	ETR 500 leading	WT	1:20
Embankment	LT	CEN (2018)	ICE3 leading	WT	1:15
Embankment	LT	CEN (2018)	TGV leading	WT	1:15
Embankment	LT	CEN (2018)	ETR 500 leading	WT	1:10
Embankment	LT	Cheli et al. (2010b)	ETR 500 leading	WT	1:10
Viaduct	LT	Cheli et al. (2010b)	ETR 500 leading	WT	1:20
Embankment	LT	Diedrichs et al. (2007b)	ICE2 leading	CFD/ RANS	1:1

Continued

Table A2.1 High-speed passenger trains.—cont'd

(B) Embankments/bridges/viaducts

Geometry	Turbulence	References	Vehicle	Type	Scale
Embankment	LT	Diedrichs et al. (2007b)	ICE2 leading	High-pressure WT	1:100
Truss Bridge	LT	Li et al. (2018c)	CRH3 three coach	MM	1:30
Embankment	LT	Schober et al. (2010)	ICE3 leading	WT	1:15
Embankment	LT	Tomasini et al. (2014)	ETR 500 leading	WT	1:45
Embankment	LT	Tomasini et al. (2014)	ETR 500 leading	WT	1:10
Flat ground and wind fences	LT	Tomasini et al. (2016)	ETR 500 leading	WT	1:15
Viaduct	ABL	Bocciolone et al. (2008)	ETR 480 leading	WT	1:20
Viaduct	ABL	Bocciolone et al. (2008)	ETR 480 trailing	WT	1:20

Table A2.2 Medium-speed passenger trains.

(A) Flat ground

Geometry	Turbulence	References	Vehicle	Type	Scale
Flat ground with track	LT	Baker (1991a,b)	APT leading	WT	1:5
Flat ground with track	LT	Baker (1991a,b)	APT leading	WT	1:25
Flat ground with track	LT	Baker (1991a,b)	APT leading	WT	1:35
Flat ground with track	LT	Baker (1991a,b)	APT leading	WT	1:50
Flat ground with STBR	LT	Sima et al. (2015)	IC4 leading	CFD/ RANS	1:15
Flat ground with STBR	LT	Sima et al. (2015)	REVCO leading	CFD/ RANS	1:15
Flat ground with STBR	LT	Gallagher et al. (2018)	Class 43 HST leading	WT	1:25

Table A2.2 Medium-speed passenger trains.—cont'd

(A) Flat ground

Geometry	Turbulence	References	Vehicle	Type	Scale
Flat ground with STBR	LT	Gallagher et al. (2018)	Class 43 HST leading	CFD/ DES	1:27
Flat ground with STBR	LT	Paradot et al. (2015)	Mark 3 coach	WT	1:15
Flat ground with STBR	LT	Paradot et al. (2015)	REVCO leading	WT	1:15
Flat ground with STBR	LT	Paradot et al. (2015)	Interregio leading	WT	1:15
Flat ground with STBR	LT	Paradot et al. (2015)	IC4 leading	WT	1:15
Flat ground with STBR	LT	Paradot et al. (2015)	IC4 trailing	WT	1:15
Flat ground with STBR	LT	Paradot et al. (2015)	ZTER leading	WT	1:15
Flat ground	ABL	Baker (1986)	APT leading	MM	1:50
Flat ground	ABL	Baker (1986)	APT trailing	MM	1:50
Flat ground with track	ABL	Baker (1991a,b)	APT leading	WT	1:50
Flat ground with track	ABL	Baker et al. (2004)	Class 390 Pendolino leading	WT	1:30
Flat ground	ABL	Dorigati et al. (2015)	Class 390 Pendolino leading	WT	1:25
Flat ground	ABL	Dorigati et al. (2015)	Class 390 Pendolino leading	MM	1:25
Flat ground	ABL	Gallagher et al. (2018)	Class 43 HST leading	MM	1:26

(B) Embankments/bridges/viaducts

Geometry	Turbulence	References	Vehicle	Type	Scale
Viaduct with parapets	LT	Barcala and Mesueguer (2007)	Talgo coach	WT	1:70

Continued

Table A2.2 Medium-speed passenger trains.—cont'd

(B) Embankments/bridges/viaducts

Geometry	Turbulence	References	Vehicle	Type	Scale
Viaduct	LT	Suzuki et al. (2003)	Sleeping car	WT	1:30
Viaduct	LT	Suzuki et al. (2003)	Passenger car	WT	1:30
Embankment	ABL	Baker (1986)	APT leading	MM	1:50
Embankment	ABL	Baker (1986)	APT trailing	MM	1:50
Topography with track	ABL	Baker et al. (2004)	Class 390 Pendolino leading	FS	1:1
Topography with track	ABL	Baker et al. (2004)	Class 390 Pendolino leading	WT	1:30
Various	ABL	Gallagher et al. (2018)	Class 43 HST leading	FS	1:1

Table A2.3 Low-speed passenger trains.

(A) Flat ground

Geometry	Turbulence	References	Vehicle	Type	Scale
Flat ground with track	LT	Baker (1991a,b)	Derby lightweight leading	WT	1:25
Flat ground with track	LT	Baker (1991a,b)	Class 141 leading	WT	1:50
Flat ground	LT	Cheli et al. (2013)	MLA Riyadh MU	WT	1:15
Flat ground	HT	Cheli et al. (2013)	MLA Riyadh MU	WT	1:15
Flat ground	LT	Diedrichs (2010)	Generic regional	WT	1:25
Flat ground	LT	Diedrichs (2010)	Generic regional	CFD/ RANS	1:1

Table A2.3 Low-speed passenger trains.—cont'd

(A) Flat ground

Geometry	Turbulence	References	Vehicle	Type	Scale
Flat ground	LT	Diedrichs (2010)	Generic regional	CFD/ DDES	1:1
Flat ground	LT	Giappino et al. (2016)	Low-speed multiple unit leading	WT	1:20
Flat ground with STBR	LT	Sima et al. (2015)	VT612 leading	CFD/ RANS	1:15
Flat ground with STBR	LT	Sima et al. (2015)	AGC leading	CFD/ RANS	1:15
Flat ground with STBR	LT	Sima et al. (2015)	AGC trailing	CFD/ RANS	1:15
Flat ground with STBR	LT	Paradot et al. (2015)	Silberling leading	WT	1:15
Flat ground with STBR	LT	Paradot et al. (2015)	M6Bx leading	WT	1:15
Flat ground with STBR	LT	Paradot et al. (2015)	VT612 leading	WT	1:15
Flat ground with STBR	LT	Paradot et al. (2015)	AGC leading	WT	1:15
Flat ground with STBR	LT	Paradot et al. (2015)	AGC trailing	WT	1:15
Flat ground with STBR	LT	Paradot et al. (2015)	ADR leading	WT	1:15
Flat ground	LT	Kwon et al. (2010)	AREX leading	WT	1:20
Flat ground	LT	Kwon et al. (2010)	AREX trailing	WT	1:20
Flat ground with track	LT	You et al. (2017)	Incheon Express EMU	WT	1:20
Flat ground with track	ABL	Baker and Sterling (2009)	Class 365 EMU leading	WT	1:30
Flat ground with track	ABL	Baker (1991a,b)	Class 141 leading	WT	1:50
Viaduct and embankment	ABL	Nakade et al. (2016)	Multiple unit	CFD/ LES	1:40

(B) Embankments/bridges/viaducts

Geometry	Turbulence	References	Vehicle	Type	Scale
Viaduct	LT	Bocciolone et al. (2008)	UIC-Z1 leading	WT	1:20
Viaduct	LT	Kikuchi and Suzuki (2015)	Multiple unit	WT	1:40
Viaduct	LT	Noguchi et al. (2017)	Multiple unit	CFD/ LES	1:40
Viaduct	LT	Suzuki et al. (2003)	Double decker	WT	1:30
Viaduct	LT	Suzuki et al. (2003)	3 car unit leading car	WT	1:40
Viaduct	LT	Suzuki et al. (2003)	3 car unit middle car	WT	1:40
Viaduct	ABL	Kikuchi and Suzuki (2015)	Multiple unit	WT	1:40
Viaduct	ABL	Kikuchi and Suzuki (2015)	Multiple unit	FS	1:1
Viaduct	ABL	Suzuki and Hibino (2016)	3 car unit leading car	WT	1:40
Viaduct	ABL	Suzuki and Hibino (2016)	3 car unit middle car	WT	1:40
Viaduct	ABL	Suzuki and Hibino (2016)	3 car unit leading car	FS	1:1
Viaduct	ABL	Nakade et al. (2016)	4 car unit leading car	CFD/ LES	1:40

Table A2.4 Freight trains

(A) Flat ground

Geometry	Turbulence	References	Vehicle	Type	Scale
Flat ground	LT	Alam and Watkins (2007)	Containers	WT	1:15
Flat ground	LT	Baker and Humphreys (1996)	Containers	WT	1:7

Table A2.4 Freight trains—cont'd

(A) Flat ground

Geometry	Turbulence	References	Vehicle	Type	Scale
Flat ground	LT	Giappino et al. (2014)	Containers	WT	1:20
Flat ground	LT	Giappino et al. (2018)	Containers	WT	1:20
Flat ground	LT	Golovanevskiy et al. (2012)	Loco and cargo wagons	WT	1:40
Flat ground	LT	Golovanevskiy et al. (2012)	Loco and cargo wagons	CFD/ RANS	1:1
Flat ground	LT	Hemida and Baker (2010)	Container	CFD/ LES	1:20
Flat ground	LT	RSSB (2012)	Containers	WT	1:25
Flat ground	LT	RSSB (2012)	Hopper wagon	WT	1:25
Flat ground	ABL	Baker and Humphreys (1996)	Containers	WT	1:50
Flat ground	ABL	Baker and Humphreys (1996)	Containers	MM	1:50
Flat ground	ABL	Kronke and Sockel (1994)	Containers	WT	1:75
Flat ground	ABL	Soper et al. (2015)	Loco and containers	MM	1:25

(B) Embankments/bridges/viaducts

Geometry	Turbulence	References	Vehicle	Type	Scale
Viaduct	LT	Suzuki et al. (2003)	Container	WT	1:30

References

Aarnio, P., Yli-Tuomi, T., Kousa, A., Makela, T., Hirsikko, A., et al., 2005. The concentrations and composition of, and exposure to, fine particles (PM2.5) in the Helsinki subway system. Atmospheric Environment 39 (28), 5059–5066. https://doi.org/10.1016/j.atmosenv.2005.05.012.

Abbasi, S., Wahlstrom, J., Olander, S., Larsson, C., Sellgren, U., 2011. A study of airborne wear particles generated from organic railway brake pads and brake discs. Wear 273 (1), 93–99. https://doi.org/10.1016/j.wear.2011.04.013.

Alam, F., Watkins, S., 2007. Effects of crosswinds on double stacked container wagons. In: Australian Fluid Mechanics Conference, Gold Coast, pp. 758–761. In: https://people.eng.unimelb.edu.au/imarusic/proceedings/16/Alam%20F.pdf.

Alfi, S., Bruni, S., Diana, G., 2011. Active control of air-spring secondary suspension to improve ride quality and safety against crosswind. Proceedings of the Institution of Mechanical Engineers Part F: Journal of Rail and Rapid Transit 225 (1), 84–98. https://doi.org/10.1243/09544097JRRT392.

Allain, E., van Kalsbeek, G., Croue, R., 2016. Comprehension of aerodynamic effects on current collection quality, especially in tunnel. In: World Congress on Rail Research, Milano, Italy. https://www.sparkrail.org/Lists/Records/DispForm.aspx?ID=23402.

Andersson, E., Häggström, J., Sima, M., Stichel, S., 2004. Assessment of train overturning risk due to strong crosswinds. Proceedings of the Institution of Mechanical Engineers Part F Journal of Rail and Rapid Transit 218 (3), 213–223. https://doi.org/10.1243/0954409042389382.

Araki, K., Fukuhara, T., Tanimoto, S., Fujii, T., 2013. A method of safety evaluation for a train under strong wind condition. In: World Congress on Rail Research, Sydney, Australia. https://www.sparkrail.org/Lists/Records/DispForm.aspx?ID=12442.

Armstrong, D., Swift, P., 1990. Lower Energy Technology Part A, Identification of Energy Use in Multiple Units. British Rail Research Report MR VS 077.

ARUP, 2014. Future of Rail, 2050. https://www.arup.com/perspectives/publications/research/section/future-of-rail-2050.

ASCE, 2012. Wind Tunnel Testing for Buildings and Other Structures. ASCE/SEI 49-12, ISBN 978-0-7844-7690-1.

Bagnold, R., 1941. The Physics of Blown Sand and Desert Dunes. Dover Earth Science, ISBN 9780486439310.

Baker, C., 1984. Determination of topographical exposure factors in complicated hilly terrain. Journal of Wind Engineering and Industrial Aerodynamics 17 (2), 239–249. https://doi.org/10.1016/0167-6105(84)90058-8.

Baker, C., 1986. Train aerodynamic forces and moments from moving model experiments. Journal of Wind Engineering and Industrial Aerodynamics 24 (3), 227–251. https://doi.org/10.1016/0167-6105(86)90024-3.

Baker, C., 1991a. Ground vehicles in high cross winds part 1: steady aerodynamic forces. Journal of Fluids and Structures 5 (1), 69–90. https://doi.org/10.1016/0889-9746(91)80012-3.

Baker, C., 1991b. Ground vehicles in high cross winds. part 2: unsteady aerodynamic forces. Journal of Fluids and Structures 5 (1), 91–111. https://doi.org/10.1016/0889-9746(91)80013-4.

Baker, C., 2001. Flow and dispersion in vehicle wakes. Journal of Fluids and Structures 15 (7), 1031–1060. https://doi.org/10.1006/jfls.2001.0385.

Baker, C., 2007. The debris flight equations. Journal of Wind Engineering and Industrial Aerodynamics 95 (5), 329–353. https://doi.org/10.1016/j.jweia.2006.08.001.

Baker, C., 2010a. The flow around high speed trains. Journal of Wind Engineering and Industrial Aerodynamics 98 (6–7), 277–298. https://doi.org/10.1016/j.jweia.2009.11.002.

Baker, C., 2010b. The simulation of unsteady aerodynamic crosswind forces on trains. Journal of Wind Engineering and Industrial Aerodynamics 98 (2), 88–99. https://doi.org/10.1016/j.jweia.2009.09.006.

Baker, C., 2013. A framework for the consideration of the effects of crosswinds on trains. Journal of Wind Engineering and Industrial Aerodynamics 123 (A), 130–142. https://doi.org/10.1016/j.jweia.2013.09.015.

Baker, C., 2014a. A review of train aerodynamics. part 1 Fundamentals. Aeronautical Journal 118 (1201), 201–228. https://www.cambridge.org/core/journals/aeronautical-journal/article/review-of-train-aerodynamics-part-1-fundamentals/1B6917D3C19F2DCA36B3E298BE621930.

Baker, C., 2014b. A review of train aerodynamics. part 2 Applications. Aeronautical Journal 118 (1202), 345–382. https://www.cambridge.org/core/journals/aeronautical-journal/article/review-of-train-aerodynamics-part-2-applications/5E449803B62928C0EBF7B4DE84F3F301?utm_source=TrendMD&utm_medium-=cpc&utm_campaign=The_Aeronautical_Journal_TrendMD_0.

Baker, C., 2015. Risk analysis of pedestrian and vehicle safety in windy environments. Journal of Wind Engineering and Industrial Aerodynamics 147, 283–290. https://doi.org/10.1016/j.jweia.2015.10.001.

Baker, C., Brockie, N., 1991. Wind tunnel tests to obtain train aerodynamic drag coefficients; Reynolds number and ground simulation effects. Journal of Wind Engineering and Industrial Aerodynamics 38 (1), 23–28. https://doi.org/10.1016/0167-6105(91)90024-Q.

Baker, C., Cheli, F., Orellano, A., Paradot, N., Proppe, C., et al., 2009. Cross-wind effects on road and rail vehicles. Vehicle System Dynamics 47 (8), 983–1022. https://doi.org/10.1080/00423110903078794.

Baker, C., Dalley, S., Johnson, T., Quinn, A., Wright, N., 2001. The slipstream and wake of a high speed train. Proceedings of the Institution of Mechanical Engineers Part F Journal of Rail and Rapid Transit 215 (2), 83–99. https://doi.org/10.1243/0954409011531422.

Baker, C., Gilbert, T., Jordan, S., 2013. The validation of the use of moving model experiments for the measurement of train aerodynamic parameters in the open air. In: World Congress on Rail Research, Sydney. https://www.sparkrail.org/Lists/Records/DispForm.aspx?ID=12376.

Baker, C., Hemida, H., Iwnicki, S., Xie, G., Ongaro, D., 2010. Integration of crosswind forces into train dynamic modelling. Proceedings of the Institution of Mechanical Engineers Part F Journal of Rail and Rapid Transit 225 (2), 154–164. https://doi.org/10.1177/2041301710392476.

Baker, C., Humphreys, N., 1996. Assessment of the adequacy of various wind tunnel techniques to obtain aerodynamic data for ground vehicles in cross winds. Journal of Wind Engineering and Industrial Aerodynamics 60, 49–68. https://doi.org/10.1016/0167-6105(96)00023-2.

Baker, C., Johnson, T., Edwards, D., 1982. Full Scale Measurements of the Aerodynamic Drag of Trains. British Rail Research Technical Memorandum TMAERO 74. https://www.sparkrail.org/Lists/Records/DispForm.aspx?ID=5177.

Baker, C., Jones, J., Lopez-Calleja, F., Munday, J., 2004. Measurements of crosswind forces on trains. Journal of Wind Engineering and Industrial Aerodynamics 92 (7–8), 547–563. https://doi.org/10.1016/j.jweia.2004.03.002.

Baker, C., Jordan, S., Gilbert, T., Quinn, A., Sterling, M., et al., 2014a. Transient aerodynamic pressures and forces on trackside and overhead structures due to passing trains. part 1 model scale experiments. Proceedings of the Institution of Mechanical Engineers Part F Journal of Rail and Rapid Transit 228 (1), 37–70. https://doi.org/10.1177/0954409712464859.

Baker, C., Jordan, S., Gilbert, T., Quinn, A., Sterling, M., et al., 2014b. Transient aerodynamic pressures and forces on trackside and overhead structures due to passing trains. part 2 standards applications. Proceedings of the Institution of Mechanical Engineers Part F Journal of Rail and Rapid Transit 228 (1), 37–70. https://doi.org/10.1177/0954409712464859.

Baker, C., Quinn, A., Sima, M., Hoefener, L., Licciardello, R., 2014c. Full-scale measurement and analysis of train slipstreams and wakes: part 1 ensemble averages. Proceedings of the Institution of Mechanical Engineers Part F Journal of Rail and Rapid Transit 229 (5), 451–467. https://doi.org/10.1177/0954409713485944.

Baker, C., Quinn, A., Sima, M., Hoefener, L., Licciardello, R., 2014d. Full-scale measurement and analysis of train slipstreams and wakes: part 2 gust analysis. Proceedings of the Institution of Mechanical Engineers Part F Journal of Rail and Rapid Transit 229 (5), 468–480. https://doi.org/10.1177/0954409713488098.

Baker, C., Sterling, M., 2009. Aerodynamic forces on multiple unit trains in cross winds. ASME Journal of Fluids Engineering 131 (10), 101113. https://doi.org/10.1115/1.3222908.

Baker, C., Sterling, M., 2018. The calculation of train stability in tornado winds. Journal of Wind Engineering and Industrial Aerodynamics 176, 158–165. https://doi.org/10.1016/j.jweia.2018.03.022.

Baker, C., Sterling, M., Figura-Hardy, G., Pope, C., 2007. The effect of crosswinds on train slipstreams. In: International Conference on Wind Engineering, ICWE12 Lubbock.

Barcala, M., Meseguer, J., 2007. An experimental study of the influence of parapets on the aerodynamic loads under cross wind on a two-dimensional model of a railway vehicle on a bridge. Proceedings of the Institution of Mechanical Engineers Part F Journal of Rail and Rapid Transit 221 (4), 487–494. https://doi.org/10.1243/09544097JRRT53.

Barlow, J., Rae, W., Pope, A., 1999. Low-Speed Wind Tunnel Testing, third ed. John Wiley & Sons, New York, ISBN 0-471-55774-9.

Barrero-Gil, A., Sanz-Andres, A., 2009. Aeroelastic effects in a traffic sign panel induced by a passing vehicle. Journal of Wind Engineering and Industrial Aerodynamics 97 (5–6), 298–303. https://doi.org/10.1016/j.jweia.2009.07.001.

BBC, 2016. How Much Diesel Pollution Am I Breathing in? http://www.bbc.co.uk/news/magazine-35717927.

BBC, 2019. Tube Particle Pollution 30 Times Higher than by Roads. https://www.bbc.co.uk/news/uk-england-london-46820584.

Beagles, A., Fletcher, D., 2013. The aerodynamics of freight: approaches to save fuel by optimising the utilisation of container trains. Proceedings of the Institution of Mechanical Engineers Part F Journal of Rail and Rapid Transit 227 (7), 635–643. https://doi.org/10.1177/0954409713488101.

Bell, J., 2015. The Slipstream and Wake Structure of High Speed Trains (Ph.D. thesis). Monash University. https://figshare.com/articles/The_slipstream_and_wake_structure_of_high-speed_trains/4688836.

Bell, J., Burton, D., Thompson, M., Herbst, A., Sheridan, J., 2014. Wind tunnel analysis of the slipstream and wake of a high-speed train. Journal of Wind Engineering and Industrial Aerodynamics 134, 122–138. https://doi.org/10.1016/j.jweia.2014.09.004.

Bell, J., Burton, D., Thompson, M., Herbst, A., Sheridan, J., 2015. Moving model analysis of the slipstream and wake of a high-speed train. Journal of Wind Engineering and Industrial Aerodynamics 136, 127–137. https://doi.org/10.1016/j.jweia.2014.09.007.

Bell, J., Burton, D., Thompson, M., Herbst, A., Sheridan, J., 2016. Flow topology and unsteady features of the wake of a generic high-speed train. Journal of Fluids and Structures 61, 168–183. https://doi.org/10.1016/j.jfluidstructs.2015.11.009.

Bell, J., Burton, D., Thompson, M., Herbst, A., Sheridan, J., 2017. A wind-tunnel methodology for assessing the slipstream of high-speed trains. Journal of Wind Engineering and Industrial Aerodynamics 166, 1–19. https://doi.org/10.1016/j.jweia.2017.03.012.

Bellfield, N., 1983. Reduction of Risk of Dewirement Using Midspan Offsets. British Rail Research IM AERO 166. https://www.sparkrail.org/Lists/Records/DispForm.aspx?ID=6375.

Belloli, M., Pizzigoni, B., Ripamonti, F., Rocchi, D., 2009. Fluid–structure interaction between trains and noise-reduction barriers: numerical and experimental analysis. WIT Transactions on the Built Environment 105, 49–60. https://doi.org/10.2495/FSI090051.

Berenger, T., Gregoire, R., 2001. Panel method applied to problems of European high-speed train interoperability. In: Schulte-Werning, B., Gregoire, R., Malfatti, M., Matschke, G. (Eds.), Notes on Numerical Fluid Mechanics and Multidisciplinary Design, TRANSAERO – A European Initiative on Transient Aerodynamics for Railway System Optimisation, vol. 79, pp. 148–159. https://doi.org/10.1007/978-3-540-45854-8_12.

Berenger, T., Le Devehat, E., Gregoire, R., Talotte, C., 1997. Etude experimentale d'un manipulateur de couche limite visant à reproduire en soufflerie les ecoulements reels se développant autour des trains à Grande Vitesse (Experimental study of a boundary layer manipulator to reproduce real flows developing around high speed trains in a wind tunnel). In: 33rd Colloquium of Applied Aerodynamics, Poitiers, France.

Bernard, M., 1995. New Knowledge about Train Resistance at Very High Speed (Tests with the TGV001 Train). SNCF.

Bierbooms, W., Cheng, P.-W., 2002. Stochastic gust model for design calculations of wind turbines. Journal of Wind Engineering and Industrial Aerodynamics 90 (11), 1237–1251. https://doi.org/10.1016/S0167-6105(02)00255-6.

BLS Ltd. Lötschberg Base Tunnel: a new Alpine rail link to connect Europe. https://www.bls.ch/en/unternehmen/projekte-und-hintergruende/neat.

Bocciolone, M., Cheli, F., Corradi, R., Muggiasca, S., Tomasini, G., 2008. Crosswind action on rail vehicles: wind tunnel experimental analyses. Journal of Wind Engineering and Industrial Aerodynamics 96 (5), 584–610. https://doi.org/10.1016/j.jweia.2008.02.030.

Bourriez, F., Soper, D., Baker, C., Sterling, M., 2019. Physical model measurement of tornado induced forces on trains. In: International Conference on Wind Engineering, Beijing.

Bradbury, W., Deaves, D., 1994. The dependence of gust factor probabilities on convective activity: analysis conducted for Eurotunnel. Meteorological Applications 1 (2), 159–164. https://doi.org/10.1002/met.5060010211.

Bradbury, W., Pottrill, R., Murtagh, V., 2003. Enhanced Permissible Speed on the West Coast Main Line: Investigations of Wind Overturning Effects, pp. 476–485. World, UK on Rail Research, Edinburgh. https://www.sparkrail.org/Lists/Records/DispForm.aspx?ID=11750.

Braun, J., Sousa, J., Pekardan, C., 2017. Aerodynamic design and analysis of the Hyperloop. AIAA Journal 55 (12), 4053–4060. https://arc.aiaa.org/doi/10.2514/1.J055634.

BRB, 1986. Tractive Resistance Tests on Unit 150-002. Testing Section Report 932.

BRB, 1991. Train Resistance Testing, Class 319 and 317 EMU's. Testing Section Report 1183.

BRB, 1994. Train Resistance Tests, Class 165 Test Type. Vehicle Testing and Commissioning 1321G.

Britcher, C., Wells, J., Renaud, B., Buvat, T., 2012. Aerodynamics of urban maglev vehicles. Proceedings of the Institution of Mechanical Engineers Part F Journal of Rail and Rapid Transit 226 (6), 561–567. https://doi.org/10.1177/0954409712441740.

Brockie, N., Baker, C., 1990. The aerodynamic drag of high speed trains. Journal of Wind Engineering and Industrial Aerodynamics 34 (3), 273–290. https://doi.org/10.1016/0167-6105(90)90156-7.

Bruno, L., Horvat, M., Raffaele, L., 2018. Windblown sand along railway infrastructures: a review of challenges and mitigation measures. Journal of Wind Engineering and Industrial Aerodynamics 177, 340–365. https://doi.org/10.1016/j.jweia.2018.04.021.

Buchanan, R., 1992. The atmospheric railway of I.K. Brunel. Social Studies of Science 22 (2), 231–243. https://doi.org/10.1177/030631292022002003.

Bukowiecki, N., Gehrig, R., Hill, M., Lienemann, P., Zwicky, C., et al., 2007. Iron, manganese and copper emitted by cargo and passenger train in Zurich (Switzerland): size-segregated mass concentrations in ambient air. Atmospheric Environment 41 (4), 878–889. https://doi.org/10.1016/j.atmosenv.2006.07.045.

Burlando, M., Freda, A., Ratto, C., Solari, G., 2010. A pilot study of the wind speed along the Rome–Naples HS/HC railway line. part 1—numerical modelling and wind simulations. Journal of Wind Engineering and Industrial Aerodynamics 98 (8–9), 392–403. https://doi.org/10.1016/j.jweia.2009.12.006.

Carassale, L., Brunenghi, M., 2013. Dynamic response of trackside structures due to the aerodynamic effects produced by passing trains. Journal of Wind Engineering and Industrial Aerodynamics 123 (B), 317–324. https://doi.org/10.1016/j.jweia.2013.09.005.

Carnevale, M., Facchinetti, A., Maggiori, L., Rocchi, D., 2016. Computational fluid dynamics as a means of assessing the influence of aerodynamic forces on the mean contact force acting on a pantograph. Proceedings of the Institution of Mechanical Engineers Part F: Journal of Rail and Rapid Transit 230 (7), 1698–1713. https://doi.org/10.1177/0954409715606748.

Carnevale, M., Facchinetti, A., Rocchi, D., 2017. Procedure to assess the role of railway pantograph components in generating the aerodynamic uplift. Journal of Wind Engineering and Industrial Aerodynamics 160, 16–29. https://doi.org/10.1016/j.jweia.2016.11.003.

Carrarini, A., 2008. Efficient models and techniques for the computational analysis of railway vehicles in cross-winds. Vehicle System Dynamics 46 (1), 77–86. https://doi.org/10.1080/00423110701882322.

CEN, 2010a. Eurocode 1: Actions on Structures — Part 1-4: General Actions — Wind Actions. EN 1991-1-4:2005+A1:2010.

CEN, 2010b. Railway Applications – Aerodynamics: Part 5: Requirements and Test Procedures for Aerodynamics in Tunnels. EN14067-5:2006+A1:2010.

CEN, 2012. Railway Applications – Current Collection Systems - Requirements for and Validation of Measurements of the Dynamic Interaction between Pantograph and Overhead Contact Line. EN 50317:2012.

CEN, 2013. Railway Applications — Aerodynamics. Part 4: Requirements and Test Procedures for Aerodynamics on Open Track. EN 14067-4:2013.

CEN, 2016a. Railway Applications — Current Collection Systems - Technical Criteria for the Interaction between Pantograph and Overhead Line. EN 50367:2012+A1:2016.

CEN, 2016b. Railway Applications — Track. Noise Barriers and Related Devices Acting on Airborne Sound Propagation — Non-acoustic Performance. Part 2 — 2: Mechanical Performance under Dynamic Loadings Caused by Passing Trains — Calculation Method. EN 16727-2-2.

CEN, 2016c. Railway applications. Gauges. Rolling stock gauge. EN 15273-3:2013+A1:2016.

CEN, 2018. Railway Applications — Aerodynamics — Part 6: Requirements and Test Procedures for Cross Wind Assessment. EN 14067-6:2018.

Cha, Y., Abassi, S., Olufsson, U., 2016. Indoor and outdoor measurement of airborne particulates on a commuter train running partly in tunnels. Proceedings of the Institution of Mechanical Engineers Part F Journal of Rail and Rapid Transit 232 (1), 3–13. https://doi.org/10.1177/0954409716642492.

Cheli, F., Corradi, R., Rocchi, D., Tomasini, G., Maestrini, E., 2010a. Wind tunnel tests on train scale models to investigate the effect of infrastructure scenario. Journal of Wind Engineering and Industrial Aerodynamics 98 (6–7), 353–362. https://doi.org/10.1016/j.jweia.2010.01.001.

Cheli, F., Corradi, R., Tomasini, G., 2012. Crosswind action on rail vehicles: a methodology for the estimation of the characteristic wind curves. Journal of Wind Engineering and Industrial Aerodynamics 104–106, 248–255. https://doi.org/10.1016/j.jweia.2012.04.006.

Cheli, F., Diana, G., Rocchi, D., Schito, P., Testa, M., et al., 2010b. A new stochastic approach for the regulation of the train velocity in presence of cross wind: an application on the Rome-Naples high-speed line. In: Computational Wind Engineering, CWE5 Chapel Hill USA. ftp://ftp.atdd.noaa.gov/pub/cwe2010/Files/Papers/403_Diana.pdf.

Cheli, F., Giappino, S., Rosa, L., Tomasini, G., Villani, M., 2013. Experimental study on the aerodynamic forces on railway vehicles in presence of turbulence. Journal of Wind Engineering and Industrial Aerodynamics 123 (B), 311–316. https://doi.org/10.1016/j.jweia.2013.09.013.

Cheli, F., Ripamonti, F., Rocchi, D., Tomasini, G., 2010c. Aerodynamic behaviour investigation of the new EMUV250 train to cross wind. Journal of Wind Engineering and Industrial Aerodynamics 98 (4), 189–201. https://doi.org/10.1016/j.jweia.2009.10.015.

Cheli, F., Ripamonti, F., Rocchi, D., Tomasini, G., Testa, M., 2008. Risk analysis of cross wind on HS/HC Rome-Naples railway line. In: Bluff Body Aerodynamics and its Application, BBAA6 Milano, Italy. http://bbaa6.mecc.polimi.it/uploads/treni/TreniPolimi1.pdf.

Cheli, F., Rocchi, D., Schito, P., Tomasini, G., 2016. Neural network algorithm for evaluating wind velocity from pressure measurements performed on a train's surface. Proceedings of the Institution of Mechanical Engineers Part F Journal of Rail and Rapid Transit 230 (3), 961–970. https://doi.org/10.1177/0954409715577968.

Chen, Z., Liu, T., Zhou, X., Niu, J., 2017. Impact of ambient wind on aerodynamic performance when two trains intersect inside a tunnel. Journal of Wind Engineering and Industrial Aerodynamics 169, 139–155. https://doi.org/10.1016/j.jweia.2017.07.018.

Cheng, Y.-H., Liu, Z.-S., Yan, J.-W., 2012. Comparisons of PM10, PM2.5, particle number, and CO2 levels inside metro trains between traveling in underground tunnels and on elevated tracks. Aerosol and Air Quality Research 12 (5), 879–891. https://doi.org/10.4209/aaqr.2012.05.0127.

Cheng, J., Xue, C., 2014. The sand-damage-prevention engineering system for the railway in the desert region of the Qinghai-Tibet plateau. Journal of Wind Engineering and Industrial Aerodynamics 125, 30–37. https://doi.org/10.1016/j.jweia.2013.11.016.

Chiu, T.W., 1991. A two-dimensional second-order vortex panel method for the flow in a cross-wind over a train and other two-dimensional bluff bodies. Journal of Wind Engineering and Industrial Aerodynamics 37 (1), 43–64. https://doi.org/10.1016/0167-6105(91)90004-G.

Chiu, T.W., 1995. Prediction of the aerodynamic loads on a railway train in a cross-wind at large yaw angles using an integrated two- and three-dimensional source/vortex panel method. Journal of Wind Engineering and Industrial Aerodynamics 57 (1), 19–39. https://doi.org/10.1016/0167-6105(94)00099-Y.

Chui, T., Squire, L., 1992. An experimental study of the flow over a train in a crosswind at large yaw angles up to 90°. Journal of Wind Engineering and Industrial Aerodynamics 45 (1), 47–74. https://doi.org/10.1016/0167-6105(92)90005-U.

Clayton, H., 1966. The Atmospheric Railway. Self-published, Lichfield.

Cleon, L., Jourdain, A., 2001. Protection of line LN5 against cross winds. In: World Congress on Rail Research, Köln, Germany.

CNN, 2007. Sandstorm Derails Train in China; 4 Die. https://web.archive.org/web/20070302073413/http://www.cnn.com/2007/WORLD/asiapcf/02/28/china.train.ap/index.html.

Cook, N., 1985. A Designer's Guide to Wind Loading of Building Structures, Part 1 Background, Wind Damage, Wind Data and Structural Classification. Building Research Establishment, Butterworths.

Cooper, R., 1975. Assessment of the Wind Effects in Relation to the Dewirements on Overhead Line Equipment, WCML, December 1974 – January 1975. British Rail Research TM AERO 9. https://www.sparkrail.org/Lists/Records/DispForm.aspx?ID=15415.

Cooper, R., 1979. Probability of trains overturning in high winds. In: International Conference on Wind Engineering. Fort Collins, pp. 1185–1194.

Cooper, R., 1984. Atmospheric turbulence with respect to moving ground vehicles. Journal of Wind Engineering and Industrial Aerodynamics 17 (2), 215–238. https://doi.org/10.1016/0167-6105(84)90057-6.

Copley, J., 1987. The three-dimensional flow around railway trains. Journal of Wind Engineering and Industrial Aerodynamics 26 (1), 21–52. https://doi.org/10.1016/0167-6105(87)90034-1.

Cornolo, G., 1990. Una leggenda che corre: breve storia dell'elettrotreno e dei suoi primati; ETR.200 - ETR.220 – ETR.240, ISBN 88-85068-23-5.

Coxon, D., 1981. Towards an Aerodynamically Neutral Pantograph. British Rail Research TM DA 32. https://www.sparkrail.org/Lists/Records/DispForm.aspx?ID=5183.

Cui, T., Zhang, W., Sun, B., 2014. Investigation of train safety domain in cross wind in respect of attitude change. Journal of Wind Engineering and Industrial Aerodynamics 130, 75–87. https://doi.org/10.1016/j.jweia.2014.04.006.

d'A Samuda, J., 1841. A Treatise on the Adaptation of Atmospheric Pressure to the Purposes of Locomotion on Railways. John Weale, London. https://archive.org/details/atreatiseonadap01samugoog/page/n6.

Daimler, 2018. The Mercedes-Benz Future Bus. The Future of Mobility. https://www.daimler.com/innovation/autonomous-driving/future-bus.html.

Davidson, P., 2005. Turbulence: An Introduction for Scientists and Engineers. Oxford University Press. ISBN 019852949.

Davis, W., 1926. The tractive resistance of electric locomotives and cars. General Electric Review 29 (10), 685–707. https://edoc.site/the-tractive-resistance-of-electric-locomotives-and-cars-pdf-free.html.

Dayman, B., Hammitt, A.G., Holway, H.P., Tucker, C.E., Vardy, A.E., 1979. Alleviation of Pressure Pulse Effects for Trains Entering Tunnels. Jet Propulsion Laboratory Publication 78-73. US Department of Transport Report UMTA-MA-06-0100-79-10, Jet propulsion laboratory, Pasadena, USA. https://rosap.ntl.bts.gov/view/dot/29764/dot_29764_DS1.pdf?.

Deb, K., 2001. Multi-objective Optimization Using Evolutionary Algorithms. Wiley, Chichester, UK.

Deb, K., Datta, R., 2010. A fast and accurate solution of constrained optimization problems using a hybrid bi-objective and penalty function approach. In: Proceedings of the IEEE WCCI 2010, Barcelona, pp. 165–172. https://ieeexplore.ieee.org/abstract/document/5586543.

Deeg, P., Jönsson, M., Kaltenbach, H.-J., Schober, M., Weise, M., 2008. Cross-comparison of measurement techniques for the determination of train induced aerodynamic loads on the trackbed. In: Bluff Body Aerodynamics and its Application, Milano, Italy. http://bbaa6.mecc.polimi.it/uploads/treni/BPR04.pdf.

DEFRA, 2017. Air Pollution in the UK 2016. UK Government Department for Environment, Food and Rural Affairs. https://uk-air.defra.gov.uk/assets/documents/annualreport/air_pollution_uk_2016_issue_2.pdf.

Demartino, C., Ricciardelli, F., 2015. Aerodynamic stability of ice-accreted bridge cables. Journal of Fluids and Structures 52, 81–100. https://doi.org/10.1016/j.jfluidstructs.2014.10.003.

Diedrichs, B., 2003. On computational fluid dynamics modelling of crosswind effects for high-speed rolling stock. Proceedings of the Institution of Mechanical Engineers Part F Journal of Rail and Rapid Transit 217 (3), 203–226. https://doi.org/10.1243/095440903769012902.

Diedrichs, B., 2006. Studies of Two Aerodynamic Effects on High-Speed Trains: Crosswind Stability and Discomforting Car Body Vibrations Inside Tunnels (Ph.D. thesis). Royal Institute of Technology (KTH). http://kth.diva-portal.org/smash/record.jsf?pid=diva2%3A11067&dswid=2522.

Diedrichs, B., 2010. Aerodynamic crosswind stability of a regional train model. Proceedings of the Institution of Mechanical Engineers Part F Journal of Rail and Rapid Transit 224 (6), 580–591. https://doi.org/10.1243/09544097JRRT346.

Diedrichs, B., Berg, M., Stichel, S., Krajnović, S., 2007a. Vehicle dynamics of a high-speed passenger car due to aerodynamics inside tunnels. Proceedings Institution of Mechanical Engineers Part F Journal of Rail and Rapid Transit 221 (4), 527–545. https://doi.org/10.1243/09544097JRRT125.

Diedrichs, B., Ekequist, M., Stichel, S., Tengstrand, H., 2004. Quasi-static modelling of wheel rail reactions due to crosswind effects for various types of high-speed rolling stock. Proceedings of the Institution of Mechanical Engineers Part F Journal of Rail and Rapid Transit 218 (2), 133–148. https://doi.org/10.1243/0954409041319614.

Diedrichs, B., Sima, M., Orellano, A., Tengstrand, H., 2007b. Crosswind stability of a high-speed train on a high embankment. Proceedings of the Institution of Mechanical Engineers Part F: Journal of Rail and Rapid Transit 221 (2), 205–225. https://doi.org/10.1243/0954409JRRT126.

Ding, Y., Sterling, M., Baker, C., 2008. An alternative approach to modelling train stability in high crosswinds. Proceedings of the Institution of Mechanical Engineers Part F: Journal of Rail and Rapid Transit 222 (1), 85–97. https://doi.org/10.1243/09544097JRRT138.

Doi, T., Ogawa, T., Masubuchi, T., Kaku, J., 2010. Development of an experimental facility for measuring pressure waves generated by high speed trains. Journal of Wind Engineering and Industrial Aerodynamics 98 (1), 55–61. https://doi.org/10.1016/j.jweia.2009.09.002.

Dorigati, F., 2013. Rail Vehicles in Crosswinds: Analysis of Steady and Unsteady Aerodynamic Effects Through Static and Moving Model Tests (Ph.D. thesis). University of Birmingham. http://etheses.bham.ac.uk/4267/.

Dorigati, F., Sterling, M., Baker, C., Quinn, A., 2015. Crosswind effects on the stability of a model passenger train — a comparison of static and moving experiments. Journal of Wind Engineering and Industrial Aerodynamics 138, 36–51. https://doi.org/10.1016/j.jweia.2014.11.009.

Downing, S.D., Socie, D.F., 1982. Simple rainflow counting algorithms. International Journal of Fatigue 4 (1), 31–40. https://doi.org/10.1016/0142-1123(82)90018-4.

Duan, Q., Ma, C., Liao, H., 2016. Experimental study on the aerodynamic admittance of railway vehicles on a truss-girder bridge. In: Bluff Body Aerodynamics and its Application, BBAA8 Boston.

Ehrendorfer, K., Sockel, H., 1997. The influence of measures near the portals of railway tunnels on the sonic boom. In: Proceedings 9th International Symposium on the Aerodynamics and Ventilation of Vehicle Tunnels. BHR Group Ltd., Aosta Valley, Italy, pp. 863–875.

Eichinger, S., Sima, M., Thiele, F., 2015. Numerical simulation of a regional train in cross-wind. Proceedings of the Institution of Mechanical Engineers Part F: Journal of Rail and Rapid Transit 229 (6), 625–634. https://doi.org/10.1177/0954409714555383.

ERRI, 1993. Resume of Test Methods to Determine the Aerodynamic Drag of Trains in the Open Air. ERRI C179/RP9.

ERRI, 1994. Loading Due to Dynamic Pressure and Suction from Railway Traffic. Effect of the Slipstreams of Passing Trains on Structures Adjacent to the Track. ERRI D189/RP1.

ERRI, 1998. Pressure Variations in Tunnels: Aerodynamic Aspects of Trains in Tunnels. Specification of a Medical Health Criterion for Pressure Changes. ERRI C218/RP5.

Eskridge, R., Hunt, J.C.R., 1979. Highway modelling part 1: prediction of velocity and turbulence fields in the wakes of vehicles. Journal of Applied Meteorology 18 (4), 387–400. https://doi.org/10.1175/1520-0450(1979)018<0387:HMPIPO>2.0.CO;2.

EU, 2007. Commission Decision of 20 December 2007 (2008/217/CE) Concerning a Technical Specification for Interoperability Relating to the 'Infrastructure' Subsystem of the Trans-European High-Speed Rail System. TSI HS INF; OJEU L 77, 19.3.2008. https://eur-lex.europa.eu/legal-content/EN/TXT/?uri=CELEX:32008D0217.

EU, 2008. Commission Decision of 21 February 2008 (2008/232/CE) Concerning a Technical Specification for Interoperability Relating to the 'Rolling Stock' Subsystem of the Trans-European High-Speed Rail System. TSI HS RST; OJEU L 84, 26.3.2008. https://eur-lex.europa.eu/legal-content/EN/TXT/?uri=uriserv:OJ.L_.2008.084.01.0132.01.ENG.

EU, 2011a. Commission Decision of 26 April 2011 (2011/291/EU) Concerning a Technical Specification for Interoperability Relating to the Rolling Stock Sub-System 'Locomotives and Passenger Rolling Stock' of the Trans-European Conventional Rail System. TSI CR LOC/PAS; OJEU L 139, 26.5.2011. https://eur-lex.europa.eu/legal-content/EN/TXT/?uri=CELEX%3A32011D0291.

EU, 2011b. Commission Decision of 26 April 2011 (2011/275/EU) Concerning a Technical Specification for Interoperability Relating to the 'Infrastructure' Subsystem of the Trans-European Conventional Rail System. TSI CR INF; OJEU L 126, 14.15.2011. https://eur-lex.europa.eu/legal-content/EN/TXT/?uri=CELEX%3A32011D0275.

EU, 2014a. Commission Regulation (EU) No 1302/2014 of 18 November 2014 Concerning a Technical Specification for Interoperability Relating to the 'Rolling Stock — Locomotives and Passenger Rolling Stock' Subsystem of the Rail System in the European Union Text with EEA Relevance. http://data.europa.eu/eli/reg/2014/1302/oj.

EU, 2014b. Commission Regulation (EU) No 1299/2014 of 18 November 2014 on the Technical Specifications for Interoperability Relating to the 'Infrastructure' Subsystem of the Rail System in the European Union Text with EEA Relevance. http://data.europa.eu/eli/reg/2014/1299/oj.

Euronews, 2018. Eight People Injured After Wind Blows a Train Carriage off the Rails in Switzerland. http://www.euronews.com/2018/01/04/eight-people-injured-after-wind-blows-a-train-carriage-off-the-rails-in-switzerland.

Farhan, I., 1991. Theoretical and Experimental Aerodynamic Analysis for High-Speed Ground Vehicles (Ph.D. thesis). Loughborough University. https://dspace.lboro.ac.uk/dspace-jspui/bitstream/2134/22236/1/Thesis-1991-Farhan.pdf.

Figura Hardy, G., 2008. Effective Management of Risk from Slipstream Effects at -Trackside and on Platforms. Appendix B: Analysis of Existing Experimental Data on Train Slipstreams Including the Effects on Pushchairs. Report on RSSB project T425. https://www.sparkrail.org/Lists/Records/DispForm.aspx?ID=9571.

Figura-Hardy, G., 2000. Pressure relief – trend and benefits of incorporating airshafts into railway tunnels. In: Proceedings of the 10th International Symposium on the Aerodynamics and Ventilation of Vehicle Tunnels, Boston, USA, pp. 989–1013.

Fletcher, G.E., 1974. Channel Tunnel Pressure Pulse Effect: Results of Recent Demonstrations. British Railways R&D Division Technical Report TM-AERO-02. https://www.sparkrail.org/Lists/Records/DispForm.aspx?ID=15362.

Flynn, D.C., 2015. A Numerical Investigation of the Effect of Crosswinds on Effects the Slipstream of a Model Scale Freight Train and Associated Effects (Ph.D. thesis). University of Birmingham. http://etheses.bham.ac.uk/6327/1/Flynn15PhD.pdf.

Flynn, D., Hemida, H., Baker, C., 2016. On the effect of crosswinds on the slipstream of a freight train and associated effects. Journal of Wind Engineering and Industrial Aerodynamics 156, 14–28. https://doi.org/10.1016/j.jweia.2016.07.001.

Flynn, D., Hemida, H., Soper, D., Baker, C., 2014. Detached-eddy simulation of the slipstream of an operational freight train. Journal of Wind Engineering and Industrial Aerodynamics 132, 1–12. https://doi.org/10.1016/j.jweia.2014.06.016.

Forasassi, G., 2016. CFD Analysis of Pressure Waves and Loads on Non-tight Trains Passing Tunnels. Master's thesis. KTH Stockholm/Politecnico d Torino. http://www.diva-portal.org/smash/get/diva2:1040644/FULLTEXT01.pdf.

Fox, J., Vardy, A., 1973. The generation and alleviation of air pressure transients by the high speed passage of vehicles through tunnels. In: International Symposium on the Aerodynamics and Ventilation of Vehicle Tunnels, Paper G3, Proceedings of the 1st International Symposium on the Aerodynamics and Ventilation of Vehicle Tunnels, Canterbury, BHRA Fluid Engineering.

Freda, A., Solari, G., 2010. A pilot study of the wind speed along the Rome-Naples HS/HC railway line. part 2-probabilistic analyses and methodology assessment. Journal of Wind Engineering and Industrial Aerodynamics 98 (8–9), 404–416. https://doi.org/10.1016/j.jweia.2009.12.005.

Fridell, E., Björk, A., Ferm, M., Ekberg, A., 2010. On-board measurements of particulate matter emissions from a passenger train. Proceedings of the Institution of Mechanical Engineers Part F: Journal of Rail and Rapid Transit 225 (1), 99–106. https://doi.org/10.1177/09544097JRRT407.

Fu, Q., Easton, J.M., 2018. Prediction of weather-related incidents on the rail network: prototype data model for wind-related delays in Great Britain. ASCE-ASME Journal of Risk and Uncertainty in Engineering Systems, Part A: Civil Engineering 4 (3), 04018027. https://doi.org/10.1061/AJRUA6.0000975.

Fujita, T., 1981. Tornadoes and downbursts in the context of generalized planetary scales. Journal of the Atmospheric Sciences 38 (8), 1511–1534. https://doi.org/10.1175/1520-0469(1981)038<1511:TADITC>2.0.CO;2.

Fujiwara, C., Suzuki, H., 2013. Research on a gust detection system using Doppler radar. JR East Technical Review 27, 29–34. https://www.jreast.co.jp/e/development/tech/pdf_27/Tec-27-29-34eng.pdf.

Fujji, T., Maeda, T., Ishida, H., Imai, T., Tanemota, K., et al., 1999. Wind-induced accidents of trains/vehicles and their measures in Japan. Quarterly Report of RTRI 40 (1), 50–55. https://doi.org/10.2219/rtriqr.40.50.

Fukuchi, G., 1975. Statistical consideration for railway vehicle overturn due to lateral winds. RTRI Quarterly Reports 16 (2), 49–53.

Gaillard, M.A., 1973. Aerodynamics of trains in tunnels. In: Proceedings of the 1st International Symposium on the Aerodynamics and Ventilation of Vehicle Tunnels, Paper J4, Canterbury. BHRA Fluid Engineering.

Gallagher, M., 2016. Experimental Investigation of the Aerodynamics of a Class 43 High Speed Train (Ph.D. thesis). University of Birmingham. http://etheses.bham.ac.uk/7269/.

Gallagher, M., Morden, J., Baker, C., Soper, D., Quinn, A., et al., 2018. Trains in cross-winds – comparison of full-scale on-train measurements, physical model tests and CFD calculations. Journal of Wind Engineering and Industrial Aerodynamics 175, 428–444. https://doi.org/10.1016/j.jweia.2018.03.002.

Garcia, J., Crespo, A., Berasarte, A., Goikoetxea, J., 2011. Study of the flow between the train underbody and the ballast track. Journal of Wind Engineering and Industrial Aerodynamics 99, 1089–1098. https://doi.org/10.1016/j.jweia.2011.07.011.

Garcia, J., Munoz-Paniagua, J., Crespo, A., 2017. Numerical study of the aerodynamics of a full scale train under turbulent wind conditions, including surface roughness effects. Journal of Fluids and Structures 74, 1–18. https://doi.org/10.1016/j.jfluidstructs.2017.07.007.

Garcia, J., Muñoz-Paniagua, J., Jimenez, A., Migoya, E., Crespo, A., 2015. Numerical study of the influence of synthetic turbulent inflow conditions on the aerodynamics of a train. Journal of Fluids and Structures 56, 134–151. https://doi.org/10.1016/j.jfluidstructs.2015.05.002.

Garreau, M., Dupont, R., 1958. Electrical locomotive pantographs. French Railway Techniques 2.

Gautier, P.-E., Sacre, C., Delauney, D., Parrot, M., Dersigny, C., et al., 2001. TGV Méditerranée high speed line safety against cross-winds: a slow-down system based on anemometric measurements and spatial short-term meteorological prediction. In: World Congress on Rail Research, Köln, Germany. https://www.sparkrail.org/Lists/Records/DispForm.aspx?ID=11567.

Gawthorpe, R., 1970. Memoranda of Two Meetings to Discuss Physiological Effects on Passengers Due to Press (Sic) Transients. British Railways Research Department Internal Memorandum IMPS-053. https://www.sparkrail.org/Lists/Records/DispForm.aspx?ID=18270.

Gawthorpe, R., 1978a. Aerodynamics of trains in the open air. Railway Engineer International 3 (3), 7–12. https://www.sparkrail.org/Lists/Records/DispForm.aspx?ID=21806.

Gawthorpe, R., 1978b. Aerodynamic problems with overhead line equipment. Railway Engineer International 3 (4), 38–40. https://www.sparkrail.org/Lists/Records/DispForm.aspx?ID=21807.

Gawthorpe, R., 1978c. Aerodynamics of trains in tunnels. Railway Engineer International 3 (4), 41–47. https://www.sparkrail.org/Lists/Records/DispForm.aspx?ID=21808.

Gawthorpe, R., 1991. Pressure comfort criteria for rail tunnel operations. In: Proc. Proceedings of the 7th International Symposium on the Aerodynamics and Ventilation of Vehicle Tunnels. BHR Group, Brighton, UK, pp. 173–188.

Gawthorpe, R., 1994. Wind effects on ground transportation. Journal of Wind Engineering and Industrial Aerodynamics 52, 73–92. https://doi.org/10.1016/0167-6105(94)90040-X.

Gawthorpe, R., 2000. Pressure effects in railway tunnels. Railways International 31 (4), 10–17. https://www.sparkrail.org/Lists/Records/DispForm.aspx?ID=22073.

Gawthorpe, R., Figura, G., Robertson, N., 1994. Pressure chamber tests of passenger comfort in tunnels. In: Proceedings of the 8th International Symposium on the Aerodynamics and Ventilation of Vehicle Tunnels. BHR Group, Cranfield, Liverpool, UK, pp. 227–243.

Gawthorpe, R., Glöckle, H., Stroud, P.G., 1988. Predicted passenger response to rail tunnel transients. In: Proceedings of the 6th International Symposium on the Aerodynamics and Ventilation of Vehicle Tunnels. BHRA Fluid Engineering, Durham UK, Cranfield.

Gawthorpe, R., Pope, C., 1976. The measurement and interpretation of transient pressures generated by trains in tunnels. In: International Symposium on the Aerodynamics and Ventilation of Vehicle Tunnels, Proceedings of the 2nd International Conference on the Aerodynamics and Ventilation of Vehicle Tunnels, Paper C3. BHRA, Cambridge UK.

Gawthorpe, R., Pope, C., Green, R., 1979a. Analysis of train drag in various configurations of long tunnel. In: Proceedings of the 3rd International Symposium on the Aerodynamics and Ventilation of Vehicle Tunnels. BHRA Fluid Engineering, Sheffield UK, pp. 247–262.

Gawthorpe, R., Pope, C., Green, R., 1979b. Analysis of Train Drag in Various Configurations of Long Tunnel. British Railways R&D Division Technical Report TM-AERO-36. https://www.sparkrail.org/Lists/Records/DispForm.aspx?ID=15376.

Gawthorpe, R., Watson, H.J., McClelland, I.L., 1984. Passenger Comfort during High Speed Rail Travel through Multiple Tunnels – Stage 1 Report Prepared for Deutsche Bundesbahn. British Rail Research Technical Report TR-AER-04. https://www.sparkrail.org/Lists/Records/DispForm.aspx?ID=6079.

Gerhardt, H., Krüger, O., 1998. Wind and train driven air movements in train stations. Journal of Wind Engineering and Industrial Aerodynamics 74, 589–597. https://doi.org/10.1016/S0167-6105(98)00053-1.

Giappino, S., Melzi, S., Tomasini, G., 2018. High speed freight trains for intermodal transportation. Wind tunnel study of the aerodynamic coefficients of container wagons. Journal of Wind Engineering and Industrial Aerodynamics 175, 111–119. https://doi.org/10.1016/j.jweia.2018.01.047.

Giappino, S., Melzi, S., Tomasini, G., Villani, M., 2014. Experimental study on the effect of crosswind on a container train with different load configurations. In: Rail Technology, Research, Development and Maintenance, Corsica, France Paper 31.

Giappino, S., Rocchi, D., Schito, P., Tomasini, G., 2016. Cross wind and rollover risk on lightweight railway vehicles. Journal of Wind Engineering and Industrial Aerodynamics 153, 106–112. https://doi.org/10.1016/j.jweia.2016.03.013.

Gil, N., Baker, C., Roberts, C., Quinn, A., 2010. Passenger train slipstream characterization using a rotating rail rig. Journal of Fluids Engineering, ASME 132 (6), 061401. https://doi.org/10.1115/1.4001577.

Gilbert, T., 2013. Aerodynamic Effects of High Speed Trains in Confined Spaces (Ph.D. thesis). University of Birmingham. https://core.ac.uk/download/pdf/18614463.pdf.

Gilbert, T., Baker, C., Quinn, A., 2013a. Gusts caused by high-speed trains in confined spaces and tunnels. Journal of Wind Engineering and Industrial Aerodynamics 121, 39–48. https://doi.org/10.1016/j.jweia.2013.07.015.

Gilbert, T., Baker, C., Quinn, A., 2013b. Aerodynamic pressures around high-speed trains: the transition from unconfined to enclosed spaces. Proceedings of the Institution of Mechanical Engineers Part F: Journal of Rail and Rapid Transit 227 (6), 609–622. https://doi.org/10.1177/0954409713494947.

Gilchrist, A., 2006. A history of engineering research on British Railways. In: Working Papers on Railway Studies Number 10, Institute of Railway Studies and Transport History, National Railway Museum and University of York, 1368-0706.

Gilchrist, A., Gawthorpe, R., Elkins, J., 1974. Investigation into the Excessive Pantograph Trajectory Amplitudes Observed on Mk IIIA Equipment in High Winds. British Rail Research TN DA 32. https://www.sparkrail.org/Lists/Records/DispForm.aspx?ID=16586.

Global News, 2017. Extreme Winds Blow Train Cars Off Track. https://globalnews.ca/video/3812559/extreme-winds-blow-train-cars-off-tracks.

Glöckle, H., 1991b. Comfort investigations for tunnel runs on the new line Würzburg-Fulda. In: Proceedings of the 7th International Symposium on the Aerodynamics and Ventilation of Vehicle Tunnels. BHR Group, Brighton UK, Cranfield, pp. 155–171.

Golovanevskiy, V., Chmovzh, V., Girka, Y., 2012. On the optimal model configuration for aerodynamic modeling of open cargo railway train. Journal of Wind Engineering and Industrial Aerodynamics 107–108, 131–139. https://doi.org/10.1016/j.jweia.2012.03.035.

Goss, W.F.M., 1898. Atmospheric resistance to the motion of railway trains. Engineer 86, 164–180.

Gottwaldt, A., 2006. Der Schienenzeppelin. Franz Kruckenberg und die Reichsbahn-Schnelltriebwagen der Vorkriegszeit 1929–1939, ISBN 978-3-88255-134-1. Freiburg.

Grappein, E., Rueter, A., 2015. Head pressure pulse in open air: full assessment by computational fluid dynamics as a new standard. Proceedings of the Institution of Mechanical Engineers Part F: Journal of Rail and Rapid Transit 229 (6), 570–580. https://doi.org/10.1177/0954409715585369.

Green, R.H., 1978. The Prediction of Train Drag and Tunnel Draught Velocities in Long Tunnels, Using the 1 D, Quasi-Steady, Incompressible Flow Theory. British Railways R&D Division Technical Report TM-AERO-33. https://www.sparkrail.org/Lists/Records/DispForm.aspx?ID=15373.

Gregoire, R., Réty, J.-M., Masbernat, F., Morinere, V., Bellenoue, M., Kageyama, T., 1997. Experimental study at scale 1/70th and numerical simulations of the generation of pressure waves and micro-pressure waves due to high-speed train-tunnel entry. In: Proceedings of the 9th International Symposium on the Aerodynamics and Ventilation of Vehicle Tunnels. BHR Group, Aosta Valley, Italy, pp. 877–904.

Guardian, 2006. Mag-lev Crash Kills 23. https://www.theguardian.com/technology/2006/sep/22/news.germany.

Guardian, 2016. A Tube for Cars? Proposal to Bury London's Traffic Says It's 'Next Best Thing to Teleportation'. https://www.theguardian.com/cities/2016/dec/02/cartube-tube-underground-cars-proposal-bury-traffic-next-best-thing-to-teleportation.

Guardian, 2017. 'Faster, Cheaper, Cleaner': Experts Disagree About Elon Musk's Hyperloop Claims. https://www.theguardian.com/sustainable-business/2017/aug/04/hyperloop-planet-environment-elon-musk-sustainable-transport.

Guiheu, C., 1981. Aerodynamic resistance of trains. In: Wind Engineering Conference, Nice Paper X-4.

Guo, D., Keming, S., Zhang, Y., Yang, G., Sun, Z., 2016. The influence of affiliated components and train length on the train wind. In: Rail Technology, Research, Development and Maintenance, Cagliari Paper 47.

Guo, Z.-J., Liu, T.-H., Chen, Z.-W., Xie, T.-Z., Jiang, Z.-H., 2018. Comparative numerical analysis of the slipstream caused by single and double unit trains. Journal of Wind Engineering and Industrial Aerodynamics 172, 395–408. https://doi.org/10.1016/j.jweia.2017.11.022.

Guo, W., Xia, H., Xu, Y.-L., 2007. Dynamic response of a long span suspension bridge and running safety of a train under wind action. Frontiers of Architecture and Civil Engineering in China 1 (1), 71–79. https://doi.org/10.1007/s11709-007-0007-1.

Hale, D., 2005. Mallard: How the 'Blue Streak' Broke the World Steam Speed Record. Aurum Press, London, ISBN 1854109391.

Han, J.-B., Kim, K.-J., 2017. Characteristics of vibration in magnetically levitated trains subjected to crosswind. Proceedings of the Institution of Mechanical Engineers Part F: Journal of Rail and Rapid Transit 232 (5), 1347–1359. https://doi.org/10.1177/0954409717721378.

Hara, H., 1961. Aerodynamic force acting on a high speed train at tunnel entrance. Bulletin of Japan Society of Mechanical Engineers 4 (15), 547–553. https://doi.org/10.1299/jsme1958.4.547. https://www.jstage.jst.go.jp/article/jsme1958/4/15/4_15_547/_pdf/-char/en.

Hara, T., Okushi, J., 1962. Model tests on the aerodynamical phenomena of high speed trains entering a tunnel. RTRI Quarterly Reports 3 (4), 6–10.

Harrison, D., 1988. Tests on a BR/Brecknell-Willis High Speed Pantograph in the MIRA Wind Tunnel. British Rail Research TM AERO 088. https://www.sparkrail.org/Lists/Records/DispForm.aspx?ID=5182.

Harrison, D., Rigby, P., 1990. Aerofoil Setting Procedure for BR/Brecknell-Willis Pantographs Fitted to Class 89, 90 and 91. British Rail Research TM AERO 95. https://www.sparkrail.org/Lists/Records/DispForm.aspx?ID=15354.

He, X., Zhou, L., Chen, Z., Jing, H., Zou, Y., Wu, T., 2018. Effect of wind barriers on the flow field and aerodynamic forces of a train-bridge system. Proceedings of the Institution of Mechanical Engineers Part F: Journal of Rail and Rapid Transit. https://doi.org/10.1177/0954409718793220.

Heine, D., Ehrenfried, K., Wagner, C., 2013. Pressure-wave studies in the tunnel-simulation facility Gottingen TSG. In: Proceedings of the 15th International Symposium on Aerodynamics, Ventilation and Fire in Tunnels, pp. 553–563 (Barcelona, Spain).

Hemida, H., Baker, C., 2010. Large-eddy simulation of the flow around a freight wagon subjected to a crosswind. Computers and Fluids 39 (10), 1944–1956. https://doi.org/10.1016/j.compfluid.2010.06.026.

Hemida, H., Baker, C., Gao, G., 2012. The calculation of train slipstreams using Large-eddy simulation. Proceedings of the Institution of Mechanical Engineers Part F: Journal of Rail and Rapid Transit 228 (1), 25–36. https://doi.org/10.1177/0954409712460982.

Hemida, H., Krajnović, S., 2008a. Exploring flow structures around a simplified ICE2 train subjected to a 30° side wind using LES. Engineering Applications of Computational Fluid Mechanics 3 (1), 28–41. https://doi.org/10.1080/19942060.2009.11015252.

Hemida, H., Krajnović, S., 2008b. LES study of the influence of train nose shape on the flow structures under cross-wind conditions. Journal of Fluid Engineering 130 (9), 091101. https://doi.org/10.1115/1.2953228.

Hemida, H., Krajnović, S., 2008c. Aerodynamic Shape Optimization of a Double-Deck Bus Subjected to a Side Wind withCFD and Response Surface Models' Internal Report 2008:04. Chalmers University of Technology Gothenburg.

Hemida, H., Krajnović, S., 2010. LES study of the influence of the nose shape and yaw angle on flow structures around trains. Journal of Wind Engineering and Industrial Aerodynamics 98 (1), 34–46. https://doi.org/10.1016/j.jweia.2009.08.012.

Henson, D.A., Fox, J.A., 1974. An investigation of the transient flows in tunnel complexess of the type proposed for the channel tunnel. Proceedings of the Institution of Mechanical Engineers 188 (1), 153–161. In: https://doi.org/10.1243/PIME_PROC_1974_188_018_02.

Henson, D., Pope, C., 1997. Alleviation of pressure transients in a main line railway tunnel. In: Proceedings of the 9th International Symposium on the Aerodynamics and Ventilation of Vehicle Tunnels. BHRA Group Ltd., Aosta Valley, Italy, pp. 849–862.

Herb, J., Hoppmann, U., Heine, C., Tielkes, T., 2007. A new approach to estimate the wind speed probability distribution along a railway track based on international standards. Journal of Wind Engineering and Industrial Aerodynamics 95 (9–11), 1097–1113. https://doi.org/10.1016/j.jweia.2007.01.018.

Hickman, A., Baker, C., Cai, X., Degado-Saborit, J., Thornes, J., 2018. Evaluaton of air quality at birmingham new street railway station. Proceedings of the Institution of Mechanical Engineers Part F: Journal of Rail and Rapid Transit 232 (6), 1864–1878. https://doi.org/10.1177/0954409717752180.

Hieke, M., Gerbig, C., Tielkes, T., Degen, K.G., 2011. Assessment of micro-pressure wave emissions from high-speed railway tunnels. In: World Congress on Rail Research, Lille, France. https://www.sparkrail.org/Lists/Records/DispForm.aspx?ID=2910.

Hieke, M., Kaltenbach, H.-J., Tielkes, T., 2009. Prediction of micro-pressure wave emissions from high-speed railway tunnels. In: Proceedings 13th International Symposium on Aerodynamics and Ventilation of Vehicle Tunnels, pp. 487–501 (New Brunswick, USA).

Hillmansen, S., 2014. Private Communication. University of Birmingham.

Holmes, J., Oliver, S., 2000. An empirical model of a downburst. Engineering Structures 22 (9), 1167–1172. https://doi.org/10.1016/S0141-0296(99)00058-9.

Hoppmann, U., Koenig, S., Tielkes, T., Matschke, G., 2002. A short-term strong wind prediction model for railway application; design and verification. Journal of Wind Engineering and Industrial Aerodynamics 90 (10), 1127–1134. https://doi.org/10.1016/S0167-6105(02)00226-X.

Howe, M.S., 1998. The compression wave produced by a high-speed train entering a tunnel. Proceedings Royal Society of London A 454, 1523–1534. https://10.1098/rspa.1998.0220.

Howe, M.S., 1999. Review of the theory of the compression wave generated when a high-speed train enters a tunnel. Proceedings Institution of Mechanical Engineers Part F Journal of Rail and Rapid Transit 213 (2), 89–104. https://doi.org/10.1243/0954409991531056.

Howe, M.S., Iida, M., Fukuda, T., Maeda, T., 2000. Theoretical and experimental investigation of the compression wave generated by a train entering a tunnel with a flared portal. Journal of Fluid Mechanics 425, 111–132. https://doi.org/10.1017/S0022112000002093.

Howe, M.S., Iida, M., Maeda, T., Sakuma, Y., 2006. Rapid calculation of the compression wave generated by a train entering a tunnel with a vented hood. Journal of Sound and Vibration 297 (1–2), 267–292. https://doi.org/10.1016/j.jsv.2006.03.039.

Howell, J., 1986. Aerodynamic response of maglev train models to a crosswind gust. Journal of Wind Engineering and Industrial Aerodynamics 22 (2–3), 205–213. https://doi.org/10.1016/0167-6105(86)90085-1.

Hoxey, R., Reynolds, A., Richardson, G., Robertson, A., Short, J., 1998. Observations of Reynolds number sensitivity in the separated flow region on a bluff body. Journal of Wind Engineering and Industrial Aerodynamics 73 (3), 231–249. https://doi.org/10.1016/S0167-6105(97)00287-0.

HS2, 2014. High Speed Two Information Paper D8: Tunnel Shafts and Portals. http://assets.hs2.org.uk/sites/default/files/hb_pdf/D8%20-%20Tunnel%20shafts%20and%20portals_0.pdf.

Huang, S., Hemida, H., Yang, M., 2016. Numerical calculation of the slipstream generated by a CRH2 high-speed train. Proceedings of the Institution of Mechanical Engineers Part F: Journal of Rail and Rapid Transit 230 (1), 103–116. https://doi.org/10.1177/0954409714528891.

Humphreys, N., 1995. High Cross Wind Gust Loads on Ground Vehicles from Moving Model Experiments (Ph.D. thesis). University of Nottingham. http://eprints.nottingham.ac.uk/11923/1/283406.pdf.

Ido, A., 2003. A study on the aerodynamic drag reduction of trains. In: World Congress on Rail Research, Edinburgh, UK, pp. 1553–1561. https://www.sparkrail.org/Lists/Records/DispForm.aspx?ID=11888.

Ido, A., Saitou, S., Nakade, K., Iikura, S., 2008. Study on under-floor flow to reduce ballast flying phenomena. In: World Congress on Rail Research, Seoul, South Korea. https://www.sparkrail.org/Lists/Records/DispForm.aspx?ID=4499.

Ido, A., Yamazaki, N., Kurita, T., Yoshioka, S., 2013. Study on under-floor flow of railway vehicle using on-track tests with a Laser Doppler Velocimetry and moving model tests with comb stagnation pressure tubes. In: World Congress on Rail Research, Sydney, Australia. https://www.sparkrail.org/Lists/Records/DispForm.aspx?ID=12430.

Iida, M., Howe, M.S., 2007. Compression wave generated by a high-speed train entering a tunnel with a hood with a long slit window. Journal of Low Frequency Noise, Vibration and Control 264 (4), 227–247. https://doi.org/10.1260/026309207783571352.

Imai, T., Fujii, K., Tanemoto, T., Shinamura, T., Maeda, T., et al., 2002. New train regulation method based on wind direction and velocity of natural wind against strong winds. Journal of Wind Engineering and Industrial Aerodynamics 90 (12–15), 1601–1610. https://doi.org/10.1016/S0167-6105(02)00273-8.

Jakubek, D., Wagner, C., 2016. Aerodynamic Shape Optimization of Train Heads Using Adjoint-Based Computational Fluid Dynamics with Different Objective Functions. In: Rail Technology, Research, Development and Maintenance, Cagliari, Italy, Paper 56.

Jang, Y.-J., Kim, D.-H., Park, W.-H., 2008. Pressure characteristics on Korean high-speed railway acoustic screen using 1/61-scaled moving model rig. In: World Congress on Rail Research, Seoul, South Korea. https://www.sparkrail.org/Lists/Records/DispForm.aspx?ID=4505.

Jing, G.Q., Zhou, Y.D., Lin, J., Zhang, J., 2012. Ballast flying mechanism and sensitivity factors analysis. International Journal of Smart Sensing and Intelligent Systems 5 (4), 928–939. https://www.exeley.com/in_jour_smart_sensing_and_intelligent_systems/doi/10.21307/ijssis-2017-515.

Johansen, F.C., 1936. The air resistance of passenger trains. Proceedings of the Institution of Mechanical Engineers 134, 91–208. In: https://doi.org/10.1243/PIME_PROC_1936_134_008_02.

Johnson, T., 1985. A Probabilistic Assessment of Blow-Off Dewirement and Associated Alleviation Methods. British Rail Research TM AERO 82. https://www.sparkrail.org/Lists/Records/DispForm.aspx?ID=5165.

Johnson, T., 1996. Strong wind effects on railway operations—16th October 1987. Journal of Wind Engineering and Industrial Aerodynamics 60, 251–266. https://doi.org/10.1016/0167-6105(96)00038-4.

Johnson, T., 1999. The need for a standardised definition of a sealing parameter. In: ERRI Conference on Cost-Effectiveness of Pressure Sealed Coaches, Utrecht, October.

Johnson, T., 2001. Measurements of the effect on pressures of a porous tunnel entrance using a moving model rig. In: World Congress on Railway Research, Köln, Germany. http://www.windresearch.org/docs/Paper%205.pdf.

Johnson, T., Dalley, S., 2000. Moving model rig tests on a tunnel with a porous entrance and with an airshaft - measurements and validation of ThermoTun predictions. In: Proceedings 10th International Symposium on the Aerodynamics and Ventilation of Vehicle Tunnels, Boston, USA, pp. 815–827.

Johnson, T., Dalley, S., 2001. 1/25 scale moving model tests for the TRANSAERO Project. In: Schulte-Werning, B., Gregoire, R., Malfatti, M., Matschke, G. (Eds.), Notes on Numerical Fluid Mechanics and Multidisciplinary Design, TRANSAERO – A European Initiative on Transient Aerodynamics for Railway System Optimisation, vol. 79, pp. 123–135. https://link.springer.com/chapter/10.1007/978-3-540-45854-8_10.

Johnson, T., Prevezer, T., Figura-Hardy, G., 2000. Tunnel pressure comfort limits examined using passenger comfort ratings. In: Proceedings 10th International Symposium on the Aerodynamics and Ventilation of Vehicle Tunnels, Boston, USA, 221-2312.

Johnston, R., Welsh, j., Schafer, M., 2001. The Art of the Streamliner. Metro Books, New York, ISBN 1-58663-146-2.

Jönsson, M., Wagner, C., Loose, S., 2012. Particle image velocimetry of the underfloor flow for generic high-speed train models in a water towing tank. Proceedings of the Institution of Mechanical Engineers Part F: Journal of Rail and Rapid Transit 228 (2), 194–209. https://doi.org/10.1177/0954409712470607.

Jordan, S., 2008. An Investigation of the Slipstreams and Wakes of Trains and the Associated Effects on Trackside People and Objects (Ph.D. thesis). University of Birmingham. http://etheses.bham.ac.uk/8029/.

Jordan, S., Johnson, T., Sterling, M., Baker, C., 2008. Evaluating and modelling the response of an individual to a sudden change in wind speed. Building and Environments 43 (9), 1521–1534. https://doi.org/10.1016/j.buildenv.2007.08.004.

Jordan, S., Sterling, M., Baker, C., 2009. Modelling the response of a standing person to the slipstream generated by a passenger train. Proceedings of the Institution of Mechanical Engineers Part F: Journal of Rail and Rapid Transit 223 (6), 567–579. https://doi.org/10.1243/09544097JRRT281.

Kaltenbach, H.-J., Gautier, P.-E., Agirre, G., Orellano, A., Schroeder-Bodenstein, K., et al., 2008. Assessment of the aerodynamic loads on the trackbed causing ballast projection: results from the DEUFRAKO project Aerodynamics in Open Air (AOA). In: World Congress on Rail Research, Seoul, South Korea. https://www.sparkrail.org/Lists/Records/DispForm.aspx?ID=4498.

Kam, W., Cheung, K., Daher, N., Sioutas, C., 2011. Particulate matter (PM) concentrations in underground and ground-level rail systems of the Los Angeles Metro. Atmospheric Environment 45 (8), 1506–1516. https://doi.org/10.1016/j.atmosenv.2010.12.049.

Kawashima, K., Iikura, S., Endo, T., Fujii, T., 2003. Experimental studies on ballast-flying phenomenon caused by dropping of accreted snow/ice from high-speed trains. RTRI Reports 17 (8), 31–36. https://jglobal.jst.go.jp/en/detail?JGLOBAL_ID=200902288655468493&rel=0.

Khandhia, Y., Gaylard, A.P., Johnson, T., 1996. CFD simulation of three dimensional unsteady train aerodynamics. In: 1st MIRA International Conference on Vehicle Aerodynamics.

Kikuchi, K., Iida, M., Fukuda, T., 2011. Optimization of train nose shape for reducing micro-pressure wave radiated from tunnel exit. Journal of Low Frequency Noise, Vibration and Active Control 30 (1), 1–19. http://journals.sagepub.com/doi/pdf/10.1260/0263-0923.30.1.1.

Kikuchi, K., Suzuki, M., 2015. Study of aerodynamic coefficients used to estimate critical wind speed for vehicle overturning. Journal of Wind Engineering and Industrial Aerodynamics 147, 1–17. https://doi.org/10.1016/j.jweia.2015.09.003.

Kim, T.-K., Kim, K.-H., Kwon, H.-B., 2011. Aerodynamic characteristics of a tube train. Journal of Wind Engineering and Industrial Aerodynamics 99 (12), 1187–1196. https://doi.org/10.1016/j.jweia.2011.09.001.

Kim, S.-W., Kwon, H.-B., Kim, Y.-G., Park, T.-W., 2006. Calculation of resistance to motion of a high-speed train using acceleration measurements in irregular coasting conditions. Proceedings of the Institution of Mechanical Engineers Part F: Journal of Rail and Rapid Transit 220 (4), 449–459. https://doi.org/10.1243/0954409JRRT74.

Kind, R., 1975. Tests to determine the wind-speeds for scouring and blow off of rooftop gravel. In: International Conference on Wind Effects on Buildings and Structures, Fourth International Conference on Wind Engineering, Heathrow, pp. 591–604.

Kirkland, C.J., 2002. The fire in the channel tunnel. Tunnelling and Underground Space Technology 17 (2), 129–132. https://doi.org/10.1016/S0886-7798(02)00014-7.

Komatsu, N., Yamada, F., Minami, T., 1999. The reduction of disturbance of the train draft pressure in passing by each other. In: World Congress on Rail Research, Tokyo, Japan. https://www.sparkrail.org/Lists/Records/DispForm.aspx?ID=11193.

Krajnović, S., 2008. Improvement of aerodynamic properties of high-speed trains by shape optimization and flow control. In: World Congress on Rail Research, Seoul, South Korea. https://www.sparkrail.org/Lists/Records/DispForm.aspx?ID=4504.

Krajnović, S., 2009a. Shape optimization of high-speed trains for improved aerodynamic performance. Proceedings of the Institution of Mechanical Engineers Part F: Journal of Rail and Rapid Transit 223 (5), 439–452. https://doi.org/10.1243/09544097JRRT251.

Krajnovic, S., 2009b. Large eddy simulation of flows around ground vehicles and other bluff bodies. Philosophical Transactions of the Royal Society A 367, 2917–2930. https://doi.org/10.1098/rsta.2009.0021.

Krönke, I., Sockel, H., 1994. Model tests about cross wind effects on containers and wagons in atmospheric boundary layers. Journal of Wind Engineering and Industrial Aerodynamics 52, 109–119. https://doi.org/10.1016/0167-6105(94)90042-6.

Kumar, A., Rickett, T., Vemula, A., Hart, J., Riley, J., et al., 2011. Aerodynamic analysis of intermodal freight trains using machine vision. In: World Congress on Rail Research, Lille, France. http://www.railway-research.org/IMG/pdf/a3_edwards_j.pdf.

Kwon, H.-B., Nam, S.-W., You, W.-H., 2010. Wind tunnel testing on crosswind aerodynamic forces acting on rail vehicles. Journal of Fluid Science and Technology 5 (1), 56–63.

Kwon, H.-B., Oh, H.-K., 2013. Decomposition and reduction of aerodynamic drag of high-speed train. In: World Congress on Rail Research, Sydney, Australia. https://www.sparkrail.org/Lists/Records/DispForm.aspx?ID=12840.

Kwon, H.-B., Park, C.-S., 2006. An experimental study on the relationship between ballast flying phenomenon and strong wind under high speed train. In: World Congress on Rail Research, Montreal, Canada. https://www.sparkrail.org/Lists/Records/DispForm.aspx?ID=10884.

Kwon, H.-B., Park, Y.-W., Lee, D.-H., Kim, M.-S., 2001. Wind tunnel experiments on Korean high-speed trains using various ground simulation techniques. Journal of Wind Engineering and Industrial Aerodynamics 89 (13), 1179–1195. https://doi.org/10.1016/S0167-6105(01)00107-6.

Lachinger, S., Reiterer, M., Kari, H., 2016. Comparison of calculation methods for aerodynamic impact on noise barriers along high speed rail lines. In: World Congress on Rail Research, Milano, Italy. https://www.sparkrail.org/Lists/Records/DispForm.aspx?ID=23675.

Lai, Y., Barkan, C., 2005. Options for improving the energy efficiency of intermodal freight trains. Transportation Research Record 1916, 47–55. https://doi.org/10.3141/1916-08.

Lai, Y., Barkan, C., Drapa, J., Ahuja, N., Hart, J., et al., 2007. Machine vision analysis of the energy efficiency of intermodal freight trains. Proceedings of the Institution of Mechanical Engineers Part F: Journal of Rail and Rapid Transit 221 (3), 353–364. https://doi.org/10.1243/09544097JRRT92.

Lai, Y., Barkan, C., Önal, H., 2008. Optimizing the aerodynamic efficiency of intermodal freight trains. Transportation Research Part E Logistics and Transportation Review 44 (5), 820–834. https://doi.org/10.1016/j.tre.2007.05.011.

Larose, G., D'Auteuil, A., 2006. On the Reynolds number sensitivity of the aerodynamics of bluff bodies with sharp edges. Journal of Wind Engineering and Industrial Aerodynamics 94 (5), 365–376. https://doi.org/10.1016/j.jweia.2006.01.011.

Larose, G., D'Auteuil, A., 2008. Experiments on 2D rectangular prisms at high Reynolds numbers in a pressurised wind tunnel. Journal of Wind Engineering and Industrial Aerodynamics 96 (6–7), 923–933. https://doi.org/10.1016/j.jweia.2007.06.018.

Lazaro, B., Gonzalez, E., Rodriguez, M., Osma, S., Iglesias, J., 2011. Characterization and modeling of flying ballast phenomena in high-speed train line. In: World Congress on Rail Research, Lille, France. https://www.sparkrail.org/Lists/Records/DispForm.aspx?ID=3395.

Le, H.-Q., Lehner, A., Sand, S., 2015. Performance analysis of ITS-G5 for dynamic train coupling application. In: International Workshop on Communication Technologies for Vehicles, Lecture Notes in Computer Science. Springer, pp. 129–140. https://doi.org/10.1007/978-3-319-17765-6_12.

Lee, Y., Rho, J., Kim, K.H., Lee, D.H., Kwon, H.B., 2015. Experimental studies on the aerodynamic characteristics of a pantograph suitable for a high-speed train. Proceedings of the Institution of Mechanical Engineers Part F: Journal of Rail and Rapid Transit 229 (2), 136–149. https://doi.org/10.1177/0954409713507561.

Li, C., Burton, D., Kost, M., Sheridan, J., Thompson, M., 2017a. Flow topology of a container train wagon subjected to varying local loading configurations. Journal of Wind Engineering and Industrial Aerodynamics 169, 12–29. https://doi.org/10.1016/j.jweia.2017.06.011.

Li, T., Hemida, H., Zhang, J., Rashidi, M., Flynn, D., 2018a. Comparisons of shear stress transport and detached eddy simulations of the flow around trains. Journal of Fluids Engineering, Transactions of the ASME 140 (11), 111108. http://fluidsengineering.asmedigitalcollection.asme.org/article.aspx?articleid=2687023.

Li, Y., Qianga, S., Liao, H., Xu, Y., 2005. Dynamics of wind-rail vehicle-bridge systems. Journal of Wind Engineering and Industrial Aerodynamics 93 (6), 483–507. https://doi.org/10.1016/j.jweia.2005.04.001.

Li, X.-Z., Wang, M., Xiao, X., Zou, Q.-Y., Liu, D.-J., 2018c. Experimental study on aerodynamic characteristics of high-speed train on a truss bridge: a moving model test. Journal of Wind Engineering and Industrial Aerodynamics 179, 26–38. https://doi.org/10.1016/j.jweia.2018.05.012.

Li, R., Xu, P., Peng, Y., Ji, P., 2016. Multi-objective optimization of a high-speed train head based on the FFD method. Journal of Wind Engineering and Industrial Aerodynamics 152, 41–49. https://doi.org/10.1016/j.jweia.2016.03.003.

Li, Z., Yang, M., Huang, S., Liang, X., 2017b. A new method to measure the aerodynamic drag of high speed trains passing through tunnels. Journal of Wind Engineering and Industrial Aerodynamics 171, 110–120. https://doi.org/10.1016/j.jweia.2017.09.017.

Li, Z., Yang, M., Huang, S., Zhou, D., 2018d. A new moving model test method for the measurement of aerodynamic drag coefficient of high-speed trains based on machine vision. Proceedings of the Institution of Mechanical Engineers Part F: Journal of Rail and Rapid Transit 232 (5), 1425–1436. https://doi.org/10.1177/0954409717731233.

Li, T., Yu, M., Zhang, J., Zhang, W., 2015. A fast equilibrium state approach to determine interaction between stochastic crosswinds and high-speed trains. Journal of Wind Engineering and Industrial Aerodynamics 143, 91–104. https://doi.org/10.1016/j.jweia.2015.04.002.

Li, T., Zhang, J., Zhang, W., 2011. An improved algorithm for fluid-structure interaction of high-speed trains under crosswind. Journal of Modern Transportation 19 (2), 75–81. https://doi.org/10.1007/BF03325743.

Li, R., Zhao, J., Zhang, S., 2009. A study of the influence of aerodynamic forces on a human body near a high-speed train. In: Browand, F., McCallen, R., Ross, J. (Eds.), The Aerodynamics of Heavy Vehicles II: Trucks, Buses, and Trains, Lecture Notes in Applied and Computational Mechanics, vol. 41. Springer, Berlin, Heidelberg. https://link.springer.com/chapter/10.1007%2F978-3-540-85070-0_24.

Li, X., Zhou, D., Jia, L., Yang, M., 2018b. Effects of yaw angle on the unsteady aerodynamic performance of the pantograph of a high-speed train under crosswind. Journal of Wind Engineering and Industrial Aerodynamics 182, 49–60. https://doi.org/10.1016/j.jweia.2018.09.009.

Lim, H., Castro, I., Hoxey, R., 2007. Bluff bodies in turbulent boundary layers: Reynolds-number issues. Journal of Fluid Mechanics 571 (1), 97–118. https://doi.org/10.1017/S0022112006003223.

Lin, C.-J., Chuah, Y., Liu, C.-W., 2008. A study on underground tunnel ventilation for piston effects influenced by draught relief shaft in subway system. Applied Thermal Engineering 28 (5–6), 372–379. https://doi.org/10.1016/j.applthermaleng.2007.10.003.

Liu, T.-H., Chen, X.-D., Li, W.-H., Xie, T.-Z., Chen, Z.-W., 2017. Field study on the interior pressure variations in high-speed trains passing through tunnels of different lengths. Journal of Wind Engineering and Industrial Aerodynamics 169, 54–66. https://doi.org/10.1016/j.jweia.2017.07.004.

Liu, H., Gu, X., Tang, W., 2012. Icing and anti-icing of railway contact wires. In: Perpinya, X. (Ed.), Reliability and Safety in Railway. Publisher: InTech, ISBN 978-953-51-0451-3. https://cdn.intechopen.com/pdfs-wm/34439.pdf.

Liu, Y., Hemida, H., Liu, Z., 2014. Large eddy simulation of the flow around a train passing a stationary freight wagon. Proceedings of the Institution of Mechanical Engineers Part F: Journal of Rail and Rapid Transit 228 (5), 535–545. https://doi.org/10.1177/0954409713488096.

Liu, H., Tian, H.-Q., Li, Y.-F., 2015. An EMD-recursive ARIMA method to predict wind speed for railway strong wind warning system. Journal of Wind Engineering and Industrial Aerodynamics 141, 27–38. https://doi.org/10.1016/j.jweia.2015.02.004.

Liu, T.-H., Tian, H.-Q., Liang, X.-F., 2010. Design and optimisation of tunnel hoods. Tunnelling and Underground Space Technology 25 (3), 212–219. https://doi.org/10.1016/j.tust.2009.12.001.

Lu, M., Li, Q., Ning, Z., Ji, Z., 2018. Study of the aerodynamic load characteristic of noise reduction barriers on high speed railway. Journal of Wind Engineering and Industrial Aerodynamics 176, 254–262. https://doi.org/10.1016/j.jweia.2018.03.031.

Lukaszewicz, P., 2001. Energy Consumption and Running Time for Trains (Ph.D. thesis). KTH, Sweden. https://pdfs.semanticscholar.org/b2a1/478bb878493fb4eee06e89f847d80e649309.pdf.

Lukaszewicz, P., 2006. Running resistance - results and analysis of full-scale tests with passenger and freight trains in Sweden. Proceedings of the Institution of Mechanical Engineers Part F Journal of Rail and Rapid Transit 221 (2), 183–193. https://doi.org/10.1243/0954409JRRT89.

Lukaszewicz, P., 2007. A simple method to determine train running resistance from full-scale measurements. Proceedings of the Institution of Mechanical Engineers Part F Journal of Rail and Rapid Transit 221 (3), 331–337. https://doi.org/10.1243/09544097JRRT88.

Maeda, T., Iida, M., Murata, K., Hukuda, T., 2000. Micro-pressure waves radiating from a tunnel portal and their mitigation. In: International Congress and Exhibition on Noise Control Engineering, Nice, France. http://www.conforg.fr/internoise2000/cdrom/data/articles/000920.pdf.

Mair, W., Stewart, A., 1985. The flow past yawed slender bodies, with and without ground effects. Journal of Wind Engineering and Industrial Aerodynamics 18 (3), 301–328. https://doi.org/10.1016/0167-6105(85)90088-1.

Maleki, S., Burton, D., Thompson, M., 2017. Assessment of various turbulence models (ELES, SAS, URANS and RANS) for predicting the aerodynamics of freight train container wagons. Journal of Wind Engineering and Industrial Aerodynamics 170, 68–80. https://doi.org/10.1016/j.jweia.2017.07.008.

Mallet, C., 1844. Report on the railroad constructed from Kingstown to Dalkey, in Ireland, upon the atmospheric system, and on the application of this system to railroads in general. Abridged Translation The Practical Mechanic and Engineer's Magazine 279. French original at: https://archive.org/stream/rapportsurleche00mallgoog#page/n8/mode/2up.

Mancini, G., Malfatti, A., Violi, A., Matschke, G., 2001. Effects of experimental bogie fairings on the aerodynamic drag of the ETR 500 high speed train. In: World Congress on Rail Research, Köln, Germany. https://www.sparkrail.org/Lists/Records/DispForm.aspx?ID=11628.

Mancini, G., Violi, A., 1999. Pressure wave effects of high speed trains running parallel on large and medium sized tunnels of Italian high speed lines. In: World Congress on Railway Research, Tokyo, Japan. https://www.sparkrail.org/Lists/Records/DispForm.aspx?ID=11280.

Masson, E., Hoefener, L., 2008. Aerodynamics in the Open Air. WP2 Crosswind Issues – Summary Report. https://www.sparkrail.org/Lists/Records/DispForm.aspx?ID=9823.

Matschke, G., Heine, C., 2002. Full-scale tests on side wind effects on trains – evaluation of aerodynamic coefficients and efficiency of wind breaking devices. In: Schulte-Werning, B., Gregoire, R., Malfatti, M., Matschke, G. (Eds.), TRANSAERO – A European Initiative on Transient Aerodynamics for Railway System Optimisation, Notes on Numerical Fluid Mechanics and Multidisciplinary Design, vol. 79, pp. 27–38. https://link.springer.com/chapter/10.1007/978-3-540-45854-8_3.

Matschke, G., Schulte-Werning, B., 1997. Measures and strategies to minimise the effect of strong cross winds on high speed trains. In: World Congress on Rail Research, Firenze, Italy. https://www.sparkrail.org/Lists/Records/DispForm.aspx?ID=2611.

Matsubayashi, K., Kosaka, T., Kitamura, T., Yamada, S., Vardy, A., Brown, J., 2004. Reduction of micro-pressure wave by active control of propagating compression wave in high speed train tunnel. Journal of Low Frequency Noise, Vibration and Active Control 23 (4), 259–270. http://journals.sagepub.com/doi/pdf/10.1260/0263-0923.23.4.259.

Michalek, T., 2018. Modification of train resistance formulae for container trains based on operational run-down tests. Proceedings of the Institution of Mechanical Engineers Part F: Journal of Rail and Rapid Transit 232 (6), 1588–1597. https://doi.org/10.1177/0954409717738690.

Ming, L., Bin, L., Miao, Y., Dahai, W., 2016. Multi-objective integrated optimization of the aerodynamic shape design of the head type for a high speed electrical multiple unit. In: Rail Technology, Research, Development and Maintenance, Cagliari, Italy Paper 61.

Mishra, A., James, D., Letchford, C., 2008. Physical simulation of a single-celled tornado-like vortex, part A: flow field characterization. Journal of Wind Engineering and Industrial Aerodynamics 96 (8–9), 1243–1257. https://doi.org/10.1016/j.jweia.2008.02.063.

Misu, Y., Ishhihara, T., 2018. Prediction of frequency distribution of strong crosswind in a control section for train operations by using onsite measurement and numerical simulation. Journal of Wind Engineering and Industrial Aerodynamics 174, 69–79. https://doi.org/10.1016/j.jweia.2017.11.020.

Miyachi, T., Iida, M., Fukuda, T., Arai, T., 2016. Nondimensional maximum pressure gradient of tunnel compression waves generated by offset running axisymmetric trains. Journal of Wind Engineering and Industrial Aerodynamics 157, 23–35. https://doi.org/10.1016/j.jweia.2016.07.015.

Mohebbi, M., Rezvani, M., 2018. Two-dimensional analysis of the influence of windbreaks on airflow over a high-speed train under crosswind using lattice Boltzmann method. Proceedings of the Institution of Mechanical Engineers Part F Journal of Rail and Rapid Transit 232 (3), 863–872. https://doi.org/10.1177/0954409717699502.

Monaco, S., Dignath, F., 2008. Structural deformation caused by aerodynamic excitations during the passage of Maglev vehicles. In: Bluff Body Aerodynamics and its Application, Milano, Italy. http://bbaa6.mecc.polimi.it/uploads/treni/pwt03.pdf.

Monnoyer, F., Lorriaux, E., Bourabaa, N., 2006. Aerodynamic optimization of railway motor coaches. In: World Congress on Rail Research, Montreal, Canada. http://www.railway-research.org/IMG/pdf/218-2.pdf.

Monreagh Heritage Centre, 2018. The Owencarrow Viaduct Disaster. https://www.monreaghulsterscotscentre.com/owencarrow-viaduct/.

Morden, J., Hemida, H., Baker, C., 2015. Comparison of RANS and detached eddy simulation results to wind-tunnel data for the surface pressures upon a class 43 high speed train. Journal of Fluids Engineering 137 (4), 041108. Paper No: FE-14-1185. https://doi.org/10.1115/1.4029261.

Most, D., 2014. The Race Underground: Boston, New York and the Incredible Rivalry that Built America's First Subway. St Martin's Press. Excerpt in Scientific American. https://www.scientificamerican.com/article/scientific-americans-owner-built-the-first-new-york-subway-excerpt/.

Muld, T., Efraimsson, G., Henningson, D., 2014. Wake characteristics of high-speed trains with different lengths. Proceedings of the Institution of Mechanical Engineers Part F Journal of Rail and Rapid Transit 228 (4), 333–342. https://doi.org/10.1177/0954409712473922.

Muld, T., Efraimsson, G., Henningsson, D., 2012. Flow structures around a high-speed train extracted using proper orthogonal decomposition and dynamic mode decomposition. Computers and Fluids 57, 87–97. https://doi.org/10.1016/j.compfluid.2011.12.012.

Muñoz-Paniagua, J., Garcia, J., Crespo, A., 2014. Genetically aerodynamic optimization of the nose shape of a high-speed train entering a tunnel. Journal of Wind Engineering and Industrial Aerodynamics 130, 48–61. https://doi.org/10.1016/j.jweia.2014.03.005.

Muñoz-Paniagua, J., Garcia, J., Lehugeur, B., 2017. Evaluation of RANS, SAS and IDDES models for the simulation of the flow around a high-speed train subjected to crosswind. Journal of Wind Engineering and Industrial Aerodynamics 171, 50–66. https://doi.org/10.1016/j.jweia.2017.09.006.

Munson, B., Okiishi, T., Huebsch, W., Rothmayer, A., 2013. Fundamentals of Fluid Mechanics, seventh ed. John Wiley & Sons, New York. ISBN:13: 978-1118116135.

Myring, D.F., 1971. Body Leakages for APT. British Railways Research IM-AERO-26. https://www.sparkrail.org/Lists/Records/DispForm.aspx?ID=13644.

Myring, D.F., 1973. An Assessment of Test Results Concerning Discomfort Caused by Transient Pressures. British Railways Research IM-AERO-58. https://www.sparkrail.org/Lists/Records/DispForm.aspx?ID=10433.

Nakade, K., 2014. Numerical simulation of flow around railway vehicle in turbulent boundary layer over flat terrain. RTRI Quarterly Reports 55, 249–254. https://www.jstage.jst.go.jp/article/rtriqr/55/4/55_249/_pdf/-char/en.

Nakade, K., Noguchi, Y., Kikuchi, K., 2016. Fluctuating aerodynamic force on railway vehicle under crosswind using large-eddy simulation. In: Bluff Body Aerodynamics and its Application, Boston, USA.

Nakamura, Y., Sakanoue, K., Minami, Y., Okada, Y., 2011. Development of pantograph for the series N700 shinkansen. In: World Congress on Rail Research, Lille, France. https://www.sparkrail.org/Lists/Records/DispForm.aspx?ID=2911.

Navarro-Medina, F., Perez-Grande, I., Sanz-Andres, A., 2015. Comparative study of the effect of several trains on the rotation motion of ballast stones. Proceedings of the Institution of Mechanical Engineers Part F Journal of Rail and Rapid Transit 229 (1), 71–88. https://doi.org/10.1177/0954409713500667.

Network Rail, 2015. A Guide to Overhead Electrification. 132787-ALB-GUN-EOH-000001. http://www.bathnes.gov.uk/sites/default/files/sitedocuments/Planning-and-Building-Control/Planning/nr_a_guide_to_overhead_electrification.pdf.

Network Rail, 2018. Weather Resilience. https://www.networkrail.co.uk/communities/environment/climate-change-weather-resilience/weather-resilience/.

Niu, J., Liang, X., Zhou, D., 2016. Experimental study on the effect of Reynolds number on aerodynamic performance of high-speed train with and without yaw angle. Journal of Wind Engineering and Industrial Aerodynamics 157, 36–46. https://doi.org/10.1016/j.jweia.2016.08.007.

Niu, J., Zhou, D., Liang, X., 2017. Numerical simulation of the effects of obstacle deflectors on the aerodynamic performance of stationary high-speed trains at two yaw angles. Proceedings of the Institution of Mechanical Engineers Part F: Journal of Rail and Rapid Transit 232 (3), 913–927. https://doi.org/10.1177/0954409717701786.

Niu, J., Zhou, D., Wang, Y., 2018. Numerical comparison of aerodynamic performance of stationary and moving trains with or without windbreak wall under crosswind. Journal of Wind Engineering and Industrial Aerodynamics 182, 1–15. https://doi.org/10.1016/j.jweia.2018.09.011.

Noguchi, Y., Suzuki, M., Nakade, K., 2017. Aerodynamic force on railway vehicles on an embankment in a turbulent boundary layer and a smooth flow. In: European and African Conference on Wind Engineering, Liege, Belgium.

Nolte, R., Wurtenberger, F., 2003. Evaluation of Energy Efficient Technologies for Rolling Stock and Train Operation of Railways. International Union of Railways (UIC), Berlin.

Onat, B., Stakeeva, B., 2014. Assessment of fine particulate matters in the subway system of Istanbul. Indoor and Built Environment 23 (4), 574–583. https://doi.org/10.1177/1420326X12464507.

Orellano, A., Kirchhof, R., 2011. Optimising the aerodynamics of high speed trains. Railway Gazette International 41–45.

Orellano, A., Sperling, S., 2009. Aerodynamic improvements and associated energy demand reduction of trains. In: Browand, F., McCallen, R., Ross, J. (Eds.), The Aerodynamics of Heavy Vehicles II: Trucks, Buses, and Trains, Lecture Notes in Applied and Computational Mechanics, vol. 41. Springer, Berlin, Heidelberg. https://link.springer.com/chapter/10.1007%2F978-3-540-85070-0_19.

Ozawa, S., 1984. Counter measures to reduce booms from exits of Shinkansen tunnels. Japanese Railway Engineering 242, 2–5.

Ozawa, S., 1990. Aerodynamic forces on trains. Japanese Society of Mechanical Engineers 900, 37.

Ozawa, S., Maeda, T., 1988. Tunnel entrance hoods for reduction of micro-pressure wave. Quarterly Report of RTRI 293, 134–1312.

Ozawa, S., Maeda, T., Matsumura, T., Uchida, K., Kajiyama, H., Tanemoto, K., 1991. Countermeasures to reduce micro-pressure waves radiating from exits of Shinkansen tunnels. In: Proceedings of the 7th International Symposium on the Aerodynamics and Ventilation of Vehicle Tunnels, Brighton, UK, pp. 253–266.

Paradot, N., Gregoire, R., Stiepel, M., Blanco, A., Sima, M., et al., 2015. Crosswind sensitivity assessment of a representative Europe-wide range of conventional vehicles. Proceedings of the Institution of Mechanical Engineers Part F Journal of Rail and Rapid Transit 229 (6), 594–624. https://doi.org/10.1177/0954409715585368.

Paradot, N., Talotte, C., Willaime, A., Guccia, L., Bouhadana, J.-L., 1999. Methodology for computing the flow around a high speed train for drag estimation and validation using wind tunnel experiments. In: World Congress on Rail Research, Tokyo, Japan. https://www.sparkrail.org/Lists/Records/DispForm.aspx?ID=11336.

Park, C.-B., Lee, B.-S., Lee, H.-W., 2013. Novel technique to reduce the aerodynamic drag of high speed trains by using SD plasma actuator. In: World Congress on Rail Research, Sydney, Australia. https://www.sparkrail.org/Lists/Records/DispForm.aspx?ID=12334.

Paul, J., Johnson, R., Yates, R., 2009. Application of CFD to rail car and locomotive aerodynamics. In: Browand, F., McCallen, R., Ross, J. (Eds.), The Aerodynamics of Heavy Vehicles II: Trucks, Buses, and Trains, Lecture Notes in Applied and Computational Mechanics, vol. 41. Springer, Berlin, Heidelberg. https://link.springer.com/chapter/10.1007%2F978-3-540-85070-0_25.

Paz, C., Suarez, E., Gil, C., 2017. Numerical methodology for evaluating the effect of sleepers in the underbody flow of a high-speed train. Journal of Wind Engineering and Industrial Aerodynamics 167, 140–147. https://doi.org/10.1016/j.jweia.2017.04.017.

Paz, C., Suarez, E., Gil, C., Concheiro, M., 2015. Numerical study of the impact of windblown sand particles on a high-speed train. Journal of Wind Engineering and Industrial Aerodynamics 145, 87–93. https://doi.org/10.1016/j.jweia.2015.06.008.

Peacock, D., 1951. Railway wind tunnel work. Journal of the Institution of Locomotive Engineers 41 (224), 606–661. In: https://doi.org/10.1243/JILE_PROC_1951_041_062_02.

Peacock, D., 1967. Wind Force on Pantographs. British Rail Research IM APT 91. https://www.sparkrail.org/Lists/Records/DispForm.aspx?ID=18460.

Peacock, D., 1971. Approximate Method of Calculation of Air Resistance of Trains in Tunnels. British Railways Research TM-AERO-29, January. https://www.sparkrail.org/Lists/Records/DispForm.aspx?ID=15371.

Pereira, I., Andre, J., 2016. Aerodynamic improvement of a compact high speed train. In: Rail Technology, Research, Development and Maintenance, Cagliari, Italy, Paper 53.

Pesava, P., Sockel, H., 2000. The effect of baffle plates on the propagation of pressure waves through a tunnel. In: Proceedings 10th International Symposium on the Aerodynamics and Ventilation of Vehicle Tunnels, Boston, USA, pp. 799–814.

Peters, J.-L., 1990. Bestimmung des aerodynamischen Widerstandes des ICE/V im Tunnel and auf freirer Strecke durch Auslaufversuche. Eisenbahntechnische Rundschau 559–564.

Pimputkar, S., 1971. The Aerodynamic Characteristics of Pantographs. British Rail Research IM AERO 25. https://www.sparkrail.org/Lists/Records/DispForm.aspx?ID=18208.

Pope, C., 1980. Theoretical Prediction Methods for Calculating Unsteady Flows in Railway Tunnels. British Rail Research TR-AER-001. https://www.sparkrail.org/Lists/Records/DispForm.aspx?ID=7395.

Pope, C., 1981. Aerodynamic Tests in the Hauenstein Tunnel – Determination of Empirical Coefficients. British Rail Research TM-AER-056. https://www.sparkrail.org/Lists/Records/DispForm.aspx?ID=6965.

Pope, C., Gawthorpe, R.G., Richards, S.P., 1982. An experimental investigation into the effect of train shape on the unsteady flows generated in tunnels. In: Paper C2, Proceedings 4th International Symposium on the Aerodynamics and Ventilation of Vehicle Tunnels. BHRA Fluid Engineering, York, UK.

Pope, C., Richards, S.P., 1984. The Slipstream and Wake Flows Generated by a Train in a Double Track Tunnel. British Rail Research TM-AER-064. https://www.sparkrail.org/Lists/Records/DispForm.aspx?ID=6306.

Premoli, A., Rocchi, D., Schito, P., Somaschini, C., Tomasini, G., 2015. Ballast flight under high-speed trains: wind tunnel full-scale experimental tests. Journal of Wind Engineering and Industrial Aerodynamics 145, 351–361. https://doi.org/10.1016/j.jweia.2015.03.015.

Premoli, A., Rocchi, D., Schito, P., Tomasini, G., 2016. Comparison between steady and moving railway vehicles subjected to crosswind by CFD analysis. Journal of Wind Engineering and Industrial Aerodynamics 156, 29–40. https://doi.org/10.1016/j.jweia.2016.07.006.

Pritchard, J., Preston, J., 2018. Understanding the contribution of tunnels to the overall energy consumption of and carbon emissions from a railway. Transportation Research Part D, Transport and Environment 65, 551–563. https://doi.org/10.1016/j.trd.2018.09.010.

Profillidis, V., 1995. Railway Engineering. Avebury. ISBN-10: 0291398286, ISBN-13: 978-0291398284.

Proppe, C., Wetzel, C., 2010. A probabilistic approach for assessing the crosswind stability of ground vehicles. Vehicle System Dynamics 48 (Suppl. 1), 411–428. https://doi.org/10.1080/00423114.2010.482158.

Proverbio, A., 2009. Numerical Simulation of a Train Traveling in a Tunnel. Thesis. Politecnico di Milano/Imperial College, London. http://citeseerx.ist.psu.edu/viewdoc/download?doi=10.1.1.459.2231&rep=rep1&type=pdf.

Querol, X., Moreno, T., Karanasiou, A., Reche, C., Alastuey, A., et al., 2012. Variability of levels and composition of PM10 and PM2.5 in the Barcelona metro system. Atmospheric Chemistry and Physics 12, 5055–5076. https://doi.org/10.5194/acp-12-5055-2012.

Quinn, A., Hayward, M., Baker, C., Schmid, F., Priest, J., et al., 2010. A full-scale experimental and modelling study of ballast flight under high-speed trains. Proceedings of the Institution of Mechanical Engineers Part F Journal of Rail and Rapid Transit 224 (2), 61–74. https://doi.org/10.1243/09544097JRRT294.

Ragunathan, R., Kim, H.-D., Setaguchi, T., 2002. Aerodynamics of high speed railway trains. Progress in Aerospace Sciences 38 (6–7), 469–514. https://doi.org/10.1016/S0376-0421(02)00029-5.

RAIB, 2009. Detachment of Containers from Freight Wagons Near Cheddington and Hardendale, 1 March 2008. Rail Accident Investigation Branch Report 12/2009. https://assets.publishing.service.gov.uk/media/547c9019ed915d4c10000177/R122009_0905027_Containers.pdf.

RAIB, 2015. Container Detachments at Scout Green, Cumbria, 7 March 2015 and Near Deeping St Nicholas, Lincolnshire, 31 March 2015. Rail Accident Investigation Branch Report 19/2015. https://assets.publishing.service.gov.uk/government/uploads/system/uploads/attachment_data/file/493134/R192015_151207_Scout_Green_DSN.pdf.

RAIB, 2017. Occupied Wheelchair Contacting a Passing Train at Twyford Station 7 April 2016. Rail Accident Investigation Branch Report 01/2017. https://assets.publishing.service.gov.uk/government/uploads/system/uploads/attachment_data/file/606091/R012017_170119_Twyford.pdf.

Railway Archive, 2018. Accident at Leven Viaduct on 27th February 1903. http://www.railwaysarchive.co.uk/eventsummary.php?eventID=70.

Railway Technology, 2018a. Shanghai-Hangzhou Maglev. https://www.railway-technology.com/projects/shanghai-maglev/.

Railway Technology, 2018b. Chuo Shinkansen Maglev Line. https://www.railway-technology.com/projects/chuo-shinkansen-maglev-line/.

RAPIDE, 2001. Railway Aerodynamics for Passing and Interaction with Dynamic Effects (Final Technical Report).

Rathakrishnan, K., Ahmad, S., Spriryagin, M., Cole, C., Sun, Y.-Q., 2013. Numerical investigation on the influence of a lateral component of a coupler force and track lateral defects on the wagon dynamics under different wind conditions. In: World Congress on Rail Research, Sydney, Australia. https://www.sparkrail.org/Lists/Records/DispForm.aspx?ID=12348.

Refan, M., Hangan, H., 2018. Near surface experimental exploration of tornado vortices. Journal of Wind Engineering and Industrial Aerodynamics 175, 120–135. https://doi.org/10.1016/j.jweia.2018.01.042.

Réty, J., Gregoire, R., 2002. Numerical investigation of tunnel extensions attenuating the pressure gradient generated by a train entering a tunnel. In: Schulte- Werning, B., Gregoire, R., Malfatti, M., Matschke, G. (Eds.), TRANSAERO – A European Initiative on Transient Aerodynamics for Railway System Optimisation, Notes on Numerical Fluid Mechanics and Multidisciplinary Design, vol. 79. Springer, pp. 239–248. https://link.springer.com/chapter/10.1007/978-3-540-45854-8_20.

Richards, S., Cooper, R., 1977. The measurement of boundary layer profiles on TC2 of APT-E and assessment of skin friction coefficient, British Rail Research Technical Memorandum TMAERO 23. https://www.sparkrail.org/Lists/Records/DispForm.aspx?ID=15365.

Rigby, P., Gawthorpe, R., 1979. Wind-tunnel Measurements to Compare the Aerodynamic Uplifts of the GEC and AMBR 1 Pantographs. British Rail Research TM AERO 40. https://www.sparkrail.org/Lists/Records/DispForm.aspx?ID=15381.

Rochard, B., Schmid, F., 2000. A review of methods to measure and calculate train resistances. Proceedings of the Institution of Mechanical Engineers Part F Journal of Rail and Rapid Transit 214 (4), 185–199. https://doi.org/10.1243/0954409001531306.

RSSB, 2009. Recommendations for Determination of Aerodynamic Rolling Moment Coefficient. Railway Group Standard GM/RT2542.
RSSB, 2011. Pantograph Sway Acceptance Requirements and Methodology. RSSB. Research Project T942. https://www.sparkrail.org/Lists/Records/DispForm.aspx?ID=719.
RSSB, 2012. Investigation of Freight Vehicle Aerodynamic Performance in Accordance with GM/RT 2142 Resistance of Railway Vehicles to Roll-Over in Gales. https://www.sparkrail.org/Lists/Records/DispForm.aspx?ID=1171.
RSSB, 2014a. Guidance on Loading Requirements for the Design of Railway Structures. GC/GN5612. https://www.rssb.co.uk/rgs/standards/gcgn5612%20iss%201.pdf.
RSSB, 2014b. Resistance of Railway Vehicles to Roll-Over in Gales. Railway Group Standard GM/RT2142. https://www.rssb.co.uk/rgs/standards/GMRT2142%20Iss%201.pdf.
RSSB, 2016a. Winter Effects on Rolling Stock, Railway Safety and Standards Board Report S248. https://www.sparkrail.org/Lists/Records/DispForm.aspx?ID=24126.
RSSB, 2018. Calculation of Enhanced Permissible Speeds for Tilting Trains. RIS-7704-INS. https://www.rssb.co.uk/rgs/standards/GCRC5521%20Iss%201.pdf.
RTRI, 2001. Clarification of Phenomenon of Ballast Thrown up by Snow/ice Falling from the Train. Major Results of Research and Development in Fiscal Year 2001. Rail Technical Research Institute. http://www.rtri.or.jp/eng/rd/seika/2001/01/safety_E02.html.
Rutschmann, S., Ehenfried, K., Dillmann, A., 2013. Validation of a potential flow model for the prediction of the aerodynamic loads on track side objects. In: World Congress on Rail Research, Sydney, Australia. https://www.sparkrail.org/Lists/Records/DispForm.aspx?ID=12470.
Sachs, K., 1973. Elektische Triebfahrzeuge. Erster Band, Allgemeine Grundlagen und Mechanischer Teil. Springer Verlag, Vienna. https://www.springer.com/gb/book/9783709143803.
Sakuma, Y., Hibino, Y., 2013. Pressure fluctuations on a 1/10th scale train model moving through a cross wind. In: World Congress on Rail Research, Sydney, Australia. https://www.sparkrail.org/Lists/Records/DispForm.aspx?ID=12814.
Sakuma, Y., Suzuki, M., Ido, A., Kajiyama, H., 2010. Measurement of air velocity and pressure distributions around high speed trains on board and on the ground. Journal of Mechanical Systems for Transportation and Logistics 3 (1), 110–118. https://doi.org/10.1299/jmtl.3.110.
Sanquer, S., Barré, C., Dufresne de Virel, M., Cléon, L.-M., 2004. Effect of cross winds on high-speed trains: development of a new experimental methodology. Journal of Wind Engineering and Industrial Aerodynamics 92 (7–8), 535–545. https://doi.org/10.1016/j.jweia.2004.03.004.
Sanz-Andrés, A., Laverón, A., Baker, C., Quinn, A., 2004a. Vehicle induced loads on pedestrian barriers. Journal of Wind Engineering and Industrial Aerodynamics 92 (5), 413–426. https://doi.org/10.1016/j.jweia.2003.12.004.
Sanz-Andrés, A., Laverón, A., Cuerva, A., Baker, C., 2004b. Vehicle-induced force on pedestrians. Journal of Wind Engineering and Industrial Aerodynamics 92 (2), 185–198. https://doi.org/10.1016/j.jweia.2003.11.002.
Sanz-Andrés, A., Navarro-Medina, F., 2010. The initiation of rotational motion of a lying object caused by wind gusts. Journal of Wind Engineering and Industrial Aerodynamics 98 (12), 772–783. https://doi.org/10.1016/j.jweia.2010.07.002.
Saussine, G., Voivret, C., Paradot, N., Allain, E., 2015. A risk assessment method for ballast flight; managing the rolling stock/infrastructure interaction. Proceedings of the Institution of Mechanical Engineers Part F Journal of Rail and Rapid Transit 229 (6), 581–593. https://doi.org/10.1177/0954409715595255.

Schetz, J., 2001. Aerodynamics of high speed trains. Annual Review of Fluid Mechanics 33, 371–414. http://www.annualreviews.org/doi/pdf/10.1146/annurev.fluid.33.1.371.

Schober, M., Weise, M., Orellano, A., Deeg, P., Wetzel, W., 2010. Wind tunnel investigation of an ICE 3 end car on three standard ground scenarios. Journal of Wind Engineering and Industrial Aerodynamics 98 (6), 345–352. https://doi.org/10.1016/j.jweia.2009.12.004.

Schulte-Werning, B., 2001. The TRANSAERO project – joint european railway research on transient aerodynamics. In: Schulte- Werning, B., Gregoire, R., Malfatti, M., Matschke, G. (Eds.), TRANSAERO – A European Initiative on Transient Aerodynamics for Railway System Optimisation, Notes on Numerical Fluid Mechanics and Multidisciplinary Design, vol. 79, pp. 11–24. https://link.springer.com/chapter/10.1007%2F978-3-540-45854-8_2.

Schulte-Werning, B., Heine, C., Matschke, G., 2003. Unsteady wake flow characteristics of high-speed trains. Proceedings Applied Maths and Mechanics 2 (1), 332–333. https://doi.org/10.1002/pamm.200310150.

Schwanitz, S., Wittkowski, M., Rolny, V., Basner, M., 2013b. Pressure variations on a train – where is the threshold to railway passenger discomfort? Applied Ergonomics 44 (2), 200–2012. https://doi.org/10.1016/j.apergo.2012.07.003.

Schwanitz, S., Wittkowski, M., Rolny, V., Samel, C., Basner, M., 2013a. Continuous assessments of pressure comfort on a train – a field-laboratory comparison. Applied Ergonomics 44 (1), 11–17. https://doi.org/10.1016/j.apergo.2012.04.004.

Sesma, I., Vinolas, J., San Emeterio, Gimenez, J., 2012. A comparison of crosswind calculations using a full vehicle and a simplified 2D model. Proceedings of the Institution of Mechanical Engineers Part F Journal of Rail and Rapid Transit 226 (3), 305–317. https://doi.org/10.1177/0954409711424094.

Shapiro, A.H., 1977. The Dynamics and Thermodynamics of Compressible Fluid Flow, vol. 1. John Wiley & Sons, ISBN 978-0-471-06691-0.

Sima, M., 2003. New unifying procedure for working with pressure tightness of rail passenger vehicles. In: Proceedings of the 11th International Symposium on the Aerodynamics and Ventilation of Vehicle Tunnels. BHR Group, Lucerne, Switzerland, pp. 743–757.

Sima, M., Eichinger, S., Blanco, A., Ali, I., 2015. Computational fluid dynamics simulation of rail vehicles in crosswind: application in norms and standards. Proceedings of the Institution of Mechanical Engineers Part F Journal of Rail and Rapid Transit 229 (6), 635–643. https://doi.org/10.1177/0954409714551013.

Sima, M., Grappein, E., Weise, M., Paradot, N., Hieke, M., et al., 2011. Presentation of the EU FP7 AeroTRAIN project and first results. In: World Congress on Rail Research, Lille France. http://www.railway-research.org/IMG/pdf/poster_sima_mikael.pdf.

Sima, M., Tietze, A., Schultz, B., Ehrenfried, K., 2016. Representing large boundary layers in slipstream moving model tests. In: Rail Technology, Research, Development and Maintenance, Cagliari, Italy, Paper 50.

Sockel, H., 2003. Formulae for the calculation of pressure effects in railway tunnel. In: Proceedings of the 11th International Symposium on the Aerodynamics and Ventilation of Vehicle Tunnels. BHR Group, Lucerne, Switzerland, pp. 581–595.

Somaschini, C., Argentini, T., Rocchi, D., Schito, P., Tomasini, G., 2018. A new methodology for the assessment of the running resistance of trains without knowing the characteristics of the track. Application to full scale experimental data. Proceedings of the Institution of Mechanical Engineers Part F Journal of Rail and Rapid Transit 232 (6), 1814–1827. https://doi.org/10.1177/0954409717751754.

Song, Y., Liu, Z., Wang, H., Zhang, J., Lu, X., Duan, F., 2018. Analysis of the galloping behaviour of an electrified railway overhead contact line using the non-linear finite element method. Proceedings of the Institution of Mechanical Engineers Part F Journal of Rail and Rapid Transit. 232 (10), 2339–2352. https://doi.org/10.1177/0954409718769751.

Soper, D., 2014. The Aerodynamics of a Container Freight Train (Ph.D. thesis). University of Birmingham. http://etheses.bham.ac.uk/5325/1/Soper14PhD.pdf https://www.springer.com/gb/book/9783319332772.

Soper, D., Baker, C., 2019. A full scale experimental investigation of passenger and freight train aerodynamics. Proceedings of the Institution of Mechanical Engineers, Part F: Journal of Rail and Rapid Transit. https://doi.org/10.1177/0954409719844431.

Soper, D., Baker, C., Jackson, A., Milne, D., Le Pen, L., et al., 2017b. Full scale measurements of train underbody flows and track forces. Journal of Wind Engineering and Industrial Aerodynamics 169, 251–264. https://doi.org/10.1016/j.jweia.2017.07.023.

Soper, D., Baker, C., Sterling, M., 2014. Experimental investigation of the slipstream development around a container freight train using a moving model facility. Journal of Wind Engineering and Industrial Aerodynamics 135, 105–117. https://doi.org/10.1016/j.jweia.2014.10.001.

Soper, D., Baker, C., Sterling, M., 2015. An experimental investigation to assess the influence of container loading configuration on the effects of a crosswind on a container freight train. Journal of Wind Engineering and Industrial Aerodynamics 145, 304–317. https://doi.org/10.1016/j.jweia.2015.03.002.

Soper, D., Flynn, D., Baker, C., Jackson, A., Hemida, H., 2018. A comparative study of methods to simulate the aerodynamic flow beneath a high speed train. Proceedings of the Institution of Mechanical Engineers, Part F: Journal of Rail and Rapid Transit 232 (5), 1464–1482. https://doi.org/10.1177/0954409717734090.

Soper, D., Gallagher, M., Baker, C., Quinn, A., 2017a. A model-scale study to assess the influence of ground geometries on aerodynamic flow development around a train. Proceedings of the Institution of Mechanical Engineers Part F Journal of Rail and Rapid Transit 231 (8), 916–933. https://doi.org/10.1177/0954409716648719.

Sourget, F., Gautier, P.-E., Cleon, L.-M., 2004. Protection against crosswind in railways; the TGV Mediterranean example. Securing Critical Infrastructures. SCI Genoble.

Spacex, 2018. Hyperloop. http://www.spacex.com/hyperloop.

Sterling, M., Baker, C., Berry, P., Wade, A., 2003. An experimental investigation of the lodging of wheat. Journal of Agricultural and Forest Meteorology 119 (3–4), 149–165. https://doi.org/10.1016/S0168-1923(03)00140-0.

Sterling, M., Baker, C., Jordan, S., Johnson, T., 2008. A study of the slipstreams of high-speed passenger trains and freight trains. Proceedings of the Institution of Mechanical Engineers Part F Journal of Rail and Rapid Transit 222 (2), 177–193. https://doi.org/10.1243/09544097JRRT133.

Stickland, M., Scanlon, T., 2001. An investigation into the aerodynamic characteristics of catenary contact wires in a cross wind. Proceedings of the Institution of Mechanical Engineers Part F: Journal of Rail and Rapid Transit 215 (4), 311–318. https://doi.org/10.1243/0954409011531602.

Sturt, R., Baker, C., Soper, D., Vardy, A., 2015. The Design of HS2 Tunnel Entrance Hoods to Prevent Sonic Booms. Railway Engineering, Edinburgh.

Sutter, K., 1930. Der Luftwiderstand auf Eisenbahnzüge in Tunneln – Ergebnisse von Versuchen im Albis-und Bötzbergtunnel der Schweizerischen Bundesbahnen (Ph.D. thesis). ETH Zürich. Nr, 581. https://www.research-collection.ethz.ch/bitstream/handle/20.500.11850/134284/eth-20990-01.pdf?sequence=1&isAllowed=y.

Suzuki, M., Hibino, Y., 2016. Field tests and wind tunnel tests on aerodynamic characteristics of train/vehicles under crosswinds. RTRI Quarterly Reports 57 (1), 55–60. https://www.jstage.jst.go.jp/article/rtriqr/57/1/57_55/_pdf/-char/en.

Suzuki, M., Nakade, K., 2013. Multi-objective design optimization of high-speed train nose. Journal of Mechanical Systems for Transport and Logistics 6, 54–64. https://doi.org/10.1299/jmtl.6.54.

Suzuki, M., Obara, K., Okura, N., 2016a. Estimation of the aerodynamic forces acting on a train using a simple tornado model. In: Paper 52 International Conference on Railway Technology: Research, Development and Maintenance. Cagliari, Italy.

Suzuki, M., Obara, K., Okura, N., 2016b. An experimental investigation of flow around a vehicle passing through a tornado. In: EPJ Web of Conferences, vol. 114, p. 02116. https://www.epj-conferences.org/articles/epjconf/abs/2016/09/epjconf_efm2016_02116/epjconf_efm2016_02116.html.

Suzuki, M., Tanemoto, K., Maeda, T., 2003. Aerodynamic characteristics of train/vehicles under cross winds. Journal of Wind Engineering and Industrial Aerodynamics 91 (1), 209–218. https://doi.org/10.1016/S0167-6105(02)00346-X.

Suzuki, M., Urakawa, Y., Satou, M., Ogawa, T., Okura, N., 2013. Aerodynamic design optimization of high-speed train shape using a multi-objective evolutionary algorithm with unsteady flow simulation. In: World Congress on Rail Research, Sydney, Australia. https://www.sparkrail.org/Lists/Records/DispForm.aspx?ID=12855.

SYSTRA, 2011. Carbon Impacts of HS2 - Factors Affecting Carbon Impacts of HSR. http://www.greengauge21.net/wp-content/uploads/SYSTRA-Factors-affecting-HSR-carbon-impacts.pdf.

Tabarra, M., Sturt, R., 2010. High speed rail tunnel aerodynamics: transient pressure and loadings on fixed tunnel equipment. In: 7th UIC World Congress on High Speed Rail, Beijing, China.

Takaishi, T., Ikeda, M., 2012. Experimental method for wind tunnel tests to simulate turbulent flow on the roof of high-speed trains. RTRI Quarterly Reports 53 (3), 167–172. https://www.jstage.jst.go.jp/article/rtriqr/53/3/53_167/_pdf.

Takei, Y., Izumi, Y., Yamada, S., Iida, M., Kikuchi, K., 2008. Evaluation method for air pressure variation and station facility member deterioration caused by high-speed train passage in stations. Quarterly Report of JRRI 49 (2), 89–95. https://doi.org/10.2219/rtriqr.49.89.

Tamura, Y., 2009. Wind induced damage to buildings and disaster risk reduction. In: Asia-Pacific Conference on Wind Engineering, APCWE7 Tapei. In: http://www.iawe.org/Proceedings/7APCWE/KS1.pdf.

Tang, Z., Feng, C., Wu, L., Zuo, D., James, D.L., 2018. Characteristics of tornado-like vortices simulated in a large-scale ward-type simulator. Boundary-Layer Meteorology 166 (2), 327–350. https://doi.org/10.1007/s10546-017-0305-7.

Temple, J., 2006. West Coast Main Line upgrade: railway tunnel pressure relief in practice. In: Proceedings 12th International Symposium on the Aerodynamics and Ventilation of Vehicle Tunnels. BHR Group Ltd., Portoroz, Slovenia.

ThermoTun Online, 2018. http://www.thermotun-online.com/index.php.

Thomas, D., Berg, M., Stichel, S., Diedrichs, B., 2015. Rail vehicle response to lateral carbody excitations imitating crosswind. Proceedings of the Institution of Mechanical Engineers Part F: Journal of Rail and Rapid Transit 229 (1), 34–47. https://doi.org/10.1177/0954409713496765.

Thomas, D., Diedrichs, B., Berg, M., Stichel, S., 2010. Dynamics of a high-speed rail vehicle negotiating curves at unsteady crosswind. Proceedings of the Institution of Mechanical Engineers Part F: Journal of Rail and Rapid Transit 224 (6), 567–579. https://doi.org/10.1243/09544097JRRT335.

Thompson, D., 2008. Railway Noise and Vibration - Mechanisms, Modelling and Means of Control. Elsevier Science, ISBN 9780080914435.

Thwaite, M., 2005. The george bennie railplane and hugh fraser airrail systems of transport. Transactions of the Newcomen Society 75 (1), 37–84. https://doi.org/10.1179/tns.2005.003.

Tian, H.-Q., 2009. Formation mechanism of aerodynamic drag of high-speed train and some reduction measures. Journal Central South University of Technology 16 (1), 161–171. https://link.springer.com/article/10.1007/s11771-009-0028-0.

Tielkes, T., 2006. Aerodynamic aspects of maglev systems. In: International Conference on Magnetically Levitated Systems and Linear Drives, Dresden, Germany. http://www.maglev.ir/eng/documents/papers/conferences/maglev2006/topic6/IMT_CP_M2006_T6_13.pdf.

Tielkes, T., Heine, C., Moller, M., Driller, J., 2008. A probabilistic approach to safeguard cross wind safety of passenger railway operation in Germany: the new DB Guideline Ril 80704. In: World Congress on Rail Research, Seoul, South Korea. https://www.sparkrail.org/Lists/Records/DispForm.aspx?ID=4501.

Tokunaga, M., Sogabe, M., Santo, T., Ono, K., 2016. Dynamic response evaluation of tall noise barrier on high speed railway structures. Journal of Sound and Vibration 366, 293–308. https://doi.org/10.1016/j.jsv.2015.12.015.

Tolmien, W., 1927. Air resistance and pressure zones around train in railway tunnels. ZVDI 71 (5), 199–203.

Tomasini, G., Cheli, F., 2013. Admittance function to evaluate aerodynamic loads on vehicles: experimental data and numerical model. Journal of Fluids and Structures 38, 92–106. https://doi.org/10.1016/j.jfluidstructs.2012.12.009.

Tomasini, G., Giappino, S., Cheli, F., Schito, P., 2016. Windbreaks for railway lines: wind tunnel experimental tests. Proceedings of the Institution of Mechanical Engineers Part F: Journal of Rail and Rapid Transit 230 (4), 1270–1282. https://doi.org/10.1177/0954409715596191.

Tomasini, G., Giappino, S., Corradi, R., 2014. Experimental investigation of the effects of embankment scenario on railway vehicle aerodynamic coefficients. Journal of Wind Engineering and Industrial Aerodynamics 131, 59–71. https://doi.org/10.1016/j.jweia.2014.05.004.

TRL, 2018. Government Gives Green Light for First Operational Vehicle Platooning Trial. https://trl.co.uk/news/news/government-gives-green-light-first-operational-vehicle-platooning-trial.

Tsai, T., Lamond, J., Lee, H., 2003. The aerodynamic effects of high-speed trains on surroundings, train operations, and people. In: World Congress on Rail Research, Edinburgh UK, pp. 452–462. https://www.sparkrail.org/Lists/Records/DispForm.aspx?ID=11748.

Tschepe, J., Nayeri, C., Paschereit, C., 2016b. Moving model drag measurement of rail vehicles in water tanks. In: Aerovehicles 2 Gothenberg, Sweden.

Tschepe, J., Nayeri, C., Scmidt, H., Paschereit, C., 2016a. Towing tank experiments for train aerodynamics. In: Rail Technology, Research, Development and Maintenance, Cagliari, Italy, Paper 49.

Tsuei, L., Savas, Ö., 2001. Transient aerodynamics of vehicle platoons during in-line oscillations. Journal of Wind Engineering and Industrial Aerodynamics 89 (13), 1085–1111. https://doi.org/10.1016/S0167-6105(01)00073-3.

Turner, J., 1977. The London Brighton and South Coast Railway, Volume 1 Origins and Formation. Batsford Books, London. ISBN:0-7134-0275-X.

UIC, 2005. Determination of Railway Tunnel Cross-Sectional Areas on the Basis of Aerodynamic Considerations, second ed. UIC 779-11.
UIC, 2013. Effect of the Slipstream of Passing Trains on Structures Adjacent to the Track, second ed. UIC 779-1.
ULTRA, 2018. Ultra Global PRT. http://www.ultraglobalprt.com/how-it-works/ultra-vehicle/.
Vardy, A.E., 1975. Ventilated approach regions for railway tunnels. Transportation Engineering Journal, ASCE 101 (4), 609–619. TE.
Vardy, A.E., 1976. The use of airshafts for the alleviation of pressure transients in railway tunnels. In: Proceedings 2nd International Symposium on the Aerodynamics and Ventilation of Vehicle Tunnels, pp. 55–612.
Vardy, A.E., 1996a. Aerodynamic drag on trains in tunnels part 1: synthesis and definitions. Proceedings of the Institution of Mechanical Engineers Part F: Journal of Rail and Rapid Transit 210 (1), 29–38. In: https://doi.org/10.1243/PIME_PROC_1996_210_324_02.
Vardy, A.E., 1996b. Aerodynamic drag on trains in tunnels part 2: prediction and validation. Proceedings of the Institution of Mechanical Engineers Part F: Journal of Rail and Rapid Transit 210 (1), 39–49. In: https://doi.org/10.1243/PIME_PROC_1996_210_325_02.
Vardy, A.E., 2008. Generation and alleviation of sonic booms from rail tunnels. Proceedings Institution of Civil Engineers, Engineering and Computational Mechanics 161 (3), 107–119. https://www.icevirtuallibrary.com/doi/full/10.1680/eacm.2008.161.3.107.
Versteeg, H., Malalasekera, W., 2007. An Introduction to Computational Fluid Dynamics: The Finite Volume Method, second ed. Pearson Education Limited.
Viana, F., Venter, G., Balabanov, V., 2010. An algorithm for fast optimal latin hypercube design of experiments. International Journal for Numerical Methods in Engineering 82 (2), 135–156. https://doi.org/10.1002/nme.2750.
Vollmer, G., 1989. Luftwiderstand von Guterwagen. Dr-Ing Dissertation. TH Darmstadt.
Wang, S., Bell, J.R., Burton, D., Herbst, A., Sheridan, J., Thompson, M., 2017. The performance of different turbulence models (URANS, SAS and DES) for predicting high speed train slipstream. Journal of Wind Engineering and Industrial Aerodynamics 165, 46–57. https://doi.org/10.1016/j.jweia.2017.03.001.
Wang, Y.-W., Wang, Y., An, Y.-R., Chen, Y.-S., 2008. Aerodynamic simulation of high-speed trains based on the Lattice Boltzmann Method (LBM). Science in China Series E Technological Sciences 51 (6), 773–783. https://doi.org/10.1007/s11431-008-0063-3.
Wang, J., Zhang, J., Zhang, Y., Xie, F., Krajnović, S., 2018. Impact of bogie cavity shapes and operational environment on snow accumulating on the bogies of high speed trains. Journal of Wind Engineering and Industrial Aerodynamics 176, 211–224. https://doi.org/10.1016/j.jweia.2018.03.027.
Watkins, S., Saunders, J., Kumar, H., 1992. Aerodynamic drag reduction of goods trains. Journal of Wind Engineering and Industrial Aerodynamics 40, 147–178. https://doi.org/10.1016/0167-6105(92)90363-F.
Wetzel, C., Proppe, C., 2007. On the crosswind stability of high speed railway vehicles. Proceedings Applied Maths and Mechanics 6 (1), 341–342. https://doi.org/10.1002/pamm.200610152.
Wikipedia, 2018a. Channel Tunnel. https://en.wikipedia.org/wiki/Channel_Tunnel.
Wikipedia, 2018b. Lötschberg Base Tunnel. https://en.wikipedia.org/wiki/L%C3%B6tschberg_Base_Tunnel.

Wilcox, D., 2002. Turbulence Modelling for CFD, second ed. DCW Industries, La Cañada CA.

Wilhelm, J., Rybach, L., 2003. The geothermal potential of Swiss alpine tunnels. Geothermics 32 (4–6), 557–568. https://doi.org/10.1016/S0375-6505(03)00061-0.

Willemson, E., 1997. High Reynolds number wind tunnel experiments on trains. Journal of Wind Engineering and Industrial Aerodynamics 69–71, 437–447. https://doi.org/10.1016/S0167-6105(97)00175-X.

Woods, W.A., Pope, C., 1976. Secondary aerodynamic effects in rail tunnels during vehicle entry. In: Proceedings 2nd International Symposium on the Aerodynamics and Ventilation of Vehicle Tunnels, Paper C5. Cambridge, UK.

Xia, C., Shan, X., Yang, Z., 2017a. Comparison of different ground simulation systems on the flow around a high-speed train. Proceedings of the Institution of Mechanical Engineers Part F: Journal of Rail and Rapid Transit 231 (2), 135–147. https://doi.org/10.1177/0954409715626191.

Xia, C., Wang, H., Shan, X., Yang, Z., Li, Q., 2017b. Effects of ground configurations on the slipstream and near wake of a high-speed train. Journal of Wind Engineering and Industrial Aerodynamics 168, 177–189. https://doi.org/10.1016/j.jweia.2017.06.005.

Xia, H., Xu, Y., Chan, T., 2000. Dynamic interaction of long suspension bridges with running trains. Journal of Sound and Vibration 237 (2), 263–280. https://doi.org/10.1006/jsvi.2000.3027.

Xia, H., Zhang, N., De Roeck, G., 2001. Dynamic analysis of train-bridge system and its application in steel girder reinforcement. Computers and Structures 79 (20–21), 1851–1860. https://doi.org/10.1016/S0045-7949(01)00115-8.

Xie, S., Qu, J., Pang, Y., 2017. Dynamic wind differences in the formation of sand hazards at high- and low-altitude railway sections. Journal of Wind Engineering and Industrial Aerodynamics 169, 39–46. https://doi.org/10.1016/j.jweia.2017.07.003.

Xiong, X.-H., Li, A.-H., Liang, X.-F., Zhang, J., 2018. Field study of high speed train induced fluctuating pressure on a bridge noise barrier. Journal of Wind Engineering and Industrial Aerodynamics 177, 157–166. https://doi.org/10.1016/j.jweia.2018.04.017.

Xiong, H.-B., Yu, W.-G., Chen, D.-W., Shao, X.-M., 2011. Numerical study on the aerodynamic performance and safe running of high-speed trains in sandstorms. Journal of Zheijang University Science A 12 (12), 971–978. https://doi.org/10.1631/jzus.A11GT005.

Xu, Y., Ding, Q., 2006. Interaction of railway vehicles with track in cross-winds. Journal of Fluids and Structures 22 (3), 295–314. https://doi.org/10.1016/j.jfluidstructs.2005.11.003.

Xu, G., Liang, X., Yao, S., Chen, D., Li, Z., 2017. Multi-objective aerodynamic optimization of the streamlined shape of high-speed trains based on the Kriging model. PLoS One 12, 1. https://doi.org/10.1371/journal.pone.0170803.

Xu, Y., Xia, H., Yan, Q., 2003. Dynamic response of suspension bridge to high wind and running train. ASCE Journal of Bridge Engineering 8 (1), 46–55. https://doi.org/10.1061/(ASCE)1084-0702(2003)8:1(46).

Xu, Y.-L., Zhang, N., Xia, H., 2004. Vibration of coupled train and cable-stayed bridge systems in cross winds. Engineering Structures 26 (10), 1389–1406. https://doi.org/10.1016/j.engstruct.2004.05.005.

Yamamoto, A., 1965. On the gradual pressure rise by a flared tunnel entrance. RTRI Quarterly Reports 6, 4.

Yan, N., Chen, X., Li, Y., 2018. Assessment of overturning risk of high-speed trains in strong crosswinds using spectral analysis approach. Journal of Wind Engineering and Industrial Aerodynamics 174, 103–118. https://doi.org/10.1016/j.jweia.2017.12.024.

Yang, Q.-S., Song, J.-H., Yang, G.-W., 2016. Moving model rig with a scale ratio of 1/8 for high speed train aerodynamics. Journal of Wind Engineering and Industrial Aerodynamics 152, 50–58. https://doi.org/10.1016/j.jweia.2016.03.002.

Yang, N., Zheng, X.-K., Zhang, J., Law, S., Yang, Q.-S., 2015. Experimental and numerical studies on aerodynamic loads on an overhead bridge due to passage of high-speed train. Journal of Wind Engineering and Industrial Aerodynamics 140, 19–33. https://doi.org/10.1016/j.jweia.2015.01.015.

Yao, S., Guo, D., Sun, Z., Yang, G., Dawei, C., 2014. Optimization design for aerodynamic elements of high speed trains. Computers and Fluids 95, 56–73. https://doi.org/10.1016/j.compfluid.2014.02.018.

Yongle, L., Hu, P., Cai, C., Zhang, M., Qiang, S., 2012. Wind tunnel study of a sudden change of train wind loads due to the wind shielding effects of bridge towers and passing trains. ASCE Journal of Engineering Mechanics 139 (9), 1249–1259. https://doi.org/10.1061/(ASCE)EM.1943-7889.0000559.

You, W., Kwon, H., Park, J., Shin, Y., 2017. Effect of wind gusts on the dynamics of railway vehicles running on a curved track. Proceedings of the Institution of Mechanical Engineers Part F: Journal of Rail and Rapid Transit 232 (4), 1103–1120. https://doi.org/10.1177/0954409717708924.

Yu, M., Liu, J., Liu, D., Chen, H., Zhang, J., 2016. Investigation of aerodynamic effects on the high-speed train exposed to longitudinal and lateral wind velocities. Journal of Fluids and Structures 61, 347–361. https://doi.org/10.1016/j.jfluidstructs.2015.12.005.

Yu, M., Zhang, J., Zhang, W., 2013. Simulation of unsteady aerodynamic loads on high-speed trains in fluctuating crosswinds. Journal of Modern Transportation 21 (2), 73–78. https://doi.org/10.1007/s40534-013-0011-1.

Yu, M., Zhang, J., Zhang, K., Zhang, W., 2015. Crosswind stability analysis of a high-speed train based on fuzzy random reliability. Proceedings of the Institution of Mechanical Engineers Part F: Journal of Rail and Rapid Transit 229 (8), 875–887. https://doi.org/10.1177/0954409714524548.

Zhang, Y., Sun, Z., Guo, D., Yang, G., 2016. Effects of accessory parts topology on the aerodynamics of high-speed trains. In: Rail Technology, Research, Development and Maintenance, Cagliari, Italy, Paper 46.

Zhang, L., Thurow, K., Stoll, N., Liu, H., 2018c. Influence of the geometry of equal-transect oblique tunnel portal on compression wave and micro-pressure wave generated by high-speed trains entering tunnels. Journal of Wind Engineering and Industrial Aerodynamics 178, 1–17. https://doi.org/10.1016/j.jweia.2018.05.003.

Zhang, J., Wang, J., Wang, Q., Xiong, X., Gao, G., 2018a. A study of the influence of bogie cut out's angles on the aerodynamic performance of a high speed train. Journal of Wind Engineering and Industrial Aerodynamics 175, 153–168. https://doi.org/10.1016/j.jweia.2018.01.041.

Zhang, L., Yang, M.-Z., Liang, X.-F., 2018b. Experimental study of the effect of wind angles on pressure distribution of train streamlined zone and train aerodynamic forces. Journal of Wind Engineering and Industrial Aerodynamics 174, 330–343. https://doi.org/10.1016/j.jweia.2018.01.024.

Zhang, L., Zhang, J., Li, T., Zhang, W., 2017. Influence of pantograph fixing position on aerodynamic characteristics of high-speed trains. Journal of Modern Transportation 25 (1), 34–39. https://link.springer.com/article/10.1007/s40534-017-0125-y.

Zhang, L., Zhang, J., Li, T., Zhang, Y., 2018d. A multi-objective aerodynamic optimization design of a high speed train head under crosswinds. Proceedings of the Institution of Mechanical Engineers Part F: Journal of Rail and Rapid Transit 232 (3), 895–912. https://doi.org/10.1177/0954409717701784.

Zhou, D., Tian, H.-Q., Zhang, J., Yang, M., 2014. Pressure transients induced by a high speed train passing through a station. Journal of Wind Engineering and Industrial Aerodynamics 135, 1–9. https://doi.org/10.1016/j.jweia.2014.09.006.

Zhu, J., Hu, Z., 2017. Flow between the train underbody and track bed around the bogie area and its impact on ballast flight. Journal of Wind Engineering and Industrial Aerodynamics 166, 20–28. https://doi.org/10.1016/j.jweia.2017.03.009.

Index

Note: 'Page numbers followed by "f" indicate figures and "t" indicate tables.'

G

H

I

R

S

T

U

V

W

TRAIN AERODYNAMICS

Fundamentals and Applications

Chris Baker, Hassan Hemida, Andrew Quinn, David Soper and **Mark Sterling**
Birmingham Centre for Railway Research and Education (BCRRE), University of Birmingham, UK
Dominic Flynn
Birmingham City University (BCU), UK
Terry Johnson
Railway Safety and Standards Board (RSSB), London, UK

In the last two decades, there has been a growth of interest in the aerodynamic behaviour of trains as a wide range of new train types and high-speed lines have come into operations around the world.

With the collaboration of experts from BCRRE, BCU and RSSB, *Train Aerodynamics: Fundamentals and Applications* examines the fundamentals and the state-of-the-art of train aerodynamics. This book includes a discussion of the experimental, numerical and analytical tools that are available, followed by a detailed description of the flow around trains of all types, mainly taken from full-scale train- and track-based tests. A wide range of aerodynamic issues that need to be taken into account in the design process for new trains and new routes are then discussed.

This comprehensive reference work is for railway engineers, train operators, train manufacturers, infrastructure managers and researchers into train aerodynamics.

Key Features

- Provides a detailed analysis and understanding of the flow field around full-scale trains
- Addresses a range of problems related to train aerodynamics: aerodynamic drag of trains; aerodynamic loading on trackside structures and people; ballast flight; pantograph aerodynamics; cross wind effects and tunnel aerodynamic issues
- Features the latest developments and progress in computational methods and experimental facilities and how can they model complex situations and contribute to improving the design of trains and infrastructure

ELSEVIER

Butterworth-Heinemann
An imprint of Elsevier
elsevier.com/books-and-journals

ISBN 978-0-12-813310-1